# TRANSFORMATION TOWARDS A SUSTAINABLE TOMORROW

## PPC & PETROMAT SYMPOSIUM 2025

International Conference

The 31st PPC Symposium on Petroleum, Petrochemicals, and Polymers and
The 16th Research Symposium on Petrochemical and Materials Technology

With

The 9th SKY Symposium (SKY 2025)

and

Workshop on Water 2025

25 - 27 June 2025

at Mandarin Hotel Bangkok and
The Petroleum and Petrochemical College, Thailand

www.ppc.chula.ac.th/ppcsymposium

PPC & PETROMAT
SYMPOSIUM 2025
International Conference

# Sponsors

PPC & PETROMAT
SYMPOSIUM 2025
International Conference

The 31st PPC Symposium on Petroleum, Petrochemicals, and Polymers and
The 16th Research Symposium on Petrochemical and Materials Technology

Chula
Chulalongkorn University

PPC & PETROMAT
SYMPOSIUM 2025
International Conference

The 31st PPC Symposium on Petroleum, Petrochemicals, and Polymers and
The 16th Research Symposium on Petrochemical and Materials Technology

# Gold Sponsor

PTTEP

PPC & PETROMAT
SYMPOSIUM 2025
International Conference

The 31st PPC Symposium on Petroleum, Petrochemicals, and Polymers and
The 16th Research Symposium on Petrochemical and Materials Technology

# Gold Sponsor

**Verasuwan Co.,Ltd**

PPC & PETROMAT
SYMPOSIUM 2025
International Conference

The 31st PPC Symposium on Petroleum, Petrochemicals, and Polymers and
The 16th Research Symposium on Petrochemical and Materials Technology

## Silver Sponsor

ptt LNG

## Bronze Sponsor

GC

PPC & PETROMAT SYMPOSIUM 2025
International Conference

The 31st PPC Symposium on Petroleum, Petrochemicals, and Polymers and
The 16th Research Symposium on Petrochemical and Materials Technology

# Exhibitor Sponsors

Anton Paar

BARA SCIENTIFIC
Solution of Success

SyncInnovation

PPC & PETROMAT
SYMPOSIUM 2025
International Conference

The 31st PPC Symposium on Petroleum, Petrochemicals, and Polymers and
The 16th Research Symposium on Petrochemical and Materials Technology

# Exhibitor Sponsors

LECO
EMPOWERING RESULTS

HKK
GYROLOK

LMS
INSTRUMENTS CO.,LTD.

Verne
Crystal

PPC & PETROMAT
SYMPOSIUM 2025
International Conference

The 31st PPC Symposium on Petroleum, Petrochemicals, and Polymers and
The 16th Research Symposium on Petrochemical and Materials Technology

# Exhibitor Sponsors

its

VOWS CRAFT INT CO., LTD.
บริษัท เวาส คราฟท์ อินท จำกัด

# *The 31st PPC Symposium on Petroleum, Petrochemicals, and Polymers and The 16th Research Symposium on Petrochemical and Materials Technology (PPC & PETROMAT SYMPOSIUM 2025) 9th SKY Symposium (SKY 2025) with Workshop on Water 2025*

***Co-organized by***

***The Petroleum and Petrochemical College,***
***Center of Excellence on Petrochemical and Materials Technology,***
***Thailand Institute of Chemical Engineering and Applied Chemistry,***
***Metallurgy and Materials Science Research Institute***
***Chulalongkorn University***
***and Shinshu University***

***at***
***Mandarin Hotel Managed by Centre Point***
***Bangkok, Thailand***

***June 25-27, 2025***
***8.00 – 17.00***

## Sessions

1. Session 1: AI Digital Tools for Process & Materials Engineering (AI)
2. Session 2: Cutting-Edge Catalysis (CA)
3. Session 3: Advanced Materials Innovation (MAT)
4. Session 4: Energy Landscape Transformation: Renewable Generation, Storage, and Conversion (Energy)
5. Session 5: Carbon & Sustainability Solutions for a Net-Zero Future (Carbon)
6. Session 6: SKY 2025 (SKY)
7. Session 7: Workshop on Water 2025 (Water)

## Participation Institutes

- Chulalongkorn University, Thailand
- Kasetsart University, Thailand
- Silpakorn University, Thailand
- Mahidol University, Thailand
- Khon Kaen University, Thailand
- King' Mongut University of Technology Ladkrabang, Thailand
- Thailand Institute of Scientific and Technological Research (TISTR), Thailand
- Petrochemical Industry Club, The Federation of Thai Industries, Thailand
- Synchrotron Light Research Institute (Public Organization), Thailand
- Vidyasirimedhi Institute of Science and Technology (VISTEC), Thailand
- Shinshu University, Japan
- Kyushu University, Japan
- Nagoya University, Japan
- The University of Tokyo, Japan
- Tokyo University of Science, Japan
- The University of Electro-Communications, Japan
- Arima Yamagata University, Japan
- Advanced Industrial Science and Technology (AIST), Japan
- Yeungnam University, South Korea
- Korea Maritime and Ocean University, South Korea

- Chulabhorn Research Institute, Thailand
- National Nanotechnology Center (NANOTEC), Thailand
- Hitachi High-Tech (Thailand) Ltd
- Indian Institute of Technology Madras, India
- PetroVietnam University, Vietnam
- Universiti Kebangaan Malaysia, Malaysia
- University of Montpellier, France
- The University of Tulsa, USA
- University of Negros Occidental-Recoletos Incorporated, Philippine
- Shanghai University, China
- University of Shanghai fir Science and Technology, China
- Chung Yuan Christian University, Taiwan
- National Taiwan University of Science and Technology, Taiwan
- National University of Singapore, Singapore
- Institut Teknologi Bandung, Indonesia
- Universitas Islam Indonesia, Indonesia
- Universitas Pembangunan Nasional, Indonesia
- University of Sri Jayewardenepura, Sri Lanka

## Conference & Post-Conference Organizing Committee

| | |
|---|---|
| Prof. Pramoch Rangsunvigit | Prof. Hathaikarn Manuspiya |
| Assoc. Prof. Siriporn Jongpatiwut | Assoc Prof. Thanyalak Chaisuwan |
| Prof. Thirasak Rirksomboon | Asst. Prof. Manit Nithitanakul |
| Mr. Surachate Chalothorn | Prof. Yutthanan Boonyongmaneerat |
| Prof. Boonyarach Kitiyanan | Asst. Prof. Ampira Charoenseang |
| Prof. Pitt Supaphol | Prof. Apanee Luengnaruemitchai |
| Prof. Suwabun Chirachanchai | Assoc. Prof. Ratana Rujiravanit |
| Assoc. Prof. Uthaiporn Suriyaprapadilok | Prof. Sirirat Jitkarnka |
| Prof. Anuvat Sirivat | Prof. Rathanawan Magaraphan |
| Asst. Prof. Kitipat Siemanond | Assoc. Prof. Stephan T. Dubas |
| Dr. Sorapat Niyomsin | Dr. Nuttapol Risangud |
| Dr. Bhumin Than-Ardna | Dr. Natthapong Sueviriyapan |
| Asst. Prof. Piya Ouraipryvan | Dr. Pensiri Silakul |
| Ms. Pariya Kongsuwan | Ms. Kaewjai Khumvilaisak |
| Mr. Suwichan Thongtam | Ms. Namon Monnawat |
| Ms. Nadchanan Poyen | Ms. Supin Chaiyaphan |
| Mr. Prasit Srikaew | Ms. Sirima Srimuang |
| Ms. Chanokporn Seaueng | Ms. Juthamas Thongliumsakul |
| Mr. Sutee Kaewsangiem | Ms. Varunee Tokul |
| Ms. Sirikorn Boonsanit | Ms. Natthapa Kamkrieng |
| Ms. Duenphen Lamphun | Ms. Nannaphat Yaphetnoy |
| Ms. Bumpenruedee Prasomseang | Mr. Suksan Putthakulanan |
| Mr. Narong Petchsuk | Mr. Aunnop Martcharat |
| Ms. Supunsa Rakprasert | Mrs. Bussayamas Boonsanit |
| Mr. Piyawat Sangpittayatron | Mr. Paticha Sammana |

## Poster Committee

| | |
|---|---|
| Prof. Benjapon Chalermsinsuwan | Prof. Sirilux Poompradub |
| Prof. Thongthai Witoon | Prof. Napida Hinchiranan |

| | |
|---|---|
| Prof. Nisanart Traiphol | Assoc. Prof. Teerawat Sema |
| Assoc. Prof. Thanakorn Chalermsinsuwan | Assoc. Prof. Sarute Ummartyotin |
| Assoc. Prof. Kanoktip Boonkerd | Assoc. Prof. Wanpen Tachaboonyakiat |
| Assoc. Prof. Sutasinee Kityakarn | Assoc. Prof. Paweena Prapainainar |
| Asst. Prof. Patraporn Luxsirikul | Asst. Prof. Sasiradee Jantasee |
| Asst. Prof. Narit Triamnak | Asst. Prof. Anyaporn Boonmahitthisud |
| Asst. Prof. Natthaphon Raengthon | Asst. Prof. Prasit Pattananuwat |
| Asst. Prof. Nuttapol Pootrakulchote | Lecturer Dr. Manunya Okhawilai |

## Chairperson

| | |
|---|---|
| Prof. Boonyarach Kitiyanan | Asst. Prof. Pichaya In-na |
| Dr. Rongrong Cheacharoen | Dr. Satita Thiangtham |
| Dr. Ratchanon Piemjaiswang | Dr. Charoen Chinwanitcharoen |
| Dr. Jinqian Qin | Dr. Nadnudda Rodthongkum |

## Technical Conference / Reviewer Committee

| | |
|---|---|
| Prof. Ben Shiau | The University of Oklahoma |
| Prof. Yong Ku Kwon | Inha University |
| Prof. Suttichai Assabumrungrat | Chulalongkorn University |
| Prof. Benjapon Chalermsinsuwan | Chulalongkorn University |
| Prof. Sirilux Poompradub | Chulalongkorn University |
| Prof. Nuttaya Pongstabodee | Chulalongkorn University |
| Assoc. Prof. Thanakorn Wasanapiarnpong | Chulalongkorn University |
| Assoc. Prof. Wanpen Tachaboonyakiat | Chulalongkorn University |
| Assoc. Prof. Soamwadee Chaianansutcharit | Chulalongkorn University |
| Assoc. Prof. Wipark Anutrasakda | Chulalongkorn University |
| Assoc. Prof. Chaluda Niamnuy | Kasetsart University |
| Assoc. Prof. Chanin Panjapornpon | Kasetsart University |
| Assoc. Prof. Pinsuda Viravathana | Kasetsart University |

| | |
|---|---|
| Assoc. Prof. Kittisak Choojun | King Mongkut's Institute of Technology Ladkrabang |
| Assoc. Prof. Suttinun Phongtamrug | King Mongkut's University of Technology North Bangkok |
| Assoc. Prof. Anawat Sungpet | King Mongkut's University of Technology Thonburi |
| Assoc. Prof. Chanatip Samart | Thammasat University |
| Assoc. Prof. Tatiya Trongsatitkul | Suranaree University of Technology |
| Assoc. Prof. Anyarat Watthanaphanit | Mahidol University |
| Asst. Prof. Bussarin Ksapabutr | Silpakorn University |
| Asst. Prof. Riezqa Andika | University of Indonesia |
| Asst. Prof. Manaswee Suttipong | Chulalongkorn University |
| Asst. Prof. Prasit Pattananuwat | Chulalongkorn University |
| Asst. Prof. Nuttapol Pootrakulchote | Chulalongkorn University |
| Asst. Prof. Mongkol Tipplook | Shinshu University |
| Asst. Prof. Sasiradee Jantasee | Rajamangala University of Technology Thanyaburi |
| Dr. Pisitpong Intarapong | King Mongkut’s University of Technology Thonburi |
| Dr. Manunya Okhawilai | Chulalongkorn University |
| Dr. Phuwadej Pornaroontham | Chulalongkorn University |
| Dr. Rajitha Gunaratne | University of Sri Jayewardenepura |
| Dr. Duong Chi Trung | Petrovietnam University |

# Proceedings Table of Contents

## Speakers Session 1-5 & ASEAN


| Oral Presentation Proceedings | Page |
|---|---|
| Asst. Prof. Jenny Rizkiana | 1 |

| ***Session 1: AI Digital Tools for Process & Materials Engineering*** | **Page** |
|---|---|
| **Oral Presentation Proceedings** | |
| AIO1-Kritsana Suwanamad | 7 |
| **Poster Presentation Proceedings** | |
| AIP2-Abdul Nggofur | 18 |
| AIP4-Affan Dulyadech | 24 |

| ***Session 2: Cutting-Edge Catalysis*** | **Page** |
|---|---|
| **Oral Presentation Proceedings** | |
| CAO1-Chiramet Thatsanakunphan | 25 |
| **Poster Presentation Proceedings** | |
| CAP1-Ari Adrianto | 31 |
| CAP3-Ungki Bella Athania | 37 |
| CAP4-Fitrah Hardhana | 43 |
| CAP5-Sasiwimol Soisom | 49 |
| CAP6-Suparatthakorn Puangjinda | 56 |
| CAP7-Maythada Ruamjaithanakul | 62 |

| ***Session 3: Advanced Materials Innovation*** | ***Page*** |
|---|---|
| **Oral Presentation Proceedings** | |
| MATO1-Pisit Phayutcharoenkun | 68 |
| **Poster Presentation Proceedings** | |
| MATP1-Phannaphat Buadang | 74 |
| MATP2-Baifern Aincharoen | 81 |
| MATP3-Krittanan Chansuk | 87 |
| MATP4-Piyapron Tipayaars | 94 |
| MATP5-Intan Eta Hidayati | 101 |
| MATP6-Puntharika Tangsopa | 107 |
| MATP7-Sonsawan Onvikij | 114 |
| MATP8-Patamavadee Tapsarn | 120 |
| MATP9-Natthanon Phonchai | 126 |
| MATP10-Lalani Kavindya Chathumalee Silva Jamuni | 133 |
| MATP11-Nicharat Amonseriroj | 139 |
| MATP12-Chamod Hasaranga Peiris | 145 |
| MATP13-Kedkaew Kanlai | 152 |
| MATP14-Duangduean Kingphan | 158 |
| MATP15-Thushani Dilandika Senanayake Wadduwa Gurunnanselage | 164 |
| MATP16-Sadeepa Mandakini Landekumbura Mudiyanselage | 171 |
| MATP17-Tarika Lomcharoenwong | 178 |
| MATP18-Medhavi Hansana Karunarathna Warusapperuma Dona | 184 |
| MATP19-Sittikorn Bawthong | 191 |
| MATP20-Pajaera Patanathabutr | 197 |
| MATP21-Piraya Bootkrut | 203 |
| MATP22-Suttida Pongsiripan | 211 |
| MATP23-Peerawit Klinsrisuk | 217 |
| MATP24-Chattrin Navapongsiri | 223 |
| MATP25-Paranee Phuking | 231 |
| MATP26-Jitrawee Suk-em | 237 |
| MATP27-Natrata Thitinardwong | 243 |

MATP29-Sutthida Iamsaard 249
MATP30-Nadine Fesya Shafira 255
MATP31-Nakamol Sansuktaweesub 262
MATP33-Firadao Bennui 268
MATP35-Pongsakorn Pandee 277
MATP37-Gamlathge Dona Dilshani Kavindi Karunathilaka 283

**Session 4: *Energy Landscape Transformation: Renewable Generation, Storage, and Conversion*** **Page**

**Poster Presentation Proceedings**

EnergyP1-Panida Thepkhun 290
EnergyP2-Thanita Sonthisawate 296
EnergyP3-Napaporn Klaijieam 302
EnergyP4-Intan Elvina 309
EnergyP5-Kangpeng Chen 315
EnergyP6-Orawee Jirachaisakul 321
EnergyP8-Nonthakan Saikhwa 327
EnergyP9-Chatthakarn Banyongponglert 335
EnergyP10-Teerapat Pongpuak 340
EnergyP11-Pemika Sathitwong 346
EnergyP12-Borin Khun 353
EnergyP14-Natthakan Rattanaphong 360
EnergyP15- Muhammad Habib Nurain 367

***Session 5: Carbon & Sustainability Solutions for a Net-Zero Future*** **Page**

**Poster Presentation Proceedings**

CarbonP2-Teerapat Rodcharoen 373
CarbonP3-Suphawadee Siriphutthanon 380
CarbonP4-Nongnapat Budsrijaroen 386
CarbonP5-Phailin Thipkonglas 392
CarbonP6-Bayu Setiawan 398
CarbonP7- Hasitha Erandani Jayasinghe Jayasinghe Koralalage 404
CarbonP8-Kittiporn Laita 411
CarbonP9-Sitinjak Ebennezer 417
CarbonP10-Usulludin Usulludin 423
CarbonP11-Chayanit Krainara 429
CarbonP12-Napaphut Dolsiririttigul 435

## *Workshop on Water 2025*

**Poster Presentation Proceedings** **Page**

WaterP11-Wasupon Wongvitvichot 441

## *SKY SYMPOSIUM 2025*

**Oral Presentation Proceedings** **Page**

SKYO24-Syamsul Bakhri 448

# Speakers Session 1-5

# & ASEAN

# Valorization of Glycerol for Monomer Plastic Production: A Pathway to Sustainable Bioplastics in Indonesia

*Jenny Rizkiana* [a,b,c,*] *Agus Tendi Ahmad Bustomi* [c], *Aghietyas Choirun Az Zahra* [a], *Virdi Chaerusani* [a]

a)Department of Bioenergy Engineering and Chemurgy, Institut Teknologi Bandung
b) Center for Catalysis and Reaction Engineering, Institut Teknologi Bandung
c) Department of Chemical Engineering, Institut Teknologi Bandung

Keywords: Glycerol; bioplastics; polyglycerol; lactic acid.

## ABSTRACT

The rapid growth of biodiesel production in Indonesia, driven by government mandates such as B30 and B35 programs, has significantly increased the generation of crude glycerol as a byproduct. For every 10 tons of biodiesel produced, approximately 1 ton of crude glycerol is generated, leading to an oversupply issue. While crude glycerol contains impurities that limit its direct application, it offers substantial potential as a renewable raw material. The valorization of this byproduct is critical to enhancing the overall sustainability and economic viability of Indonesia's biodiesel industry. One promising approach to glycerol valorization is its conversion into monomers for bioplastic production. Through chemical and biological pathways, glycerol can be transformed into high-value compounds such as lactic acid, propylene glycol, and propylene. Lactic acid serves as a precursor for polylactic acid (PLA), a leading biodegradable plastic, while propylene glycol and propylene are essential for producing various polymeric materials. These pathways not only provide a sustainable alternative to petrochemical-based plastics but also create opportunities for Indonesia to develop a circular bioeconomy. Harnessing glycerol for bioplastic monomer production thus aligns with national goals for waste minimization, renewable resource utilization, and industrial innovation in the green economy sector.

***rizkiana@itb.ac.id**

## INTRODUCTION

The demand for renewable energy sources has significantly reshaped the global fuel market in recent decades, with biodiesel emerging as a key player in decarbonization strategies. In Indonesia, the rapid growth of biodiesel production has been primarily driven by national energy diversification goals, sustainable development commitments, and the vast availability of palm oil feedstock. The Indonesian government, through Presidential Regulation No. 66/2018 has aggressively expanded the biodiesel mandate, currently reaching B35 (35% biodiesel blending) with aspirations to scale it further. According to the Ministry of Energy and Mineral Resources (ESDM), biodiesel production in Indonesia rose from 7.2 million kiloliters in 2019 to over 10 million kiloliters in 2023, making Indonesia the largest biodiesel producer globally (ESDM, 2023; USDA GAIN Report, 2023).

PPC & PETROMAT SYMPOSIUM 2025

However, this expansion has led to the generation of large quantities of glycerol as a byproduct. For every 100 kg of biodiesel produced, approximately 10 kg of crude glycerol is generated, amounting to an estimated 1 million metric tons annually in Indonesia alone. This figure is expected to increase in line with the government's push toward B40 and higher blending mandates. While glycerol is a non-toxic, biodegradable compound with diverse potential uses, the oversupply of crude glycerol poses a significant challenge. Without proper downstream utilization, this surplus can create environmental concerns and result in market saturation, which depresses its economic value. Studies have reported that in regions with unbalanced glycerol valorization infrastructure, crude glycerol prices may even turn negative (Pagliaro & Rossi, 2008; Behr et al., 2008).

In parallel, the world is facing an urgent need to transition away from petrochemical-derived plastics, driven by escalating environmental issues associated with plastic waste and carbon emissions. Indonesia, as the second-largest contributor to ocean plastic pollution (Jambeck et al., 2015), faces increasing international and domestic pressure to develop biodegradable and bio-based plastic alternatives. Although the country has launched initiatives like the "Indonesia Plastic Action Partnership", the core issue remains the shortage of locally sourced, renewable plastic monomers. Most bio-based plastics currently depend on imported building blocks like polylactic acid (PLA) or bio-ethylene glycol, which increases costs and limits scalability.

Based on these factors, this article examines the conversion pathways of glycerol into plastic. The goal is to assess how glycerol valorization can contribute to a circular, sustainable plastic economy, leveraging biodiesel byproducts to create a high-value downstream industry for bio-based polymer manufacturing.

## POTENTIAL PRODUCT FROM GLYCEROL

The increasing availability of glycerol as a byproduct of biodiesel production has prompted interest in its valorization into high-value chemical intermediates, particularly for use in the plastic industry. Among the most promising applications is the transformation of glycerol into various plastic precursors or monomers, which can serve as building blocks for bioplastics and other polymeric materials (Pagliaro & Rossi, 2008). Table 1 shows the list of potential products from glycerol and their functions in bioplastics or biopolymers.

One of the most notable monomers derived from glycerol is 1,3-propanediol (1,3-PDO). This compound can be synthesized through microbial fermentation or catalytic hydrogenolysis of glycerol and is used as a key monomer in the production of polytrimethylene terephthalate (PTT)—a bio-based polyester with applications in textiles and packaging (Mu et al., 2006; Wright & Palkovits, 2010). The production of 1,3-PDO not only adds value to glycerol but also offers a renewable alternative to petroleum-derived monomers.

Another important derivative is glycerol carbonate, which can be produced via transesterification or carboxylation of glycerol. This compound serves as a versatile intermediate in the synthesis of biodegradable polycarbonates and non-isocyanate

polyurethanes (NIPUs). Its low toxicity and high reactivity make it an attractive candidate for green chemistry applications (Rokicki et al., 2015).

Glycerol acrylates and methacrylates represent another category of glycerol-derived monomers with significant industrial relevance. These derivatives are typically used in the production of acrylic resins, adhesives, and UV-curable coatings, offering the advantage of functionality and flexibility in polymer design. Their introduction into acrylic polymer chains enhances hydrophilicity and thermal stability (Zhou et al., 2014).

**Table 1** lists of potential bioplastic precursor from glycerol

| Chemical | Role in Plastics | Notes |
|---|---|---|
| 1,3-Propanediol (1,3-PDO) | Monomer | Used to produce polytrimethylene terephthalate (PTT), a bio-based polyester. |
| Glycerol carbonate | Monomer/Intermediate | Used in biodegradable polycarbonates and non-isocyanate polyurethanes (NIPUs). |
| Glycerol acrylates/methacrylates | Monomer | Used in acrylic resins, coatings, and adhesives. |
| Polyglycerols | Polyol | Used in polyurethane production and biodegradable polymers. |
| Epichlorohydrin | Monomer | Used to synthesize epoxy resins, often for adhesives and coatings. |
| Allyl alcohol | Monomer/Intermediate | Precursor for allyl-based resins and thermosetting polymers. |
| Succinic acid | Diacid monomer | Used in polybutylene succinate (PBS) and other polyesters. |
| Lactic acid | Monomer | Can be converted to PLA (polylactic acid), a major bioplastic. |

Polyglycerols, which are produced by the oligomerization or etherification of glycerol, function as polyols in polyurethane synthesis. Depending on their molecular weight, they can be used to tailor the mechanical and thermal properties of polyurethanes, making them suitable for applications in foams, elastomers, and coatings. Moreover, polyglycerols are also used in the food and cosmetic industries due to their non-toxic and biodegradable nature (Behr & Eilting, 2008).

Additionally, epichlorohydrin, a critical monomer in epoxy resin production, can be synthesized from glycerol via chlorination and ring closure. The use of glycerol as a feedstock for epichlorohydrin reduces reliance on propylene and opens the door to bio-based epoxy materials with wide-ranging uses in coatings, adhesives, and composites (Pagliaro & Rossi, 2008).

Allyl alcohol, another intermediate, can be produced from glycerol and serves as a precursor to allyl resins, which are widely employed in the production of thermosetting

PPC & PETROMAT SYMPOSIUM 2025

plastics and crosslinked polymers. Its role in enhancing resin toughness and chemical resistance makes it valuable in industrial composites (Dasari et al., 2005).

Succinic acid, while not directly synthesized from glycerol, can be derived through biochemical routes and plays an essential role as a diacid monomer in the production of polybutylene succinate (PBS) and other biodegradable polyesters. It complements glycerol-derived diols in polyester synthesis, contributing to the formation of fully bio-based polymers (Werpy & Petersen, 2004).

## GLYCEROL CONVERSION TO POLYGLICEROLS

Recent advances in glycerol valorization have focused on the efficient synthesis of polyglycerols using a range of catalytic systems. Homogeneous base catalysts like NaOH remain widely used due to their high activity and simple reaction setup, achieving yields above 70% at around 240°C, though they require post-reaction neutralization and purification (Weber & Barth, 2002). In contrast, solid base catalysts such as MgO and CaO offer easier separation and reusability, with comparable yields around 65–70% under similar conditions (Sutterlin et al., 2008).

Acidic catalysts, including $H_2SO_4$ and Amberlyst-15, provide moderate yields (~55–60%), with the latter preferred for food-grade applications due to its milder and non-corrosive nature (Pagliaro & Rossi, 2008). Additionally, bifunctional catalysts like hydrotalcite-derived Mg-Al oxides demonstrate enhanced selectivity and recyclability, offering a promising balance of efficiency and sustainability (Liu et al., 2010).

**Table 2** recent development of glycerol conversion to polyglycerol

| Catalyst Type | Catalyst System | Temp (°C) | Yield (%) | Notes | Reference |
|---|---|---|---|---|---|
| Homogeneous base | NaOH | ~240 | >70 | High activity, requires neutralization | Weber & Barth, 2002 |
| Homogeneous acid | $H_2SO_4$ | ~220 | ~60 | Effective, but corrosive and non-food grade | Behr & Eilting, 2008 |
| Solid base | MgO, CaO | 240 | 65–70 | Reusable, simpler work-up | Sutterlin et al., 2008 |
| Solid acid | Amberlyst-15 | 200–220 | ~55 | Mild, food-grade applications | Pagliaro & Rossi, 2008 |
| Bifunctional catalyst | Hydrotalcite (Mg-Al) | 240 | 70–75 | Selective and recyclable | Liu et al., 2010 |
| Microwave-assisted | NaOH + microwave | ~200 | ~80 | Fast, energy-efficient | Reddy et al., 2013 |

Innovative methods like microwave-assisted synthesis using NaOH have shown improved energy efficiency and faster reaction rates, with yields reaching ~80% diglycerol (Reddy et al., 2013). These developments underscore the potential of catalytic process optimization in producing polyglycerols for diverse applications ranging from bioplastics to food emulsifiers and polyurethane foams.

PPC & PETROMAT SYMPOSIUM 2025

## GLYCEROL CONVERSION TO LACTIC ACID

Table 3 presents a comparative overview of recent advancements in the catalytic and biocatalytic conversion of glycerol to lactic acid, a high-value platform chemical with growing applications in biodegradable plastics, pharmaceuticals, and food additives.

**Table 3** Recent development of glycerol conversion to lactic acid

| Catalyst Type | Catalyst System | Temp (°C) | Yield (%) | Advantages | Reference |
|---|---|---|---|---|---|
| Homogeneous base + metal salt | NaOH + $SnCl_2$ | 180 | 80 | High conversion, cost-effective | Zhou et al., 2008 |
| Homogeneous base + Cu(II) salt | NaOH + $Cu(NO_3)_2$ | 160 | 85 | High selectivity, relatively mild conditions | Yang et al., 2012 |
| Solid base catalyst | MgO, CaO | 200 | 60 | Reusable, low toxicity | Yao et al., 2014 |
| Solid acid catalyst | HZSM-5, Amberlyst-15 | 180 | 50 | Mild acid site control | Pagliaro & Rossi, 2008 |
| Biocatalyst (enzyme) | Lactobacillus spp. + glycerol | 37 | 90 | High selectivity, operates at low temp | Silva et al., 2015 |
| Metal oxide catalyst | $CuO/ZrO_2$, $Ru/Al_2O_3$ | 200 | 75 | Robust system, potential for scale-up | Liu et al., 2011 |

Among the most efficient systems are biocatalytic processes using Lactobacillus species, which ferment glycerol under mild, anaerobic conditions (around 37 °C) to produce lactic acid with very high yields (up to 90%) (Silva et al., 2015). On the catalytic side, homogeneous base-metal systems such as NaOH combined with $Cu(NO_3)_2$ or $SnCl_2$ have shown excellent performance, offering high selectivity (80–85%) at moderate temperatures (160–180 °C) (Zhou et al., 2008; Yang et al., 2012).

Heterogeneous solid base catalysts, such as MgO and CaO, provide the advantage of reusability and lower toxicity, with lactic acid yields around 60% under thermal conditions (Yao et al., 2014). These catalysts are promising for continuous flow operations and reduce the need for complex separation processes. Recent work on metal oxide catalysts such as $CuO/ZrO_2$ and $Ru/Al_2O_3$ highlights their potential for scalable lactic acid production, combining robustness with reasonable conversion efficiencies (~75%) (Liu et al., 2011).

## CONCLUSIONS

The conversion of glycerol into bioplastic precursors presents a strategic opportunity to address glycerol oversupply from biodiesel production while supporting the transition to sustainable materials. As demonstrated by various studies, glycerol can be transformed into valuable monomers for producing biodegradable plastics. Technologies for glycerol valorization span biological fermentation and chemical catalysis, each with growing

PPC & PETROMAT SYMPOSIUM 2025

efficiency and selectivity. Innovations like microwave-assisted synthesis, solid catalysts, and continuous-flow systems are improving scalability and energy efficiency. However, key challenges remaining are improving process economics and ensuring regulatory compliance for end-use materials. With aligned policy and industrial support, glycerol-derived bioplastics could play a major role in advancing circular economy goals and reducing plastic-related emissions.

## REFERENCES

**Behr, A., & Eilting, J. (2008).** Glycerol as a raw material in organic synthesis. *Green Chemistry*, 10(1), 13–30.

**Dasari, M. A., Kiatsimkul, P. P., Sutterlin, W. R., & Suppes, G. J. (2005)**. Low-pressure hydrogenolysis of glycerol to propylene glycol. *Applied Catalysis A: General*, 281(1–2), 225–231.

**Liu, H., et al. (2010).** Etherification of glycerol over solid base catalysts. *Catalysis Communications*, 11(7), 597–601.

**Liu, Z., & Zhang, F. (2011).** Catalytic performance of $CuO/ZrO_2$ in the selective oxidation of glycerol to lactic acid. *Chemical Engineering Journal*, 168(3), 1226–1230.

**Mu, Y., Teng, H., Zhang, D. J., Wang, W., & Xiu, Z. L. (2006**). Microbial production of 1,3-propanediol by *Klebsiella pneumoniae* using crude glycerol from biodiesel preparations. *Biotechnology Letters*, 28(21), 1755–1759.

**Pagliaro, M., & Rossi, M. (2008).** *The Future of Glycerol: New Uses of a Versatile Raw Material*. Royal Society of Chemistry.

**Reddy, V. K., & Prasad, R. B. N. (2013).** Microwave-assisted synthesis of diglycerol from glycerol. *Industrial Crops and Products*, 44, 383–386.

**Rokicki, G., Piotrowska, A., & Parzuchowski, P. G. (2015).** Glycerol carbonate as a monomer for polycarbonates and polyurethanes. *Polimery*, 60(9), 569–576.

**Silva, G. P., et al. (2015).** Lactic acid production from glycerol using Lactobacillus strains. *Bioresource Technology*, 185, 92–99.

**Sutterlin, W. R., Suppes, G. J., & Sutterlin, B. (2008).** Etherification of glycerol with solid catalysts. *Applied Catalysis A: General*, 347(2), 180–187.

**Weber, M., & Barth, T. (2002).** Base-catalyzed synthesis of polyglycerol from glycerol. *Journal of the American Oil Chemists' Society*, 79(5), 521–525.

**Wright, W. R. H., & Palkovits, R. (2010**). Development of heterogeneous catalysts for the conversion of glycerol to value-added products. *ChemSusChem*, 3(8), 929–940.

**Yang, F., Hanna, M. A., & Sun, R. (2012).** Catalytic conversion of glycerol to lactic acid by alkaline hydrothermal reaction. *Bioresource Technology*, 116, 190–194.

**Yao, G., Wang, Y., & Wang, S. (2014).** Conversion of glycerol into lactic acid using MgO and CaO catalysts. *Catalysis Communications*, 47, 58–62.

**Zhou, C.-H., Beltramini, J. N., Fan, Y.-X., & Lu, G. Q. (2008).** Chemoselective catalytic conversion of glycerol as a biorenewable source to valuable commodity chemicals. *Chemical Society Reviews*, 37(3), 527–549.

PPC & PETROMAT SYMPOSIUM 2025

# Session 1-AI Digital Tools for Process & Materials Engineering (AI)

# Data-Driven NARX Modeling and MPC Control for Nonlinear CSTR Systems

*Kritsana Suwanamad*[b], *Apinan Soottitantawat*[*a,b]

[a)] *Center of Excellence in Particle and Materials Processing Technology, Department of Chemical Engineering, Faculty of Engineering, Chulalongkorn University, Bangkok, 10330, Thailand*
[b)] *Bio-Circular-Green-economy Technology & Engineering Center, Department of Chemical Engineering, Faculty of Engineering, Chulalongkorn University, Bangkok, 10330, Thailand*

Keywords: CSTR, NARX, Neural network, MPC control

## ABSTRACT

Continuous Stirred Tank Reactor (CSTR) is a basic reactor unit widely used in the chemical, petrochemical, and food industries. Because it can consistently control the concentration and temperature of the reactants, controlling these parameters is crucial for ensuring product safety and quality. However, the CSTR system exhibits nonlinear behaviour and complex dynamics, which make it challenging to build a model for use in control systems such as Model Predictive Control (MPC). This research proposes a model approach to generate simulated data and then uses a NARX neural network model to learn the nonlinear behaviour of the system. The resulting model has an accuracy value of $R2 = 0.9952$. In addition, the MPC parameter tuning using SLSQP, PSO, and GA was compared. It was found that GA gave the best results in finding the global optimum and effectively reducing the offset. The control system was tested in two scenarios, between the servo test and the regulatory test. The experimental results show that the system can track the initial value well and respond to Gaussian noise quickly and stably, demonstrating the potential of integrating NARX with MPC and GA to control non-linear processes efficiently.

***apinan.s@chula.ac.th**

## INTRODUCTION

Continuous Stirred Tank Reactor (CSTR) is one of the most important chemical reactor units and is widely used in industrial processes such as chemical, petrochemical and food industries because it has the ability to continuously control the operating conditions, especially in terms of temperature and chemical concentration, which directly affect the safety and quality of the product [1]. However, the CSTR system has nonlinear characteristics and exhibits complex dynamic behaviors, which hinders the use of linear models for accurate control. Therefore, it is necessary to develop a model that can properly capture these nonlinear characteristics [2-5].

Model Predictive Control (MPC) is a widely popular control strategy because it can predict the behaviour of the system in advance and adjust the control values under various constraints effectively [2, 6-8]. However, the efficiency of MPC directly depends on the accuracy of the system model [2, 8]. Therefore, recent research has applied artificial neural models such as Nonlinear Autoregressive with Exogenous Inputs (NARX) to learn the behaviour of the system from real data that is highly nonlinear and uncertain [2, 3, 9].

PPC & PETROMAT SYMPOSIUM 2025

This research will focus on improving the efficiency of MPC to control CSTR accurately and quickly. This research presents an approach to using NARX as a process model with MPC along with tuning the MPC parameters using various optimization algorithms: Sequential Least Squares Programming (SLSQP) suitable for smooth optimization problems, Particle Swarm Optimization (PSO), and Genetic Algorithm (GA) that models natural evolutionary processes [7, 8]. Comparing these three algorithms in the context of CSTR control via servo test and regulatory test will help identify the most suitable approach for industrial scale non-linear control systems [3, 9].

## EXPERIMENTAL

*A. System overview*

The CSTR is a chemical reactor system used in the chemical, petrochemical and food industries [1]. The characteristic of CSTR is that when mixed uniformly throughout the reactor, the composition of the output is the same as the reactor [1, 10]. Figure 1 shows a schematic representation of CSTR [10]. Therefore, CSTR is usually designed to control temperature and concentration within the required range for safety and to produce quality products [10].

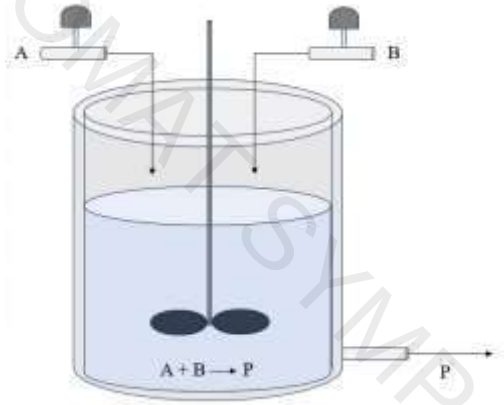


**Figure 1:** Continuous Stirred Tank Reactor (CSTR) [10]

*B. Data generation*

This research has applied the model from Thamminaidu et al. [10] to create data simulating the system response by randomly selecting uniform input values in the range [-1,1] with a total of 550 data points to cover the frequency band of the system. Then, the data is normalized to be neutral and the data for training and testing the NARX model is divided into 80% and 20% of the simulated data set.

*C. NARX model*

This NARX model is an important type of discrete time nonlinear system that can be shown in Eq 1 [11].

$$y(n+1) = f[y(k),\ldots,y(k-d_y+1);u(k-i),u(k-i-1),\ldots,u(k-i-d_u+1)] \quad (1)$$

PPC & PETROMAT SYMPOSIUM 2025

where $d_u \geq 1$, $d_y \geq 1$, and $d_u \leq d_y$ represent the sequence of the input and output memory, respectively, and $u(k) \in R$ and $y(k) \in R$ represent the model's input and output at n time steps. The delay term known as the process's dead time is represented by the parameter i ($i \geq 0$) [11].

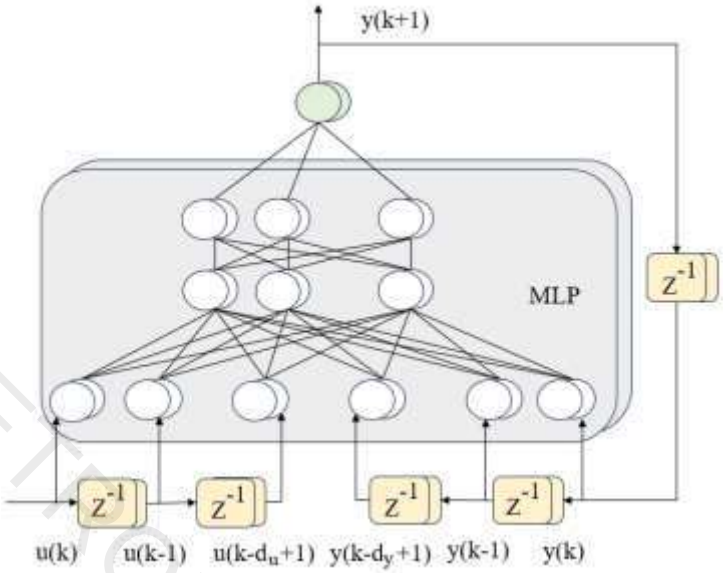


**Figure 2:** NARX structure [11]

There are two main modes used for training the NARX model. The first mode is the parallel mode, in which the predicted output of the network is fed back into the input as part of the standard NARX structure which is shown in Figure 3. The second mode is the series-parallel mode, in which the actual output is used for feedback instead of the predicted output which is shown in Figure 4. The main advantage of the SP mode is that it preserves a true feed forward structure, which allows for the use of constant backpropagation during training. Therefore, in this study, the NARX network is first trained using the series-parallel mode and then converted to the parallel mode for prediction purposes [11].

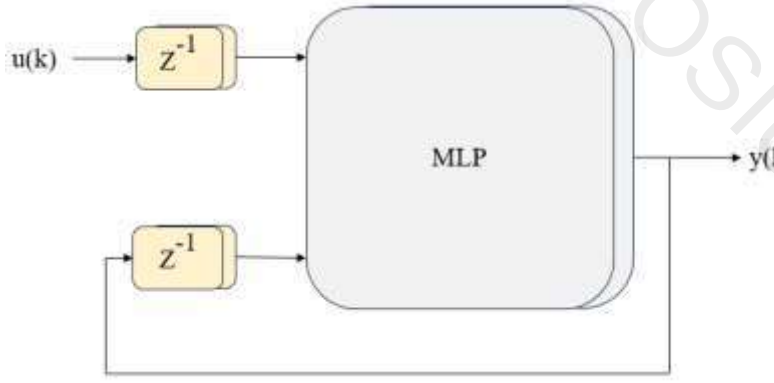


**Figure 3:** Parallel structure of NARX model [11]

PPC & PETROMAT SYMPOSIUM 2025

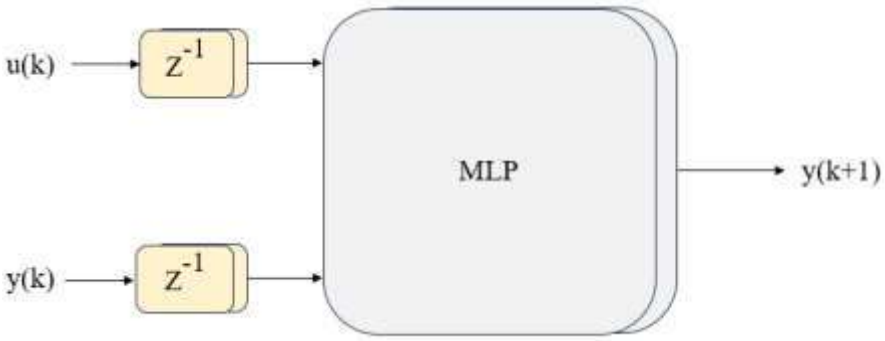


**Figure 4:** Series-Parallel structure of NARX model [11]

This research creates NARX using MLPRegressor (Neural Network) to estimate a non-linear function that relates the past data of output $y(k-1)$ and input u(k−1) to the current output $y(k)$. NARX structure has 32, 64 and 32 hidden layers respectively to use the data obtained from data generation to train the model using series parallel and after testing is complete, when testing the model will switch to parallel mode to predict the process model value for model simulation with MPC control [12].

*D. MPC controller*

Model-based predictive control (MPC) systems use a system model to predict the future state of the system and generate a control vector that minimizes a defined cost function over the prediction period, taking into account disturbances and system constraints which is shown in Eq 2-7. At each sampling time, only the first control input from the computed vector is used, and the remaining inputs are discarded. The process then repeats at the next time step. Constraints can be imposed on the dynamics of the actuators, the controlled variables, and the controlled outputs [13, 14].

$$\min \sum_{k=0}^{N_p-1} Q\cdot(\hat{y}_k - y_{ref})^2 + \sum_{k=0}^{N_p-1} R\cdot(u_k - u_{k-1})^2 \quad (2)$$

Control Constraints: $u_{min} \le u_k \le u_{max}$ (3)

Rate of Change Constraints: $\Delta u_{min} \le u_k - u_{k-1} \le \Delta u_{max}$ (4)

Output Constraints: $y_{min} \le y_k \le y_{max}$ (5)

State Constraints: $x_{min} \le x_k \le x_{max}$ (6)

Terminal Constraints: $x_{k+N_p} \in X_f$ (7)

This approach allows the controller to remain robust to time varying disturbances and parameter changes while maintaining tight control within the defined operating limits.

*E. Optimization algorithm*

This research will focus on three optimization methods including Sequential Least Squares Quadratic Programming (SLSQP), Genetic Algorithm (GA), and Particle Swarm Optimization (PSO) were tuned the input sequence of the Model Predictive Control (MPC)

PPC & PETROMAT SYMPOSIUM 2025

for a nonlinear CSTR system. These optimizers were used to solve the cost function and constraints defined in the MPC formulation.

*F. Testing scenarios*

This research will investigate two tests of the entire system: a servo test and a regulatory test.

1. Servo test

Servo testing is an evaluation of a controller's ability to track setpoint changes. The research will determine a reference line for the system output to change at pre-determined time intervals to ensure that the output can accurately track the changing reference line with minimal steady-state error, rapid rise time, and no excessive overshoot [15].

2. Regulatory test

Regulatory test is a control designed to check the robustness of the controller to external disturbances, modeled as Gaussian noise added to the process. This research simulates potential situations that can occur in a CSTR system, such as feed fluctuations, with the objective of maintaining the process output at a constant setpoint while minimizing the impact of the disturbances [15].

## RESULTS AND DISCUSSION

*A. NARX modeling*

This research has applied the model from research [1] to create data to train and test the NARX model as process model in the control system. The results are shown in Figure 5 and Table 1.

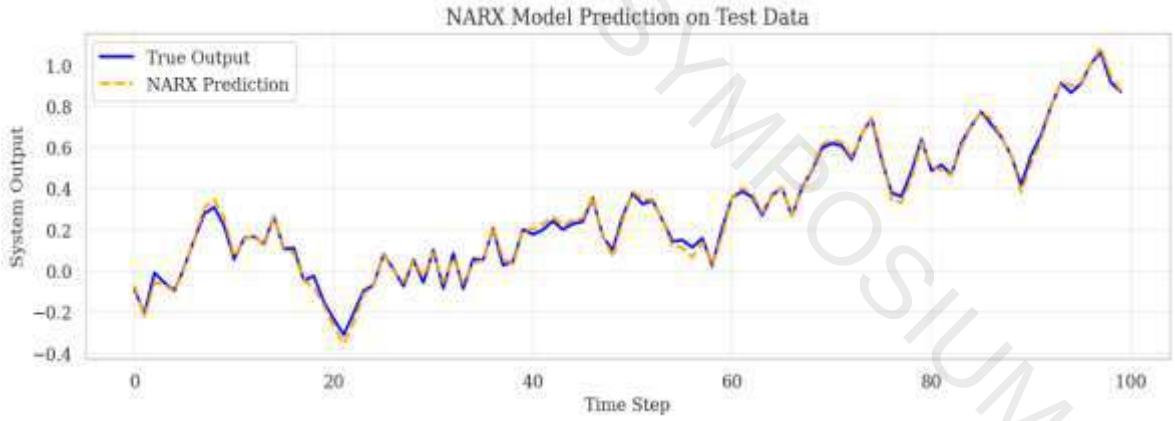


**Figure 5:** NARX model prediction on test data

**Table 1:** Evaluation NARX model with dataset

| Evaluation | Training set | Testing set |
|---|---|---|
| MAE | $1.57 \times 10^{-2}$ | $1.83 \times 10^{-2}$ |
| MSE | $4.00 \times 10^{-4}$ | $5.00 \times 10^{-4}$ |
| $R^2$ | 0.99 | 0.99 |

PPC & PETROMAT SYMPOSIUM 2025

From Figure 5 and Table 1, it shows that the NARX model that was created can represent the process model for CSTR system because the error between the actual value and the predicted value is very small and there is no overfitting as tested from the training and testing sets of MSE, MAE. In addition, the $R^2$ of the model is close to 1, which means that the model of this research is considered to have very high accuracy up to 0.9952.

*B. Evaluation optimizer*

This research evaluates the optimization methods of MPC control to find the most suitable method for use with MPC control for CSTR system by comparing SLSQP, GA and PSO as shown in Figure 6 and Table 2.

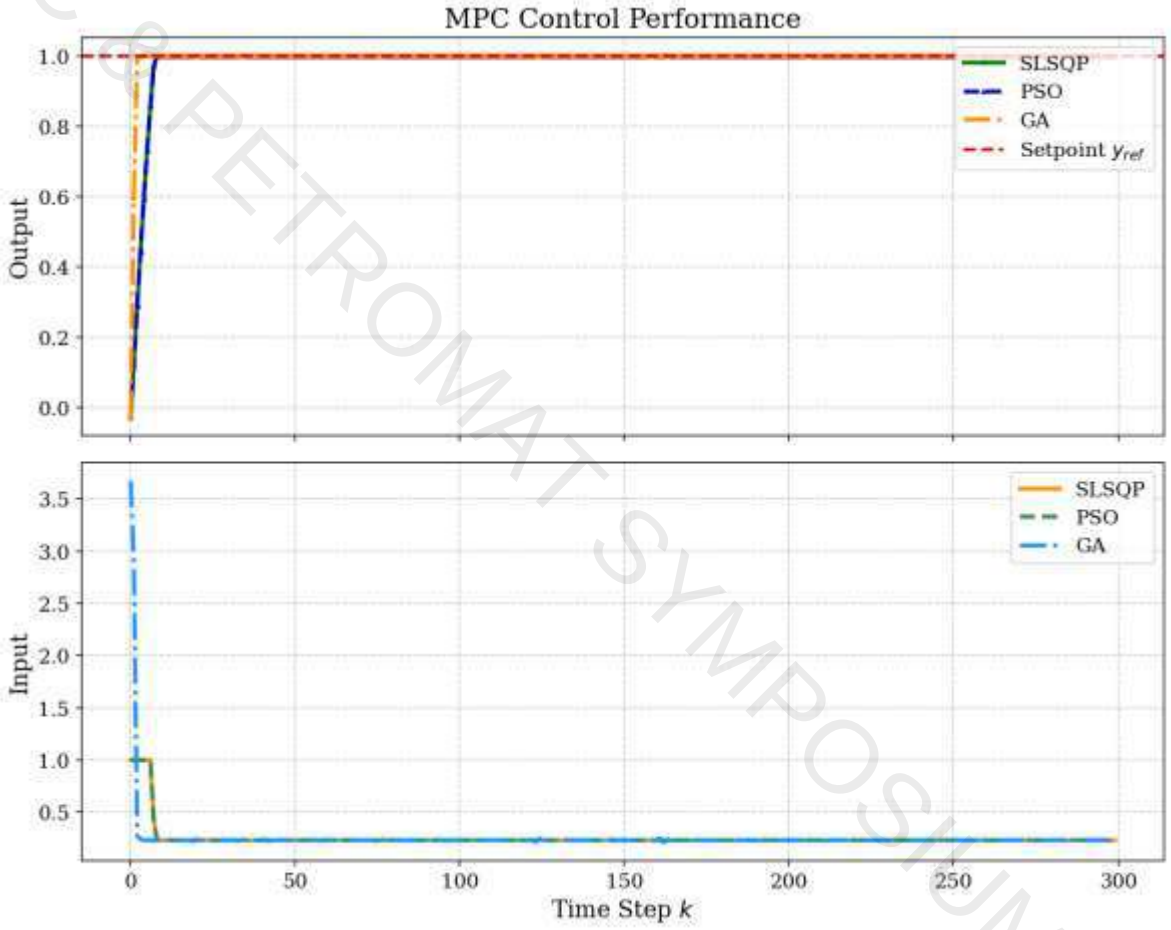


**Figure 6:** MPC control evaluation between SLSQP, GA and PSO

**Table 2:** Evaluation control performance between SLSQP, GA and PSO

| Evaluation | SLSQP | GA | PSO |
|---|---|---|---|
| Rising time (sec) | 6.00 | 1.00 | 6.00 |
| Overshoot (%) | 0.00 | 0.00 | 0.00 |
| Undershoot (%) | - | - | - |
| Offset | 0.00 | 0.00 | 0.00 |

PPC & PETROMAT SYMPOSIUM 2025

| | | | |
|---|---|---|---|
| IAE | 4.01 | 1.48 | 4.02 |
| ISE | 2.89 | 1.22 | 2.89 |
| ITAE | 8.08 | 6.46 | 8.41 |

From the Table 2 comparing the efficiency of SLSQP, GA and PSO algorithms in tuning MPC parameters for CSTR system, it was found that Genetic Algorithm (GA) shows the best control results in all aspects, especially in terms of Rising Time, taking only 1.00 seconds to reach the setpoint and the lowest accumulate errors (IAE, ISE and ITAE) when GA is compared with SLSQP and PSO, which shows that GA has the ability to make the system reach the setpoint quickly and stably.

*C. Servo test*

This research conducted a servo test control system to examine the new tracking setpoint when the setpoint was changed at different times at 0, 100 and 200 seconds, which can be shown in Figure 7.

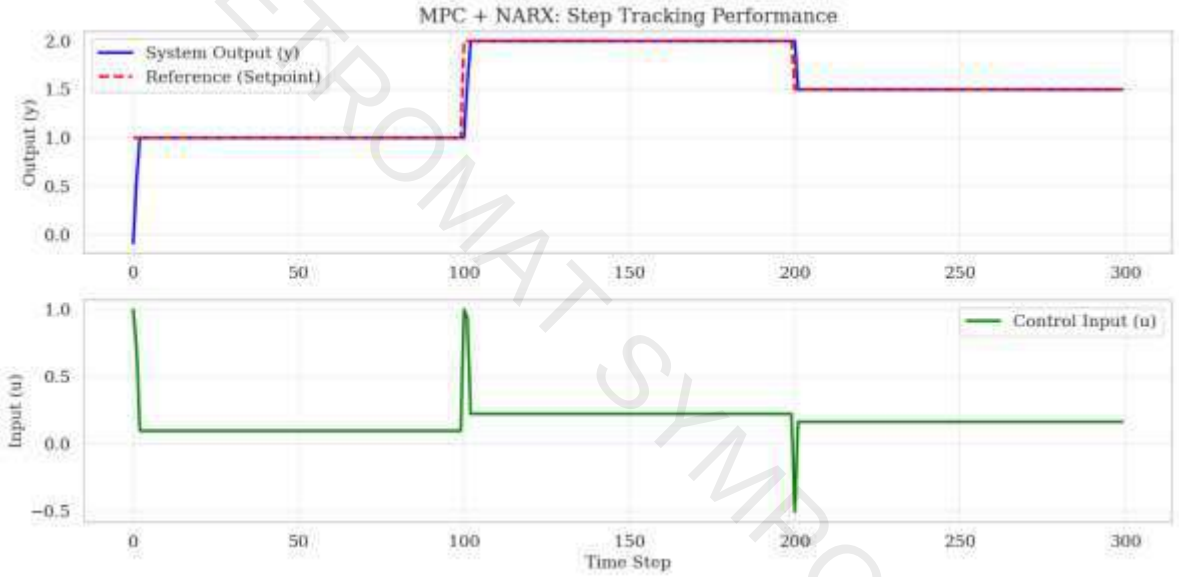


**Figure 7:** Servo test

From Figure 7, it sees that the combined control system between the MPC control and the NARX model can track the reference value accurately and stably. The system output can respond to the change of the reference value in each period quickly with low overshoot and return to the steady state, which shows the accuracy of the NARX model in predicting the process behaviour and the efficiency of the MPC in controlling the system. In addition, the control signal (input) changes only during the setpoint change and remains constant during the system entering the steady state, indicating the effective control. As a result, the system can be controlled efficiently under the condition of no disturbance.

*D. Regulatory test*

This research conducted a regulatory test by adding disturbance to examine the MPC control system combined with NARX model to determine whether it can maintain the

PPC & PETROMAT SYMPOSIUM 2025

setpoint value in two cases between a small disturbance (D = 0.01) and a large disturbance (D = 0.1) which can be shown in Figures 8 and 9.

Case 1: Random disturbance (D = 0.01)

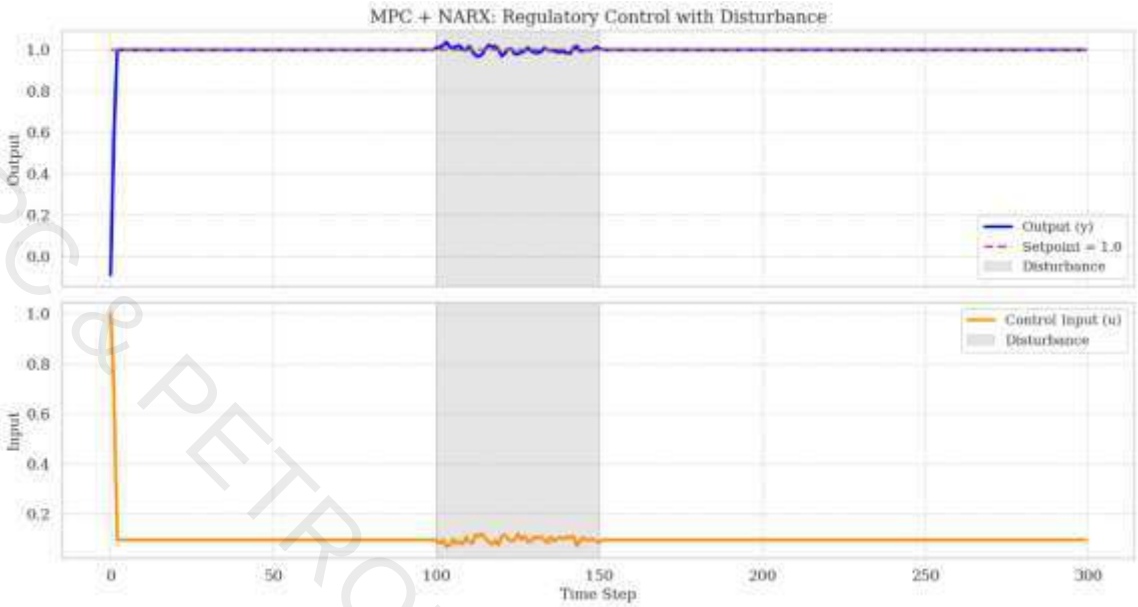


**Figure 8:** Regulatory test (Random disturbance D = 0.01)

From Figure 8 in the case of small disturbance (D = 0.01) inserted in the period of 100-150 seconds, it was found that the MPC control system combined with the NARX model can still obtain a stable reference value (setpoint = 1.0) despite slight fluctuations during the disturbance period, which shows the ability of the control system to respond well to external uncertainties. The control signal is slightly adjusted during the disturbance period to compensate for the impact of the disturbance that interferes with the system and returns to a constant value when the disturbance ends. This shows that the MPC combined with NARX has the ability to control in a manner and is somewhat resistant to disturbance, which is suitable for application in real systems that may be affected by disturbances.

Case 2: Random disturbance (D = 0.1)

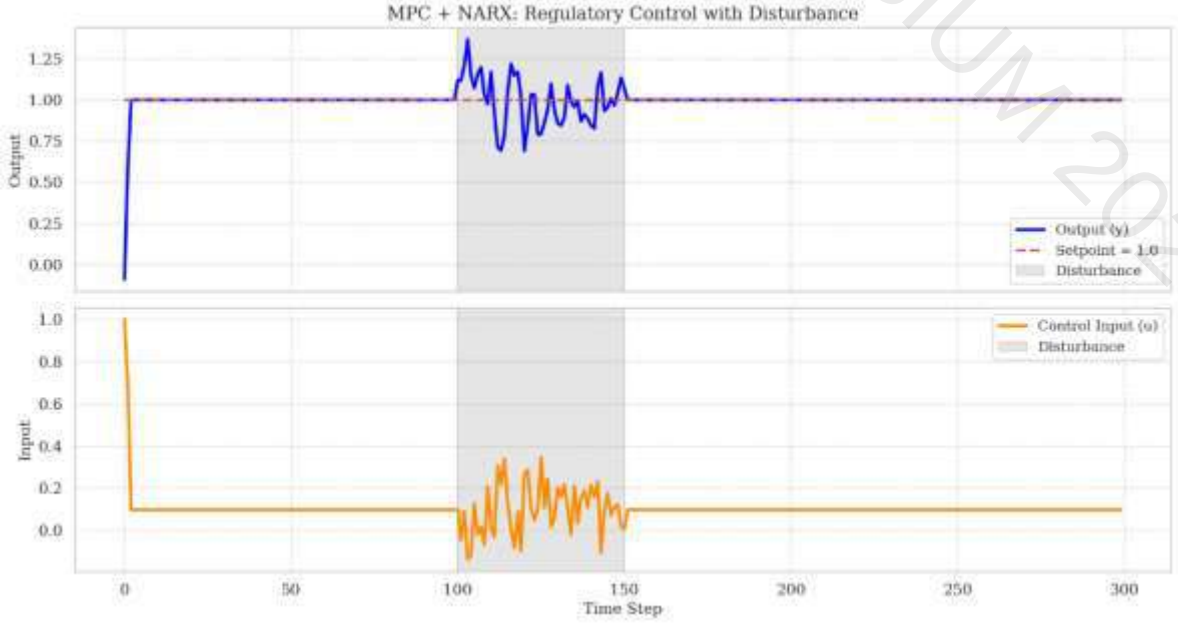


PPC & PETROMAT SYMPOSIUM 2025

**Figure 9:** Regulatory test (Random disturbance D = 0.1)

In the case of regulatory test with high disturbance (D = 0.1), the result shows that the disturbance is introduced at time 100 sec, the system shows a significantly more volatile response, with the output deviating up to about 1.3, which is significantly beyond the setpoint, and continuous oscillation throughout the disturbance range. Such response reflects the challenge of MPC control with NARX model in dealing with large disturbance. Although after the end of the disturbance range at time 150 sec, the system can return to the setpoint, it takes longer than the case with no disturbance or with small disturbance. In addition, the control signal value fluctuates more in the disturbance range, indicating the MPC 's attempt to adjust the control value to counteract the impact of continuous disturbance. In conclusion, in the case of large disturbance, the system is still controllable but its efficiency is reduced, and there are obvious oscillations in both output and input, but it can still cope with the challenge of high disturbance.

From the study of both cases, the research investigated the regulatory test of MPC control system together with NARX model which can be shown in Table 3.

**Table 3:** Evaluation regulatory case (D = 0, 0.01 and 0.1)

| Criteria | D = 0 | D = 0.01 | D = 0.1 |
|---|---|---|---|
| Maximum deviation | $5.00 \times 10^{-4}$ | $2.00 \times 10^{-2}$ | $3.20 \times 10^{-1}$ |
| Overshoot (%SP) | 0.00 | 2.00 | 30.00 |
| control input (AVG) | 0.10 | 0.11 | 0.16 |
| Deviation of input | $2.00 \times 10^{-4}$ | $1.50 \times 10^{-2}$ | 0.11 |

From Table 3, it can be concluded that without disturbance, the system shows accurate control capability, with the output value following the setpoint well and the control input usage is constant and very low. However, with a disturbance of 0.01, even though the deviation and overshoot increase slightly, the system can still maintain stability, with the input starting to adjust itself to offset the disturbance effect well. However, when the disturbance increases to 0.1, the obvious effect is the overshoot and oscillation of the output significantly more, especially in the disturbance range, causing the system to take longer time to return to the setpoint. In addition, it is found that the control input usage changes more (both the average and the fluctuation), reflecting the burden of the controller in trying to deal with the system variability.

## CONCLUSIONS

This research presents the application of NARX model combined with MPC control for the control of a CSTR continuous stirred tank reactor system. The developed NARX model trained on the model obtained in previous research shows high accuracy with very low error estimates of MSE, MAE and coefficient of determination $R^2$ of 0.9952, indicating the model's accuracy in representing the real process.

This research compares the efficiency of SLSQP, GA and PSO algorithms in optimizing MPC input signal for CSTR system. It is found that Genetic Algorithm (GA) shows the best control performance in all aspects, especially in terms of Rising Time, which

PPC & PETROMAT SYMPOSIUM 2025

takes only 1.00 seconds to reach the setpoint and has the lowest cumulative error (IAE, ISE and ITAE) when comparing GA with SLSQP and PSO, which shows that GA has the ability to make the system reach the setpoint quickly and stably.

In addition, the research has tested the servo control system, MPC control system with NARX, showing accurate tracking of setpoint values, fast response, less overshoot, and stable behaviour. The change of the control signal occurs only when the setpoint changes. In the regulatory control test, the system can maintain its performance when there is a small disturbance (D = 0.01) with a small deviation and can quickly return to a steady state, which shows the robustness of the controller. However, when there is a larger disturbance (D = 0.1), the system shows a larger behaviour of the output vibration and overshoot, and it takes longer to return to a steady state and has a more severe change of the control signal, which shows an increase in control effort. However, the MPC control system with NARX can handle and support large disturbances, which can be applied to real industries where there is a lot of noise and disturbances interfering with the system.

## ACKNOWLEDGEMENTS

I would like to thank myself for my efforts, my curiosity, my determination, my intentions, and my persistence in facing obstacles throughout the research. This is an important step in developing my academic potential and creativity, and it is something that has made my dreams come true from what I could not achieve while studying.

I would like to thank my family for being my support at all times, both emotionally and unconditionally, which has given me the strength to move forward steadily.

I would like to thank my girlfriend who has always been by my side, encouraging me, understanding me, and supporting me fully throughout the research.

I would like to express my deepest gratitude to Associate Professor Dr. Apinan Sutthithanthawach, the main advisor of this research, for providing advice, guidelines, and inspiration to conduct the research. I would also like to thank Chulalongkorn University and the Bio-Circular-Green-economy Technology & Engineering Center, Department of Chemical Engineering, Faculty of Engineering, for providing research funding and valuable resources for this work.

## REFERENCES

1. Jingjing, D., S. Chunyue, and L. Ping, *Modeling and control of a continuous stirred tank reactor based on a mixed logical dynamical model.* Chinese Journal of Chemical Engineering, 2007. **15**(4): p. 533-538.
2. Shrivastava, P., *Modeling and control of CSTR using model based neural network predictive control.* arXiv preprint arXiv:1208.3600, 2012.
3. Nikolakopoulou, A. and R.D. Braatz, *Polynomial NARX-based nonlinear model predictive control of modular chemical systems.* Computers & Chemical Engineering, 2023. **177**: p. 108272.
4. Krishnan, A., et al. *Model predictive control of a CSTR: A comparative study among linear and nonlinear model approaches*. in *2017 Indian Control Conference (ICC)*. 2017. IEEE.

PPC & PETROMAT SYMPOSIUM 2025

5. Shyamalagowri, M. and R. Rajeswari, *Modeling and simulation of non linear process control reactor-continuous stirred tank reactor.* International Journal of Advances in Engineering & Technology, 2013. **6**(4): p. 1813.
6. Al-Gherwi, W., H. Budman, and A. Elkamel, *A robust distributed model predictive control based on a dual-mode approach.* Computers & Chemical Engineering, 2013. **50**: p. 130-138.
7. Kouvaritakis, B. and M. Cannon, *Model predictive control.* Switzerland: Springer International Publishing, 2016. **38**(13-56): p. 7.
8. Qin, S.J. and T.A. Badgwell, *A survey of industrial model predictive control technology.* Control engineering practice, 2003. **11**(7): p. 733-764.
9. Billings, S.A., *Nonlinear system identification: NARMAX methods in the time, frequency, and spatio-temporal domains*. 2013: John Wiley & Sons.
10. Thamminaidu, V. and K. Shihabudheen. *Model predictive control (MPC) of system identified continuous stirred tank reactor (CSTR) with constraints*. in *2021 IEEE 6th International Conference on Computing, Communication and Automation (ICCCA)*. 2021. IEEE.
11. Xie, H., H. Tang, and Y.-H. Liao. *Time series prediction based on NARX neural networks: An advanced approach*. in *2009 International conference on machine learning and cybernetics*. 2009. IEEE.
12. Diaconescu, E., *The use of NARX neural networks to predict chaotic time series.* Wseas Transactions on computer research, 2008. **3**(3): p. 182-191.
13. Afram, A. and F. Janabi-Sharifi, *Theory and applications of HVAC control systems–A review of model predictive control (MPC).* Building and environment, 2014. **72**: p. 343-355.
14. Bonassi, F., et al. *An Offset-Free Nonlinear MPC scheme for systems learned by Neural NARX models*. in *2022 IEEE 61st conference on decision and control (CDC)*. 2022. IEEE.
15. Deulkar, A.M. and A.B. Patil, *Temperature control of continuous stirred tank reactor using model predictive controller.* International Journal of Industrial Electronics and Electrical Engineering, 2015. **3**.

PPC & PETROMAT SYMPOSIUM 2025

# RAPID TRACEABILITY AND AUTHENTICATION OF CRUDE PALM OIL FINGERPRINTING USING $^1$H NMR SPECTROSCOPY COMBINED WITH CHEMOMETRIC ANALYSIS

*Abdul Nggofur [a], Tawan Sooknoi[b], Ketsada Sutthiumporn [c], Natthapong Sueviriyapan [a], Siriporn Jongpatiwut* *[a],*

[a] The Petroleum and Petrochemical College, Chulalongkorn University, Bangkok, Thailand
[b] Department of Chemistry, King Mongkut's Institute of Technology Ladkrabang, Bangkok, Thailand
[c] Department of Energy Business, Ministry of Energy, Bangkok, Thailand

Keywords: chemometric analysis; crude palm oil; geographic origin; machine learning; $^1$H NMR spectroscopy

## ABSTRACT

The growing demand for Crude Palm Oil (CPO) emphasizes the need for traceability and authenticity in confirming its geographical origin to preserve product quality and support sustainable practices. A rapid method for identifying the geographical source of CPO was established using $^1$H Nuclear Magnetic Resonance ($^1$H NMR) spectroscopy coupled with chemometric analyses and machine learning (ML). Principal Component Analysis (PCA), t-distributed Stochastic Neighbor Embedding (t-SNE), and Uniform Manifold Approximation and Projection (UMAP) for dimensionality reduction and clustering were used to examine a dataset of 100 CPO samples from Thailand, Indonesia, Malaysia, and the Philippines. Random Forest (RF) evaluated Feature Importance (FI), revealing different chemical fingerprints linked to each geographic origin, while Leave-One-Out Cross-Validation (LOOCV) attained an accuracy of 98%. Compared to conventional gas chromatography (GC)-based fingerprinting, this $^1$H NMR–ML approach enables rapid, non-destructive analysis with minimal sample preparation. Advanced algorithms (such as PCA, t-SNE, UMAP, RF) efficiently extract and classify complex, non-linear patterns in high-dimensional spectra toward achieving high accuracy and robustness. The workflow is objective and scalable, reducing operator bias and enabling high-throughput verification. Collectively, these strengths ensure more reliable, efficient, and user-friendly authentication of palm oil origin and composition with potential extension to other edible oils.

*siriporn.j@chula.ac.th

PPC & PETROMAT SYMPOSIUM 2025

## INTRODUCTION

Crude palm oil (CPO), a leading type of vegetable oil globally, is the primary product derived from the oil palm industry (Phoon, et al., 2018). Oil palm is currently the highest-yielding oil crop and is extensively utilized across multiple industries, including food, confectionery, cosmetics, detergents, and biofuels (Absalome, et al., 2020). The oil palm tree thrives in tropical climates, particularly in Southeast Asia, with countries such as Malaysia, Indonesia, and Thailand serving as major cultivation regions (Rozali, et al., 2023). Thailand ranks in global palm oil production. Although the oil palm industry has been highly successful, ensuring global sustainability remains a key challenge. Current traceability systems rely heavily on documentation and digital records, which are prone to errors. Analytical tools can play a vital role in enhancing traceability and supporting more robust sustainability certification (Rozali, et al., 2023) to improve this framework.

Various analytical techniques combined with chemometric methods have been employed to trace the origin of palm oil. For example, Tres et al. used gas chromatography with flame ionization detection (GC-FID) and proton-transfer-reaction mass spectrometry PTR-MS to analyze fatty acids and volatile compounds in CPO samples from Southeast Asia, Africa, and South America, applying partial least squares discriminant Analysis (PLS-DA) for classification (Tres, et al., 2013). Meanwhile, Rozali et al. employed fourier transform infrared spectroscopy (FTIR) combined with orthogonal partial least squares discriminant analysis (OPLS-DA), to classify Malaysian CPO samples based on geographical origin and production time with high accuracy (Rozali, et al., 2023). However, these techniques are generally time-consuming and require complex operations, as they involve numerous sample preparation steps prior to analysis (Shi, et al., 2019).

Hydrogen nuclear magnetic Resonance ($^1$H NMR) offers a rapid, non-destructive approach for analyzing complex mixtures such as vegetable oils. It enables the simultaneous quantification of multiple compounds with high selectivity, repeatability, and automation, making it ideal for quality assessment (Shi, et al., 2019). To maximize its potential, it is essential to integrate advanced data analysis techniques, such as chemometrics and machine learning. These tools enhance pattern recognition, improve predictive accuracy, and reduce human error when processing complex datasets from NMR, spectroscopy, and chromatography (Joshi, 2023).

This study aimed to develop a model using $^1$H NMR data combined with chemometric analysis and machine learning techniques to classify 100 crude palm oil (CPO) samples from Indonesia (ID), Malaysia (MY), the Philippines (PH), and Thailand (TH). We hypothesize that chemometric and machine learning techniques can successfully differentiate CPO samples from different countries based on their fatty acid composition. To validate this hypothesis, chemometrics plays a key role in preprocessing and extracting meaningful information from complex spectral data, thereby enhancing the quality of the input features used by machine learning algorithms. By combining these high-quality features with supervised and unsupervised machine learning approaches, the model effectively identified patterns, preserved the data structure, and accurately predicted the geographic origin of CPO samples for reliable traceability.

PPC & PETROMAT SYMPOSIUM 2025

## EXPERIMENTAL AND ANALYTICAL APPROCAHES

*A. Samples Collection*

A total of 100 samples were collected from four countries (Thailand, Malaysia, Indonesia, and the Philippines), with 25 samples collected from each country. These samples were gathered to enable a comprehensive evaluation of the authenticity and quality of edible palm oil using advanced spectroscopic techniques.

*B. $^1$H NMR Spectroscopy*

Crude palm oil samples were prepared for $^1$H NMR analysis using a JEOL JNM-ECZ-400R/S1 spectrometer. 0.02 grams of CPO was measured into 25 individual vials using glass pipettes (Shi, et al., 2019). Another set of 25 glass pipettes was used to add 1 mL of chloroform-d ($CDCl_3$), a deuterated solvent, to each vial to ensure thorough mixing and uniform dispersion of the oil. After proper homogenization, the mixtures were transferred into 25 NMR tubes for 400 MHz analysis. Each sample was analyzed six times using the NMR spectrometer, yielding a total of 600 spectra.

*C. Chemometric Analysis*

The spectral data was extracted and saved in CSV format. Prior to dimensionality reduction, the data underwent preprocessing through scaling and normalization techniques, which standardized the features to ensure equal contribution and prevent bias from varying scales. This careful preprocessing enables dimensionality reduction methods such as PCA, UMAP, and t-SNE to capture the true underlying structure of the data more effectively (Meyer, et al., 2022), model evaluation was conducted using Leave-One-Out Cross-Validation (LOOCV), a stringent and reliable validation method (Pang, et al., 2023).

## RESULTS AND DISCUSSION

*A. $^1$H NMR Spectroscopy*

Figure 1 shows the stacked $^1$H NMR spectra of the CPO samples collected from four different countries: TH, MY, ID, PH. Each spectrum is annotated with the respective proton signals labeled A - I, which correspond to the chemical shifts described in Table 1. The spectral patterns indicate that although the chemical shift positions are consistent among all samples, the integrated peak areas vary between countries.

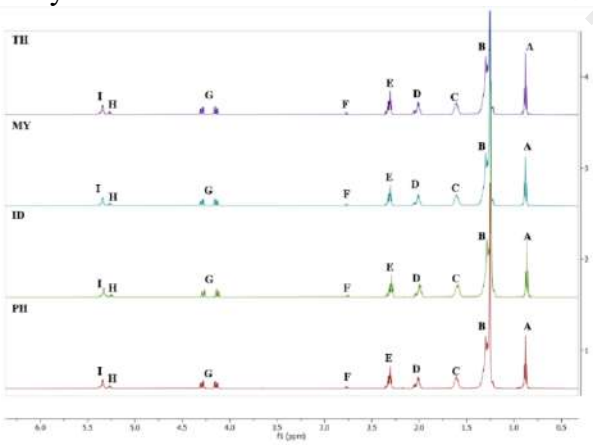


**Figure 1.** Stacked $^1$H NMR spectra of CPO samples from different country

PPC & PETROMAT SYMPOSIUM 2025

**Table 1.** Assigned $^{1}$H NMR chemical shifts.

| Signal | Chemical shift δ (ppm) | Proton | Compound |
|---|---|---|---|
| A | 0.94 .. 0.83 | –CH=CH–CH$_2$–C**H$_3$** | Terminal methyl group |
| B | 1.35 .. 1.22 | (C**H$_2$**)n | Aliphatic |
| C | 1.67 .. 1.57 | –C**H$_2$**–CH$_2$–COOH | Methylene group |
| D | 2.09 .. 1.95 | –C**H$_2$**–CH=CH– | Methylene group |
| E | 2.38 .. 2.26 | –C**H$_2$**–COOH | Methylene group to ester |
| F | 2.79 .. 2.75 | –CH=CH–C**H$_2$**–CH=CH– | Methylene group |
| G | 4.35 .. 4.01 | –C**H$_2$**–OCO–R | Glycerol (triacylglycerols) |
| H | 5.29 .. 5.23 | C**H**–OCO–R | Glycerol (triacylglycerols) |
| I | 5.42 .. 5.29 | –C**H**=C**H**– | Olefinic protons |

Because the proton environments remain consistent across all CPO samples regardless of geographic origin, the relative peak areas can be used to compare the concentrations of different functional groups. The distinction between the CPO samples is based on the variations in their integrated areas. These differences in signal intensity reflect the relative abundance of specific molecular groups, making the area under each peak a critical parameter for compositional analysis. The integrated area of the $^{1}$H NMR signals is directly proportional to both the number of hydrogen atoms in each functional group and their relative abundance, enabling accurate and data-driven differentiation between the samples.

*B. Chemometric Analysis*

Principal component analysis (PCA) is one of the most used linear techniques for unsupervised dimensionality reduction. It aims to retain the global Euclidean structure of high-dimensional data by capturing the directions of the greatest variance from the $^{1}$H NMR data. Figure 2(a) illustrates how PCA assumes that the data have a linear structure, which may not accurately reflect the true underlying structure when the data follow a nonlinear distribution. This assumption can limit ability of PCA to reveal complex patterns in the dataset. To overcome this constraint, nonlinear techniques such as t-distributed stochastic neighbor embeddings (t-SNE) have been developed to better preserve local patterns, particularly in complex datasets such as those encountered in hyperspectral or spectroscopic analyses (Silva andMelo-Pinto, 2023). Figure 2(b) displays the t-SNE result, which captures local relationships more effectively, although it may compromise the global structure and underperform in scenarios where clear class separation or interpretability is required.

PPC & PETROMAT SYMPOSIUM 2025

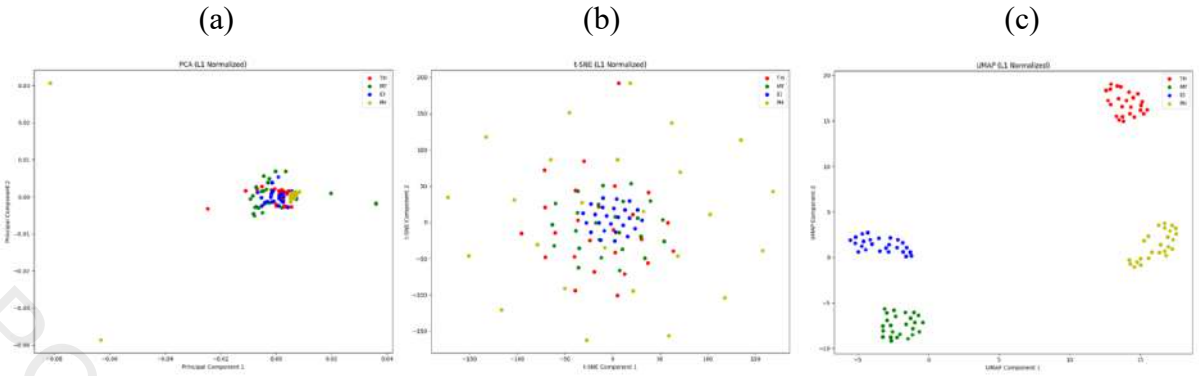


**Figure. 2** Scatter Plot of **(a)** PCA and, **(b)** t-SNE and **(c)** UMAP of CPO from available samples

In response to these challenges, uniform manifold approximation and projection (UMAP) has emerged as a robust alternative. UMAP is designed to maintain both global and local data structures while efficiently handling non-linear manifolds. When applied as an unsupervised dimensionality reduction technique, UMAP successfully separated four distinct clusters corresponding to CPO samples from TH, MY, ID, and TH, as illustrated in Figure 2(c). To assess the discriminative value of these clusters, a classification analysis was conducted, the results of which are summarized in Table 2, presenting the performance of a Random Forest model trained on the original normalized features. The classification was performed using Leave-One-Out Cross-Validation (LOOCV), demonstrating the robustness of the pipeline and achieving an overall classification accuracy of 95%.

**Table 2.** Performance metrics of Random Forest classifier using Leave-One-Out Cross-Validation (LOOCV)

| Label | precision | recall | f1-score | support |
|---|---|---|---|---|
| TH | 1.00 | 0.88 | 0.94 | 25 |
| MY | 1.00 | 0.96 | 0.98 | 25 |
| ID | 0.96 | 1.00 | 0.98 | 25 |
| PH | 0.86 | 0.96 | 0.91 | 25 |
| Accuracy | | | 0.95 | 100 |

## CONCLUSIONS

This study demonstrates the effectiveness of combining $^{1}$H NMR spectroscopy, chemometric analysis, and machine learning to classify CPO samples according to their geographic origin. By applying normalization and scaling techniques prior to dimensionality reduction, meaningful structural patterns in the data were maintained. UMAP was used as an unsupervised technique to reduce data dimensionality, followed by Random Forest as a supervised classification model. The pipeline was rigorously evaluated LOOCV, achieving 95% accuracy with high precision, recall, and f1-score across all classes. These findings highlight the potential of integrating spectral data and machine learning for the high-resolution authentication and traceability of crude palm oil based on its geographic origin.

PPC & PETROMAT SYMPOSIUM 2025

## ACKNOWLEDGEMENTS

The authors gratefully acknowledge the ASEAN/Non-ASEAN scholarship, Chulalongkorn University, and the Department of Energy Business, Ministry of Energy, for their financial support. Appreciation is extended to PT. Sinar Mas Agro Resources and Technology Tbk (PT SMART Tbk), PT. Harapan Sawit Cemerlang, Pathum Vegetable Oil Co., Ltd., and PPP Green Complex Public Co., Ltd., Agumil Philippines, INC., Univanich Inc., Sime Darby Oils Langat Refinery Sdn Bhd for providing the CPO samples.

## REFERENCES

Absalome, M. A., Massara, C.-C., Alexandre, A. A., Gervais, K., Chantal, G. G.-A., Ferdinand, D., Rhedoor, A. J., Coulibaly, I., George, T. G., Brigitte, T., Marion, M. and Jean-Paul, C. (2020). Biochemical properties, nutritional values, health benefits and sustainability of palm oil. *Biochimie*, *178*, 81-95. https://doi.org/https://doi.org/10.1016/j.biochi.2020.09.019

Joshi, P. B. (2023). Navigating with chemometrics and machine learning in chemistry. *Artif Intell Rev*, 1-26. https://doi.org/10.1007/s10462-023-10391-w

Meyer, B. H., Pozo, A. T. R. and Nunan Zola, W. M. (2022). Global and local structure preserving GPU t-SNE methods for large-scale applications. *Expert Systems with Applications*, *201*, 116918. https://doi.org/https://doi.org/10.1016/j.eswa.2022.116918

Pang, Y., Wang, Y., Lai, X., Zhang, S., Liang, P. and Song, X. (2023). Enhanced Kriging leave-one-out cross-validation in improving model estimation and optimization. *Computer Methods in Applied Mechanics and Engineering*, *414*, 116194. https://doi.org/https://doi.org/10.1016/j.cma.2023.116194

Phoon, K. Y., Ng, H. S., Zakaria, R., Yim, H. S. and Mokhtar, M. N. (2018). Enrichment of minor components from crude palm oil and palm-pressed mesocarp fibre oil via sequential adsorption-desorption strategy. *Industrial Crops and Products*, *113*, 187-195. https://doi.org/https://doi.org/10.1016/j.indcrop.2018.01.039

Rozali, N. L., Azizan, K. A., Singh, R., Syed Jaafar, S. N., Othman, A., Weckwerth, W. and Ramli, U. S. (2023). Fourier transform infrared (FTIR) spectroscopy approach combined with discriminant analysis and prediction model for crude palm oil authentication of different geographical and temporal origins. *Food Control*, *146*, 109509. https://doi.org/https://doi.org/10.1016/j.foodcont.2022.109509

Shi, T., Zhu, M., Zhou, X., Huo, X., Long, Y., Zeng, X. and Chen, Y. (2019). 1H NMR combined with PLS for the rapid determination of squalene and sterols in vegetable oils. *Food Chemistry*, *287*, 46-54. https://doi.org/https://doi.org/10.1016/j.foodchem.2019.02.072

Silva, R. and Melo-Pinto, P. (2023). t-SNE: A study on reducing the dimensionality of hyperspectral data for the regression problem of estimating oenological parameters. *Artificial Intelligence in Agriculture*, *7*, 58-68. https://doi.org/https://doi.org/10.1016/j.aiia.2023.02.003

Tres, A., Ruiz-Samblas, C., van der Veer, G. and van Ruth, S. M. (2013). Geographical provenance of palm oil by fatty acid and volatile compound fingerprinting techniques. *Food Chemistry*, *137*(1), 142-150. https://doi.org/https://doi.org/10.1016/j.foodchem.2012.09.094

PPC & PETROMAT SYMPOSIUM 2025

# Optimized Machine Learning Approach for Prediction of Characteristic Curvature (Cc) of Ionic Surfactants using Molecular Descriptors

*Affan Dulyadech*[a], *Natthapong Sueviriyapan*[a], *Uthaiporn Suriyapraphadilok*[a], *Ampira Charoensaeng*[a,*]

[a]*The Petroleum and Petrochemical College, Chulalongkorn University*

Keywords: Characteristic curvature, Machine Learning, SHAP, Surfactant

## ABSTRACT

Microemulsion phase behavior can be predicted using the hydrophilic-lipophilic deviation concept, with characteristic curvature (Cc) as a key parameter that reflects the balance between hydrophilicity and lipophilicity. Conventional Cc determination is time-consuming and hardly scalable. To address this challenge, a proof-of-concept machine learning framework was developed, surpassing traditional methods due to its potential to capture nonlinear relationships between 2D molecular descriptors and provide insights into feature importance through interpretability tools. A curated dataset (31 anionic surfactants) was compiled from the literature, with initial testing focused on a single surfactant system. To ameliorate the limited sample size, rigorous statistical validation was implemented, including k-fold cross-validation and bootstrap resampling, to ensure model robustness. Molecular descriptors were generated using RDKit, followed by systematic feature selection to prevent overfitting. Several regression models were evaluated, with tree-based models outperforming linear approaches. The Gradient Boosting Regressor achieved optimal performance ($R^2 = 0.74$, RMSE = 0.40, MAE = 0.35) on the tested set. The SHAP analysis identified topological and electronic descriptors as most predictive of Cc values. Despite sample size constraints, cross-validation confirms statistical validity with future expansion to larger available datasets and diverse surfactant classes expected to enhance model generalizability. This methodology enables rapid, interpretable, and scalable predictions, supporting the efficient formulation of microemulsions.

***ampira.c@chula.ac.th**

## INTRODUCTION

Microemulsions are well-known thermodynamically isotropic stable systems consisting of surfactant and with/without cosurfactant(s), water, and oil, which form spontaneously under specific conditions (Salager et al., 2005). Microemulsions are characterized by their small droplet size, ultralow interfacial tension, and high solubilization capacity, making them invaluable in various industrial applications (Salager et al., 2005). Winsor (Winsor, 1948) classifies microemulsions into four types (Winsor I-IV) based on the balance of phases. Furthermore, the Hydrophilic-Lipophilic Deviation (HLD) equation offers a more quantitative approach, enabling precise predictions of phase transitions. One critical variable in the HLD equation is the surfactant characteristic curvature (Cc), which reflects the balance between the hydrophilic and lipophilic portions of the molecule (Leng & Acosta, 2023). Various experimental methods have been employed to measure Cc. However, these methods have several limitations, including limited accuracy, time consumption, and the requirement for specialized equipment (Lemahieu *et al.*,

PPC & PETROMAT SYMPOSIUM 2025

2022; Sheng, 2011). Recent advancements in machine learning (ML) offer a promising alternative to overcome these limitations. By integrating molecular descriptors with quantitative representations of molecular structures, ML algorithms can accurately and efficiently predict Cc values, which is comparable to experimental methods. The use of ML in combination with molecular descriptors can improve prediction accuracy and enable the discovery of complex, non-linear relationships that are difficult to identify using conventional approaches (Seddon et al., 2022). This study proposes the development of ML models for predicting the Cc values of surfactants using molecular descriptors from the RDKit library by leveraging techniques such as normalization and transformation, feature selection, and hyperparameter tuning. Finally, to provide transparent, chemically interpretable feature importances, the Shapley Additive exPlanations (SHAP) method was applied. This study aimed to optimize the model for robust predictions and an interpretable model. Ultimately, this approach can lead to results that confirm the applicability of ML in predicting surfactant Cc values, thereby enhancing the prediction of microemulsion behavior and improving the design and optimization of the formulations for industrial applications.

## METHODS

A. Data Preparation and Preprocessing

The Cc values and molecular structures of 31 anionic surfactants were extracted from the literature (Chen *et al.*, 2022; Lemahieu *et al.*, 2022; Leng & Acosta, 2023; Witthayapanyanon *et al.*, 2008). The structural formulas were redrawn in ChemDraw, exported as canonical SMILES, and processed in a Python/RDKit pipeline within VS Code. Each SMILES underwent a round-trip consistency check (SMILES → Mol → canonical SMILES), and records failing the check or duplicating an existing entry were discarded. Subsequently, the target data distribution was explored. RDKit then generated a full suite of 2-D descriptors.

Feature selection proceeded in two stages: descriptors with zero or near-zero variance (threshold = 0) were excised and for any pair displaying |Pearson r| > 0.80, the descriptor less correlated with Cc was removed, retaining the descriptor more strongly correlated with Cc. The remaining descriptors were rescaled and placed on a common scale for subsequent modeling. From the data distribution results, we decided to stabilize and correct the skew of the variable (Cc) using a Yeo-Johnson power transformation (Riani *et al.*, 2023). This workflow ultimately yields a compact, informative, and statistically well-behaved descriptor matrix suitable for the robust prediction of surfactant Cc values.

B. Machine Learning Benchmark

Three linear regressors (Ordinary Least Squares, Lasso, and Elastic Net) and four tree-based models (Decision Tree, Random Forest, Gradient Boosting Regressor (GBR), and XGBoost) were benchmarked on z-standardized descriptors. At the same time, Cc remained on its original scale. A stratified 20 % holdout set provided preliminary $R^2$ scores to identify promising

PROCEEDINGS PETROMAT SYMPOSIUM 2025

algorithm families. Their test $R^2$ values were used to determine the most promising algorithm family for further optimization.

C. Model Optimization

Model optimization was performed as follows:

Step 1: Scaling protocol: We compared four different methods of data scaling: (1) StandardScaler for features with non-transformed target variables, and (2) StandardScaler for features with transformed target variables, (3) RobustScaler for features with non-transformed target variables, and (4) RobustScaler for features with transformed target variables.

Step 2: Hyperparameter tuning: For every algorithm and scaling combination, a grid search was conducted inside a nested cross-validation framework (inner grid search, outer 5- and 10-fold splits) to obtain an unbiased estimate of the generalization error despite the limited sample size.

Step 3: Selection of the optimal pipeline: All optimized models across various scaling methods and two types of k-fold were compared to identify the best approach for model optimization. We will directly compare the model's performance (as measured by validation and test $R^2$) to select the one with the highest performance.

Step 4: Final model selection: All fine-tuned algorithms with the best optimization approach were compared again in this step, as in Step 3. The best model was selected by comparing its performance (as measured by Test $R^2$).

D. Model Evaluation and Analysis

Performance Matrix Analysis

The performance of the final model was evaluated using three complementary metrics: the coefficient of determination ($R^2$), root-mean-square error (RMSE), and mean absolute error (MAE), to capture both the proportion of explained variance and absolute prediction accuracy.

SHAP Analysis

Model interpretability employed SHAP.

1. Feature importance: mean |SHAP| bar plot ranking descriptors.
2. Global feature effect: beeswarm plot overlaid with individual SHAP values to reveal directionality.
3. Local feature effect: Waterfall plots decompose extreme predictions, illuminating how each feature affects individual data points.

**RESULTS AND DISCUSSION**

Following the given preprocessing and optimization, Figure 1 displays the model performance results of the GBR with 10-fold cross-validation across various scaling methods. From the results, the pipeline that paired robust scaled descriptors with a Yeo-Johnson transformed target and a GBR regressor validated by 10-fold nested cross-validation emerged as the most reliable (outer-fold $R^2 = 0.72$). The nested grid search converged on a deliberately

PPC & PETROMAT SYMPOSIUM 2025

conservative hyperparameter set: n_estimators = 1,200, learning_rate = 0.02, max_depth = 3, min_sample_leaf = 5, subsample = 0.8, and max_feature = sqrt, to balance the expressive power against the risk of overfitting a 31-compound dataset. The resulting model reproduces the training data almost perfectly ($R^2$ = 0.97, RMSE = 0.21, MAE = 0.11) and explains three-quarters of the variance in the stratified 20 % hold-out set ($R^2$ = 0.74, RMSE = 0.40, MAE = 0.35).

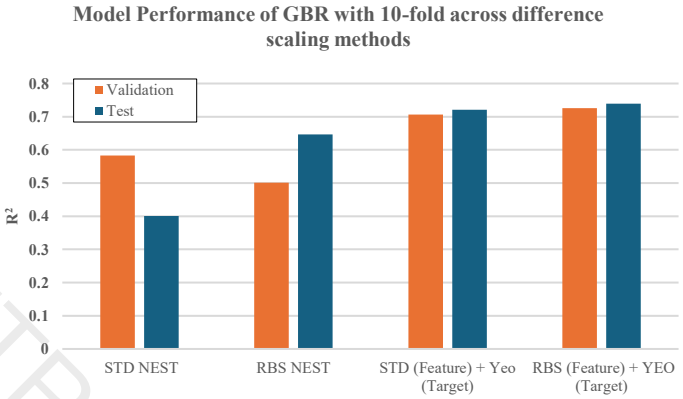


**Figure 1.** Model Performance of GBR with 10-fold cross-validation across different scaling methods

Figure 2 visualizes this performance, with blue circles (training) and green circles (test) clustering tightly around the red line (ideal prediction). Only a handful of larger test residuals are attributable to branched or highly substituted surfactants that are underrepresented in the training pool. The modest generalization gap (test-to-train RMSE ratio of approximately 1.9) is, therefore, consistent with the small-sample regime. It indicates that the final model captures the dominant nonlinear structure-property relationships governing the characteristic curvature (Boukelkal *et al.*, 2024; Chowdhury *et al.*, 2021). These results show promising potential for developing a predictive framework for surfactant Cc prediction.

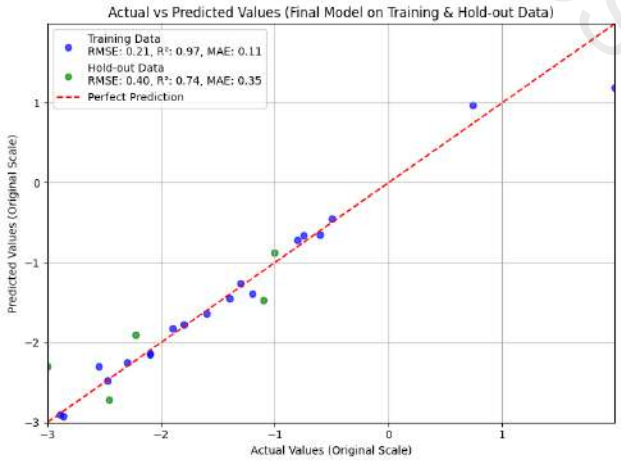


**Figure 2:** The model prediction result. The blue points represent the training data, while the green points represent the testing data.

PPC & PETROMAT SYMPOSIUM 2025

Additionally, SHAP analysis was used to unpack the “black box” and identify the molecular descriptors that drive GBR predictions. Figure 3 ranks the features by their mean |SHAP| value, that is, their average absolute impact on the output across all molecules (Boukelkal *et al.*, 2024). The molecular weight (MolWt) dominates, underscoring the intuitive link between surfactant size, particularly tail length, and curvature preference: heavier, longer-tailed anionics generally push the microemulsion toward more negative Cc values. Two BCUT terms follow: BCUT2D_MRLOW, which reflects low-eigenvalue Burden coefficients weighted by molar refractivity (a proxy for polarizability and volume), and BCUT2D_MWLOW, the analogous mass-weighted index. Their prominence suggests that the dispersive volume and mass distribution influence the ease with which the tail region accommodates curved interfaces. Hall-Kier α (branching index) and MaxAbsEStateIndex (largest absolute electrotopological state) appear next, showing that branching and extreme localized charges fine-tune the balance between head-group hydration and tail packing. Lower-ranked but still influential variables, MinAbsEStateIndex, PEOE_VSA6 (partial-charge surface area bin), SMR_VSA4 (log P surface area bin), Ipc (information content), and EState_VSA4, capture subtler aspects of the electronic distribution and hydrophobic surface topology . These descriptors explain how the size and shape (geometric terms) and charge distribution (electronic terms) work in concert to dictate the characteristic curvature, offering chemically interpretable levers for rational surfactant design.

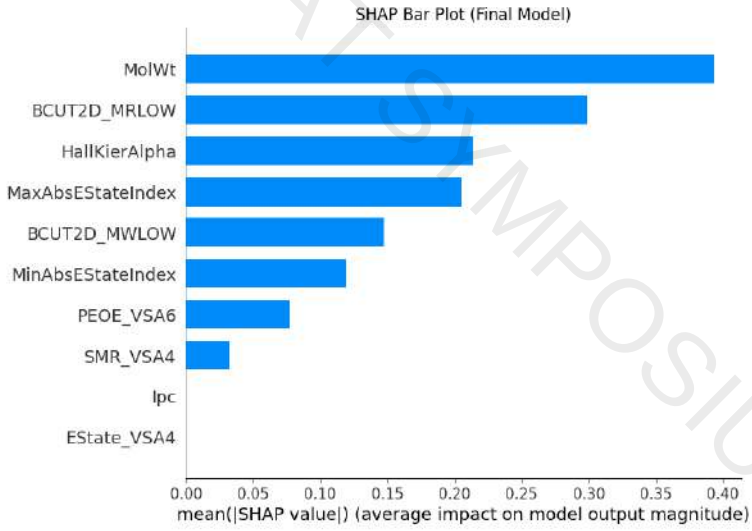


**Figure 3.** The mean absolute SHAP values for the rank descriptors in our final model.

## CONCLUSION

This study establishes a proof-of-concept, data-driven workflow for predicting the Cc of ionic surfactants directly from readily calculated 2-D molecular descriptors. A carefully curated set of 31 anionic surfactants, stringent descriptor selection, and nested cross-validation helped extract the maximum signal from a small but chemically diverse dataset. The final GBR model, trained on robust-scaled descriptors and a Yeo-Johnson transformed target, explained 97% of the

PPC & PETROMAT SYMPOSIUM 2025

variance in the training partition and 74% in an external hold-out set, with a sub-unit RMSE. SHAP interrogation confirmed that intuitive size- and polarity-related descriptors (MolWt, BCUT indices, Hall-Kier branching, and extreme E-state values) dominated the prediction, providing chemically interpretable levers for future surfactant design. Despite the modest sample size, the study demonstrates that ML can reliably learn the nonlinear structure-property relationships governing Cc, and, in doing so, lays the groundwork for rapid virtual screening and rational surfactant design as larger, multi-class datasets become available. Future work should expand the dataset to include additional surfactant classes and incorporate three-dimensional descriptors to enhance predictive power and mechanistic insight further.

## ACKNOWLEDGEMENTS

The author would like to thank the Petroleum and Petrochemical College, Chulalongkorn University for the full scholarship. This research supported by The development of environmentally corrosion inhibitors for sustainable industrial development. (Fundamental Fund, DISF67630021) Chulalongkorn University.

## REFERENCES

Boukelkal, N., Rahal, S., Rebhi, R., & Hamadache, M. (2024). QSPR for the prediction of critical micelle concentration of different classes of surfactants using machine learning algorithms. Journal of Molecular Graphics and Modelling, 129, 108757. https://doi.org/https://doi.org/10.1016/j.jmgm.2024.108757

Chen, C., Shen, H., Harwell, J. H., & Shiau, B.-J. (2022). Characterizing oil mixture and surfactant mixture via hydrophilic-lipophilic deviation (HLD) principle: An insight in consumer products development. Colloids and Surfaces A: Physicochemical and Engineering Aspects, 634, 127599. https://doi.org/https://doi.org/10.1016/j.colsurfa.2021.127599

Chowdhury, S., Lin, Y., Liaw, B. Y., & Kerby, L. (2021). Evaluation of Tree Based Regression over Multiple Linear Regression for Non-normally Distributed Data in Battery Performance. https://doi.org/10.48550/arXiv.2111.02513

Lemahieu, G., Ontiveros, J. F., Gaudin, T., Molinier, V., & Aubry, J.-M. (2022). The Salinity-Phase-Inversion method (SPI-slope): A straightforward experimental approach to assess the hydrophilic-lipophilic-ratio and the salt-sensitivity of surfactants. Journal of Colloid and Interface Science, 608, 549-563. https://doi.org/https://doi.org/10.1016/j.jcis.2021.09.155

Leng, Z., & Acosta, E. (2023). The characteristic curvature (Cc) definition and its use in assessing Cc for single ionic surfactants. Journal of Surfactants and Detergents, 26(3), 287-301. https://doi.org/https://doi.org/10.1002/jsde.12653

Riani, M., Atkinson, A. C., & Corbellini, A. (2023). Automatic robust Box–Cox and extended Yeo–Johnson transformations in regression. Statistical Methods & Applications, 32(1), 75-102. https://doi.org/10.1007/s10260-022-00640-7

Salager, J.-L., Antón, R., Sabatini, D., Harwell, J., Acosta, E., & Tolosa, L. (2005). Enhancing solubilization in microemulsions—State of the art and current trends. Journal of Surfactants and Detergents, 8, 3-21. https://doi.org/10.1007/s11743-005-0328-4

Seddon, D., Müller, E. A., & Cabral, J. T. (2022). Machine learning hybrid approach for the prediction of surface tension profiles of hydrocarbon surfactants in aqueous solution. Journal of

PPC & PETROMAT SYMPOSIUM 2025

Colloid and Interface Science, 625, 328-339. https://doi.org/https://doi.org/10.1016/j.jcis.2022.06.034
Sheng, J. J. (2011). Chapter 7 - Surfactant Flooding. In J. J. Sheng (Ed.), Modern Chemical Enhanced Oil Recovery (pp. 239-335). Gulf Professional Publishing. https://doi.org/https://doi.org/10.1016/B978-1-85617-745-0.00007-3
Winsor, P. A. (1948). Hydrotropy, solubilisation and related emulsification processes. Transactions of The Faraday Society, 44, 376-398.
Witthayapanyanon, A., Harwell, J. H., & Sabatini, D. A. (2008). Hydrophilic–lipophilic deviation (HLD) method for characterizing conventional and extended surfactants. Journal of Colloid and Interface Science, 325(1), 259-266. https://doi.org/https://doi.org/10.1016/j.jcis.2008.05.061

PPC & PETROMAT SYMPOSIUM 2025

# Session 2-Cutting-Edge Catalysis (CA)

# NOVEL SYNTHESES OF $SrTiO_3/g\text{-}C_3N_4$ PHOTOCATALYSTS FOR ENHANCED PHOTOCATALYTIC HYDROGEN EVOLUTION

*Chiremet Thatsanakunlaphan*[a], *Akawat Sirisuk*[*,a,b]

[a] Center of Excellence on Catalysis and Catalytic Reaction Engineering, Department of Chemical Engineering, Faculty of Engineering, Chulalongkorn University, Bangkok, 10330, Thailand
[b] Bio-Circular-Green economy Technology & Engineering Center, Department of Chemical Engineering, Faculty of Engineering, Chulalongkorn University, Bangkok, 10330, Thailand

Keywords: Photocatalysis; Hydrogen evolution; Strontium titanate; Graphitic carbon nitride; Heterostructure

## ABSTRACT

The strontium titanate/graphitic carbon nitride ($SrTiO_3/g\text{-}C_3N_4$, STO/CN) composites have been widely used as photocatalysts in the hydrogen evolution system. The traditional multi-step synthesis process of these photocatalysts provides the complications, such as consuming operational time and energy. To address this issue, two different simple techniques have been comparatively investigated, namely, the one-pot hydrothermal synthesis and the two-step process. The one-pot hydrothermal synthesis uses urea and melamine as the precursors to produce $g\text{-}C_3N_4$ (CN) and also uses titanium (IV) n-butoxide (TBOT) and strontium nitrate ($Sr(NO_3)_2$) as the precursors for $SrTiO_3$ (STO), leading to CN-decorated STO. On the other hand, the two-step process first synthesizes urea and melamine as CN via a thermal polymerization process, followed by the hydrothermal treatment of TBOT and $Sr(NO_3)_2$ onto the CN surface. All synthesized catalysts are characterized using scanning electron microscopy (SEM), X-ray diffraction (XRD), photoluminescence (PL) spectroscopy, and UV-Vis diffuse reflectance spectroscopy (UV-Vis DRS). Both methods facilitate strong interfacial contact between CN and STO and reduce electron-hole pair recombination. Compared to the conventional synthesis method, these methods are not only faster but also more environmentally friendly and cost-effective, making them highly attractive for scalable production while improving photocatalytic performance. As a result, the STO/CN-2 composites synthesized by the two-step method demonstrated the highest hydrogen evolution efficiency, reaching 721 μmol/g under visible light irradiation. These findings highlight the advantages of simpler synthesis methods for producing efficient photocatalysts available for further solar-driven hydrogen production.

***akawat.s@chula.ac.th**

## INTRODUCTION

In recent years, sustainable energy has been increasingly developed to address global concerns about climate change and the limited availability of fossil fuel resources (Ghoniem, 2011). Hydrogen energy has become a promising substitute due to its high energy density and zero carbon emission when derived from renewable sources. Among effective production methods, photocatalytic water splitting using solar energy stands out for its potential in sustainable and eco-friendly hydrogen generation (Hisatomi, T.; Kubota, J.; Domen, K., 2014). In this process, strontium titanate ($SrTiO_3$, STO) serves as a photocatalyst under UV light irradiation. However, the limited visible light absorption and rapid charge recombination reduce its photocatalytic efficiency (Mu, L., et al., 2016). To improve the

PPC & PETROMAT SYMPOSIUM 2025

photocatalytic properties of this material, a development of its composite with graphitic carbon nitride (g-$C_3N_4$, CN) is considered. This composite material offers some significant advantages such as a performing the photocatalytic reaction under visible light and possessing excellent thermal and chemical stabilities. Therefore, synthesizing CN with STO to form a composite photocatalyst is beneficial to improve thermal and chemical stabilities, solar light absorption, and encourage charge separation, leading to higher photocatalytic hydrogen production efficiency.

Typically, the traditional synthesis process of $SrTiO_3$/ g-$C_3N_4$ (STO/CN) composite is complicated due to the multi-step requirement (Xiao, F.; et al., 2020 and Ferreira, M. A.; et al., 2020). To provide novel synthesis methods, this study aims to comparatively study the utilization of two different simple techniques, including the one-pot solvothermal synthesis and the two-step process. The resulting materials from these techniques were characterized via scanning electron microscopy (SEM), X-ray diffraction (XRD), photoluminescence (PL) spectroscopy, and UV-Vis diffuse reflectance spectroscopy (UV-Vis DRS). This research will contribute to the advantages of simpler synthesis methods for producing efficient photocatalysts available for solar hydrogen production.

## EXPERIMENTAL

### *A. Chemicals*

All reagents were obtained from commercial suppliers. Strontium nitrate ($Sr(NO_3)_2$, 99.99%), triethanolamine (TEOA, $N(CH_2CH_2OH)_3$, 99%), and ethylene glycol ($C_2H_6O_2$, 99.5%) were purchased from Sigma-Aldrich Co. LLC (USA). Titanium(IV) n-butoxide (TBOT, $C_{16}H_{36}O_4Ti$, >99.0%), melamine ($C_6H_6N_6$, 99%), and urea ($CO(NH_2)_2$, 99.5%) were obtained from Thermo Fisher Scientific Inc. (UK). Ethanol absolute ($C_2H_6O$, 99.9%), methanol ($CH_3OH$, 99.9%), and sodium hydroxide (NaOH, 99%) were supplied by QReC (New Zealand). All experiments were performed with deionized water.

### *B. Synthesis of STO/CN composites by the one-pot solvothermal method*

In the one-pot solvothermal method, 4.28 g of urea was first dissolved in 45 mL of ethylene glycol and stirred until the homogeneous solution was received. Then, 3 g of melamine was added and stirred for 10 min, followed by 1.71 mL of TBOT. After that, 10 mL of 0.5 M $Sr(NO_3)_2$ solution was added dropwise, followed by 5 mL of 5 M NaOH solution. The mixture was stirred for 1 h, then transferred to an autoclave and heated at 180 °C for 24 h. After cooling to room temperature, the product was collected by vacuum filtration, washed with deionized water and ethanol until the pH was neutral, and dried at 60 °C for 12 h to obtain STO/CN powder. The samples were labeled STO/CN-1.

### *C. Synthesis of STO/CN composites by the two-step process*

In a two-step process, the first step involved thermal polycondensation to prepare CN. 4.28 g of urea and 3 g of melamine were thoroughly mixed, placed in a covered crucible, and calcined in a muffle furnace at 550 °C for 4 h with a heating rate of 2 °C/min. After cooling,

PPC & PETROMAT SYMPOSIUM 2025

yellow CN powder was obtained. The second step used the solvothermal method to decorate STO on the surface of CN. Here, 1.71 mL of TBOT was dissolved in 45 mL of ethylene glycol while stirring. Then, 0.3 g of the prepared CN powder was dispersed into the TBOT solution. Next, 10 mL of 0.5 M $Sr(NO_3)_2$ solution was added dropwise, followed by 5 mL of 5 M NaOH solution. The mixture was stirred for 1 h before being transferred to an autoclave and heated at 180 °C for 24 h. After cooling to room temperature, the product was collected by vacuum filtration, washed with deionized water and ethanol until the pH was neutral, and dried at 60 °C for 12 h to yield the STO/CN powder. The final products were named STO/CN-2.

*D. Synthesis of STO/CN composites by the conventional multi-step process*

The STO/CN composites were prepared through a multi-step process (Kong, C.; et al., 2022). First, CN nanosheets were synthesized by a thermal condensation polymerization method. 4.28 g of urea and 3 g of melamine were placed in a covered crucible and heated in a muffle furnace at 550 °C for 4 h with a heating rate of 2 °C/min to obtain bulk CN powder. This bulk powder was then further heated at 500 °C for 2 h at a rate of 5 °C/min to produce CN nanosheets. Next, STO was synthesized by the solvothermal method. In this step, 1.71 mL of TBOT was dissolved in 45 mL of ethylene glycol under constant stirring. Then, 10 mL of 0.5 M $Sr(NO_3)_2$ solution was added slowly, followed by 5 mL of 5 M NaOH. The mixture was stirred for 1 h, transferred to an autoclave, and heated at 180 °C for 24 h. After the reaction, the product was washed with deionized water and ethanol until the pH was neutral, dried at 60 °C for 12 h, and ground into STO powder. In the final step, STO/CN composites were formed via a two-step self-assembly method. 0.3 g of CN nanosheets were dispersed in 50 mL of methanol and sonicated for 1 h. Then, 0.7 g of STO powder was added, then sonicated for 30 min and stirred for 12 h. The resulting mixture was dried at 60 °C for 12 h and ground into powder. Finally, this powder was calcined at 400 °C for 1 h with a heating rate of 3 °C/min and ground again to obtain the final STO/CN-BM composite, which served as a benchmark for comparison with other synthesis methods used in this study.

*E. Photocatalyst characterization*

The morphology was determined by SEM. The crystal structures and phase compositions were analyzed using XRD with Cu Kα radiation (λ = 1.5406 Å) operated at 45 kV and 30 mA. The diffraction patterns were recorded in the 2θ range of 10 to 80°. The optical absorbance and band gap energy were investigated using UV-Vis DRS with a wavelength range of 200 to 800 nm. The band gap energy was estimated from the Tauc plot. PL spectra were recorded at room temperature using fluorescence spectroscopy with an excitation wavelength of 300 nm to investigate the charge carrier recombination behavior of the samples.

*F. Photocatalytic hydrogen evolution*

Photocatalytic hydrogen evolution was conducted in a submersion-type reactor. For each experiment, 0.5 g/L of photocatalyst was dispersed in 500 mL of an aqueous solution containing 10 vol% triethanolamine (TEOA) as a sacrificial agent. The suspension was stirred and purged with nitrogen gas for 1 h to remove air. The reaction system was

PPC & PETROMAT SYMPOSIUM 2025

illuminated for 4 h using a 250 W visible light source. The gas samples from the reactor headspace were collected every 30 min and analyzed using gas chromatography with a thermal conductivity detector.

## RESULTS AND DISCUSSION

### *A. Morphological analysis*

The morphologies of the synthesized photocatalysts were characterized using SEM. In Figure 1(a), STO/CN-1 showed a rod-like and rough structure, while STO/CN-2 exhibited a more uniform and compact aggregation, indicating better interfacial contact, as shown in Figure 1(b). In contrast, STO/CN-BM presented spherical and less aggregated particles, suggesting weaker interaction between STO and CN, as shown in Figure 1(c). The morphology of STO/CN-2 was expected to facilitate more efficient charge separation and photocatalytic activity.

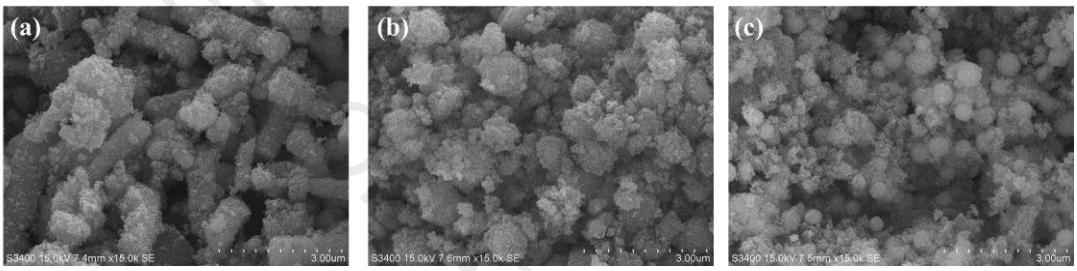


**Figure 1** SEM images of (a) STO/CN-1, (b) STO/CN-2, and (c) STO/CN-BM composites.

### *B. Crystalline structure*

The crystal structure of the synthesized photocatalysts was characterized using XRD, as shown in Figure 2. All samples exhibited diffraction patterns corresponding to the cubic perovskite structure of $SrTiO_3$ (JCPDS No. 35-0734), confirming the successful crystallization of STO in all cases. In addition, additional diffraction peaks matching those of $SrCO_3$ (JCPDS No. 05-0418) were observed, indicating the presence of residual $SrCO_3$ after the synthesis process. The diffraction peaks of g-$C_3N_4$ (JCPDS No. 87-1526) were also detected in all samples, suggesting potential dispersion and interaction of CN on STO surface.

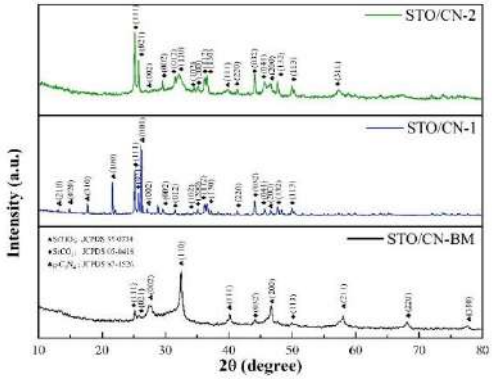


**Figure 2** XRD patterns of various synthesized photocatalysts.

PROCEEDINGS OF PPC & PETROMAT SYMPOSIUM 2025

*C. Optical properties*

The optical properties of the synthesized photocatalysts were analyzed using UV-Vis DRS and band gap energies, as presented in Figures 3(a) and 3(b), respectively. In Figure 3(a), all samples exhibited absorption in the visible region. STO/CN-BM showed an absorption edge approximately 414 nm, while STO/CN-1 and STO/CN-2 displayed absorption edges at approximately 473 nm and 480 nm, respectively. These right shifts indicated enhanced visible-light absorption due to the incorporation of CN on STO. Regarding these shifts, the estimated band gap energies from the Tauc plots in Figure 3(b) were 2.96 eV, 2.49 eV, and 2.45 eV for STO/CN-BM, STO/CN-1, and STO/CN-2, respectively. The reduced band gaps in STO/CN-1 and STO/CN-2 confirmed the successful formation of heterojunctions between STO and CN, enabling more efficient absorption of visible light and potentially enhancing the photocatalytic activity under solar irradiation.

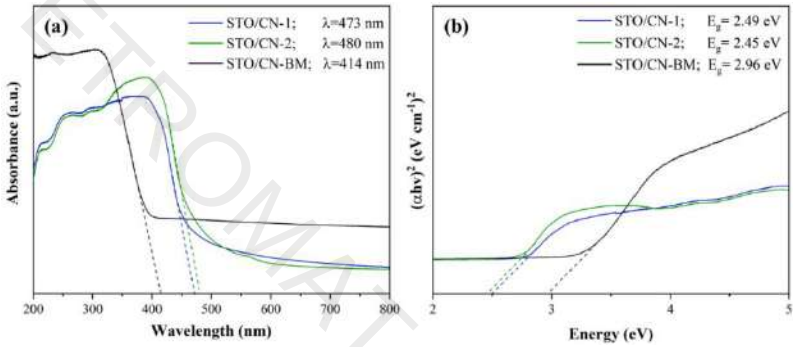


**Figure 3** UV-Vis spectra (a) and band gap energies (b) of various synthesized photocatalysts.

The PL spectra of the synthesized photocatalysts are presented in Figure 4. Among the three samples, STO/CN-BM exhibited the highest PL intensity, suggesting a higher recombination rate of charge carriers. In contrast, the STO/CN-1 and STO/CN-2 samples showed significantly lower PL intensities, suggesting more efficient charge separation and reduced recombination. In particular, STO/CN-2 displayed the lowest PL intensity, implying the most effective suppression of electron-hole recombination among these samples. These results suggested that the formation of a heterojunction between STO and CN effectively enhanced charge carrier separation, which could contribute to improved photocatalytic activity.

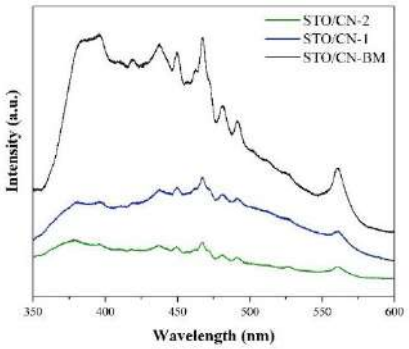


**Figure 4** PL spectra of various synthesized photocatalysts.

PPC & PETROMAT SYMPOSIUM 2025

*D. Photocatalytic hydrogen performance*

The photocatalytic hydrogen evolution shown in Figure 5 indicates the photocatalytic efficiency of various STO/CN composites. STO/CN-2 exhibited the highest hydrogen evolution of 721 μmol/g. In contrast, STO/CN-1 and STO/CN-BM showed the hydrogen evolution of 454 and 218 μmol/g, respectively. These results suggested that the synthesis process used for STO/CN-2 was the most effective in enhancing photocatalytic activity, likely due to improved charge separation and better interfacial contact between STO and CN.

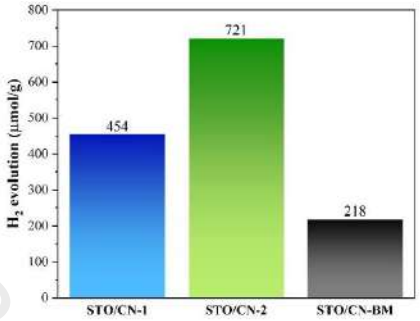


**Figure 5** Photocatalytic hydrogen evolution of various synthesized photocatalysts.

## CONCLUSIONS

In conclusion, both the one-pot and two-step synthesis methods successfully produced STO/CN composites with improved photocatalytic hydrogen evolution performance. The STO/CN-1 and STO/CN-2 exhibited better photocatalytic activity, which was attributed to the higher light absorption, more efficient charge separation, and reduced recombination when compared with STO/CN-BM. As a result, these simplified methods provide significant novelty in terms of process efficiency and material performance available for further solar-driven hydrogen production.

## ACKNOWLEDGEMENTS

The authors gratefully acknowledge the support and research funding from the Center of Excellence on Catalysis and Catalytic Reaction Engineering (CECC) and the Malaysia-Thai Joint Administration (MTJA).

## REFERENCES

**Cao, S.; Yu, J. (2014)** J. Phys. Chem. Lett. 5 **(12)**, 2101–2107.
**Hisatomi, T.; Kubota, J.; Domen, K. (2014)** Chem. Soc. Rev. 43 **(22)**, 7520–7535.
**Ghoniem, A. F. (2011)** Prog. Energy Combust. Sci. 37 **(1)**, 15–51.
**Mu, L.**; **et al. (2016)** Energy Environ. Sci. 9 **(7)**, 2463–2469.
**Kong, C.; et al. (2022)** J. Alloys Compd. 924, 166629.
**Xiao, F.; et al. (2020)** Environ. Sci. Pollut. Res. 27 **(6)**, 5788–5796.
**Ferreira, M. A.; et al. (2020)** Mater. Sci. Semicond. Process. 108, 104887.

PPC & PETROMAT SYMPOSIUM 2025

# $LaNi_{0.85}Sr_{0.15}O_3$ PEROVSKITE AS A CATALYST FOR GLYCEROL TRANSFORMATION TO 1,2-PROPANEDIOL

*Ari Adrianto* [a], *Sirirat Jitkarnka** [a,b]

[a] The Petroleum and Petrochemical College, Chulalongkorn University, Bangkok, Thailand
[a,b] Center of Excellence on Petrochemical and Materials Technology, Bangkok, Thailand

Keywords: Glycerol, 1,2-propanediol, perovskites, hydrogenolysis

## ABSTRACT

The catalytic conversion of glycerol into renewable 1,2-propanediol offers a promising approach for biomass valorization. To prevent agglomeration-induced deactivation during the reaction, a catalyst with high thermal stability, surface acidity, and effective hydrogenolysis activity is required. The process involves initial dehydration of glycerol to acetol over Lewis acid sites, followed by hydrogenation to form 1,2-propanediol. $LaNiO_3$-based perovskites are attractive due to La-enhanced glycerol conversion and NiO-facilitated hydrogenation. In this work, strontium (Sr) was introduced into $LaNiO_3$ to modulate its acid–base properties and improve metal dispersion, enhancing hydrogenolysis performance. The Sr-doped perovskite, $LaNi_{0.85}Sr_{0.15}O_3$, was synthesized hydrothermally and calcined at 800°C. Catalytic testing was conducted at 180 °C for 4 h in a PARR reactor using pure glycerol as feed. Products were analyzed by GC-TOF/MS, and catalyst properties were examined using XRD, XRF, BET, $NH_3$-TPD, and $CO_2$-TPD. Among the samples tested, $LaNi_{0.85}Sr_{0.15}O_3$ showed superior performance with 63.8% 1,2-propanediol selectivity and 98.2% glycerol conversion. Sr increased surface acidity (0.348 mmol/g) to promote dehydration and basicity (0.648 mmol/g) to stabilize intermediates. These synergistic effects directed the reaction toward selective hydrogenolysis, suppressing side reactions. It was found that Sr promoted hydrogenolysis pathway, resulting in higher 1,2-propanediol production and less unwanted products.

***sirirat.j@chula.ac.th**

## INTRODUCTION

Due to climate change and limited petroleum resources, renewable energy has become a priority in scientific discourse. Despite this focus, biodiesel usage is high, requiring appropriate management actions. Biorefineries can use glycerol to make cosmetic goods like 1,2-propanediol and lactic acid. Hydrogenolysis-oxidation is an efficient glycerol conversion method with high yields and low temperatures. This pathway commences with glycerol dehydration into acetol, catalyzed by Lewis acid sites, followed by hydrogenation to yield 1,2-propanediol (Dimitratos *et al*., 2009). Subsequently, the oxidation of 1,2-propanediol produces lactaldehyde, ultimately leading to lactic acid formation (Feng *et al*., 2014). Many research have focused on metal oxide catalysts because

PPC & PETROMAT SYMPOSIUM 2025

to its large surface area, exposed surface atoms, and active sites, which accelerate catalytic reaction. SrO performs better than MgO and CaO on glycerol conversion, among other catalytic features. SrO also had good carbon balance and produced the most lactic acid from glycerol reforming (Liu and Ye, 2015). Additionally, Sr loading to single $La_2O_3$ oxide improves glycerol conversion catalysis (Yu *et al*., 2023). Despite these encouraging results ,typical metal oxides frequently have poor thermal stability, electrical structure, or surface qualities. Designing and developing more efficient metal oxides with improved electrical,chemisorptive, and catalytic characteristics is necessary to address these issues. Perovskite oxides ($ABO_3$) have received attention in recent years due to their flexible structure and exceptional catalytic capabilities. Renowned perovskite $LaNiO_3$ facilitates rapid charge transfer (Hernández *et al*., 2015). Glycerol conversion was found enhanced using other perovskite supports such as $Pt/LaAlO_3$ and $Pt/LaCrO_3$ (Inns *et al.*, 2021). Previously, the modification of $ABO_3$ perovskite-type oxide by the A-site doping has been revealed to be one of the effective methods to further improve the catalytic reaction. For instance, Ca substitution in $LaNiO_3$ ($La_{0.5}Ca_{0.5}NiO_3$) significantly improved $H_2$ production during glycerol reforming by modifying the electronic environment of Ni sites (Wu *et al*., 2014).
Based on previous studies, this study investigated the catalytic performance of Sr-doped $LaNiO_3$ perovskite ($LaNi_{0.85}Sr_{0.15}O_3$), aiming to improve glycerol conversion into 1,2-propanediol.

## EXPERIMENTAL

*A. Catalyst Preparation*

A solution was made by mixing 0.010 mol Lanthanum Nitrate Hexahydrate ($La(NO_3)_3.6H_2O$), 0.010(1-x) mol Nickel Nitrate ($Ni(NO_3)_2.6H_2O$), and 0.010x mol Strontium (IV) nitrate $Sr(NO_3)_2$ with 30 mL of deionized water. The solution was then swirled at 500 rpm. An appropriate quantity of KOH 6M regulated pH to 13. The mixture was placed in a hydrothermal autoclave reactor and heated at 220ºC for 48 hours after 1 hour of stirring. After that, the $LaNi_{0.85}Sr_{0.15}O_3$ precipitate was rinsed with deionized water and ethanol until pH reached 7, then filtered on the Whatman 42 paper. Likewise, $LaNiO_3$ perovskite oxide was prepared using the same procedure. Next, the catalysts were oven-dried overnight at 65ºC. Final calcination took about 3 hours at 800ºC with a heating rate of 3ºC/min in a furnace.

*B. Catalyst Characterization*

The catalysts obtained in the study underwent thorough characterization employing a variety of techniques. Powder X-Ray Diffraction (XRD) was employed to investigate crystal structure and chemical composition of the samples. X-ray fluorescence spectrometer (XRF) was employed to quantify the elemental composition of the catalysts. Additionally, Field Emission Scanning Electron Microscopy (FE-SEM) was conducted to examine the surface morphology of the catalysts. The BET method, performed with a Quantachrome Autosorb-IQ-MP, measured the specific area, pore volume, and pore size distribution. Furthermore, the $NH_3$-TPD and $CO_2$-TPD were performed to determine acid-basic properties of the catalysts.

PPC & PETROMAT SYMPOSIUM 2025

*C. Catalytic Activity Testing*

The catalytic activity testing was accomplished in a PARR Reactor with automated temperature control and a stirrer. First, 1 g of catalyst and 40 ml of 99.5% glycerol were placed into the PARR reactor. Then, the reactor was flushed to remove the air with 99% of $N_2$ gas for around 15 minutes. This part can remove any air in the system of the reactor. The activity testing experiments were conducted at 180°C under auto-pressure for 4 hours of reaction without $H_2$ and $O_2$ feed. Then, the centrifuged machine was used to detach the solid catalyst from the liquid products. GC-TOF/MS (LECO) in 1D-Mode was employed to analyze for the composition of liquid products before and after the reaction.

## RESULTS AND DISCUSSION

*A. Catalyst Characterization*

The crystalline phases were analyzed using X-ray diffraction patterns, as depicted in Figure 5.2. The distinct and prominent peaks (2θ) at 14.46°, 26.16°, 29.16°, 30.02°, 39.57°, 44.37°, 46.16°, 48.63°, 52.24°, 53.83°, 55.53°, and 56.05° correspond to $La_2O_3$ (PDF No. 01-074-1144). The presence of NiO is detected at 37.28° and 43.30° (PDF No. 00-004-0835). The peaks observed at 32.50° in the X-ray diffraction (XRD) pattern correspond to the $LaNiO_3$ compound, whereas the peaks observed at 42.98° correspond to the SrO. The introduction of Sr into the $LaNiO_3$ structure is preliminarily evidenced by slight shifts and changes in the peak intensities in the XRD patterns. Thus, the integration of Sr into the lattice structure may provoke the formation of A-site modified perovskite structures, which is likely because Sr has a similar larger ionic radius than La, and competes for the insertion of the A site in the perovskite structure as indicated by the X-Ray Diffraction (XRD) peak observed at 33.18°. The FE-SEM results (Figure 1b) show that $LaNiO_3$ has well-defined cubic and rectangular-shape grains with a smooth structure. As Sr is introduced, the surface morphology of the perovskite becomes porous and less defined. At x=0.15, the crystals start to agglomerate, becoming larger with more highly irregular shapes as it can be seen in 100X magnification.

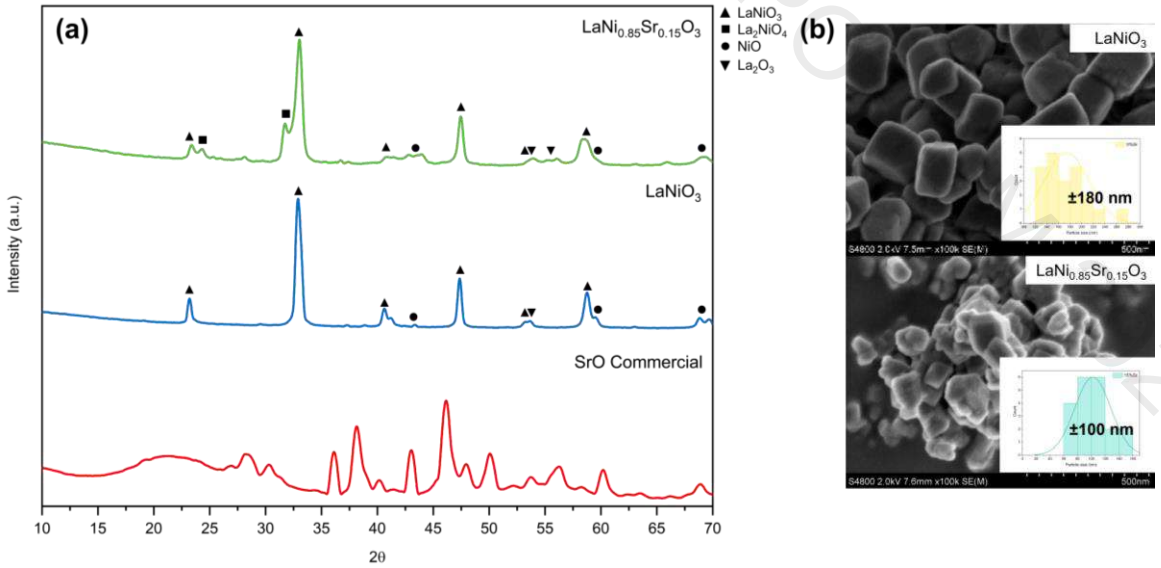


**Figure 1.** (a) XRD and (b) FE-SEM Characterization over $LaNi_{0.85}Sr_{0.15}O_3$.

Table 1 shows the specific surface area, total pore volume, and pore diameter of $LaNi_{0.85}Sr_{0.15}O_3$ catalysts. In general, $LaNiO_3$-based catalysts have a low specific surface area (1.6 $m^2/g$). The further insertion of Sr in $LaNiO_3$ results in a slight decrease in surface area (1.2 $m^2/g$). However, after the Sr insertion, the surface area significantly increases due to the effect on lattice strain or distortion (Zhang *et al*., 2022). Moreover, it can be seen that the total pore volume is in the range of 0.010-0.021 $cm^3/g$, while the average pore diameter
in the range of 4.47-15.49Å. Concurrently, X-ray Fluorescence (XRF) analysis in Table 1 shows a notable increase in La content with elevated Sr loading, despite a constant initial La quantity, which is attributed to the emergence of a secondary $La_2NiO_4$ phase, confirmed by a new peak at 33.6° in the X-ray diffraction (XRD) pattern (Maas *et al.*, 2022).

**Table 1.** Physical properties of $LaNi_{0.85}Sr_{0.15}O_3$

| Catalyst | Relative concentration (wt%)[a] | | | $S_{BET}$ ($m^2/g$)[b] | Total Pore Volume ($cm^3/g$)[b] | Average Pore Diameter (Å)[b] |
|---|---|---|---|---|---|---|
| | La | Ni | Sr | | | |
| $LaNiO_3$ | 50.0 | 29.7 | - | 1.6 | 0.021 | 15.49 |
| $LaNi_{0.85}Sr_{0.15}O_3$ | 60.6 | 22.3 | 3.3 | 7.0 | 0.010 | 4.47 |

(a) determined using XRF, and (b) examined using BET technique

The acidity and basicity of the catalysts are summarized in Table 2 as determined using the $NH_3$-TPD and $CO_2$-TPD techniques, respectively. The $NH_3$-TPD analysis shows that when Sr was incorporated into $LaNiO_3$, the strong acid density decreases, whereas the weak one drastically increases. $LaNiO_3$ as the parent catalyst, has the total acidity of 0.354 mmol/g and the total basicity of 0.196 mmol/g. Therefore, incorporating Sr into $LaNiO_3$ structure causes a decrease in the total acidity, especially the weak acid density. For $CO_2$-TPD analysis, with the Sr loading, the density of strong basic sites generally increases. Therefore, $LaNi_{0.85}Sr_{0.15}O_3$ possesses a high basicity (0.648 mmol/g) and high weak acid density (0.236 mmol/g). By illustrating a distinct modification of the acid-base properties via Sr doping, the effect on glycerol reforming transformation to 1,2-propanediol is subsequently discussed in this work.

**Table 2.** Acid-basic properties of $LaNi_{0.85}Sr_{0.15}O_3$

| Catalyst | Acid density (mmol/g) | | | Basic density (mmol/g) | | | Ratio (A:B) |
|---|---|---|---|---|---|---|---|
| | Weak | Strong | Total | Weak | Strong | Total | |
| $LaNiO_3$ | 0.036 | 0.318 | 0.354 | 0.173 | 0.023 | 0.196 | 2:1 |
| $LaNi_{0.85}Sr_{0.15}O_3$ | 0.236 | 0.112 | 0.348 | 0.079 | 0.569 | 0.648 | 1:2 |

PPC & PETROMAT SYMPOSIUM 2025

*B. Catalytic activity*

The glycerol transformation was conducted in a PARR reactor at 180ºC for 4 hours using pure glycerol as the feed. The non-catalyst case only gives 14.6% conversion, indicating that without a catalyst, the reactions are not likely to occur in the bulk (Figure 2a). $LaNiO_3$ as a catalyst can substantially increase the conversion to 91.4%, whereas SrO as a commercial catalyst shows moderate glycerol 62.7% conversion. Further improvements are accomplished on the introduction of Sr-doped $LaNiO_3$. The introduction of Sr into $LaNiO_3$ (x=0.15) enhances the catalytic performance, to 98.2% conversion.

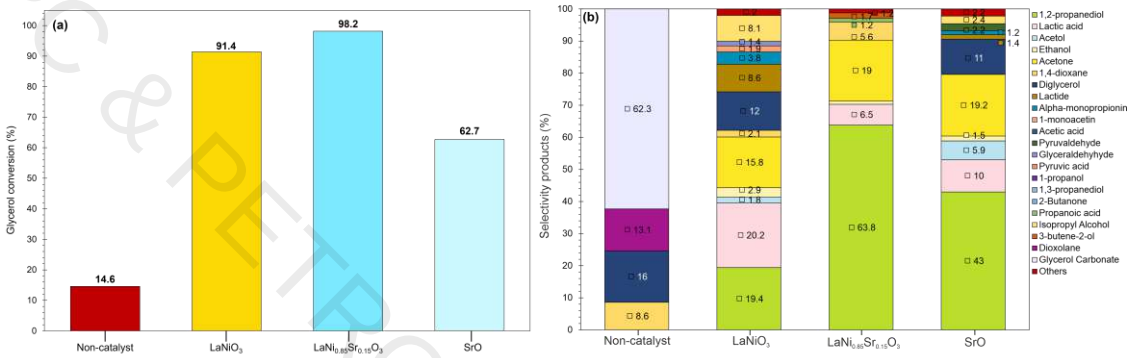


**Figure 2.** (a) Glycerol conversion, and (b) selectivity products over $LaNi_{0.85}Sr_{0.15}O_3$ catalyst.

Figure 2b presents the selectivity of various products over a series of $LaNi_{0.85}Sr_{0.15}O_3$ catalyst. The non-catalytic case only produces some undesired products such as glycerol carbonate (9.1%), dioxane (1.3%), diglycerol (2.3%), and dioxolane (1.6%). Additionally, the SrO commercial catalyst produces 43.0% 1,2-PDO selectivity in addition to lactic acid (10%) and acetol (5.9%). As the parent catalyst, $LaNiO_3$ exhibits a broader product distribution, giving 19.4% 1,2-PDO and 20.2% lactic acid selectivity. Sr loading reveals a distinct impact on 1,2-PDO formation. $LaNi_{0.85}Sr_{0.15}O_3$ exhibits a shift towards selectivity of 1,2-PDO (63.8%) and lactic acid (6.5%), demonstrating the influence of Sr doping on changing both redox and acid-basic properties. With the Sr loading, the selectivity for 1,2-PDO increases, which is attributed to the optimal balance of basic sites, as evidenced by TPD analysis. Figure 3 shows that Sr-O species inside the $LaNiO_3$ perovskite structure affect both hydrogenolysis and condensation reactions, thereby favoring the formation of 1,2-PDO as a targeted product. Furthermore, it is well known that certain products, including the highly selective 1,4-dioxane, easily condense over basic catalysts. According to the findings, Sr plays two crucial roles in $LaNiO_3$; that are, (1) it tunes the optimal acid-basic properties, (2) promotes $La_2NiO_4$ formation, (3) produces less undesirable product, and (4) enhances the catalyst's resistance to deactivation, boosting its overall efficiency (Di Cosimo *et al*., 2014; Umar *et al*., 2019).

PPC & PETROMAT SYMPOSIUM 2025

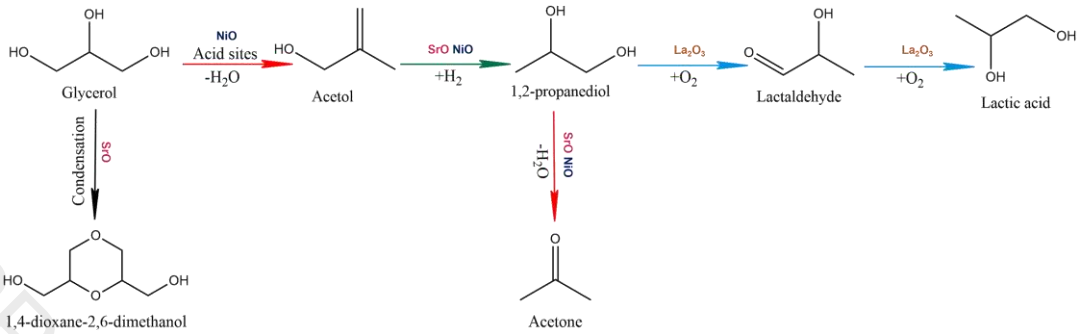


**Figure 3.** Influences of Sr in $LaNi_{0.85}Sr_{0.15}O_3$ catalyst on the pathways.

## CONCLUSIONS

The insertion of Sr into $LaNiO_3$ perovskite catalysts significantly influences both the physical properties and catalytic performance. In terms of physical properties, increasing Sr loading altered the morphology. Sr at x=0.15 resulted in agglomeration and the deformation of perovskite structure. In addition, this work has proven that the insertion of Sr in $LaNiO_3$ significantly enhanced the formation of 1,2-propanediol, boosted glycerol conversion, and produced less undesirable products. Using pure glycerol as a feedstock, $LaNi_{0.85}Sr_{0.85}O_3$ gave 62.8% 1,2-propanediol yield due to the promoted oxygen vacancies.

## ACKNOWLEDGEMENTS

The author would like to acknowledge for the Fundamental Fund (BCG66630025) and the ASEAN Scholarship from Chulalongkorn University.

## REFERENCES

**Dimitratos, N., Lopez-Sanchez, J. A., Meenakshisundaram, S., Anthonykutty, J. M., Brett, G., Carley, A. F., ... & Hutchings, G. J.** (2009). Selective formation of lactate by oxidation of 1, 2-propanediol using gold palladium alloy supported nanocrystals. Green Chemistry, 11 **(8)**, 1209-1216.

**Feng, Y., Yin, H., Gao, D., Wang, A., Shen, L., & Meng, M.** (2014). Selective oxidation of 1, 2-propanediol to lactic acid catalyzed by hydroxylapatite nanorod-supported Au/Pd bimetallic nanoparticles under atmospheric pressure. *Journal of Catalysis*, *316*, 67-77.

**Hernández, D., López, D., & Fernández, J. J.** (2015). Catalytic performance of $Ni/La_2O_3$ materials in glycerol valorization for acetol and syngas production. Applied Catalysis A: General, 499, 13-18.

**Wu, G., Li, S., Zhang, C., Wang, T., & Gong, J.** (2014). Glycerol steam reforming over perovskite-derived nickel-based catalysts. *Applied Catalysis B: Environmental*, *144*, 277-285.

**Zhang, Y., Guo, L., Xu, Q., Zhang, Q., Li, J., & Ma, Q.** (2022). Effect of Sr-doping on the photocatalytic performance of $LaNiO_3$− σ. *Catalysts*, *12*(11), 1434.

**Maas, K., Wulles, C., Roque, J. M. C., Ballesteros, B., Lafarge, V., Santiso, J., & Burriel, M. (2022).** Role of p $O_2$ and film microstructure on the memristive properties of $La_2NiO_4$+ δ/$LaNiO_3$− δ bilayers. *Journal of Materials Chemistry A*, *10*(12), 6523-6530.

PPC & PETROMAT SYMPOSIUM 2025

# Ketonization of Biodiesel over Nanoflower MnO/γ-$Al_2O_3$ Catalysts: Effect of Synthesis Temperature

*Ungki Bella Athania* [a], *Siriporn Jongpatiwut**[a,b]

[a] The Petroleum and Petrochemical College, Chulalongkorn University, Bangkok, Thailand
[b] Center of Excellence on Petrochemical and Materials Technology, Bangkok, Thailand

Keywords: Biodiesel, Catalysts, Ketonization, Nanoflower, Temperature

## ABSTRACT

The growing surplus of biodiesel necessitates advanced valorization strategies. This study presents an efficient catalytic process to convert low-value biodiesel into high-value ketones via hydrolysis-ketonization reaction. First, biodiesel was hydrolyzed into fatty acids, which were then subjected to ketonization using nanoflower (NF) manganese oxide (MnO) catalysts supported on gamma-alumina (γ-$Al_2O_3$). The γ-$Al_2O_3$ support enhances ketonization efficiency by promoting the hydrolysis of biodiesel into fatty acids with addition of water. Four MnO/γ-$Al_2O_3$ catalysts with nanoflower morphologies were synthesized via hydrothermal methods at 120°C (12 h) and 140°C (2, 4, and 12 h). Nanoflower catalysts were characterized using BET, XRD, XPS, FE-SEM, TPR, and HR-TEM. Ketonization reactions of biodiesel were conducted in a fixed-bed reactor at 380°C (WHSV 1.03 $h^{-1}$) for 6 h time of stream. The NF 140-2H MnO/γ-$Al_2O_3$ catalyst demonstrated the highest performance, achieving 87.6% conversion and 50.2% ketone yield. This highest performance was attributed to its high surface area (65.5 $m^2/g$) and its high oxygen vacancy concentration (72.3%). These findings provide valuable insights for designing efficient catalytic systems for biodiesel valorization and offer an economically viable route to sustainable chemical production from low-value biodiesel streams.
***siriporn.j@chula.ac.th**

## INTRODUCTION

Biodiesel, derived from vegetable oils or animal fats, offers an opportunity to produce higher-value chemicals beyond its conventional use as fuel. Through ketonization, biodiesel's FAME can be converted into ketones, which have greater industrial value than biodiesel itself. The resulting ketones can be further upgraded into high-performance biolubricants, biowaxes or even biofuels with better cold-flow properties compared to conventional biodiesel (Ohkuma, 2010). This valorization strategy improves the economic viability of biodiesel production by diversifying its applications. Instead of being limited to the fuel market, biodiesel-derived ketones enter higher-margin chemical markets while maintaining environmental benefits over petroleum-based alternatives (Oliver-Tomas et al., 2017). The ketonization process is efficiently catalyzed by MnO supported on γ-$Al_2O_3$, which facilitates the removal of carboxyl groups from FAME while forming new C-C bonds. The redox properties of oxygen vacancy enhance catalytic activity and selectivity, minimizing unwanted side reactions (Cai et al., 2024). These catalysts will be characterized using several techniques including field emission scanning electron microscope (FE-SEM),

PPC & PETROMAT SYMPOSIUM 2025

surface area analyzer with Brunauer-Emmett-Teller (BET) method, X-ray diffraction (XRD), temperature-programmed reduction of $H_2$ ($H_2$-TPR), X-ray photoelectron spectroscopy (XPS), and high-resolution transmission electron microscopy (HR-TEM).

## EXPERIMENTAL

*A. Feed Preparation*

Biodiesel (B100, PPP Green Complex Company) was used directly without pretreatment and injected into the syringe pump.

*B. Catalyst Preparation*

1. Nanoflower MnO Catalysts

Nanoflower (NF) MnO were obtained by a hydrothermal method. The main materials that are used in this synthesis are 0.25 g potassium permanganate ($KMnO_4$), 0.1 g manganese (II) sulphate monohydrate ($MnSO_4.H_2O$) and 0.05 g cethylmethyl ammonium bromide (CTAB). Each of them dissolved in 25 mL deionized water and the resulting solution is placed in an autoclave and heated in oven at 120 $^oC$ for 12 h and 140 $^oC$ for 2, 4 and 12 h. After hydrothermal treatment, the precipitate is collected, washed multiple times using deionized water until the pH reaches 7 and then dried in an oven for 12 h. The obtained NF MnO catalysts were then calcined in muffle furnace at 500 $^oC$ for 3 h at heating rate of 1 $^oC$/min.

2. Nanoflower MnO / $\gamma$-$Al_2O_3$ Catalyst

A solution of NF MnO catalyst with different pretreatments was prepared by dispersing 0.25 g of each MnO catalyst in 125 mL ethyl alcohol using sonicator for 2 h. Before that, $\gamma$-$Al_2O_3$ was calcined at 500 $^oC$ for 3 h (1 $^oC$/min ramp). Therefore, NF MnO catalyst was doped onto 10 g of $\gamma$- $Al_2O_3$ using dip coating technique and dried in the oven for 2 h at 120 $^oC$. The prepared catalysts were designated as 2.5 wt% of MnO/$\gamma$- $Al_2O_3$ catalysts.

*C. Catalytic Activity Testing*

The ketonization reaction of biodiesel was conducted in fixed bed reactor at atmospheric pressure, using 5 g of NF $MnO_2$/$\gamma$-$Al_2O_3$ catalyst. Prior to the reaction, the catalyst was reduced at 380 °C for 2 hours under a $H_2$ flow of 100 mL/min. The reaction was carried out at 380 °C with biodiesel fed at 6 mL/h via a syringe pump and injection of water using $N_2$ gas at the flowrate of 100 mL/min to the reactor for 6 h time of stream. Heating wires were installed along the feed line, product line, and glass trap to prevent solidification. The solid and gas products were collected every 2 h. Solid products were analyzed using gas chromatography - flame ionization detector (GC-FID, Agilent 7890A with an auto-injector and DB-5HT column), while gas products were analyzed using gas chromatography - flame ionization detector (GC-FID, Hewlett Packard II 5890 with an HP-AL/S column). Compound identification was performed using gas chromatography – mass spectrometry (GC-MS, Leco Instrument with Rtx-PAH column).

*D. Catalyst Characterization*

X-ray diffraction (XRD, Rigaku) with CuKα radiation (λ = 0.15406 nm) at 40 kV was employed to determine the crystal structure, with scans performed over a 2θ range of 5–80 at a rate of 4 °/min and a step size of 0.02 °/s. Morphology of the catalysts was analyzed

PPC & PETROMAT SYMPOSIUM 2025

using field emission scanning electron microscopy (FE-SEM, Shimadzu S-4800), while surface area and pore diameter were measured via the Brunauer-Emmett-Teller (BET) method on a QS-evo MP analyzer. The chemical states (Mn and O) of the catalyst were investigated using X-ray photoelectron spectroscopy (XPS, Kratos Axis Ultra DLD) and the spectra were deconvoluted using CasaXPS 2.3.26PR1.0 software, Reducibility was assessed through temperature-programmed reduction of $H_2$ ($H_2$-TPR) on MicroActive Autochem II 2920. The interplanar spacing measurement and oxygen vacancy identification were determined by high resolution transmission electron microscopy (HR-TEM, JEM-3100F) and ImageJ 1.54g software was used to refine TEM images by inverse fast Fourier transform (IFFT) technique.

## RESULTS AND DISCUSSION

### *A. Catalyst Characterization Result*

The SEM images in Figure 1 clearly demonstrate the successful formation of nanoflower (NF) morphologies from different pretreatment temperature (120-140°C) and duration of oven time (2-12 hours). Although different catalyst synthesis conditions, all catalysts exhibited well-defined flower-like morphology with petal arrangements.

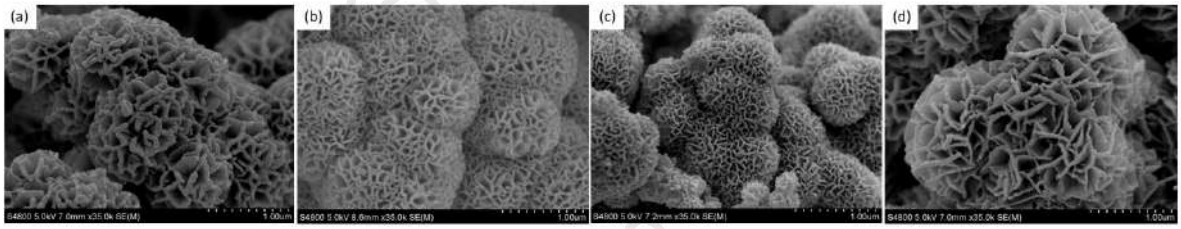


**Figure 1.** SEM images of nanoflower MnO catalysts:
**(a)** NF120-12H, **(b)** NF140-2H, **(c)** NF140-4H, and **(d)** NF140-12H

The BET analysis shows different results of surface area in different synthesis pretreatment. The NF 140-12H catalyst, synthesized at the highest temperature for the longest duration, displayed the largest surface area (99.22 $m^2/g$) followed by NF140-4H (75.27 $m^2/g$), NF 120-12H (71.13 $m^2/g$) and NF 140-2H (65.45 $m^2/g$).

**Table 1.** Summary of BET surface area and pore size of NF MnO catalysts

| Catalyst | BET Surface Area ($m^2/g$) | Average Pore Size (nm) |
|---|---|---|
| NF 120-12H | 71.13 | 5.57 |
| NF 140-2H | 65.45 | 6.61 |
| NF 140-4H | 75.27 | 6.28 |
| NF 140-12H | 99.22 | 6.51 |

Crystallinity of NF MnO catalysts analyzed by XRD instrument by identifying the XRD patterns in Figure 2. Figure 2(a) shows the XRD patterns of fresh catalysts and represents a single phase of α-$MnO_2$ with tetragonal crystal structure (JCPDS# 44-0141). After reduction process (Figure 2b), XRD confirms that α-$MnO_2$ was reduced to MnO. Additionally, the color of catalysts change from brownish black into green powder.

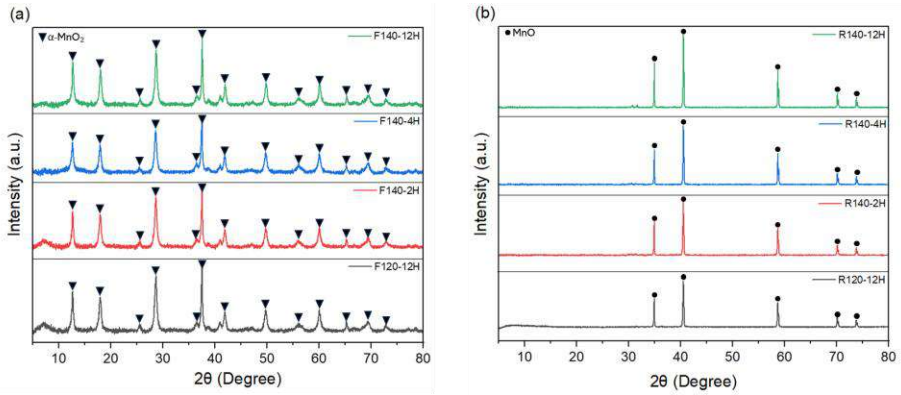


**Figure 2.** XRD result of NF MnO catalysts: **(a)** Fresh catalysts, **(b)** Reduced catalysts

$H_2$-TPR profile demonstrates that all reduction peaks of the nanoflower MnO catalysts are below the reduction temperature of 380 °C, indicating the better reducibility under operational conditions.

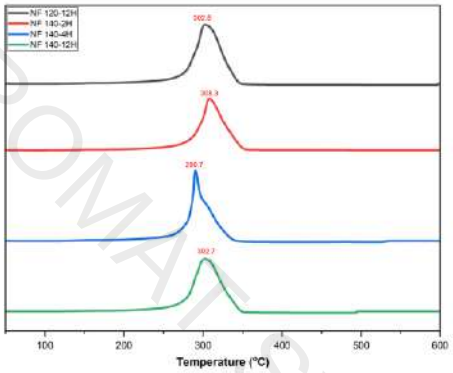


**Figure 3.** $H_2$-TPR profile of NF MnO Catalysts

The XPS shows quantification of Mn and O species for NF MnO catalysts. As shown in Table 2, the fresh catalysts were predominantly composed of $Mn^{3+}$ (66-73%) and $Mn^{4+}$ (26-34%) species, with no detectable $Mn^{2+}$. However, after reduction, all catalysts exhibited high concentration of $Mn^{2+}$ (45-56%) along with a corresponding decrease in $Mn^{4+}$ content (12-22%). Reduced NF 140-2H catalyst, demonstrated the highest oxygen vacancy concentration (72.3%) followed by NF 140-4H (64.14%), NF 120-12H (62.91%), and NF 140-12H (55.18%).

**Table 2.** Quantitative result O and Mn spectra of fresh and reduced catalysts

| Catalyst | O | | | Mn | | |
|---|---|---|---|---|---|---|
| | $O_L$ | $O_V$ | $O_S$ | $Mn^{2+}$ | $Mn^{3+}$ | $Mn^{4+}$ |
| NF 120-12H | 27.75% | 42.31% | 29.94% | - | 73.47% | 26.52% |
| NF 120-12H (reduced) | 2.25% | 62.91% | 34.84% | 53.8% | 30.25% | 15.91% |
| NF 140-2H | 12.44% | 38.99% | 48.58% | - | 66.52% | 33.48% |
| NF 140-2H (reduced) | 11.36% | 72.3% | 16.33% | 45.6% | 32.29% | 22.11% |
| NF 140-4H | 32.95% | 46.04% | 21.02% | - | 66.73% | 33.26% |
| NF 140-4H (reduced) | 3.45% | 64.14% | 32.41% | 50.47% | 35.45% | 14.09% |
| NF 140-12H | 20.53% | 39.89% | 39.58% | - | 68.85% | 31.15% |
| NF 140-12H (reduced) | 13.46% | 55.18% | 29.06% | 56.04% | 31.38% | 12.58% |

PPC & PETROMAT SYMPOSIUM 2025

Figure 5 presents high-resolution TEM (HR-TEM) images of NF MnO catalysts, where the red circles distinctly mark the presence of oxygen vacancies as the defect sites created by missing oxygen atoms in the crystal lattice that detected by IFFT technique. The measured values correspond to the interplanar spacing (d-spacing) of TEM images, designated as observed d-spacing ($D_{obs}$) are correlated with calculated d-spacing ($D_{calc}$) from XRD spectra, which confirmed the crystal facet as indicated by XRD spectra of reduced catalysts in Figure 2(b).

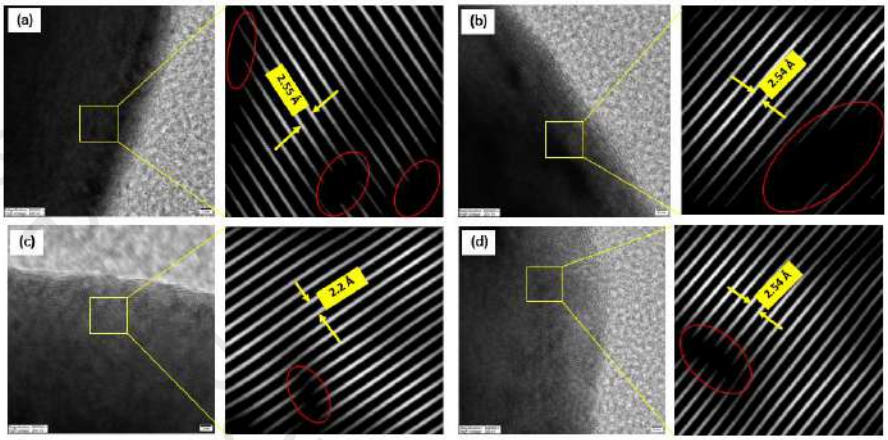


**Figure 5.** TEM Images for NF MnO Catalysts:
**(a)** NF120-12H, **(b)** NF140-2H, **(c)** NF140-4H, and **(d)** NF140-12H

**Table 3.** Interplanar Spacing (d-spacing) measurement of NF MnO catalysts

| Catalyst | Crystal Structure[1] | Lattice Parameter[1] | Dcalc (Å)[1] | Dobs (Å)[2] | Crystal Facet[1] |
|---|---|---|---|---|---|
| NF 120-12H | | | 2.55 | 2.55 | [1,1,1] |
| NF 140-2H | Cubic | a=b=c | 2.55 | 2.54 | [1,1,1] |
| NF 140-4H | Manganosite | 4.415 Å | 2.21 | 2.20 | [2,0,0] |
| NF 140-12H | | | 2.55 | 2.54 | [1,1,1] |

[1] XRD, [2] HR-TEM

*B. Catalytic Activity Testing Results*

The ketonization of biodiesel performance was evaluated for 6 h time of stream at 380 °C at atmospheric condition using four catalysts of MnO with 2.5 wt.% loading onto γ-$Al_2O_3$ support (2.5% Nanoflower 120-12H MnO/γ-$Al_2O_3$ (NF 120-12H), 2.5% Nanoflower 140-2H MnO/γ-$Al_2O_3$ (NF 140-2H), 2.5% Nanoflower 140-4H MnO/γ-$Al_2O_3$ (NF 140-4H) and 2.5% Nanoflower 140-12H MnO/γ-$Al_2O_3$ (NF 140-12H)). All catalytic testing results revealed that NF 140-2H achieved the highest biodiesel conversion (87.6%) and total ketones yield (50.2%), while maintaining excellent stability (>80.0% conversion after 6 h) compared to the NF120-12H, NF 140-4H and NF 140-12H. Blank γ-$Al_2O_3$ was also tested under the same conditions and showed low catalytic activity, confirming that the observed ketonization performance is primarily driven by the MnO active phase rather than the support itself.

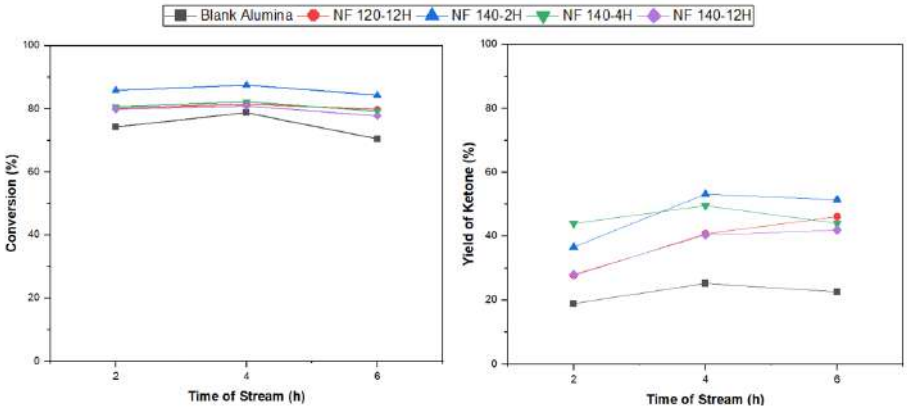


**Figure 6.** Catalytic Activity Testing for NF MnO/γ-$Al_2O_3$ support

## CONCLUSIONS

The comprehensive study of NF MnO/γ-$Al_2O_3$ catalysts identifies NF 140-2H as the best catalyst in biodiesel ketonization, owing to its desired nanoflower structure and surface properties. XRD confirms the presence of MnO phase, while TPR result show the reduction peak is below the reduction temperature (380 ºC). XPS and TEM revealed that NF 140-2H possesses the highest oxygen vacancy concentration (72.3%) among the tested catalysts. This also supported by its high surface area (65.5 $m^2/g$) and high pore diameter (6.6 nm). Additionally, TEM image confirms the presence of oxygen vacancy through IFFT technique as identified by black void area. These parameters are correlated to its higher catalytic performance that achieving high conversion (87.6%) and higher total ketones yield (50.2%). This finding underscore that optimal reducibility and the formation of oxygen vacancies are the key drivers of high catalytic performance on biodiesel ketonization.

## ACKNOWLEDGEMENTS

This research and innovation activity is funded by National Research Councils of Thailand (NRCT). The author would like to thank the research support from The Petroleum and Petrochemical College, Chulalongkorn University and for Graduate Scholarship for ASEAN and Non-ASEAN Countries from Chulalongkorn University.

## REFERENCES

**Cai, B., Lin, F., Guo, X., & Li, Y.** (2024). Catalytic Acetone Oxidation over MnOx Catalysts: Regulating Their Crystal Structures and Surface Properties. Processes, **12(2)**.

**Ohkuma, T.** (2010). Asymmetric hydrogenation of ketones: tactics to achieve high reactivity, enantioselectivity, and wide scope. Proc Jpn Acad Ser B Phys Biol Sci, **86(3)**, 202-219.

**Oliver-Tomas, B., Renz, M., & Corma, A.** (2017). High Quality Biowaxes from Fatty Acids and Fatty Esters: Catalyst and Reaction Mechanism for Accompanying Reactions. Industrial & Engineering Chemistry Research, **56(45)**, 12870-12877.

PPC & PETROMAT SYMPOSIUM 2025

# SULFONIC ACID-MODIFIED Zr -KIT-6 AS A SOLID ACID CATALYST FOR GLYCEROL ACETYLATION TO PRODUCE TRIACETIN, A HIGH-VALUE BIO-ADDITIVE

*Fitrah Hardhana* [a], *Apanee Luengnaruemitchai* [a,*], *Shih-Yuan Chen* [b, c,*], *Takehisa Mochizuki* [b,c]

[a)] The Petroleum and Petrochemical College, Chulalongkorn University, Pathumwan, Bangkok 10330, Thailand
[b)] Synthetic Fuel Production and Evaluation Research Team (FPET), Integrated Research Center for CCUS Implementation`
[c)] Energy Catalyst Technology Research Group, Energy Process Research Institute (EPRI)
National Institute of Advanced Industrial Science and Technology (AIST) 16-1 Onogawa, Tsukuba, Ibaraki 305-8569, Japan.

Keywords: Acetylation reaction, Triacetin, Glycerol conversion, Solid acid catalyst, KIT-6

## ABSTRACT

The acetylation of glycerol with acetic acid is effective for producing acetin compounds, particularly triacetin, a value-added bio-additive for fuel. KIT-6, with its three-dimensional bicontinuous cubic structure, large pore size, thick pore walls, and high thermal stability, was used as a support for solid acid catalysts. We developed a method to prepare Zr-incorporated KIT-6 materials using post-synthesis, followed by sulfonic acid surface modification, yielding sulfonic acid-modified Zr-KIT-6 catalyst for glycerol acetylation to produce triacetin. Zr-KIT-6 containing zirconia clusters (i.e., $ZrO_x$), which act as Lewis acid sites on the pore walls, showed minimal catalytic activity. However, these surface $ZrO_x$ clusters anchored sulfonic acid groups, forming sulfonic acid-modified Zr-KIT-6 with surface sulfonic acid groups ($–SO_3H$), denoted as S-Zr-KIT-6, that act *as* efficient Brønsted acid sites for glycerol acetylation. Among the prepared S-Zr-KIT-6 catalysts with different sulfonic acid and Zr loadings, S-7Zr-KIT-6, with a high BET surface area of 718 $m^2$ $g^{-1}$ and total acidity of 1.02 mmol $H^+$ $g^{-1}$, completely converts glycerol at 115 °C for 8 h, achieving 45% triacetin selectivity and a production rate of 5.63 mmol triacetin $g^{-1}$ $h^{-1}$. These findings highlight the importance of balanced acid site types and mesoporous structure in maximizing glycerol acetylation toward triacetin production

***apanee.l@chula.ac.th *sy-chen@aist.go.jp**

## INTRODUCTION

Scientist are increasingly focused on developing sustainable, economical chemical processes to decrease their reliance on fossil fuels. Biomass-derived products derived from organic polyfunctional molecules offer a promising alternative to petrochemical based materials. Biodiesel is a mixture of fatty acid methyl ester (FAME) produced by the transesterification of triglycerides with methanol, which generates 10 wt% of crude glycerol as a by-product (Koranian, *et al.*, 2022). Glycerol, a byproduct of biodiesel production, can be valorized into high-value acetylglycerols. The acetylation of glycerol with acetic acid is a promising method, offering environmental and cost advantages over the use of acetic anhydride (Perez, *et al.*, 2022). This process yield a mixture of mono-, di-, and tri-acetyl glycerides (MAG, DAG, and TAG). Among these acetin derivatives, triacetin has been widely used in various applications including as a biodiesel additive (Hidayati, *et al.*, 2021). When blended with biodiesel, triacetin can enhance cold flow characteristics, octane ratings, engine performance and decrease greenhouse gas emissions (Zada, *et al.*, 2022). Acid catalysts, particularly heterogeneous ones, are favored for glycerol acetylation because they are less toxic and ease of separation. The pore size of the catalyst is essential in the formation of

triacetin. The three-dimensional bicontinuous cubic structure of KIT-6 mesoporous silica, with their high thermal stability, large pore diameter, and large surface area, has attracted much attention in the acetylation of glycerol with acetic acid (Guillet-Nicolas, *et al.*, 2016). KIT-6 mesoporous silica's unique pore interconnecting enhances the reactant and product diffusion, leading to high pore accessibility (Moritz, 2015). Additionally, the acidic properties of KIT-6 materials can be improved by incorporating active metals such as Zr, Sn, and Ti. Incorporating heteroatoms in mesoporous silica allows for precise control over surface properties, including hydrophobicity and acidity/basicity. *(*Yimer, *et al.*, 2024).

## EXPERIMENTAL

*A. Synthesis of Mesoporous Silica (KIT-6), Zr-Modified Mesoporous Silica (Zr-KIT-6), and Sulphonic-Zirconia Modified Mesoporous Silica (S-KIT-6 and S-7Zr-KIT-6)*

4 g of Pluronic P123 was vigorously stirred with 176.69 g of 0.5 M HCl solution in a polypropylene bottle at 35℃ for 3 h. After complete dissolution, 5.112 g of butanol was added, and the mixture was stirred vigorously for 1 h at the same temperature. After getting a clear solution, 12.677 g of tetraethyl orthosilicate (TEOS) was introduced, and the solution was further stirred for 24 h at 35°C. The resulting mixture was then aged hydrothermally at 100°C for 24 h. The white precipitate formed was filtered without washing, then dried at 100°C for 24 h. Finally, the powder was calcined at 550°C for 6 h with a heating rate of 1°C/min, forming KIT-6 material (Kim, *et al.*, 2005).

For Zr-modified KIT-6, $ZrOCl_2.8H_2O$ was used as the zirconium precursor to modify the KIT-6 support via the impregnation method. Different Si/Zr molar ratios corresponding to different Zr loadings (2.5, 5, 7, 10) were prepared. KIT-6 and Zr precursor were stirred in dry ethanol for 8 h. After 8 h of stirring, the catalyst was filtered and thoroughly washed with ethanol three times. The catalyst was then dried at 100°C for 24 h and calcined at 550°C for 6 h (Gutiérrez and Klimova, 2011). Hereafter, the catalysts will be denoted as xZr-KIT-6, where x represents the specific Si/Zr molar ratio.

For sulfonic acid-Zr-KIT-6, 1.5 g of Zr-KIT-6 was stirred with 30 mL of 1.5 M $H_2SO_4$ for 24 h at 25°C, then the solution was sonicated for 30 min. After sonication, the solution was filtered and washed with methanol three times. Then the obtained solid was dried for 12 h at 100°C and calcined at 550°C for 3 h (Guo, *et al.*, 2023). The S-xZr-KIT-6 was obtained, where S is the notation of sulphate.

*B. Characterization*

The specific surface area, total pore volume and average pore size were analyzed using $N_2$ physisorption utilizing a QS-evo MP (Quantachrome, USA). The specific surface area was determined using the Brunauer-Emmett-Teller (BET) method, based on 57 adsorption and desorption data points. Prior to the measurement, the sample was outgassed at 110 ℃ for 15 h under high vacuum to eliminate volatile adsorbates from the surface. Nitrogen ($N_2$) gas was adsorbed onto the catalyst surface at -196 ℃. The pore size distribution was evaluated using Barrett-Joyner-Halenda (BJH) method, based on data from the desorption branch. The pore volume reached a $P/P_0$ ratio of 0.8. The crystalline structure of the cayalyst was analyzed using a Rigaku Smartlab X-ray diffractometer using CuKα radiation (1.5406 Å). Small angle X-ray

scattering patterns (SAXS) was conducted with a range between 0.5° to 3° (2θ angle), a resolution of 0.02° per step and a scanning speed of 0.5°/min. The acid capacities of the materials were determined by acid–base titration using NaCl solution as an ion-exchange agent. A 50 mg sample was ion-exchanged with 20 mL of 2 M NaCl solution at ambient temperature at least 24 h, then followed by filtering and washing with 3 mL of deionized water. The filtrates were then titrated with a 0.01 M NaOH solution (Chen, *et al.*, 2011). Temperature-programmed desorption of ammonia ($NH_3$-TPD) utilizing the Microtrac BEL, BELCAT II, was used to measure the relative acid site strength and the overall acidity of the produced catalysts. In a standard experiment, 100 mg of the material was outgassed at 200°C for one hour while He (30 ml $min^{-1}$) was flowing as a carrier gas, and then it was cooled to 100°C. After that, the sample was exposed to $NH_3$/He gas for one hour at 100 °C at a flow rate of 60 ml $min^{-1}$. The reactor temperature was raised from 100 to 600 °C at a heating rate of 10°C $min^{-1}$ after the physically adsorbed ammonia molecules were eliminated by purging with helium flow until the baseline was flat

*C. Catalytic activity*

The acetylation of glycerol with acetic acid was conducted in a 100-mL three-necked round-bottom flask equipped with a vertical condenser, heating mantle, silicone oil bath, and magnetic stirring. In a typical experiment, 10 g of glycerol (99.5% Qrec) and a 1:9 molar ratio of glycerol to acetic acid (99.8% Qrec) were poured to the flask, together with 0.5 g of the catalyst (5 wt% glycerol). The response time was measured after attaining the desired temperature. After the reaction time was completed, the reaction flask was cooled to ambient temperature, and the catalyst was recovered by vacuum filtration (Kanimozhi, *et al.*, 2018). The glycerol and acetin products were analyzed using an Agilent 7890B gas chromatography (GC) system equipped with an HP-5 column and a flame ionization detector (FID). The 0.1 g of products were diluted in 45 mL of ethanol and 30 $\mu L$ of butanol (internal standard). The prepared sample (0.2 $\mu L$) was introduced into the column at a split ratio of 6:1. The oven temperature was initially set at 70 °C and gradually increased to 180 °C and 250 °C at rates of 5 °C/min and 10 °C/min, respectively. The FID temperature was set to 310 °C. Equations (1-2) were employed to calculate glycerol conversion and acetin selectivity.

$$\text{Glycerol conversion} = \frac{\text{Initial mole of glycerol} - \text{remained mole of glycerol}}{\text{Initial mole of glycerol}} \times 100 \quad (1)$$

$$\text{Selectivity } (S_i, \%) = \frac{\text{mole of i product}}{\text{total moles product of converted glycerol}} \times 100 \quad (2)$$

where i denotes the monoacetin, diacetin or triacetin products

## RESULT AND DISCUSSION

*A. Physicochemical properties of KIT-6, S-KIT-6, 7Zr-KIT-6, and S-7Zr-KIT-6 catalysts*

The physicochemical properties and acidity of KIT-6, S-KIT-6, 7Zr-KIT-6, and S-7Zr-KIT-6 were examined. Table 1 reveals that the KIT-6 and S-KIT-6 catalysts have comparable surface area of 631 $m^2/g$. 7Zr-KIT-6 has a lower surface area of 608 $m^2/g$ compared to the other catalysts, due to pore blockage caused by addition of Zr (Gopinath, *et al.*, 2017). The highest surface area is achieved by S-7Zr-KIT-6 (718 $m^2/g$). The pore volume of KIT-6 is 0.7 $cm^3/g$, whereas S-KIT-6, 7Zr-KIT-6, and S-7Zr-KIT-6 have the pore volume of 0.6 $cm^3/g$. S-7Zr-KIT-6 has a higher surface area due to its reduced pore diameter compared to the others, resulting in an increased surface area

PPC & PETROMAT SYMPOSIUM 2025

(Ren, *et al.*, 2013). The acidity of KIT-6 catalysts was tuned by employing sulphonic acid and Zr loading using the post-synthesis method. The highest acidity among all catalysts is 1.022 mmol/g (or 0.771 mmol/g obtained from $NH_3$-TPD), achieved by S-7Zr-KIT-6. This confirms that combining sulphonic acid and Zr can enhance the acidity of the KIT-6 (Guo, *et al.*, 2023). The interplanar spacing (d-spacing) was determined from the first peak, corresponding to the (211) reflection, and the unit cell parameter ($a_0$) was derived as $a_0 = 6^{1/2}d_{211}$ (Uchoa, *et al.*, 2022). The enhancement of wall thickness of Zr incorporated into KIT-6, S-KIT-6, and S-7Zr-KIT-6 catalysts after post-functionalization caused by Zr incorporated in KIT-6 was also found by Rachmat, *et al.*, 2017. Fig.1 illustrates the small angle XRD (SAXS) patterns of the catalysts and one main peak located at a 2θ value around 0.9°−1.2°, corresponding to the (211) or (220) planes. This peak signifies the presence of a highly ordered mesoporous structure of the prepared catalysts.

**Table 1.** Physicochemical properties of the KIT-6, 7Zr-KIT-6, S-KIT-6 and S-Zr-KIT-6 catalysts.

| Catalyst | Surface area[a] ($m^2/g$) | Pore volume[b] ($cm^3/g$) | Pore diameter[b] (nm) | $d_{211}$[c] (nm) | Unit cell ($a_0$)[d] (nm) | Wall thickness[e] (nm) | Acidity | |
|---|---|---|---|---|---|---|---|---|
| | | | | | | | Titration (mmol/g) | $NH_3$-TPD (mmol/g) |
| KIT-6 | 631 | 0.7 | 5.1 | 9.01 | 22.07 | 5.21 | 0.082 | 0.044 |
| 7Zr-KIT-6 | 608 | 0.6 | 5.3 | 8.83 | 21.64 | 5.24 | 0.272 | 0.537 |
| S-KIT-6 | 631 | 0.6 | 4.4 | 9.01 | 22.07 | 5.25 | 0.269 | 0.510 |
| S-Zr-KIT-6 | 718 | 0.6 | 3.6 | 8.49 | 20.80 | 5.26 | 1.022 | 0.771 |

KIT-6 prepared following molar ratio of compositions: 1.5TEOS: 0.017P123: 1.83HCl: 1.7BuOH: 195$H_2O$

[a] obtained from the BET method.

[b] obtained from the maximum of BJH method desorption pore size distribution.

[c] obtained from the d-spacing reflected of intense (211) peak by SAXS analysis

[d] obtained from the position of the (211) diffraction as $a_0 = 6^{1/2}d_{211}$

[e] wall thickness = $a_0/2$ - pore diameter

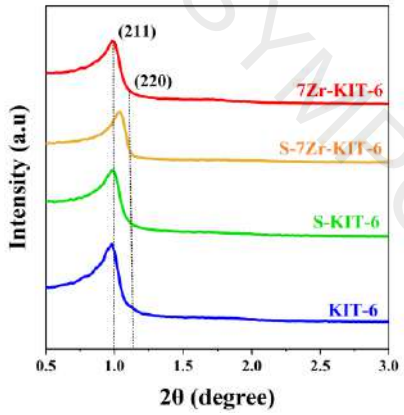


**Figure 1.** Representative small-angle XRD (SAXS) patterns of KIT-6, 7Zr-KIT-6, S-KIT-6, and S-7Zr-KIT-6.

*B. Catalytic Performance of the Prepared Catalysts*

Fig.2. illustrates the catalytic performance of the KIT-6, 7Zr-KIT-6, S-KIT-6, and S-7Zr-KIT-6 catalysts. The results demonstrate that complete glycerol conversion (100%) can be obtained under the following reaction conditions: 0.5 g catalyst loading, a 1:9 glycerol to acetic acid molar ratio, a temperature of 115 °C, and a reaction time of 8 h. The KIT-6 catalyst achieved 27% monoacetin, 56% diacetin, and 17% triacetin selectivity, attributed to its minimal acidity. For S-KIT-6 and 7Zr-KIT-6 (b and c), the selectivity does not much increase for all mono-, di-, and triacetin products.

PPC & PETROMAT SYMPOSIUM 2025

S-7Zr-KIT-6 attained the maximum selectivity for triacetin at 45%. Therefore, the S-7Zr-KIT-6 catalyst was chosen for use in this studies. This result agrees well with other work using sulfate siliceous zirconia catalyst functionalized mesoporous silica (SSZ-550) for the acetylation reaction. A 90% glycerol conversion was achieved with selectivities of 14%, 30% and 46% towards monoacetin, diacetin and triacetin, respectively, under similar conditions using a 2 wt% catalyst at 80 °C (Abida and Ali, 2020).

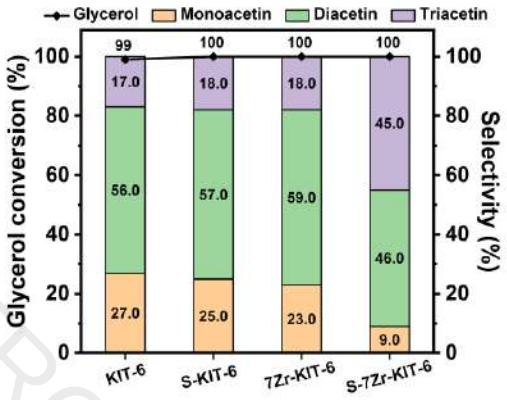


**Figure 2.** Catalytic performances of the prepared catalysts under reaction condition: 0.5 g catalyst loading (5 wt% of total feedstock volume), a 1:9 molar ratio of glycerol to acetic acid, a reaction temperature of 115 °C, and a reaction time of 8 h.

## CONCLUSION

This study demonstrated the efficacy of sulfonic acid-Zr-KIT-6 prepared by a post-synthesis method, for the acetylation of glycerol with acetic acid. Our finding showed the synergy between the structure of KIT-6 with the enhanced acidity tuned by Zr and sulfonic acid functionalization. The presence of strong acid sites quantified by $NH_3$-TPD and acid-base titration is attributed to high activity for this reaction. The S-7Zr-KIT-6 catalysts showed high catalytic activity, achieving 100% glycerol conversion and high triacetin selectivity. The combination of Zr and sulfonic acid was the key parameter for achieving a triacetin selectivity of 45%, compared to that of KIT-6 support at 115 °C (17% triacetin selectivity).

## ACKNOWLEDGEMENTS

The authors would like to thank the financial support from the Petroleum and Petrochemical College, Chulalongkorn University; and scholarship from the Graduate Scholarship for ASEAN and NON-ASEAN countries, Chulalongkorn University.

## REFERENCES

Abida, K. and Ali, A. (2020). Sulphuric acid-functionalized siliceous zirconia as an efficient and reusable catalyst for the synthesis of glycerol triacetate. Chemical Papers, 74(10), 3627-3639.

Chen, S.-Y., Yokoi, T., Tang, C.-Y., Jang, L.-Y., Tatsumi, T., Chan, J. C. C. and Cheng, S. (2011). Sulfonic acid-functionalized platelet SBA-15 materials as efficient catalysts for biodiesel synthesis. Green Chemistry, 13(10), 2920-2930.

PPC & PETROMAT SYMPOSIUM 2025

Gopinath, S., Kumar, P. S. M., Arafath, K. A. Y., Thiruvengadaravi, K. V., Sivanesan, S. and Baskaralingam, P. (2017). Efficient mesoporous $SO_4^{2-}$/Zr-KIT-6 solid acid catalyst for green diesel production from esterification of oleic acid. Fuel, 203, 488-500.

Guillet-Nicolas, R., Ahmad, R., Cychosz, K. A., Kleitz, F. and Thommes, M. (2016). Insights into the pore structure of KIT-6 and SBA-15 ordered mesoporous silica – recent advances by combining physical adsorption with mercury porosimetry. New Journal of Chemistry, 40(5), 4351-4360.

Guo, L., Xie, W. and Xu, X. (2023). A robust mesoporous sulfated zirconium-doped KIT-6 solid acid catalyst for the hydrolysis of microcrystalline cellulose. Journal of Chemical Technology & Biotechnology, 99, 551-561.

Gutiérrez, O. and Klimova, T. (2011). Effect of the support on the high activity of the (Ni)Mo/ZrO 2–SBA15 catalyst in the simultaneous hydrodesulfurization of DBT and 4,6-DMDBT. Journal of Catalysis, 281, 50-62.

Hidayati, N., Sari, R. P. and Purnama, H. (2021). Catalysis of glycerol acetylation on solid acid catalyst: a review. Jurnal Kimia Sains dan Aplikasi, 23(12), 414-423.

Kanimozhi, S., Ramani, V. and Pandurangan, A. (2018). Effects of alumina on GO and KIT-6 supports for the acetylation of glycerol. New Journal of Chemistry, 42, 18942-18950.

Kim, T.-W., Kleitz, F., Paul, B. and Ryoo, R. (2005). MCM-48-like Large Mesoporous Silicas with Tailored Pore Structure: Facile Synthesis Domain in a Ternary Triblock Copolymer−Butanol−Water System. Journal of the American Chemical Society, 127(20), 7601-7610.

Koranian, P., Huang, Q., Dalai, A. K. and Sammynaiken, R. (2022). Chemicals Production from Glycerol through Heterogeneous Catalysis: A Review. Catalysts, 12(8), 897-925.

Moritz, M. G.-M., M. (2015). Mesoporous materials as multifunctional tools in biosciences: principles and applications. Materials Science and Engineering, 49, 114-151.

Perez, F., Gatti, M., Nichio, N. and Pompeo, F. (2022). Bio-additives from glycerol acetylation with acetic acid: Chemical equilibrium model. Journal of Engineering Mechanics, 15, 100502-100512.

Rachmat, A., Trisunaryanti, W., Sutarno and Wijaya, K. (2017). Synthesis and characterization of sulfated zirconia mesopore and its application on lauric acid esterification. Materials for Renewable and Sustainable Energy, 6(3), 13.

Ren, Y., Ma, Z., Morris, R. E., Liu, Z., Jiao, F., Dai, S. and Bruce, P. G. (2013). A solid with a hierarchical tetramodal micro-meso-macro pore size distribution. Nature Communications, 4(1), 2015.

Uchoa, A., Valle, C., Moreira, D., Bañobre-López, M., Gallo, J., Dias, F., Anderson, M. and Ricardo, N. (2022). Synthesis of a KIT-6 mesoporous sulfonic acid catalyst to produce biodiesel from cashew nut oil. Brazilian Journal of Chemical Engineering, 39, 1001–1011.

Yimer, A. M., Assen, A. H., Ait Said, H., Elamri, A., Lakbita, O., Rousseau, A., Adil, K., Benyoucef, H., Daafi, Y. and Belmabkhout, Y. (2024). Direct synthesis of multiple heteroatoms functionalized mesoporous silica adsorbents from phosphate industry mining byproducts. Decontaminating water from Pb(ii) ions as an application case. Journal of Materials Chemistry A, 12(43), 29669-29683.

Zada, B., Kwon, M. and Kim, S.-W. (2022). Current Trends in Acetins Production: Green versus Non-Green Synthesis. Molecules, 27(7), 2255-2269.

PPC & PETROMAT SYMPOSIUM 2025

# Experimental and Simulated Insights of Photocatalytic Degradation of Methylene Blue Using $TiO_2$ as a Photocatalyst in a Microchannel Reactor

*Sasiwimol Soisom* [a], *Paravee Vas-Umnuay**,[a]

[a] Center of Excellence in Particle and Material Processing Technology, Department of Chemical Engineering, Chulalongkorn University, Bangkok 10330 Thailand.

Keywords: Photocatalysis, $TiO_2$, Microchannel

## ABSTRACT

In recent decades, the concern over dye contamination in water sources, particularly methylene blue (MB), has garnered significant attention due to its effects on humans and the environment. This study investigated the photodegradation of methylene blue within a microchannel reactor employing a titanium dioxide ($TiO_2$) photocatalyst film. The microchannel reactor provides constant illumination and reduces diffusion distances within the reactor. The study considered the different chamber widths within the microchannel reactor, varying from 1 to 3 mm. MATLAB simulates convection-diffusion dynamics, using the Langmuir-Hinshelwood kinetic mechanism for analyzing kinetic effects. The experimental results showed 77%, 33%, and 30% MB degradation at 1, 2, and 3 mm widths. The simulation results from experiments showed that the apparent rate constant ($k$) for widths of 1, 2, and 3 mm were 3.53, 2.03, and 1.97 × $10^{-5}$ mol/$m^2$·s, respectively. The adsorption equilibrium constants ($K$) for widths of 1, 2, and 3 mm were 5.00, 5.01, and 6.09 $m^3$/mol ,respectively. The results indicate that a decrease in chamber width enhances the efficiency of methylene blue degradation, leading to a significant rise in the apparent rate constant,while the adsorption equilibrium constant exhibits little variation. This suggests that decreasing the reactor's width is essential to enhancing the efficiency of the MB degradation process.

***paravee.V@chula.ac.th**

## INTRODUCTION

Water is crucial for human life, especially in domestic and industrial settings. The water used by these activities is becoming more contaminated. Likewise, the annual increase in water-contaminated dyes, such as methylene blue (MB), from the textile industry contributes to the growing water pollution problem [1]. MB contains a heterocyclic aromatic molecular structure ($C_{16}H_{18}ClN_3S$) and absorbs light at 665 nm, causing a significant risk to environmental and human health [2].

Development of dye degradation methods for wastewater treatment has been conducted due to concerns about MB contamination in water sources. The most popular approach identified is photocatalysis of dye degradation due to its cost-effectiveness and reusability [3]. Furthermore, studies and developments have been conducted on reactors to enhance photocatalytic efficiency over the traditional batch method. This leads to the design of a microchannel reactor, including narrow channels with a photocatalyst applied to the lower channel wall. This design ensures uniform incoming light and short diffusion distances,

PPC & PETROMAT SYMPOSIUM 2025

thus increasing photocatalytic degradation efficiency [4]. The photocatalyst commonly used for dye degradation is $TiO_2$, due to its resistance to light and chemical corrosion, and its robust photoactivity [5].

This work investigates the photodegradation of methylene blue in a microchannel reactor using a $TiO_2$ photocatalytic film. Experiments were conducted to compare differences in width within the microchannel reactor, during which the chamber width was varied to 1, 2, and 3 mm. The experimental results were subsequently simulated in MATLAB to solve the 2D diffusion-reaction equations, applying the Langmuir-Hinshelwood kinetic mechanism to investigate the related kinetic effects.

## EXPERIMENTAL

### *A. Chemicals*

Methylene blue ($C_{16}H_{18}ClN_3S.xH_2O$, 99%, QRëC), Titanium (IV) isopropoxide ($Ti[OCH(CH_2)_2]_4$, >98%, Thermo Scientific), Hydrochloric acid (HCl, 37%, Quality Reagent Chemical), Ethyl alcohol ($C_2H_5OH$, >99.9%, Quality Reagent Chemical), Deionized water (DI water), Isopropyl alcohol ($C_3H_7OH$, CARLO ERBA Reagents).

### *B. $TiO_2$ photocatalyst film preparations*

$TiO_2$ photocatalyst solution was synthesized using the sol-gel method. A 0.35 M solution of titanium (IV) isopropoxide (TTIP) was prepared by dissolving 1.061 mL of TTIP in 5 mL of ethyl alcohol. Separately, a 0.04 M hydrochloric acid (HCl) solution was prepared by dissolving 0.048 mL of HCl in 5 mL of ethyl alcohol. The HCl solution was then added dropwise to the continuously stirred TTIP solution until the mixture became clear. The resulting $TiO_2$ photocatalyst solution was applied onto an FTO glass substrate using the convective deposition method. The coated glass was then placed on a hot plate and heated at 70 °C for 15 min. This coating process was repeated three times, followed by annealing the sample at 500 °C for 1 h.

### C. *Experimental set-up for MB photocatalytic degradation test*

In this experiment, the internal width of the chamber was modified to 1, 2, and 3 mm. An MB solution with a concentration of 2 mg/l was injected from the bottom of the reactor at flow rates of 0.05, 0.10, and 0.15 ml/min with a syringe pump, corresponding to chamber widths of 1, 2, and 3 mm, respectively, to maintain uniform residence times across all chamber widths. A 100 W UV lamp was used as the light source, directed at the light-receiving area in the center of the reactor, as shown in Figure 1. Each experiment was carried out in darkness for 30 minutes, subsequently followed by 180 min in light conditions. Samples were also collected to measure absorbance using a UV-visible spectrophotometer at 664 nm, the peak absorption wavelength of MB.

PPC & PETROMAT SYMPOSIUM 2025

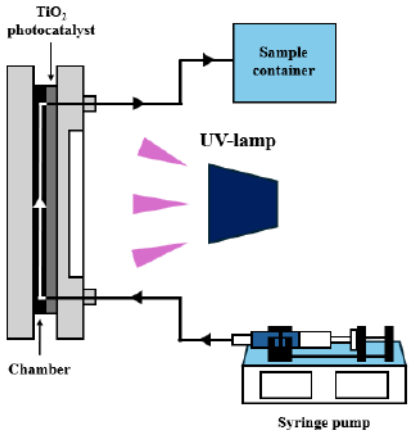


**Figure 1.** *Experimental set-up for MB photocatalytic degradation test*

*D. Modeling with MATLAB*

The MB photocatalytic degradation 2D domain model was simulated via the finite element method using MATLAB version R2022b, as illustrated in Figure 2. Within the reactor, the length of the channel is 40 mm, while the width ranges from 1 to 3 mm. One wall of the reactor is coated with a $TiO_2$ photocatalyst, accelerating the degradation reaction, while the opposite wall remains non-reactive. For the reason of simplicity, the physical properties of water are taken into consideration for the dilution of the MB solution [6].

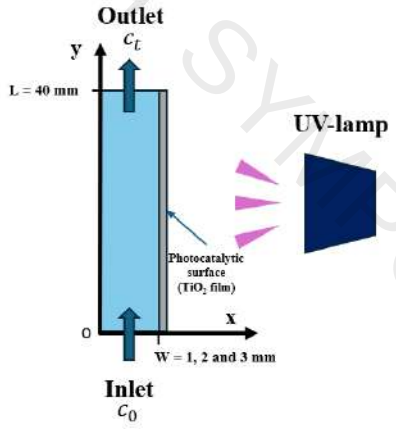


**Figure 2.** *The MB photocatalytic degradation 2D domain model.*

The MB solution is a single phase exhibiting laminar flow. The analysis considers a steady-state condition with a Newtonian and incompressible fluid, including a no-slip boundary condition at both the wall and the catalyst surface. The continuity equation (Eq. (1)) and the motion equation (Eq. (2)) are employed for analysing the MB solution flowing through the y-axis from bottom to top.

PPC & PETROMAT SYMPOSIUM 2025

$$\rho \nabla \vec{u} = 0 \quad (1)$$

$$\rho \left(\frac{\partial \vec{u}}{\partial t}\right) + \vec{u} \cdot \nabla \vec{u} = -\nabla \vec{p} + \mu \nabla^2 \vec{u} \quad (2)$$

In Eqs. (1) and (2), $u$ represents the velocity vector (m/s), $\rho$ denotes the fluid density (kg/m³), $\mu$ denotes the dynamic viscosity of the fluid (kg/m·s), and $p$ indicates the fluid pressure (Pa).

The convection-diffusion equation presented in Eq. (3) is employed to analyze mass transfer in the bulk within the microchannel reactor [7].

$$\frac{\partial \vec{c}}{\partial t} + \nabla \cdot (-D \nabla \vec{c} + \vec{c}\vec{u}) = 0 \quad (3)$$

In Eq. (3), $c$ represents the concentration of MB in bulk (mol/m³), and $D$ is the diffusion coefficient for dilute MB (equal to 1 x $10^{-9}$ m²/s). The unsteady state condition is considered. The flow velocity in the y-axis and diffusion in the x-axis. The $TiO_2$ photocatalyst absorbs MB concentration from bulk into its surface. The catalytic surface reaction ($r$) is analyzed applying the flux boundary condition as shown in Eq. (4).

$$\frac{\partial c_s}{\partial t} + (-D \nabla c_s) = r \quad (4)$$

where $c_s$ is the surface concentration of MB. The rate of elimination of organic pollutants is usually determined by the Langmuir-Hinshelwood kinetic model, as shown in Eq. (5).

$$r = \frac{kKc_s}{1+Kc_s} \quad (5)$$

where $k$ represents the apparent rate constant and $K$ represents the adsorption constant. Given that the surface reaction occurs more rapidly than the diffusion reaction, it could be assumed that the surface concentration of MB is insignificant relative to the bulk concentration of MB, as shown in Eq. (6) [8].

$$r = \frac{kKc}{1+Kc} \quad (6)$$

*E. Characterization*

The crystallinity and phase formation of the $TiO_2$ photocatalytic film were analyzed via X-ray diffraction (BRUKER D8 DISCOVER) employing detector scan mode and Cu Kα1 (λ=1.5406Å) radiation within the 2θ range of 10°– 60°. The morphology and thickness of the $TiO_2$ photocatalytic film were studied using a scanning electron microscope. Furthermore, a UV-vis spectrophotometer (Shimadzu UV-2600) was utilized to measure the absorbance of methylene blue within the 400-800 nm region to determine the change in MB concentration.

PPC & PETROMAT SYMPOSIUM 2025

## RESULTS AND DISCUSSION

### *A. $TiO_2$ photocatalyst characterizations*

The crystallinity and phase formation of the $TiO_2$ film analyzed using XRD is shown in Figure 3. The $TiO_2$ film exhibited peaks at 2θ values of 25.38°, 38.2°, 48.22°, 54.26°, and 55.24°, corresponding to the planes (101), (004), (200), (105), and (211), respectively, confirming the anatase phase of $TiO_2$ [9]. At 52.25°, there is a peak in FTO glass. The anatase phase of $TiO_2$ is frequently employed in dye degradation due to its large band gap energy, enabling it to absorb more organic compounds compared to the rutile and brookite phases [10].

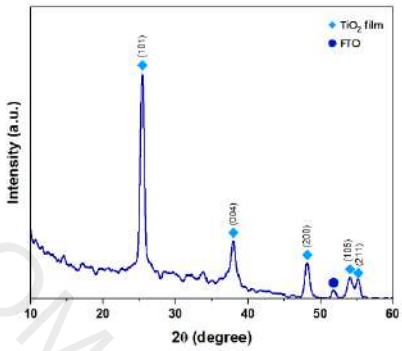


**Figure 3.** *The XRD pattern of the $TiO_2$ film.*

The morphology of the $TiO_2$ film was analyzed using SEM, as shown in Figure 4. Figure 4a, the top-section image, shows that the synthesized $TiO_2$ film is smooth, with no fractures, and exhibits closely aligned particles. In Figure 4b, the cross-sectional image shows that the $TiO_2$ film adheres completely to the FTO glass surface, with an average thickness of 240 nm.

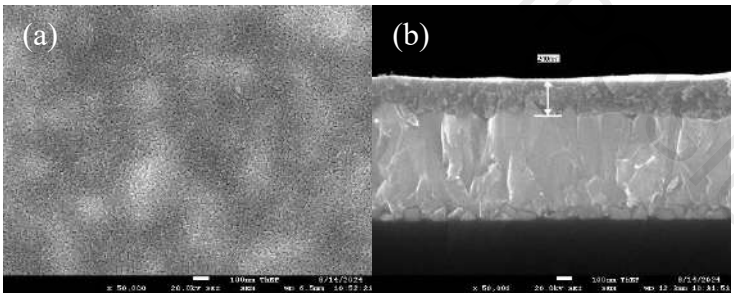


**Figure 4.** *The SEM image of the $TiO_2$ film: (a) top-section, (b) cross-section.*

### *B. The MB photodegradation and kinetic simulation results.*

Figure 5a-c shows the effect of MB degradation using a $TiO_2$ film, with chamber widths of 1, 2, and 3 mm. The study investigated the ratio of concentration change over time to the initial concentration ($C_t/C_0$) as a function of time. The experiment results indicated that the MB photodegradation with the widths of 1, 2, and 3 mm obtained degradation of 77%,

33%, and 30%, respectively. Upon analyzing the experimental results for kinetic effects via MATLAB simulation, the apparent rate constant ($k$) values at widths of 1, 2, and 3 mm have
been determined to be 3.53, 2.03, and 1.97 × $10^{-5}$ mol/m²·s, respectively. While the adsorption constant ($K$) values were 5.00, 5.01, and 6.09 m³/mol, respectively. This indicates that the apparent rate constant diminishes as chamber width increases, as the greater width impacts the diffusion of MB to the $TiO_2$ surface, hence leading to reduced degradation of MB. Similar values of the obtained adsorption constants indicated an adsorption of $TiO_2$,which was not affected by changes in chamber width.

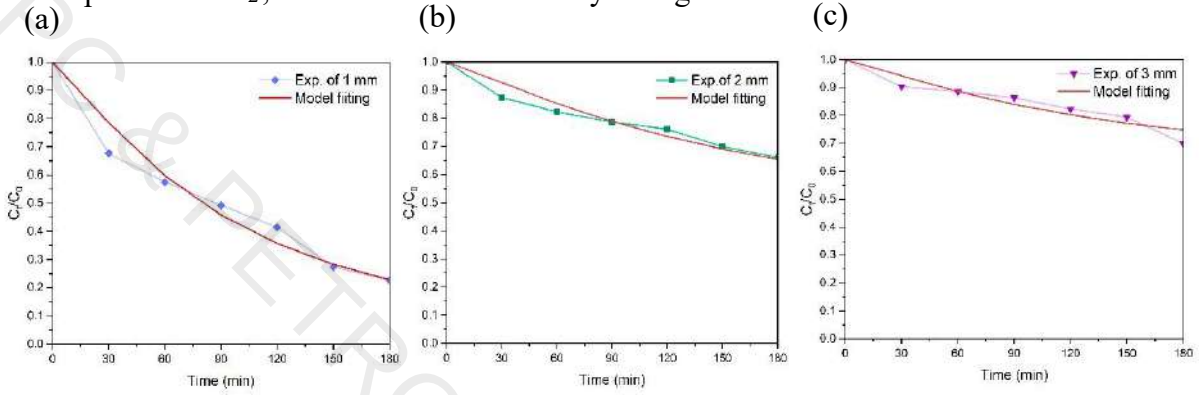


**Figure 5**. *The effect of MB degradation using a $TiO_2$ film with different chamber widths: (a) 1 mm, (b) 2 mm, and (c) 3 mm.*

## CONCLUSIONS

In the investigation of MB degradation using the $TiO_2$ film, an increase in the chamber width of the reactor resulted in a decreased $C_t/C_0$ value, indicating lower efficiency in MB degradation. Simulation of the experimental results using MATLAB revealed that the apparent rate constant ($k$) decreased with an increase in chamber width, which indicates a reduced likelihood of MB diffusing to the surface of the $TiO_2$ photocatalyst, which consequently led to a decrease in MB degradation efficiency. The obtained values of the adsorption constant ($K$) were comparable, suggesting that the ability to adsorb $TiO_2$ remained relatively unchanged with variations in chamber width.

## REFERENCES

1. **Shabir, M., et al.** (2022). *A review on recent advances in the treatment of dye-polluted wastewater*. **112**, p. 1-19. Journal of Industrial and Engineering Chemistry.
2. **Oladoye, P.O., et al.** (2022). *Methylene blue dye: Toxicity and potential elimination technology from wastewater*. **16**. Results in Engineering.
3. **Gao, Z., et al.** (2021). *Continuous-Flow Photocatalytic Microfluidic-Reactor for the Treatment of Aqueous Contaminants, Simplicity, and Complexity: A Mini-Review*. **13 (8)**. Symmetry.
4. **Das, S. and V.C. Srivastava** (2016). *Microfluidic-based photocatalytic microreactor for environmental application: a review of fabrication substrates and techniques, and operating parameters*. **15 (6)**, p. 714-30. Photochem Photobiol Sci.

PPC & PETROMAT SYMPOSIUM 2025

5. **Lailatul, N. Z., et al.** (2019). *Sol-gel Preparation of Different Crystalline Phases of $TiO_2$ Nanoparticles for Photocatalytic Degradation of Methylene Blue in Aqueous Solution*. **7 (1)**, p. 39-45. American Journal of Nanomaterials.
6. **Fayazeh, R., et al.** (2021). *Simulation of photocatalytic degradation of methylene blue in planar microreactor with integrated ZnO nanowires*. Journal of Applied Research in Water and Wastewater.
7. **Corbel, S., et al.** (2012). *Modelling and design of microchannel reactor for photocatalysis*. **7 (3)**, p. 203-209.Virtual and Physical Prototyping.
8. **Corbel, S., et al.** (2014). *Mass transfer measurements and modeling in a microchannel photocatalytic reactor*. **92 (4)**, p. 657-662. Chemical Engineering Research and Design.
9. **Wiranwetchayan, O., et al.** (2017). *Effect of alcohol solvents on $TiO_2$ films prepared by sol–gel method*. **326**, p. 310-315. Surface and Coatings Technology.
10. **Teoh, W.Y., et al.** (2012). *Progress in Heterogeneous Photocatalysis: From Classical Radical Chemistry to Engineering Nanomaterials and Solar Reactors*. **3 (5)**, p. 629-39. J Phys Chem Lett.

PPC & PETROMAT SYMPOSIUM 2025

# Studied the activity of doping Fe in $LaNiO_3$ perovskite for the dry reforming of methane

Suparatthakorn Puangjinda[a], Merika Chanthanumataporn[*,a,b]

[a] Center of Excellence on Catalysis and Catalytic Reaction Engineering, Department of Chemical Engineering, Faculty of Engineering, Chulalongkorn University, Bangkok, 10330, Thailand
[b] Bio-Circular-Green-economy Technology & Engineering Center, BCGeTEC, Department of Chemical Engineering, Faculty of Engineering, Chulalongkorn University, Bangkok, Thailand 10330

Keywords : Doping Fe; Dry reforming of methane; Perovskite catalysts; Sol-gel

## ABSTRACT

The dry reforming of methane reaction uses two types of catalysts: noble metals (such as Rh, Ru, Pt, and others) and transition metals (including Ni, Co, Fe, and others). Currently, transitional metals are mainly used due to their low prices and high activity; however, their activity decreases quickly due to carbon deposits on the catalyst surface. $LaNi_{(1-x)}Fe_xO_3$ (where $0.1<x<0.5$) was synthesized using the sol-gel method to investigate the effect of varying amounts of Fe in $LaNiO_3$ perovskite on the catalyst's performance during the dry reforming of methane reaction. The experiment involved $LaNi_{(1-x)}Fe_xO_3$ performing DRM at 700 °C for 6 hours, using a $CH_4$:$CO_2$ molar ratio of 1:1 and a total flow rate of 40 mL/min. The analysis indicated that a decrease in the iron content led to decreases in other compound phases and more significant square morphology. The experimental results of the dry reforming of the methane reaction indicated that $LaNi_{0.5}Fe_{0.5}O_3$ became the catalyst, demonstrating the highest performance of this research. The catalyst resulted in around 27% conversion of $CH_4$, 47% conversion of $CO_2$, and $H_2$/CO ratio of 0.58.

* merika.c@chula.ac.th

## INTRODUCTION

Carbon monoxide (CO) and hydrogen are produced via the dry reforming of methane, which transforms methane and carbon dioxide into synthesis gas. Synthesis gas becomes a precursor for many chemical reactions, facilitating the production of an extensive range of chemical compounds. Subsequent chemical reactions can produce a range of chemicals, including methanol, ethanol, fuels, and hydrocarbons.[1, 2]

Perovskite catalyst is a catalyst used in the dry reforming of methane because it has excellent thermal resistance and can prevent coke formation on the catalyst surface. The structure of perovskite is $ABO_3$, where A is a rare earth, making it a support with Oxygen in the oxide state, and B is a transition metal, acting as an active site.[2] Most research studies use Ni-based catalysts

PPC & PETROMAT SYMPOSIUM 2025

because they are inexpensive transition metals that respond well to the dry reforming of methane. B has been developed in the form of bimetallic metal by adding other elements such as Zn, Fe, Cu, etc., to enhance the qualities of the catalyst, such as preventing coke deposition, reducing sintering, etc.[1, 2] Sania Maria de Lima et al.[3] was observed that when comparing $LaNiO_3$ with $LaNiO_3$ containing a small amount of iron, the addition of iron enhances stability, with the activity being lower than that of $LaNiO_3$ without iron. Xiao Song et al.[4] found that adding a small amount of iron to $LaNiO_3$ and $La_2NiO_4$ will enhance the carbon resistance properties of the catalyst, leading to the stability of mixed perovskite catalysts in the atmosphere and the enhancement of metal-support interaction.

The objective of the research is to compare the Fe ratios in the $LaNi_{(1-x)}Fe_xO_3$ catalyst and analyze its properties using XRD, BET, SEM, and ICP to better understand the chemical and physical characteristics of the $LaNi_{(1-x)}Fe_xO_3$ catalyst, which was synthesized using the sol-gel method and the amount of iron used during this experiment will be between 0.1 and 0.5 using reaction testing conditions, which are 700°C for 6 h, $CH_4$:$CO_2$ = 1, and WHSV = 6 $L•(h•g_{cat})^{-1}$, to identify the suitable ratio for dry reforming of methane.

## EXPERIMENTAL

### A. Materials and Synthesis Method

Materials used in this study are Nickel (II) nitrate hexahydrate ($Ni(NO_3)_2·6H_2O$), Lanthanum nitrate hexahydrate ($La(NO_3)_3·6H_2O$), Iron (III) nitrate nonahydrate ($Fe(NO_3)_3·9H_2O$), Citric acid monohydrate ($C_6H_8O_7·H_2O$), Ammonia solution 25% ($NH_4OH$)

### B.Synthesis of $LaNi_{(1-x)}Fe_xO_3$ by sol-gel method

$LaNi_{(1-x)}Fe_xO_3$ with varying Fe doping amount ($0.1<x<0.5$) was synthesized using the sol-gel method.[5] Nickel (II) nitrate hexahydrate ($Ni(NO_3)_2·6H_2O$), Lanthanum nitrate hexahydrate 99%( $La(NO_3)_3·6H_2O$), and iron (III) nitrate hexahydrate ($Fe(NO_3)_3·9H_2O$) were dissolved together in 100 mL of deionized water. Then citric acid (CA) and ethylene diamine tetraacetic acid (EDTA) were added into the above solution with a molar ratio of metal ion: CA: EDTA = 1: 1: 1.5. Aqueous ammonia was dropped slowly into the mixture solution until pH = 4.0-5.0 with vigorous stirring. The mixture was maintained at 80 °C until all the water had evaporated, resulting in a transparent gel. The resulting xerogel underwent calcination through a three-step process. The initial phase involved the combustion of the precursor at 300 °C for 4 hours in air to remove the organic components. Subsequently, the temperature was increased to 750 °C for 3 hours, followed by a rise to 850 °C for a final 3 hours to form $LaNi_{(1-x)}Fe_xO_3$ catalysts, which are identified as LNF-x, where x represents a molar amount of Fe.

### C. Characterization

BET was measured for surface area, pore volume, and pore size. FE-SEM was used to measure the morphology of the catalysts. X-ray diffractometer was used to measure the structural phase of catalysts by using the $2\theta = (20\text{-}80^o)$ range at 298 K with CuKα radiation source. ICP identifies metallic elements to analyze the composition of elements generated via catalyst synthesis.

PPC & PETROMAT SYMPOSIUM 2025

### D. Catalytic evaluation

The measurement of catalytic activity was performed in a quartz tubular fixed-bed continuous-flow reactor at atmospheric pressure. The total amount of 0.5 g of the catalyst was carefully set in the center of the reactor. Before the reaction, the catalyst was reduced in a 20% $H_2/N_2$ mixture at 750°C for 1 h. After reduction, the temperature was decreased to 700°C, and a reactant gas comprising an equimolar mixture of $CH_4$ and $CO_2$ was introduced into the reactor. The gas composition of reactants and products was analyzed by using a gas chromatograph (GC-8A) equipped with a TCD detector. In all tests, the catalyst performances were evaluated by the conversion of $CH_4$ and $CO_2$, selectivity to $H_2$ and CO, and $H_2$/CO ratio, which are calculated as: $CH_4$ and $CO_2$ conversion: [6]

$$\text{Conversion X (\%)} = \left(\frac{M_{in}-M_{out}}{M_{in}}\right) \times 100 \quad (1)$$

Selectivity to $H_2$ and CO:

$$\text{Selectivity X (\%)} = \frac{M_{\text{out of product}}}{M_{total\ product}} \times 100 \quad (2)$$

$H_2$/CO ratio:

$$\frac{H_2}{CO}\ \text{ratio} = \frac{M_{\text{out of product } H_2}}{M_{\text{out of product CO}}} \quad (3)$$

Where $M_{in}$ and $M_{out}$ represent the molar flow rate with units of mol/min $CH_4$, CO, $CO_2$, and $H_2$ entering and leaving the reactor, respectively.[6, 7]

## RESULTS AND DISCUSSION

### A. Characterization of synthesized catalysts

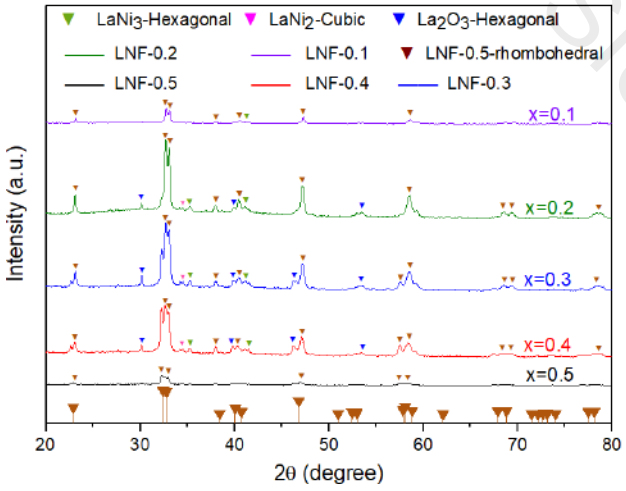


**Figure 1** XRD pattern of as-synthesized LNF-x catalyst

PPC & PETROMAT SYMPOSIUM 2025

Figure 1 illustrates the XRD pattern of the as-synthesized LNF-x catalyst. The outcome indicates that the phase in each ratio remains consistent, specifically the rhombohedral phase[8] (PDF 04-006-1883-ICDD). Additionally, each ratio of Fe presents supplementary phases, including the $LaNi_3$ hexagonal phase, $LaNi_2$ cubic phase, and $La_2O_3$ hexagonal phase.

**Table 1** Inductively coupled plasma atomic emission spectroscopy analyses and Textural properties of LNF-x catalysts

| sample | Mole (%) | | | Fe/Ni | Surface area ($m^2/g$) | Pore Volume ($cm^3/g$) |
|---|---|---|---|---|---|---|
| | La | Ni | Fe | | | |
| LNF-0.5 | 49.92 | 24.88 | 25.19 | 1.01 | 2.08 | $1.97x10^{-3}$ |
| LNF-0.4 | 49.41 | 30.09 | 20.50 | 0.68 | 1.27 | $2.25x10^{-3}$ |
| LNF-0.3 | 48.87 | 35.63 | 15.51 | 0.44 | 2.42 | $3.55x10^{-3}$ |
| LNF-0.2 | 48.60 | 39.85 | 11.55 | 0.29 | 2.03 | $2.49x10^{-3}$ |
| LNF-0.1 | 49.27 | 44.72 | 6.00 | 0.13 | 2.59 | $4.48x10^{-3}$ |

Table 1 presents an analysis of metallic elements to determine the composition derived from the synthesis and surface area of the LNF-x catalyst, reflecting the ratio of doped Fe within the catalyst structure as compared to the theoretical ratio. The ICP results indicate that the quantity of Ni is marginally greater than that of Fe, resulting in a slight deviation of the doped Fe ratio from the theoretical expectations. The BET results discovered that all catalyst ratios were in the identical rhombohedral phase, characterized by low surface area and low pore volume. Upon the reduction of Fe, the surface area and pore volume experienced only marginal increases. In comparison, LNF-0.5 showed a large surface area but a small pore volume, as the SEM image showed big, similar cubic shapes mixed, while LNF-0.4 had big, similar cubic shapes along with a small surface area and a large pore volume. In the two examples, it was observed that as the pore volume rose, the larger, similar cubic formations progressively disappeared.

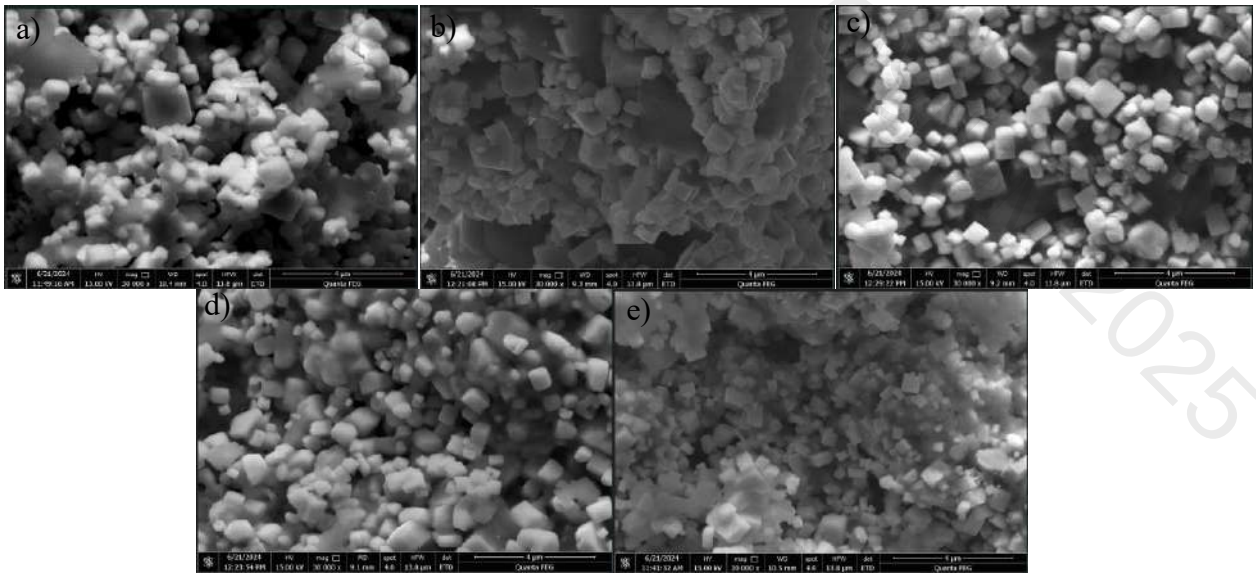


PPC & PETROMAT SYMPOSIUM 2025

**Figure 2** FE-SEM images of as-synthesized LNF-x catalyst: a) LNF-0.5, b) LNF-0.4, c) LNF-0.3, d) LNF-0.2, and e) LNF-0.1

Figure 2 shows an examination of the shape of the $LaNi_{(1-x)}Fe_xO_3$ catalyst based on SEM results. The catalysts exhibit a similar cubic shape. The analysis of ICP and SEM indicates that a reduction in the amount of Fe leads to a more obvious similar cubic shape.

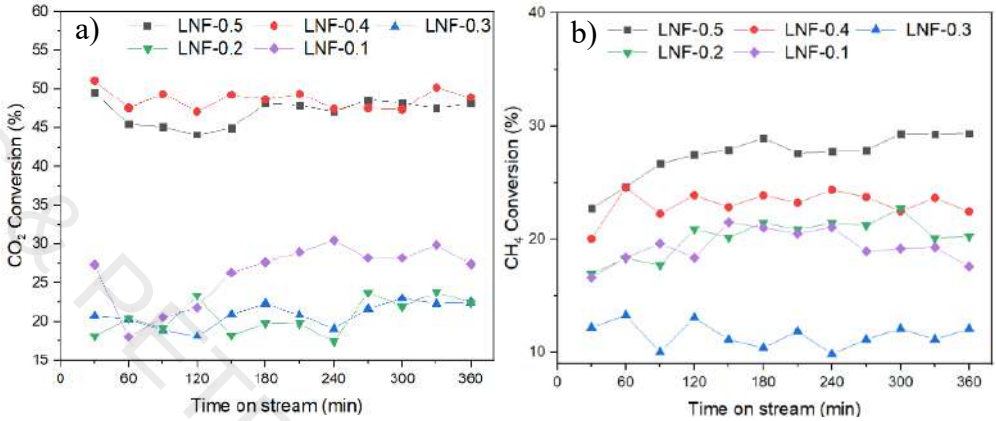


Figure 3 a) $CH_4$ conversion and b) $CO_2$ conversion of LNF-x catalyst at 700 ºC, $CH_4$:$CO_2$ = 1:1, WHSV = 6 L•(h•$g_{cat}$)$^{-1}$

Figure 3 presents an analysis of the experimental outcomes from the dry reforming of methane conducted at 700 °C. The results showed that LNF-(0.4-0.5) exhibits $CH_4$ and $CO_2$ conversion rates of approximately 20-30% and 44-51%, respectively, while LNF-(0.1-0.3) has conversion rates of approximately 9-23% and 18-30%, respectively. XRD analysis revealed that LNF-0.5 exhibits no peaks corresponding to other compounds, just displaying the rhombohedral phase, which facilitates a favorable reaction. In contrast, LNF-0.4 begins to exhibit peaks of additional compounds, resulting in diminished reactivity due to reduced oxygen bonding on the surface, as the addition of other compounds inhibits the reaction.[9]

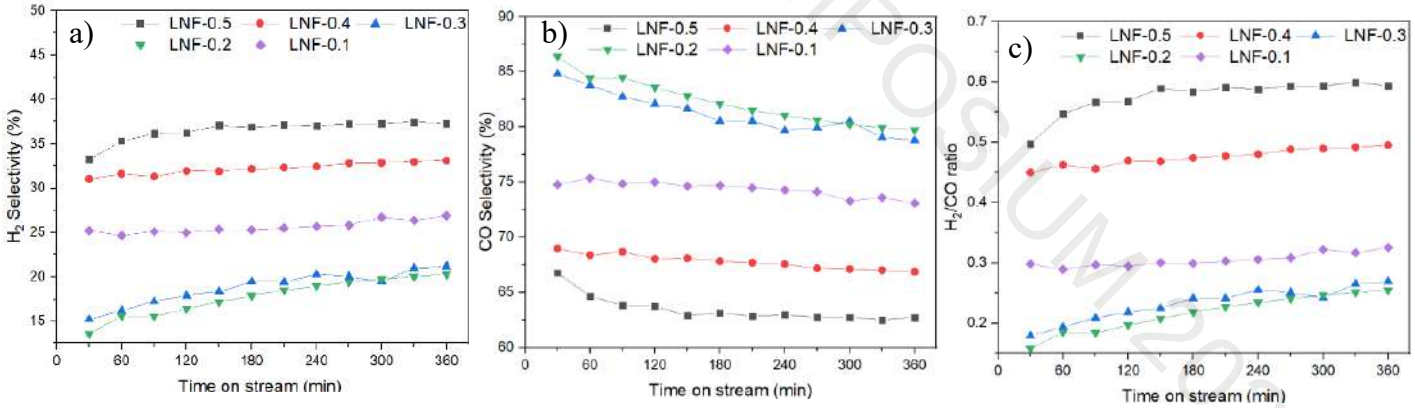


Figure 4 a) $H_2$ selectivity, b) CO selectivity, and c) $H_2$/CO ratio of LNF-x catalyst at 700 ºC, $CH_4$:$CO_2$ = 1:1, WHSV = 6 L•(h•$g_{cat}$)$^{-1}$

Figure 4, the experimental results for the dry reforming of methane at 700°C. The study indicated that LNF-(0.4-0.5) exhibits $H_2$ and CO selectivity values of approximately 31-37% and 62-69%, respectively, with an $H_2$/CO ratio ranging from 0.45 to 0.59. In contrast, LNF-(0.1-0.3)

demonstrates H2 and CO selectivity values of roughly 13-25% and 75-87%, respectively, with an H2/CO ratio between 0.15 and 0.32. XRD analysis revealed that LNF-0.5 exhibited no peaks corresponding to other compounds, just displaying the rhombohedral phase, which facilitated optimal reactivity. In comparison, LNF-0.4 began to show peaks of additional compounds, resulting in less reactivity and reduced production of $H_2$ and CO, due to the influence of oxygen bonding on the surface.[9]

## CONCLUSIONS

This research focuses on the effect of increasing the iron ratio from 0.1 to 0.5 in the dry reforming of methane via the sol-gel method. The experimental results indicate that the synthesized catalyst with an iron ratio of 0.5 is the most effective, as it exhibits a rhombohedral phase without the addition of other compounds. This leads to a greater influence on the bonding of oxygen at the surface compared to catalysts with different ratios that have additional phases identified in XRD analysis. Moreover, the catalysts exhibit comparable surface areas and adopt analogous cubic shapes.

## REFERENCES


1. Aramouni, N.A.K., et al., *Catalyst design for dry reforming of methane: Analysis review.* Renewable and Sustainable Energy Reviews, 2018. **82**: p. 2570-2585.
2. Bhattar, S., et al., *A review on dry reforming of methane over perovskite derived catalysts.* Catalysis Today, 2021. **365**: p. 2-23.
3. de Lima, S.M. and J.M. Assaf, *Ni–Fe Catalysts Based on Perovskite-type Oxides for Dry Reforming of Methane to Syngas.* Catalysis Letters, 2006. **108**(1-2): p. 63-70.
4. Song, X., et al., *Effects of Fe partial substitution of La 2 NiO 4 /LaNiO 3 catalyst precursors prepared by wet impregnation method for the dry reforming of methane.* Applied Catalysis A: General, 2016. **526**: p. 132-138.
5. Jahangiri, A., H. Aghabozorg, and H. Pahlavanzadeh, *Effects of Fe substitutions by Ni in La–Ni–O perovskite-type oxides in reforming of methane with CO2 and O2.* International Journal of Hydrogen Energy, 2013. **38**(25): p. 10407-10416.
6. Rabelo-Neto, R.C., et al., *CO2 reforming of methane over supported LaNiO3 perovskite-type oxides.* Applied Catalysis B: Environmental, 2018. **221**: p. 349-361.
7. Liu, C., et al., *Dry reforming of methane by LaNiO3 perovskite oxide: Cu-substituted improving reactivity and stability.* International Journal of Hydrogen Energy, 2025. **101**: p. 617-626.
8. Bonmassar, N., et al., *In Situ-Determined Catalytically Active State of LaNiO3 in Methane Dry Reforming.* ACS Catalysis, 2019. **10**(2): p. 1102-1112.
9. *<Structural features and activity for CO oxidation of LaFe~Ni~.~O3+~ catalysts.pdf>.*


PROCEEDINGS PETROMAT SYMPOSIUM 2025

# SYNTHESIS AND CATALYTIC ACTIVITY OF HIGH-ENTROPY METAL SULFIDES FOR OXYGEN EVOLUTION REACTION

*Maythada Ruamjaithanakul* [a], *Sakulsuk Unarunotai* [a], *Numpon Insin* *[a,b]

[a] Department of Chemistry, Faculty of Science, Chulalongkorn University, Bangkok 10330, Thailand
[b] Photocatalysts for Clean Environment and Energy Research Unit, Faculty of Science, Chulalongkorn University, Bangkok, 10330, Thailand

Keywords: High-entropy metal sulfides, electrocatalyst, oxygen evolution reaction

## ABSTRACT

High-Entropy Materials (HEMs), which are composed of at least five different metal elements, are intended to operate as electrocatalysts for the oxygen evolution reaction (OER) in water-splitting. High-entropy metal sulfides (HEMSs) are parts of HEMs that can provide excellent catalytic activity in the OER. However, attempts to synthesize HEMSs frequently encounter difficulties in integrating several metal components into the structure. In this research, FeCoNiCuZnS HEMSs were synthesized by solvothermal methods and by a solid-state reaction using various single metal sulfides. The synthesized materials were characterized using XRD, SEM, TEM and ICP-OES techniques. The FeCoNiCuZnS HEMSs showed a mixed structure of two cubic phases with metallic components of both +2 and +3 ions, increasing the charge transfer property of the material and making it a great electrocatalyst. When utilized as an OER catalyst, compared with five types of single metal sulfides, the HEMS showed high OER activity with a low overpotential of 222 mV at 10 mAcm $^{-2}$ in 1.0 M KOH with stability for up to 6 hours. HEMSs were successfully synthesized and have the potential to be useful in electrocatalysis applications

***numpon.i@chula.ac.th**

## INTRODUCTION

Nowadays, energy demand is increasing due to industrial development and extreme population growth. Therefore, there is a need to research and develop sustainable alternative energy to replace fossil energy. Electrochemical water-splitting is one of the key green technologies for producing hydrogen energy, as hydrogen fuel is a renewable energy with no pollution, making it an attractive alternative to fossil fuels. The water splitting reaction is divided into two parts: hydrogen evolution reaction (HER), and oxygen evolution reaction (OER) at the cathode and anode, respectively. Currently, the development of this technology is hindered by the slow kinetics and complicated mechanism of OER due to the complex four-electron transfer process. The well-known and commercially available catalysts, $RuO_2$ and $IrO_2$, are used as OER.[1] However, the scarcity of noble metals and inferior stability in alkaline solutions have limited their use in industry.[2] Recently, non-precious metal or transition metal compound catalysts, such as metal oxides, chalcogenides, hydroxides etc., have been developed to be efficient electrocatalysts. Among these materials, transition metal sulfides showed effective electrical conductivity and OER activity under alkaline due to the surface reconstruction process and low cost.[3, 4]

PPC & PETROMAT SYMPOSIUM 2025

Recently, high-entropy materials (HEMs), which are composed of at least five different metal elements, have been applied in various applications.[5] The definition is given based on Boltzman hypothesis, where entropy (S) is the degree of disorder, uncertainty or randomness in the system.[6] The configuration entropy of mixing ($S^{mix}_{config}$) depends on number of components and atomic fraction in the structure (Eq. 1), which is defined as the HEMs when $S^{mix}_{config} \geq 1.5R$. According to thermodynamics, the Gibbs free energy of mixing ($\Delta G_{mix}$) shows that as the term $\Delta S_{mix}$ increases, the $\Delta G_{mix}$ becomes more negative, resulting in more stable materials, which is beneficial to the application of HEMs in various applications.[6]

$$\Delta S^{mix}_{conf} = -R \sum_{i=1}^{N} x_i \ln x_i \quad (1)$$

Where, R is the ideal gas constant, N is the number of components, while $x_i$ represent the atomic fraction of components.

High-entropy metal sulfides (HEMSs) are parts of HEMs that can provide excellent catalytic activity in water splitting owing to remarkable structural properties, catalytic activity, and outstanding electrical conductivity.[7] However, attempts to synthesize HEMSs frequently encounter difficulties in integrating several metal components into the structure. Previous reports have shown the synthesis using pulse thermal decomposition process and ball-milling process, in which high energy and longtime were required.

In this study, we report the design and fabrication of HEMSs via a combination of solvothermal and solid-state reactions, aiming to reduce the energy and time required for synthesis while enhancing their electrocatalytic activity toward the oxygen evolution reaction (OER).

## EXPERIMENTAL

### *A. Synthesis of HEMSs using single metal sulfides process*

Each metal sulfides were first synthesized using a solvothermal process. Metal nitrates source (1.0 mmol each) and thiourea 1-2 mmol were dissolved in 40 mL ethylene glycol. Homogeneously mixed solution was transferred to a 100 mL Teflon-lined stainless-steel autoclave for solvothermal reaction at 200-220°C for 18 h. The resulting powders were washed with water several times and then dried at 60°C. Second, HEMS were prepared by mixed 5 metal sulfides and used solid-state reaction process at 1000°C for 6 h under $N_2$ gas (gas flow furnace).

### *B. Synthesis of HEMSs using mixed metal sulfides process*

As-synthesized HEMSs were first synthesized using a solvothermal process. Equimolar metal nitrates source (1.0 mmol each) and thiourea 10 mmol were dissolved in 40 mL ethylene glycol. Homogeneously mixed solution was transferred to a 100 mL Teflon-lined stainless-steel autoclave for solvothermal reaction at 220°C for 18 h. The resulting powders were washed with water several times and then dried at 60°C. Second, HEMS were prepared by solid-state reaction process at 1000°C for 6 h under $N_2$ gas (gas flow furnace).

### *C. Characterizations*

X-ray powder diffraction (XRD: a Rigaku SmartLab 30kV with Cu Kα radiation), scanning electron microscope (SEM: JEOL JSM-IT100 at 20kV), transmission electron microscope (TEM: FEI TECNAI G2 20), inductively coupled plasma emission optical spectrometry (ICP-OES, Thermo iCAP 6500 Duo) will be used to study the structure, morphology, and chemical composition of materials.

PPC & PETROMAT SYMPOSIUM 2025

*D. Electrochemical testing*

The electrocatalyst-treated glassy carbon electrode (E-GCE) was prepared as follows: HEMSs electrocatalyst powder:carbon black = 1:1 and 5%wt Nafion were dispersed in a 2-propanol under ultrasonic energy. After 30 min of ultrasonication, a certain amount of the above-mentioned ink was drop-casted on the GCE, then was dried in a hot air oven for 2 h to fabricate the working electrodes. The active materials loading on GCE were 509 μg/cm$^2$. Electrochemical measurements were carried out using Palm Sens 4 potentiostat with a standard three-electrode mode in a 1.0 M KOH solution 10mL as the electrolyte, using the electrocatalyst-treated glassy carbon electrode (E-GCE), a platinum wire, and Ag/AgCl as the working, counter, and reference electrode, respectively. Electrochemical performance was specified via linear sweep voltammetry (LSV) with a scan speed of 5 mV/s, and the stability were tested using by chronopotentiometry and chronoamperometry.

## RESULTS AND DISCUSSION

*A. Characterizations*

The HEMS synthesis affects material characteristics, with solvothermal processes being heat and pressure-based processes that use less energy, and solid-state processes that can improve the stability of the material structure. The single metal sulfides process is to synthesize the five metal sulfides first and then mix them in a solid-state reaction, while the mixed metal sulfides process is to mix the five metal sulfides in a solvothermal reaction and then continue the solid-state reaction.

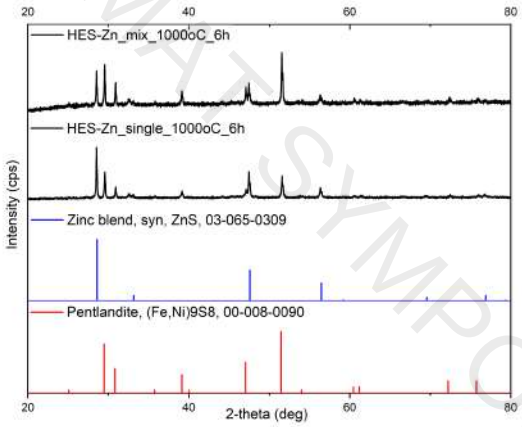


**Figure 1.** XRD Pattern of FeCoNiCuZnS using single metal process (FeCoNiCuZnS-single) and mixed metal process (FeCoNiCuZnS-mix)

The phase structures of the HEMSs FeCoNiCuZnS using single metal process (FeCoNiCuZnS-single) and mixed metal process (FeCoNiCuZnS-mix) were analyzed by XRD characterization. **Figures 1** show the XRD patterns of FeCoNiCuZnS-single and FeCoNiCuZnS-mixed which are prepared in different process, all diffraction peaks of the materials can be match with the 2 cubic phase structure corresponding to PDF #00-008-0090, which showed the distinct peaks at 29.46°, 30.81°, 39.13°, 47.02°, and 51.44° corresponding to (311), (222), (331), (511) and (440) planes of pentlandite, respectively. And another cubic structure mixed match with PDF #03-065-0309, which showed the distinct peaks at 28.61°, 33.15°, 47.59°, and 56.47° corresponding to (111), (200), (220), and (311) planes of zinc blend, respectively. XRD pattern shows that both synthesis processes produce materials with the same mixed two cubic structure but different ratios structures, with the single metal sulfides process represent a higher ratio of zinc blend structures than

PPC & PETROMAT SYMPOSIUM 2025

the mixed metal sulfides process. The crystallite size was calculated from the peak at 29.46° with 105.6 and 103.5 nm of FeCoNiCuZnS-single, and FeCoNiCuZnS-mixed, respectively.

**Figure 2(a-d)** shows the SEM image of the as-prepared HEMSs. FeCoNiCuZnS-single has a non-uniform distribution of spherical shapes, which is aggregated into the big particles, and it has particle size around 10μm. While, FeCoNiCuZnS-mixed has a spherical shape with particle size 1-2μm.

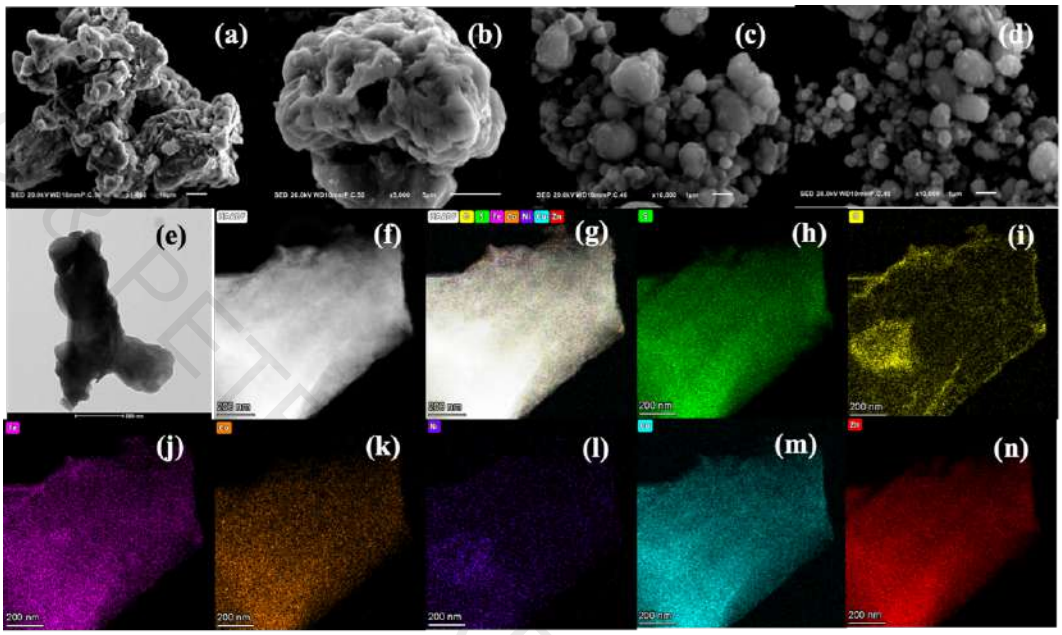


**Figure 2.** SEM images of the (a-b) FeCoNiCuZnS-single, and (c-d) FeCoNiCuZnS-mixed. (e) TEM images, (f) HAADF image, and (g-n) elemental mapping of FeCoNiCuZnS-single.

The atomic ratio of each metal elements in HEMS FeCoNiCuZnS was analyzed by ICP-OES , as shown in **Table 1.** The atomic ratios of 5 metals, Fe, Co, Ni, Cu and Zn, were 0.89, 0.94, 1.00, 1.09 and 1.20, respectively, which approximates the metal atomic ratio in the FeCoNiCuZnS (1:1:1:1:1). **Figure 2(e-n)** shows the TEM image and Energy dispersive X-ray (EDX) analysis of the as-prepared HEMS FeCoNiCuZnS-single. It has a uniform distribution of metal and sulfur elements.

**Table 1.** ICP-OES concentration of HEMS FeCoNiCuZnS-single

| Element | % Atom | Atomic ratio |
|---|---|---|
| Fe | 17.38 | 0.89 |
| Co | 18.30 | 0.94 |
| Ni | 19.53 | 1.00 |
| Cu | 21.29 | 1.09 |
| Zn | 23.50 | 1.20 |

*B. Electrochemical testing*

The OER performance of the as-synthesized samples was evaluated using linear sweep voltammetry (LSV). As shown in **Figure 3(a-b)**, the (FeCoNiCuZn)S-single exhibited a lower overpotential of 222 mV at a current density of 10 mA $cm^{-2}$ ($\eta_{10}$) and 425 mV at 100 mA $cm^{-2}$ ($\eta_{100}$), compared to the (FeCoNiCuZn)S-mixed. This enhanced performance is attributed to its high crystallinity and structural stability, which facilitate improved catalytic efficiency. In addition, the

HEMS ((FeCoNiCuZn)S-single) exhibited superior OER activity compared to the five metal sulfides synthesized under identical conditions, as well as the commercial catalyst $RuO_2$ as shown in **Table 2.,** showing that multi-element (high entropy) is attributed to the synergistic interactions among the constituent metal elements. In addition, metal sulfides can undergo surface reconstruction into active oxy/hydroxide derivatives (the true active species), which lowers the energy barrier and enhances catalytic activity. Similarly, metal sulfates are also capable of transforming into these active phases under OER conditions[3, 6]. The stability of the catalyst was evaluated using chronoamperometry and chronopotentiometry, as shown in **Figure 3(c-d)**, with continuous operation for up to 6 and 11 hours, respectively. These results confirm that the catalyst demonstrates good electrochemical stability under OER conditions.

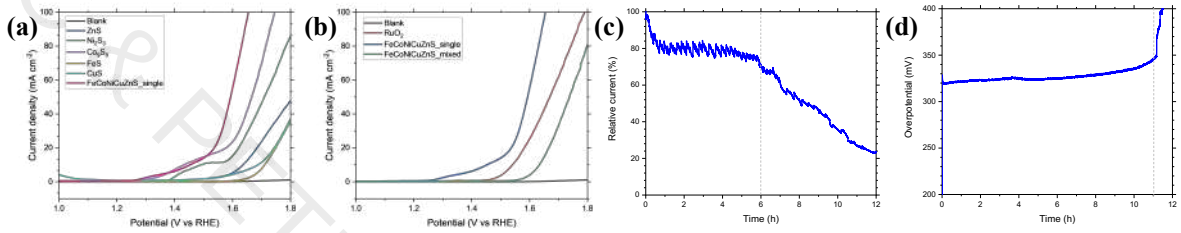


**Figure 3.** Oxygen evolution reaction (OER) performance. (a-b) at a scan rate of 5 mV $s^{-1}$ of various materials. (c) Chronoamperometry of FeCoNiCuZnS-single at the fixed overpotential of 300 mV (d) Chronopotentiometry of FeCoNiCuZnS-single at a current density of 10 mA $cm^{-2}$

**Table 2.** Comparison of the OER activity of FeCoNiCuZn, $IrO_2$, and various metal sulfides.

| Element | Overpotential (mV) | |
|---|---|---|
| | $\eta_{10}$ | $\eta_{100}$ |
| FeS | 481 | 962 |
| $Co_9S_8$ | 203 | 516 |
| $Ni_2S_3$ | 263 | 602 |
| CuS | 458 | 873 |
| ZnS | 407 | 928 |
| $RuO_2$ (comercials) | 311 | 560 |
| FeCoNiCuZnS-mixed | 404 | 607 |
| FeCoNiCuZnS-single | 222 | 425 |

## CONCLUSIONS

HEMSs synthesized from single-metal sulfide precursors exhibit superior electrocatalytic performance compared to mixed-metal counterparts. The HEMSs, (FeCoNiCuZn)$S_x$-single material, featuring a mixed cubic structure with +2 and +3 oxidation states, shows enhanced charge transfer and excellent oxygen evolution reaction (OER) activity, with a low overpotential and good stability. These results highlight the promise of HEMSs as efficient electrocatalysts for sustainable energy applications.

## ACKNOWLEDGEMENTS

This work is funded by the Development and Promotion of Science and Technology Talents Project (DPST) scholarship, Graduate School Thesis Grant, Chulalongkorn University, and the Department of Chemistry, Faculty of Science, Chulalongkorn University.

PPC & PETROMAT SYMPOSIUM 2025

## REFERENCES

(1) Lee, Y.; Suntivich, J.; May, K. J.; Perry, E. E.; Shao-Horn, Y. Synthesis and Activities of Rutile IrO2 and RuO2 Nanoparticles for Oxygen Evolution in Acid and Alkaline Solutions. *The Journal of*
*Physical Chemistry Letters* **2012**, *3* (3), 399-404.
(2) Liu, J.; Zheng, Y.; Jiao, Y.; Wang, Z.; Lu, Z.; Vasileff, A.; Qiao, S. Z. NiO as a Bifunctional Promoter for RuO(2) toward Superior Overall Water Splitting. *Small* **2018**, *14* (16), e1704073.
(3) Hu, Y.; Zheng, Y.; Jin, J.; Wang, Y.; Peng, Y.; Yin, J.; Shen, W.; Hou, Y.; Zhu, L.; An, L.; et al. Understanding the sulphur-oxygen exchange process of metal sulphides prior to oxygen evolution reaction. *Nature Communications* **2023**, *14* (1), 1949.
(4) Wang, W.; Wang, A.; Xu, J.; Li, H.; Yu, M.; Dong, A.; Li, Z.; Zhao, C.; Cheng, F.; Wang, W. Surface reconstruction of pyrite-type transition metal sulfides during oxygen evolution reaction. *Journal of Colloid and Interface Science* **2024**, *657*, 334-343.
(5) Schweidler, S.; Botros, M.; Strauss, F.; Wang, Q.; Ma, Y.; Velasco, L.; Cadilha Marques, G.; Sarkar, A.; Kübel, C.; Hahn, H.; et al. High-entropy materials for energy and electronic applications. *Nature Reviews Materials* **2024**, *9* (4), 266-281.
(6) Nguyen, T. X.; Su, Y.-H.; Lin, C.-C.; Ting, J.-M. Self-Reconstruction of Sulfate-Containing High Entropy Sulfide for Exceptionally High-Performance Oxygen Evolution Reaction Electrocatalyst. *Advanced Functional Materials* **2021**, *31* (48), 2106229.
(7) Feng, C.; Chen, M.; Zhou, Y.; Xie, Z.; Li, X.; Xiaokaiti, P.; Kansha, Y.; Abudula, A.; Guan, G. High-entropy NiFeCoV disulfides for enhanced alkaline water/seawater electrolysis. *Journal of Colloid and Interface Science* **2023**, *645*, 724-734.

PPC & PETROMAT SYMPOSIUM 2025

# Session 3-Advanced Materials Innovation (MAT)

# A Novel Hydrothermal Synthesis Process of MIL-53(Al) using Bamboo Biochar as a Sustainable Precursor for $CO_2$ Adsorption

~~Pisit Phayutcharoenkun~~ [a], Samson Bamidele Akindoye [a], Rajendran Chandran [a], Phuet Prasertcharoensuk [a]

[a] Department of Chemical Engineering, Chulalongkorn University

Keywords: Metal-Organic Frameworks (MOFs), Biochar, Composite, Carbon Dioxide Adsorption

## ABSTRACT

Among the numerous MOFs members, MIL-53(Al) framework is one of the most interesting structures due to the breathing effect and has been widely investigated for hydrogen storage and water treatment. It is built up by the interconnection of infinite trans chains of corner-sharing $AlO_4(OH)_2$ octahedral by 1,4-benzenedicarboxylate ligands. MIL-53 crystallizes in a "wine rack" structure (Pnma, a = 17.129(2) Å, b = 6.628(1) Å, c = 12.182(1) Å, $\alpha = \beta = \gamma = 90°$) with large internal pores held open by excess solvent and unreacted ligand in the as-synthesized state. Another challenge is the synthesis process and raw materials for production, synthetic-method development has been playing a major role in the advancement of this field. Due to the complex and expensive synthesis process, researchers around the world are working to improve manufacturing processes and search for alternative raw materials to assemble the structure for reducing the cost of MIL-53 synthesis while maintaining its physical properties and purity. This work investigates the potential of bamboo biochar as alternative material for metal-organic frameworks (MOFs)'s synthetic to tackle the problem of costly production. The utilization of biochar, a carbonaceous substance obtained from organic matter, has garnered attention due to its ability and the price.

*** Phuet.p@chula.ac.th**

## INTRODUCTION

Until relatively recent times, most technological developments have been linked to metamorphisms of materials. Multifunctional materials are the materials that perform multiple functions in a system due to their specific properties. Multifunctional materials can be both naturally existing and specially engineered. The integration of materials science and engineering is essential to improving structures, applications, and manufacturing processes.[1] Metal–organic frameworks (MOFs) are versatile porous materials that hold huge potential with a broad range of applications. It is constructed by connecting metal ions/clusters with organic linkers in the network structure (1-D, 2-D, or 3-D, leading to the generation of periodic network crystalline structures with high porosities and large surface areas, which promote their potential applications in various fields of science and technology.[2] These properties, together with the extraordinary degree of variability for both the organic and inorganic components of their structures, make MOFs of interest for potential applications in clean energy, most significantly as storage media for gases such as hydrogen and methane, and as high-capacity adsorbents to meet various separation needs.

PPC & PETROMAT SYMPOSIUM 2025

Additional applications in membranes, thin-film devices, catalysis, and biomedical imaging are increasingly gaining importance.[3]

Among the numerous MOFs members, MIL-53(Al) framework is one of the most interesting structures due to its breathing effect and has been widely investigated for hydrogen storage and water treatment. It is built up by the interconnection of infinite trans chains of corner-sharing $AlO_4(OH)_2$ octahedral by 1,4-benzenedicarboxylate ligands. [4] MIL-53 crystallizes in a "wine rack" structure (Pnma, a = 17.129(2) Å, b = 6.628(1) Å, c = 12.182(1) Å, $\alpha = \beta = \gamma = 90°$) with large internal pores held open by excess solvent and unreacted ligand in the as-synthesized state.[5]

Another challenge is the synthesis process and raw materials for production, synthetic-method development has been playing a major role in the advancement of this field. Due to the complex and expensive synthesis process, researchers around the world are working to improve manufacturing processes and search for alternative raw materials to assemble the structure to reduce the cost of MIL-53 synthesis while maintaining its physical properties and purity.[6]

Although innovations in MOFs have advanced from laboratories to engineering and applications, MOF commercialization is still in a growing stage and is greatly impeded by limitations associated with their mass productivity and properties. This thesis investigates the potential of bamboo biochar as an alternative material for metal-organic frameworks (MOFs)'s synthetic to tackle the problem of costly production. The utilization of biochar, a carbonaceous substance obtained from organic matter, has garnered attention due to its ability and price.

## EXPERIMENTAL

### *A. Materia*

Activated biochar

Bamboo biochar 98% from Thai Carbon & Graphite Co., Ltd. And Potassium Hydroxide (KOH) 98% from J.T. Barker.

MIL-53(Al)

Aluminium Nitrate ($Al(NO_3)_3 \cdot 9H_2O$) 98% from DAEJUNG, 1,4-Benzenedicarboxylic Acid (BDC or terephthalic acid), 98% from Sigma Aldrich, and DI water.

### *B. Methodology*

Activation of biochar using KOH

Commence by quantifying the preferred quantity of charcoal and potassium hydroxide (KOH). The optimal ratio of potassium hydroxide (KOH) to biochar may vary depending on the specific use, although a commonly recommended initial proportion is approximately 1:1 (KOH: Biochar). In a glass container, add the KOH to the biochar while stirring continuously. The reaction between KOH and biochar generates heat and can be exothermic, so be cautious. If necessary, add a small amount of distilled or deionized water to the mixture to create a paste-like consistency. This helps facilitate the activation process. Transfer the mixture to an oven and heat it at a controlled temperature (commonly around 300-800°C) for a specified period (typically several hours). The heat activates the biochar and transforms it into activated carbon. Allow the biochar that has been activated to cool to the ambient temperature. Rinse the activated charcoal with water to eliminate any surplus KOH and other contaminants. You may need to repeat this washing process several times

PPC & PETROMAT SYMPOSIUM 2025

until the pH of the washed biochar reaches a stable and acceptable level. After washing, dry the activated biochar in an oven to remove any remaining moisture. This is typically done at a lower temperature than the activation step. Store the activated biochar in a dry and sealed container to prevent it from reabsorbing moisture and impurities from the environment.

Synthesizing of MIL-53(Al)-BDC using activated biochar

$Al(NO_3)_3 \cdot 9H_2O$ (1.915 g, 5.0 mmol), and activated biochar (0.3 g) were dissolved in distilled water (25 mL) and adjusted pH then placed in a Teflon-lined steel autoclave and heated up at 220 °C for 72 hours. At the end of reaction time, the autoclave was cooled down to room temperature. The resulting crude was filtered and washed with deionized water several times and the wet white powder was dried under vacuum for overnight at 100 °C to obtain as-MIL-53(Al)-BDC. Then, the as-MIL(Al)-BDC was calcined at 330 °C during 72 hours under vacuum to obtain lp-MIL-53(Al)-BDC. After the calcination, lp-MIL-53(Al)-BDC was cooled down to obtain the npMIL-53(Al)-BDC by the water presence into the pores. The classic activation process was carried out on MIL-53(Al)-BDC, it was heated up to 180 °C under vacuum for 2 hours. Thus, lp-MIL-53(Al)-BDC was obtained, stored in a dedicator and characterized.

Characterizations of MOF

A variety of methods are used to characterize a metal-organic framework (MOF) to determine its structure, porosity, surface area, chemical composition, and other characteristics. The following are some standard techniques for MOF characterization in the laboratory:

X-ray diffraction (XRD): Determining the crystal structure of MOFs necessitates the use of XRD. It provides information about the size of the crystals, the purity of the phases, and the characteristics of the unit cell. It also helps in determining the arrangement of atoms within the lattice of the material.

Gas adsorption analysis involves conducting measurements of gas adsorption at various temperatures using techniques such as nitrogen or argon adsorption. This process yields information on the material's porosity, surface area, pore size distribution, and pore volume. The Brunauer-Emmett-Teller (BET) method is extensively used for calculating surface area.

Transmission Electron Microscopy (TEM) and Scanning Electron Microscopy (SEM) can be used to capture high-resolution images of MOF samples at micro- and nano-scale levels. TEM provides detailed information about the size, shape, and distribution of the particles, while SEM focuses on imaging at a larger scale.

Fourier Transform Infrared Spectroscopy (FTIR): The information provided by FTIR spectroscopy about chemical bonding, organic linker presence, and functional group identification in MOFs are all helpful.

Thermogravimetric Analysis (TGA): The existence of volatile components in MOFs, thermal stability, and decomposition temperatures can all be ascertained using TGA, which analyses weight changes in response to temperature.

*C. $CO_2$ adsorption-desorption analysis*

Before analysis, the adsorbent material (100 mg) was preheated at 200 °C for 24 hours. A desorption study of $CO_2$ was performed using a Temperature-Programmed Desorption (TPD) instrument. 5% $CO_2$ in He was used to study the basicity properties of materials and

PPC & PETROMAT SYMPOSIUM 2025

adsorption–desorption behaviour. The TPD analysis was carried out from 50 to 720 °C at a heating rate of 10 °C/min under flowing He (50 ml/min).

## RESULTS AND DISCUSSION

### *A. Structural Characterization*

XRD patterns confirmed the successful synthesis of MIL-53(Al)-BDC, exhibiting characteristic peaks corresponding to its crystalline structure. Both Al-MIL-53-BDC and MIL-53(Al)-BDC/Biochar has consistent peaks from SC-XRD structural simulations at 10.313, 12.645, 14.455, 15.317, 17.319, 17.798, 18.565, 20.470, 21.237, 24.101, 25.251, and 26.869 respectively. Moreover, the xrd peak of biochar obtained from bamboo pyrolysis also showed unequivocally amorphous behavior as shown in Figure 1.

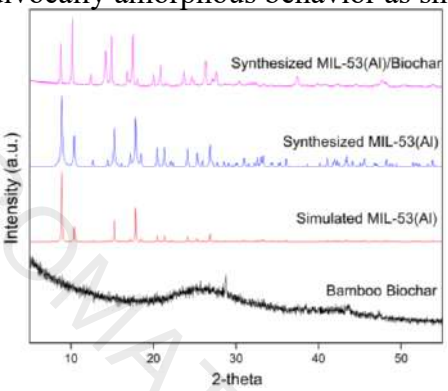


Figure 1: PXRD patterns of Bamboo Biochar, MIL-53(Al)-BDC simulated patterns, MIL-53(Al)-BDC from synthesis, and MIL-53(Al)-BDC /Biochar.

The morphology of materials was determined using SEM microscopy. SEM image in Figures 2a and 2b revealed typical parallelepiped and trapezoidal prism-shaped crystals of MIL-53(Al)-BDC and MIL-53(Al)-BDC/Biochar, respectively. Figure 2b shows the non-uniform particles of biochar evincing amorphousness in the system.

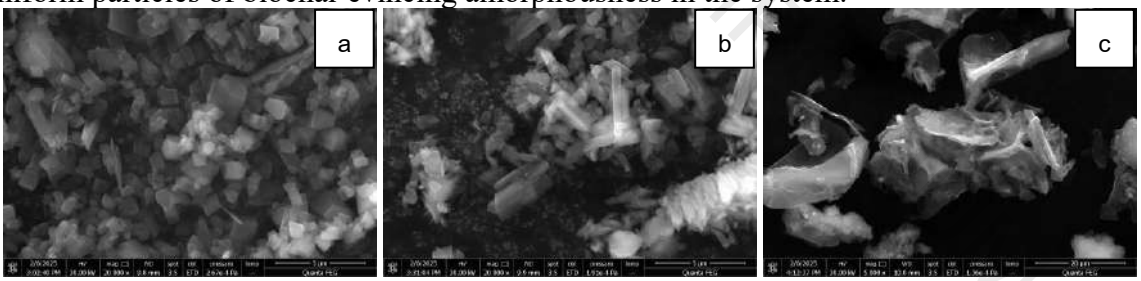


Figure 2: SEM images of (a) MIL-53(Al)-BDC, (b) MIL-53(Al)-BDC/Biochar, and (c) Bamboo Biochar.

The thermogravimetric analysis (TGA) provides information about the synthesized materials (Figure 3). The lower temperature peak corresponds to the release of the guest molecules (water within the pores) at 150 °C, while the higher temperature (340 °C) peak is related to the decomposition of uncoordinated terephthalate that is captured inside the pores. At 540 °C, structural decomposition occurs due to the dissociation of the terephthalic from the framework.

PPC & PETROMAT SYMPOSIUM 2025

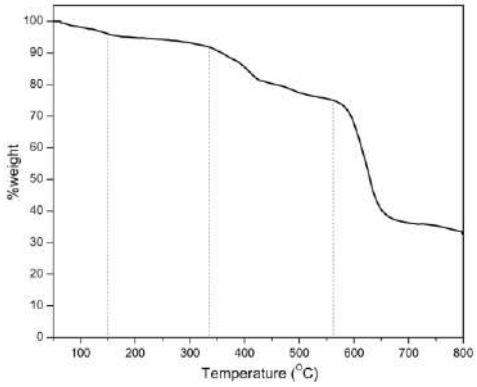


Figure 3: Thermal decomposition results from TGA of MIL-53(Al)-BDC/Biochar

Figure 4 depicts the $N_2$ adsorption-desorption isotherm of MIL-53(Al)-BDC/Biochar. We can notice an isotherm of type IV exhibiting a hysteresis loop with a large hysteresis typical of the breathing effect. The specific surface area is about 806 m²/g.

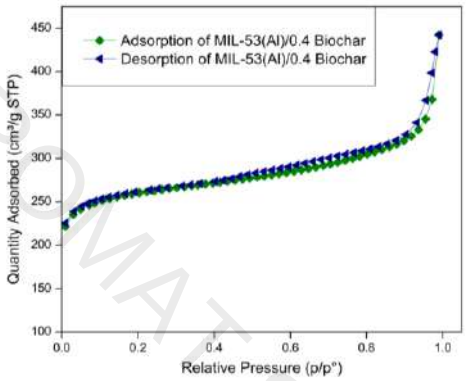


Figure 4: Nitrogen (77 K) sorption measurement of MIL-53(Al)-BDC/Biochar.

*B. Adsorption-desorption of $CO_2$*

For $CO_2$ sorption studies, a clear peak corresponding to $CO_2$ release was detected at 520-620 °C around 11 mmol/g as shown in Figure 5. Hamid Reza Mahdipoor et al. (2021) revealed MIL-53 synthesized by Al as metal center is capable to adsorb 10 mmol/g of $CO_2$ gas at ambient temperature and 2 MPa.[7] From the above information, it can be concluded that MIL-53(Al) synthesized using biochar has the potential for practical application.

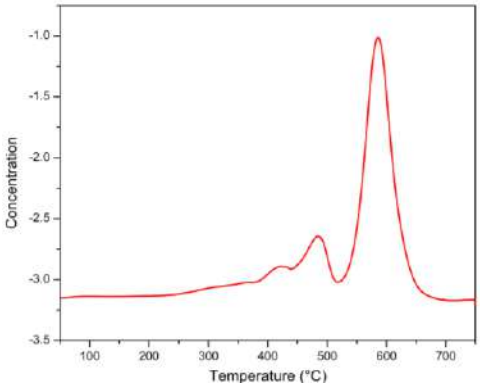


Figure 5: Carbon Dioxide sorption measurement of MIL-53(Al)-BDC/Biochar.

PPC & PETROMAT SYMPOSIUM 2025

## CONCLUSIONS

The MIL-53(Al)-BDC/biochar porous material developed in this study offers a sustainable and efficient solution for carbon dioxide capture. Its high adsorption capacity, structural stability, and cost-effectiveness make it a promising candidate for large-scale applications in air treatment. The material could absorb carbon dioxide gas up to 11 mmol/g.

## ACKNOWLEDGEMENTS

The authors gratefully acknowledge the supporting and research funding from Department of Chemical Engineering, Faculty of Engineering, Chulalongkorn University.

## REFERENCES

**Ferreira, B.L.**, Nóvoa, P.J.R.O., Marques, A. T. (2016). Multifunctional Material Systems: A state-of-the-art review. Composite Structures, 151, 3-35.

**Yusuf, V. F.**, Malek, N. I., Kailasa, S. K. (2022). Review on Metal–Organic Framework Classification, Synthetic Approaches, and Influencing Factors: Applications in Energy, Drug Delivery, and Wastewater Treatment. ACS Omega, 70(49).

**Zhou, H.**, Long, J. R., Yaghi, O. M. (2012). Introduction to Metal–Organic Frameworks. Chemical Reviews, 112(2).

**Qian, X.**, Yadian, B., Wu, R., Long, Y., Zhou, K., Zhu, B., Huang, Y. (2013). Structure stability of metal-organic framework MIL-53 (Al) in aqueous solutions. International Journal of Hydrogen Energy, 38(36), 16710-16715.

**Ashling, C. W.**, Johnstone, N, D., Widmer, R. N., Hou, J., Collins, M. S., Sapnik, A. F., Bumstead, A. M., Midgley, P. A., Chater, P. A., Keen, D. A., Bennett, T. D. (2019) Synthesis and Properties of a Compositional Series of MIL-53(Al) Metal–Organic Framework Crystal-Glass Composites. Journal of the American Chemical Society, 141(39).

**Paul, T.**, Juma, A., Alqerem, R., Karanikolos, G., Arafat, H. A., Dumée L. F. (2023). Scale-up of metal-organic frameworks production: Engineering strategies and prospects towards sustainable manufacturing. Journal of Environmental Chemical Engineering, 11(5), 111112.

**Mahdipoor, H. R.,** Halladj, Rouein., Babakhani, E. G., Amjad-Iranagh, S., Ahari, J. S. (2021). Synthesis, characterization, and CO2 adsorption properties of metal organic framework Fe-BDC. The Royal Society of Chemistry's, 11, 5192-5203.

PPC & PETROMAT SYMPOSIUM 2025

# Carboxymethyl Cellulose/Cellulose Nanofiber/Zinc Oxide Nanocomposite Hydrogel for Wearable Glucose Sensor Application

*Phannaphat Buadang*[a], *Thitiyaporn Phookum*[b], *Nadnudda Rodthongkum*[*,c], *Pranut Potiyaraj*[a]

[a] Department of Materials Science, Faculty of Science, Chulalongkorn University, Bangkok, 10330, Thailand
[b] Nanoscience and Technology Interdisciplinary Program, Chulalongkorn University, Bangkok, 10330, Thailand
[c] Department of Chemistry, Faculty of Science, Chulalongkorn University, Bangkok, 10330, Thailand
[d] Center of Excellence in Responsive Wearable Materials, Chulalongkorn, University, Bangkok, 10330, Thailand

Keywords: Non-invasive sensor, Carboxymethyl cellulose, Cellulose nanofiber, Zinc Oxide

## ABSTRACT

Non-invasive wearable sensors are increasingly important for health monitoring, especially in diabetes management where the invasive and painful finger-prick blood glucose method necessitates alternative solutions. Sweat-based glucose sensors, utilizing absorbent hydrogels that exhibit visible color changes in response to sweat glucose levels, offer a user-friendly, needle-free approach. Biocompatibility is paramount, making cellulose-based materials a promising foundation. In this work, we focus on fabricating a novel carboxymethyl cellulose (CMC)/cellulose nanofibers (CNF)/zinc oxide (ZnO) hydrogel crosslinked with citric acid for application in non-invasive wearable glucose sensors. The incorporation of carboxymethyl cellulose (CMC) enhances water solubility and allows for hydrogel formation upon crosslinking with 10 wt% citric acid, which was found to be sufficient for stable structural integrity. To improve the hydrogel's mechanical properties, 1 wt% cellulose nanofibers (CNF) were integrated, balancing swelling capacity and compressive strength. Furthermore, 0.2 wt% zinc oxide (ZnO) nanoparticles were incorporated to provide significant antibacterial properties and ensure cytocompatibility, thereby preventing bacterial growth on the sensor and ensuring safety for prolonged skin contact. The resulting CMC/CNF/ZnO hydrogel, crosslinked with citric acid, is specifically tailored for its ability to selectively and visibly respond to glucose concentrations within the physiological range found in sweat. This innovative hydrogel offers significant promise for the development of real-time, painless, and non-invasive glucose monitoring systems for enhanced diabetic care and management.

*** Corresponding author e-mail: nadnudda.r@chula.ac.th**

## INTRODUCTION

Non-invasive wearable sensors are increasingly vital for health monitoring, especially in diabetes management. Without regular glucose monitoring, blood sugar can reach dangerously high levels, potentially leading to diabetic shock. Given that traditional finger-prick blood tests are invasive and painful, there's a strong drive to develop non-invasive glucose sensors. While various biofluids like tears, saliva, and urine can be used for glucose detection, their limited availability (tears) or high contaminant levels (saliva, urine) make them less ideal than sweat. Consequently, sweat-sensing hydrogel-based platforms have emerged as promising candidates due to their excellent liquid absorbency, flexibility, and mechanical properties. These user-friendly patches utilize hydrogels that visually change

PPC & PETROMAT SYMPOSIUM 2025

color in response to sweat glucose levels, offering a convenient, needle-free alternative for continuous monitoring. Biomaterials designed for human contact prioritize biocompatibility. Our hydrogel design leverages the inherent hydrophilicity of cellulose, utilizing carboxymethyl cellulose (CMC) for its enhanced water solubility and ability to form crosslinkable structures. Citric acid (10 wt%) effectively crosslinks CMC, yielding stable hydrogels with high swelling capacity, though requiring post-neutralization for skin safety. To bolster mechanical properties, cellulose nanofibers (CNF) were incorporated as reinforcement. Furthermore, zinc oxide (ZnO) nanoparticles provided essential antibacterial properties and cytocompatibility, ensuring safe skin contact. This optimized hydrogel enables colorimetric glucose detection within a 0-0.5 mM range, spanning relevant physiological levels in human sweat, saliva, and ocular fluids, with 0.3 mM glucose serving as a critical cut-off for distinguishing between normal and diabetic patients. We have focused on fabricating a CMC/CNF/ZnO hydrogel, crosslinked with citric acid, engineered for non-invasive wearable glucose sensor application. The as prepared hydrogel's ability to sensitively respond to glucose in sweat offers a compelling pathway towards real-time and painless glucose monitoring for enhanced diabetic care.

## EXPERIMENTAL

*A. Materials and reagents*

Sodium carboxymethyl cellulose (CMC) (average Mw 250,000 g/mol and degree of substitution at 1.2), citric acid, glucose oxidase (GOx) from Aspergillus Niger (type VII ≥15,000 units/g solid), phosphate buffer saline (PBS) tablet, and 3,3′,5,5′-tetramethylbenzidine (TMB) were purchased from Sigma-Aldrich. Cellulose nanofiber (CNF), which was prepared by supermass colloidal at 3.0 % solid in water, was supplied from Cellulose Lab. Zinc oxide (ZnO) nanoparticle was received from XF Nano, Inc. D(+)Glucose anhydrous was from Carlo Erba Reagents. Dimethyl sulfoxide (DMSO) was obtained from Fisher Scientific International, Inc.

*B. Preparation of CMC/CNF/ZnO nanocomposite hydrogel*

To prepare CMC hydrogel, the CMC powder at 1, 2, 3, 5, and 7 wt% was dissolved in DI water and stirred by a magnetic stirrer until completely dissolved. The 10 wt% citric acid was applied to the CMC-based solution as a crosslinking agent and stirred until homogenous. The hydrogel solution was heated in the oven at 80°C for 24-48 hours for water removal and crosslink reaction.

To prepare CMC/CNF nanocomposite hydrogel, the CMC powder at 2 wt% was used. After the CMC solution was well dissolved. The CNF powder at 0.5, 1, 2, and 3 wt% was incorporated. After CMC/CNF solutions were well dispersed. The citric acid at the same concentration was added. The oven was also used for CMC-based hydrogel preparation.

To prepare CMC/CNF/ZnO nanocomposite hydrogel, the ZnO powder at 0.2 wt% was included in a well-dispersed solution of 2 wt% CMC and 1 wt% CNF, then citric acid was added and heated under the same conditions.

The dried hydrogels were neutralized by immersion in DI water and PBS buffer solution, respectively. The neutralized hydrogels were dried out to be ready to integrate with the colorimetric sensor part.

PROCEEDINGS OF PPC & PETROMAT SYMPOSIUM 2025

*C. Integration of colorimetric sensor part into CMC/CNF/ZnO nanocomposite hydrogel*

The TMB 7.5 mM was prepared by dissolving it in DMSO. The dried neutralized hydrogels were dropped with TMB 7.5 mM and incubated 30 minutes at room temperature. Then, the mixture of enzymes GOx and HRP at a ratio of 120:30 U/ml, which was dissolved in PBS buffer solution, was dropped into the hydrogels and incubated for 30 minutes at room temperature. To determine the colorimetric performance for sensor application, the glucose solutions at 0.01, 0.025, 0.05, 0.1, 0.2, 0.3, 0.4, and 0.5 wt% were dropped into ready-to-use hydrogels, and the color change was observed with different time intervals.

*D. Characterization of CMC/CNF/ZnO nanocomposite hydrogel*

For swelling property, the dried CMC/CNF nanocomposite hydrogels were weighed in the range of 0.3-0.45 mg. The hydrogels were immersed in DI water and weighed at different time intervals. The percentage of swelling ratio was calculated by the following equation.

$$Swelling\ ratio\ (\%) = \frac{W_{swell} - W_{dry}}{W_{dry}} \times 100$$

Where $W_{dry}$ refers to the dry hydrogel as the initial weight and $W_{swell}$ refers to the weight of the swollen hydrogel at different times.

For transmission electron microscopy (TEM) morphology analysis, the three solutions were prepared: 1 wt% CNF, 0.2 wt% ZnO, and the mixture of 1 wt% CNF and 0.2 wt% ZnO. All three conditions were dispersed in DI water. The solutions were dropped into TEM grids and dried at room temperature before being observed by JEM-1400Flash electron microscopy, Japan.

The three sample conditions, which be observed by scanning electron microscopy (SEM) morphology analysis and Fourier transform infrared spectroscopy (FTIR), included 2 wt% CMC hydrogel, 2 wt% CMC and 1 wt% CNF hydrogel, and 2 wt% CMC with 1 wt% CNF and 0.2 wt% ZnO hydrogel. For SEM, the swelled freeze-dried samples were observed via a JEOL Model IT 500 HR instrument (Japan). The energy dispersive x-ray spectroscopy (EDX) was used to confirm the existence and dispersion behavior of Zn in hydrogel. For FTIR, the dried samples were observed using Nicolet iS50 (Thermo Scientific Fisher, USA), the dried hydrogels were observed with attenuated total reflectance (ATR) mode.

The cytocompatibility property was tested using the MTT assay against L929 mouse fibroblast cells. The seed cell was attached and grown in a 96-well plate for 24 hours at 37ºC, 5% $CO_2$. The hydrogels were sterilized in an autoclave at 121ºC for 20 minutes and incubated in culture medium Dulbecco's Modified Eagle Medium (DMEM) for 24 hours before being added into the well plate. The culture medium in the well plate was exchanged for hydrogel extract and was incubated for 48 hours. The MTT solution at a final concentration of 0.5 mg/mL was prepared and added into each well and incubated at 37°C in a humidified incubator for 2 hours. Carefully aspirated the medium, then added 100 µL of DMSO into each well. Measure absorbance at 570 nm using an EnSight Multimode Plate Reader (PerkinElmer) with Kaleido software. The percentage of cell viability was calculated by the following equation.

$$Cell\ viability\ (\%) = \frac{Abs_{sample}}{Abs_{control}} \times 100$$

PPC & PETROMAT SYMPOSIUM 2025

Where $Abs_{control}$ refers to absorbance of the control condition (without hydrogel extract) and $Abs_{sample}$ refers to absorbance of each sample (with hydrogel extract) condition.

For the potential of colorimetric sensors, The color change of the hydrogels after applying the glucose solution was collected, and the color intensity was measured via ImageJ software.

## RESULTS AND DISCUSSION

### *A. Optimization of CMC and CNF concentration*

The hydrogels with different CMC concentrations were formed. The 2 wt% of CMC concentration is the minimum required for stable hydrogel structure.

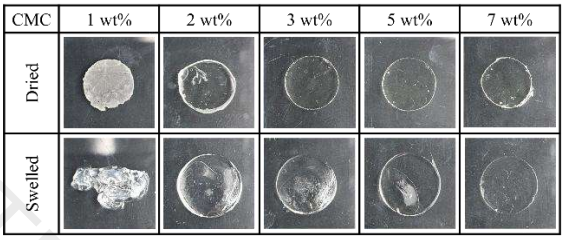


**Table 1.** Dried and swelled of various concentration of CMC hydrogels crosslinked with citric acid

The various CNF concentrations were incorporated into 2 wt% CMC hydrogels. The swelling ratio of CMC hydrogels with different CNF concentrations was shown in Fig 1. The more CNF added, the less swelling of hydrogels were observed. The 1 wt% CNF is optimized due to its reasonable swelling ratio and can be able to handle without damage.

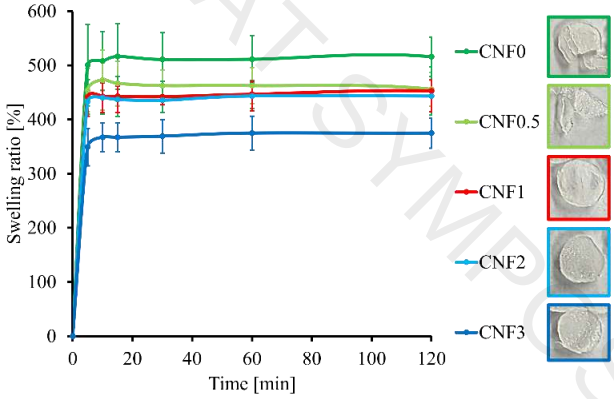


**Fig 1.** Swelling ratio at different time intervals of various CNF concentrations in CMC hydrogels

### *B. TEM morphology analysis*

The CNF were the nano fibers with width ≤300 nm. The ZnO were nanoparticles with widths in the range of 100-200 nm. The nanocomposite of CNF and ZnO is uniformly dispersed across the CNF network.

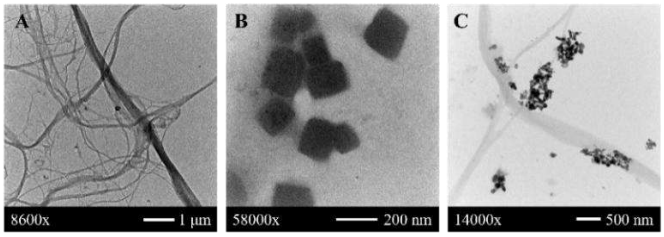


**Fig 2.** TEM image of CNF (A), ZnO (B), and nanocomposite of CNF and ZnO (C)

PPC & PETROMAT SYMPOSIUM 2025

*C. SEM-EDX morphology analysis*

CNF can be crosslinked with citric acid, the same as CMC, causing CNF to increase crosslink density in hydrogel and decrease pore size, respectively, as shown in Fig 3. The smaller pore makes it more difficult for hydrogel to absorb the liquid. Therefore, the swelling ratio decreased as shown in Fig 1.

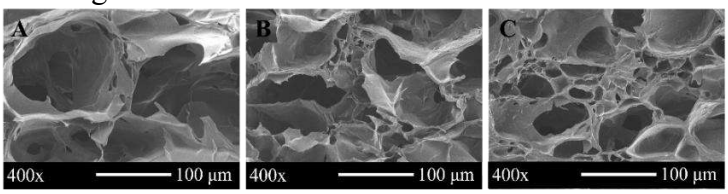


**Fig 3.** SEM image of CMC hydrogel (A), CMC/CNF (B), and CMC/CNF/ZnO nanocomposite hydrogel (C)

The SEM-EDX spectrum can confirm the existence of Zn in CMC/CNF/ZnO nanocomposite hydrogel, as the Zn peak. In addition, the mapping also showed well-dispersed Zn on the surface of the hydrogel.

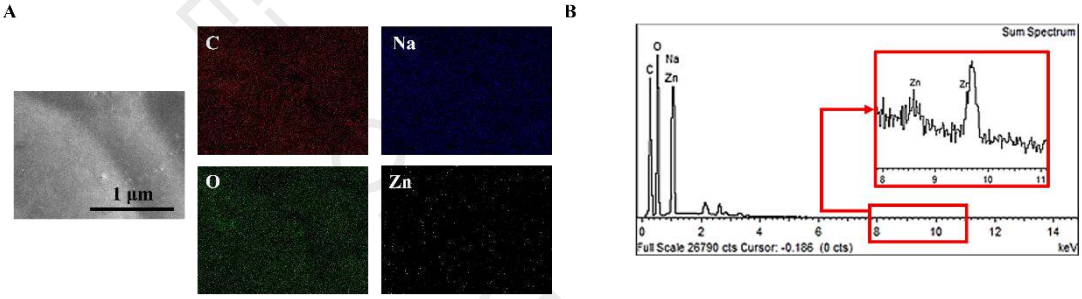


**Fig 4.** SEM-EDX mapping (A) and spectrum (B) of CMC/CNF/ZnO nanocomposite hydrogel

*D. FT-IR chemical composition analysis*

The crosslinking reaction was shown on peak 1730 $cm^{-1}$ as carbonyl group (C=O) stretching vibrations in an ester bond. There is obviously a larger O-H board area in hydrogel added by ZnO due to the increase of hydrogen bonding between ZnO and the hydroxyl group of CMC chains, as in other studies.

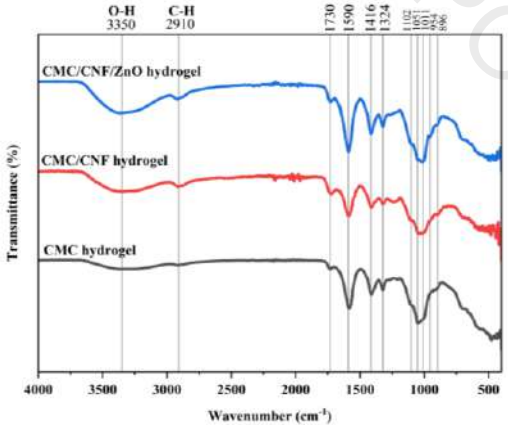


**Fig 5.** FTIR spectrum of CMC-based hydrogels

*F. Cytocompatibility property*

The 2 wt% CMC with 1 wt% CNF and 0.2 wt% ZnO hydrogel was extracted and tested via MTT assay. The cell viability of the control and the hydrogel extract shows no significant

difference. The cell viability in the hydrogel extract condition was higher than 80%, indicating great biocompatibility properties.

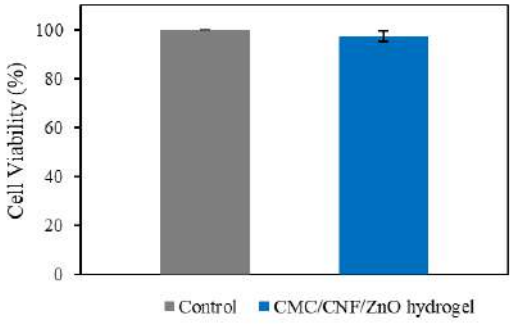


**Fig 6.** Cell viability with coculturing CMC/CNF/ZnO nanocomposite hydrogels

*G. Colorimetric glucose sensor performance*

The color change of the hydrogels was observed every 5 minutes after glucose solution application, with 30 minutes identified as the optimal reaction time. The gray channel proved most suitable for quantifying color intensity. As depicted in Fig 7, the CMC/CNF/ZnO nanocomposite hydrogel exhibited a clear color change trend across various glucose concentrations. The resulting calibration curve, plotting glucose concentration against mean color intensity, demonstrated a strong linear relationship. The glucose sensor achieved a low limit of detection (LOD) of 0.01 mM and a wide linear detection range of 0.0-0.5 mM, effectively covering glucose levels found in human sweat.

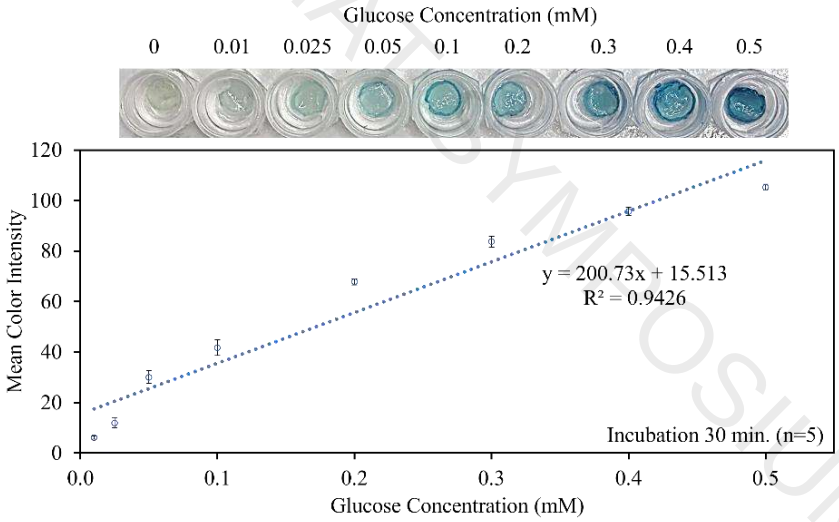


**Fig 7.** Photo of color and standard calibration plot of CMC/CNF/ZnO nanocomposite hydrogel

## CONCLUSIONS

In this research, we successfully fabricated a novel CMC/CNF/ZnO nanocomposite hydrogel, addressing key design considerations for robust and functional biosensing. Our findings indicate that a 2 wt% CMC concentration is the minimum requirement for forming a stable hydrogel structure, while the incorporation of 1 wt% CNF optimizes the swelling ratio and significantly improves the hydrogel's handling properties. The uniform dispersion of ZnO nanoparticles within the hydrogel further enhances its performance. Critically, the developed CMC/CNF/ZnO nanocomposite hydrogel exhibits excellent biocompatibility,

PPC & PETROMAT SYMPOSIUM 2025

making it suitable for direct skin contact. As a glucose sensor, the hydrogel demonstrated a strong linear relationship between glucose concentration and sensor response, achieving a low limit of detection (LOD) of 0.01 mM and a wide linear detection range of 0.0-0.5 mM. This work highlights the potential of cellulose-based nanocomposites in creating effective biosensor.

## ACKNOWLEDGEMENTS

This work was supported by Center of Excellence in Responsive Wearable Materials, Chulalongkorn, University and the Department of Material Science, Chulalongkorn University.

## REFERENCES

**de Lima, G. F., de Souza, A. G. and Rosa, D. d. S.** (2020) Macromol. Symp. **394 (1)**, 2000126.
**Jung, S., Kim, J., Bang, J., Jung, M., Park, S., Yun, H. and Kwak, H. W.** (2023) Carbohydr. Polym. **317**, 121090.
**Oh, S. Y., Hong, S. Y., Jeong, Y. R., Yun, J., Park, H., Jin, S. W., Lee, G., Oh, J. H., Lee, H., Lee, S.-S. and Ha, J. S.** (2018) ACS Appl. Mater. Interfaces. **10 (16)**, 13729-13740.
**Passornraprasit, N., Siripongpreda, T., Ninlapruk, S., Rodthongkum, N. and Potiyaraj, P.** (2022) Int J Biol Macromol. **213**, 1037-1046.
**Priyadarshi, R., Kumar, B. and Rhim, J. W.** (2020) Int J Biol Macromol. **162**, 229-235.
**Promphet, N., Thanawattano, C., Buekban, C., Laochai, T., Lormaneenopparat, P., Sukmas, W., Rattanawaleedirojn, P., Puthongkham, P., Potiyaraj, P., Leewattanakit, W. and Rodthongkum, N.** (2024) Anal Chim Acta. **1312**, 342761.
**Xu, X., Wang, J., Sun, T. C., Li, Q. and Ning, R. D.** (2024) Regen Ther. **26**, 956-966.

PPC & PETROMAT SYMPOSIUM 2025

# IODIDE EXTRACTION USING TETRAALKYLAMMONIUM SALT-BASED DEEP EUTECTIC SOLVENT

*Baifern Aincharoen* [a,b], *Narong Praphairaksit* [a], *Apichat Imyim**[a,b]

[a] Department of Chemistry, Faculty of Science, Chulalongkorn University, Bangkok, Thailand
[b] Center of Excellence on Petrochemical and Materials Technology, Chulalongkorn University, Bangkok, Thailand

Keywords: iodide, extraction, deep eutectic solvent, tetraalkylammonium salts

## ABSTRACT

Iodine is an essential micronutrient, and its accurate quantification in food and biological samples is necessary. However, the determination of iodide in real samples is challenging due to its typically low concentration and the limitations of direct analytical techniques resulting from matrix interferences. This study aims to develop an efficient extraction method utilizing liquid-liquid extraction with a deep eutectic solvent (DES) composed of tetrabutylammonium chloride and thymol. The DES was used for the extraction of iodide, followed by quantification using inductively coupled plasma optical emission spectrometry (ICP-OES). The influence of various parameters, such as DES types, molar ratios, and pH, were examined to optimize conditions for maximal extraction efficiency. The optimal molar ratio of tetrabutylammonium chloride and thymol was 1:8, and the optimum pH was 5–7, without the need for pH adjustment. Under these optimized conditions, the method achieved an extraction efficiency of 97.4%. The results demonstrate that the developed DES enables effective extraction of iodide from aqueous samples. This hydrophobic DES presents a promising and efficient alternative for iodide extraction and quantification in samples.

***apichat.i@chula.ac.th**

## INTRODUCTION

Iodine is a trace element necessary for synthesizing thyroid hormones, which control an individual's metabolism, growth, and development. Health concerns like goiter, cognitive impairments, and thyroid disorders, including hyperthyroidism and hypothyroidism, may occur from both low and high iodine intakes.[1] Iodine is commonly found in natural waters, soils, and foods in the forms of iodide and iodate ions.[2] The accurate measurement of iodide in food, water, and biological samples is crucial for public health. Direct quantification becomes a challenge due to the low iodide concentration of the sample and interference from complex sample matrices. Traditional methods such as the Sandell-Kolthoff (S-K) reaction, ion chromatography, and colorimetry are known to lack sufficient sensitivity, accuracy, and the ability to deal with complex sample matrices.[3-5] Consequently, accurate measurements require the extraction of iodide and/or the removal of the matrices to eliminate these issues.

Liquid-liquid extraction (LLE) is a technique for separating compounds within two immiscible solvents, enhancing detection by concentrating analytes.[6] It is effective for extracting iodide due to the separation efficiency as well as the flexibility of the solvents

PPC & PETROMAT SYMPOSIUM 2025

used. However, this process is usually complicated because iodide must be oxidized to a more easily extractable form.[7, 8]

Recently, deep eutectic solvents (DESs) have gained a lot of attention, in particular hydrophobic DESs (HDESs), due to their easy synthesis, tunable properties, and greater phase separation from water.[9, 10]

This work aims to develop a tetraalkylammonium salt-based DES that will be used to extract iodide directly from aqueous solutions without conversion, followed by quantification using ICP-OES (Inductively Coupled Plasma Optical Emission Spectrometry).

## EXPERIMENTAL

*A. Reagents and materials*

All chemicals and reagents used were of analytical grade, and all solutions were prepared using Milli-Q deionized water. Tetrabutylammonium chloride, decanoic acid, and thymol were purchased from Tokyo Chemical Industry (TCI). Tetrabutylammonium bromide, menthol, and choline chloride were obtained from Thermo Scientific, while tetraethylammonium chloride was purchased from Fluka Analytical. Sodium hydroxide and nitric acid (Merck) were used to adjust the pH. A stock standard solution of iodide was prepared using potassium iodide (Sigma-Aldrich). Sulfuric acid and hydrochloric acid, supplied by Merck, were used in the stripping study.

*B. DES preparation*

The DESs listed in **Table 1** were prepared by mixing the designated hydrogen bond acceptor (HBA) and hydrogen bond donor (HBD) in specified molar ratios in screw-capped bottles. The mixtures were stirred and heated at 70°C until a homogeneous liquid was obtained.

**Table 1.** List of DESs

| Hydrogen bond acceptor (HBA) | Hydrogen bond donor (HBD) | Molar ratio (HBA:HBD) |
|---|---|---|
| Choline chloride (ChCl) | Thymol (Thy) | 1:4 |
| Tetrabutylammonium chloride (TBACl) | Decanoic acid (Dec) | 1:2 |
| Tetrabutylammonium chloride (TBACl) | Thymol (Thy) | 1:1, 1:2, 1:3, 1:4, 1:8, 1:10 |
| Tetrabutylammonium chloride (TBACl) | Menthol (Men) | 1:2 |
| Tetraethylammonium chloride (TEACl) | Thymol (Thy) | 1:2 |
| Tetrabutylammonium bromide (TBABr) | Thymol (Thy) | 1:2 |

*C. Liquid-Liquid extraction procedure*

An aqueous iodide solution with a concentration of 50 mg/L was prepared. For each extraction experiment, 10 mL of the iodide solution was added to 1 mL of the DES in a centrifuge tube. The mixture was shaken vigorously for 2 minutes using a vortex mixer to ensure thorough contact between the phases, then centrifuged at 4000 rpm for 10 minutes to achieve phase separation. The aqueous phase (lower layer) was carefully separated using a syringe with a needle. The collected solution was filtered through a 0.45 µm nylon syringe

PPC & PETROMAT SYMPOSIUM 2025

filter, and the iodide concentration was determined using ICP-OES. The percentage of extraction efficiency (%Extraction) was calculated as shown in **Equation 1**,

$$\%\text{Extraction} = \left(\frac{C_i - C_f}{C_i}\right) \times 100 \quad \textbf{Equation 1}$$

where $C_i$ and $C_f$ represent the iodide concentration before and after extraction, respectively.

*D. Stripping procedure*

After the iodide extraction, 10 mL of acid solution was added directly into the centrifuge tube containing the extracted DES. The mixture was vortexed for 2 minutes using a vortex mixer, followed by centrifugation at 4000 rpm for 10 minutes to facilitate the back extraction of iodide into the aqueous phase. After phase separation, the aqueous phase (lower layer) containing the stripped iodide was carefully collected using a syringe with a needle. The collected solution was then filtered through a 0.45 µm nylon syringe filter, and the iodide concentration was determined using ICP-OES, which measured the iodide stripped by the acid. The percentage of stripping efficiency (%Stripping) was calculated as shown in **Equation 2**,

$$\%\text{Stripping} = \left(\frac{C_{stripping\ acid}}{C_{DES}}\right) \times 100 \quad \textbf{Equation 2}$$

where $C_{stripping\ acid}$ and $C_{DES}$ represent the iodide concentrations in the acid after stripping and in the DES phase after extraction, respectively.

And $C_{DES}$ can be calculated as shown in **Equation 3**.

$$C_{DES} = C_i - C_{remaining\ in\ aqueous} \quad \textbf{Equation 3}$$

## RESULTS AND DISCUSSION

*A. DES selection*

This research aimed to develop hydrophobic deep eutectic solvents (HDESs) for iodide extraction by employing quaternary ammonium salts as hydrogen bond acceptors (HBAs) and various hydrogen bond donors (HBDs). The mechanism involves ion exchange between the iodide ion and the anion of the quaternary ammonium salt, and phase separation for the iodide transfer.[11] The selection of appropriate HBAs and HBDs is critical to achieve the ultimate extraction performance. A number of DESs were prepared, and their extraction efficiencies were assessed. According to the results in **Figure 1(a)**, TBACl:Thy had the highest extraction efficiency at 89.8% followed by TBABr:Thy at 84.0%. The rest of the synthesized DESs, ChCl:Thy, TBACl:Men, and TBACl:Dec, showed much lower extraction efficiencies in the range of 10.7% to 18.3%, while TEACl:Thy was able to achieve a moderate extraction efficiency at 26.6%. Based on these observations, TBACl:Thy was selected for further experiments due to its superior extraction capability.

To determine the optimum TBACl to Thy ratio for enhancing the iodide extraction, various ratios of both components were evaluated. As shown in **Figure 1(b)**, the extraction efficiency increased with increased thymol content, reaching 97.4% at a 1:8 ratio, before slightly decreasing to 96.3% at 1:10. These results suggest that higher thymol content improves iodide extraction efficiency, likely due to increased hydrophobicity, which facilitates the phase separation. Based on these results, the 1:8 TBACl:Thy ratio was chosen for further investigation as it provided the highest extraction efficiency.

PPC & PETROMAT SYMPOSIUM 2025

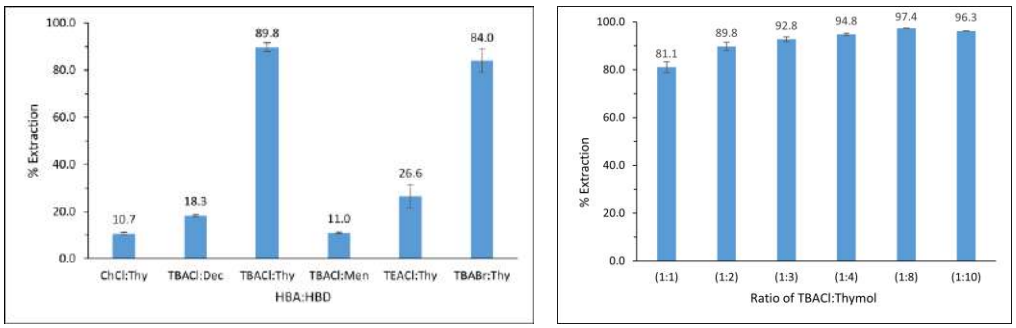


**Figure 1. (a)** Effect of DES types on the extraction percentage, **(b)** Effect of TBACl:Thymol ratios on the extraction percentage.

*B. Characterization of DES*

The formation of DES from tetrabutylammonium chloride (TBACl) and thymol (Thy) was confirmed by Fourier transform infrared spectroscopy (FTIR). As shown in **Figure 2(a)**, the main peak from the FTIR spectra was the O-H stretching band, which was absent in TBACl but was present in thymol at 3182 $cm^{-1}$ and shifted to 3259 $cm^{-1}$ in the DES, which indicated hydrogen bonding. Additionally, the C=C stretching band (1618 $cm^{-1}$) from thymol's aromatic ring and the C-O stretching band (1240 $cm^{-1}$) of the phenolic group were also retained in the DES, which confirms thymol's structure. Moreover, the C-N stretching band (1032 $cm^{-1}$) from TBACl was present in both TBACl and DES spectra. Due to the 8:1 ratio of Thy to TBACl, the DES spectrum was dominated by the thymol spectrum.

$^1$H NMR, alongside DMSO as solvent, was employed as a characterization technique for the synthesized DES. As shown in **Figure 2(b)**, the DES spectrum shows proton signals from TBACl and thymol. In the spectrum, signals at 2.47 ppm and 3.42 ppm are assignable to residual DMSO and $H_2O$, respectively. The hydroxyl proton (-OH) associated with thymol appears at 9.10 ppm (position 1), while other aromatic protons in thymol appear at 6.90, 6.57, and 6.49 ppm for positions 4, 2, and 3, respectively. Aliphatic protons on thymol at positions 7, 8, 5, and 6 are observed at 3.08, 2.13, and 1.08 ppm, respectively. Peaks at 3.08, 1.49, 1.23, and 0.88 ppm can be assigned to the protons of TBACl at positions A, B, C, and D, respectively. This confirms the successful formation of the DES in an 8:1 thymol:TBACl ratio.

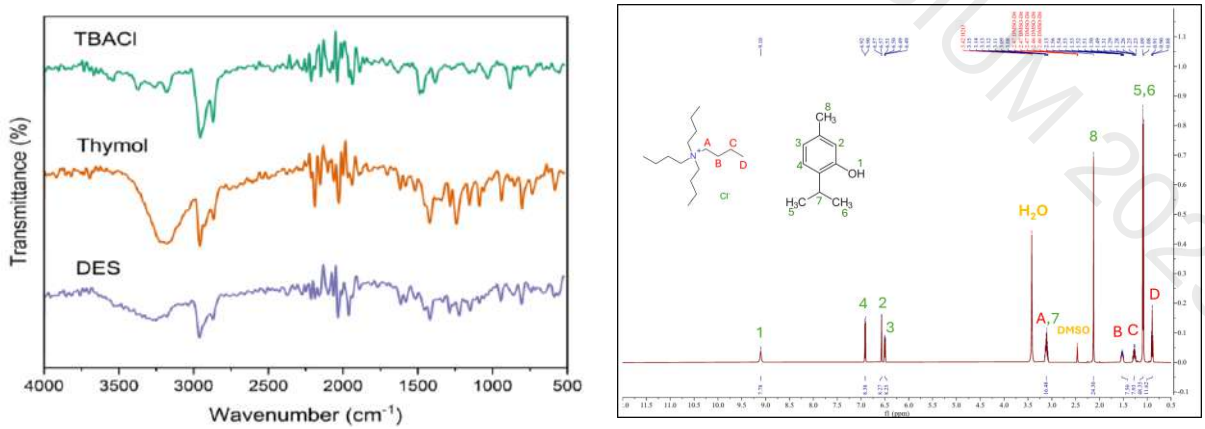


**Figure 2. (a)** FTIR spectra of TBACl, Thy, and DES, **(b)** $^1$H-NMR spectrum of DES.

PPC & PETROMAT SYMPOSIUM 2025

*C. Effect of pH*

The pH of the solution may significantly affect the form of iodide, influencing its extraction efficiency. For example, under acidic conditions, iodide ($I^-$) may be converted into iodine ($I_2$), while under alkaline conditions, it may exist as iodate ($IO_3^-$).[12] The relationship between pH and the percentage of iodide extraction is shown in **Figure 3**. At pH 1, the extraction efficiency of iodide remains low, around 70.3%. This is likely because, under strongly acidic conditions, iodide ($I^-$) may be converted into iodine ($I_2$), which is not extracted by the DES. However, the extraction efficiency remained consistently high at pH 3, 5, 7, and 11, with values of 97.2%, 97.3%, 97.1%, and 97.4%, respectively. During this range, the extraction efficiency remains relatively stable, as iodide ($I^-$) stays in its ionic form, which is effectively extracted by the DES. Therefore, in this work, the pH of the solution was not adjusted (approximately 5-7), as changes in pH did not significantly affect the extraction efficiency.

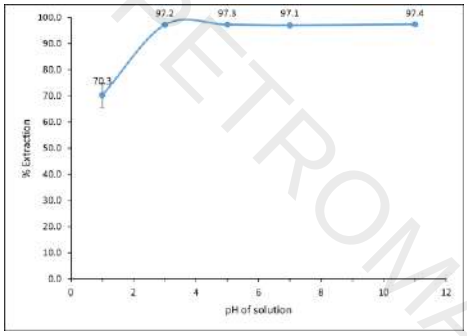


**Figure 3**. Effect of pH solution on the extraction percentage.

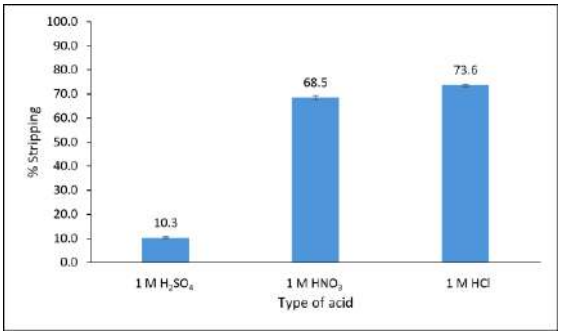


**Figure 4**. Effect of acid types on the stripping percentage.

*D. Iodide stripping*

Various types of acid, including sulfuric acid ($H_2SO_4$), nitric acid ($HNO_3$), and hydrochloric acid (HCl), were evaluated as stripping agents for the extracted iodide. The acid concentration was maintained at a constant level of 1.0 M for each acid, with a contact time of 2 minutes at room temperature. The stripping efficiencies are shown in **Figure 4**. The results indicate that 1.0 M sulfuric acid ($H_2SO_4$) resulted in the lowest stripping efficiency, with only 10.3% of iodide being removed from the DES phase. In contrast, both 1.0 M nitric acid ($HNO_3$) and 1.0 M hydrochloric acid (HCl) were significantly more effective in stripping iodide, with efficiencies of 68.5% and 73.6%, respectively. These data suggest that the type of acid plays a significant role in the stripping efficiency. Therefore, HCl was selected for further experiments. Future studies could investigate the underlying mechanisms in greater detail, such as the impact of acid concentration, contact time, and volume of acid solution to further optimize the stripping process.

## CONCLUSIONS

In conclusion, iodide extraction was successfully achieved using hydrophobic DES based on the principle of liquid-liquid extraction. The deep eutectic solvent (DES), composed of tetrabutylammonium chloride (TBACl) and thymol (Thy), exhibited high efficiency in extracting iodide. Iodide was transferred from the aqueous phase to the DES phase, demonstrating efficient extraction, followed by the determination of iodide remaining in the aqueous phase using ICP-OES. The optimization of both the extraction and stripping

PPC & PETROMAT SYMPOSIUM 2025

processes was evaluated. The results demonstrate that the developed DES enables effective extraction of iodide from aqueous samples.

**ACKNOWLEDGEMENTS**

The authors would like to acknowledge the workstation in the Environmental Analytical Research Unit (EARU), Department of Chemistry, Faculty of Science, Chulalongkorn University.

**REFERENCES**

(1) Rohner, F.; Zimmermann, M.; Jooste, P.; Pandav, C.; Caldwell, K.; Raghavan, R.; Raiten, D. J. Biomarkers of nutrition for development-iodine review. *The Journal of Nutrition* 2014, 144 (8), 1322S-1342S.

(2) Fuge, R.; Johnson, C. C. Iodine and human health, the role of environmental geochemistry and diet, a review. *Applied Geochemistry* 2015, 63, 282-302.

(3) Huang, C. J.; Lee, L. H.; Cheng, C. P.; Yao, S. F.; Chen, H. S.; Hwu, C. M.; Tang, K. T.; Wang, F. F.; Shih, C. W.; Yang, C. C.; Huang, W. S. Measurements of elemental iodine in soy sauces in taiwan using a modified microplate method. *Frontiers in endocrinology* 2023, 14, 1058695.

(4) Rong, L.; Lim, L. W.; Takeuchi, T. Determination of iodide in seawater samples by ion chromatography with chemically-bonded poly(ethylene glycol) stationary phase. *Journal of Chromatography A* 2006, 1128 (1), 68-72.

(5) Chen, J.; Lin, Q.; Li, Q.; Li, W.-T.; Zhang, Y.-M.; Wei, T.-B. A highly selective colorimetric chemosensor for detection of iodide ions in aqueous solution. *RSC Advances* 2016, 6 (89), 86627-86631.

(6) Liu, Y. Chapter 5 - Liquid–liquid extraction. In *HiGee Chemical Separation Engineering*, Liu, Y. Ed.; Elsevier 2024, 159-206.

(7) Zaruba, S.; Vishnikin, A. B.; Andruch, V. A novel vortex-assisted liquid–liquid microextraction approach using auxiliary solvent: determination of iodide in mineral water samples. *Talanta* 2016, 149, 110-116.

(8) Kaykhaei, M. A.; Kaykhaii, M.; Hashemi, M.; Sargazi, M. Dispersive liquid-liquid microextraction coupled with micro-volume spectrophotometry for determination of total iodine in urine samples. *Journal of the Chilean Chemical Society* 2016, 63, 3947-3949.

(9) Smith, E. L.; Abbott, A. P.; Ryder, K. S. Deep eutectic solvents (DESs) and their applications. *Chemical Reviews* 2014, 114 (21), 11060-11082.

(10) Osch, D. J. G. P. V.; Zubeir, L. F.; Bruinhorst, A. V. D.; Rocha, M. A. A.; Kroon, M. C. Hydrophobic deep eutectic solvents as water-immiscible extractants. *Green Chemistry* 2015, 17 (9), 4518-4521.

(11) Katsuta, S.; Sugimoto, A. Use of ionic liquids for extraction separation and concentration of iodide ions in brine samples. *Analytical Sciences* 2023. 39, 785-789.

(12) Yan, C.; Zhang, B.; He, Z.; Liu, Y. The mechanism and influential factors for radioactive iodide adsorption: A review. *Separation and Purification Technology* 2025 ,363, 131954.

PPC & PETROMAT SYMPOSIUM 2025

# Development of bacterial cellulose-based wound dressing materials containing zeolite, nanocarbon, chitosan functionalized-SiNPs, marigold flower extract, and natural deep eutectic solvent

*Krittanan Chansuk* [a], *Ratana Rujiravanit* [a,b], *Takeshi Hagio* [c]

[a] The Petroleum and Petrochemical College, Chulalongkorn University, Bangkok, Thailand
[b] Center of Excellence on Petrochemical and Materials Technology, Bangkok, Thailand
[c] Department of Materials Chemistry, Faculty of Engineering, Shinshu University, Matsumoto, Japan

Keywords: Bacterial cellulose, Marigold flower extract, Silica nanoparticles, Nanocarbon, Wound dressing

## ABSTRACT

Bacterial cellulose (BC), valued for its outstanding moisture retention, biocompatibility, and structural similarity to the human skin extracellular matrix, shows great potential for wound dressing applications. However, its healing performance can be further enhanced by incorporating functional materials. In this study, BC-based composite hydrogels were developed by integrating BEA zeolite, carbon nanoparticles, and chitosan-functionalized silica nanoparticles (CS-SiNPs), along with marigold flower extract. BEA zeolite, synthesized from rice husk-derived silica nanoparticles by the dry-gel conversion method, enabled exudate absorption and antioxidant carrier capability. Nanocarbon synthesized via solution plasma processing offers high reactivity and intrinsic antioxidant potential. CS-SiNPs, produced through plasma-assisted functionalization and glutaraldehyde crosslinking, improved nanoparticle dispersibility and biocompatibility. Marigold flower extract rich in lutein, carotenoids, and flavonoids was prepared using a natural deep eutectic solvent (NADES), enhancing anti-inflammatory, antioxidant, and tissue-regenerative activities. The three incorporated components, i.e. BEA zeolite, carbon nanoparticles, and CS-SiNPs were individually compared based on their influence on water holding capacity (WHC), water absorption capacity, antioxidant activity, and the absorption and desorption behaviour of carotenoids and flavonoids from the marigold flower extract. The comparative evaluations demonstrated that these composite hydrogels could improve the wound healing potential of BC. These findings suggested that BC composite hydrogels containing BEA zeolite, carbon, and CS-SiNPs are promising candidates for advanced wound dressing applications.

*** ratana.r@chula.ac.th**

## INTRODUCTION

Chronic and infected wounds remain a significant burden to healthcare systems worldwide, often requiring prolonged treatment and posing a high risk of complications. Traditional wound dressings such as gauze or cotton provide only passive protection and lack the ability to promote healing. As the demand for advanced wound care materials continues to grow, the development of multifunctional dressings that combine biocompatibility with therapeutic properties such as antioxidant activity has become increasingly important.

Wound healing is a biologically regulated process consisting of four distinct yet overlapping stages are hemostasis, inflammation, proliferation, and remodelling. An ideal

PPC & PETROMAT SYMPOSIUM 2025

wound dressing should provide a moist environment, protect the wound from microbial infection, allow gas exchange, and support tissue regeneration. Bacterial cellulose (BC), a biopolymer synthesized by *Komagataeibacter* species, has gained attention in wound care applications due to its high-water retention, mechanical stability, and biocompatibility. However, its lack of intrinsic bioactivity such as antioxidant functions limits its efficacy for advanced therapeutic use.

To enhance the performance of BC, this study incorporates three different reinforcing agents into the BC matrix, i.e. zeolite, nanocarbon, and chitosan-functionalized silica nanoparticles (CS-SiNPs). Zeolite (BEA-type) is a crystalline microporous material known for its high surface area and ion-exchange capabilities, making it suitable for drug adsorption and release. Nanocarbon synthesized via solution plasma processing offers high reactivity and intrinsic antioxidant potential. Chitosan-functionalized SiNPs introduce surface amine groups that can not only act as interaction sites with bioactive compounds but also contribute to antioxidant activity. These reinforcing agents are expected to improve the physical properties of BC and facilitate controlled delivery of active compounds.

Marigold (*Tagetes erecta Linn.*) extract, rich in carotenoids and flavonoids, was selected as a natural bioactive agent to be loaded into the BC composites. The phytochemicals in the marigold extract possess strong antioxidant activity and play a role in modulating oxidative stress in wound environments. To enhance their solubility and diffusion into the BC matrix, Natural Deep Eutectic Solvents (NADES) were employed as eco-friendly, biocompatible extraction and loading media. Overall, this research aims to develop multifunctional BC-based wound dressings with improved loading capacities of bioactive compounds, release control, and antioxidant performance through synergistic integration of selected reinforcing agents and NADES-mediated marigold extract.

## EXPERIMENTAL

### *A. Materials and chemicals*

Bacterial cellulose (BC) was produced using *Komagataeibacter nataicola* TISTR 975 obtained from the Thailand Institute of Scientific and Technological Research (TISTR). Marigold (*Tagetes erecta Linn.*) flowers were purchased from a local market in Bangkok, Thailand. Rice husk ash (RHA) was sourced from a rice mill in Suphanburi province and used as a precursor for silica nanoparticles (SiNPs). Urea was purchased from Krungthepchemi Co., Ltd., while choline chloride was purchased from Pengbo technology, China. Both were used for preparing Natural deep eutectic solvent (NADES) Tetraethylammonium hydroxide (TEAOH) for BEA zeolite synthesis was obtained from Sigma-Aldrich. Glutaraldehyde was purchased from Merck. Shrimp chitosan (particle size: <1.5 mm., %DD: 90-95%, Molecular weight: ~250 kDa) was purchased from Marine Bio Resources Co., Lid., Samut Sakhon, Thailand.

### *B. Preparation of BC pellicles*

*Komagataeibacter nataicola* TISTR 975 was cultured in a sterile medium containing 4.0% (w/v) D-glucose and 2.0% (w/v) yeast extract under static conditions at 30 °C to produce BC pellicles. After cultivation, the pellicles were purified by boiling in 4% NaOH solution to eliminate residual cells and medium components. Subsequently, they were soaked in 1.5% acetic acid solution and rinsed with deionized water until neutral pH was achieved.

PPC & PETROMAT SYMPOSIUM 2025

*B. Preparation of beta zeolite from silica nanoparticles*

Beta (BEA-type) zeolite was synthesized via a dry gel conversion (DGC) method using silica nanoparticles (SiNPs) extracted from rice husk ash as a silica source. A synthesis mixture containing SiNPs (1.815g), tetraethylammonium hydroxide (TEAOH, 8.26g), sodium hydroxide (NaOH, 0.5g), and aluminium sulfate (0.15g) was prepared, ultrasonicated, and aged at 80ºC for 4 hr. The dried gel was transferred to a Teflon-lined autoclave and heated at 180 °C under static conditions for 12–36 hours. The resulting solid was dried and calcined at 450 °C for 12 hours to remove the organic contaminants and obtain crystalline beta zeolite.

*C. Preparation and NaOH-modified nanocarbon by solution plasma process*

Nanocarbon was prepared via solution plasma process (SPP) by discharging 70 mL of palm oil in a reactor equipped with silver electrodes under a condition of 1.64 kV, 15 kHz, 2 µs pulse width and 0.5 mm gap for 4 hours. The product was collected by centrifugation (12,000 rpm, 15 min, 4 °C), washed with hexane, and dried at 70 °C. The dried powder was then modified by stirring in 0–10 M NaOH (0.1g/10mLNaOH) at 60 °C for 24 hours, followed by neutralization and drying. This treatment was intended to alter the surface chemistry and improve the reactivity of nanocarbon.

*D. Preparation of chitosan functionalized-SiNPs by solution plasma process (SPP)*

Chitosan-functionalized silica nanoparticles (CS-SiNPs) were prepared by dispersing 0.3% (w/v) SiNPs into 70 mL of 0.2% (w/v) chitosan solution in 0.1 M acetic acid, followed by plasma treatment using a bipolar pulsed power supply (1.64 kV, 20 kHz, 2 µs pulse width, 0.5 mm gap) for 0-4 hours. After plasma exposure, 4.48 mL of glutaraldehyde was added (chitosan: glutaraldehyde = 1:8 w/w) and stirred for 1 hour. The resulting particles were collected by centrifugation to separate CS-SiNPs from solution, washed with DI water, and dried at 70 °C for 12 hours.

E. *Fabrication of BC/BEA, BC/CS-SiNPs, and BC/nanocarbon Composites*

For each formulation, 100 mg of BEA zeolite, CS-SiNPs, and NaOH-treated nanocarbon was dispersed in 10 mL of deionized water and sonicated for 30 minutes to ensure homogeneous suspension. A purified BC pellicle (2.5 cm diameter, 3-4 mm thickness) was immersed in the respective suspension and autoclaved at 121 °C for 30 minutes. The autoclaving process was repeated for two cycles to ensure the diffusion of the particles into the BC matrices. The resulting BC composites were rinsed with deionized water and sonicated for 15 minutes to remove any loosely bound particles prior to further use.

F. *Marigold Extraction and Evaluation of BC Composite Absorption, Desorption, and Antioxidant Activity*

Marigold (*Tagetes erecta Linn.*) petals were oven-dried at 60 °C, ground, and extracted using a natural deep eutectic solvent (NADES) composed of choline chloride and urea at a 1:2 molar ratio. The extract was diluted with water (50%w/w of NADES), and 20 mL of the dilute solution was used to immerse BC-based composites (BC/BEA, BC/CS-SiNPs, BC/nanocarbon). Absorption was performed over 0-1440 minutes at 40 °C in a shaking water bath, and desorption was conducted in a phosphate buffer saline (PBS) solution (pH 7.4) under similar conditions. Flavonoid and carotenoid contents were quantified using

PPC & PETROMAT SYMPOSIUM 2025

UV–Vis spectrophotometry, and antioxidant activity was determined via DPPH and ABTS assays.

## RESULTS AND DISCUSSION

### *A. Characterization of bacterial cellulose*

The purified bacterial cellulose (BC) was analyzed to confirm its chemical structure and morphology. FTIR spectra showed characteristic peaks of cellulose I at ~3345 $cm^{-1}$ (O–H stretching), 2900 $cm^{-1}$ (C-H stretching), and 1055 $cm^{-1}$ (C-O-C stretching). XRD analysis revealed diffraction peaks at 14.4°, 16.8°, and 22.5°, corresponding to the ($1\bar{1}0$), (110), and (200) planes, indicating a highly crystalline cellulose I structure (Wang et al., 2017). The crystallinity index was calculated to be 86.79±0.05%. FE-SEM images showed a nanofibrous 3D network with fiber and pore size diameters of 57.56±19.98 nm and 1.46±0.45 µm respectively, supporting its high surface area and porosity suitable for composite formation.

### *B. Characterization of BEA Zeolite*

Beta-zeolite (BEA) zeolite was successfully synthesized from rice husk ash - derived silica nanoparticles (SiNPs) using a dry gel conversion (DGC) method. X-ray diffraction (XRD) analysis confirmed that the diffraction pattern of the synthesized zeolite closely matched that of a commercial BEA reference, achieving a high crystallinity index (CI) of 87.5±0.62%. Field-emission scanning electron microscopy (FE-SEM) images revealed that the material consisted of uniform clusters of intergrown sub-micrometer particles with an average size of 0.83 ± 0.13 µm and a microporous texture consistent with BEA topology.

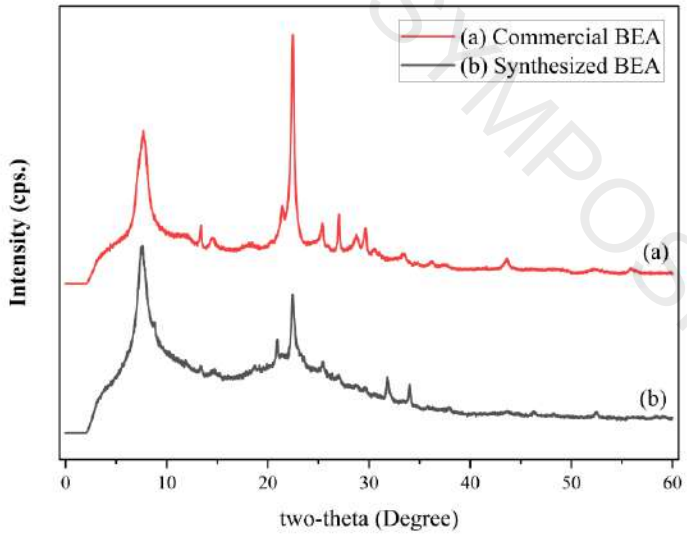


**Figure 1.** XRD patterns of (a) commercial BEA zeolite and (b) synthesized BEA zeolite.

### *C. Characterization of nanocarbon synthesized by solution plasma process.*

Nanocarbon synthesized from palm oil via the solution plasma process (SPP) was characterized as an amorphous carbon embedded with silver nanoparticles (AgNPs). The presence of crystalline, face-centered cubic (FCC) silver, which originated from the erosion

PPC & PETROMAT SYMPOSIUM 2025

of silver electrodes during plasma discharge, was confirmed by X-ray diffraction (XRD) (Fatemeh et al., 2017). Transmission electron microscopy (TEM) revealed that the AgNPs had an average size of 5.32±1.40 nm. Raman spectroscopy indicated that the synthesized nanocarbon had a degree of graphitic ordering ($I_D/I_G$ ratio = 0.938) higher than activated carbon (Islam et al., 2021). To improve dispersion in water, the synthesized nanocarbon was modified with 1M NaOH. The NaOH-modified nanocarbon possessed increased colloidal stability by attaining the zeta potential value of -35.03 ± 0.70 mV.

*D. Preparation of CS-functionalized SiNPs by solution plasma process*

Chitosan-functionalized silica nanoparticles (CS-SiNPs) were successfully synthesized via a solution plasma process (SPP) with subsequent glutaraldehyde crosslinking. The deposition of chitosan on SiNPs was primarily confirmed by a change of zeta potential values from a negative value for bare SiNPs (-22.17±0.15 mV) to a positive value of +23.20 ± 0.52 mV for CS-SiNPs. This resulted in enhanced colloidal stability and reduced average aggregate size. Elemental analysis provided definitive chemical evidence of the deposition of CHNS on SiNPs by showing an increase in nitrogen content from 0% to 5% and carbon content from 2.59% to 6.45% after deposition of SiNPs with chitosan (Budnyak et al., 2015).

*E. Characterization of bacterial cellulose composites containing different reinforcing agents*

Bacterial cellulose (BC) composites were successfully fabricated by incorporating various reinforcing agents, i.e., BEA zeolite, nanocarbon, SiNPs, and CS-SiNPs. During the fabrication process, reinforcing agents were first dispersed in deionized water and sonicated for 30 minutes to ensure homogeneous suspension and prevent particle agglomeration. Subsequently, BC pellicles were immersed in these suspensions and subjected to two cycles of autoclaving at 121°C for 30 minutes per cycle. This repeated autoclaving applied pressure, which facilitated the penetration and diffusion of the reinforcing particles into the BC pellicle and matrix. The loading contents of each reinforcing agent were determined by STA. The loading contents of BC/BEA, BC/carbon, BC/SiNPs, and BC/CS-SiNPs in the corresponding composites were 53.45%, 35.51%, 50.09%, 41.69%, respectively. FE-SEM analysis further verified the incorporation of the reinforcing agents in the BC matrix by revealing the distribution of the reinforcing particles throughout the three-dimensional network of the BC matrix.

PROCEEDINGS OF PPC & PETROMAT SYMPOSIUM 2025

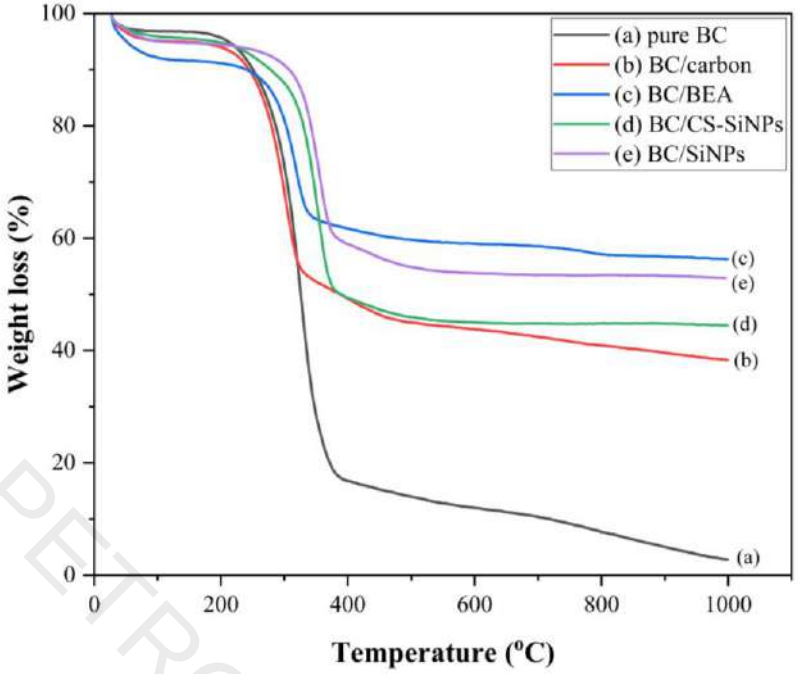


**Figure 2.** STA thermograms of (a) pure BC, (b) BC/carbon, (c) BC/BEA, (d) BC/CS-SiNPs and (e) BC/SiNPs composite determined under nitrogen atmosphere.

*F. Determination of absorption, desorption and antioxidant activity of bacterial cellulose/ reinforcing agent composites containing marigold flower extract*

The absorption and desorption of bioactive compounds from marigold extract were evaluated through the determination of total carotenoid and total flavonoid content. All BC composites showed enhanced absorption capacity compared to pure BC. It was found that the BC/chitosan-functionalized SiNPs (BC/CS-SiNPs) composite exhibited the highest uptake for both flavonoids (184.88±3.36 mg quercetin/100 mg BC) and carotenoids (53.70±2.23 mg lutein/100 mg BC). The composites demonstrated sustained release profiles. Among the studied BC composites, the BC/CS-SiNPs yielded the highest cumulative desorption for both flavonoids (36.20±0.73%) and carotenoids (26.76±1.49%) after immersion for 1440 minutes. Importantly, the extracts desorbed from the BC composites exhibited potent antioxidant activity, as confirmed by high radical scavenging values in both DPPH and ABTS assays. These results confirm the successful development of a functional composite with enhanced loading and controlled release of active compounds for wound healing applications.

## CONCLUSIONS

This research successfully developed functional bacterial cellulose (BC) composites by incorporating various reinforcing agents, including BEA zeolite, nanocarbon, silica nanoparticles (SiNPs) and chitosan-functionalized silica nanoparticles (CS-SiNPs). The resulting BC composites demonstrated enhanced capacity to absorb bioactive compounds, such as flavonoids and carotenoids from the marigold extract, and provided a sustained release profile. The released compounds exhibited potent antioxidant activity, confirming

PPC & PETROMAT SYMPOSIUM 2025

the potential of these composites as advanced wound dressing materials with improved wound healing function.

## ACKNOWLEDGEMENTS

The authors would like to gratefully thank the Petroleum and Petrochemical College, Chulalongkorn University and Center of Excellence on Petrochemical and Materials Technology (PETROMAT) for their support to this research work. This research is also supported by the 90th Anniversary of Chulalongkorn University, Ratchadapisek Somphot research funds

## REFERENCES

**Budnyak, T. M., Pylypchuk, I. V., Tertykh, V. A., Yanovska, E. S., & Kolodynska, D. (2015).** Synthesis and adsorption properties of chitosan-silica nanocomposite prepared by sol-gel method. Nanoscale research letters, **10**, 1-10.

**Fatemeh, K., Mohammad Javad, M., & Samaneh, K.** (2017). The effect of silver nanoparticles on composite shear bond strength to dentin with different adhesion protocols. Journal of applied oral science, **25**, 367-373.

**Islam, Z., Watthanaphanit, A., Chae, S., Niitsu, K., & Saito, N.** (2021). Structure and properties of nanocarbons-encapsulated WC synthesized by solution plasma process in palm oils. Materials Express, **11(9)**, 1602-1607.

**Wang, S.-S., Han, Y.-H., Ye, Y.-X., Shi, X.-X., Xiang, P., Chen, D.-L., & Li, M.** (2017). Physicochemical characterization of high-quality bacterial cellulose produced by Komagataeibacter sp. strain W1 and identification of the associated genes in bacterial cellulose production. RSC advances, **7(71),** 45145-45155.

PPC & PETROMAT SYMPOSIUM 2025

# Essential Oil Stabilization by Liquid-Core Hydrogel Composites with NADES in Liquid Core and Either Carbon or Silica Nanoparticles Reinforcement

*Piyapron Tipayaars* [a], *Ratana Rujiravanit* [a,b], *Takeshi Hagio* [c]

[a] The Petroleum and Petrochemical College, Chulalongkorn University, Bangkok, Thailand
[b] Center of Excellence on Petrochemical and Materials Technology, Bangkok, Thailand
[c] Department of Materials Chemistry, Faculty of Engineering, Shinshu University, Matsumoto, Japan

Keywords: Liquid-core hydrogel, Natural deep eutectic solvent, Lavender essential oil, Carbon nanoparticles, Silica nanoparticles

## ABSTRACT

Essential oil aromatherapy can complement holistic care for neurodegenerative diseases, but clinical uptake is limited by the rapid loss of key volatile organic compounds (VOCs). We designed liquid-core hydrogel beads that preserve and release lavender essential oil, rich in linalool, linalyl acetate, and β-caryophyllene, in a controlled manner. The core contains natural deep eutectic solvents (choline chloride/ethylene glycol, choline chloride/ glycerol, or choline chloride/xylitol), whose dense hydrogen-bond networks markedly reduce VOC evaporation. A triple-layer shell comprising of calcium alginate, chitosan, and glutaraldehyde-crosslinked chitosan provided mechanical integrity and diffusion gating. Carbon nanoparticles having an average particle size of 228 ± 30 nm, that were prepared from palm oil with the aid of solution plasma, dispersed in the shell would act as internal adsorbents, while rice husk-derived silica nanoparticles with an average particle size of 49 ± 10 nm could enhance thermal stability and stiffness. Scanning electron microscopy confirmed a core–shell architecture with an average core volume of ≈ 287 mm³, which is in a feasible range for both systemic and localized medical use. The composite beads showed superior retention of the three target VOCs and sustained release profiles, demonstrating an effective strategy for stabilising therapeutically valuable essential oils.
*** ratana.r@chula.ac.th**

## INTRODUCTION

Rapid population ageing is reshaping global demographics. By 2030, one-in-six people will be ≥ 60 years old, a shift that is already driving sharp increases in age-related neurodegenerative disorders such as Alzheimer's and Parkinson's diseases, together with anxiety, agitation, and sleep disturbance that accompany them. Pharmacological regimens alleviate symptoms only partially, motivating complementary, patient-friendly approaches that enhance quality of life without adding drug burden.

Olfactory stimulation with essential oils (EO) fits this need because volatile aroma molecules reach limbic and cortical regions within minutes, modulating mood, cognition, and autonomic balance. Lavender essential oil is especially attractive; its principal volatile organic compounds (VOCs)—linalool, linalyl acetate, and caryophyllene—exert anxiolytic, anti-inflammatory, and potential neuroprotective actions documented in both pre-clinical and early clinical studies (Satou, 2024). Yet these benefits seldom translate beyond the

PPC & PETROMAT SYMPOSIUM 2025

laboratory, because heat, light, and oxygen accelerate VOCs evaporation and oxidation, leading to unpredictable dosing and short shelf life.

To overcome this bottleneck, we engineered liquid-core hydrogel beads that stabilize and control lavender EO's release. The core contains natural deep eutectic solvents (NADES), that were choline chloride and ethylene glycol, choline chloride and glycerol, or choline chloride and xylitol. The dense hydrogen-bond networks in NADES markedly lower vapor pressure of VOCs and provide intrinsic antioxidative protection. Encasing this core, a triple-layer shell comprising of calcium alginate, chitosan, and glutaraldehyde-crosslinked chitosan conferred mechanical robustness and tunable diffusion pathways. Furthermore, carbon nanoparticles embedded in the shell would act as internal VOCs adsorbents, while rice husk ash-derived silica nanoparticles enhance thermal stability and stiffness.

The effect of NADES formulations present in the liquid-core solutions on oil-loading capacity and VOCs retention was examined. On the other hand, the effects of carbon and silica nanoparticles present in the shells on mechanical properties and thermal stability of the beads as well as VOCs retention, were investigated. By integrating green solvents, biopolymer engineering, and plant-derived nanomaterials, this platform offers a scalable route for delivering plant-derived volatiles to an ageing population, potentially enriching non-pharmacological care of neurodegenerative disease.

## EXPERIMENTAL

### *A. Materials and chemicals*

Lavender essential oil was purchased from AP operations company limited, Thailand. Choline chloride was purchased from Pengbo technology, China. Glycerol, xylitol,and xanthan gum were purchased from Krungthepchemi Co. Ltd., Thailand. Ethylene Glycol was purchased from (laboratory grade) was purchased from Kemaus. Sodium alginate was purchased from Acros Organics. Calcium chloride was purchased from Ajax Finechem. Shrimp chitosan (particle size < 1.5 mm, degree of deacetylation: 90–95%, molecular weight ~250 kDa) was purchased from Marine Bio Resources Co., Ltd., Samut Sakhon, Thailand. Glutaraldehyde (synthesis grade, 25 %w/w) was purchased from Loba chemie pvt.ltd. Silver wires (99.9%) and ceramic tubes were purchased from Nilaco Corporation, Japan. Refined palm olein cooking oil was purchased locally under the brand Oleen. Rice husk ash was complementarily supplied by Khao C.P. Co., Ltd. (Suphanburi Rice Mill).

### *B. Preparation of natural deep eutectic solvents (NADES)*

Natural deep eutectic solvents (NADES) were prepared by combining choline chloride (hydrogen-bond acceptor) with the chosen hydrogen bond donor, glycerol, ethylene glycol, or xylitol, at molar ratios of 1:0.5, 1:1, 1:2, 1:3, and 1:4 (HBA:HBD). Each mixture was heated to 90 °C with continuous magnetic stirring until a clear, homogeneous liquid formed, confirming single-phase eutectic formation across all compositions. The functional groups of NADES were investigated by Fourier-transform infrared (FTIR) analysis was performed using a Thermo Nicolet Nexus 670 spectrometer in ATR mode over the range of 4000–400 $cm^{1}$.

### *C. Preparation of nanocarbon by solution plasma process*

Seventy milliliters of palm oil were poured into a glass beaker fitted with two silver electrodes (0.5 mm inter-electrode gap) connected to a bipolar pulse power supply. Plasma

PROCEEDINGS OF PPC & PETROMAT SYMPOSIUM 2025

was generated 15 kV, 2 μs pulse width, and 80 kHz frequency until the oil turned opaque black, indicating carbon formation. The suspension was then centrifuged at 12,000 rpm, 4 °C for 15 min to separate carbon powder from the residual liquid. The synthesized carbon was characterized by Fourier-transform infrared spectroscopy (FTIR; Thermo Nicolet Nexus 670, ATR mode, 4000–400 $cm^{1}$), X-ray diffraction (XRD; Rigaku, Smart Lab, 2θ range 5–90°), Raman spectroscopy (Raman; XploRA PLUS), and transmission electron microscopy (TEM; JEOL JEM-2100).

*D. Modification of synthesized nanocarbon powder by NaOH*

The as-prepared carbon powders were submerged in aqueous NaOH solutions of 1M for 24 h to introduce surface oxygenated sites. After thorough rinsing with deionized water to neutral pH, the samples were oven-dried at 80 °C, yielding NaOH-modified nanocarbons ready for further use.

*E. Preparation of silica nanoparticles from rice husk ash*

Raw rice husk ash was rinsed with deionized water, oven-dried (80 °C, 24 h) and refluxed in 4 M HCl (120 °C, 2 h) to remove heavy metal impurities. After washing until neutral and drying, the acid-treated ash was dispersed in 5 M NaOH and refluxed (120 °C, 2 h) to extract silica as sodium silicate. The hot slurry was filtered, and the filtrate was titrated with 5 M $H_2SO_4$ under vigorous stirring until pH ≈ 2, leading to precipitation of amorphous silica. The resulting silica was washed to neutral pH by repeated centrifugation (12,000 rpm, 15 min) and oven-dried at 80 °C for 24 h, yielding silica nanoparticles. The synthesized silica was characterized by Fourier-transform infrared spectroscopy (FTIR; Thermo Nicolet Nexus 670, ATR mode, 4000–400 $cm^{1}$), X-ray diffraction (XRD; Rigaku, Smart Lab, 2θ range 5–90°).

*F. Preparation of liquid-core hydrogel beads.*

Lavender essential oil/NADES core liquids were prepared by dissolving $CaCl_2$ (2 % w/w) and xanthan gum (0.1 % w/w) in a selected NADES, then add 2 g of lavender essential oil together with Tween 80 (oil:tween 80 = 3:2, w/w) and gently blending them into the NADES. A primary gelling bath consisting of 0.5 % (w/v) sodium alginate in deionized water was prepared. After that, each functional filler, that are carbon 0.1 % (w/v) or silica 0.5 % (w/v), was added into the primary gelling bath. A 1 % (w/v) chitosan solution (in 1 % v/v acetic acid) served as the secondary gelling medium. By using a 5 mL syringe, the core liquid was dripped into the alginate bath under gentle stirring (100 rpm), allowing gel to form for 20 min. Beads were then rinsed with DI water, transferred to the chitosan bath, and immersed for a further 15 min, and washed again. Finally, the beads were immersed in 2.5 % (v/v) glutaraldehyde for 30 min to generate crosslinking at the outer chitosan layer, then thoroughly washed and stored for subsequent analyses.

*G. Characterization of hydrogel beads*

The thermal stability of the hydrogel beads was evaluated using simultaneous thermal analysis (STA 449 F3 Jupiter) over a temperature range of 30–1000 °C.

Mechanical properties of the hydrogel beads were evaluated using a universal testing machine (Instron 2K). Compression tests were performed at a pre-test speed of 5.0 mm/s, a test speed of 1.0 mm/s, and a post-test speed of 10 mm/s, with a compression distance of 90% of the sample height at room temperature.

PPC & PETROMAT SYMPOSIUM 2025

The chemical composition of the lavender essential oil used was analyzed using gas chromatography-mass spectrometry (GC–MS) performed on a LECO GC×GC Thermal Modulator Pegasus 4D. Gas chromatography (GC) using an Agilent 7820A system equipped with an FID detector was employed to determine the volatile retention capacity of the hydrogel beads by quantifying the headspace concentration of volatile compounds from the liquid-core hydrogel beads.

## RESULTS AND DISCUSSION

*A. natural deep eutectic solvents (NADES)*

The optimal molar ratios for clear NADES formation were 1:2 for choline chloride to ethylene glycol (ChCl/ETG) and choline chloride to glycerol (ChCl/GLY), and 1:1 for choline chloride to xylitol (ChCl/XLY). The clear appearance of each liquid indicates strong hydrogen bonding between choline chloride and the hydrogen bond donor (HBD). Viscosity followed the order: ChCl/XLY (1491.47 mPa·s) > ChCl/GLY (256.50 mPa·s) > ChCl/ETG (61.03 mPa·s), correlating with the number of hydroxyl groups in the HBD. FTIR spectra confirmed hydrogen bonding in NADES by shift of the O–H stretching from ~3200 $cm^{-1}$ (from glycerol and choline chloride) to ~3300 $cm^{-1}$. A peak at ~950 $cm^{-1}$ (C–N stretching) further confirms the presence and interaction of choline chloride and HBD within the NADES.

*B. nanocarbon prepared from palm oil by solution plasma process*

The production yield of carbon increased with the longer plasma discharge times. It was found that the highest yield was obtained at 240 minutes. Raman spectroscopy revealed that the synthesized carbon had an I_D/I_G ratio of 0.96, lower than the 1.28 ratio of the commercial activated carbon, indicating fewer defects and higher graphitic crystallinity (Puech, 2019). The XRD pattern of the synthesized carbon, as shown in Figure 1a, featured a broad peak at 2θ = 18.93 degrees, which corresponds to the disordered arrangement of carbon atoms. Peaks at (111), (200), (220), and (311) confirmed the presence of silver from the solution plasma process. (Girgis, 2007) (Bakti, Gareso, & Rauf, 2018). TEM images, as shown in Figure 1b, confirmed the amorphous phase of the synthesized carbon and showed silver particles, the d-space of silver metal released from silver electrode rods (d=0.233 nm). The average particle size of the synthesized carbon was 3.48 ± 0.76 nm (n =200). EDX analysis further confirmed the presence of silver originating from the plasma electrodes.

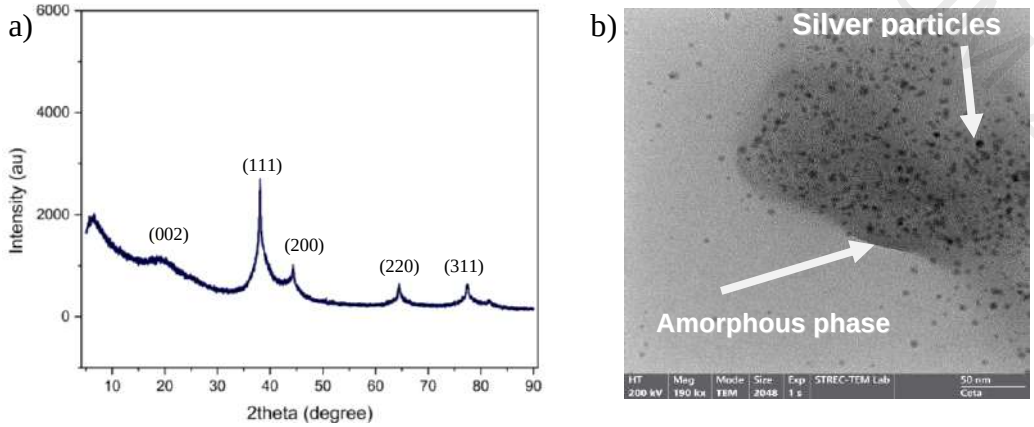


Figure 1. a) XRD patterns and b) TEM images of synthesized carbon.

*C. Characterization of NaOH-modified nanocarbon powder*

Nanocarbon, after the treatment with 1 M NaOH, showed the lowest value of zeta potential (–34.77 mV) and the smallest particle size compared with other NaOH concentrations, indicating the highest colloidal stability. This improvement is due to the introduction of oxygen-containing functional groups like the hydroxyl group onto the surface of nanocarbon, enhancing hydrophilicity and surface charge.

*D. silica nanoparticles from rice husk ash*

Silica nanoparticles synthesized from rice husk ash showed characteristic FTIR peaks, as shown in Figure 2a, at 3481 $cm^{-1}$ (O–H stretching), 1624 $cm^{-1}$ (OH bending), 955 $cm^{-1}$ (Si–OH stretching), and 1061 $cm^{-1}$ and 796 $cm^{-1}$ (Si–O–Si stretching), suggesting the successful formation of silica. XRD analysis revealed a broad peak at $2\theta = 23.2°$, indicating an amorphous structure. the silica nanoparticles with an average particle size of 49.36 ± 9.58 nm (n =200).

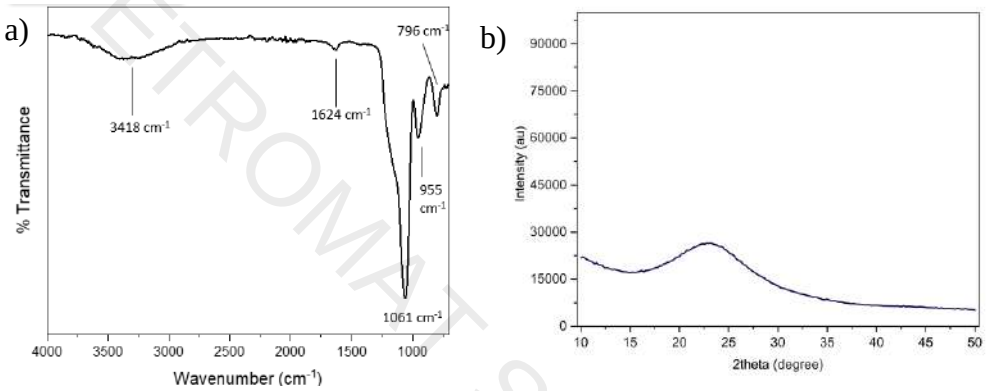


Figure 2. a) FTIR spectrum and b) XRD patterns of synthesized silica nanoparticles.

E. *Characterization of liquid-core hydrogel beads*

The liquid-core hydrogel beads containing different reinforcing agents exhibited distinct visual appearances. The nanocarbon-reinforced beads were dark and opaque, while the nanosilica-reinforced beads were clear and translucent, reflecting the inherent properties of the incorporated nanomaterials. Moreover, scanning electron microscopy (SEM) images, as shown in Figure 3a, of the liquid-core hydrogel beads with NADES were successfully formed with a liquid core surrounded by a double-layered shell. The inner shell consists of a calcium-crosslinked alginate layer, while the outer layer is formed by chitosan and further crosslinked with glutaraldehyde. In terms of thermal behaviours, as shown in Figure 3b, simultaneous thermal analysis revealed that both nanosilica- and nanocarbon-loaded beads underwent slower degradation and retained a higher residual mass compared to the non-reinforced beads. This indicated the enhanced thermal stability.

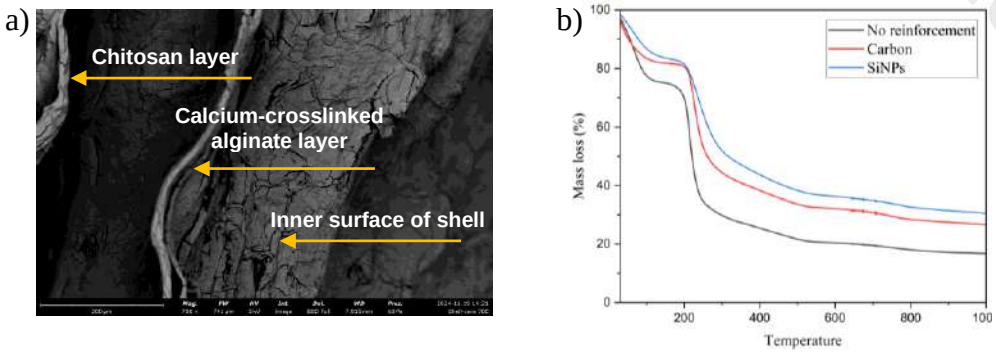


Figure 3. a) SEM images of the liquid-core hydrogel bead, b) STA thermograms of liquid-core hydrogel beads with and without a reinforcing agent determined under nitrogen gas. under nitrogen gas.



PPC & PETROMAT SYMPOSIUM 2025

From a mechanical perspective, as shown in Figure 4, nanocarbon-reinforced beads exhibited the highest compressive strain (45.54± 14.5%), followed by non-reinforced beads (39± 5.1%) and nanosilica-reinforced beads (33.75± 5.6%), indicating enhanced flexibility due to nanocarbon. In terms of compressive stress, nanosilica-reinforced beads showed the highest value (2.4 ± 0.4 kPa), compared to nanocarbon (0.8 ± 0.4 kPa) and non-reinforced beads (0.56 ± 0.06 kPa), suggesting improved structural resistance. Silica nanoparticles markedly increased the compressive modulus to 6.12 kPa, indicating strong reinforcement, while carbon nanoparticles had minimal effect (1.75 kPa), close to the control (1.70 kPa). Thus, silica was more effective in enhancing mechanical strength.

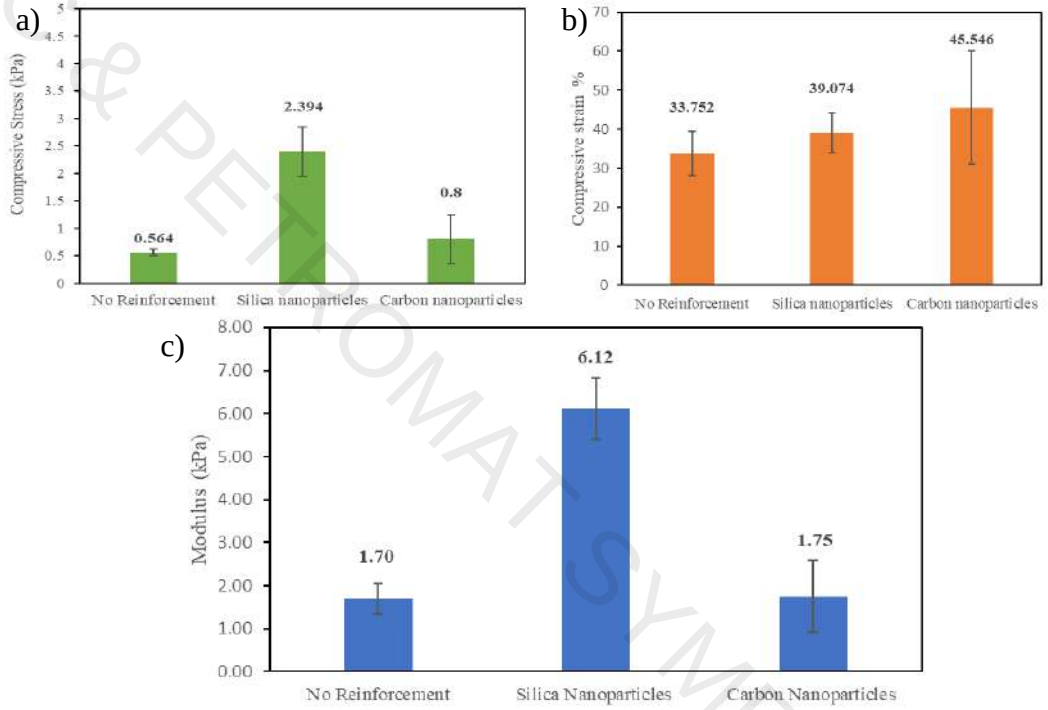


Figure 4. Mechanical properties of liquid-core beads using a reinforcing agent in alginate Layer a) Compressive strain, b) Compressive strain at break, and c) Modulus. (n=5).

GC-MS analysis of lavender essential oil, as shown a Figure 6, revealed a complex profile of volatile organic compounds, among which linalool, linalyl acetate, and β-caryophyllene are the predominant constituents (Dong, 2020). These three compounds were selected as representative markers for further retention analysis due to their high abundance.

Subsequent GC headspace analysis demonstrated that the release of volatile compounds from liquid-core hydrogel beads varied significantly depending on the type of reinforcement. The unreinforced beads exhibited the highest headspace concentrations, indicating the lowest retention efficiency, with 29.18 mg/mL of linalool, 36.50 mg/mL of linalyl acetate, and 50.78 mg/mL of β-caryophyllene. In contrast, the nanocarbon-reinforced beads showed the greatest reduction in volatile release, with 15.64 mg/mL of linalool, 22.93 mg/mL of linalyl acetate, and 39.56 mg/mL of β-caryophyllene, suggesting enhanced adsorption and restricted diffusion. The nanosilica-reinforced beads demonstrated intermediate performance, releasing 23.58 mg/mL of linalool, 32.20 mg/mL of linalyl

PPC & PETROMAT SYMPOSIUM 2025

acetate, and 44.37 mg/mL of β-caryophyllene. These findings highlight the positive effect of structural reinforcement on the volatile retention performance of hydrogel systems.

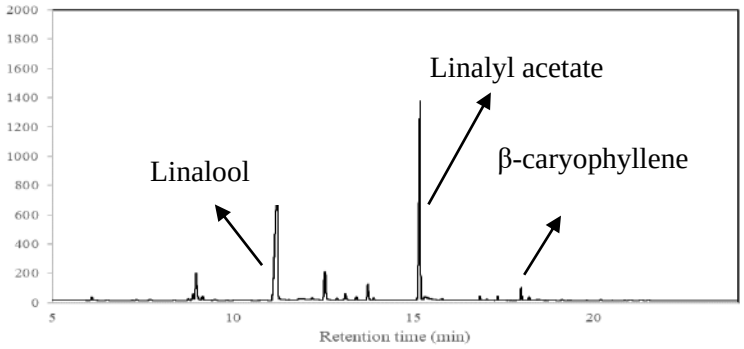


Figure 6 Gas Chromatography chromatogram of lavender essential oil.

## CONCLUSIONS

In summary, the incorporation of nanocarbon and nanosilica as reinforcing agents in the liquid-core hydrogel beads could enhance their thermal stability, mechanical strength, and volatile compound retention. The differences imparted by each reinforcing agent influenced both the appearance and performance of the beads—nanocarbon improved flexibility and adsorption, while nanosilica beads enhanced compressive strength. Notably, the reinforced beads exhibited improved retention of linalool, linalyl acetate, and β-caryophyllene, that are the main volatile constituents in lavender essential oil.

## ACKNOWLEDGEMENTS

The authors would like to express their sincere gratitude to the Petroleum and Petrochemical College, Chulalongkorn University, for its valuable support to this research work.

## REFERENCES

Bakti, A.I., Gareso, P.L., and Rauf, N. (2018). Characterization of active carbon from coconut shell using X-ray diffraction (X-RD) and SEM-EDX techniques. Jurnal Penelitian Fisika dan Aplikasinya (JPFA), 8(2), 115-122.

Dong, G., Bai, X., Aimila, A., Aisa, H.A., and Maiwulanjiang, M. (2020). Study on lavender essential oil chemical compositions by GC-MS and improved pGC. Molecules, 25(14), 3166.

Girgis, B.S., Temerk, Y.M., Gadelrab, M.M., and Abdullah, I.D. (2007). X-ray diffraction patterns of activated carbons prepared under various conditions. Carbon letters, 8(2), 95-100.

Puech, P., Kandara, M., Paredes, G., Moulin, L., Weiss-Hortala, E., Kundu, A., Ratel-Ramond, N., Plewa, J.-M., Pellenq, R., and Monthioux, M. (2019). Analyzing the Raman spectra of graphenic carbon materials from kerogens to nanotubes: what type of information can be extracted from defect bands? C, 5(4), 69.

Satou, T., Kamagata, M., Nakashima, S., Mori, K., and Yoshinari, M. (2024). Effects of Inhaled Linalool on the Autonomic Nervous System in Awake Mice. Natural Product Communications, 19(2), 1934578X241232273.

PPC & PETROMAT SYMPOSIUM 2025

# BIOBASED EPOXY POLYMERIC FILMS DERIVED FROM RUBBER SEED OIL

*Intan Eta Hidayati* [a], *Thanyalak Chaisuwan* [b,c], *Suwabun Chirachanchai* [b], *Sorapat Niyomsin*[b,c]

[a)] The Petroleum and Petrochemical College, Chulalongkorn University
[b)] Center of Excellence in Bioresources to Advanced Materials (B2A-CE), The Petroleum and Petrochemical College, Chulalongkorn University, Bangkok, Thailand
[c)] Machine Learning for Polymers and Materials Discovery Research Unit, The Petroleum and Petrochemical College, Chulalongkorn University, Bangkok 10330, Thailand

**Keywords:** Rubber seed oil, Bio-based polymers, Epoxy polymeric films, Sustainable materials

## ABSTRACT

The growing demand for sustainable materials has accelerated interest in bio-based polymers as alternatives to petroleum-derived products. Rubber seed oil (RSO) is an abundant underutilized by product of rubber cultivation in Thailand. This study investigates the transformation of RSO through amidation, methacrylation, and epoxidation to produce polymerizable and curable monomers. The modified monomers were subsequently subjected to radical polymerization, followed by curing with polyethyleneimine (PEI) to form polymeric films. The FTIR and NMR analyses confirmed the presence of the expected functional groups. The mechanical and thermal properties demonstrated flexibility and thermal stability, making them suitable for applications and sustainable polymeric materials. This work highlights the potential of converting plant-based oils into high value polymeric materials, promoting green chemistry and contributing to the development of environmentally friendly alternatives in the polymer industry.

*Sorapat.N@chula.ac.th

## INTRODUCTION

In recent years, there has been growing interest in using renewable resources to develop sustainable materials, driven by the need to reduce environmental impact and dependence on non-renewable resources. This shift has attracted attention from both academia and industry, seeking eco-friendly alternatives to petrochemical products. The use of renewable resources has led to the creation of materials that offer both environmental and economic benefit. Rubber seed oil, with its high availability and fatty acids, is a prominent renewable resource. Its oil content, typically 50-60%, contains a mix of fatty acids, including palmitic acid, stearic acid, oleic acid, and predominantly linoleic acid, which can be modified and polymerized into biodegradable materials with properties similar to petrochemical-based products (Obanla et al., 2019). This makes rubber seed oil an attractive, sustainable substitute for conventional vegetable oils, supporting the development of circular economy.

This study explores the potential of converting fatty acids from rubber seed oil into functional monomers that can be polymerized to produce various polymers with tailored properties. Rubber seed oil is rich in unsaturated fatty acids, in an ideal source for synthesizing monomers, which can be modified to exhibit specific physical, chemical, and mechanical characteristics. These monomers can then be used in applications such as

PPC & PETROMAT SYMPOSIUM 2025

biodegradable plastics, coatings, adhesives, and medical devices. By focusing on unsaturated fatty acids, which offer flexibility, strength, and resistance to oxidation, the research aims to create innovative, customizable materials from renewable plant-based resources. The transformation process involves extracting and chemically modifying fatty acids, using their inherent reactive sites, such as double bonds and carboxylic acid groups, to enable polymerization and the formation of high-performance polymers (Xia, Quirino, & Larock, 2013).

Additionally, this study investigates the incorporation of rubber seed oil into epoxy resin formulations to improve their environmental sustainability. Modifying these resins with elastomeric components can also produce epoxy elastomers, enhancing flexibility and durability (Derawi & Salimon, 2010). This research aims to green chemistry and sustainable materials science by offering renewable feedstock for value-added materials, such as epoxy bio-elastomers, addressing resource depletion and promoting environmental sustainability.

## EXPERIMENTAL

*A. Materials*

Rubber seed oil was extracted by compression. 2-(methylamino) ethanol and 4-(dimethylamino) pyridine (DMAP) were purchased from Tokyo Chemical Industry Co. Ltd., Japan. Methacrylic anhydride, sodium hydroxide (NaOH), sodium sulfate anhydrous ($Na_2SO_4$), meta-chloroperoxybenzoic acid (m-CPBA) and polyethyleneimine (PEI) were purchased from Sigma Aldrich, United States. Dichloromethane (DCM), chloroform ($CHCl_3$), sodium chloride (NaCl), ethanol, methanol and toluene were purchased from RCI LabScan Co., Ltd., Thailand. 2,2’ Azobis(2-methylpropionitrile) (AIBN) was purchased from Loba Chemie Co., Ltd., India. Sodium bicarbonate ($NaHCO_3$) was purchase from Carlo Ebra Co., Ltd., Italy.

*B. Synthesis of Rubber seed oil-epoxy polymer*

The amidation reaction was initiated by mixing 2-(methylamino) alcohol (0.3138 mol), rubber seed oil (0.1533 mol) and sodium ethoxide (0.005 mol). The reaction mixture was heated to 110$^{o}$C and continuously stirred for 3 hours, resulting in the formation of rubber seed oil-amide monomer (RSM). The process then proceeded to methacrylation, where RSM (0.28 mol), methacrylate anhydride (0.28 mol) and DMAP (0.0028 mol) were heated to 65$^{o}$C and stirred for 12 hours, resulting in the formation of rubber seed oil-acrylate monomer (RSMA). Subsequently, an epoxidation reaction was carried out, wherein RSMA (0.252 mol), m-CPBA (0.2 mol) and sodium carbonate (0.252 mol) were stirred in an ice-water bath for 1 hour, followed by stirring at room temperature for 24 hours to produce rubber seed oil-acrylate epoxy monomer (ERSMA). The purification process after each reaction step, the solution was dissolved in DCM and washed twice with sodium chloride solution. Then anhydrous sodium sulfate was added. The product was filtered, and DCM was removed by rotary evaporation to obtain a monomer. Polymerization was carried out via free radical polymerization by mixing ERSMA (14.3 mmol), AIBN (0.143 mmol) in 1,4-Dioxan (6.5 ml). The mixture was purged under nitrogen atmosphere for 1 hour and placed in an oil bath at 80$^{o}$C. The reaction was stirred continuously for 12 hours. The polymerization solution, which was then precipitated into cold diethyl ether to obtain epoxy polymer (EP). The purification procedure was repeated twice before vacuum drying.

PROS PETROMAT SYMPOSIUM 2025

*C. Preparation of Polymeric films*

Rubber seed oil-based epoxy resin was prepared by curing EP with polyethyleneimine (PEI) in the presence of a catalyst (DMAP, 0.5 wt%) for 2 hours. The process involved placing measured amounts of EP, polyethyleneimine (PEI) and chloroform into a 20 mL vial, which was then be thoroughly stirred to create a uniform mixture. To eliminate any trapped air bubbles, the mixture underwent ultrasonication. Then, the solution was poured into a polytetrafluoroethylene (PTFE) mold and left to dry in a fume hood at room temperature for 24 hours. After this, the mixture was cured in a vacuum at 90$^{o}$C for 6 hours, 150$^{o}$C for 3 hours and 180$^{o}$C for 30 minutes. The product was labelled as EP-PEI. To evaluate the impact of PEI content on crosslinking density, $EP_x$-$PEI_y$ samples were prepared, where x represents the epoxy mol ratio and y the amine ratio in the feed mixture.

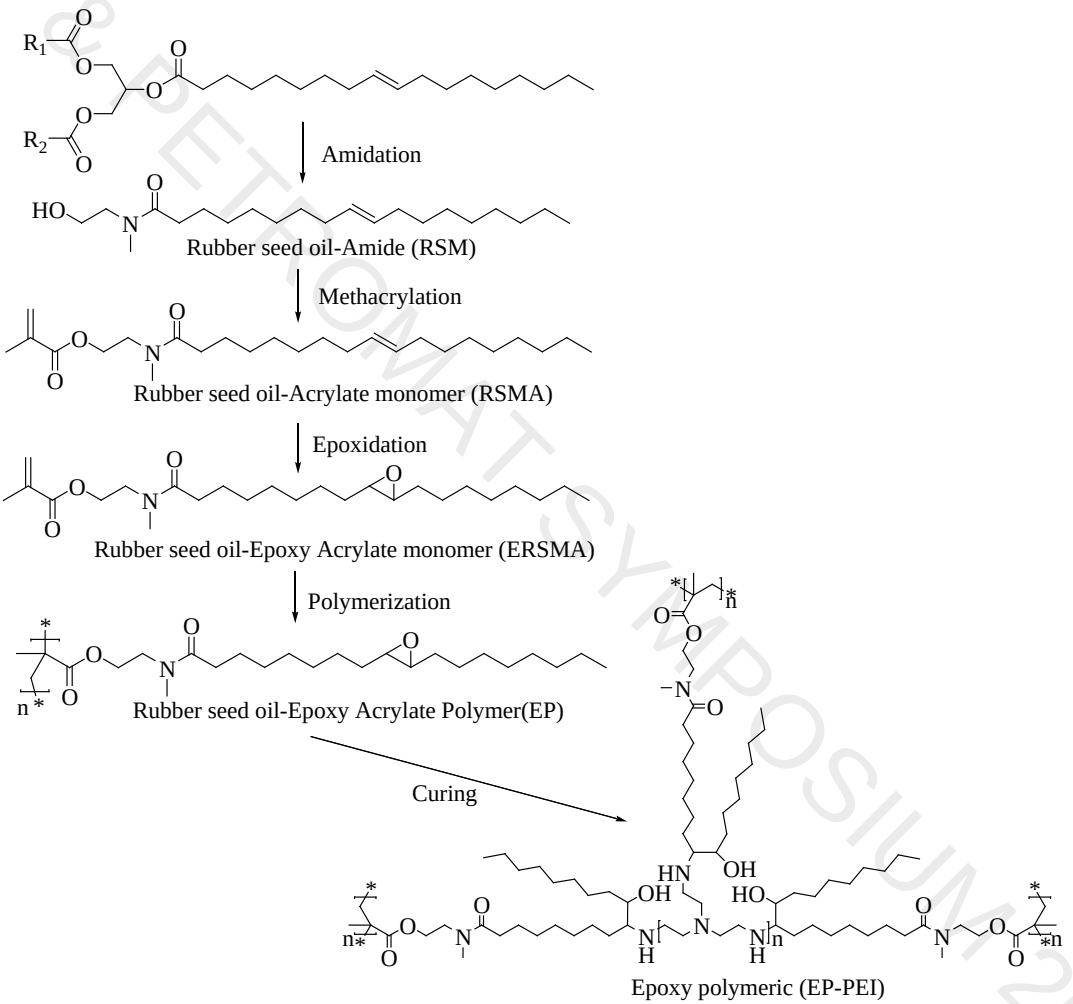


**Figure 1** Schematic of epoxy polymeric (EP-PEI).

*D. Characterizations*

The synthesized materials were characterized by various analytical techniques. Proton ($^{1}$H-NMR) and carbon ($^{13}$C-NMR) Nuclear Magnetic Resonance spectra were recorded using a Bruker AVANCE 500 MHz Ultra Shield Plus at 25°C. Fourier-transform infrared (FTIR)

PPC & PETROMAT SYMPOSIUM 2025

spectroscopy was conducted on a Bruker ALPHA FTIR in the wavenumber range of 4000-500 $cm^{-1}$. Thermal properties were analyzed using a TA Q50 thermogravimetric analyzer (TGA) over a temperature range of 30°C to 600°C, with a heating rate of 10°C/min under a nitrogen flow. Calorimetric measurements were performed using a NETZSCH proteus differential scanning calorimeter (DSC). Viscoelastic properties were measured using a Discovery DMA 850 dynamic mechanical analyzer (DMA), with a heating rate of 5°C/min and a frequency set at 10 Hz.

## RESULTS AND DISCUSSION

### *A. Characterization of EP and $EP_x$-$PEI_y$*

FTIR spectra support the breakdown of the triglyceride bond in rubber seed oil (RSO), as the ester peak at 1742 $cm^{-1}$ disappeared (Figure 1(a)). The appearance of peaks at 3375 $cm^{-1}$ (OH group) and 1620 $cm^{-1}$ (C=O Amide) in rubber seed oil-amide (RSM) indicated functional group changes. The C=O stretching peak at 1715 $cm^{-1}$ and C=C methacrylate peak at 1615 $cm^{-1}$ confirmed the incorporation of methacrylate to form RSMA. In ERSMA, a new peak at 840 $cm^{-1}$ showed the presence of an epoxy group, and the absence of C=C peak at 1640 $cm^{-1}$ confirmed radical polymerization. FTIR analysis during curing, shown in Figure 1(b), revealed the disappearance of the primary amine (3210 $cm^{-1}$) and epoxy (840 $cm^{-1}$) peaks, indicating effective ring-opening between epoxy of EP and PEI as curing agents. A new peak at 3375 $cm^{-1}$ confirmed the formation of hydroxyl groups. Increasing the amine-to-epoxy ratio enhanced crosslinking, as indicated by stronger FTIR signals and broader hydroxyl peaks at 3375 $cm^{-1}$, suggesting a more complete reaction and robust structure (Mu et al., 2020).

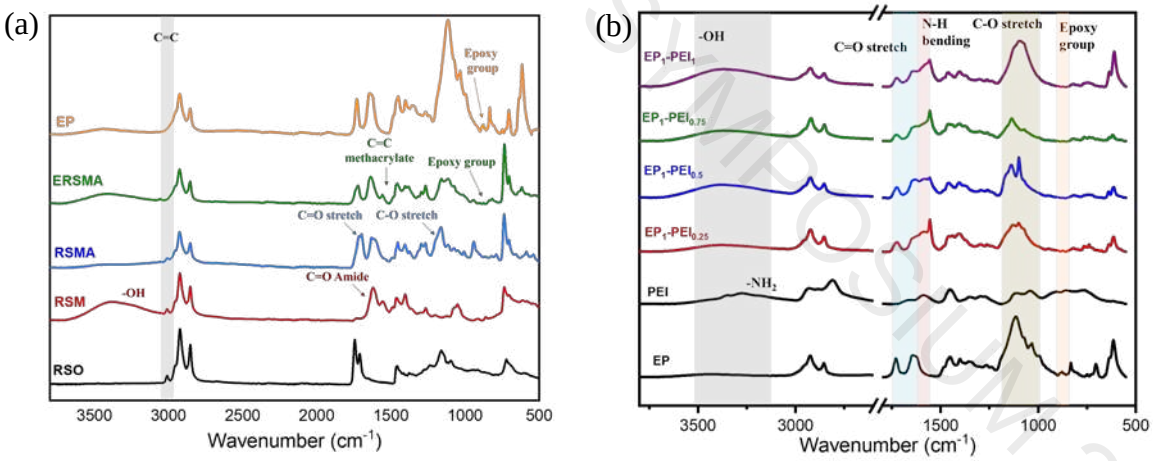


**Figure 2** FTIR spectra of (a) RSO, RSM, RSMA, ERSMA and EP, (b) $EP_x$-$PEI_y$.

### *B. Thermal properties*

TGA thermograms indicate approximately 2% mass loss at lower temperatures (around 100 -150 $^oC$) (Figure 2 (a)). At higher temperatures (above 200$^oC$), $EP_1$-$PEI_1$, with the highest PEI content exhibits decomposition at higher temperature, suggesting enhanced thermal stability. DSC thermograms demonstrated a clear increase in glass transition temperature (Tg) with raising PEI content (Figure 2(b)). Formulations with lower PEI content show a more flexible polymer structure characterized by lower Tg values, whereas higher PEI

content promotes more extensive curing, leading to a denser and more rigid polymer network with elevated Tg. These findings highlight the key role of curing agent concentration in controlling cure degree, crosslink density, and the polymer's thermal stability (Prasob & Sasikumar, 2019).

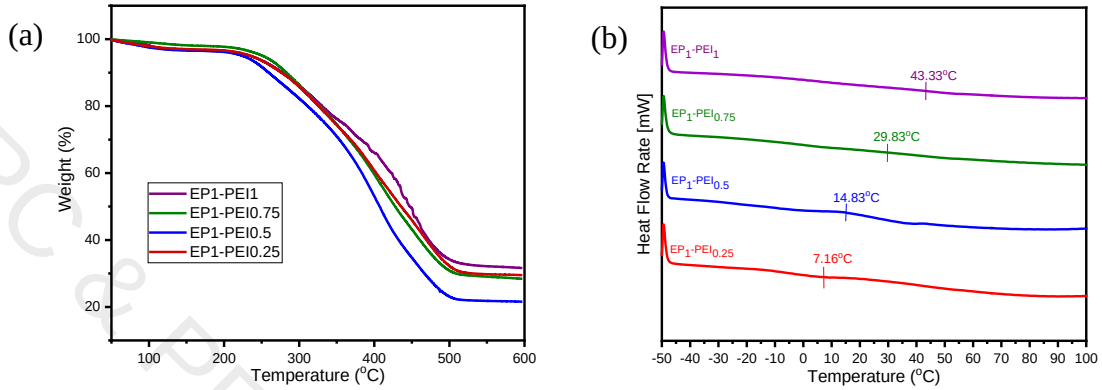


**Figure 3** (a) TGA curves, (b) DSC curves of $EP_x$-$PEI_y$.

*C. Mechanical properties*

The dynamic mechanical behavior of $EP_x$-$PEI_y$ was evaluated using DMA, with Figure 3 shown temperature-dependent changes in storage modulus and loss tangent. The storage modulus initially slightly decreased corresponding to the transition from rigid glassy state, then rapidly dropped and finally plateaued in the rubbery state, reflecting thermal transition (Yang et al., 2023). Figure 3(a) shows the temperature increases, the storage modulus of the $EP_1$-$PEI_{0.75}$ sample becomes higher than $EP_1$-$PEI_{0.5}$, indicating increased stiffness due to a higher degree of crosslinking. This enhanced crosslinking improves the material's strength and thermal stability. In contrast, $EP_1$-$PEI_{0.5}$ exhibits lower stiffness, likely due to fewer crosslinks, making it more flexible under heat. EP1-PEI1, with the highest PEI content, was too brittle for DMA testing, while $EP_1$-$PEI_{0.25}$ was too sticky and thin, indicating incomplete curing. Figure 3(b) shown the glass transition temperature (Tg), determined from the peaks in the loss tangent curves decreased with decreasing PEI content indicating that lower PEI content reduced the glass transition temperature of the materials.

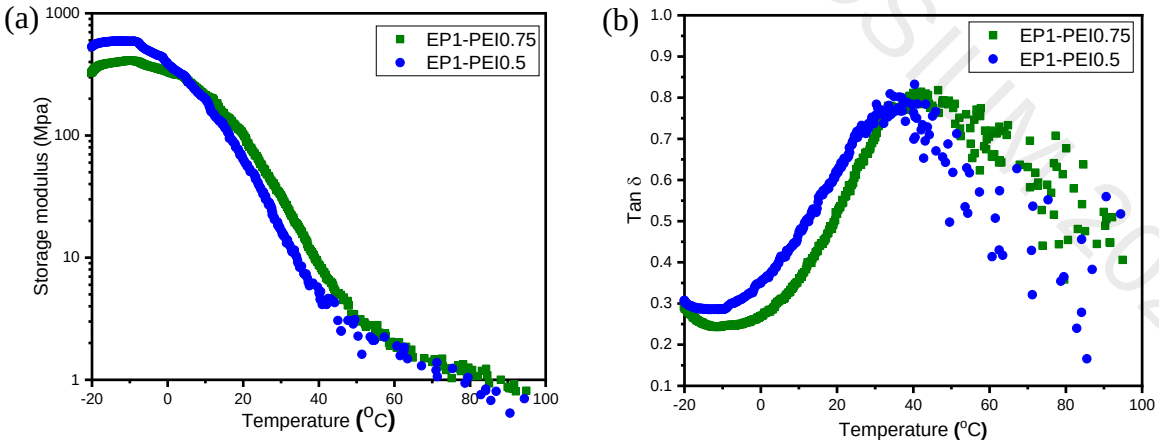


**Figure 4** DMA curves of (a) storage modulus and (b) loss tangent as a function of temperature for $EP_x$-$PEI_y$.

## CONCLUSIONS

This study successfully synthesized rubber seed oil-acrylate epoxy monomers through amidation, methacrylation, and epoxidation, followed by free radical polymerization to produce rubber seed oil-acrylate epoxy polymer (EP). These polymers were cured with polyethyleneimine (PEI) to create fully biobased epoxy films. The curing mechanism, involving ring-opening between EP and PEI, formed a strong cross-linked network observed by FTIR. In addition, thermal properties were assessed using TGA and DSC, while mechanical performance was evaluated through DMA. Among the tested formulations, the $EP_1$-$PEI_{0.75}$ film demonstrated the best thermal stability, highlighting its potential for advanced applications. This study contributes to the development of sustainable, eco-friendly polymeric materials using renewable resources like rubber seed oil.

## ACKNOWLEDGEMENTS

The authors would like to express their gratitude to the Petroleum and Petrochemical College of Chulalongkorn University, and ASEAN & NON-ASEAN Scholarship of Chulalongkorn University, SATREPS, and High potential research group scholarships.

## REFERENCES

**Auvergne,R., Caillol, S., David, G., Boutevin, B., & Pascault, J.-P.** (2014). Biobased thermosetting epoxy: present and future. *Chemical reviews*, 114(2), 1082-1115.

**Derawi, D., & Salimon, J.** (2010). Optimization on epoxidation of palm olein by using performic acid. *Journal of Chemistry*, 7(4), 1440-1448.

**Mu, S., Zhang, Y., Zhou, J., Wang, B., & Wang, Z.** (2020). Recyclable and mechanically robust palm oil-derived epoxy resins with reconfigurable shape-memory properties. *ACS Sustainable Chemistry & Engineering*, 8(13), 5296-5304.

**Obanla, O., Udonne, J., Ajani, O., Ojewumi, M., Omodara, O., & Oni, B.** (2019). Studies of the in-situ epoxidation of Rubber (Havea Bransiliensis) seed oil by performic acid. Journal of Physics.

**Prasob, P., & Sasikumar, M.** (2019). Viscoelastic and mechanical behavior of reduced graphene oxide and zirconium dioxide filled jute/epoxy composite at different temperature conditions. *Materials Today Communications*, 19, 252-261.

**Xia, Y., Quirino, R., L., & Larock, R. C.** (2013). Bio-based thermosetting polymers from vegetable oils. *Journal of Renewable Materials*, 1(1), 3-27.

**Yang, X., Li, j., Wang, Y., Tan, L., Han, L., Lu, J., Li, M., Fang, D., Huang, X., & Xu, Y. h.** (2023). Synthesis and Characterization of Fully Biobased Epoxy Elastomers Prepared from Different Plant Oils. *ACS Sustainable Chemistry & Engineering*, 11(38), 13950-13961.

PPC & PETROMAT SYMPOSIUM 2025

**Full Paper Template**

# GLUCOSE-MEDIATED REDUCTION OF SILVER IONS: A COST-EFFECTIVE APPROACH TO NANOPARTICLE SYNTHESIS

*Puntharika Tangsopa* [a,b], *Manop Panapoy* [a], *Nattawut Chaiyut* [a], *Bussarin Ksapabutr*[*, a]

[a] Department of Materials Science and Engineering, Faculty of Engineering and Industrial Technology, Silpakorn University, Nakhon Pathom, Thailand
[b] Center of Excellence on Petrochemical and Material Technology, Chulalongkorn University

Keywords: Silver nanoparticle, Green synthesis, Glucose

## ABSTRACT

Silver nanoparticles (AgNPs) have demonstrated immense potential for diverse applications, including biosensing, wastewater treatment, catalysis, antimicrobial agents, and biomedical engineering. Green synthesis of metallic nanoparticles is recognized as one of the simplest, most convenient, cost-effective, and environmentally friendly methods that minimize the involvement of toxic chemicals. In this study, AgNPs were synthesized using a microwave-assisted method with glucose as the reducing agent, which facilitated the reduction of $Ag^{+}$ ions to $Ag^{0}$. The pH of the solution was controlled by the addition of NaOH. The conditions for the green synthesis of AgNPs were a silver nitrate solution concentration of 0.1 mM, glucose solution concentration of 2 mM, and pH 9.5. Response Surface Methodology (RSM) was then employed to compare the experimental absorbance values with statistical predictions, yielding an $R^2$ value of 0.9862, indicating a close agreement between the observed and predicted absorbance values. The AgNPs obtained from the microwave heating process exhibited a surface plasmon resonance band centered at 413 nm and demonstrated high stability in aqueous suspensions as indicated by a zeta potential value of -26.2 mV. Dynamic light scattering analysis revealed that the average diameter of AgNPs was 79 nm.

*** ksapabutr_b@su.ac.th**

## INTRODUCTION

Silver nanoparticles (AgNPs) are prominent nanomaterials that have attracted considerable attention across various scientific disciplines due to their unique physical, chemical, and biological characteristics, including stability and plasmonic effect-induced optical properties. These attributes render them suitable for diverse applications, such as biosensing, wastewater treatment, catalysis, and biomedical engineering (Farooqi et al., 2024). Currently, green synthesis methods are increasingly favored because of their convenience, simplicity, and environmentally benign nature. Conventional methods for synthesizing nanoparticles typically involve the reaction of metal salts with heat, which can be implemented through various means. Microwave irradiation is an interesting alternative because of its enhanced energy efficiency compared with traditional heating methods. Furthermore, studies have indicated that the biosynthesis of nanoparticles using microwave irradiation exhibits higher efficiency than conventional heating methods (Phoemthaisong et al., 2023, Thanasakonpong et al., 2023) The synthesis of AgNPs relies on redox reactions, where metal ions are reduced to form stable nanoparticles. Commonly employed reducing agents include sodium borohydride ($NaBH_4$), hydrazine ($N_2H_4$), and formaldehyde

PPC & PETROMAT SYMPOSIUM 2025

(HCHO), which are associated with toxicity and potential environmental residues (Hashemirad et al., 2025). Consequently, glucose is increasingly preferred as a reducing agent because of its natural origin and is found in sources such as grapes, apples, bananas, carrots, and radishes. Glucose facilitated the reduction of $Ag^{+}$ ions to $Ag^{0}$. The reducing agents exhibited optimal performance under alkaline conditions. In other words, the addition of an alkali can accelerate the reaction time, and hydroxide ion (OH-) compounds such as sodium hydroxide (NaOH) are commonly utilized as accelerators by regulating the concentration of free metal ions in the solution (Putri et al., 2019; Swensson et al., 2018). In this work, a rapid and green method for microwave-assisted biological synthesis was developed using glucose as the reducing agent and sodium hydroxide as the accelerator. Additionally, the influence of different experimental variables, namely $AgNO_3$ concentration and glucose concentration used in the synthesis, was investigated using Response Surface Methodology (RSM).

## EXPERIMENTAL

### *A. Materials*

Silver nitrate ($AgNO_3$) was supplied by Carlo Erba Reagent (Italy). Glucose ($C_6H_{12}O_6$) was purchased by Reckitt Benckiser (Thailand). Sodium hydroxide (NaOH) and sodium chloride (NaCl) were purchased from RCI Labscan (Thailand). All reagents were employed in their commercially available without additional purification, and all solutions were prepared using deionized (DI) water.

### *B. Synthesis of AgNPs and Experimental design by RSM*

A 25 mM sodium hydroxide solution was added to 20 ml of glucose solutions (0.5 - 4 mM) at ambient temperature and continuously stirred magnetically for 20 min. The pH of the mixture was adjusted (9, 9.5, 10, and 10.5). Subsequently, 5 ml of a silver nitrate solution (0.025 – 0.3 mM) was added to the mixture over a period of 10 min. The resulting mixture was then placed in a microwave oven at 800 W for 100 s. Upon removal from the microwave, 0.05 ml of a NaCl solution was added as a stabilizing agent. For all UV-Vis spectrophotometric studies, Response Surface Methodology (RSM) combined with Central Composite Design (CCD) was employed to optimize the levels of effective variables for AgNP synthesis and analyze their relationships. The two significant variables were glucose and $AgNO_3$ concentrations (at a constant pH of 9.5). All the parameters were investigated at different levels.

### *C. Detection and characterization of AgNPs*

The initial detection was performed by visual observation. Following microwave irradiation, a change from colorless to yellow was observed in the solution. The formation of AgNPs was confirmed using an Ultraviolet-Visible-Near Infrared (UV-VIS-NIR) spectrophotometer (UV-3600i Plus, Shimadzu) in the 300-800 nm wavelength range. The size distribution profile, polydispersity index (PDI), zeta analysis, and particle size distribution of the synthesized AgNPs were investigated by Dynamic Light Scattering (DLS) using a Zetasizer Nano ZS instrument (Malvern).

PPC & PETROMAT SYMPOSIUM 2025

## RESULTS AND DISCUSSION

The UV-visible spectra shown in Figure 1(a) illustrate the influence of glucose solution concentration on the formation of AgNPs. In the absence of glucose, the solution remained colorless and the UV-visible spectrum was relatively flat, indicating no AgNP formation (Cheviron et al., 2014). However, upon addition of glucose, the solution turned yellow, consistent with previous reports (El-Rafie et al., 2014; Hemmati et al., 2019; Pattnaik et al., 2023). Under thermal and alkaline conditions, the glucose solution is typically oxidized to gluconate and other products that act as reducing agents, facilitating the reduction of $Ag^{+}$ ions to $Ag^{0}$ and potentially serving as stabilizing agents.

Figure 1(b) shows the influence of pH on the synthesis of AgNPs. In the absence of NaOH, the SPR absorbance was lower than that of the sample with NaOH, indicating that NaOH acted as a rate enhancer by controlling the concentration of free metal ions in the solution (Swensson et al., 2018; Putri et al., 2019). Increasing the pH from 9 to 9.5 resulted in an increase in the maximum absorbance. At higher pH levels, the rates of the reaction, reduction, and nucleation of $Ag^{+}$ ions were enhanced. Furthermore, no significant changes were observed at pH values above 9.5 (Hemmati et al., 2019).

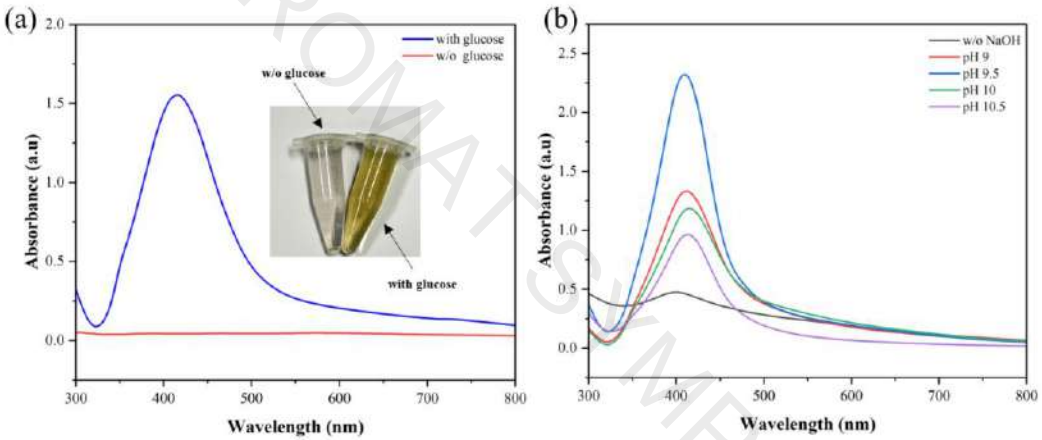


**Figure 1.** UV-visible absorption spectra of the synthesized AgNPs, showing the effects of (a) glucose concentration and (b) pH.

The surface response analyses depicted in Figures 2(a) and 2(b) clearly demonstrate that the concentrations of $AgNO_3$ and glucose significantly influenced AgNP biosynthesis. As the concentration of $AgNO_3$ increased from lower values to approximately 0.1–0.2 mM, the absorbance rapidly increased (transitioning from blue to red regions). However, if the concentration was increased excessively (e.g., beyond 0.25 mM), the absorbance began to decrease again (returning to the blue region). The observed decrease in absorbance may be attributed to the agglomeration of nanoparticles (Kamal et al., 2016; Putri et al., 2019). Similarly, as the glucose concentration increased from lower values, the overall absorbance tended to rise, particularly in regions where $AgNO_3$ concentration was moderate. Nevertheless, at very low glucose concentrations (e.g., 0.5–1.0 mM), the absorbance remains low even when the $AgNO_3$ concentration is optimal. Consequently, to achieve maximum absorbance (red regions), it was evident that both $AgNO_3$ and glucose concentrations needed to be within their respective optimal ranges simultaneously. Multiple

PPC & PETROMAT SYMPOSIUM 2025

regression analysis was performed on the experimental data to develop a regression model between the maximum absorbance value and independent variables. The results obtained from the Central Composite Design (CCD) were integrated into a second-order polynomial equation. The relationship between the experimental factors and maximum absorbance is expressed by the following equation:

$$\text{Absorbance} = 2.914 - 0.680x + 1.202y - 3.531x^2 - 0.241y^2 + 2.432xy$$

where x represents the concentration of $AgNO_3$ (mM) and y represents the concentration of glucose (mM). Based on the analysis of variance (ANOVA), the F-value of the model was calculated to be 71.62, indicating the model's significance. A p-value of 0.0001, which was less than 0.05, further confirmed the significance of the model terms. The calculated coefficient of determination ($R^2$) was 0.9862, implying that the model accounts for 98.62% of the total variability. A relatively low coefficient of variation (CV = 8.18%) further indicated the high accuracy and reliability of the model. Furthermore, as shown in Figure 2(c), the normal probability plot of the residuals indicates that all the residual values are aligned along a straight line without significant deviation.

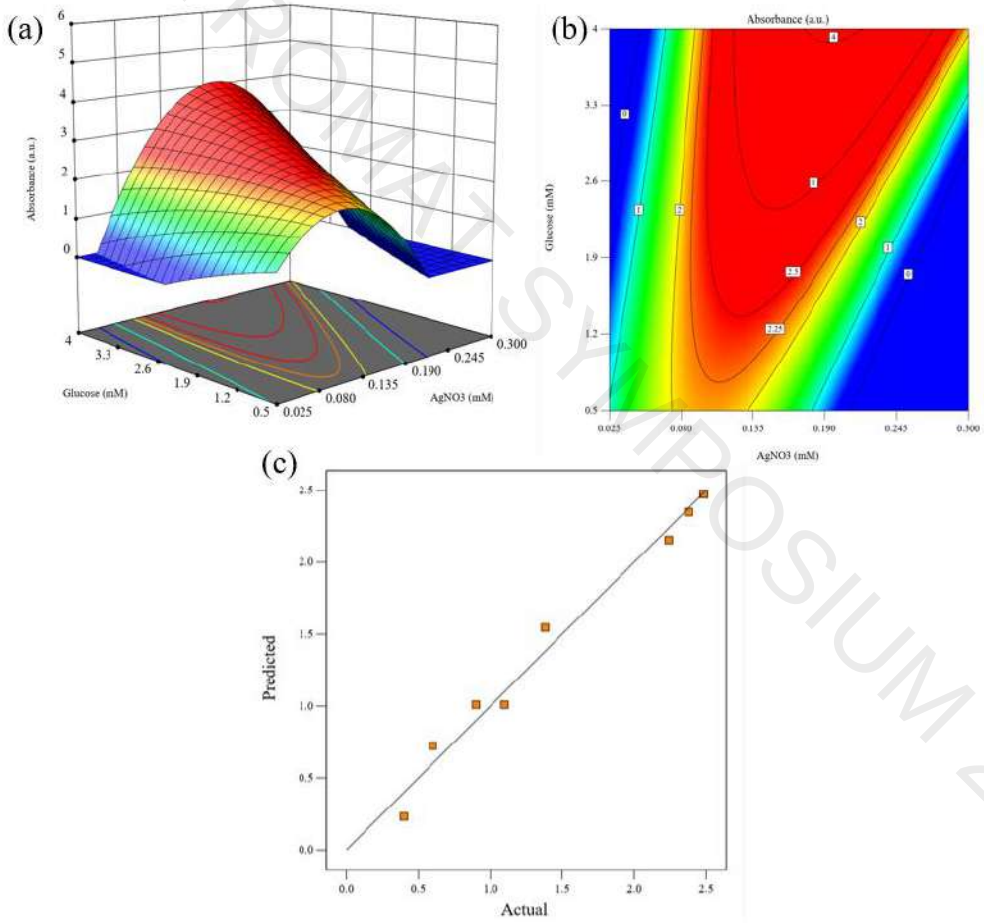


**Figure 2.** (a) Three-dimensional response surface, (b) contour plots showing the absorbance of AgNPs as a function of glucose and $AgNO_3$ concentration, and (c) normal probability plot of internally studentized residuals for the quadratic model of SPR intensity.

PPC & PETROMAT SYMPOSIUM 2025

The optimal criteria for achieving the maximum absorbance (Abs) using minimal concentrations of $AgNO_3$ and glucose are presented in Table 1. The results indicated that the optimal conditions were 0.113 mM $AgNO_3$ and 1.388 mM glucose (at a constant pH of 9.5 and reaction time of 100 s). A comparison between the model and the experimental results is presented in Table 2. When the glucose concentration was fixed at 2 mM, the optimal $AgNO_3$ concentration was 0.123 mM. The simulated Abs value under these conditions was 2.744, which was in close agreement with the experimental value of 2.475 obtained with 0.1 mM $AgNO_3$ (%error = 9.8%).

**Table 1.** Optimization constraints.

| Name | Goal | Lower Limit | Upper Limit | Lower Weight | Upper Weight |
|---|---|---|---|---|---|
| $AgNO_3$ | minimize | 0.025 | 0.3 | 1 | 1 |
| Glucose | minimize | 0.5 | 4 | 1 | 1 |
| Abs | maximize | 1 | 4 | 1 | 1 |
| **Number** | **$AgNO_3$** | **Glucose** | **Abs** | **Desirability** | |
| 1 | 0.113 | 1.3888 | 2.481 | 0.603 | selected |

**Table 2.** Comparison between simulation and experimental results.

| Name | Goal | Lower Limit | Upper Limit | Lower Weight | Upper Weight |
|---|---|---|---|---|---|
| $AgNO_3$ | minimize | 0.025 | 0.3 | 1 | 1 |
| Glucose | 2 | 0.5 | 4 | 1 | 1 |
| Abs | maximize | 1 | 4 | 1 | 1 |
| | **$AgNO_3$** | **Glucose** | **Abs** | **Desirability** | |
| Simulation | 0.123 | 2.000 | 2.744 | 0.603 | selected |
| Experimental | 0.100 | 2.000 | 2.475 | | |

The formation of AgNPs was monitored using UV-Vis spectroscopy. The absorption spectrum of the microwave-synthesized AgNPs, prepared under conditions of 0.1 mM $AgNO_3$, 2 mM glucose, pH 9.5, and 100 s reaction time, is presented in Figure 3 in the visible region of the electromagnetic spectrum (380–450 nm). The UV-Vis spectrum showed maximum absorption at 413 nm, confirming the formation of AgNPs and the concomitant color change of the reaction medium from colorless to yellow, which is a result of the surface plasmon resonance phenomenon (El-Rafie et al., 2014). Furthermore, the absorption peak was narrow and symmetrical, indicating good dispersion and homogeneous nature of the nanoparticles (Car and Krstulović, 2022; Velgosová and Mražíková, 2017).

Zeta potential measurements were conducted to study the zeta potential of the microwave-synthesized AgNPs (Figure 4a). The analysis revealed a prominent peak at -26.2 mV, suggesting remarkable stability. This is consistent with the established criterion for stable colloidal systems, where zeta potential values typically fall within the range of ± 30 mV. The observed negative zeta potential confirmed the colloidal nature of the AgNPs in the solution. Furthermore, a high negative zeta potential implies significant electrostatic

PPC & PETROMAT SYMPOSIUM 2025

repulsion among the particles, which effectively inhibits agglomeration and contributes to the high stability of the colloidal dispersion (Liaqat et al., 2022, Vinayagam et al., 2024).

For the measurement of nanoparticle size and size distribution in solution, the size distribution profile and polydispersity index (PDI) of AgNPs were investigated by DLS technique, as shown in Figure 4(b). The synthesized AgNPs exhibited a PDI of 0.4, a value below 0.5. This low PDI signifies a lack of significant particle aggregation, leading to improved stability and a relatively monodisperse system (Alzubaidi et al., 2023; Moosavy et al., 2023; Varadavenkatesan et al., 2021). This observation aligns well with the determined zeta potential (-26.2 mV). Furthermore, the particle size distribution (Figure 3b) displayed a single distinct peak at 135 nm (100%), reinforcing the monodisperse characteristics of the nanoparticles. Consequently, the average particle size of AgNPs was determined to be 79 nm.

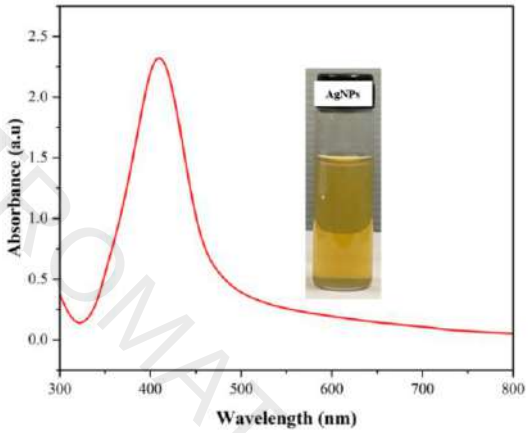


**Figure 3.** UV-visible absorption spectrum of the synthesized AgNPs.

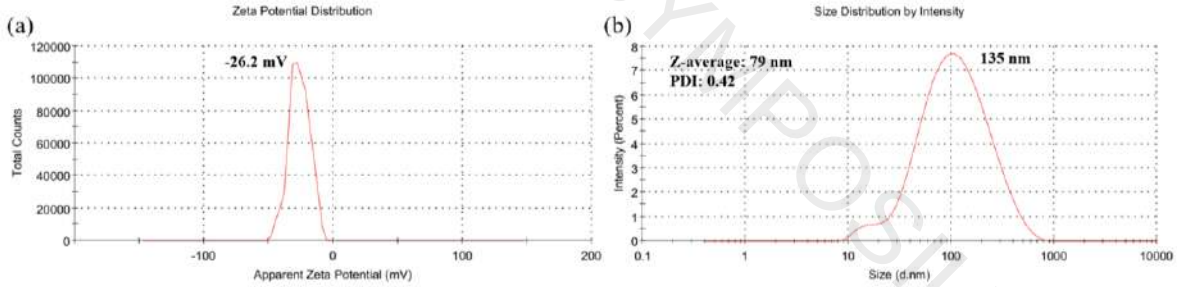


**Figure 4.** DLS spectrum of the synthesized AgNPs (a) zeta potential and (b) size distributions.

## CONCLUSIONS

An environmentally friendly and cost-effective green method for the microwave synthesis of AgNPs was successfully implemented using glucose as the reducing agent. Glucose effectively reduced the $Ag^{+}$ ions to $Ag^{0}$, leading to the formation of AgNPs. Response Surface Methodology (RSM) analysis revealed that the concentrations of both $AgNO_3$ and glucose solutions had a significant effect on the formation of AgNPs. Additionally, the pH also influenced the AgNPs. A comparison between the simulated and experimental results indicated that the absorbance values were in close agreement (9.8% error). This method

produced highly stable spherical AgNPs with a monodisperse size distribution and an average particle diameter of 79 nm.

## ACKNOWLEDGEMENTS

The authors thank the Department of Materials Science and Engineering, Faculty of Engineering and Industrial Technology, Silpakorn University. The authors also thank the Hub of Talent: Sustainable Materials for Circular Economy, National Research Council of Thailand (NRCT).

## REFERENCES

**Alzubaidi, A. K., Al-Kaabi, W. J., Ali, A. A., Albukhaty, S., Al-Karagoly, H., Sulaiman, G. M., Asiri, M. & Khane, Y.** (2023). Applied Sciences, **13,** 2182.
**Car, J. & Krstulović, N.** (2022). Nanomaterials, **12,** 3302.
**Cheviron, P., Gouanvé, F. & Espuche, E.** (2014). Carbohydrate polymers, **108,** 291-298.
**El-Rafie, M., Ahmed, H. B. & Zahran, M.** (2014). International scholarly research notices, **2014,** 702396.
**Farooqi, M. A., Bae, S., Kim, S., Bae, S., Kausar, F., Farooqi, H. M. U., Hyun, C. G. & Kang, C. U.** (2024). Scientific Reports, **14,** 22922.
**Hashemirad, F.-S., Kavoosi, G. & Dadfar, S. M. M.** (2025). LWT, **223,** 117797.
**Hemmati, S., Retzlaff-Roberts, E., Scott, C. & Harris, M. T.** (2019). Journal of Nanomaterials, **2019,** 9641860.
**Kamal, S., Vimala, J., Sahoo, P., Ghosal, P. & Durai, L.** (2016). Defence Science Journal, **66**.
**Liaqat, N., Jahan, N., Anwar, T. & Qureshi, H.** (2022). Frontiers in chemistry, **10 ,**952006.
**Moosavy, M.-H., de la Guardia, M., Mokhtarzadeh, A., Khatibi, S. A., Hosseinzadeh, N. & Hajipour, N.** (2023). Scientific Reports, **13,** 7230.
**Pattnaik, C., Mishra, R., Sahu, A. K., Sahoo, L. N., Sahoo, N. K., Tripathy, S. K. & Sahoo, S.** (2023). Sensors & Diagnostics, **2,** 647-656.
**Phoemthaisong, T., Ksapabutr, B., Chaiyut, N. & Panapoy, M.** (2023). IOP Conference Series: Materials Science and Engineering, **1280,** 012013.
**Putri, G. E., Gusti, F. R., Sary, A. N. & Zainul, R.** (2019). Journal of Physics: Conference Series, **1317,** 012027.
**Swensson, B., Ek, M. & Gray, D.** (2018). ACS Omega, **3(8)**, 9449-9452.
**Thanasakonpong, A., Ksapabutr, B. & Panapoy, M.** (2023). IOP Conference Series: Materials Science and Engineering, **1280,** 012016.
**Varadavenkatesan, T., Pai, S., Vinayagam, R. & Selvaraj, R.** (2021). Materials Chemistry and Physics, **272,** 125017.
**Velgosová, O. & Mražíková, A.** (2017). AIP Conference Proceedings, **1918**.
**Vinayagam, R., Nagendran, V., Goveas, L. C., Narasimhan, M. K., Varadavenkatesan, T., Chandrasekar, N. & Selvaraj, R.** (2024). Materials Chemistry and Physics, **313,** 128787.

PPC & PETROMAT SYMPOSIUM 2025

# Facile One-Step Low-Temperature Synthesis of Sub-100 nm Silver Nanowires via Polyol Method

*Sonsawan Onvikij* [a,b], *Manop Panapoy* [a] , *Nattawut Chaiyut* [a], *Bussarin Ksapabutr*[*, a]

[a] Department of Materials Science and Engineering, Faculty of Engineering and Industrial Technology, Silpakorn University, Nakhon Pathom, Thailand
[b] Center of Excellence on Petrochemical and Material Technology, Chulalongkorn University

Keywords: Silver nanowire , AgNWs , Polyol method , Low temperature

## ABSTRACT

Silver nanowires (AgNWs) are one-dimensional nanostructures composed of silver atoms, typically with diameters ranging from 10 to several hundred nanometers in length. AgNWs are regarded as promising materials for diverse technological applications because of their high electrical conductivity, mechanical flexibility, and optical transparency. This study investigated the controlled synthesis of AgNWs via the polyol method and examined the effects of polyvinylpyrrolidone (PVP) concentration, reaction time (3, 5 and 8 h) and temperature (110, 120 and 130 °C) on the nanowires. The synthesized nanowires were characterized using UV-Vis spectroscopy, scanning electron microscopy (SEM), and X-ray diffraction (XRD). The results demonstrated successful nanowire formation at 120°C. It was observed that increasing the reaction time and temperature resulted in an increase in nanowire diameter. The optimal synthesis conditions were determined to be 120°C for 3 h, Nanowires with the smallest average diameter of $57.24 \pm 23.36$ nm

***ksapabutr_b@su.ac.th**

## INTRODUCTION

Silver nanowires (AgNWs) are one-dimensional (1D) metallic nanomaterials that have gained considerable attention in scientific research due to their excellent properties and wide range of potential applications. These include high electrical conductivity, mechanical flexibility, and unique optical, thermal, and catalytic properties.(Kumar et al., 2021). Such characteristics make AgNWs important materials for the development of modern and emerging technologies. In recent years, various methods have been developed for synthesizing AgNWs. Among them, the polyol synthesis method is the most widely used due to its simplicity, scalability, and ability to control nanowire shape and size effectively. In this process, polyvinylpyrrolidone (PVP) is used as a capping agent to control the growth at the nanowire tips, while ethylene glycol (EG) serves as both the solvent and reducing agent to convert silver nitrate ($AgNO_3$) into silver nanowires. (Yamamoto et al., 2022) investigated the effects of different control agents such as NaCl, $CuCl_2$, and NaBr on the aspect ratio of AgNWs. Their findings showed that NaBr resulted in the lowest aspect ratio compared to the other agents. Another effective additive, ferric chloride ($FeCl_3$), acts as an oxidizing agent to regulate nanowire growth. It promotes the formation of longer, purer AgNWs with desirable structures suitable for use in transparent conductive films or flexible electronic devices.

PPC & PETROMAT SYMPOSIUM 2025

## EXPERIMENTAL

### *A. Materials*

Silver nitrate (99.8%) was obtained from CARLO ERBA, ferric chloride ($FeCl_3$) (93%) was obtained from CARLO ERBA. PVP powder ( Mw 1,300,000) was supplied from Sigma-Aldrich. Ethylene glycol 99% (EG) was obtained from CARLO ERBA. Deionized (DI) water and absolute ethanol were used for washing and redispersion.

### *B. Synthesis of Silver Nanowires (AgNWs)*

The synthesis of silver nanowires (AgNWs) was carried out using a polyol method. Initially,0.1 g of PVP was dissolved in 12.5 mL of ethylene glycol under magnetic stirring at room temperature until a clear solution was obtained. In a separate container, 0.125 g of $AgNO_3$ was dissolved in 1.75 g of 600 µM $FeCl_3$ solution, also under magnetic stirring until fully dissolved.(Li et al., 2018) The PVP solution was then gradually added to the $AgNO_3$/$FeCl_3$ solution and gently shaken to ensure homogeneous mixing. The final mixture was placed in a 200 mL silicon oil bath and heated at three different temperatures 110 °C, 120 °C and 130 °C for 3, 5 and 8 hours (Mao et al., 2012) respectively, to promote the growth of AgNWs.(CAO et al., 2023, Salam et al., 2024)

### *C. Purification and Redispersion*

After the reaction, the mixture was removed from the heat source and allowed to cool naturally to room temperature. The AgNWs were separated by centrifugation at 4500 rpm for 10 minutes and washed several times alternately with deionized water and absolute ethanol to remove any remaining impurities (Jarrett and Crook, 2016). The purified AgNWs were redispersed in ethanol for further analysis and application.

### *D. Characterization of Silver Nanowires (AgNWs)*

The synthesized silver nanowires were characterized using various analytical techniques to investigate their morphological, structural, and optical properties, UV–Visible Spectroscopy (UV–Vis) used to monitor the optical absorption characteristics of AgNWs. Characteristic peaks were typically observed around 355 nm and 390 nm, indicating the presence of nanowire structures. Scanning Electron Microscopy (SEM) employed to observe the morphology, diameter and length distribution of the synthesized AgNWs. SEM images provided information on wire uniformity and aspect ratio. X-ray Diffraction (XRD) used to confirm the crystalline structure of the AgNWs.(Mao et al., 2012). The diffraction peaks were compared with standard silver patterns to verify phase purity and crystallinity. These characterization methods provided essential insights into the quality and applicability of the AgNWs for potential use in transparent conductive films and flexible electronic devices.

## RESULTS AND DISCUSSION

To analyze and characterize the optical properties of silver nanowires (AgNWs), ultraviolet-visible (UV-Vis) spectroscopy was employed as an analytical tool. It is well known that the

nanoscale structure of silver, particularly differences in shape and morphology, significantly influences the surface plasmon resonance (SPR) phenomenon (Sohn et al., 2019). As shown in Figure 1. the UV-Vis spectrum displays characteristic features of AgNWs, with two distinct absorption peaks observed at 355 nm and 390 nm, which are attributed to the transverse plasmon resonance modes of silver nanowires (Silva et al., 2024, Vijila et al., 2016). Notably, the emergence of a shoulder peak around 355 nm indicates the initial formation of silver nanowires. In addition, an absorption peak observed at approximately 460–470 nm corresponds to the typical plasmonic resonance of silver nanoparticles (AgNPs) (Sun et al., 2002). The spectral data reveal a redshift (a shift toward longer wavelengths) in the absorption peaks as the reaction time increases, suggesting a progressive increase in both the length and diameter of the silver nanowires during the growth process.

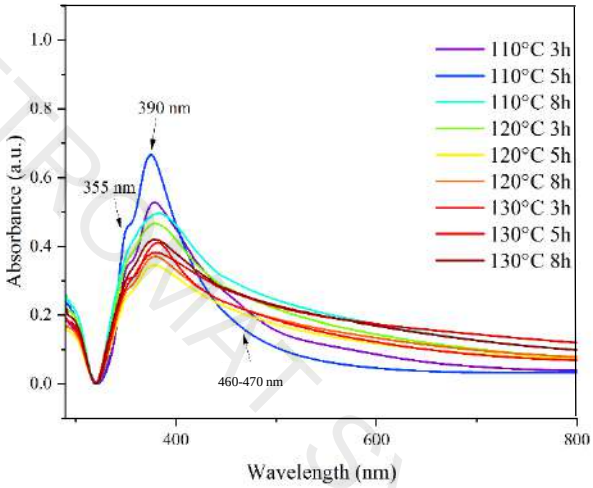


Figure 1. Normalized UV-Vis extinction spectra of silver nanowires dispersed in ethanol at different temperatures.

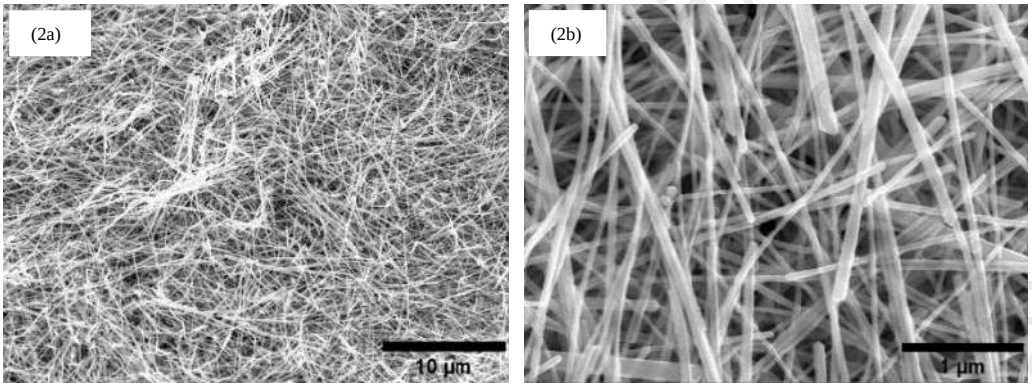


Figure 2. SEM images of silver nanowires synthesized at 120 °C for 3 hours: (2a) at 5.0 kx magnification and (2b) at 50.0 kx magnification.

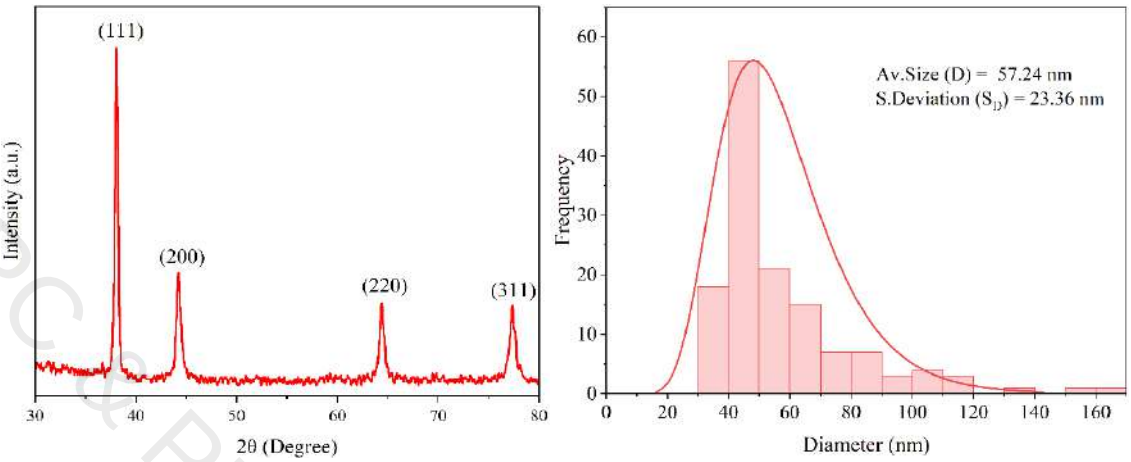


Figure 3. (3a) XRD pattern of AgNWs and (3b) Histogram of AgNWs under synthesis conditions diameter distribution : 120 °C, 3h

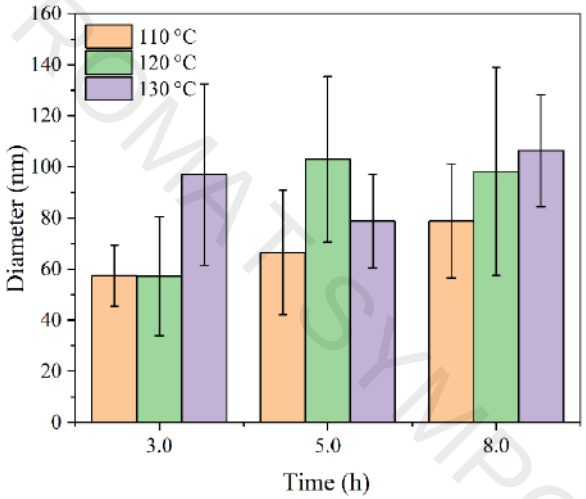


Figure 4. Effect of temperature and time on AgNWs diameter.

As shown in Figure 2. scanning electron microscopy (SEM) images of silver nanowires (AgNWs) synthesized under various experimental conditions are presented. Under the condition of 120 °C for 3 hours, the AgNWs exhibit a long and slender morphology with a relatively uniform thickness. However, silver nanoparticles were also observed dispersed within the imaged area. The crystalline structure of the silver nanowires was further examined using X-ray diffraction (XRD) analysis, as shown in Figure 3a. The XRD pattern of the AgNWs reveals four distinct diffraction peaks corresponding to the crystallographic planes (111), (200), (220) and (311). These diffraction peaks confirm the presence of a face-centered cubic (FCC) crystalline structure of metallic silver, consistent with standard reference data (JCPDS No. 04-0783). (Jang et al., 2017, Nagasundari et al., 2021, Tang et al., 2014). According to the histogram analysis shown in Figure 3b, the average diameter of AgNWs synthesized at 120 °C for 3 hours was approximately 57.24 ± 23.36 nm.(Ali et al., 2021). The synthesis condition that yielded the largest average diameter was at 130 °C for 8 hours, resulting in nanowires with an average diameter of approximately 87.60 ± 8.60 nm. The trend shown in Figure 4. indicates that both the synthesis temperature and reaction time significantly influence the diameter of the silver nanowires. As temperature and time increase,

PPC & PETROMAT SYMPOSIUM 2025

more $Ag^+$ ions are reduced to silver atoms, leading to a greater number of atoms available for the self-assembly process. This results in the formation of longer and thicker silver nanowires. (Septiningrum et al., 2019)

## CONCLUSIONS

In this study, the orthogonal experimental method was employed to synthesize silver nanowires (AgNWs) under various reaction conditions. The resulting nanowires were then characterized and compared to evaluate the influence of synthesis parameters. The experimental results revealed that the condition of 120 °C for 3 hours produced AgNWs with the most uniform diameter distribution and the smallest average diameter, measured at $57.24 \pm 23.36$ nm. Furthermore, analysis of all experimental conditions indicated that increasing the reaction temperature and synthesis duration leads to a larger average nanowire diameter, suggesting that these parameters play a critical role in controlling the dimensional properties of the synthesized AgNWs.

## ACKNOWLEDGEMENTS

The authors thank the Department of Materials Science and Engineering, Faculty of Engineering and Industrial Technology, Silpakorn University. The authors also thank the Hub of Talent: Sustainable Materials for Circular Economy, National Research Council of Thailand (NRCT).

## REFERENCES

**Ali, F., Ali, Z., Younas, U., Ahmad, A., Mooin-ud-din, G., Pervaiz, M., Luque, R., Ahmad, I., Ashraf, A. & Albaqami, M.** (2021).
**CAO, K. T., TRAN, K. K. & Thi, H.** (2023). Journal of Metals, Materials and Minerals, **33,** 1727-1727.
**Jang, H.-W., Kim, Y.-H., Lee, K.-W., Kim, Y.-M. & Kim, J.-Y.** (2017). APL Materials, **5**.
**Jarrett, R. & Crook, R.** (2016). Materials Research Innovations, **20,** 86-91.
**Kumar, A., Shaikh, M. O. & Chuang, C.-H.** (2021). Nanomaterials, **11,** 693.
**Li, Y., Guo, S., Yang, H., Chao, Y., Jiang, S. & Wang, C.** (2018). RSC advances, **8,** 8057-8063.
**Mao, H., Feng, J., Ma, X., Wu, C. & Zhao, X.** (2012). Journal of nanoparticle research, **14,** 1-15.
**Nagasundari, S. M., Muthu, K., Kaviyarasu, K., Al Farraj, D. A. & Alkufeidy, R. M.** (2021). Surfaces and Interfaces, **23,** 100931.
**Salam, A. A., Ebrahim, S., Soliman, M. & Shokry, A.** (2024). Scientific Reports, **14,** 20986.
**Septiningrum, F., Roza, L. & Fauzia, V.** (2019). IOP Conference Series: Materials Science and Engineering, **622,** 012031.
**Silva, B. P., Silva, W. C. d., Saraiva, S. R. & Otubo, L.** (2024). Journal of the Brazilian Chemical Society, **35,** e-20240120.
**Sohn, H., Park, C., Oh, J.-M., Kang, S. W. & Kim, M.-J.** (2019). Materials, **12,** 2526.
**Sun, Y., Yin, Y., Mayers, B. T., Herricks, T. & Xia, Y.** (2002). Chemistry of Materials, **14,** 4736-4745.

PPC & PETROMAT SYMPOSIUM 2025

**Tang, Y., He, W., Wang, S., Tao, Z. & Cheng, L.** (2014). Journal of Materials Science: Materials in Electronics, **25,** 2929-2933.
**Vijila, C. M., Rahman, K. A., Parvathy, N. & Jayaraj, M.** (2016). AIP Conference Proceedings, **1731,** 080073.
**Yamamoto, E. G., Dantas, M. P., Yamanishi, G., Soares, F. B., Urbano, A., Lourenço, S. A. & Cava, C. E.** (2022). Applied Nanoscience, **12,** 205-213.

PPC & PETROMAT SYMPOSIUM 2025

# FABRICATION POLY-5-AMINOINDOLE:POLY(4-STYRENESULFONIC ACID) LOADED LOCUST BEAN GUM:XANTHAN GUM HYDROGEL METRIX FOR SKIN CANCER DRUG TRANSDERMAL DELIVERY VIA IONTOPHORESIS

*Patamavadee Tapsarn, Anuvat Sirivat**

Conductive and Electroactive Polymers Research Unit, The Petroleum and Petrochemical College, Chulalongkorn University, Bangkok, 10330, Thailand

Keywords : Transdermal delivery, Iontophoresis, conductive polymer

## ABSTRACT

Melanoma is an aggressive type of skin cancer due to its ability to rapidly spread to various organs. For treatment, the oral drug administration is preferred for its convenience. However, the oral route faces challenges such as the first-pass metabolism, pH-dependent absorption, and delayed onset of action. Therefore, transdermal drug delivery (TDDS) offers an alternative route to overcome these limitations. This work developed an iontophoresis-assisted transdermal patch using a Locust Bean Gum (LCB) and Xanthan Gum (XG) hydrogel matrix, incorporated with a conductive polymer, poly-5-aminoindole:poly(4-styrenesulfonic acid) (PAIn:PSS), and Imatinib as the model drug. The vitro release study showed that incorporating PAIn:PSS enhanced the drug release, while the application of an electric field significantly improved skin permeation through electrorepulsion. These findings highlight the potential of the Imatinib/PAIn:PSS/LCB:XG hydrogel for controlled transdermal drug delivery.

***anuvat.s@chula.ac.th**

## INTRODUCTION

Skin cancers are the most common type of cancer worldwide. Treatment options include oral administration, injections, and transdermal drug delivery systems (Hasan *et al.* 2023). Among these, transdermal drug delivery is particularly suitable for skin cancer, as it allows direct delivery of the drug to the target site—the skin. However, conventional transdermal patches are limited in terms of the types and sizes of drug molecules they can effectively deliver, due to reliance on passive diffusion (Jeong *et al.* 2021).

Iontophoresis is a technique that uses a mild electric current to facilitate the transport of drugs through the skin. This method can overcome the limitations of traditional patches by enhancing and controlling drug diffusion across the skin barrier (Fukuta *et al.* 2020).

Poly-5-aminoindole (PAIn) is a type of conductive polymer synthesized from the monomer 5-aminoindole, containing an amino group at the 5-position of the indole ring. PAIn exhibits good electrical conductivity and is employed in various applications such as sensors, biosensors, biomedical electronics, and corrosion protection (Broda *et al.* 2014).

Poly(4-styrenesulfonic acid) (PSS) is a water-soluble polyelectrolyte featuring sulfonic acid groups (-$SO_3H$) attached to a polystyrene backbone (Kogej 2012). It is widely

PPC & PETROMAT SYMPOSIUM 2025

used in chemistry, materials science, and biomedical engineering due to its ionic and hydrophilic properties (Wang *et al.* 2021).

Locust bean gum (LCB) is a natural polysaccharide derived from the seeds of the carob tree (*Ceratonia siliqua*), commonly used as a thickener, stabilizer, and gelling agent in both food and pharmaceutical formulations (Verma *et al.* 2019).

Xanthan gum is a high-molecular-weight polysaccharide produced by the bacterium Xanthomonas campestris via fermentation of simple sugars. It is widely utilized as a thickener, stabilizer, and gelling agent in food, pharmaceuticals, and biomedical applications, including hydrogel-based drug delivery systems (Zhang *et al.* 2023).

In this work, water-soluble PAIn:PSS was synthesized. Imatinib was selected as a model drug for skin cancer treatment. Both PAIn:PSS and Imatinib were incorporated into LCB:XG hydrogel matrices to investigate the release behaviour of Imatinib under the influence of applied electric fields and the incorporated conductive polymers.

## EXPERIMENTAL

*A. Synthesis of Imatinib loaded PAIn:PSS*

Imatinib and PAIn:PSS were dissolved in 15 mL of deionized (DI) water and stirred for 7 days at room temperature. The concentration of PAIn:PSS was varied to be at 0.5% w/v (0.075 g) and 1.0% w/v (0.15 g). Imatinib was added at a fixed amount of 0.4 g, corresponding to the 10% intended daily dosage. The optimal loading of Imatinib in the PAIn:PSS matrix, as well as the interactions between Imatinib and PAIn:PSS, were evaluated using Simultaneous Thermal Analysis (STA).

*B. Preparation of Imatinib/PAIn:PSS loaded LCB:XG hydrogels*

The suitable concentration of PAIn:PSS was used to prepare the hydrogel. First, LCB and XG powders were dissolved in 30 mL of deionized (DI) water, stirred, and heated at 70 °C. The Imatinib/PAIn:PSS solution was then added to the gel mixture and stirred until a homogeneous solution was obtained. The resulting solution was poured into a petri dish, dried in an oven overnight, and subsequently freeze-dried. The cross-sectional morphology of the hydrogel was investigated using a field emission scanning electron microscope (FE-SEM).

*C. The in-vitro Imatinib release and release kinetic study*

In-vitro Imatinib release study was investigated by the modified Franz diffusion cell. The modified Franz diffusion cell consisted of 2 parts: the donor and acceptor parts. The receptor part contained the PBS solution (pH 7.4) at 37°C. The hydrogels were placed over a nylon net on the receptor part. Imatinib was released through the hydrogel and the nylon net into the PBS solution. The 0.1 mL of solution was collected from the acceptor part and replaced with the same volume of fresh PBS at various times. The amount of the Imatinib was measured by the UV–Visible spectrophotometer at the wavelength of 283 nm.

Drug release mechanisms were investigated by the Korsmeyer-Peppas model as shown in equation (1);

$$M_t/M_\infty = kt^n \quad (1)$$

PPC & PETROMAT SYMPOSIUM 2025

where Mt / M∞ is the fraction of drug released from the porous LCB:XG matrices at .time t, k is the kinetic constant, t is the release time (h), n is the diffusion scaling exponent, used to identify the release mechanisms of the Imatinib (Wu *et al.* 2019)

The diffusion coefficient (D) was obtained from the Higuchi's equation (2) from the slope of amount of drug released versus the square root of time (h):

$$Q = M_t/A = 2C_0(Dt/)^{1/2} \quad (2)$$

where $M_t$ is the amount of drug released (g), A is the diffusion coefficient area ($cm^2$), $C_0$ is the initial drug concentration in the matrix ($g/cm^3$), and D is the diffusion coefficient of the drug ($cm^2/s$) (Siepmann *et al.* 2011).

## RESULTS AND DISCUSSION

*A. The optimum concentration of PAIn:PSS loaded Imatinib*

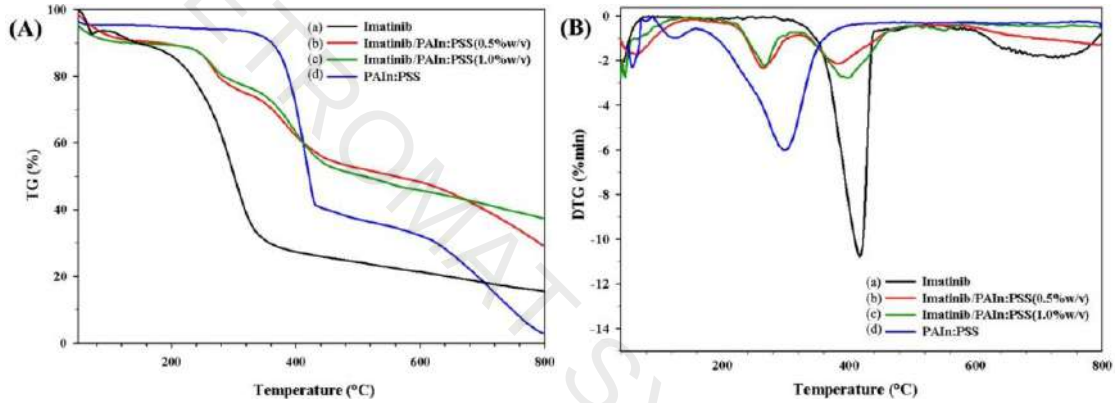


**Figure 1** (A) STA thermograms and (B) Derivatives of (a) Imatinib; (b) Imatinib/PAIn:PSS 0.5%w/v; (c) Imatinib/PAIn:PSS 1.0%w/v; and (D) PAIn:PSS.

The STA thermograms of Imatinib were shown in **Figure 1(A)-(B)**. Imatinib exhibits two thermal decomposition stages: the first stage corresponds to moisture loss at 42.9°C, while the second stage represents the decomposition of Imatinib at 417.5°C (Mucha et al., 2016). For Imatinib/PAIn:PSS(0.5% w/v and 1.0% w/v), new decomposition peaks were observed at 264.1°C and 266.7°C, respectively, corresponding to the decomposition of PAIn:PSS. Additionally, decomposition temperatures at 382.9°C and 398.0°C were recorded, which are attributed to the decomposition of Imatinib. The new peaks and shifts in major decomposition temperatures suggest that Imatinib molecules interacted with PAIn:PSS via the electrostatic interactions.

Based on the amount of PAIn:PSS loaded with Imatinib, both Imatinib/PAIn:PSS (0.5% w/v and 1.0% w/v) successfully incorporated Imatinib, as confirmed by the STA thermogram, which indicate interactions between the two components. However, the higher concentration of PAIn:PSS in the 1.0% w/v formulation may lead to increased toxicity (Kašpárková et al., 2019). Therefore, Imatinib loaded PAIn:PSS (0.5% w/v) was selected for incorporation into the LCB:XG hydrogel.

PPC & PETROMAT SYMPOSIUM 2025

*Characterization of Imatinib/PAIn:PSS loaded LCB:XG hydrogels*

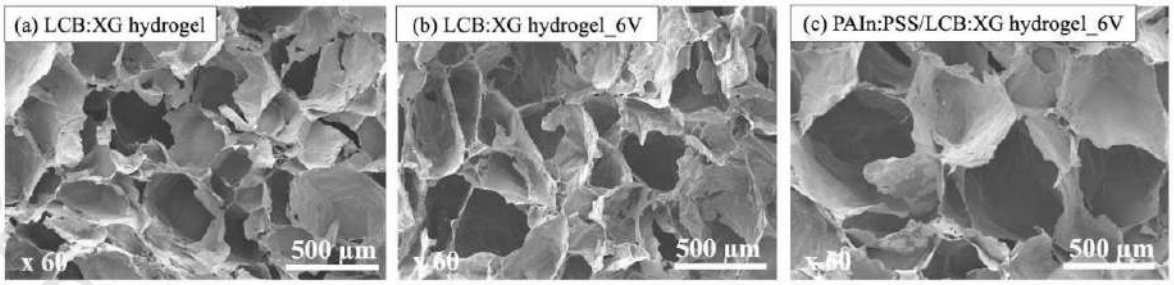


**Figure 2** The cross-section morphology of: (a) LCB:XG hydrogel; (b) LCB:XG hydrogel_6V; (c) PAIn:PSS/LCB:XG hydrogel_6V.

The cross-sectional images of the LCB:XG hydrogels are shown in **Figure 2(a)**. Upon application of an electric field at 6 V **[Figure 2(b)]**, the pore size of the hydrogel slightly increased compared to the condition without an applied electric field. This indicates that the applied electric field promoted pore enlargement compared to the LCB:XG hydrogel without the field, an effect attributed to enhanced electrostatic repulsion. The LCB:XG hydrogel matrix contained charged functional groups, and the applied electric field intensified the electrostatic repulsion within the polymer network, leading to expansion of the polymer chains and formation of larger pores.

The effect of incorporating a conductive polymer is presented in **Figure 2(c)**. The hydrogel containing PAIn:PSS was subjected to an electric field of 6 V. The results demonstrate that the pore size was significantly larger than that of the pure LCB:XG hydrogel. This is likely due to the ability of PAIn:PSS, as a conductive polymer, to transport charge under an electric field, thereby further enhancing electrostatic repulsion within the hydrogel matrix and promoting greater pore expansion (Boonprakong et al., 2024).

*C. Characterization of Imatinib/PAIn:PSS loaded LCB:XG hydrogels*

**Table 1** Kinetics factors and diffusion coefficients of Imatinib released

| Sample | Electric voltage (V) | Power law | | Higuchi | D ($cm^2/s$) | %Release | Time to equilibrium (h) |
|---|---|---|---|---|---|---|---|
| | | n | K ($T^{-n}$) | $k_H$ ($T^{-n}$) | | | |
| LCB:XG hydrogel | 0 V | 0.74 | 0.52 | 0.05 | $1.45 \times 10^{-11}$ | 43.14 | 2.81 |
| | 6 V | 0.44 | 0.26 | $3.00 \times 10^{-5}$ | $4.14 \times 10^{-11}$ | 74.03 | 6.55 |
| PAIn:PSS /LCB:XG hydrogel | 6 V | 0.90 | 0.30 | $3.00 \times 10^{-5}$ | $5.02 \times 10^{-11}$ | 84.56 | 5.29 |

The amounts of Imatinib released are shown in the **Table 1**. Under applied electric fields, the amount of Imatinib release increased compared to the condition without the electric fields from 43.14% to 74.03%. Moreover, the diffusion coefficient increased from $1.45 \times 10^{-11}$ $cm^2/s$ to $4.14 \times 10^{-11}$ $cm^2/s$. At higher electric field strengths, the release of

Imatinib and its diffusion coefficient were enhanced due to the electro repulsion. This mechanism originated from the repulsion of positively charged Imatinib by the anode electrode, generating a driving force that facilitated the migration of drug molecules away from the electrode (Paradee et al., 2021).

The amount of Imatinib released from PAIn:PSS/LCB:XG hydrogels was investigated under an applied electric field of 6 V. Compared to the condition without PAIn:PSS, the amount of Imatinib released increased from 74.03% to 84.56%, while the diffusion coefficient increased from $4.14 \times 10^{-11}$ cm²/s to $5.02 \times 10^{-11}$ cm²/s. This enhancement is attributed to the incorporation of PAIn:PSS, which disrupted the existing crosslinking within the hydrogel matrix, leading to a reduction in crosslink density. The resulting larger pore sizes facilitated an increased release of Imatinib. (Guo et al., 2019).

## CONCLUSIONS

A PAIn:PSS concentration of 0.5% w/v was found to be optimal for loading Imatinib, as determined by STA analysis. The Imatinib/PAIn:PSS complex was incorporated into the LCB:XG hydrogel to facilitate Imatinib release via iontophoresis. The in vitro Imatinib release study showed that the amount of Imatinib released and the diffusion coefficient increased with the incorporation of PAIn:PSS, as the conductive polymer expanded the pore size of the LCB:XG hydrogel, enhancing the release pathway. Furthermore, both the amount and rate of Imatinib release were improved under an applied electric field due to electrostatic repulsion forces. Therefore, the Imatinib/PAIn:PSS-loaded LCB:XG hydrogel demonstrates potential for enhanced Imatinib transdermal delivery.

## ACKNOWLEDGEMENTS

We are deeply appreciative of the full scholarship generously provided by the Petroleum and Petrochemical College (PPC). We also gratefully acknowledge the support for this work from the Conductive and Electroactive Polymers Research Unit of Chulalongkorn University. I would like to thank the 90th Anniversary of Chulalongkorn University Scholarship and the National Research Council of Thailand (NRCT) for funding.

## REFERENCES

**Broda, B. and Inzelt, G. (2014)**. Preparation and characterization of poly(5-aminoindole) by using electrochemical quartz crystal nanobalance technique. Acta Chim Slov, 61(2), 357-365.

**Fukuta, T., Oshima, Y., Michiue, K., Tanaka, D. and Kogure, K**. (2020). Non-invasive delivery of biological macromolecular drugs into the skin by iontophoresis and its application to psoriasis treatment. Journal of Controlled Release, 323(323-332.

**Hasan, N., Nadaf, A., Imran, M., Jiba, U., Sheikh, A., Almalki, W. H., Almujri, S. S., Mohammed, Y. H., Kesharwani, P. and Ahmad, F. J**. (2023). Skin cancer:

PPC & PETROMAT SYMPOSIUM 2025

understanding the journey of transformation from conventional to advanced treatment approaches. Mol Cancer, 22(1), 168.

**Jeong, W. Y., Kwon, M., Choi, H. E. and Kim, K. S**. (2021). Recent advances in transdermal drug delivery systems: a review. Biomaterials Research, 25(1), 24.

**Kogej, K**. (2012). Chapter Seven - Polyelectrolytes and Surfactants in Aqueous Solutions: From Dilute to Concentrated Systems. Advances in Planar Lipid Bilayers and Liposomes. A. Iglič, Academic Press. **16:** 199-237.

**Siepmann, J. and Peppas, N. A**. (2011). Higuchi equation: Derivation, applications, use and misuse. International Journal of Pharmaceutics, 418(1), 6-12.

**Verma, A., Tiwari, A., Panda, P. K., Saraf, S., Jain, A. and Jain, S. K. (2019)**. Chapter 8 - Locust bean gum in drug delivery application. Natural Polysaccharides in Drug Delivery and Biomedical Applications. M. S. Hasnain and A. K. Nayak, Academic Press**:** 203-222.

**Wang, Y., Wu, S., Yin, Q., Jiang, B. and Mo, S**. (2021). Tuning thermoelectric performance of Poly(3,4-ethylenedioxythiophene): Poly (styrene sulfonate)/Polyaniline composite films by nanostructure evolution of polyaniline. Polymer Testing, 94(107017.

**Wu, I. Y., Bala, S., Škalko-Basnet, N. and di Cagno, M. P**. (2019). Interpreting non-linear drug diffusion data: Utilizing Korsmeyer-Peppas model to study drug release from liposomes. European Journal of Pharmaceutical Sciences, 138(105026.

**Zhang, H., Yan, Z., Xie, F., Tian, Y. and Ai, L**. (2023) Rheological Properties and Kinetics of Gelation of Binary Polymers between Xanthan Gum and Locust Bean Gum. Polymers **15**, DOI: 10.3390/polym15234604

PROCEEDINGS OF PETROMAT SYMPOSIUM 2025

# EFFECTS OF SODIUM DODECYL SULFATE ON THE PREPARATION OF AG/RHA-$SiO_2$ NANOCOMPOSITES FOR SURFACE COATING APPLICATIONS

*Napat Nakyam* [a], *Kanyanat Kanlueang* [a], *Natchawadee Akewikanon* [a], *Natthanon Phonchai*[*, a,b]

[a] Department of Materials Science and Engineering, Silpakorn University, Nakorn Phathom, Thailand
[b] Center of Excellence on Petrochemical and Materials Technology, Bangkok, Thailand

Keywords: Rice husk ash, Nanocomposites, Silver nanoparticles, Silica nanoparticles

## ABSTRACT

This research aims to investigate the effect of sodium dodecyl sulfate (SDS), an anionic surfactant, on the preparation and physicochemical properties of nanocomposites prepared by incorporating silver nanoparticles (Ag NPs) and rice husk ash-based silica nanoparticles (RHA-$SiO_2$ NPs), referred to as "Ag/RHA-$SiO_2$ NC". The result shows a significant decrease in the average particle size compared with the no added SDS. However, increasing SDS concentration does not change the average particle size in the nanocomposite system. The surface stabilization that occurred from the addition of SDS was observed and discussed. The result from the Vickers microhardness tester promotes a 16.41% increase in surface-microhardness of the polymethyl methacrylate (PMMA) sheet coated with the nanocomposite prepared from 16 mM of SDS. Moreover, the PMMA sheet coated with nanocomposite also exhibits a clear zone with Staphylococcus aureus (S. aureus), as shown in antibacterial testing. This work may be attributed to fabricating multifunctional nano-scale materials for surface coating applications.

***Phonchai_n@su.ac.th**

## INTRODUCTION

Over the past decades, polymethyl methacrylate (PMMA) has been commonly used in prosthodontic applications, including dental bases and teeth retainers [1, 2]. However, this polymer contains some limitations, such as high surface abrasion and bacterial accumulation. Therefore, improving both micro-hardness and antibacterial properties on the PMMA surface is an attractive topic for several materials scientists [3-5]. In Thailand, rice husk is one of the most observed agricultural wastes. Thus, to evaluate rice husk waste and fabricate a novel antibiotic agent, it is worthwhile to prepare the Ag NPs and RHA-$SiO_2$ NPs nanocomposite (Ag/RHA-$SiO_2$ NC). The goal of this work is to improve the microhardness as well as initiate the antibacterial property of the PMMA surface by coating with Ag/RHA-$SiO_2$ NC. In this work, we present sodium dodecyl sulfate (SDS), one of the negatively charged surfactants, to prevent the agglomeration and enhance the colloidal stability of the nanocomposite. The electrostatic repulsion was employed to stabilize the components within the nanocomposite, which enhances the physical and antibacterial properties of coated PMMA. We believe that the silver ions released from Ag/RHA-$SiO_2$ NC destroy the cell wall and reduce the growth rate of bacteria around the PMMA surface.

PPC & PETROMAT SYMPOSIUM 2025

## EXPERIMENTAL

*A. Synthesis of Ag/RHA-$SiO_2$ NC*

In this study, silica nanoparticles were synthesized from rice husk ash (RHA) using the sol-gel method. The surface of the silica obtained was modified with an anionic surfactant, sodium dodecyl sulfate (SDS), to reduce particle agglomeration and enhance colloidal stability. Silver nanoparticles (Ag NPs) were synthesized by reducing silver ions with a chemical reducing agent, and a capping agent was added to control the particle size and dispersion. These Ag NPs were then mixed with silica nanoparticles modified SDS to prepare a highly dispersed Ag/RHA-$SiO_2$ NC, utilizing SDS concentrations of 4, 16, 32, and 64 mM.

*B. Preparation of PMMA sheet, coating, and antibacterial testing*

To prepare PMMA sheets, 15 g of PMMA was dissolved in 50 ml of acetone to form a PMMA solution. The PMMA sheets were cast by using this solution casting and dried completely. A highly dispersed Ag/RHA-$SiO_2$ NC at 2 ml was coated onto the surface of the PMMA. The coated samples were subsequently analyzed for their mechanical properties using a Vickers microhardness tester. The antibacterial activity was evaluated against bacteria by observing the clear zone formed on nutrient agar plates.

## RESULTS AND DISCUSSION

*A. Synthesis of RHA-$SiO_2$ nanoparticles and surface modification with SDS*

The morphology and particle size of RHA-$SiO_2$ NPs obtained from a scanning electron microscope (SEM) are shown in Fig.1. The results show the irregular shape of synthesised nanoparticles with well dispersed in Fig.1(a). The average particle size from the dynamic light scattering (DLS) technique was detected at 110.13 nm. Fig.1(b) presents the structural changes in RHA-$SiO_2$ NPs when added with SDS 16 mM. It is found that the silica particles have a rough surface due to the particle agglomeration, creating a connected structure. However, the average particle size reported by DLS is 80.14 nm in this sample. We suggest that the sample preparation on the SEM technique and hydrogen bonding between the SDS head group with the silanol group on the silica surface may have a major effect on the induced particles [6].

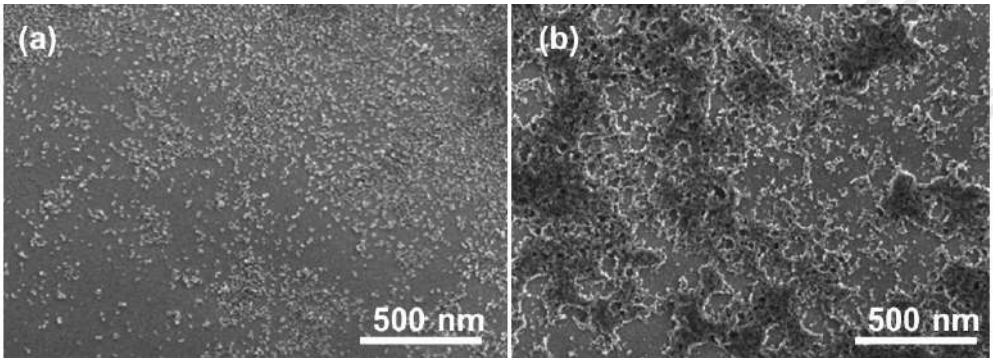


Fig.1 SEM image of (a) RHA-$SiO_2$ NPs and (b) RHA-$SiO_2$ NPs with SDS 16 mM

PPC & PETROMAT SYMPOSIUM 2025

The addition of SDS solution into colloids of RHA-$SiO_2$ NPs promotes the systematic trend seen in Fig.2 (a) and (b). The zetapotential values and average particle size tend to decrease with the SDS concentration. We believe that the head group of SDS will repel against O- of silica nanoparticles, resulting in a more negative zeta potential value and the reduction of average particle size. Until the concentration of SDS was increased to a range of 16 to 64 mM, the negative value of the zeta potential and the average particle size showed unchanged data. Our result is nearly the report of Vatanparast and coworkers, which explains the relationship between the surface-active site of silica nanoparticles and SDS concentration. At high SDS concentration, the hydrodynamic size and the zeta-potential values of $SiO_2$ nanoparticles will be disturbed by Sodium ions ($Na^+$), which come from the counter ions of SDS [7].

The FT-IR spectra of RHA-$SiO_2$ NPs with SDS were observed and discussed in Fig.2(c). The chemical bond composition of Silica nanoparticles showed O-H stretching at around 3400 $cm^{-1}$, O-H bending at around 1630 $cm^{-1}$, indicating O-H at the surface of nano-silica, and around 790, 960, 1100 $cm^{-1}$ indicating Si-O-Si symmetric stretching of bonds in the structure of nano-silica. The chemical bond composition of sodium dodecyl sulphate (SDS) showed C-H stretching, S=O stretching, S-O-C and S-O stretching at wavenumber 2900, 1200, 1000, and 590 $cm^{-1}$, respectively. The chemical bond composition of Silica nanoparticles added with 16 mM SDS showed the changing vibration signal of O-H stretching, which was broadened due to the change of O-H stretching bond at the surface of nano silica. However, the Si-O-Si stretching area did not change, and there was a shifting of some components, indicating that when the materials were mixed, only the RHA-$SiO_2$ NPs surface was disturbed. For further understanding, we propose the schematic representation of RHA-$SiO_2$ NPs modified with SDS presented in Fig.2 (d).

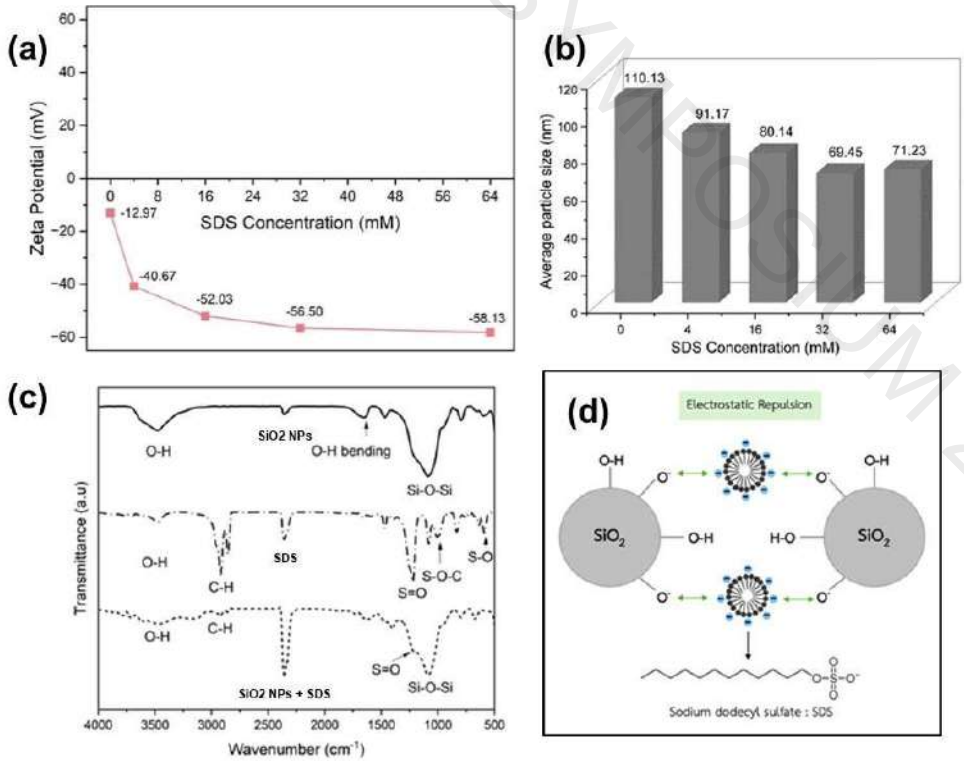

Fig.2 (a) Zeta potential and (b) average particle size of colloids of RHA-$SiO_2$ NPs plotted with varying SDS concentration. (c) FT-IR spectra and (d) schematic representation of RHA-$SiO_2$ NPs modified with SDS.

*B. Synthesis of Ag/RHA-$SiO_2$ NC*

Fig.3(a) presents a SEM image of silver nanoparticles synthesized by using ascorbic acid as a reducing agent with the onset of colloid solution. The red laser light represents the Tyndall effect observed in the colloid solution, according to the scattering of light when it travels through the nanoparticles. We found the well-dispersed round shape of silver nanoparticles resulting in a pale-yellow colloid solution. Mixing silver nanoparticles with the RHA-$SiO_2$ NPs modified by SDS 16 mM shows no difference in colloid solution when detected with the naked eye, but the SEM image reveals the agglomeration of silver and silica nanoparticles displayed in Fig.3(b). We propose that the accumulation was induced by $Na^+$, the counter ions of SDS, when the nanocomposite was prepared by using up to 16 mM of SDS concentration. However, the SEM image was collected from the dried nanoparticles sample that contained the anionic surfactant; this may affect the obtained morphology.

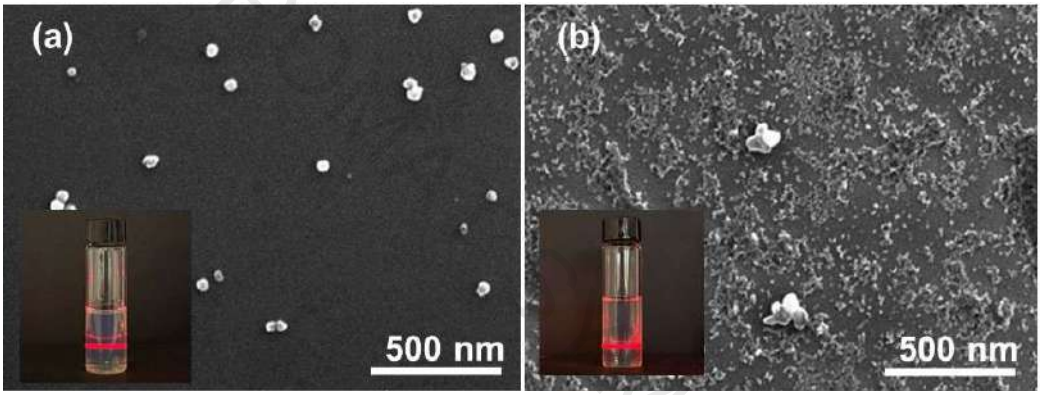


Fig.3 SEM image with picture of colloid (onset) of (a) Silver nanoparticle and (b) Ag/RHA-$SiO_2$ NC added by SDS 16 mM

The zeta potential values, representing the surface charge of the nanoparticles, were reported in Fig.4(a). The results show the insignificant change when the SDS concentration was increased, while the system containing only RHA-$SiO_2$ NPs exhibits the opposite trend. Our group believes that the head moiety of SDS will bind with the citrate groups surrounding silver nanoparticles; this binding occurs more than the O-H groups of the silica nanoparticles. For a deeper understanding, more experiments were required.

Fig.4(b) compares the average particle size between pure RHA-$SiO_2$ NPs and Ag/RHA-$SiO_2$ NC by increasing the SDS concentration. The result shows a lower average particle size compared with the pure counterpart observed in all of the nanocomposite systems. We suggest that adding Ag NPs, prepared using trisodium citrate as a capping agent, into the RHA-$SiO_2$ NPs system repels both nanoparticles themselves by the electrostatic repulsion mechanism. Consequently, adding SDS to the nanocomposite system results in a decrease in the average particle size. According to the reason mentioned above, this electrostatic

PROCEEDINGS PPC & PETROMAT SYMPOSIUM 2025

repulsive interaction plays a crucial role in the smaller size of the nanocomposite. However, increasing SDS concentration does not affect the average particle size in this system. We believe that the $Na^+$ from SDS can interact electrostatically with citrate anion, which covers Ag NPs, resulting in no change in the average particle size of the nanocomposite system [8].

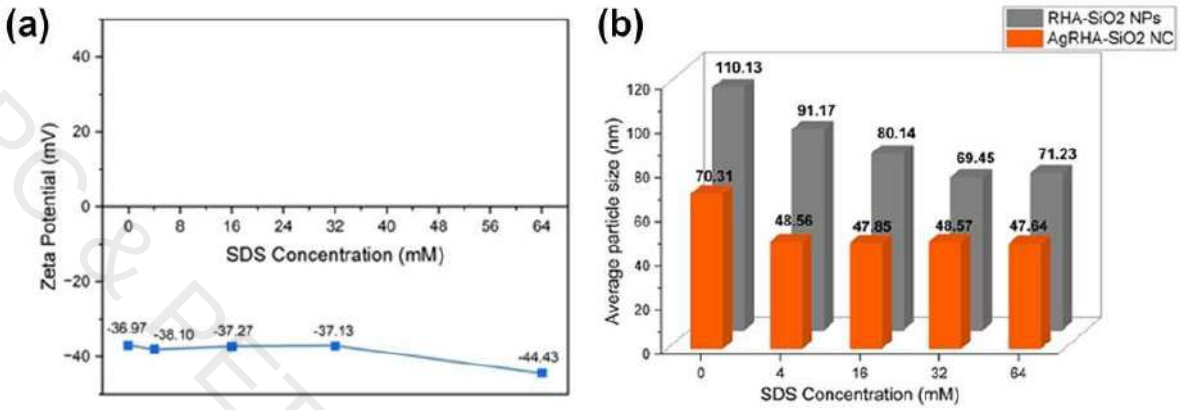


Fig.4 (a) Zeta potential and (b) average particle size of Ag/RHA-$SiO_2$ nanocomposite plotted against SDS concentration.

*C. Coating Ag/RHA-$SiO_2$ NC on PMMA surface and antibacterial testing*

Fig. 5 shows a PMMA sheet coated with 2 ml of mixer between Ag NPs and RHA-$SiO_2$ NPs with varying SDS concentration. It is observed that the transparency of the coated layer varies depending on the SDS concentration. The highly dispersed layer was detected at the systems added with 4 and 16 mM of SDS, while increasing the SDS concentration to 32 and 64 mM exhibits a turbid surface. According to our system prepared in DI water solution, SDS controls the reversible assembly of silica nanoparticles at water–hydrocarbon interfaces. At low SDS concentrations, nanoparticles coexist at the interface, but at higher concentrations, they migrate toward the aqueous phase due to increased electrostatic interactions [9]. The results from using a Vickers microhardness tester demonstrate that the PMMA sheet coated with Ag NPs and RHA-$SiO_2$ NPs modified with SDS at concentrations of 4, 16, 32, and 64 mM show the microhardness values at 1.69, 1.79, 1.70, and 1.66 HV, respectively. This demonstrates that surface Ag/RHA-$SiO_2$ NC modification with SDS significantly improved the hardness of the sheet. The sample coated with Ag/RHA-$SiO_2$ nanocomposite modified with SDS concentration 16 mM exhibited the highest hardness, an increase of 16.41% compared with the pure PMMA sheet.

PPC & PETROMAT SYMPOSIUM 2025

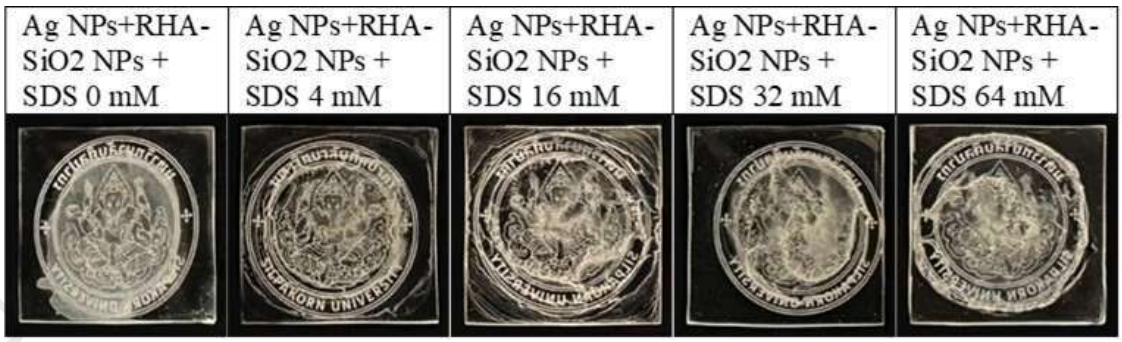


Fig.5 PMMA sheet coated with silver nanoparticles and RHA-$SiO_2$ nanoparticles with varying SDS concentration.

## CONCLUSIONS

This research explores the effects of sodium dodecyl sulphate (SDS) on the preparation and properties of Ag/RHA-$SiO_2$ NC for surface coating applications. The study shows that SDS plays a key role in stabilizing the nanocomposite and reducing particle size compared with the system. However, further increases in SDS concentration do not significantly alter the particle size. The coated PMMA sheet demonstrates a 16.41% increase in surface microhardness when using a nanocomposite prepared with 16 mM SDS. This study highlights the potential of SDS-modified Ag/RHA-$SiO_2$ NC in improving PMMA's mechanical properties and antibacterial performance, providing a way for multifunctional surface coatings. These findings suggest promising applications for dentistry, biomedical coatings, and protective materials.

## ACKNOWLEDGEMENTS

The authors would like to thank the Department of Materials Science and Engineering, Faculty of Engineering and Industrial Technology, Silpakorn University, for financial support, and also the Center of Excellence on Petrochemical and Materials Technology, Chulalongkorn University, for collaborative assistance in this study.

## REFERENCES

1. **Alqutaibi, A.Y., et al.** (2023), *Polymeric Denture Base Materials: A Review.* Polymers, 15(15): p. 3258.
2. **Zafar, M.S.** (2020), *Prosthodontic Applications of Polymethyl Methacrylate (PMMA): An Update.* Polymers, 12(10): p. 2299.
3. **Fatalla, A.A., M.S. Tukmachi, and G.H. Jani**. (2020), *Assessment of some mechanical properties of PMMA/silica/zirconia nanocomposite as a denture base material.* IOP Conference Series: Materials Science and Engineering, 987(1): p. 012031.
4. **Lhosupasirirat, S., et al.** (2018), *Improved Hardness of Nanocomposite Films on PMMA Sheet Using Beadmilled-SiO2 Nanoparticle in Dowanol PM.* Materials Science Forum, 911: p. 61-65.

PPC&PETROMAT SYMPOSIUM 2025

5. **Juan Carlos, F.-A., et al.** (2020), *Antimicrobial Poly (methyl methacrylate) with Silver Nanoparticles for Dentistry: A Systematic Review.* Applied Sciences, 10(11): p. 4007.
6. **Qiao, B., et al.** (2016), *Surface modification to produce hydrophobic nano-silica particles using sodium dodecyl sulfate as a modifier.* Applied Surface Science, 364: p. 103-109.
7. **Vatanparast, H., et al.** (2018), The Role of Electrostatic Repulsion on Increasing Surface Activity of Anionic Surfactants in the Presence of Hydrophilic Silica Nanoparticles. Scientific Reports Vol. 8 Issue 1 Pages 7251.
8. **Bo Fu, Jiakun Chen, Yatian Cao, et al.** (2024), Sodium dodecyl sulfate-modified ZIF-8 for sensitive detection of tetracycline in foods under synergistic adsorption of sodium dodecyl sulfate, Microchemical Journal, Volume 197.
9. **Mohammed, S., I. Kuzmenko, and G. Gadikota** (2022), *Reversible assembly of silica nanoparticles at water–hydrocarbon interfaces controlled by SDS surfactant.* Nanoscale, 14(1): p. 127-139.

PPC & PETROMAT SYMPOSIUM 2025

# DEVELOPMENT OF UV CURABLE PBZ/CNT NANOCOMPOSITE FOR 3D-PRINTABLE ELECTRODE FOR ENERGY STORAGE

*Lalani Kavindya Chathumalee Silva Jamuni* [a], *Thanyalak Chaisuwan* [*a,b]

[a] The Petroleum and Petrochemical College, Chulalongkorn University, Bangkok, Thailand
[b] Center of Excellence on Petrochemical and Materials Technology, Bangkok, Thailand

Keywords: Polybenzoxazine, Nanocomposite, UV Curable Resin

PROCEEDINGS OF PPC & PETROMAT SYMPOSIUM 2025

## ABSTRACT

Developing scalable and high-performance electrode materials is a much-needed innovation for energy storage technology. In this study, a novel UV-curable MWCNT/PBZ composite was designed for an energy storage electrode. The research was conducted in two phases. In the first phase, multi-wall carbon nanotubes (MWCNTs) were functionalized using benzoxazine monomer (BZ-F) to enhance the dispersion and compatibility in the composite matrix. Surface modification of MWCNTs' surface was confirmed through X-ray photoelectron spectrophotometer (XPS) and differential scanning calorimeter (DSC). The functionalized MWCNT (M-OCNT) loading was varied from 1 wt.% to 7 wt.%, and electrical conductivity showed the optimum performance for the 5 wt.% M-OCNT composite as 0.5 S/cm. The scanning electron microscope (SEM) further confirmed the uniform distribution of MWCNTs within the matrix. In the second phase, the benzoxazine matrix (BZ-M) was developed as UV-curable using glycidyl methacrylate (GMA), enabling its use in 3D printing. Fourier transform infrared spectroscopy (FTIR) was used to confirm the successful photopolymerization. The optimized MWCNT/PBZ composite shows promising electrical properties, making it a viable candidate for energy storage electrode application. This study suggests that combining advanced composite materials with additive manufacturing method could enhance next-generation energy storage devices.
* **thanyalak.c@chula.ac.th**

## INTRODUCTION

Growing demand for sustainable energy sources has increased the growth of renewable energy sources globally. However, the intermittent nature of renewables (wind and solar power) needs effective and sustainable energy storage technology to guarantee an uninterrupted energy supply. Rechargeable batteries have become the preferred energy storage method, and lithium-ion batteries are prominent due to their properties such as high energy density and commercial feasibility. However, the limited resource availability, environmental concerns, and safety difficulties emerged alternative materials and architectures for next-generation energy storage systems. To solve these issues, polymer-based electrodes have gained more attention due to their design flexibility, environmental friendliness, and molecular structure adjustability that enable the incorporation of conductive functionalities that are needed for the end product applications. Polybenzoxazine is a high-performance thermosetting polymer that has superior thermal stability, excellent mechanical strength, high dimensional stability, and low shrinkage during polymerization. These interesting properties emerged in the usage of polybenzoxazine as a material for electrodes of energy storage devices (Ishida, 2011; Katanyoota et al., 2010; Kiskan, 2018; Kiskan et al., 2011).

However, polybenzoxazine is low inherent conductivity limits the direct usage in electrode applications. This limitation can be overcome by using conductive fillers such as carbon nanotubes (CNTs). CNTs are widely used as conductive fillers due to their excellent electrical conductivity, mechanical reinforcement, and good structural stability. When CNTs are incorporated into a polybenzoxazine matrix, surface modification needs to be done to obtain better results as nanocomposite (Chen et al., 2006). Currently, advanced manufacturing methods like three-dimensional (3D) printing of complex electrode structures, have shown significant promise in enhancing electrochemical performance. 3D printing allows accurate control of complex electrode structures and the formation of customized designs in multiscale to engineer ion and electron conduction paths. Although PBZ-based printable materials are emerging, studies on UV-curable MWCNT/PBZ composite designed for electrode applications remain limited. This study addresses this need by developing a new UV-curable MWCNT/PBZ composite as a high performance electrode material for rechargeable energy storage systems. By combining the mechanical and thermal benefits of PBZ, the electrical conductivity of MWCNTs, and the geometric versatility of 3D printing, this approach offers a scalable route to fabricate high performance electrodes.

## EXPERIMENTAL

### *A. Materials*

Paraformaldehyde 95% and Aniline 99% were purchased from Sigma-Aldrich. Bisphenol-F was purchased from Ken Seika Corporation. 1,6-Diaminohexaane was purchased from Fluka Chemicals. Bisphenol-A 99% was purchased from Tokyo Chemical Industry Co.Ltd. Formaldehyde 37%, Chloroform 99.8% and 1,4 Dioxan were purchased from RCI Lab Scan, Co., Ltd. Toluene and ethanol AR grade were purchased from Quality Reagent Chemical. MWCNT was obtained from Nanocy, Belgium. Glycidyl methacrylate was purchased from Tokyo Chemical Industry Co.Ltd. Diphenyl (2,4,6- trimethylbenzoyl) phosphine oxide (TPO) was purchased from Skin Recipes.

### *B. Synthesis of Benzoxazine for Polymer Matrix (BZ-M)*

Bisphenol F, paraformaldehyde, and 1,6 diaminohexane (molar ratio 1.1: 4:1) were mixed with toluene/ethanol solvent (2/1, v/v) and added into a 250 mL round bottom glass flask equipped with a condenser, oil bath and a magnetic stirrer. The reaction mixture was refluxed for 6 hours at 100 °C. The solvent was evaporated using a rotary evaporator at 80 °C, and the residue was re-dissolved it in dichloromethane. After being rinsed with 0.1 M sodium hydroxide solution and distilled water, the solutioncwas dried for 24 hours at 55 °C in a vacuum oven.

### *C. Synthesis of Benzoxazine for MWCNT Modification (BZ-F)*

Benzoxazine for MWCNT surface modification was synthesized by using a solventless method using bisphenol A, paraformaldehyde, and aniline (molar ratio 1: 4: 2). The mixture was mixed at 110 °C and stirred until it was clear and no bubble formation.

### *D. Functionalization of Oxidized MWCNTs – (M-OCNT)*

The CNT was oxidized prior to surface modification as follows; 0-50 °C for 30 min, 50-350 °C for 5 hours, and 350 °C for 2 hours (holding). The dispersion of MWCNTs in the solvent was achieved by an ultrasonication bath (45kHz at 40 °C). The 0.1 g of oxidized-MWCNT (OCNT) was added to 10 ml of chloroform and sonicated for 30 min before

PPC & PETROMAT SYMPOSIUM 2025

adding the BZ-F. Then, 0.1 g of BZ-F was dissolved in another 10 ml of chloroform and added into the OCNT mixture. Then the mixture was sonicated again for 60 min.

*E. Preparation of MWCNT/PBZ Nanocomposite*

The MWCNT/PBZ nanocomposites were prepared using the solvent method. A quantity of modified M-OCNT prepared as procedure *D* was added into the system composed of 5.0 g of BZ-M monomer and 30 ml of 1,4 dioxane. The weight ratio of BZ-M to M-OCNT varied from 1%, 3%, 5%, 6% and 7%. The resulting mixtures were sonicated for 5 min by an ultrasonication probe, and then the mixture was stirred for 3 h at room temperature. Then the mixture was poured into a silicon mold and vacuum oven at 45 °C for 24 h. Then the composite samples were cured as stepwise as follows: 160 °C for 1 h, 180 °C for 1 h, 200 °C for 1 h, 220 °C for 1 h, and 240 °C for 4 h in a curing oven.

*F. Preparation of UV-Curable Benzoxazine Matrix*

The UV-curable benzoxazine matrix was prepared by adding GMA into the benzoxazine matrix solution and stirring it for 24 hours at 60 °C. The ratio of the GMA: OH was 1:1. Then the UV curing was conducted using an ELEGOO Saturn S printer for 180 s. After that, UV specimens were washed through acetone and Deionized (DI) water, and post-cured in the oven as mentioned earlier.

*G. Instrument and Characterization.*

Chemical structures of the synthesized polymers were characterized by Fourier transform infrared spectroscopy (FTIR), Thermo SCIENTIFIC NICOLET iS5 FTIR in the wavenumber range 600-4000 $cm^{-1}$. The thermal properties were tested using the NETZSCH Proteus differential scanning calorimeter (DSC) under a nitrogen flow. The surface chemistry of the modified MWCNT was studied using an X-ray photoelectron spectrophotometer (XPS, Kratos Axis Ultra DLD). The morphologies and dispersion of the CNTs were investigated using field-emission scanning electron microscopy (FESEM) with a Hitachi/S-4800. The resistances of the CNT/PBZ composites were tested using a four-point probe technique.

## RESULTS AND DISCUSSION

*A. FTIR Characterization*

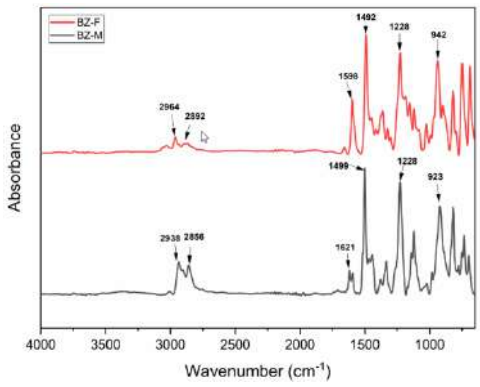


Figure 1. FTIR of BZ-F and BZ-M

Figure 1 shows FTIR spectra of BZ-F and BZ-M monomers. The absorption peaks observed at 923/942 $cm^{-1}$ and 1499/ 1492 $cm^{-1}$ correspond to the trisubstituted benzene ring, confirming the presence of the benzoxazine ring (Taskin et al., 2013). The absorption band at 1228 $cm^{-1}$ is attributed to the asymmetric stretching vibration of the C-O-C group of the oxazine ring. Also, the peaks at 2938/2964 $cm^{-1}$ and 2856/ 2892 $cm^{-1}$ correspond to the $CH_2$ stretching vibration (Tj et al., 2021).

PPC & PETROMAT SYMPOSIUM 2025

*B. XPS – Benzoxazine Functionalized MW*CNTs

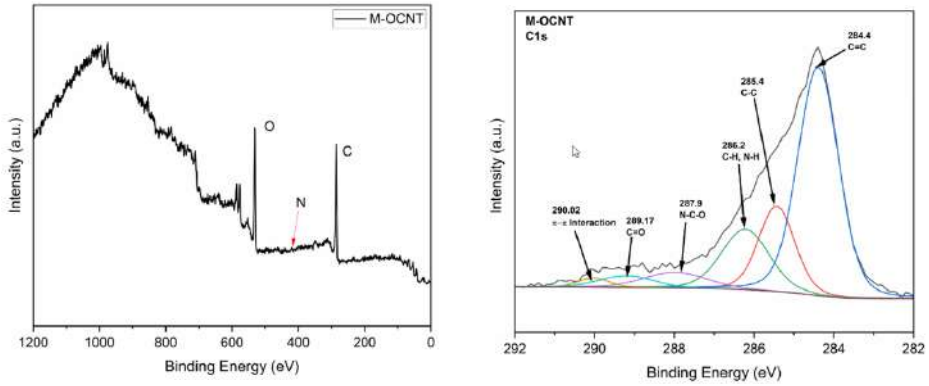


Figure 2. XPS spectrum M-OCNT wide scan (a), and C1s spectrum

The elemental composition of M-OCNTs was performed using XPS to confirm the grafting of BZ-F monomer on the MWCNT's surface. The wide-scan XPS spectrum of M-OCNTs is shown in Figure 2a, and no clear N1s peak was observed, possibly due to the low nitrogen content of the benzoxazine and single scan mode of the wide scan. Narrow scan analysis was conducted to enhance detection, which indicated the presence of nitrogen bonds. The high resolution C1s spectrum (Figure 2b) shows peaks at 284.4 and 285.4 eV for C=C and C-C, respectively. Peaks at 286.2, 287.9,289.1and 290.0 eV were assigned to C-H/N-H, N-C-O, C=O, and π-π interactions, confirming successful surface modification of CNTs (Chen et al., 2006; Wang et al., 2012).

*C. Themal Properties of M-OCNTs*

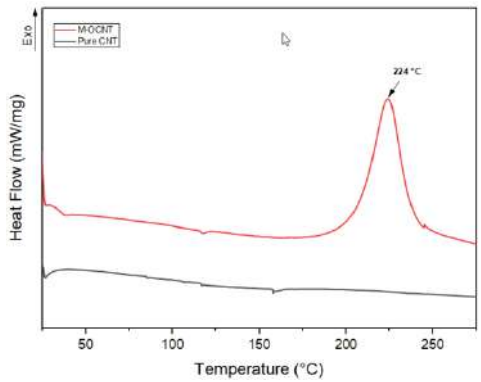


Figure 3.Thermal properties of M-OCNTs

Successful functionalization of MWCNTs with benzoxazine monomer was confirmed by using DSC analysis. M-OCNT and pristine MWCNTs were examined. Only the M-OCNT sample shows a clear exothermic peak at around 224 ºC, as seen in Figure 3. The peak is due to the thermal reaction during the ring-opening polymerization of the benzoxazine monomer on the MWCNT surface. On the other hand, the pure MWCNTs do not show detectable exothermic peaks confirming no thermal transition such as cross-linking and polymerization within the temperature range. The absence of an exothermic peak in the control sample also supports the idea that the benzoxazine is present on the surface of MWCNTs after modification.

*D. Conductivity Test*

The electrical conductivity of prepared MWCNT/PBZ nanocomposites is shown in Figure 4. The conductivity of the nanocomposite shows strong dependence on the MWCNT wt% and the highest conductivity was achieved at 5 wt% of MWCNT as 0.5 S/cm.

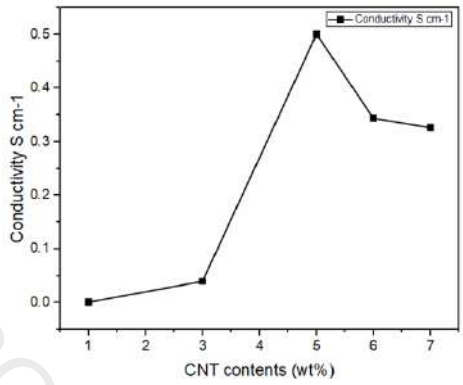


Figure 4. Conductivity of nanocomposites

This is due to the formation of an effective percolation network within the BZ-M matrix.The M-OCNT wt% below 5 wt%, conductivity is low due to the poor connectivity between the M-OCNTs in the matrix due to the inadequate M-OCNTs to form the electron conductive pathway. A very high concentration of M-OCNTs also shows poor conductivity than the 5 wt% M-OCNTs content due to the excess M-OCNTs agglomeration and disrupted conductive pathways.

## *E. Morphology of Composites*

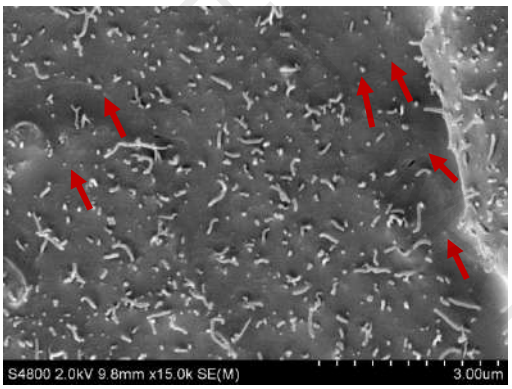


Figure 5. SEM of 5 wt% nanocomposite

The SEM micrograph of the 5 wt% M-OCNT composite illustrates good and homogeneous dispersion in the BZ-M matrix (Figure 5). The M-OCNTs are well embedded with no signs of agglomeration indicating good interfacial interaction between the matrix and the M-OCNTs. The red arrows show the embedded M-OCNTs in the matrix that do not come out from the matrix like others. Homogeneous distribution of M-OCNT is critical in efficient electron transport to enable the formation of a conductive network.

These morphological features are evidence of improved electrical conductivity observed at this composite and demonstrate that the 5 wt% loading of M-OCNT is optimal to match dispersion and conductivity in the composite system.

## *F.* FTIR Analysis of UV Curable Resin

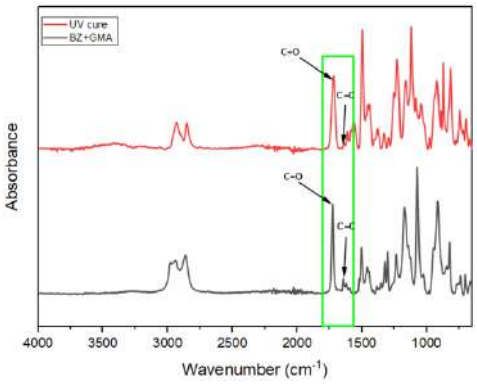


Figure 6. FTIR of UV curable resin

The FTIR analysis compares the chemical structures of the GMA incorporated BZ-M resin before and after UV curing. The before curing sample show a clear peak at 1638 $cm^{-1}$ for the C=C stretching vibration of methacrylate groups. After UV exposure, the peak intensity was significantly decreased, confirming efficient polymerization of C=C bonds. This is indicates the selective polymerization of methacrylate double bonds without benzoxazine ring-opening after UV curing.

## CONCLUSIONS

This study describes a two-phase development of a UV curable MWCNT/PBZ composite for energy storage applications. Modification of MWCNTs with benzoxazine monomer (BZ-F) improved dispersion and conductivity. The 5 wt% M-OCNT composite showed optimum performance due to the homogeneous dispersion of M-OCNTs within the polymer matrix. The benzoxazine matrix (BZ-M) was chemically grafted with GMA to make it UV curable and potentially 3D printable, as confirmed by FTIR analysis. Combining this resulting nanocomposite and UV curable resin will be a promising solution for scalable, high performance energy storage applications.

## ACKNOWLEDGEMENTS

The authors gratefully acknowledges The Petroleum and Petrochemical College, and Center of Excellence on Petrochemical and Materials Technology, Chulalongkorn University (Thailand) for ASEAN and non-ASEAN scholarship program and funding of this research work.

## REFERENCES

Chen, Q., Xu, R., & Yu, D. (2006). Multiwalled carbon nanotube/polybenzoxazinenanocomposites: Preparation, characterization and properties. *Polymer*, *47*(22), 7711-7719. https://doi.org/https://doi.org/10.1016/j.polymer.2006.08.058

Ishida, H. (2011). Chapter 1 - Overview and Historical Background of Polybenzoxazine Research. In H. Ishida & T. Agag (Eds.), *Handbook of Benzoxazine Resins* (pp. 3-81). Elsevier. https://doi.org/https://doi.org/10.1016/B978-0-444-53790-4.00046-1

Katanyoota, P., Chaisuwan, T., Wongchaisuwat, A., & Wongkasemjit, S. (2010). Novel polybenzoxazine-based carbon aerogel electrode for supercapacitors. *Materials Science and Engineering: B*, *167*(1), 36-42. https://doi.org/https://doi.org/10.1016/j.mseb.2010.01.024

Kiskan, B. (2018). Adapting benzoxazine chemistry for unconventional applications. *Reactive and Functional Polymers*, *129*, 76-88. https://doi.org/https://doi.org/10.1016/j.reactfunctpolym.2017.06.009

Kiskan, B., Ghosh, N. N., & Yagci, Y. (2011). *Polym. Int.*, *60*(2), 167.

Taskin, O. S., Kiskan, B., & Yagci, Y. (2013). Polybenzoxazine Precursors As Self-Healing Agents for Polysulfones. *Macromolecules*, *46*(22), 8773-8778. https://doi.org/10.1021/ma4019153

Tj, M., Hariharan, A., Balaji, K., & Alagar, M. (2021). Studies on Syntheses, Spectral, Thermal and Hydrophobic Behavior of Cardanol Based Tetra Functional Benzoxazines. *Polymer Science, Series A*, *63*(6), 679-689. https://doi.org/10.1134/S0965545X21350133

Wang, Y.-H., Chang, C.-M., & Liu, Y.-L. (2012). Benzoxazine-functionalized multi-walled carbon nanotubes for preparation of electrically-conductive polybenzoxazines. *Polymer*, *53*(1), 106-112. https://doi.org/https://doi.org/10.1016/j.polymer.2011.11.040

PPC & PETROMAT SYMPOSIUM 2025

# DERIVATIZED CYCLODEXTRINS AS FUNCTIONAL MATERIALS FOR ENHANCED ISOMER SEPARATION BY GAS CHROMATOGRAPHY

*Nicharat Amonseriroj* [a,b], *Aroonsiri Shitangkoon* *[a,b]

[a)] Department of Chemistry, Faculty of Science, Chulalongkorn University, Bangkok 10330 Thailand
[b)] Center of Excellence on Petrochemicals and Materials Technology, Chulalongkorn University, Bangkok 10330 Thailand

Keywords: isomer, cyclodextrin, gas chromatography

## ABSTRACT

Efficient separation of aromatic isomers is important and useful in industries and environmental monitoring, due to their widespread use and varying levels of toxicity. This research investigated and optimized conditions for isomer separation by gas chromatography using (2,3-di-*O*-methyl-6-*O*-*tert*-butyldimethylsilyl)--, - and - cyclodextrins as stationary phases with 15-meter-long capillary columns. Three groups of isomers included xylenes, (trifluoromethyl)acetophenones and methylphenols were analytes of interest. Types of cyclodextrin and column temperature were investigated to achieve complete resolution of each group of isomers. The results demonstrated that the size of cyclodextrin ring affected selectivity and elution order. Only -cyclodextrin derivative could completely separate all three groups of isomers under optimized isothermal conditions. Moreover, it provided shorter analysis time compared to commercial columns and/or polysiloxane-based stationary phases. This work demonstrated the strategic condition optimization of existing functional materials, offering a practical pathway to enhance analytical performance without novel material synthesis. The findings contribute to smart material utilization in chromatographic systems, supporting both analytical advancement and environmental safety.

***aroonsiri.s@chula.ac.th**

## INTRODUCTION

Isomers are compounds with identical molecular formulas. Although isomers have different structures, they may have similar chemical and physical properties. These similarities make the separation and identification of individual isomers a significant analytical challenge. In petrochemical industries, aromatic isomers such as *o*-xylene, *m*-xylene, *p*-xylene and ethylbenzene are widely utilized in various applications. However, they showed different toxicities and environmental impacts. For example, occupational and environmental safety regulations specify different permissible exposure limits for each xylene isomer. Therefore, effective analytical techniques that can distinguish between structurally similar isomers are critical for regulatory compliance, environmental monitoring, and risk assessment [1,2]. Due to their volatility and small molecular size, these aromatic isomers were typically analyzed using gas chromatography (GC). However, most conventional polysiloxane or polyethylene glycol stationary phases often failed to achieve complete isomer resolution or separation with reasonable analysis time [3].

PPC & PETROMAT SYMPOSIUM 2025

Cyclodextrins (CDs), cyclic oligosaccharides composed of 5 or more glucose units. Three common CDs are α-, β-, and γ-CDs with 6, 7, and 8 glucose units, respectively. CDs possess a hydrophobic internal cavity and hydrophilic exterior, enabling selective host-guest interactions with a wide range of analytes. In addition, CDs contain 30-40 chiral centers per molecule, allows them to effectively differentiate structurally similar isomers and chiral compounds [4]. Previous study reported the use of octakis(2,3-di-*O* -methoxymethyl-6-*O*-*tert*-butyldimethylsilyl)-γ-CD as a GC stationary phase for separation of enantiomers. A total of 125 pairs of enantiomers could be separated [5]. Many CD derivatives have shown promises as GC stationary phases due to their unique molecular structure [6].

In this study, (2,3-di-*O*-methyl-6-*O*-*tert*-butyldimethylsilyl)--, - and -CDs mixed in polysiloxane were used as GC stationary phases to separate aromatic isomers. Three groups of isomers included xylenes, methylphenols and (trifluoromethyl)acetophenones were analytes of interest. Size of cyclodextrin and column temperature were investigated to achieve complete resolution of each group of isomers. Elution order and analysis time obtained from derivatized CD stationary phases and polysiloxane stationary phase were compared.

## EXPERIMENTAL

### *A. Chemicals*

All isomers and solvents were purchased from various vendors (Sigma-Aldrich, TCI, Merck) and were used without purification. Group 1 included 4 isomers of *o*-xylene (o); *m* -xylene (m); *p*-xylene (p); and ethylbenzene (E). Group 2 included 3 methylphenols (2MP;3MP; and 4MP) and 5 dimethylphenols (2,4DMP; 2,5DMP; 2,6DMP; 3, 4DMP; and 3,5DMP). Group 3 included 3 isomers of (trifluoromethyl)acetophenones (2T; 3T and 4T).
Each group of isomers were dissolved in pentane or dichloromethane to obtain a final concentration of ~10 mg/mL for each analyte.

### *B. GC stationary phases*

Capillary columns (15 m long, 0.25 mm i.d.) were coated with 0.25 m film of stationary phase [7]. Four types of stationary phases were used in this work included polysiloxane OV-1701 and three derivatized CDs (Figure 1) separately mixed in polysiloxane OV-1701. Column efficiency was tested with *n*-alkanes. All columns showed good efficiency of 3,400-4,200 plates/m.

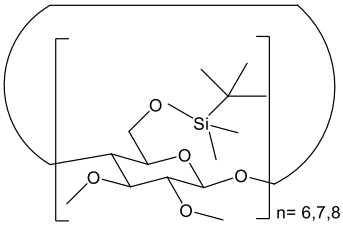


ACD: n = 6
BCD: n = 7
GCD: n = 8

Figure 1. Structure of (2,3-di-*O*-methyl-6-*O*-tert-butyldimethylsilyl)-CDs

PPC & PETROMAT SYMPOSIUM 2025

*C. GC analyses*

All separations were performed on an Agilent 7890B gas chromatograph, with a split injector (250 °C, split ratio 100:1) and a flame ionization detector (250 °C). Hydrogen was used as a carrier gas at 50 cm/sec. Column temperature was adjusted and optimized until a complete separation (minimum resolution of 1.5 of the least separated peak pair) for each group of isomers was obtained with short analysis time. Analyses of isomer mixtures were performed at least in duplicate (retention times were within 0.002 minute).

## RESULTS AND DISCUSSION

*A. Group 1*

The (2,3-di-*O*-methyl-6-*O*-*tert*-butyldimethylsilyl) derivatives of -, - and -CDs were separately mixed with polysiloxane OV-1701 and used as GC stationary phases, referred to as ACD, BCD, and GCD columns, respectively. To determine the optimum column temperature for separation of each group of isomers, a temperature program was initially used and elution temperature of analytes was obtained. Figure 2 showed a chromatogram for the separation of group 1 isomers obtained from ACD column using temperature program. ACD provided excellent separation of 4 isomers with elution order of E, p, o, m. Next, the elution temperature was used for an isothermal run. The column temperature was then adjusted until a complete separation with shortest analysis time was achieved. At optimum column temperature of 83 °C, group 1 isomers could be separated in less than 2 minutes on ACD column (Figure 3a), about 3.3 times faster than temperature program run.

Separations of group 1 isomers were attempted on BCD, GCD, and OV-1701 columns using the same procedures as ACD column. As shown in Figure 3b, BCD column showed complete separation of group 1 isomers at 85 °C in 1.73 minutes with different elution order than ACD column, indicating the effect of CD ring size on the interaction with analytes. The large-size GCD column could not provide complete separation between E and p isomers even at low temperature of 40 °C (Figure 3c). While OV-1701 column could not separate p and m isomers (Figure 3d). The elution order obtained from OV-1701 column followed the boiling points of analytes and was different than other three CD-based columns since there was no additional interaction from CD.

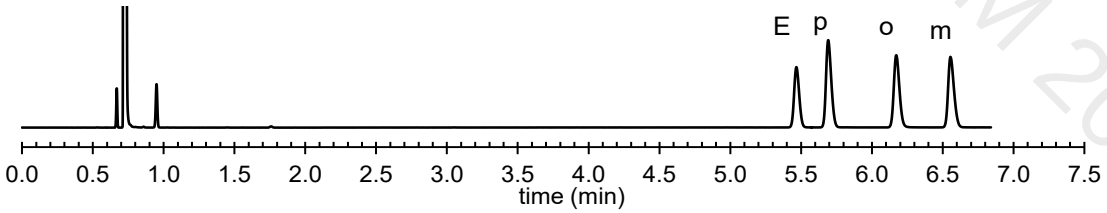


Figure 2. Separation of group 1 isomers on ACD column (temperature: 40-180 °C, rate 3.2 °C/min).

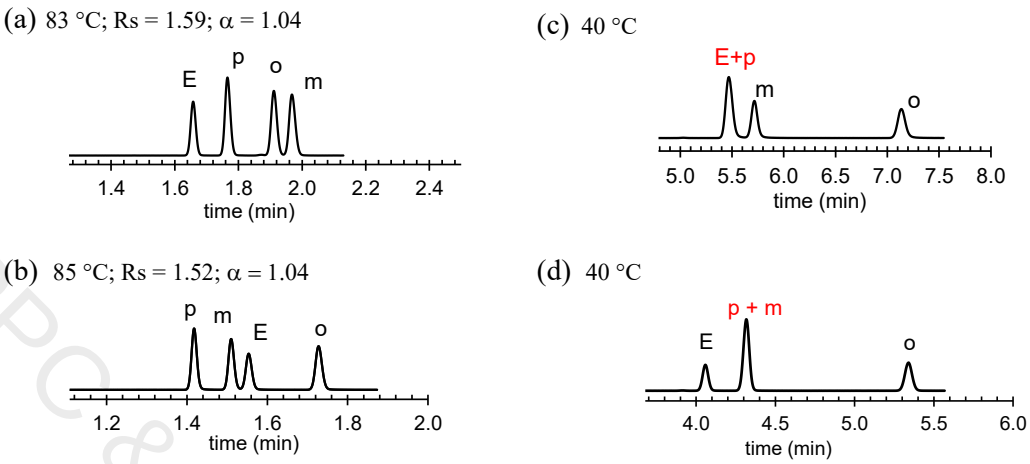


Figure 3. Separation of group 1 isomers on (a) ACD, (b) BCD, (c) GCD, and (d) OV-1701 columns. Resolution (Rs) and selectivity (α) of the least separated peak pair were reported.

*B. Group 2*

Isomers of methylphenols were divided into 2 subgroups according to the number of aromatic substitutions. Separation of three isomers of methylphenols (2MP, 3MP, 4MP) on OV-1701 column was not satisfied even at low temperature, as 4MP and 3MP isomers were barely resolved. However, three derivatized CDs significantly improved the separation of three methylphenols. The elution orders on three columns were similar. At their optimum conditions, analyses of three methylphenols on ACD and BCD columns could be achieved at 182 °C in less than 0.9 minute (Figure 4a). While GCD column required lower column temperature and slightly longer analysis time of 1.42 minutes (Figure 4a).

Next, separation of five isomers of dimethylphenols was investigated (2,3-dimethylphenol was not available). OV-1701 column did not provide satisfied result, as 2,4DMP and 2,5DMP isomers were coeluted at every condition investigated. On the other hand, three CD columns successfully separated five dimethylphenols (Figure 4b). At optimum condition, ACD column could separate five isomers in 1.38 minutes with the elution order of 2,6DMP; 2,4DMP; 2,5DMP; 3,4DMP; 3,5DMP. BCD column showed better selectivity enhancement and could complete the separation in 1.02 minutes, but with different elution order than ACD column. However, large-size GCD column required lower column temperature and longer analysis time of 10.94 minutes. These results emphasized the effect of CD ring size and shape on the interaction with different analytes, resulting in different selectivity and elution order.

PPC & PETROMAT SYMPOSIUM 2025

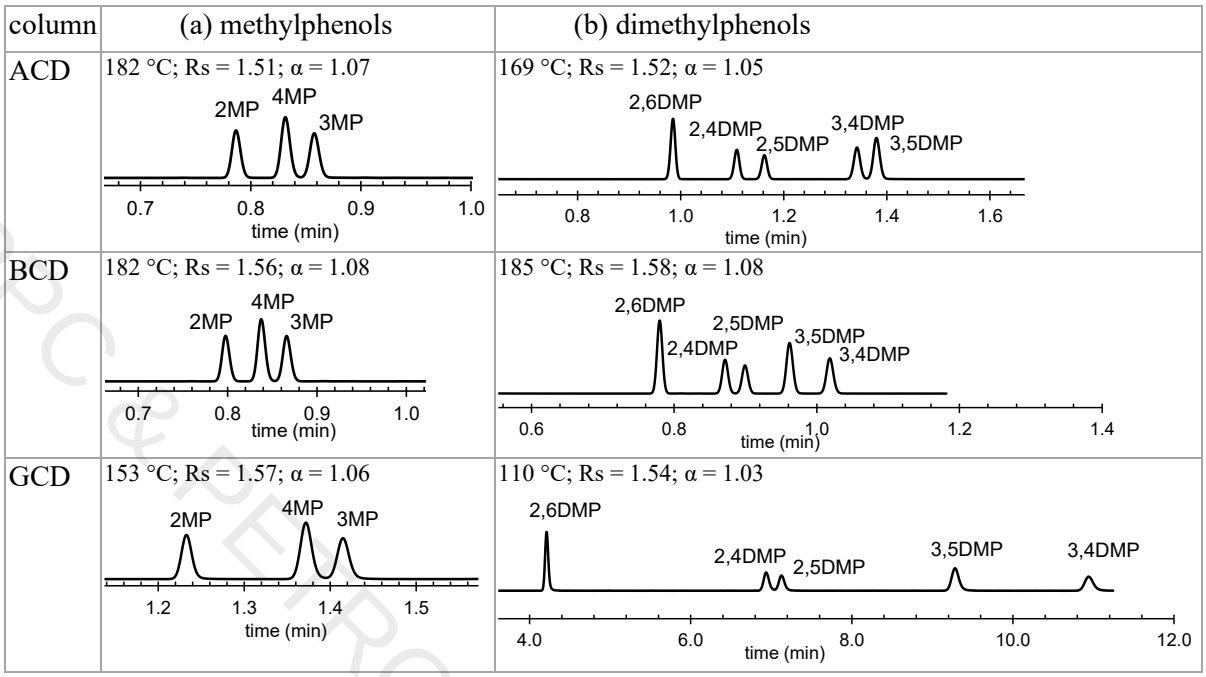


Figure 4. Separation of group 2 isomers (a) methylphenols and (b) dimethylphenols on ACD, BCD, and GCD columns. Resolution (Rs) and selectivity (α) of the least separated peak pair were reported.

*C. Group 3*

Last, separation of three (trifluoromethyl)acetophenone isomers were studied. Similar to group 1 and group 2 isomers, OV-1701 column did not provide satisfied result for group 3 isomers, as 3T and 4T isomers were coeluted at every condition investigated. Three CD derivatives showed selectivities towards group 3 isomers to a different extent. ACD column could not provide satisfied result, as 2T and 4T isomers were partially separated. Lower temperature was not studied as peaks became broader and analysis time was too long. However, BCD and GCD columns provided complete separation, but with different elution order, in 3.35 and 4.35 minutes, respectively (Figure 5).

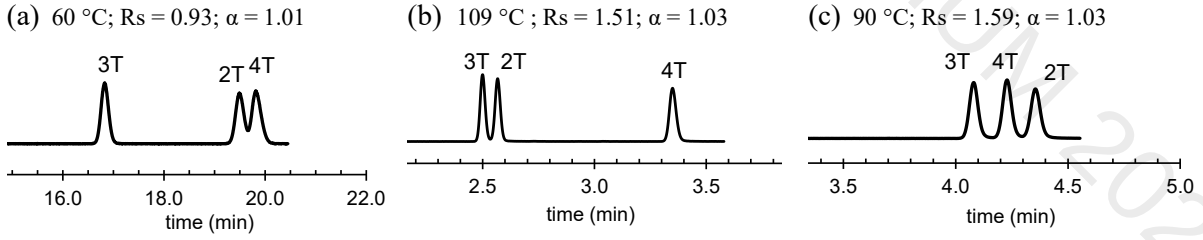


Figure 5. Separation of group 3 isomers on (a) ACD, (b) BCD, and (c) GCD columns. Resolution (Rs) and selectivity (α) of the least separated peak pair were reported.

PPC & PETROMAT SYMPOSIUM 2025

## CONCLUSIONS

This study investigated the role of cyclodextrin derivatives as smart functional materials and reinforce their potential in advanced chromatographic systems. Through the use of existing materials and optimizing operating conditions rather than developing entirely new ones, this research contributes to the practical advancement of innovative materials for high-performance chemical analysis.

The results demonstrated that each CD-based GC column provided unique selectivity and effectively separated aromatic isomers of various functional groups, while polysiloxane OV-1701 column failed to fully resolve the isomers in this study. Although all CD derivatives shared identical substituents, their differing ring sizes significantly affected selectivity and elution order. For isomers with a single aromatic ring, the medium-size BCD column provided fast and efficient separation, and useful for future industrial applications.

However, analytes this study were limited to aromatic isomers, and performance with other chemical groups was not explored. Nonetheless, the selectivity observed suggests that CD-based stationary phases are suitable for separating compounds with similar structures or functional groups beyond aromatics. Future work will expand the application of these materials to a broader range of analytes to further demonstrate their capability in complex separations relevant to environmental, petrochemical, and pharmaceutical laboratories.

## ACKNOWLEDGEMENTS

Authors would like to thank Professor Gyula Vigh for providing derivatized CDs used in this work.

## REFERENCES

[1] **Loba Chemie**. (2024). *Material Safety Data Sheet: o-Xylene for Synthesis*. Retrieved from https://www.lobachemie.com/lab-chemical-msds/MSDS-oXYLENE-CASNO-95-47-06498-TH.aspx (accessed February 17, 2024).
[2] **Fisher Scientific.** (2024). *Material Safety Data Sheet: m-Xylene*. Retrieved from https://fscimage.fishersci.com/msds/95260.htm (accessed February 17, 2024).
[3] **Sun, T., Chen, R., Huang, et al**. (2023). Anal. Chim. Acta **1251**, 340979.
[4] **Singh, N., and Sahu, O.** (2019). *4 - Sustainable cyclodextrin in textile applications. In The Impact and Prospects of Green Chemistry for Textile Technology*, I. Shahid ul & B. S. Butola (Eds.) pp. 83-105. Woodhead Publishing.
[5] **Takahisa, E. and K.-H. Engel**. (2005) J. Chromatogr. A. **1063 (1)**, 181-192.
[6] **Xiao, Y., et al.,** (2012) J. Chromatogr. A, 2012. **1269**, 52-68.
[7] **Grob, K.** (1986). *Making and Manipulating Capillary Columns for Gas Chromatography*, Hüthig Verlag, Heidelberg

PPC & PETROMAT SYMPOSIUM 2025

# INVESTIGATION ON IN-SITU ION SWELLING OF POLYELECTROLYTE MULTILAYERS (PEMS) USING LIGHT INTERFERNCE SPECTROSCOPY

*Chamod Hasaranga Peiris* [a], *Stephan Thierry Dubas* *[a,b]

a The Petroleum and Petrochemical College, Chulalongkorn University, Bangkok 10330, Thailand
b Center of Excellence on Petrochemical and Materials Technology, Bangkok 10330, Thailand

Keywords: Polyelectrolytes Multilayers (PEMs), Light Interference Spectroscopy (LIS), In-situ Swelling, Layer-by-layer, Thin-film interference

## ABSTRACT

Polyelectrolytes Multilayers (PEMs) and layer-by-layer assemblies exhibit dynamic swelling responses to ionic environments and solvent compositions, making them ideal solutions for ion-selective membranes, biomedical coatings, and energy devices. By exposing the PEM to various salt type and concentration, structural changes of the ion pairing in the multilayer networks can occur by electrostatic screening. The study of these swelling effects remains unclear and extremely challenging to investigate in real-time circumstances. Using Light Interference Spectroscopy (LIS), a noninvasive optical method based on thin-film interference, the present investigation offers a real-time assessment of the in-situ, ion-induced swelling of PEMs. The PEMs were built via layer-by-layer deposition and subjected to different amounts of organic solvents and monovalent salts. Ion-specific and solvent-induced swelling behavior were shown by observing the shifts in the interference peak (λ max), with KCl exhibiting a more noticeable influence than NaCl. Verifying the LIS sensitivity along with recent works, KCl red shift exhibits steeper slope of 74.53 nm/moldm-3 as opposed to NaCl 59.86 nm/moldm-3. Acetone acts conversely by contracting PEM layers resulting in a blue shift in absorbance pattern (-155.97 nm/moldm-3). This approach offers a helpful foundation for studying dynamic film behavior and developing responsive materials for innovative uses.

***stephan.d@chula.ac.th**

## INTRODUCTION

Advancements in present membrane technology, PEMs have managed to stand in a niche spot in the membrane industry in recent decades. This considerable interest in PEM in a wide range of applications in the membrane industry is drawn towards itself due to its adoptable characteristics under many different environments. The spontaneous complex formation of polyanion and polycation resulting in a versatile polyelectrolyte complex, studied by many researchers recently, reveals its dynamic characteristics with ionic strength, pH, and dielectric gradients, as well as its chemical stimuli responses (Kastinen et al., 2024; Khavani et al., 2022; Konyali et al., 2023). Despite being a “jack of all trades” in the applied membrane industry, the theoretical understanding of this dynamic characteristic stayed dormant due to the complexity of swelling studies. Understanding the real-time swelling dynamics of PEMs is necessary for optimizing their performance in a range of applications, including ion-selective membranes, biomedical coatings, and electrolyte transport in energy devices.

PPC & PETROMAT SYMPOSIUM 2025

Quartz Crystal Microbalance Dissipation mode (QCM-D) has been the typical approach for assessing and monitoring PEM swelling and layer growth investigations for the last few years. According to a recent study by Konyali et al. (2023) (Konyali et al., 2023), QCM-D has been used to track solvent-induced swelling and PEM stability, explaining dynamic ion interactions and structural integrity under various circumstances. However, this approach of dissipation offers indirect measurement of frequency damping proportionate to membrane weight growth, but its operation requires a certain level of advanced technical understanding. Similarly, Hegaard and Thormann (2023) used ellipsometry and atomic force microscopy (AFM) to study the effects of composition, salt concentration, and ion selectivity on the pH responsiveness of covalently crosslinked chitosan and alginate dialdehyde multilayer films (Hegaard & Thormann, 2023).

It is practically challenging to generate adequate real-time data for a complete analysis within a limited amount of time using these discussed methods. Providing an accurate platform to study the dynamics of swelling itself with these techniques is burdened by a vast knowledge requirement to handle QCM, ellipsometry, and AFM when it comes to real-time investigation of in-situ swelling and contractions of PEM. As a reliable alternative, LIS stands as a highly sensitive, noninvasive method to track swelling and contraction dynamics of thin films in real time. LIS allows exact observation of film thickness variations at the nanoscale scale, offering a greater understanding of ion-polymer interactions in PEMs by measuring the interference patterns of reflected light from PEM layers.

This work describes a novel approach that uses LIS to analyze the in-situ swelling of PEMs in various ionic and dielectric conditions. The primary goal of this work will be to investigate the effects of various monovalent salts on the swelling behavior of PEMs, as well as to investigate solvent-induced contraction mechanisms.

## EXPERIMENTAL

### *A. PEM Fabrication*

A solution of 10 mM PSS (polystyrene sulfonate) was made in 1M NaCl solution; in contrast, a solution of 10 mM PDADMAC (poly(diallyldimethylammonium) chloride) was prepared. We bought electrolytes, solvent materials, acetone, KCl, NaCl, PSS, PDAD, and acid solutions from Sigma Aldrich. Every chemical and solvent that was supplied was used exactly as it was, without any additional purification or processing

Silicon wafers should be dipped alternately in the prepared PSS and PDADMAC solutions to create the multilayer structure. Prior to layer-by-layer assembly, silicon wafer slides were free of any organic contaminants. For the cleaning procedure of Si substrates, "Piranha Solution" was made by mixing a 2:1 ratio of concentrated sulfuric acid with 30% hydrogen peroxide and dipping all prepared wafers in it for 15 minutes (Dubas & Schlenoff, 1999). After the extensive cleaning, the Si slides were carefully rinsed with deionized water. These substrates were then prepared for layer-by-layer assembly by sonication in ethanol (30 minutes), followed by washing twice with DI water.

The silicon wafer was immersed in the PSS solution for one minute, with mild vertical movements manually ensuring 6 dips per minute to facilitate uniform coating. After dipping in the PSS solution, the wafer was washed with flowing deionized water for 1 minute to remove surplus polyelectrolyte layers. The coated silicon wafer was then immersed in the PDADMA solution for 1 minute before repeating the operation. The rinse approach is repeated until the requisite layers are deposited on top of the silicon substrate.

PPC & PETROMAT SYMPOSIUM 2025

*B. LIS for Swelling Analysis*

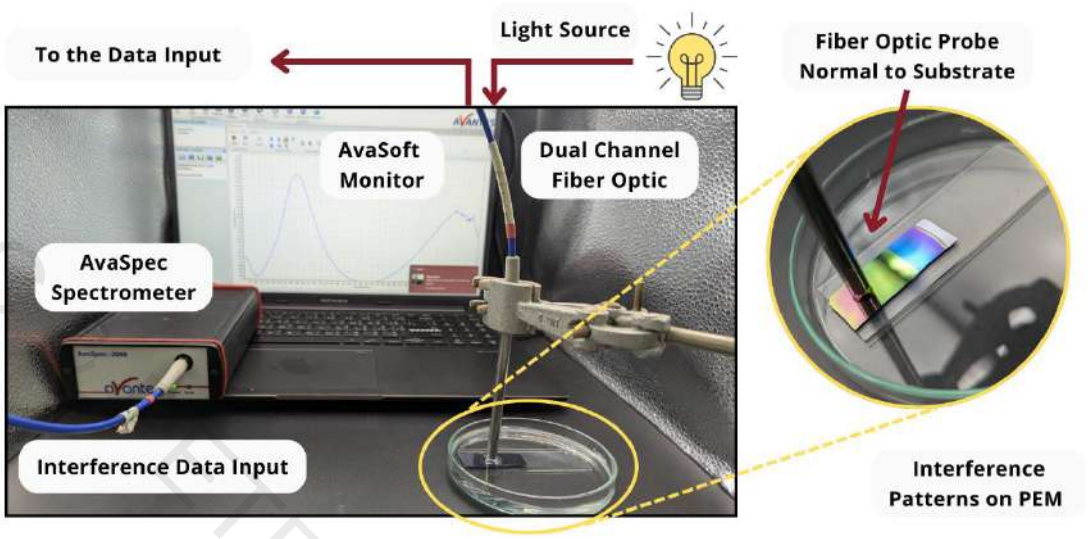


Figure 1: LIS experimental setup used for the swelling analysis

Light Interference Spectroscopy (LIS) was used to track the real-time changes in interference patterns when the solutions and their concentrations were changed while the produced PEMs were submerged in previously prepared solutions (solvents and salt solutions). To investigate the red and blue shift that happens as concentration changes, the absorbance spectrum was acquired. The changes in PEM thickness over time as a function of concentration or solvent percentages were calculated using the obtained shifts generated from LIS. As illustrated in Figure 2, increment of layer thickness even at nanoscale level were represented in LIS as absorbance where it plotted as a redshift to quantitatively represent thickness change.

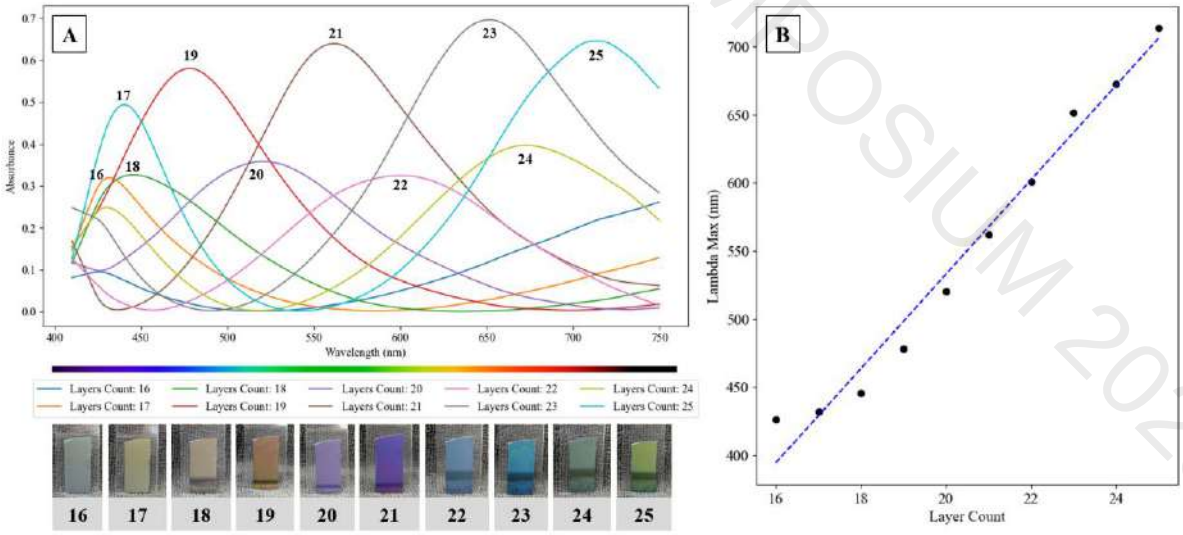


Figure 2: A—Light Interference Spectra Taken by Increasing Polyelectrolyte Layer by Layer. B – Increment of λmax of each spectrum taken by increasing the layers of PEM

PPC & PETROMAT SYMPOSIUM 2025

## RESULTS AND DISCUSSION

*A. Ion transport promoting PEM Swelling*

Polyelectrolyte multilayers (PEMs) are highly adjustable thin films made using the layer-by-layer process that are frequently employed in responsive coatings, membranes, and sensors. One of the important dynamic features of PEMs is ion-induced swelling, in which ions from the medium around it penetrate the film, disrupt electrostatic connections, and cause an increase in film thickness due to osmotic pressure and hydration effects. (Figure 3 – C). Light Interference Spectroscopy (LIS), a non-destructive optical approach based on thin-film interference, is the best way to record the real-time swelling response. (Figure 3 – A). Whenever ions migrate into the PEM structure, the thickness difference affects the interference pattern of reflected light, causing observable alterations in the interference peak ($\lambda_{max}$). This shift is closely related to film swelling, making LIS an effective instrument for in-situ, time-resolved monitoring of ion-film interactions at the nanoscale. As shown in Figure 3 – B, these interference patterns shown on top of the PEM surface can be observed using LIS as a spectral pattern where $\lambda_{max}$ sensitively responds to the thickness variances.

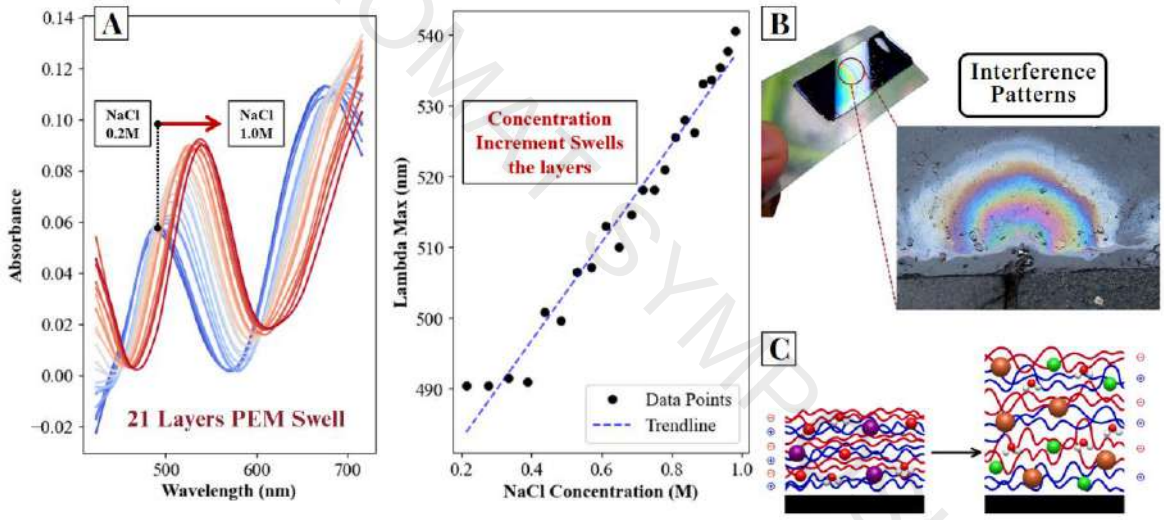


Figure 3: A - Red Shift Represented as Absorbance Spectral Shift as a Variable of Ionic Strength. B - Interference Patterns on Silicon Wafer Visible to the Naked Eye. C - Schematic Presentation of Polyelectrolyte Chain Swelling with Ion Replacement.

*B. In-situ ion transport and swelling of PEM (Red Shift)*

Internal ion transport is one of the subtle ways of understanding the dynamic characteristic of PEM when it comes to investigating the ionic strength effect on swelling. The absorbance spectra in Figure 4 – A demonstrate clear spectral red-shifts in λ max as salt concentration increases from 0.40 to 1.2 mol/dm³. Although KCl and NaCl both regularly cause spectrum shifts, KCl always causes a larger shift at every concentration point. This suggests that $K^+$

PROCEEDINGS FROM PPC & PETROMAT SYMPOSIUM 2025

ions cause more swelling in the PEM matrix than $Na^+$ ions because of their stronger hydration shell and stable equilibrium calculated using DFT calculations.

The increase in λ max, which can be accurately recorded in real time with LIS, indicates an increase in PEM thickness or refractive index because of ion uptake and matrix expansion. Figure 4 – B quantifies the swelling behavior by plotting λ max against salt concentration and calculating the slopes for NaCl and KCl. A more noticeable swelling response is confirmed by the steeper slope for KCl (74.53 nm/mol·dm$^{-3}$) as opposed to NaCl (59.86 nm/mol·dm$^{-3}$).

The way that ion-specific interactions affect the PEM structure is demonstrated by the growing gap ($\Delta\lambda_{max}$) between the two ion types over concentration ranges. This behavior emphasizes how crucial ion valency and hydration energy are in controlling PEM swelling, which is important information for developing sensitive coatings and sensors.

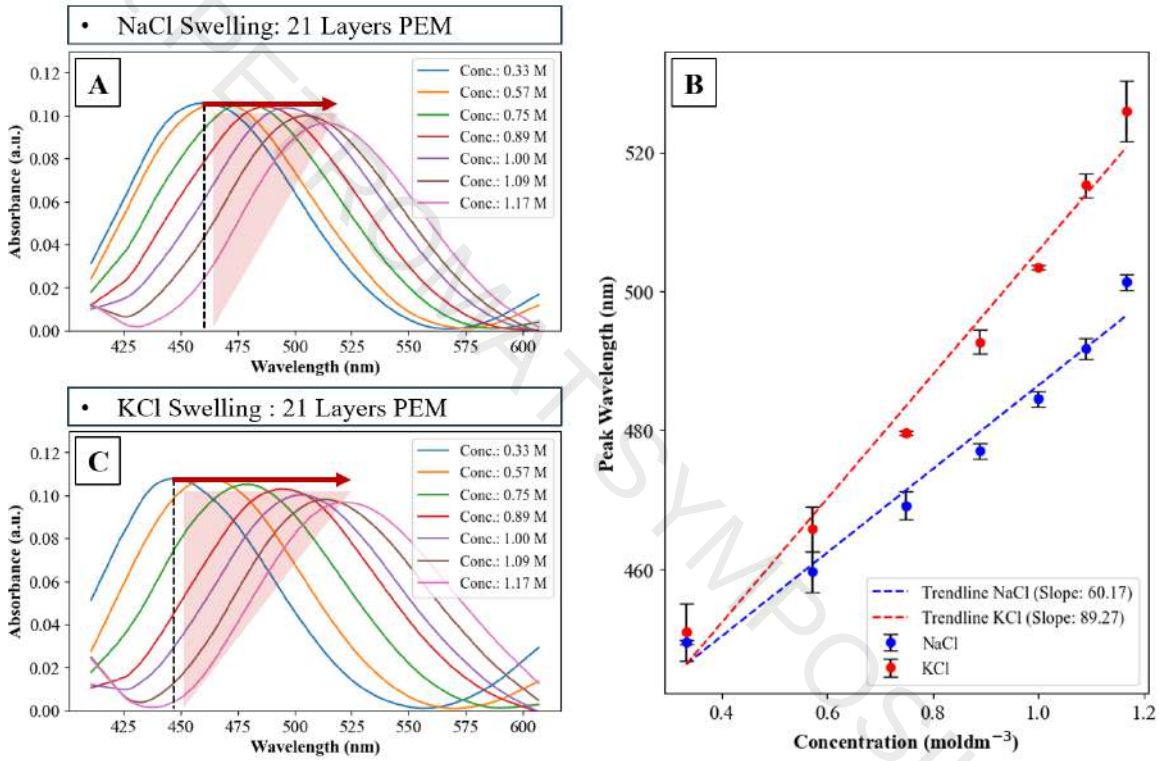


Figure 4: A, C- Spectral Patterns of Absorbance of KCl and NaCl under Different Concentration Brackets. B - λ max peak shift over concentration in KCl and NaCl (Gap of Delta λ max Study)

*C. Solvent induced contraction of PEM (Blue Shift)*

As shown in Figure 4, concentration of electrolytes increments results in the PEM layers swelling as it monitored in LIS with absorbance red shift. Similarly, the solvent induced shrinkage of PEM monitored as a blue shift of the absorbance peak in LIS in this section. The dehydration of PEM influenced by acetone triggers the thickness reduction or densification of PEM layers. 25 layered PEM shrinkage with acetone further monitored with LIS as shown in Figure 5. Figure 5 – A, blue triangle showed this inverse shift which denoted

as blue shift of absorbance peak, represents the shrinking ability of the acetone qualitatively with the help of shrinking pattern.

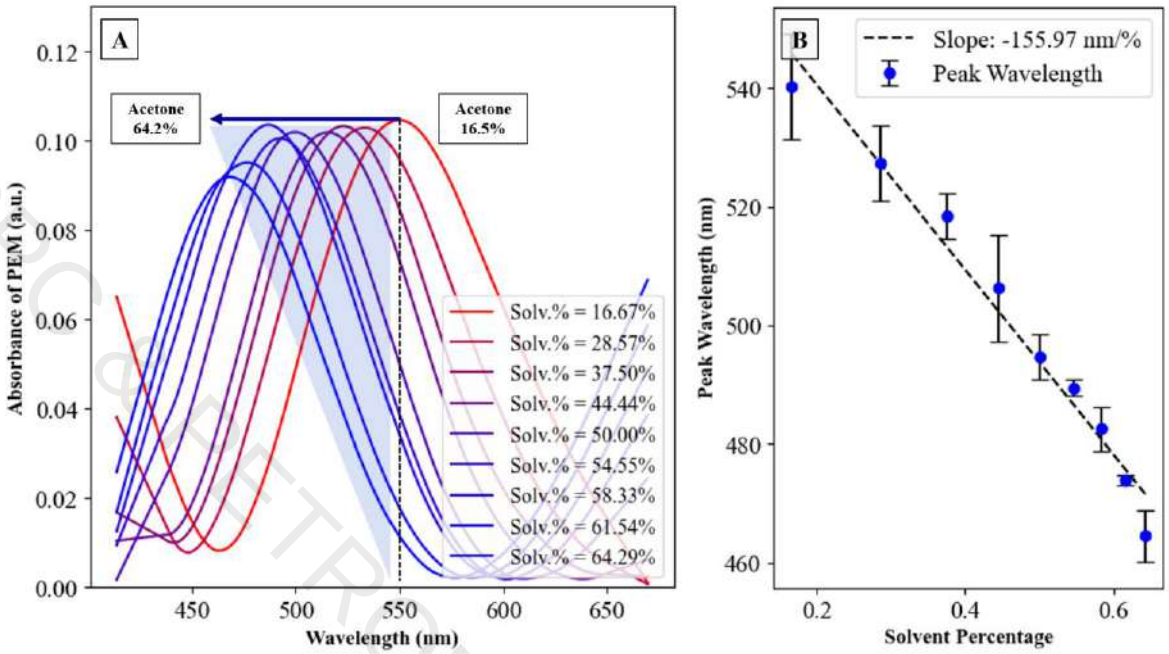


Figure 5: A - Spectral Blue Shift represented with LIS absorbance patterns under the effect of acetone. B - λ Max Shifts: Blue Shift vs Solvent Percentage

A significant blue shift in the absorbance spectra as the acetone percentage increases in the solvent mixture represents the solvent-induced contraction of PEM layers. The remaining water squeezing out from the membrane and drying it reveals this blue shift. As acetone content rises from ~17% to ~67%, λ max shifts progressively to shorter wavelengths (Figure 5 – A). This shift is likely due to solvent-induced dehydration or contraction of the PEM, reducing its effective thickness and altering its refractive index.
These blue shifts demonstrate the PEM's sensitivity to ionic environments but also to organic solvents, suggesting potential utility in organic solvent sensing or filtration membranes. The quantitative analysis can be carried out with λ max vs. solvent % plotted since this shows a direct relationship of swelling with the λ max shift derived from Beer – Lambert law (Figure 5 – B). Reliable swelling or contraction behavior is indicated by the constant slope and low error bars, highlighting LIS's potential as a strong instrument for real-time solvent–film interaction research. These kinds of insights can direct the creation of solvent-responsive PEM systems for separation technologies, microfluidics, or smart packaging.

## CONCLUSION

In conclusion, LIS makes it possible to monitor PEM swelling in real time, noninvasively, and with great sensitivity and accuracy. The structural alterations in the film brought on by ion penetration and hydration are immediately reflected in the observed optical shifts. This method provides a useful framework for researching the behavior of dynamic films and creating responsive materials for cutting-edge applications.

PPC & PETROMAT SYMPOSIUM 2025

## ACKNOWLEDGEMENT

I would like to express my deepest gratitude to the Petroleum & Petrochemical College, Chulalongkorn University, for providing me with invaluable knowledge and research opportunities. My sincere appreciation to the ASEAN & Non-ASEAN Scholarship and the 90th Anniversary of Chulalongkorn University Scholarship for their financial support.

## REFERENCES

**Dubas, S. T., & Schlenoff, J. B. (1999)**. Factors controlling the growth of polyelectrolyte multilayers. *Macromolecules*, *32*(24), 8153–8160. https://doi.org/10.1021/ma981927a

**Hegaard, F., & Thormann, E. (2023)**. Influence of Ionic Strength and Specific Ion Effects on Polyelectrolyte Multilayer Films with pH-Responsive Behavior. *Langmuir*, *39*(14), 5012–5020. https://doi.org/10.1021/acs.langmuir.2c03515

**Kastinen, T., Batys, P., Tolmachev, D., Laasonen, K., & Sammalkorpi, M. (2024).** Ion-Specific Effects on Ion and Polyelectrolyte Solvation. *ChemPhysChem*, *25*(15). https://doi.org/10.1002/cphc.202400244

**Khavani, M., Batys, P., Lalwani, S. M., Eneh, C. I., Leino, A., Lutkenhaus, J. L., & Sammalkorpi, M. (2022).** Effect of Ethanol and Urea as Solvent Additives on PSS-PDADMA Polyelectrolyte Complexation. *Macromolecules*, *55*(8), 3140–3150. https://doi.org/10.1021/acs.macromol.1c02533

**Konyalı, E., Cengiz, H. Y., Müftüler, A., & Deligöz, H. (2023).** Monitoring the salt stability and solvent swelling behavior of PAH-based polyelectrolyte multilayers by quartz crystal microbalance with dissipation. *Polymer Engineering and Science*, *63*(10), 3328–3342. https://doi.org/10.1002/pen.26447

PPC & PETROMAT SYMPOSIUM 2025

# Synthesis and Characterization of zeolite from pottery stone

Kedkaew Kanlai [a, *], Thanakorn Wasanapiarnpong [b], Apirat Theerapapvisetpong [b], Nithiwach Nawaukkaratharnant [a, b]

[a] Metallurgy and Materials Science Research Institute, Chulalongkorn University, Bangkok, 10330, Thailand
[b] Upcycled Materials from Industrial and Agricultural Wastes Research Unit, Department of Materials Science, Faculty of Science, Chulalongkorn University, Bangkok, 10330, Thailand

Keywords: Zeolite, Pottery stone, Alkali fusion process, $CO_2$ adsorption

## ABSTRACT

In Thailand, rhyolite stone which is usually called pottery stone, is found in northern and western area. It is mainly composed of silica and alumina so that it has an opportunity to be used as raw material for zeolite synthesis. Zeolite was successfully synthesized from pottery stone using alkali fusion process followed by crystallization process. Herein, the effect of weight ratios of pottery stone and sodium hydroxide on phase transformation after firing and the effect of hydrothermal time were investigated. The results indicated that the optimal weight ratio of pottery stone to sodium hydroxide for the alkali fusion process was 1 to 1.2, which effectively transformed crystalline phases in the raw material, such as quartz, kaolinite, and muscovite, into water-soluble phases. Moreover, zeolite X could be synthesized by pottery stone as confirmed by XRD after crystallization. The specific surface area and $CO_2$ adsorption capacity presented 706.70 $m^2/g$ and 17.45 wt%, respectively.

* **Kedkaew.k@chula.ac.th**

## INTRODUCTION

In Thailand, rhyolite stone which is usually called pottery stone, is found in northern and western area. It is mainly composed of more than 70% silica ($SiO_2$), with alumina ($Al_2O_3$) as a minor component (Coffman et al., 2015). Normally, pottery stone is utilized in ceramic industries such as sanitary ware, refractory materials, and insulators.

Zeolite is an aluminosilicates material with three-dimensional structure. It's composed of the networks of $[SiO_4]^{4-}$ and $[AlO_4]^{5-}$ tetrahedral sharing with oxygen atoms which contain alkali or alkali-earth metals residing within the pores of the structure (Khaleque et al., 2020, Eluwa et al., 2025). The structural type depends on the difference positive charge of the cations from neutralizing the negative charge on the lattice effect to porosity and pore size of zeolite (Jacobs et al., 2001). The zeolite exhibits high surface area, high porosity, and fast diffusion characteristics. These unique properties make them highly effective in various applications including adsorption (Xu et al., 2025), catalyst (Ávila et al., 2025, Mardiana et al., 2025), ion exchange (Ismail et al., 2010), and water treatment (Chi et al., 2025). Zeolite can be synthesized using various raw materials which are composed of $SiO_2$ and $Al_2O_3$ such as clay minerals and waste (Jiang et al., 2011, Sangita et al., 2016). Recent studies have reported the use of kaolin as raw material for zeolite synthesis. For instance, zeolite has been successfully synthesized from natural kaolin clay and sodium hydroxide via the

PPC & PETROMAT SYMPOSIUM 2025

fusion/hydrothermal method (Mokhtar et al., 2025). Additionally, low-grade kaolin containing muscovite and quartz impurities has been effectively utilized to synthesize zeolite by heating route, followed by hydrothermal crystallization (Fan et al., 2025). Moreover, zeolite synthesis requires adjusting the alkaline base ratio and reaction conditions of crystallization process such as solid/water ratio, temperature and aging and crystallization time (Qiang et al., 2019).

To enhance the value of pottery stone, using it as raw material for zeolite synthesis is interesting. The purpose of this study is to investigate the optimal ratio of pottery stone and sodium hydroxide and parameters for zeolite synthesis using alkaline fusion followed by crystallization method.

## EXPERIMENTAL

*A. Materials*

The pottery stone in this study was obtained from western area of Thailand. The chemical composition was shown in Table 1 and phase composition was presented in Fig. 1. The pottery stone is mainly composed of $SiO_2$ (69.19 wt%) and $Al_2O_3$ (16.86 wt%) with the phase of quartz, kaolinite, and muscovite. In alkali fusion process using NaOH 99% purity.

**Table 1** Chemical composition of pottery stone.

| Chemical composition | $SiO_2$ | $Al_2O_3$ | $Na_2O$ | $K_2O$ | $Fe_2O_3$ | Others | LOI |
|---|---|---|---|---|---|---|---|
| wt% | 69.19 | 16.86 | 0.05 | 2.39 | 1.97 | 1.95 | 7.60 |

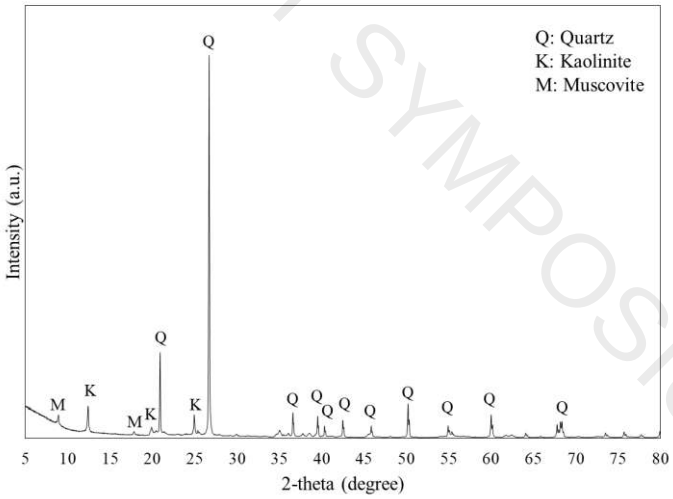


**Fig. 1.** XRD pattern of pottery stone.

*B. Zeolite synthesis*

The pottery stone, ground using vibratory disc mill, was dry mixed with NaOH in weight ratio of 1:0.8, 1:1.2, and 1:1.6 and then fused at 800 °C for 2 h. The fused powder was mixed with reverse osmosis (RO) water at weight ratio of 1:4, respectively. The dispersion was then stirred at room temperature for 1 h followed by heating at 90 °C in oil bath for 8, 12, and 24 h. The powder product was filtered with RO water until the pH reached 9 and was then dried at 100 °C overnight to obtain zeolite.

PPC & PETROMAT SYMPOSIUM 2025

*C. Characterizations*

Chemical composition of raw material examined by X-ray fluorescence (XRF, Rigaku ZSX Primus III+). Phase composition of raw material, fused material and product determined by X-ray diffraction (XRD, Bruker D8 Advance). The morphology examined by scanning electron microscopy (SEM, Hitachi SU3500). The specific surface area and $CO_2$ adsorption capacity measured by gas adsorption analyzer (Micromeritics 3Flex).

## RESULTS AND DISCUSSION

*A. Effect of pottery stone and NaOH ratios on phase transformation of alkaline fused product*

The XRD patterns of fused products with different pottery stone to NaOH ratios (1:0.8, 1:1.2 and 1:1.6) were shown in Fig. 2. The result indicates that the optimal weight ratio was 1:1.2 which the crystalline phases of the pottery stone which are quartz, kaolinite, and muscovite, were effectively transformed to sodium silicate and sodium aluminum silicate after fusing at 800 °C for 2 h. Therefore, this ratio is sufficient for preparing the fused product. Moreover, the soluble phases are suitable for zeolite synthesis process.

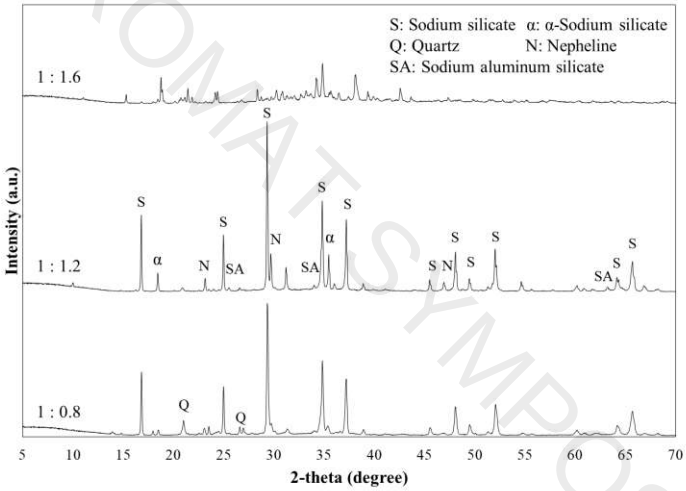


**Fig. 2.** XRD patterns of fused products.

*B. Effect of crystallization time*

The effect of crystallization time on phase formation of zeolite product was focused. The crystallization times at 90 °C were 8, 12, and 24 h. XRD patterns, as shown in Fig. 3, confirmed the formation of zeolite phases. The result shows that at 8 h, sodium aluminum silicate hydrate (PDF no. 00-047-0751), sodium aluminum silicate (PDF no. 00-048-0731) and small amount of zeolite X (PDF no. 00-012-0228) were detected. When the time was extended to 12 h, peaks of zeolite X (PDF no. 00-038-0237) were detected as the main phase and of the trace of zeolite P was observed. While the time was increased to 24 h, the intensity of the peaks of zeolite P increased, which influenced the surface area of the synthesized material. The result can be confirmed that the crystallization time has significant effect on zeolite formation.

PPC & PETROMAT SYMPOSIUM 2025

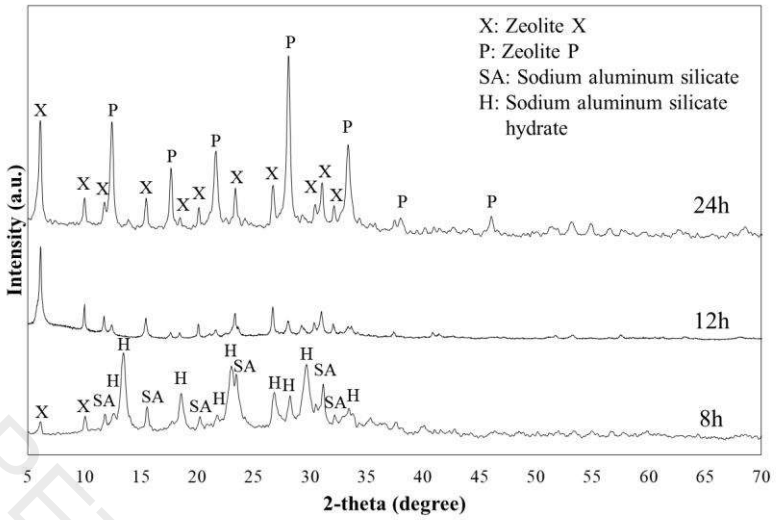


**Fig. 3.** XRD patterns of synthesized zeolite at different crystallization times.

The morphology of selected product, prepared at 90 °C for 12 h was presented in Fig. 4. From the SEM images, octahedral crystalline zeolite X particles with sizes below 4 μm can be observed, which appeared agglomerated. Furthermore, the synthesized zeolite exhibits a high specific surface area of 706.70 $m^2/g$ and a $CO_2$ adsorption capacity of 17.45 wt% as shown in Table 2. The result indicates its potential applicability in adsorption processes (Pérez-Botella et al., 2022).

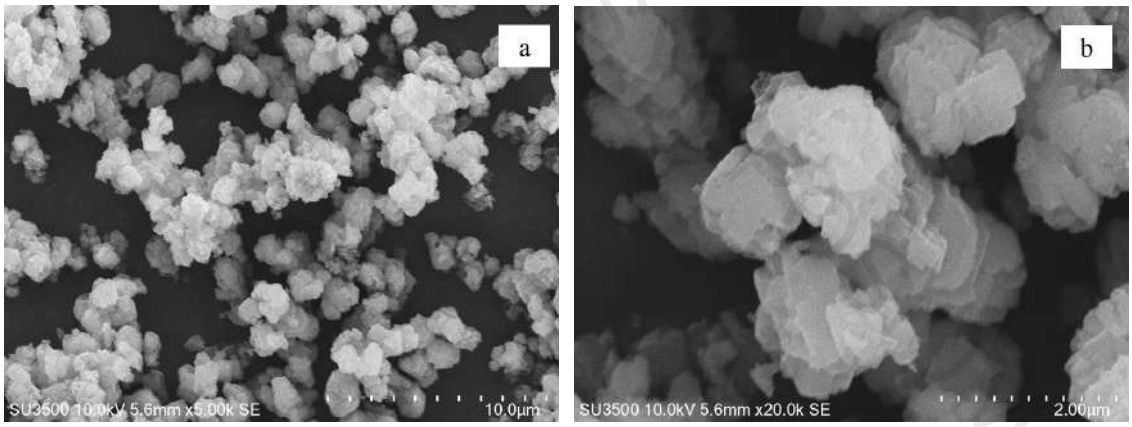


**Fig. 4.** SEM image of synthesized zeolite. a) X5,000 b) X20,000

**Table 2** Specific surface area and $CO_2$ adsorption of synthesized zeolite X.

| Properties | Value |
|---|---|
| Specific surface area ($m^2/g$) | 706.70 |
| $CO_2$ adsorption at 25 °C, 250 mmHg (wt%) | 17.45 |

## CONCLUSIONS

Zeolite was successfully synthesized from pottery stone using alkali fusion process followed by crystallization. The results obtained in this study can lead to the following conclusions:

- The ratio of pottery stone to NaOH significantly influences the phase transformation during the alkali fusion process. The optimal weight ratio of 1:1.2 results in the most effective conversion of crystalline phases into soluble phases at a fusing temperature of 800 °C for 2 h.
- Crystallization time has a significant effect on the phase composition of the synthesized zeolite. Zeolite X was successfully synthesized from pottery stone at 90 °C for 12h as confirmed by XRD. The specific surface area and $CO_2$ adsorption capacity were 706.70 $m^2/g$ and 17.45 wt%, respectively.

## ACKNOWLEDGEMENTS

This work was supported by Department of Primary Industries and Mines and Upcycled Materials from Industrial and Agricultural Wastes Research Unit, Department of Materials Science, Faculty of Science, Chulalongkorn University.

## REFERENCES

**Ávila, M. I., Alonso-Doncel, M. M., Cueto, J., Briones, L., Gómez-Pozuelo, G., Escola, J. M., Serrano, D. P., Peral, A. and Botas, J. A.** (2025). Production of high value-added phenolic compounds through lignin catalytic pyrolysis over ion-exchanged hierarchical ZSM-5 and Beta zeolites. *Catalysis Today*, **456**, 115343.

**Chi, S., Baik, Y., Oh, C., Kim, J.-C. and Choi, M.** (2025). Hydrophobic zeolites as efficient adsorbents for removing chloroform in drinking water. *Microporous and Mesoporous Materials*, **395**, 113690.

**Coffman, S. and Rasic, J. T.** (2015). Rhyolite characterization and distribution in central Alaska. *Journal of Archaeological Science*, **57**, 142-157.

**Eluwa, V. C., Kovo, A. S., Abdulkareem, A. S., Tijani, J. O. and Mustapha, S.** (2025). Hydrothermal synthesis of kaolin based zeolite A for use in the deodourisation of poultry litter. *Next Research*, **2 (3)**, 100443.

**Fan, J., Liu, X., Yang, M., Liu, M., Ma, Q., Fu, L., Min, X. and Huang, Z.** (2025). Synthesis of zeolite 4A from low-grade kaolin containing muscovite and quartz via ultrafast Joule heating route: A comparison with conventional calcination. *Applied Clay Science*, **275**, 107889.

**Ismail, A. A., Mohamed, R. M., Ibrahim, I. A., Kini, G. and Koopman, B.** (2010). Synthesis, optimization and characterization of zeolite A and its ion-exchange properties. *Colloids and Surfaces A: Physicochemical and Engineering Aspects*, **366 (1)**, 80-87.

**Jacobs, P., Flanigen, E. M., Jansen, J. and van Bekkum, H.** (2001). *Introduction to zeolite science and practice.*pp., Elsevier.

PPC & PETROMAT SYMPOSIUM 2025

**Jiang, J. L., Gu, X., Duan Mu, C. S., Du, W. G. and Wu, J.** (2011). Synthesis of Pure Zeolite X from Palygorskite Clay Using a Two-Stage Method. *Advanced Materials Research*, **236-238**, 767-770.

**Khaleque, A., Alam, M. M., Hoque, M., Mondal, S., Haider, J. B., Xu, B., Johir, M. A. H., Karmakar, A. K., Zhou, J. L., Ahmed, M. B. and Moni, M. A.** (2020). Zeolite synthesis from low-cost materials and environmental applications: A review. *Environmental Advances*, **2**, 100019.

**Mardiana, S., Kusnadi, A., Arcana, I. M., Ismunandar and Kadja, G. T. M.** (2025). Realizing mesoporous *MRE zeolites using polyethylene glycol and their catalytic evaluation in palm oil and polyethylene cracking. *Results in Chemistry*, **15**, 102244.

**Mokhtar, A., Abdelkrim, S., Hachemaoui, M., Boukoussa, B., Djelad, A., Sassi, M., Issam, I., Patole, S. P., Viscusi, G. and Abboud, M.** (2025). Optimization of zeolite LTA formation from kaolin using fusion/hydrothermal method: Crystallization parameters and Box-Behnken experimental design. *Applied Clay Science*, **275**, 107877.

**Pérez-Botella, E., Valencia, S. and Rey, F.** (2022). Zeolites in Adsorption Processes: State of the Art and Future Prospects. *Chemical Reviews*, **122 (24)**, 17647-17695.

**Qiang, Z., Shen, X., Guo, M., Cheng, F. and Zhang, M.** (2019). A simple hydrothermal synthesis of zeolite X from bauxite tailings for highly efficient adsorbing CO2 at room temperature. *Microporous and Mesoporous Materials*, **287**, 77-84.

**Sangita, K., Prasad, B. and Udayabhanu, G.** (2016). Synthesis of Zeolite from Waste Fly Ash by Using Different Methods. *Asian Journal of Chemistry*, **28 (7)**, 1435-1439.

**Xu, Q., Lu, J., Zhou, Z. and Jin, Y.** (2025). FAU zeolites from coal/rice husk co-combustion ash (co-ash) for CO2 adsorption: Synthesis, characterization, adsorption and regeneration performance. *Separation and Purification Technology*, **369**, 133147.

PROCEEDINGS PPC & PETROMAT SYMPOSIUM 2025

# ARAGONITE PLATE CALCIUM CARBONATE FROM GREEN MUSSEL SHELLS AS A FILLER IN POLY(LACTIC ACID) FOR 3D PRINTING APPLICATIONS

*Duangduean KINGPHAN[a], Chutiparn LERTVACHIRAPAIBOON[b], Prompong PIENPINIJTHAM[c], Sanong EKGASIT*[c]*

[a]Petrochemical and Polymer Science Program, Faculty of Science, Chulalongkorn University Bangkok 10330, Thailand
[b]National Nanotechnology Center, National Science and Technology Development Agency Pathum Thani 12120, Thailand
[c]Department of Chemistry, Faculty of Science, Chulalongkorn University Bangkok 10330, Thailand

Keywords: Green mussel shell, Calcium Carbonate ($CaCO_3$), Aragonite plate, Poly(lactic acid, 3D printing filament

## ABSTRACT

Plate-shaped calcium carbonate ($CaCO_3$) with aragonite polymorph was derived from green mussel shells. This $CaCO_3$ was employed as a filler in poly(lactic acid), PLA, before utilizing as bio-polymer composite filaments. The mechanical and thermal properties of the PLA/$CaCO_3$ composites were examined. The incorporation of $CaCO_3$ led to an increase in the glass transition temperature (Tg) compared to neat PLA. A cold crystallization temperature (Tcc) observed only in the PLA/$CaCO_3$ composites, indicating that the addition of $CaCO_3$ alters the crystallization behavior of PLA. Tensile strength improved with $CaCO_3$ content up to 5 wt% and declined with more filler loading. PLA/$CaCO_3$ composites were successfully extruded into filaments with a standard diameter of 1.79 mm, suitable for common 3D printing applications. This approach offers a cost-effective alternative filament for educational and training purposes.

**Corresponding author e-mail: sanong.e@chula.ac.th**

## INTRODUCTION

Additive manufacturing (AM), commonly known as 3D printing is a technique that fabricates objects by depositing materials layer by layer. The technique enables the creation of complex shapes directly through customizable computer-aided design (CAD) models, eliminating the needs for molds or tooling. Among the various AM processes, fused deposition modeling (FDM) which employs thermoplastic filament is the most accessible due to its simplicity and affordability. Regarding this, poly(lactic acid) (PLA) is one of the most widely used filament in FDM systems because of its low melting temperature, excellent dimensional stability, and ease of processing. Moreover, its biodegradability, relatively low warping during printing and lower toxic fumes emission compared to other thermoplastics like ABS, contributes to PLA popularity in educational and home-use applications. However, PLA suffers from low mechanical properties; therefore, incorporation of filler materials are particularly beneficial due to their potential to enhance PLA properties as demonstrated in previous studies with both organic and inorganic fillers such as talc [1], organoclay [2], alumina [3], and titanium dioxide [4].

Among the possible materials used in polymer applications, calcium carbonate ($CaCO_3$) is typically used as an additive filler in polymers due to its low toxicity, cost-

PPC & PETROMAT SYMPOSIUM 2025

effective, and biocompatibility. For example, $CaCO_3$ is used in polyvinyl chloride (PVC) to improve flexibility and rigidity[5] or in polypropylene (PP) and polyethylene (PE) to enhance stiffness and reduce shrinkage [6]. Although the use of synthetic $CaCO_3$ in thermoplastic has been widely reported, few have explored the use of Bio-$CaCO_3$ derived from natural sources such as marine mollusk shells, which typically contain aragonite, a polymorph of $CaCO_3$ with a distinctive plate-like morphology. Green mussel (Perna viridis) aquaculture, especially along the Gulf of Thailand, plays a vital role in the local economy due to its high yield, rapid growth, and low farming costs. Thailand produces approximately 70,000 tons of green mussels annually, with the shell composed of about 60% $CaCO_3$, making up a large portion of its mass. Previous studies have shown that green mussel shells consist of stratified layers of pseudo-hexagonal aragonite plates, each measuring 200–400 nm in thickness and 3–5 μm in lateral size. These plates are bonded together in a brick-and-mortar structure through natural organic binders such as proteins, lipids, and polysaccharides [7, 8].

In this study, the possibility of using micro-$CaCO_3$ with aragonite polymorph produced from Green mussel shell as bio-filler material for polylactic acid (PLA) was demonstrated. $CaCO_3$ was compounded together with PLA before extrusion to produce PLA/$CaCO_3$ filament for use in FDM-based 3D printing system. This approach has the potential for cost-effective filament production, particularly for educational and training applications. Moreover, by repurposing green mussel shells waste and utilizing biodegradable PLA, this work contributes to reducing environmental impacts from waste disposal while promoting sustainable use of resources and responsible material consumption.

## EXPERIMENTAL

### *A. Materials*

Raw green mussel shells were obtained from Laem Yai district, Samut Songkram Province, Thailand. Potassium hydroxide (KOH), 30%wt Hydrogen peroxide ($H_2O_2$) were obtained from Merck. Poly(lactic acid) (PLA) pellets (grade 4043D) with Melt Flow Index (MFI) of 6 g/10 min (210 °C, 2.16 kg) was obtained from NatureWorks LLC, USA.

### *B. $CaCO_3$ Preparation from Green Mussel Shells*

Raw green mussel shells were first cleaned with tap water to remove residual tissue and surface contaminants, then air-dried at ambient temperature. The dried shells were immersed in 1 M KOH for two weeks to eliminate the green organic layer on the outer surface before thoroughly washed with water and dried again. The shells were then subjected to heat treatment in an oven at 300 °C for 1 hour then soaked in 30 wt% $H_2O_2$ to remove any residual organic matter. Finally, the shells were then ground and sieved through a 300-mesh sieve (54 μm) to be used as filler in poly(lactic acid) (PLA) composites. The morphology of the obtained $CaCO_3$ particles was observed by a scanning electron microscope (SEM, JEOL, JSM-6510A) with an acceleration 15 kV.

### *C. Composite Preparation*

PLA pellets and $CaCO_3$ powder were thoroughly dried before compounding. The materials were first mixed using an internal mixer at 180 °C and 60 rpm to produce a masterbatch containing 30 wt% $CaCO_3$. This masterbatch was mixed with virgin PLA to

PROCEEDINGS OF PPC & PETROMAT SYMPOSIUM 2025

obtain final filler contents of 3, 5, 7, and 10 wt%. The mixtures were extruded using a single-screw extruder (ThermoHaake Polydrive) with a temperature profile of 180°C, 190°C, 200°C, 200°C, and 190°C from feed zone to die. Filament extrusion conditions were optimised by adjusting the extrusion and spooler speeds to maintain a consistent diameter. Filament dimensions were measured at multiple angles using digital callipers to ensure uniformity. The PLA/$CaCO_3$ composite functional group were analyzed using the Attenuated total reflection–Fourier transform infrared spectroscopy (ATR–FTIR, Thermo Scientific Nicolet iS5) in a range of 400-4000 $cm^{-1}$ with a resolution of ±16 $cm^{-1}$. Thermal properties were investigated using differential scanning calorimetry (DSC, Perkin Elmer, Pyris 1) under a heat flow rate 15 °C/min. The sample (~10 mg) was loaded into a standard alumina pan. Tensile performance, including tensile strength and elongation at break of neat PLA and PLA/$CaCO_3$ composite were measured at room temperature using a universal testing machine (Instron 5567) following ASTM D638-22 type IV specimens, and each condition was tested five times.

*D. 3D printing*

A commercial FDM-based 3D printer (Creality, Ender-7) was employed for the printing process. In this study, the developed PLA/$CaCO_3$ composite filament was extruded and deposited layer by layer through the nozzle of the 3D printer with specimen dimensions conforming to ASTM D638-22 type IV dog bone specimen. Process parameters used for printing by the FDM method: Bed temperature 55 °C, Nozzle temperature 215 °C, Printing speed 60 mm/s, Layer height 300 µm, and lay down pattern −45°/+45°.

## RESULTS AND DISCUSSION

*A. Characterization of $CaCO_3$ derives from green mussel shells.*

SEM image and size distribution of $CaCO_3$ filler derived from green mussel shells are shown in Figure 1. The $CaCO_3$ particles exhibit a plate-like morphology with a smooth surface, consistent with aragonite crystals typically found in bivalve shells such as abalone and oyster shell. The particle size distribution analysis (n = 300) indicated that the obtained $CaCO_3$ possesses a narrow size distribution with an average bisector length of 3.72 µm.

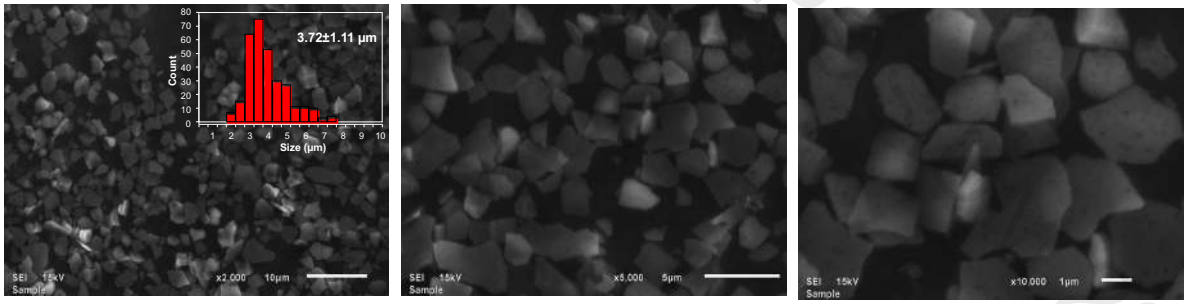


Figure 1. SEM images of $CaCO_3$ derived from green mussel shells at varying magnification.

*B. Characterization of PLA/$CaCO_3$ Composite*

Figure 2a show the ATR–FTIR spectra of the obtained $CaCO_3$ along with the PLA/$CaCO_3$ composites at various $CaCO_3$ contents. According to the spectra, the $CaCO_3$ derived from green mussel shells exhibited characteristic peaks of aragonite crystal form at 699 and 712 $cm^{-1,}$ which correspond to -$CO_3$ in-plane bending ($\upsilon_4$) vibration. In addition, a strong band at 1444 $cm^{-1}$ corresponding to -$CO_3$ Asymmetric stretching ($\upsilon_3$) and 858, 1082 $cm^{-1}$

relative to -$CO_3$ out-of-plane bending ($\upsilon_2$), and -$CO_3$ symmetric stretching ($\upsilon_1$) respectively, can also be observed. As for neat PLA, the sample exhibits a strong C=O stretching vibration peak at wavenumbers of 1746 $cm^{-1}$ along with 1181, 1085 $cm^{-1,}$ attributed to the -C-O stretching of the ether bond. Each PLA/$CaCO_3$ composite didn't present an obvious shift of characteristic peaks of PLA, indicating no chemical interaction between PLA and $CaCO_3$.

Next, DSC was performed to evaluate the effect of $CaCO_3$ particles on the thermal properties of PLA. The DSC thermograms of neat PLA and PLA/$CaCO_3$ composites with different filler contents are shown in Figure 2b with the data summarized in Table 1. It can be observed that the glass transition temperature ($T_g$) slightly increases as a function of $CaCO_3$ content from 59 °C of neat PLA up to 62.7 °C at 10 %wt $CaCO_3$ due to the filler restricting the movement of polymer chains. While cold crystallization temperature (Tcc) of PLA present $CaCO_3$ particles appear the cold crystallization peak indicated that the filler facilitates earlier crystallite formation contribute to increase overall crystallinity. A slight reduction in overall melting temperature ($T_m$) was also observed compared to neat PLA. Neat PLA is primarily amorphous, which shows a single endothermic melting peak. On the other hand, PLA/$CaCO_3$ composite displayed two distinct peaks, indicating increase in the PLA crystallinity caused by $CaCO_3$ particles. This behavior is attributed to the fusion of pre-existing crystals formed during processing with the α- and α′-crystals developed during cold crystallization, leading to overlapping melting transitions[9].

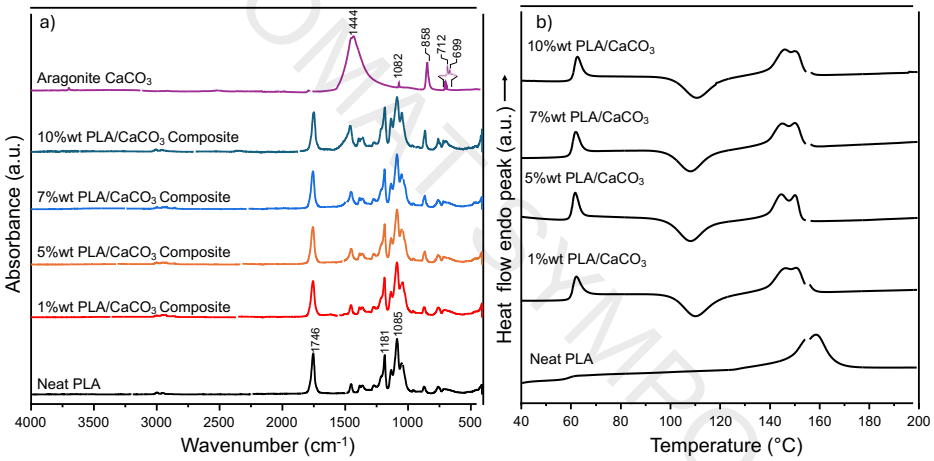


Figure 2. a) ATR-FTIR spectra of $CaCO_3$ and PLA/$CaCO_3$ composite at various contents, and b) DSC curves of neat PLA and PLA/$CaCO_3$ composite.

**Table 1** Thermal properties as measured by DSC of PLA/$CaCO_3$ composites. The table indicated the glass transition temperature (Tg), crystallization temperature (Tcc), and melting temperature (Tm) values for each sample.

| Sample | $T_g$ (°C) | $T_{cc}$ (°C) | $T_{m1}$ (°C) | $T_{m2}$ (°C) |
|---|---|---|---|---|
| Neat PLA | 59.0 | - | 159.0 | - |
| 1%wt PLA/$CaCO_3$ | 61.3 | 111.5 | 149.0 | 152.6 |
| 5%wt PLA/$CaCO_3$ | 59.8 | 109.2 | 146.5 | 152.5 |
| 7%wt PLA/$CaCO_3$ | 59.8 | 109.1 | 148.0 | 152.2 |
| 10%wt PLA/$CaCO_3$ | 62.7 | 111.5 | 147.7 | 151.1 |

PROCEEDINGS PPC & PETROMAT SYMPOSIUM 2025

The filament produced from PLA with 5 wt% $CaCO_3$ demonstrated a uniform cylindrical shape with a relatively consistent diameter of 1.79 mm, maintained within a tolerance of 0.05 mm, as shown in Figure 3a. The surface appeared smooth, indicating the uniform dispersion of $CaCO_3$ particles throughout the PLA. Dog-bone specimens printed from the filament displayed consistent geometry and smooth edges as shown in Figure 3b, confirming that the PLA/$CaCO_3$ composite filament was compatible with FDM printing and produced 3D objects without visible defects.

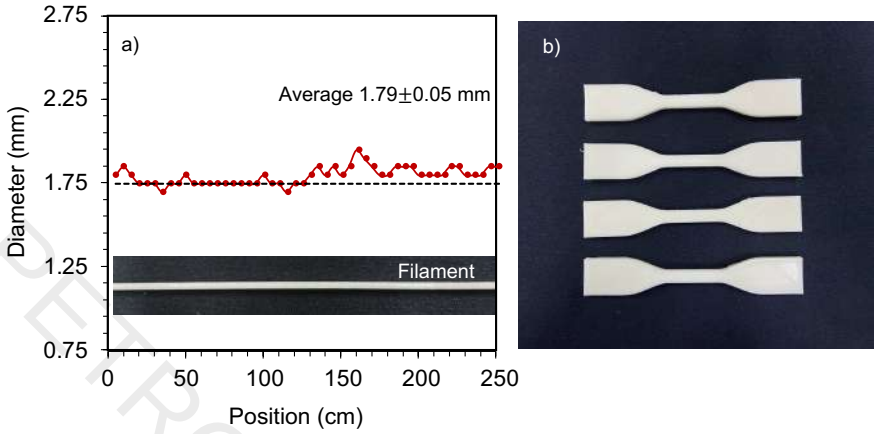


Figure 3. (a) Diameter profile of 5 wt% PLA/$CaCO_3$ composite filament along a 250 cm length. The inset shows the resulting composite filament, and (b) printed dog bone specimens via FDM printing.

The tensile properties of PLA/$CaCO_3$ composites are shown in Figure 4. A slight increase in tensile strength was observed at 1 %wt and 5 %wt $CaCO_3$ loading, which can be attributed to the better interfacial interaction between the filler and PLA at low concentration. However, $CaCO_3$ loading up to 7 %wt results in a decrease in tensile strength due to poor interfacial adhesion and filler agglomeration, which create stress concentration points. However, elongation at break presents a significant decrease compared to neat PLA. This reduction is attributed to the restricted mobility of polymer chains under plastic deformation caused by the presence of rigid filler particles.

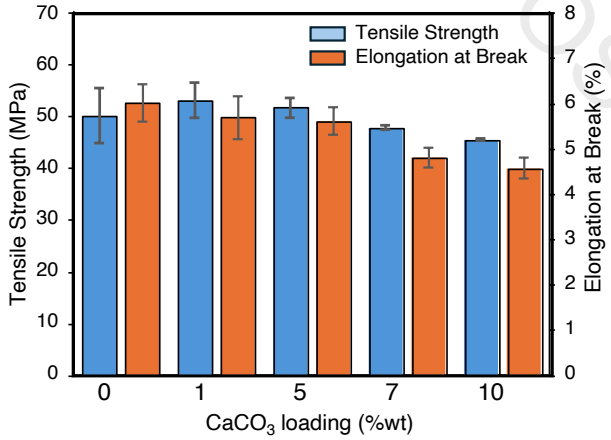


Figure 4. The Tensile performance of PLA/$CaCO_3$ composites with various contents of $CaCO_3$ shows the mechanical performance of the composite compared with virgin PLA.

PPC & PETROMAT SYMPOSIUM 2025

## CONCLUSIONS

In summary, the $CaCO_3$ derived from green mussel shells with a plate-like aragonite morphology was used as a bio–filler in the composite. When combined with a PLA matrix, $CaCO_3$ acted as a nucleating agent, as evidenced by a shift in cold crystallization temperature and a distinct melting peak. Mechanical testing revealed that moderate filler loadings (1–5 wt%) maintained or slightly improved tensile strength, while higher contents reduced ductility due to limited polymer chain mobility. The extruded filament exhibited a consistent diameter of $1.79 \pm 0.05$ mm and a smooth surface, supporting stable extrusion via FDM printing. Overall, this study demonstrates promising bio–filler from mussel shell-derived $CaCO_3$, and sustained PLA–based FDM filaments.

## ACKNOWLEDGEMENTS

The author would like to thank the Petrochemistry and Polymer Science Program, Faculty of Science, Chulalongkorn University, for the scholarship throughout this research.

## REFERENCES

1. Petchwattana, N., S. Covavisaruch, and S. Petthai, *Influence of talc particle size and content on crystallization behavior, mechanical properties and morphology of poly(lactic acid).* Polymer Bulletin, 2014. **71**(8): p. 1947-1959.
2. Coppola, B., et al., *3D Printing of PLA/clay Nanocomposites: Influence of Printing Temperature on Printed Samples Properties.* Materials, 2018. **11**(10): p. 1947.
3. Lule, Z. and J. Kim, *Nonisothermal Crystallization of Surface-Treated Alumina and Aluminum Nitride-Filled Polylactic Acid Hybrid Composites.* Polymers, 2019. **11**(6): p. 1077.
4. Petchwattana, N. and B. Narupai, *Synergistic Effect of Talc and Titanium Dioxide on Poly(lactic acid) Crystallization: An Investigation on the Injection Molding Cycle Time Reduction.* Journal of Polymers and the Environment, 2019. **27**(4): p. 837-846.
5. Lin, H., Y.-b. Dong, and L.-y. Jiang, *Preparation of calcium carbonate particles coated with titanium dioxide.* International Journal of Minerals, Metallurgy and Materials, 2009. **16**(5): p. 592-597.
6. Awan, M.O., et al., *Development of HDPE composites with improved mechanical properties using calcium carbonate and NanoClay.* Physica B: Condensed Matter, 2021. **606**: p. 412568.
7. Matthews, S. and A. Asadov, *Plasma Spraying of CaCO3 Coatings from Oyster and Mussel Shell.* Journal of Thermal Spray Technology, 2020. **29**(5): p. 1144-1171.
8. Lertvachirapaiboon, C., et al., *Selective colors reflection from stratified aragonite calcium carbonate plates of mollusk shells.* J Struct Biol, 2015. **191**(2): p. 184-9.
9. Deetuam, C., et al., *Isothermal cold crystallization kinetics and properties of thermoformed poly(lactic acid) composites: effects of talc, calcium carbonate, cassava starch and silane coupling agents.* Iranian Polymer Journal, 2020. **29**(2): p. 103-116.

PPC & PETROMAT SYMPOSIUM 2025

# DEVELOPMENT OF COPPER NANOPARTICLES EMBEDDED POROUS POLYVINYL CHLORIDE MEMBRANES FOR HEXAVALENT CHROMIUM REMOVAL FROM WASTEWATER

*Thushani Dilandika Senanayake W.G*[a], *Jitima Preechawong* [a] *Jirasuta Chungprempree*[a], *Aung Kyaw Moe*[a], *Manit Nithitanakul** [a]

[a] The Petroleum and Petrochemical College, Chulalongkorn University, Bangkok, Thailand

Copper nanoparticles, PVC nanocomposite membrane, Non-solvent induced phase separation

## ABSTRACT

Hexavalent chromium [Cr(VI)] is a highly toxic heavy metal commonly found in industrial wastewater, posing significant environmental and public health risks. This study presents the development of a porous polyvinyl chloride (PVC) membrane incorporated with copper nanoparticles (CuNPs) for the effective removal of Cr(VI) from wastewater. Non-solvent induced phase separation (NIPS) technique was used to fabricate the membranes. Various DMAc/water gelation bath compositions were investigated to optimize pore structure and minimize Cu leaching. Scanning electron microscope (SEM) analysis showed that 40/60 DMAc/water bath composition resulted in the most uniform porous morphology which is suitable for adsorption applications. Energy Dispersive X-ray (EDX) analysis confirmed improved Cu retention on both the top and bottom membrane surfaces under this condition. The successful incorporation of CuNPs into the membrane matrix was further validated by X-ray diffraction (XRD). Contact angle measurements demonstrated enhanced hydrophilicity with CuNPs content. Cr(VI) adsorption showed that CuNPs incorporation significantly improved removal efficiency. The findings suggest that incorporating CuNPs into porous PVC membranes offer promising potential for Cr(VI) remediation in wastewater treatment applications.

***manit.n@chula.ac.th**

## INTRODUCTION

One of the most hazardous and carcinogenic heavy metals found in wastewater from the metallurgical, textile dyeing, leather tanning, and electroplating industries is hexavalent chromium [Cr(VI)]. Its high solubility and mobility in water make it a serious environmental hazard by contaminating groundwater and drinking water sources. Cr(VI) exposure poses significant health risks, including respiratory issues, liver and kidney damage, and cancer. Due to these dangers, the World Health Organization (WHO) has set strict limits on Cr(VI) levels in drinking water [1], causing the need for efficient and sustainable removal technologies.

Earlier, conventional Cr(VI) removal methods such as chemical precipitation, ion exchange, adsorption, and membrane filtration have been used [2]. Chemical methods are effective, yet often involve high costs and generate sludge, leading to secondary pollution. Adsorbents like activated carbon and metal oxides show promise but face regeneration and disposal challenges [3]. Membrane-based techniques are gaining attention due to their

PPC & PETROMAT SYMPOSIUM 2025

selective removal capabilities and reduced secondary waste. However, membrane performance relies heavily on material properties and structure. Porous polymeric membranes are particularly effective for Cr(VI) removal as they combine adsorption and filtration functions. Their performance is influenced by porosity, surface chemistry, and the incorporation of active materials. The non-solvent induced phase separation (NIPS) method can be recognized as a widely used technique to produce membranes with controlled pore structures [4]. Metal nanoparticles, especially copper (Cu) and iron (Fe), have shown excellent potential for Cr(VI) removal due to their high surface reactivity and reducing ability. Cu nanoparticles can reduce Cr(VI) to the less toxic Cr(III) form and enhance removal of Cr from water [5]. However, possible challenges like nanoparticle stability and leaching in aqueous environments must be addressed. Polyvinyl chloride (PVC) is a durable, chemically resistant, and also cost-effective polymer, which is suitable for NIPS-based membrane fabrication. Incorporating Cu nanoparticles into PVC membranes can enhance Cr(VI) removal while maintaining mechanical and chemical stability.

Several studies have explored CuNPs incorporated PVC membranes for Cr(VI) removal. Yet, key performance factors, such as nanoparticle concentration, membrane porosity, and stability, remain underexplored. The influence of water parameters like pH and metal ion concentration on removal efficiency also needs to be investigated. This study focuses on the preparation of a CuNPs incorporated PVC membrane via NIPS for Cr(VI) removal from wastewater. Zero-valent CuNPs will act as reducing agents. The effects of pH, initial Cr(VI) concentration and CuNPs content on the Cr(VI) uptake capacity were investigated. Also, the impact of gelation bath composition on membrane porosity were examined. Membrane characterization included adsorption behavior, morphology, porosity, pore size, mechanical properties, and hydrophilicity were also studied.

## EXPERIMENTAL

### *A. Preparation of CuNP colloid*

CuNPs were prepared using $CuCl_2$ as the metal precursor. PVP (polyvinylpyrrolidone) and $NaBH_4$ were used as the reducing agent and capping agent for the nanoparticles, respectively. $NaBH_4$ was dissolved in DMF, whereas $CuCl_2$ and PVP were dissolved in DMAc. While stirring at 1000 rpm, the $NaBH_4$ solution was gradually added dropwise to the $CuCl_2$ and PVP solutions. To slow down the oxidation of CuNP, the reaction was carried out in an ice bath. After adding all the $NaBH_4$ solution, the mixture was left for an hour to make sure the reaction had finished.

### *B. Membrane Preparation*

Porous PVC film membranes were prepared using the NIPS technique. PVC powder was dissolved in DMAc to create a uniform casting solution. To guarantee the complete dissolution of PVC, the mixture was constantly agitated for two hours at 90 °C at 250 rpm. Then the prepared CuNP-DMAc colloid was added to the PVC-DMAc solution. It was agitated at 250 rpm and 60°C for about 15 minutes. After an even mixture was obtained, the solution was allowed to stand for ten minutes to eliminate any air bubbles. A doctor's blade was used to evenly cast the solution onto a sterilized glass surface at a thickness of 200 μm. Next, the casted film was immediately immersed in a gelation bath and left for an

PPC & PETROMAT SYMPOSIUM 2025

hour. To get rid of any water-soluble contaminants, the membrane was then extensively rinsed with DI water [6].

*C. Adsorption Study*

2.8288 grams of $K_2Cr_2O_7$ were dissolved in 1 L of DI water to prepare the standard stock solution of Cr(VI) ions (1000 ppm). To achieve the required concentration, this stock solution was diluted with DI water and used in the adsorption tests. For the adsorption tests, 1 cm*1 cm film pieces from samples were immersed in 10 ml of working standard solution. The solutions were agitated at room temperature at 400 rpm for 24 hours. Following the removal of the film samples from the solutions, the remaining Cr(VI) ions were examined using UV-VIS at a wavelength of 354 nm. The tests were carried out to investigate the effects of pH, initial Cr(VI) concentration, and CuNP content.

The amount of Cr(VI) adsorbed on the membrane was calculated as,

$$\text{Adsorbed Cr(VI)} = \frac{(C_0 - C_1) \times V}{m}$$

where, $C_0$ and $C_1$ are the Cr(VI) concentration before and after the adsorption, respectively, V is the volume of the Cr(VI) solution and m is the weight of the membrane sample.

## RESULTS AND DISCUSSION

*A. Morphology of prepared films*

Figure 1 show SEM cross-sectional images of membranes prepared under different conditions. Figure 1(a) demonstrated that the morphology of channels and voids was significantly influenced by the gelation bath composition. As the solvent (DMAc) content in the bath increased, both the number and size of pores increased, up to 40 wt% DMAc. However, at 60 wt%, the number of visible pores sharply decreased. This behavior was attributed to changes in the solvent–non-solvent exchange rate. Higher DMAc content slowed down water diffusion into the polymer solution, resulting in delayed demixing and fewer pores. According to Figure 1(b), with 1 wt% CuNPs, the membrane exhibited a dense structure with few visible pores, indicating a slow exchange rate and delayed phase separation. At 4 wt%, the membranes showed extensive finger-like macro-voids and open porosity. This progression from dense to highly porous morphology indicated that CuNPs influenced the kinetics and thermodynamics of membrane formation, potentially acting as pore formers and modifying the phase separation behavior.

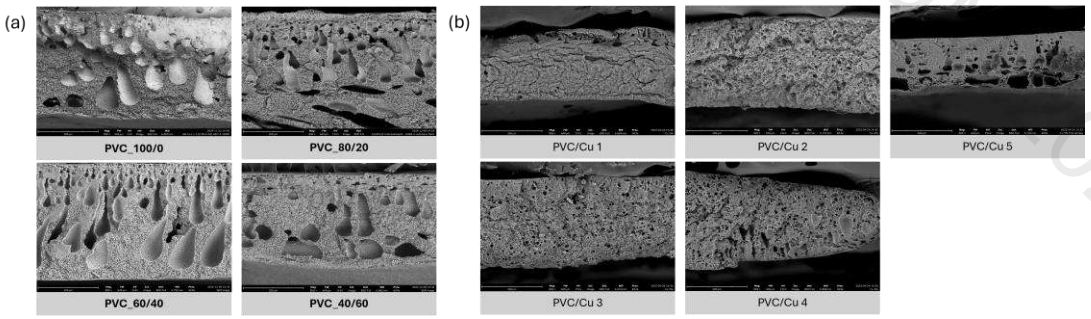


Figure 1: SEM images of cross section of film membranes (a) water/DMAc gelation bath ratios PVC_100/0, PVC_80/20, PVC_60/40, PVC_40/60 (b) CuNP contents PVC/Cu 1 (1 wt%), PVC/Cu 2 (2 wt%), PVC/Cu 3 (3 wt%), PVC/Cu 4 (4wt%), and PVC/Cu 5 (5 wt%).

PPC & PETROMAT SYMPOSIUM 2025

*B. EDX Analysis*

A key challenge in incorporating CuNPs into membranes was preventing their leaching during immersion in the gelation bath [7]. Different water/DMAc ratios were tested to identify conditions minimizing Cu leaching. As shown in Figure 2, across all bath compositions, the bottom surface retained more Cu, suggesting that leaching was more prominent from the top surface. EDX mapping images showed that the 60/40 (water/DMAc) ratio exhibited the highest Cu retention. This was attributed to a moderated solvent–non-solvent exchange rate. Even under optimized conditions, some Cu leaching continued as Cu loading increased from 1 to 5 wt%. Figure 3 shows that 2 wt% Cu loading resulted in the highest retention, with 3.43% and 5.61% atomic wt% on the top and bottom surfaces, respectively. At higher loadings, surface Cu content decreased due to insufficient surface trapping during phase inversion. According to Figure 3, 60/40 (water/DMAc) gelation bath composition was identified as the optimized composition for film preparation.

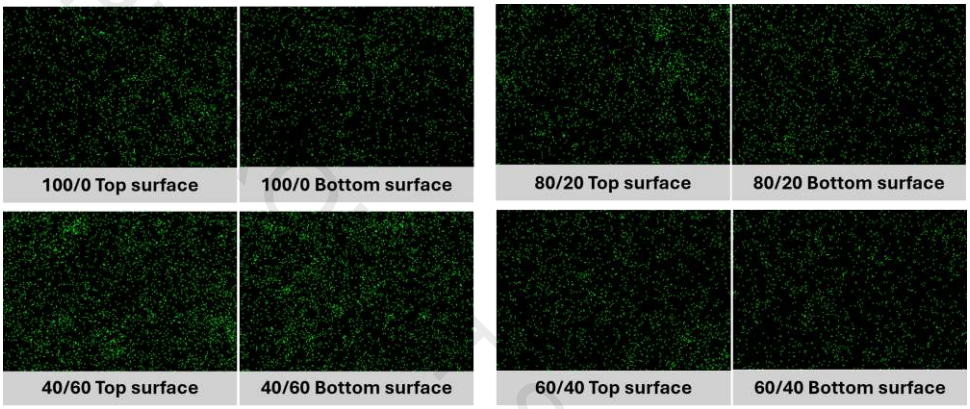


Figure 2: EDX mapping of film membranes in different water/DMAc gelation bath ratios PVC_100/0, PVC_80/20, PVC_60/40, PVC_40/60.

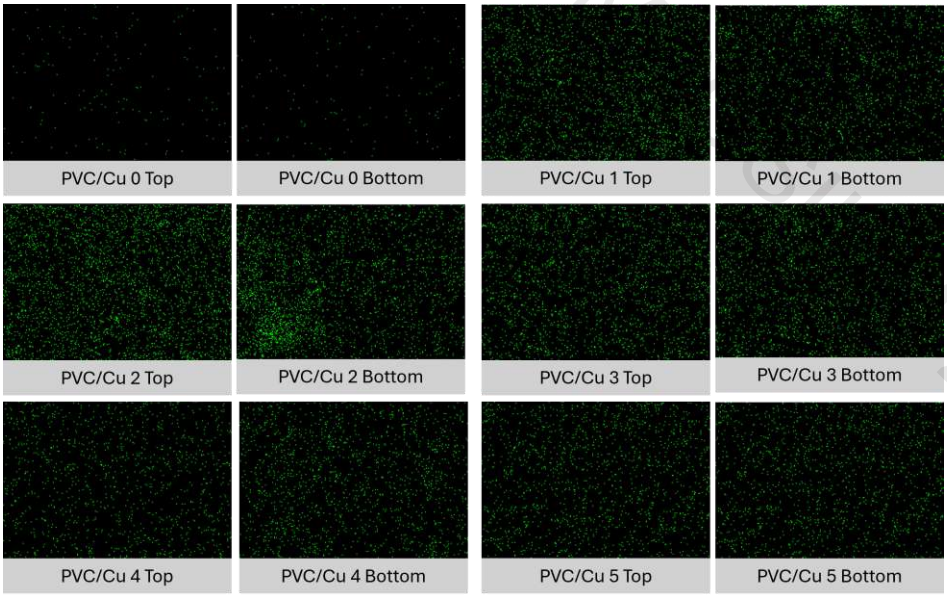


Figure 3: EDX mapping of film membranes with different CuNP contents PVC/Cu 1 (1wt%), PVC/Cu 2 (2 wt%), PVC/Cu 3 (3 wt%), PVC/Cu 4 (4 wt%), PVC/Cu 5 (5 wt%).

*B. XRD Analysis*

To examine the structural features and crystallinity of the films, XRD analysis was conducted. Figure 4 shows that neat PVC give broad and diffuse peaks centered near 2θ ≈ 16° and 25°, which were characteristic of its semicrystalline nature. As Cu concentration increased, distinct sharp peaks appear around 2θ ≈ 45.5°, 56.53°, and 75.4°, corresponding to the (111), (200), and (220) planes of metallic copper. These peaks confirmed the successful incorporation of CuNPs within the polymer matrix. Peak intensities notably increased from 3 wt% Cu onward, indicating an increased presence of crystalline Cu. Additionally, a peak around 31.7° was observed, corresponding to CuO, suggesting some oxidation of copper.

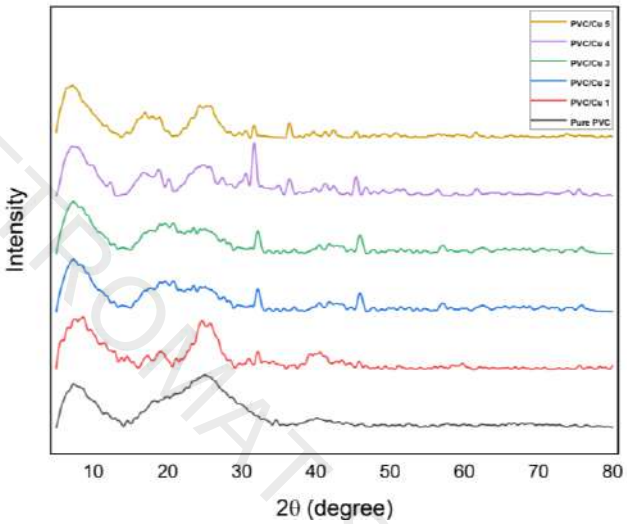


Figure 4: XRD Spectrum of film membranes

*D. Contact angle measurements*

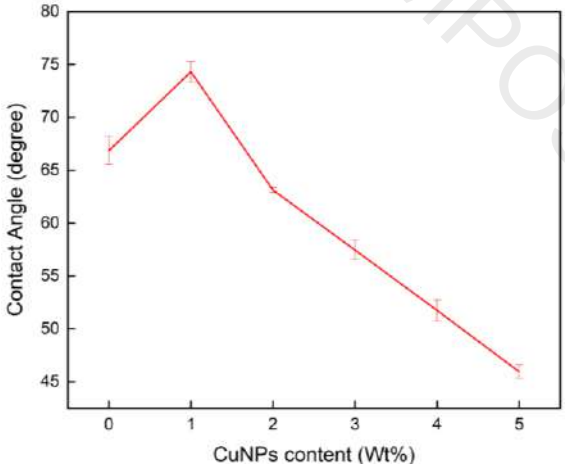


Figure 5: Water contact angle measurements of film membranes

Figure 5 exhibits the water contact angle measurements of the prepared films, revealing a decreasing trend as CuNP content increased from 0 to 5 wt%. Interestingly, the membrane with 1 wt% Cu showed the highest contact angle, indicating the most hydrophobic surface.

PPC & PETROMAT SYMPOSIUM 2025

This finding correlated with SEM images which showed a dense structure at 1 wt%, limiting water penetration. Beyond this concentration, the contact angle steadily decreased, indicating increased hydrophilicity. The enhanced hydrophilicity was primarily due to morphological changes induced by CuNP incorporation. As shown in Figure 2, higher Cu loadings resulted in more porous structures due to accelerated solvent–non-solvent exchange during phase inversion. Additionally, surface chemistry contributed to this effect. Oxidation of exposed CuNPs forms hydrophilic species such as CuO and $Cu(OH)_2$, which promote water adsorption [8]. These polar groups, combined with the sponge-like membrane structure, facilitate greater water affinity and transport within the membrane.

*E. Adsorption study*

The Cr(VI) uptake capacity of the prepared membranes was evaluated at 20 ppm Cr(VI) concentration, and the results showed in Figure 6. A notable increase in uptake capacity was observed with increasing CuNP content, rising from 0.92 mg/g for the pristine PVC membrane to a maximum of 2.47 mg/g at 2 wt% Cu loading. This enhancement was attributed to the redox activity of $Cu^0$, which effectively reduced toxic Cr(VI) to less harmful, water-insoluble Cr(III), which eased the adsorption. At lower Cu concentrations, better nanoparticle dispersion resulted in higher surface area and improved reactivity, enhancing Cr(VI) removal. However, at Cu loadings beyond 2 wt%, the uptake capacity declined sharply, reaching as low as 0.28 mg/g at 5 wt%. This decline was likely due to increased leaching of CuNPs during the membrane formation process, reducing the available reactive sites. At higher Cu contents, the removal mechanism shifts from reduction to primarily physical adsorption within the porous structure. These results suggested that 2 wt% CuNP was the optimal concentration for maximizing Cr(VI) removal via a combined adsorption-reduction mechanism.

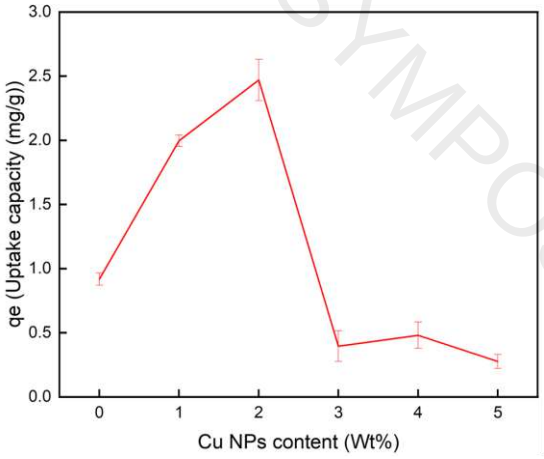


Figure 6: Cr(VI) Uptake capacity variation upon CuNPs content

## CONCLUSIONS

In this study, CuNPs incorporated porous PVC membranes were fabricated via the NIPS method for Cr(VI) removal. A 60/40 water/DMAc bath composition was identified as the

PPC & PETROMAT SYMPOSIUM 2025

optimal condition which aids morphology and minimal Cu leaching. SEM analysis revealed how the CuNP content affected the porous structure of the film membrane. XRD analysis confirmed the successful CuNP incorporation into the polymer matrix. Contact angle measurements exhibited that the incorporation of the CuNPs increased the hydrophilicity of the membrane. Adsorption study revealed that 2 wt% CuNP content as the optimal condition for the Cr(VI) uptake capacity. This finding suggests that the optimized CuNP content not only enhances the membrane's structural properties but also significantly improves its performance in environmental applications, particularly in the removal of chromium ions from aqueous solutions and use in wastewater treatment processes.

## ACKNOWLEDGEMENTS

The Petroleum and Petrochemical College, Chulalongkorn University, Bangkok, Thailand. ASEAN and NON-ASEAN scholarship program, Chulalongkorn University, Bangkok, Thailand.

## REFERENCES

1. Moffat, I., et al., *Hexavalent Chromium in Drinking Water.* Journal AWWA, 2018. **110**(5).
2. Owlad, M., et al., *Removal of Hexavalent Chromium-Contaminated Water and Wastewater: A Review.* Water, Air, and Soil Pollution, 2008. **200**(1-4): p. 59-77.
3. Zafar, A., et al., *Strategies of Toxic Chromium (Vi) Mitigation from Tannery Effluents: A Review.* International Journal of Advanced Research, 2024. **12**(06): p. 269-283.
4. Ho, C.-C., J.F. Su, and L.-P. Cheng, *Fabrication of high-flux asymmetric polyethersulfone (PES) ultrafiltration membranes by nonsolvent induced phase separation process: Effects of H2O contents in the dope.* Polymer, 2021. **217**.
5. Ahmed, I.A., et al., *Investigation the Effects of Green-Synthesized Copper Nanoparticles on the Performance of Activated Carbon-Chitosan-Alginate for the Removal of Cr(VI) from Aqueous Solution.* Molecules, 2021. **26**(9).
6. Gao, H., et al., *'Green' fabrication of PVC UF membranes with robust hydrophilicity and improved pore uniformity.* Desalination, 2023. **568**.
7. Huang, J., Z. Shu, and Y. Zhang, *Fabrication and performance of a polyethersulfone nanofiltration membrane impregnated with a mesoporous silica–poly(1-VInylpyrrolidone) nanocomposite.* Polymer Composites, 2015. **38**(5): p. 908-917.
8. Ha, J., *Superhydrophilic Surface Creation and Its Temporal Transition to Hydrophobicity on Copper via Femtosecond Laser Texturing.* Coatings, 2024. **14**(9).

PPC & PETROMAT SYMPOSIUM 2025

# FACTORS INFLUENCING THE EMULSION STABILITY IN HIPE DERIVED POROUS BEADS FOR COPPER NANOPARTICLE-BASED CONTROLLED RELEASE IN SOIL ENRICHMENT

*Sadeepa Mandakini Landekumbura Mudiyanselage* [a], *Jithima Preechawong* [a] *Jirasuta Chungprempree* [a], *Aung Kyaw Moe* [a], *Manit Nithitanakul* *[a]

[a] The Petroleum and Petrochemical College, Chulalongkorn University, Bangkok, Thailand

Keywords: HIPE, Cu NPs, Degradation, highly porous beads

## ABSTRACT

The integration of copper nanoparticles (CuNPs) into high internal phase emulsion (HIPE) derived degradable porous beads offers a promising approach in sustainable agriculture by reducing the frequent fertilization and minimizing environmental impact. This study aims to fabricate highly porous beads using a water-in-oil HIPE system, in which colloidal CuNPs are immobilized for controlled release. Polylactic acid (PLA) dissolved in dichloromethane (DCM) served as the continuous phase, while the internal-aqueous phase (volume >74%) comprised gelatin, polyvinyl alcohol (PVA) and colloidal CuNPs, stabilized by an oil soluble surfactant. Gelatin acts as a sacrificial porogen in the system. Results indicated that the stability of HIPE system was enhanced by gelation of the internal phase, system pH neutrality and increased PLA content. The stability of the HIPE was also influenced by surfactant type, aqueous-to-oil phase ratio, and the physicochemical properties of the CuNP colloid. Due to their highly porous nature and degradable characteristics, the resulting HIPE derived beads are promising candidates for controlled release of CuNPs and other active agents into soil, supporting environmentally friendly and sustainable agricultural applications.

***manit.n@chula.ac.th**

## INTRODUCTION

Copper (Cu) has multifaceted roles in plants, including nutrition and antimicrobial activity which highlights the significance of Cu for enhancing crop productivity and sustainability in agriculture (Kumar et al., 2021). As an essential micronutrient, Cu is involved in pivotal physiological and biochemical processes of plant growth and development including chlorophyll synthesis, enzymatic functions and protein and carbohydrate metabolism as well as fungicidal and bactericidal approaches (Rai et al., 2018). Recently, the advancements with Cu based nanomaterials gained huge attention as a promising tool for sustainable agriculture in plant nutrition and disease management.

Rather than directly applying CuNPs to plants, immobilization in polymeric carriers has gained huge attention from novel research studies since it offers more sustainable and efficient CuNPs delivery in agricultural practices. Direct application of Cu to plants can impose several disadvantages including phytotoxicity, soil accumulation and environmental persistence, and microbial community disruption (Perfileva et al., 2025). To avoid the

PPC & PETROMAT SYMPOSIUM 2025

above-mentioned drawbacks, encapsulation of CuNPs in polymeric carriers can be pointed out as a promising approach since it offers several advantages including controlled and gradual release of Cu, reducing the risk of phytotoxicity and soil accumulation. Moreover, polymeric carriers could enhance Cu bioavailability, ensuring efficient plant uptake and maintaining healthy soil microbiota ensuring overall soil health (Rather et al., 2020).
The proposed polymeric carrier was fabricated by employing high internal phase emulsion (HIPE) technique which is known to yield highly porous structures possessing hierarchical interconnected pores, high surface area and tunable porosity. These inherent characteristics of HIPE derived materials make them ideal for versatile applications including controlled release systems (Zhang & Guo, 2013). Typically, the dispersed phase of the HIPE, which is known as the internal phase, takes up >74% of the total volume of the emulsion which acts as the template for creating the porous structure while the continuous phase containing the polymer creates the solid external structure of the porous material. In this study, HIPE derived porous beads were prepared using PLA as the polymer due to its nontoxic and biodegradable nature which is suitable for soil related applications. The effect of variation of PLA content, gelation of the internal phase, type of surfactant, aqueous-to-oil phase ratio, and the effect of physicochemical properties of the CuNPs colloid on the emulsion stability was essentially investigated. Gelatin was employed as the sacrificial porogen to create highly porous beads to deliver CuNPs in a controlled manner into soil.

## EXPERIMENTAL

*A. Preparation of the internal phase*
First the internal aqueous phase was prepared as per the following steps. Initially, DI water was heated up to 50 $^{o}$C and then gelatin (Type B) was stirred until it fully dissolved. The pH of the system was adjusted to ~6-7 using 1 M NaOH solution before adding PVA to the system. Then PVA powder was dissolved in the gelatin aqueous solution at about 80 $^{o}$C. After fully dissolving PVA, pH neutralized colloidal CuNP solution was added and well stirred in the aqueous system and it was kept aside to let the aqueous solution cool down and turn into gel state before mixing with the oil phase.

*B. Preparation of the continuous phase*
PLA pellets were fully dissolved in DCM until a very viscous solution was obtained. Then, the surfactant was added to the system and stirred until it is fully dissolved in the oil phase.

*C. Preparation of the HIPE*
Prepared oil phase was stirred using an overhead stirrer while slowly adding the internal aqueous phase in the gel state. When the total volume of the internal phase is added, the rotation speed was increased, and the system was stirred for 2 more minutes until the system forms a highly viscous white paste like HIPE.
HIPEs were prepared to investigate the emulsion stability upon variation of several factors including PLA content (1%, 3%, 6%, 8%, 10%), volume ratio of aqueous phase to oil phase (IP vol.%: 16%, 25%, 40%, 74%, 80%), surfactant type (span 80, span 80/tween 80, increased span 80/tween 80, Hypermer B246), physicochemical properties of CuNPs colloidal (pH and presence of salt in the CuNPs colloid).
Then the already prepared HIPE was dropwise added into a container having liquid nitrogen using a syringe needle to form HIPE beads via cryogenic solidification method.

PPC & PETROMAT SYMPOSIUM 2025

The formed beady structures were then collected and kept in the deep freezer until all DCM are evaporated and form the solid bead structures. After solidification, the beads were well stirred with warm water at 50 $^{o}$C to wash and remove gelatine and PVA from the system to obtain porous beads. Finally, the beads were collected and dried in an oven at 60 $^{o}$C overnight.

The morphological properties of the prepared HIPE derived porous beads were observed from FE-SEM and tabletop-SEM and the Cu content was characterized by SEM-EDX analysis. To investigate the thermal properties as well as to observe the remaining Cu content, STA was conducted on the prepared porous beads.

## RESULTS AND DISCUSSION

### *A. Influence of factors on emulsion stability*

The HIPE stability was observed to increase with the increasing amount of PLA in the continuous phase. Since PLA can act as a co-stabilizer and enhance the interfacial film strength, it can reduce the droplet coalescence in the HIPE system (Wang et al., 2019). Hence, increased PLA content can improve HIPE stability. Moreover, with increasing gelation of the aqueous internal phase, the HIPE stability increases due to the physical strengthening of the structure by the gel network and hence prevent the droplet coalescence by reducing mobility. When the internal phase becomes gelled and less mobile, droplets can behave more like active solid fillers and enhance the overall rigidity of the system (Liu et al., 2022). This structural reinforcement by gelled internal phase results in enhanced stability of the HIPE. When the volume ratio of the aqueous phase to oil phase gradually increases, the viscosity of the system increases until a critical threshold point is achieved. Beyond this point, the emulsion system viscosity drastically drops with the continual addition of the internal phase due to droplet deformation and coalescence leading to phase separation. Hence, a surfactant is essential for a stable HIPE to retain the droplets in the uncoalesced state. Without proper structuring from an emulsifier or a gelator, when the internal aqueous phase volume exceeds ~74%, the continuous phase film thickness between internal phase droplets weakens and coalesce resulting phase separated HIPE (Li et al., 2021).

A well stabilized HIPE was obtained while increasing the internal phase to continuous phase volume ratio when a surfactant was employed in the preparation stage. Compared to Span 80 alone, and Span 80 and Tween 80 together, a superior HIPE stability was achieved with Hypermer B246. Since Hypermer B246 is a polymeric, nonionic surfactant, it can form a more elastic and thicker interfacial film as well as better steric protection which leads to prevention of the droplet coalescence and enhanced HIPE stability in contrast with small molecular surfactants like span 80 and tween 80 which only form thinner interfacial layers that are more prone to rupture. The pH of the system has a significant influence on the stability of HIPE since it affects the charge, solubility and structure of emulsifiers and other components in HIPE hence the nature of the interfacial film between the internal phase droplets. In this study, the low pH values of the system have caused phase separation of the HIPE within several minutes. Since Gelatin type B (pH ~4.7-5.4) aqueous solution makes the internal phase pH lower than neutral pH, it resulted in phase separation and

PPC & PETROMAT SYMPOSIUM 2025

lower stability of HIPE. But with pH adjusting to ~6-7 before mixing with the oil phase using 1 M NaOH, the HIPE stability increased.

Figure 1: CuNP colloid before and after dialysis

A pre-prepared colloidal CuNPs solution was employed as the Cu source to be immobilized in the HIPE derived porous beads in this study. HIPE stability was directly influenced by the physicochemical properties of the CuNP colloid. Since the pH of the CuNP was ~2, when the CuNP colloid containing aqueous phase mixed with the continuous phase, the HIPE tends to phase separate within a few minutes in acidic conditions. But with pH adjusted CuNP colloid, a stable HIPE was obtained. Other than pH, the presence of salts in the colloidal CuNP solution negatively impacts HIPE stability. Salt ions in the CuNP colloid modulates interfacial interactions by screening the electrostatic repulsions between droplets and results in emulsion destabilization at moderate to high salt ion concentrations. When the CuNP colloid was purified to remove salt ions via dialysis, the addition of it into the HIPE system did not lead to the HIPE destabilization.

Figure 2: Variation of HIPE stability

*B. Morphological analysis*

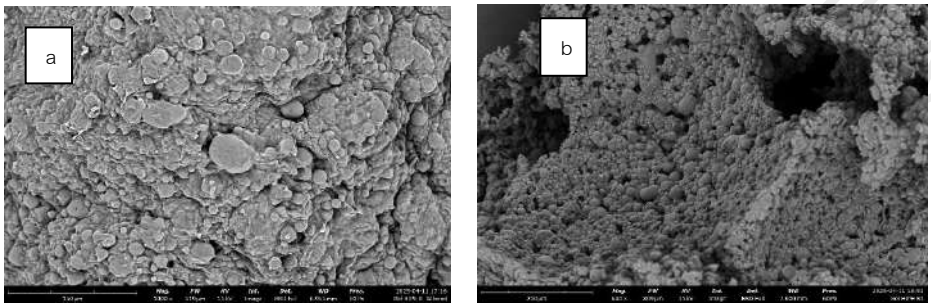


Figure 3: SEM images of a) HIPE derived beads before washing b) after washing

The morphology of the prepared HIPE derived beads were observed using Tabletop SEM and the SEM (S4800, Hitachi, Japan) images show the resultant porosity of the material

and changes of the morphology before and after gelatin and PVA removal by washing as shown in Figure 3a) and 3b). The addition of colloidal Cu NPs solution (pH ~2) decreases the emulsion stability if not adjust the pH into neutral. With pH adjusted to ~6-7, the emulsion stability was enhanced as well as the pore structures seem to be open a bit compared to the HIPE derived beads without CuNP. The EDX analysis results confirm the immobilization of CuNPs in the HIPE structure and after washing, CuNPs seem to be visible clearly, upon removal of gelatin.

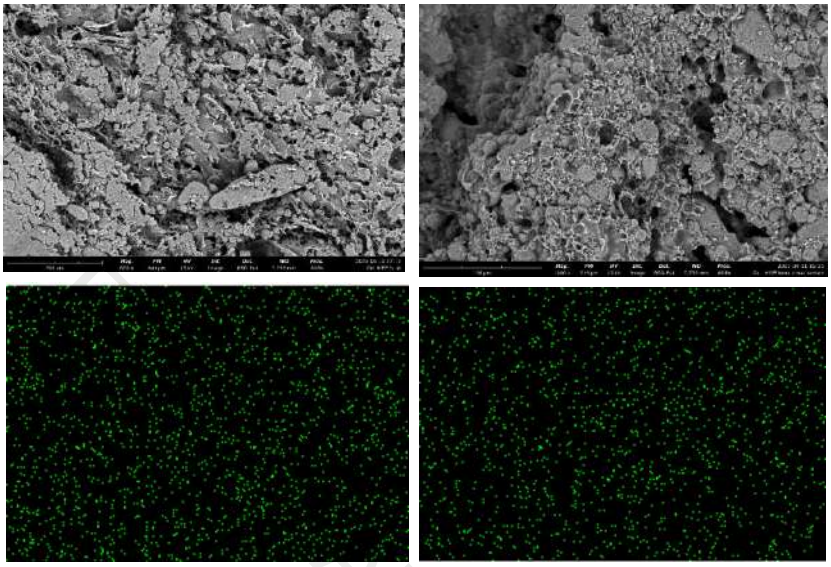

Figure 4: SEM and EDX images of CuNP immobilized HIPE beads a) before washing b) after washing to remove the porogen

*C. FTIR analysis of HIPE derived beads*

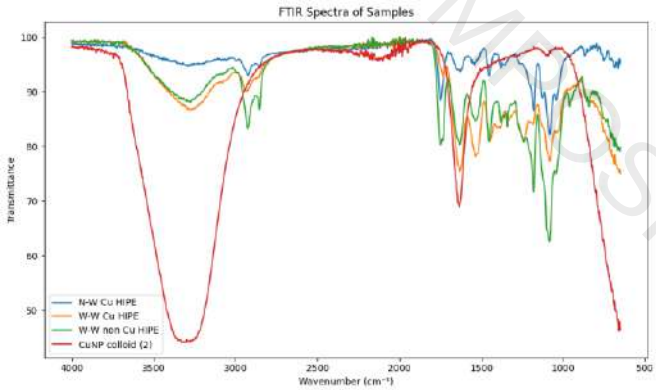


Figure 5: FTIR spectra of samples

FTIR analysis (Nicolet iS5, Thermofisher, USA) was conducted to study the changes between samples prepared using different conditions. Here colloidal CuNPs immobilized in HIPE derived porous beads and pristine beads well washed (W-W) and not washed (N-W) states compared with the spectrum of colloidal CuNPs.

*D. Thermal analysis*

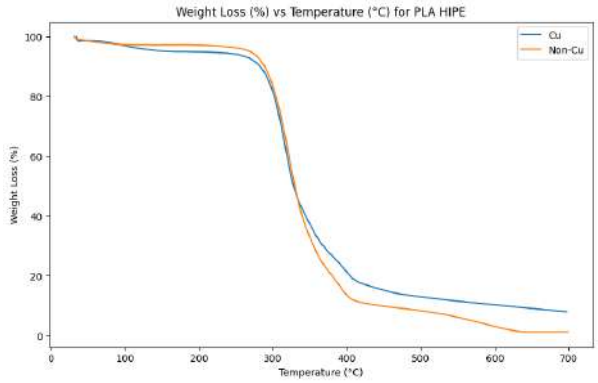


Figure 6: STA analysis of HIPE beads before and after Cu immobilization

Simultaneous thermal analysis (449F3 Jupiter, NETZSCH, Germany) was carried out to study the thermal behaviour of HIPE derived beads. From the STA thermogram, prepared beads start to thermally degrade around 300 °C. As per the results, it was suggested that even after washing, immobilized CuNPs remain entrapped in the HIPE derived beads. Hence, this material is suitable as a promising CuNP controlled release system for soil enrichment.

## CONCLUSIONS

In this study, PLA porous beads were prepared by HIPE technique as CuNPs carrier for soil enrichment. When the gelation of the internal phase increased, the stability of the HIPE was also increased. Emulsion stability was enhanced when Hypermer B246 was employed as the surfactant. When increasing the polymer content from 1 wt.% to 6 wt.%, the resulting HIPE seems to demonstrate an increased stability, and when polymer content was higher than 6 wt.% no significant enhancement in HIPE stability was observed. Along with the aqueous-to-oil phase ratio, HIPE stability varied significantly with the increment in the aqueous internal phase. Moreover, the physicochemical properties of the CuNPs colloid including pH, and salt content influence directly on the emulsion stability. This porous material formed using HIPE technique could be a great candidate as a CuNPs carrier for gradual release for soil enrichment. Further modifications of the material could effectively enhance the versatility of the beads in soil enrichment by encapsulating various agrochemicals and nutrients as well as water absorption for sustainable agriculture.

## ACKNOWLEDGEMENTS

- The Petroleum and Petrochemical College, Chulalongkorn University, Bangkok, Thailand.
- ASEAN and NON-ASEAN graduate scholarship program, Chulalongkorn University, Bangkok, Thailand.

PPC & PETROMAT SYMPOSIUM 2025

## REFERENCES

**Kumar, V., Pandita, S., Singh Sidhu, G. P., Sharma, A., Khanna, K., Kaur, P., Bali, A. S., & Setia, R.** (2021). Copper bioavailability, uptake, toxicity and tolerance in plants: A comprehensive review. *Chemosphere*, *262*, 127810. https://doi.org/10.1016/j.chemosphere.2020.127810

**Li, K., Zhang, Z., & Dong, S.** (2021). High internal phase emulsions and their applications in functional material preparation. *Chinese Science Bulletin*, *66*(14), 1703-1716. https://doi.org/10.1360/tb-2020-1454

**Liu, Y., Lee, W. J., Tan, C. P., Lai, O. M., Wang, Y., & Qiu, C.** (2022). W/O high internal phase emulsion featuring by interfacial crystallization of diacylglycerol and different internal compositions. *Food Chem*, *372*, 131305. https://doi.org/10.1016/j.foodchem.2021.131305

**Perfileva, A. I., Sukhov, B. G., Kon'kova, T. V., Strekalovskaya, E. I., & Krutovsky, K. V.** (2025). Diversity of copper-containing nanoparticles and their influence on plant growth and development. *Plant Physiol Biochem*, *220*, 109575. https://doi.org/10.1016/j.plaphy.2025.109575

**Rai, M., Ingle, A. P., Pandit, R., Paralikar, P., Shende, S., Gupta, I., Biswas, J. K., & da Silva, S. S.** (2018). Copper and copper nanoparticles: role in management of insect-pests and pathogenic microbes. *Nanotechnology Reviews*, *7*(4), 303-315. https://doi.org/10.1515/ntrev-2018-0031

**Rather, B. A., Masood, A., Sehar, Z., Majid, A., Anjum, N. A., & Khan, N. A.** (2020). Mechanisms and Role of Nitric Oxide in Phytotoxicity-Mitigation of Copper. *Front Plant Sci*, *11*, 675. https://doi.org/10.3389/fpls.2020.00675

**Wang, Y., Azhar, U., He, J., Chen, H., Zhao, J., Pang, A. M., & Geng, B.** (2019). A facile fabrication of porous fluoro-polymer with excellent mechanical properties based on high internal phase emulsion templating using PLA as co-stabilizer. *RSC Adv*, *9*(69), 40513-40522. https://doi.org/10.1039/c9ra08226c

**Zhang, T., & Guo, Q.** (2013). High internal phase emulsion (HIPE) organogels prepared from charge-driven assembled polymer organogels. *Chem Commun (Camb)*, *49*(100), 11803-11805. https://doi.org/10.1039/c3cc47263a

PPC & PETROMAT SYMPOSIUM 2025

# A Smart Strip for Grading Used Cooking Oil via Colorimetric Detection of Free Fatty Acids

*Tarika Lomcharoenwong* [a], *Atitiya Saedan* [d], *Pranee Rattanawaleedirojn* [a,c], *Kanokwan Saengkiettiyut* [a], *Sarute Ummartyotin* [d], *Jutiporn Yukird* [a], *Nadnudda Rodthongkum* [b,c,*]

[a] Metallurgy and Materials Science Research Institute, Chulalongkorn University, Bangkok, Thailand
[b] Department of Chemistry, Faculty of Science, Chulalongkorn University, Bangkok, Thailand
[c] Center of Excellence in Responsive Wearable Materials, Metallurgy and Materials Science Research Institute, Chulalongkorn University, Bangkok, Thailand
[d] Department of Materials and Textile Technology, Faculty of Science and Technology, Thammasat University, Pathum Thani, Thailand

Keywords: Oleic acid, Cooking oil, Acid-base titration

## ABSTRACT

A user-friendly modified cellulose paper-based device has been developed for rapid assessment of cooking oil quality, a crucial step in grading used oil before its conversion into biodiesel. The method employs a colorimetric acid–base titration between immobilized sodium carbonate ($Na_2CO_3$) and oleic acid, used as a model free fatty acid indicative of oil degradation. The device was fabricated by immobilizing phenolphthalein indicator and three concentrations of $Na_2CO_3$ (0.02, 0.08, and 0.2 M) as primary standards onto the paper substrate, forming detection zones. Upon immersion in an oil sample containing oleic acid, a visible color change from pink to colorless in the detection zones signifies a neutralization reaction. The device demonstrated a linear detection range of 0–4% v/v oleic acid, effectively encompassing the critical 3.0% v/v threshold commonly used to assess significant oil degradation. The rectangular paper format incorporates three spatially separated detection zones, enabling semi-quantitative analysis without instrumentation. The number of pink zones that lose their color directly correlates to the oleic acid concentration in the oil sample. Successful application of this platform to real used cooking oil samples demonstrates its significant potential for rapid, low-cost, and on-site assessment of oil quality, facilitating efficient biodiesel production processes.

*** Nadnudda.R@chula.ac.th**

## INTRODUCTION

The extensive consumption of deep-fried food in Thailand contributes to the annual use of more than one million tons of cooking oil, consequently generating a substantial quantity of used cooking oil each year[1]. Transforming this waste stream into biodiesel offers a promising strategy for advancing circular economy principles and meeting the increasing demand for alternative energy sources. Used cooking oil is especially appealing for biodiesel production due to its inherent low cost and abundance. Nevertheless, the physicochemical degradation that occurs during repeated high-temperature frying poses a significant challenge, as it compromises oil quality and negatively impacts the efficiency of subsequent biodiesel conversion processes.

A key parameter associated with the deterioration of used cooking oil is the formation of free fatty acids (FFAs), which are produced via hydrolysis of triglycerides[2]. Elevated FFA content not only reduces the oxidative stability of biodiesel but also hinders

transesterification efficiency and increases production costs due to the need for additional pretreatment steps[3]. Therefore, the rapid and accurate assessment of FFA concentration is crucial for determining the suitability of used cooking oil as a biodiesel feedstock.

The conventional analytical techniques used for FFA quantification include titration[4], gas chromatography (GC)[5], high-performance liquid chromatography (HPLC)[6], Fourier-transform infrared spectroscopy (FT-IR)[7], and nuclear magnetic resonance (NMR)[8]. Despite offering high sensitivity and precision, conventional methods typically demand sophisticated instrumentation, specialized personnel, and laborious sample preparation. The titration method, although widely employed, is notably time-consuming, consumes substantial volumes of organic solvents, and produces considerable chemical waste, thereby presenting environmental and operational difficulties. Moreover, its inherent reliance on fixed laboratory infrastructure restricts its utility for on-site quality assessment.

To overcome these limitations, the present study introduces a cellulose-based colorimetric platform for the semi-quantitative determination of FFA content in used cooking oil. The proposed device integrates a colorimetric acid–base titration system using immobilized sodium carbonate ($Na_2CO_3$) and phenolphthalein indicator onto a paper substrate containing three detection zones. Oleic acid, a representative FFA commonly found in degraded oils, was used as a model compound. Upon contact with the sample, the number of zones that exhibit a color change (from pink to colorless) is directly correlated with the concentration of FFAs present.

This paper-based sensing approach offers several advantages, including its low cost, ease of use, minimal reagent consumption, and potential for rapid, on-site assessment without specialized equipment or extensive training. Its successful application to real used cooking oil samples clearly demonstrates its practical utility for quality screening before biodiesel production. Furthermore, we developed a smartphone application for quantitative readout of % FFA, which helps eliminate human eye error. Ultimately, this work significantly contributes to developing accessible and sustainable tools for energy resource management, especially in resource-limited or decentralized settings.

## EXPERIMENTAL

*A. Materials*

Sodium carbonate ($Na_2CO_3$) and phenolphthalein indicator were obtained from Sigma-Aldrich (USA). Oleic acid (analytical grade) was purchased from PanReac AppliChem (Spain). Fresh cooking oil and used cooking oil samples were collected from a local market. Whatman No. 1 filter paper was used as the cellulose substrate for paper-based devices.

*B. Preparation of Modified Paper-Based Colorimetric Titration Strips*

Cellulose-based filter paper was cut into rectangular strips and patterned using an inkjet printer with water-resistant ink to define hydrophobic barriers and restrict fluid flow. Each strip featured three circular detection zones with a diameter of 4 mm. The detection zones were functionalized by sequentially dispensing 2.5 µL of 1% w/v phenolphthalein solution

PPC & PETROMAT SYMPOSIUM 2025

followed by 5.0 µL of $Na_2CO_3$ solution. Three different $Na_2CO_3$ concentrations were used: 0.02 M, 0.08 M, and 0.2 M, each applied to a separate detection zone to enable semi-quantitative analysis based on color change response.

*C. Colorimetric titration method*

The free fatty acid (FFA) content in oil samples was determined following the Standard Operating Procedure (SOP) ARL-20210301, which is based on the AOCS Official Method Ab 5-49. In this method, a titration was performed using a standardized sodium carbonate ($Na_2CO_3$) solution as the titrant. Phenolphthalein was used as the pH indicator to visually detect the endpoint, indicated by the disappearance of the pink colour, which corresponds to the neutralization of free fatty acids present in the sample.

## RESULTS AND DISCUSSION

*A. Colorimetric Detection of Free Fatty Acids Using a Modified Paper-Based Platform*

The modified cellulose paper-based device was fabricated using a rectangular sheet of cellulose-based paper designed for ease of handling and visual observation. Each strip featured three circular detection zones, each 4 mm in diameter, allowing simultaneous detection and internal comparison. To prepare the sensing zones, 2.5 µL of phenolphthalein solution and 5.0 µL of $Na_2CO_3$ solution were immobilized on the surface of the paper. The immobilization process ensured a consistent distribution of reagents, enabling reliable reactivity during testing. To evaluate the device's response to varying levels of free fatty acids (FFAs), three concentrations of $Na_2CO_3$ (0.02, 0.08, and 0.2 M) were employed in different detection zones. This gradient allowed the device to function as a semi-quantitative tool for detecting a range of FFA concentrations. Upon immersion in oil samples containing FFAs, with oleic acid serving as a model FFA, a visible color change from pink to colorless occurred in the detection zones. The pink hue, characteristic of the basic form of phenolphthalein, gradually disappeared as the acid in the sample neutralized the carbonate base.

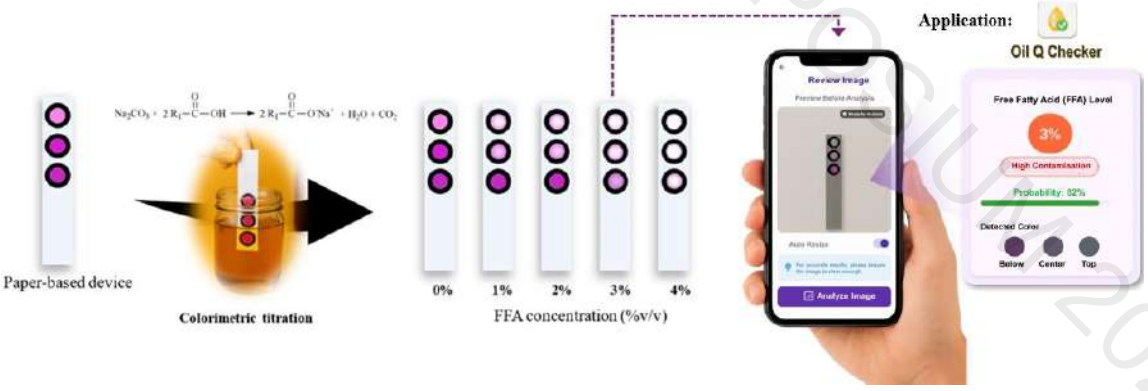


**Figure 1** Paper-based device for free fatty acid detection via acid–base neutralization, along with a standard color chart of FFA concentrations ranging from 0 to 4 %v/v with smartphone readout.

This observable color transition provided a straightforward visual indication of the acid–base neutralization reaction, and the intensity of discoloration correlated with the FFA concentration. As illustrated in Figure 1, the device was accompanied by a standard color chart corresponding to FFA levels ranging from 0 to 4 %v/v, allowing the user to visually match and estimate the FFA concentration in real samples. The system demonstrated a measurable and consistent response within this linear range, confirming its potential as a simple, low-cost, and equipment-free tool for evaluating FFA levels in real cooking oil samples.

*B. Validation of modified cellulose paper-based platforms for FFA quantification in real samples*

A cellulose-based paper device was successfully utilized for the quantification of free fatty acids (FFAs) in real used cooking oil samples. The detection principle relied on acid–base titration, where sodium carbonate immobilized on the paper reacted with oleic acid in the sample. Phenolphthalein was employed as a pH indicator, and the fading of its pink color upon acid neutralization was used as a visual cue for FFA presence. The extent of color disappearance, observable to the naked eye, served as a semi-quantitative measure of FFA concentration, as shown in Fig. 2 and Table 1. Six used cooking oil samples were collected from the local restaurants and analyzed using the developed paper-based platform. The FFA levels were estimated visually and compared with values obtained from a standard AOCS Official Method Ab 5-49.

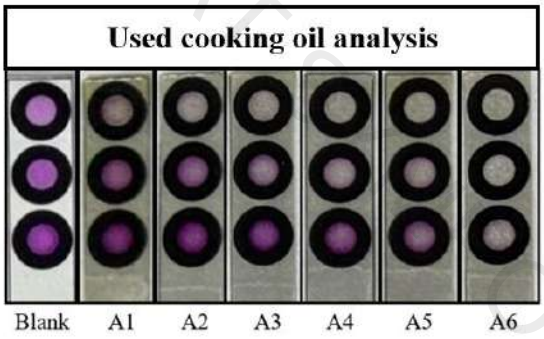


**Figure 2** Visual appearance of the modified cellulose paper-based device after dipping in real samples.

The paper-based colorimetric sensor results showed FFA content within the ranges of 0-1%, >1%-3%, >1%-3%, >3%-4%, >3%-4%, and >4%v/v for the respective samples. Corresponding measurements from the AOCS method were 0.8%, 1.3%, 2.3%, 3.1%, 4.0% and 5.9% v/v. These findings demonstrate good consistency between the two methods, confirming the reliability of the paper-based system. Furthermore, the paper device successfully identified samples that exceeded the commonly accepted degradation threshold of 3.0% FFA. This highlights the potential of the platform for rapid screening of oil quality without the need for laboratory-based instrumentation or technical expertise. The simplicity and cost-effectiveness of the method make it particularly suitable for field use, especially in settings such as local food vendors or small-scale biodiesel production

facilities. Overall, the visual titration results align well with the standard method, validating the device's practicality and reinforcing its value as a portable tool for assessing oil degradation through FFA content in real cooking oil samples.

**Table 1 The comparison of oleic acid concentrations in used cooking oil samples**

| Sample | Oleic acid concentration (%v/v) | |
|---|---|---|
| | Naked eye | Titration [a] |
| A1 | 0< x ≤ 1 | 0.8 |
| A2 | 1< x ≤3 | 1.3 |
| A3 | 1< x ≤3 | 2.3 |
| A4 | 3< x ≤4 | 3.1 |
| A5 | 3< x ≤4 | 4.0 |
| A6 | >4 | 5.9 |

[a] Based-on SOP ARL-20210301 (adapted from AOCS Method Ab 5-49).

*C. Stability evaluation of the modified cellulose paper-based device for FFA quantification in real samples*

To evaluate the operational stability and shelf-life of the modified cellulose-based paper device, a storage stability assessment was performed by maintaining the fabricated strips under ambient conditions for a duration of four weeks. This study aimed to determine whether the immobilized phenolphthalein and $Na_2CO_3$ retained their functional integrity and colorimetric responsiveness over time in the absence of refrigeration, thereby simulating real storage and usage conditions. A real cooking oil sample (A2), previously quantified to contain 1.3 %v/v FFA via a conventional titration method, was employed as the analytical matrix. At weekly intervals (0, 1, 2, 3, and 4 weeks), stored test strips were exposed to the sample, and the resultant colorimetric responses were evaluated against a pre-established reference chart corresponding to FFA concentrations ranging from 0 to 4 %v/v. As illustrated in Figure 3, the device demonstrated sustained visual performance throughout the entire storage period, showing no apparent degradation in the intensity or quality of the color change. Its detection zones consistently produced a discoloration pattern indicating an FFA content in the range of 1–3% v/v, which closely matched the expected value from the reference titration analysis.

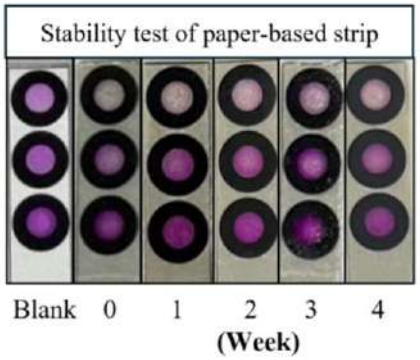


**Figure 3** Stability tested of modified cellulose paper-based strip in sample A2

PPC & PETROMAT SYMPOSIUM 2025

*D. Smartphone Application for Quantitative FFA Readout*

To improve convenience and accuracy in quantitative FFA analysis, a smartphone application was developed for digital colorimetric analysis of the cellulose-based paper device. The app captures images using the smartphone camera and compares the colour data to a standard chart of FFA concentrations (0–4% v/v), as shown in Figure 1.

The application automatically detects the detection zone, analyzes the colour intensity, and calculates the corresponding FFA percentage. Validation with real used cooking oil samples (A1–A6), previously evaluated by naked-eye inspection and titration, showed consistent results. This confirms the application's reliability for field and on-site screening.

## CONCLUSIONS

We developed a user-friendly cellulose paper-based device for rapid, semi-quantitative free fatty acid (FFA) content determination in used cooking oil. This colorimetric platform uses immobilized $Na_2CO_3$ and phenolphthalein, providing a 0–4% v/v oleic acid detection range that covers the critical 3.0% v/v FFA degradation threshold. The device showed strong correlation with standard AOCS titration when validated with real samples, confirming accuracy and reliability. It also exhibited excellent operational stability (four weeks ambient storage) and enables quantitative %FFA readout via a smartphone application. This low-cost, portable, and easy-to-use system offers a promising solution for rapid used cooking oil quality screening, supporting sustainable resource management.

## ACKNOWLEDGEMENTS

The authors would like to thank Center of Excellence in Responsive Wearable Materials, Chulalongkorn, University, Soi Chula 12, Phayathai Road, Pathumwan, Bangkok, 10330, Thailand.

## REFERENCES

1. **วิทยา อุลสมบูรณ์.** (2014). ปฏิวัติน้ำมันทอดซ้ำจากกระทะสู่วาระแห่งชาติ พิมพ์ครั้งที่ 4. แผนงานพัฒนาวิชาการ และกลไกคุ้มครองผู้บริโภคด้านสุขภาพ จุฬาลงกรณ์มหาวิทยาลัย. กรุงเทพฯ.
2. **Choe, E. and Min, D. B.** (2007). *J. Food Sci*. **72 (5)**, 77-86.
3. **Gerpen, J. V.** (2005). *Fuel Process. Technol.* **86 (10)**, 1097-1107.
4. **Bazina, N. and He, J.** (2018). *J Food Sci Technol*. **55 (8)**, 3085-3092.
5. **Wan, P. J.,Dowd, M. K.,Thomas, A. E. and Butler, B. H.** (2007). *J. Am. Oil Chem. Soc.* **84 (8)**, 701-708.
6. **Li, G.,You, J.,Suo, Y.,Song, C.,Sun, Z.,Xia, L.,Zhao, X. and Shi, J.** (2011). *Food Chem.* **125 (4)**, 1365-1372.
7. **Al-Alawi, A.,van de Voort, F. R.,Sedman, J. and Ghetler, A.** (2006). *SLAS Technol*. **11 (1)**, 23-29.
8. **Di Pietro, M. E.,Mannu, A. and Mele, A.** (2020). *Processes*. **8 (4)**.

PPC & PETROMAT SYMPOSIUM 2025

# ELECTROCHEMICAL IMPEDANCE SPECTROSCOPY ANALYSIS OF ION TRANSPORT IN POLYELECTROLYTE MEMBRANES

*Medhavi Hansana Karunarathna Warusapperuma Dona*[a], *Stephan Thierry Dubas**[a,b]

a The petroleum and Petrochemical College, Chulalongkorn University, Bangkok 10330, Thailand
b Center of Excellence on Petrochemical and Materials Technology, Bangkok 10330, Thailand

Keywords: Polyelectrolyte complex membranes, EIS, Ion transportation, Annealing

## ABSTRACT

Polyelectrolyte complex (PEC) membranes have emerged as promising materials for selective ion transport in separation applications. Membrane-based ion transport offers more advantages when compared to modern technologies since it can be operated with low energy consumption and high efficiency. Thin PEC membranes were prepared by co-precipitation of cationic poly(diallyldimethylammoniumchloride) (PDADMAC) and anionic poly((sodium-4-styrenesulfonate) (PSS) followed by compression. Stoichiometric and non-stoichiometric membranes were prepared by tuning the molar composition ratios to 1:1, 2:1 and 1:2, respectively. To improve the ion paring within the membrane, they were annealed with NaCl overnight and rinsed. Electrochemical impedance spectroscopy (EIS) was used to study the ion transport properties of the membranes as a function of salt concentration. Annealing results revealed a decrease in ion-transport resistance over time, likely due to the reduced structural complexity of the PSS and PDADMAC chains. However, $K^+$ demonstrated the lowest ion transport resistance through PEC membrane (34Ω) for the 1:2 stoichiometry compared to 1:1 and 2:1 for annealed samples. Therefore, the results indicated that the ion transport through the membranes is influenced by the ionic annealing, membranes' structure, ion size, and charge density. Importantly, this insight can guide to optimize the designs for applications including cross flow polymerizations and battery separators.

***Stephan.d@chula.ac.th**

## INTRODUCTION

Ion transport is a fundamental and crucial process in biological systems and membrane-based technologies enabling energy conversions. It offers the advantage of enhanced efficiency, scalability, energy savings etc. Thus, significant advancement in membrane-based ion transporting has been made for processes like water purification[1], desalinations[2], battery separators[3,4], cross flow polymerizations[5] etc. However, much research has been intensified into efficient and sustainable novel membrane materials. In that case, PEC membranes offer advanced properties compared to Nafion[6], ceramic/polymeric micro- or ultrafiltration (MF/UF) membranes etc. by permitting precise adjustment of fixed charge concentration via stoichiometry or choice of polyelectrolytes (PEs). Unlike polysulfone, PVDF which degrades in organic media[7], PECs exhibit stability in a wide pH range. Further, the choice of PECs has inherently possessed hydrophilic groups which reduce the

PPC & PETROMAT SYMPOSIUM 2025

foulant adhesion and biofilms formation compared to PVDF. Furthermore, PECs are fabricated via water-based-co precipitation method[8] which is a much greener process than other membrane synthesis processes.

PEC formation is mainly based on entropic release of counterions and the formation of ionic interactions from the ionic sites of polymer[9]. The assembly of PEC is represented in following equilibrium equation (1). The pivotal contribution from Schlenoff and coworkers[10] have made these PECs to be processable via ultracentrifugation and extrusion.

$$Pol^{+}Pol^{-} + M_{aq}^{+} + X_{aq}^{-} \longrightarrow Pol{+}X_c^{-} + Pol{-}M_c^{+} \quad (1)$$

Despite their broad applications, the effects of monovalent and divalent ions on PEC membrane structure and resistivity remain unclear, requiring further study for optimization. Further, it also requires a powerful characterization technique to collect detailed resistivity information. In that case, EIS serves as a powerful tool to probe these transport properties[11]. This study aims to investigate the ion transport behavior of PEC membranes composed of PDADMAC and PSS with varying stoichiometries (1:1, 2:1, and 1:2(PDADMAC: PSS)) and we hypothesis that ionic annealing in high salt concentration (without heating) can enhance the ionic pathways through rearrangements of PEC membranes. By employing EIS, we seek to elucidate the relationship between membrane composition and ion transport resistance, particularly for $Na^+$ and $K^+$ ions. Understanding these relationships will inform the design of PEC membranes optimized for applications in crossflow polymerization processes and battery separator technologies.

## EXPERIMENTAL

*A. Preparation of Polyelectrolyte Complex*

The PEC was prepared by mixing two oppositely charged polyelectrolytes solutions. PDADMAC and PSS were each dissolved in DI water with 1 M NaCl added during stirring. Then, both solutions were mixed to produce a ball of polyelectrolyte complex. To prepare the membrane, the complex mixture ball was placed in between two Polytetrafluoroethylene (PTFE) sheets and kept a 0.15 mm thick aluminum as a spacer. Then, the hot pressing was heated to 70 °C and compressed the mixture for 3 min. in 2000psi force.

*B. Dye and electrolyte uptake*

To confirm the stoichiometric and non-stoichiometries behavior, prepared membranes were soaked in methyl blue (cationic dye/MB), methyl orange (anionic dye/MO), and in a mixture of MB and MO to confirm the selectivity. For that, dried (60 °C for 24 hrs) 3$cm^2$ of membranes were used. To evaluate electrolyte uptake, membranes were dipped in the 2.0 M NaCl, KCl solutions also.

*C. Ionic annealing of PEC membranes*

The prepared membranes were dried and cut with 1.5 cm diameter. Then, the cut samples were annealed in 2M NaCl solution for 24 hours and were checked the ionic resistivity via EIS. The real time annealing behavior was also tested via EIS within 11 hours in 2M NaCl solution by placing 10 min. interval. To further confirm the annealing, methyl orange (MO) (20ppm) diffusion through annealed and not annealed PECs were experimented.

PPC & PETROMAT SYMPOSIUM 2025

*D. Preparation of membranes for the resistivity measurement*

The annealed samples were mounted with H-cells. Electrolyte solutions were changed as NaCl, KCl. Further, 1.0, 1.5, 2.0, 2.5M concentration series were used to examine the membrane behavior.

## RESULTS AND DISCUSSION

To confirm the ionic nature of the prepared 1:1, 2:1 and 1:2 membranes, dye uptake was studied.

*A. Dye uptake*

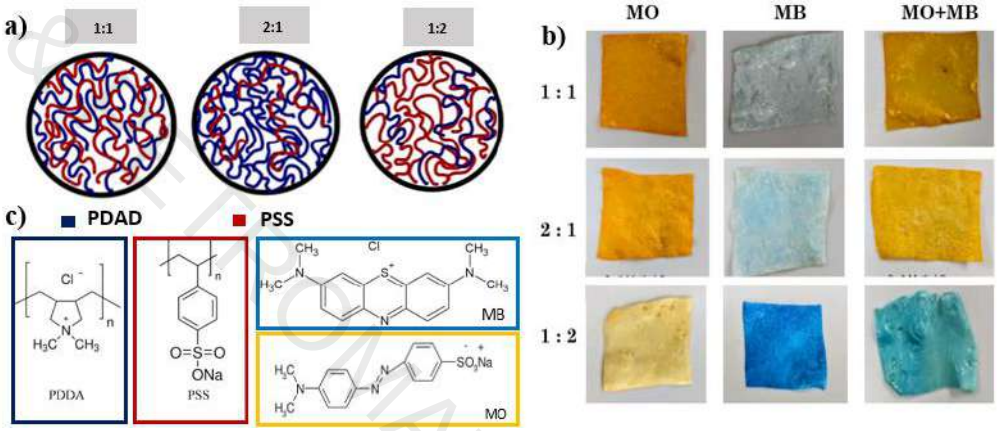


**Figure 1** a. Schematic representation of stoichiometric and non-stoichiometric membrane structure b. PSS, PDAD, Methyl Blue (MB), and Methyl Orange (MO) structures c. Methyl Blue (MB), Methyl Orange (MO) and mixture of MB and MO.

However, after 24 hours of soaking, the 1:2 membrane was exhibited a blue color, as expected, due to the presence of excess PSS groups that remain unbound. In contrast, the 2:1 membrane, which contains excess PDADMAC, showed orange color in MO solution and less blue color in MB solution. Surprisingly, 1:1 behaved similarly to 2:1, which suggests that stoichiometric membranes have excess cationic nature. This observation was further confirmed by soaking membrane in green solution (mixture of MB and MO). The results consistently showed that the 1:2 membrane exhibited a blue coloration, while the 1:1 and 2:1 membrane displayed an orange coloration. The reason is, although it was stoichiometric, more polycations were in the 1:1 membrane. Furthermore, the stability of the membranes with respect to different salt types and concentrations were analyzed by salt uptake test in the following section.

*B. KCl and NaCl uptake and swelling*

Electrolyte uptake for all the membranes at 2.0M concentration of NaCl and KCl is depicted in Figure 2a, and corresponding swelling behavior is shown in Figure 2b. According to the data given in electrolyte uptake, the highest uptake percentage of 2.0M KCl was for 1:2 membrane which was 97.407% and 82.845% for 2.0 M NaCl. The error bars for this 1:2 membrane were larger because of the excessive uptake which led to more swollen membranes (Figure 2b) and making it difficult to completely remove surface water.

PPC & PETROMAT SYMPOSIUM 2025

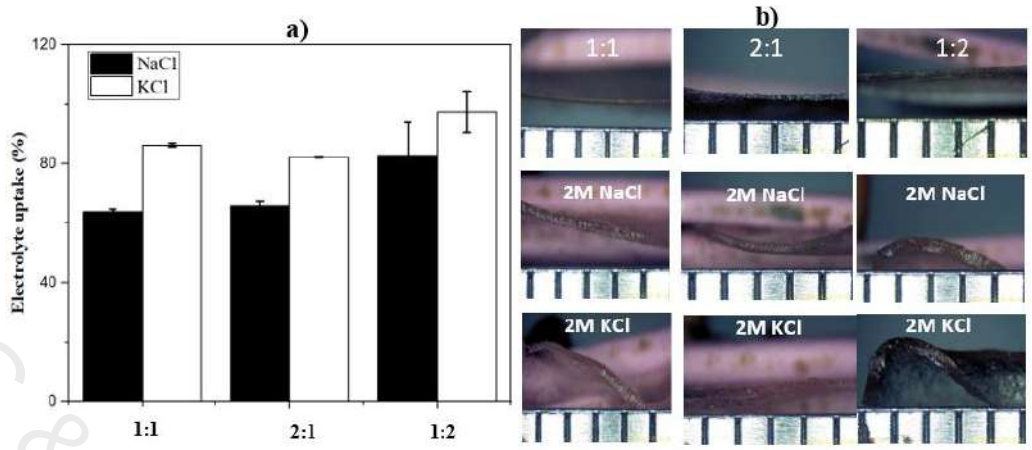


**Figure 2** a. 2.0M NaCl and KCl uptake on all stoichiometries b. Swelling of all stoichiometric membranes using optical microscopy.

Based on these results, it can be concluded that excess negative chargers in the 1:2 membrane attract more KCl than NaCl. Since the salts has same anion, much effect on the membranes' electrolyte uptake was based on the cations; $K^+$ and $Na^+$. When compared to $Na^+$ and $K^+$, their behaviour differs due to the size of the ion and the hydration shell. Although $K^+$ ion is larger in atomic radius than $Na^+$, its hydration shell is smaller in $K^+$ than $Na^+$, making more ions absorbed in to the negatively charged membrane.

However, it is advisable to precondition the membranes before conducting ion transport studies to enhance ion pairing in the membranes containing excess salts. NaCl was selected for this purpose as it also acts as a plasticizer during membrane preparation. Further, NaCl 2.0M is not highly effective at causing membrane swelling and the membrane tends to lose its mechanical strength by absorbing a greater number of cations such as $K^+$

*C. Annealing of PEC membranes*

EIS was used to examine the ion transport in the membrane as a function of time during annealing. In this study, 1:1 PEC membrane was analyzed with EIS, UV-Vis spectroscopy to represent the overall behavior. Figure 3a shows the Nyquist plots with real and imaginary impedance. Accordingly, the Nyquist plot exhibits depressed semicircular arcs followed by a Warburg tail which represents the membrane impedance and ion diffusion rate respectively. In the beginning, in Figure 3b the Nyquist curve displayed a large semicircle diameter, a lower angle with respect to the real impedance (Z') axis, and a long tail. However, over time, the semicircle diameter decreased, the angle with real impedance axis becomes higher, and the tail length becomes shorter which represents the membrane resistance drops, enhanced ion diffusion, less ion accumulation near the membrane and ideal diffusion respectively.

Briefly, high ionic concentration of salts leads to rearrangement of PSS and PDADMAC, leading to resulting in a more ordered membrane structure. Further, more $Na^+$ and $Cl^-$ reduces electrostatic repulsion between oppositely charged polyelectrolyte groups and allowing them to come closer and form more stable ion pairs. Therefore, in the beginning, ion transport through the membrane was limited to the membrane, possibly due to the high

PPC & PETROMAT SYMPOSIUM 2025

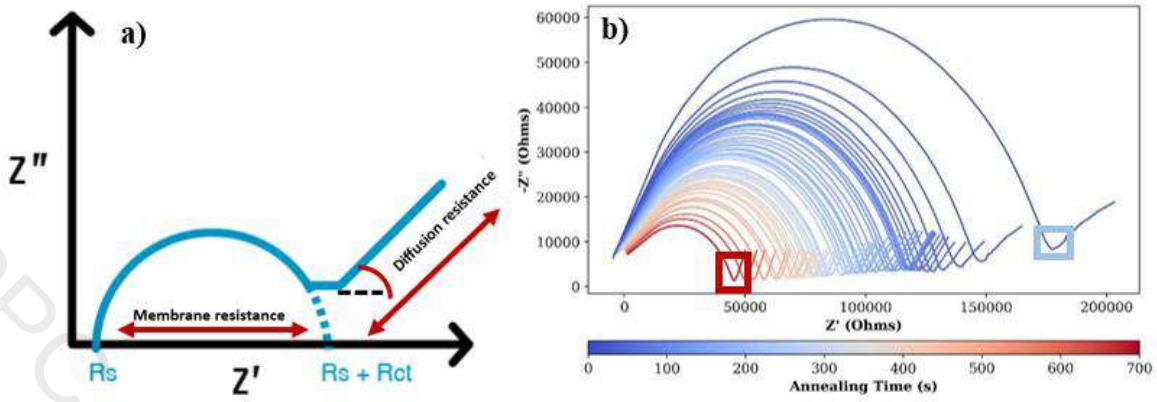


**Figure 3** a. Schematic representation of Nyquist plot b. Annealing of 1:1 PEC membrane in 2M NaCl within 10 min. time intervals.

tortuosity, incomplete swelling or tight polymer packing. Thus, overall, the system was not yet equilibrated, and ions had higher resistance to transport in the beginning. However, in the later stages, ion pathways became clearer due to the swelling of the membrane, reorganization of polymer chains, and equilibration with electrolyte and ions experienced lower resistance to transport. Accordingly, with time, membranes altered their pathways for easier ion transportation.

*D. Dye diffusion through annealed and non-annealed membranes*

To investigate this behavior, concentration-driven diffusion of methyl orange (MO) was examined using an H-cell setup. Both annealed and non-annealed 1:1 PEC membranes were placed between the two compartments. Here, the results show that UV spectrum

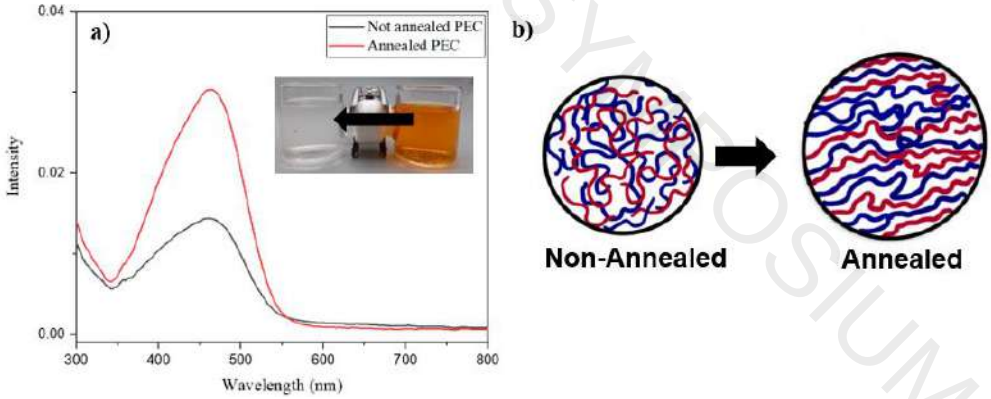


**Figure 4** a. UV-Vis spectra of Methyl Orange diffusion through annealed (1:1) and non-annealed (1:1) membranes b. Schematic representation of annealing.

related to annealed samples has more MO intensity (peak 460nm) in DI water compartment compared to non-annealed compartment after 24 hours. This observation further confirms that annealing leads to rearrangements of PSS and PDADMAC chains, reducing complexity and facilitating ion movement through PEC membrane. These findings highlight the importance of annealing PECs prior to conducting further ion-transport studies.

*E. KCl and NaCl ion resistivity via EIS*

**Table 1** EIS data of PEC membranes' resistivity to salts

| *Conc.* | *1: 1 (Ohms)* | | *1: 2 (Ohms)* | | *2: 1 (Ohms)* | |
|---|---|---|---|---|---|---|
| *Moldm-3* | **NaCl** | **KCl** | **NaCl** | **KCl** | **NaCl** | **KCl** |
| **1.0** | 116.72 | 88.74 | 111.02 | 82.41 | 124.50 | 84.17 |
| **1.5** | 83.20 | 59.63 | 77.16 | 55.80 | 82.45 | 61.10 |
| **2.0** | 68.22 | 48.43 | 62.77 | 45.02 | 66.21 | 49.34 |
| **2.5** | 45.50 | 37.85 | 50.51 | 34.78 | 51.90 | 38.77 |

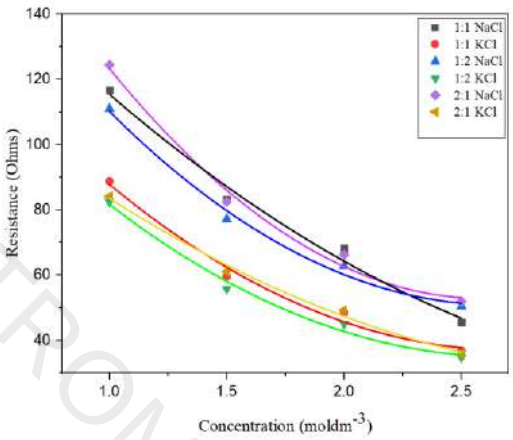


**Figure 5** Summary of Nyquist plots data for NaCl and KCl resistance for 1.0, 1.5, 2.0, 2.5 moldm$^{-3}$ concentrations.

Both NaCl and KCl demonstrated lower resistance as their concentrations increased from 1M to 2.5M (Figure 5, Table 1). On the other hand, 1:2 PEC membrane exhibited the lowest ion resistance—45 Ω for NaCl and 34 Ω for KCl compared to 2:1(51Ω, 38Ω) and 1:1 (50Ω, 37Ω) stoichiometries. In PSS-rich membranes, the enhanced charge density and greater swelling capacity (section B) enable more efficient cation transport, reducing overall ionic resistance. These membranes not only attract cations but also facilitate their movement. This overall result suggests that while the membrane undergoes some structural rearrangement to facilitate ionic pathways, these membranes not only attract cations but also facilitate their movement. Further, despite being larger, $K^+$ ions can traverse annealed PEC membranes more efficiently than $Na^+$ due to their weaker hydration shell, higher mobility, and lower interaction with the fixed charges within the membrane.

## CONCLUSIONS

In this study, EIS revealed a reduction in resistivity upon annealing the membranes in 2 M NaCl. UV–vis spectroscopy of dye diffusion through annealed and non-annealed membranes showed increased diffusion in the annealed samples, supporting the hypothesis that annealing enhances the reorganization of ionic pathways. Additionally, $K^+$ ions exhibited lower ionic resistance than $Na^+$, which is attributed to differences in ion size and hydration properties. These findings indicate that ionic annealing, membrane structure, and ion-specific transport behavior are critical for applications such as battery separators and crossflow polymerization. Moreover, this system shows potential as a cost-effective alternative to commercially available Nafion membranes.

PPC & PETROMAT SYMPOSIUM 2025

## ACKNOWLEDGEMENTS

The author sincerely acknowledges The Petroleum and Petrochemical College, Chulalongkorn University and the ASEAN and non-ASEAN scholarship programme.

## REFERENCES

1. **Zhang, M., Guan, K., Ji, Y., Liu, G., Jin, W., & Xu, N. (2019).** Controllable ion transport by surface-charged graphene oxide membrane. *Nature Communications*, 10.
2. **Zhang, M., Zhao, P., Li, P., Ji, Y., Liu, G., & Jin, W. (2021).** Designing Biomimic Two-Dimensional Ionic Transport Channels for Efficient Ion Sieving. *ACS nano*.
3. **Zuo, P., Ye, C., Jiao, Z., Luo, J., Fang, J., Schubert, U., McKeown, N., Liu, T., Yang, Z., & Xu, T. (2023).** Near-frictionless ion transport within triazine framework membranes. *Nature*, 617, 299 - 305.
4. **Zuo, P., Xu, Z., Zhu, Q., Ran, J., Ge, L., Ge, X., Wu, L., Yang, Z., & Xu, T. (2022).** Ion Exchange Membranes: Constructing and Tuning Ion Transport Channels. *Advanced Functional Materials*, 32.
5. **Luangaramvej, P., Wijitsettakun, P., Plengplung, P., & Dubas, S. T. (2021).** In-situ polymerization of polyaniline in PDADMAC/PSS complex membranes: Effect of the polyelectrolyte stoichiometry. *Journal of Applied Polymer Science, 139*(4), e51684.
6. **Krishna, A., Lindhoud, S., & de Vos, W. M. (2021).** Hot-pressed polyelectrolyte complexes as novel alkaline stable monovalent-ion selective anion exchange membranes. *Journal of Colloid and Interface Science, 593*, 11–20.
7. **Sadman, K., Delgado, D. E., Won, Y., Wang, Q., Gray, K. A., & Shull, K. R. (2019).** Versatile and high-throughput polyelectrolyte complex membranes via phase inversion. *ACS Applied Materials & Interfaces, 11*(15), 16018–16026.
8. **Durmaz, E. N., Kaya, T., Yildiz, H. B., Tufani, A., & Okay, O. (2021).** Polyelectrolytes as building blocks for next-generation membranes with advanced functionalities. *ACS Applied Polymer Materials, 3*(9), 4347–4374.
9. **Rumyantsev, A. M., Zhulina, E. B., & Borisov, O. V. (2023).** Surface-immobilized interpolyelectrolyte complexes formed by polyelectrolyte brushes. *ACS Macro Letters, 12*(12), 1587–1592.
10. **Schaaf, P., & Schlenoff, J. B. (2015).** Saloplastics: Processing compact polyelectrolyte complexes. *Advanced Materials, 27*(15), 2420–2432.
11. **Lazanas, A.C. and M.I. Prodromidis, (2023).** Electrochemical Impedance Spectroscopy─A Tutorial. *ACS Measurement Science Au,* 3(3), 162

PPC & PETROMAT SYMPOSIUM 2025

# BIOSYNTHESIZED ZINC OXIDE NANOPARTICLES BY HYDROALCOHOLIC PLANT EXTRACTS FOR PLA/PEG BIOCOMPOSITES

*Sittikorn Bawthong* [a,b], *Nattakarn Hongsriphan* [a,b] , *Pajaera Patanathabutr* [a,b]

[a] Department of Materials Science and Engineering, Faculty of Engineering and Industrial Technology Silpakorn University
[b] Center of Excellence on Petrochemical and Material Technology, Chulalongkorn University

Keywords: Green synthesis, Zinc oxide nanoparticles , PLA/PEG biocomposites , Active food packaging

## ABSTRACT

The development of sustainable nanocomposite materials incorporating biofunctional nanomaterials has attracted significant interest for environmentally friendly applications, particularly in antimicrobial packaging. Zinc oxide nanoparticles (ZnO-NPs) are especially promising due to their inherent antimicrobial and UV-blocking properties. This study focused on the green synthesis of ZnO-NPs using hydroalcoholic extracts of *Andrographis paniculata* leaves and *Garcinia mangostana* peels, both rich in phytochemicals that serve as natural reducing and stabilizing agents. Total phenolic content (TPC) analysis revealed substantially higher concentrations in *Garcinia mangostana* peel (153 mg GAE/g) compared to *Andrographis paniculata* leaves (13 mg GAE/g), with an optimal ethanol–water extraction ratio of 75:25 (v/v). Fourier-transform infrared spectroscopy (FTIR ) confirmed the presence of phenolic compounds involved in ZnO-NPs formation. X-ray diffraction (XRD) verified the crystalline wurtzite structure of ZnO, while scanning electron microscopy (SEM) and energy-dispersive X-ray spectroscopy (EDX) were used to assess nanoparticle morphology, size, and elemental composition. The biosynthesized ZnO-NPs were subsequently incorporated into polylactic acid (PLA)/polyethylene glycol (PEG) composites (80:20 w/w) master batch to evaluate their performance in biodegradable films. These results highlight the potential of phytomediated ZnO-NPs as multifunctional nanofillers for active food packaging applications.

*** Bawthong_S@su.ac.th**

## INTRODUCTION

Nanotechnology enables the creation of nanocomposite films with enhanced gas barrier and antimicrobial properties for sustainable food packaging, while blending biodegradable polylactic acid (PLA) with polyethylene glycol (PEG) improves its flexibility and processability. Zinc oxide nanoparticles (ZnO-NPs) are added to PLA/PEG films to enhance antibacterial activity, UV protection, gas barrier properties, and mechanical strength, while green synthesis using plant extracts offers an eco-friendly alternative to conventional chemical methods. *Andrographis paniculata* leaves and *Garcinia mangostana* peel, rich in phenolics and flavonoids, serve as eco-friendly plant extracts that act as natural reducing and stabilizing agents for the green synthesis of biocompatible ZnO nanoparticles suitable for food-related applications. This study aims to synthesize green ZnO-NPs and incorporate them into PLA/PEG blends to produce biodegradable active packaging films.

PPC & PETROMAT SYMPOSIUM 2025

## EXPERIMENTAL

*A. Materials*

Both *Andrographis paniculate* leaves (APL) and *Garcinia mangostana* peels (GMP) were sourced from local cultivators in Uthai Thani and Chanthaburi provinces of Thailand,respectively. Zinc acetate dihydrate (99.5%) and polyethylene glycol (PEG 6000, lab grade)were purchased from KemAus. Polylactic acid (PLA 4043D) were purchased from SMART BIO PLASTIC Co., Ltd. The total phenolic content was analyzed using the Folin–Ciocalteu reagent and gallic acid monohydrate (98%) were supplied by CTi & SCIENCE Co., Ltd. Sodium hydroxide(99% AR.grade), 95% ethanol(Solvent grade), and deionized water were used as solvents.

*B. Plant extracts preparation*

Both plants were washed, dried at 50 °C for 6 hours, and ground into powder. A total of 5 g of dried plant powder was extracted with 100 mL of 75% ethanol (ethanol:water = 75:25, v/v), which was selected based on prior evaluation of extraction efficiency. The extraction was performed at a solid-to-solvent ratio of 1:20 (w/v) by stirring at 70 °C for 2 hours. After cooling, the mixture was vacuum filtered, and the crude extract was stored at 4 °C for further experiments. Based on the total phenolic content (TPC), the phenolic concentration in the extract was estimated to be approximately 0.625 mg/mL for Andrographis paniculata, and 7.675 mg/mL for *Garcinia mangostana*, expressed as gallic acid equivalents (GAE). FTIR spectroscopy (4000–600 $cm^{-1}$) and UV-Vis spectroscopy (200–800 nm) were used to analyze the functional groups and UV absorption properties, respectively.

*C. Characterization of Plant extracts*

Total phenolic content (TPC) of the plant extract as measurement using the Folin–Ciocalteu method. Results were expressed as milligrams of gallic acid equivalents per gram of extract (mg GAE/g dry weight).Chemical functional groups of the plant extract were analyzed by FTIR (Vertex 70, Bruker, Germany) using ATR mode, with spectra recorded from 600 to 4000 $cm^{-1}$ at 4 $cm^{-1}$ resolution.The ultraviolet-visible (UV-Vis-1280,Shimazu) light absorption of the plant extract was analyzed using a UV-Vis Spectrophotometer, scanning wavelengths from 200 to 800 nm.

*D. Synthesis of zinc oxide nanoparticles (ZnO Nps)*

Zinc oxide nanoparticles were synthesized by mixing 75 mL of plant extract with 25 mL of 0.2 M zinc acetate dihydrate solution (extract-to-zinc acetate ratio of 3:1, v/v). The mixture was stirred at 500 rpm and 70 °C for 1 hour. The pH was adjusted and maintained at 12 using 3 M NaOH, followed by an additional 2 hours of stirring under the same conditions.(Dappula et al., 2023) The resulting precipitate was centrifuged at 6000 rpm for 30 minutes at 25 °C, washed with deionized water, and oven-dried at 80 °C for 2 hours. The dried product was then calcined at 800 °C for exactly 1 hour to yield ZnO nanoparticles.

*E. Characterization of zinc oxide nanoparticles (ZnO NPs)*

The crystalline structure of ZnO nanoparticles was analyzed using XRD (XRD-6100, Shimazu) with Cu Kα radiation (λ = 1.5418 Å), operating at 30 kV and 20 mA, over a 2θ range of 20–90°. Morphology and particle size were examined using SEM (MIRA3 Tescan) at 20,000×and50,000×magnification with 15 kV accelerating voltage. Samples

were gold-coated to prevent charging at 30 sec. Powdered samples were compacted before XRD analysis. EDX attached to SEM was used to confirm elemental composition (Zn, O, and trace N, P, K) of the synthesized ZnO nanoparticles.EDX analysis was performed using EDAX APEX with a resolution of 131.5 eV. Elemental quantification was conducted using the built-in Smart Quant method with standardless ZAF correction.

*F. Composite compounding and processing*

PLA, PEG, and ZnO nanoparticles were initially blended at a ratio of 80:20:1 using a twin-screw extruder (SHJ-25, China) operated at 100 °C (zone 1), 140 °C (zone 2), 170 °C (zone 3), and 190 °C at the die head. and 50 rpm to produce a masterbatch, which was then pelletized. The masterbatch was subsequently mixed with neat PLA at 80:20 and 60:40 ratios (neat PLA to masterbatch) to achieve final PLA:PEG:ZnO-NPs compositions of 96:4:0.2 and 92:8:0.4, respectively. These blends were processed into films via cast film extrusion using zone temperatures of 140 °C (zone 1), 160 °C (zone 2), and 180 °C (die head), operated at a screw speed of 60 rpm.

## RESULTS AND DISCUSSION

Figure 1 show that Total phenolic content (TPC) varied with plants. *Andrographis paniculate* leaves showed highest TPC in 100% ethanol (19.91 mg GAE/g) (Adaramola et al., 2018), while *Garcinia mangostana* peels showed highest TPC in 50% ethanol (194.29 mg GAE/g) (Suttirak& Manurakchinakorn, 2014), highlighting the effectiveness of ethanol –water mixtures.

However, 50% ethanol caused gel formation and filtration issues, while 100% ethanol evaporated rapidly. Therefore,75% ethanol was selected as optimal for its high yield, easier handling. FTIR spectra of *Andrographis paniculate* leaves and *Garcinia mangostana* peels extract exhibit similar peaks, indicating shared functional groups. A broad peak at 3200 –3600 $cm^{-1}$ corresponds to O–H stretching, prominent in water-rich extracts due to hydroxyl groups from water, ethanol, and phenolics. Peaks at 2800–3000 $cm^{-1}$, associated with C–H stretching,are stronger in ethanol-rich extracts, reflecting ethanol and organic compounds. Additionally, a peak near 1640 $cm^{-1}$ suggests C=O stretching or H–O–H bending vibrations and peaks at 1450–1600 $cm^{-1}$ (C=C stretching) suggest aromatic rings, while 1000–1100 $cm^{-1}$ (C –O stretching)reflects phenolics and ethanol. The 875 $cm^{-1}$ peak, seen in *Garcinia mangostana* peel, indicates aromatic C–H bending. The ethanol:water ratio influences peak intensity, affecting compound extraction based on solvent polarity. (Dappula et al., 2023)

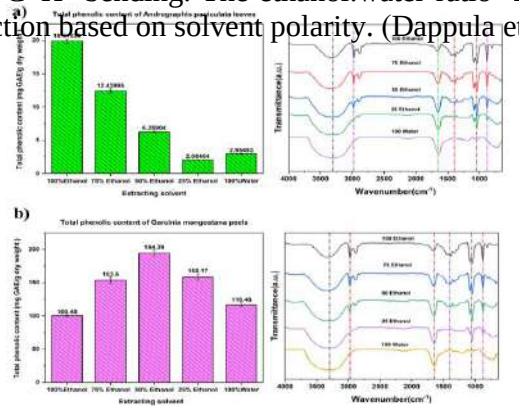


**Figure 1.** Total phenolic content and FTIR spectra of a) *Andrographis paniculate* leaves extract b) *Garcinia mangostana* peels extract.

PROCEEDINGS OF PPC & PETROMAT SYMPOSIUM 2025

Figure 2 show XRD patterns of ZnO–MGP, ZnO–APL, and commercial ZnO show characteristic peaks of hexagonal wurtzite ZnO at specific 2θ values. The biosynthesized ZnO-NPs displayed peak positions similar to commercial ZnO, confirming successful crystallization. Slight variations in peak intensity and width, especially in ZnO–MGP, suggest smaller crystallite sizes or morphological differences due to phytochemical influence. This indicates both plant extracts effectively guided ZnO formation for potential functional use.(Jaithon et al., 2024)

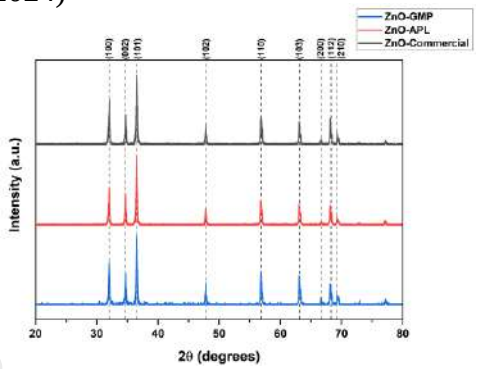


**Figure 2.** XRD patterns of ZnO nanoparticles synthesized from *Andrographis paniculate* leaves (APL) and *Garcinia mangostana* peels (GMP) , compared with commercial ZnO.

SEM images in Figure 3 show that ZnO nanoparticles synthesized using *Andrographis paniculate* leaves (a, b) are predominantly spherical with minimal aggregation and an average diameter of 286.60 nm. In contrast, ZnO nanoparticles from *Garcinia mangostana* peels (d, e) exhibit rod-like shapes, greater aggregation, and a larger average size of 443.04 nm (Jaithon et al., 2024). These morphological differences arise from variations in phytochemical composition, which affect particle nucleation and growth; *Andrographis paniculata leaves* likely enhance stabilization, yielding smaller, more uniform particles, while *Garcinia mangostana* peels promote crystal growth, resulting in larger, anisotropic structures. Both plant extracts effectively enable green synthesis, though their distinct physicochemical properties suggest different potential applications (Cao et al., 2021).

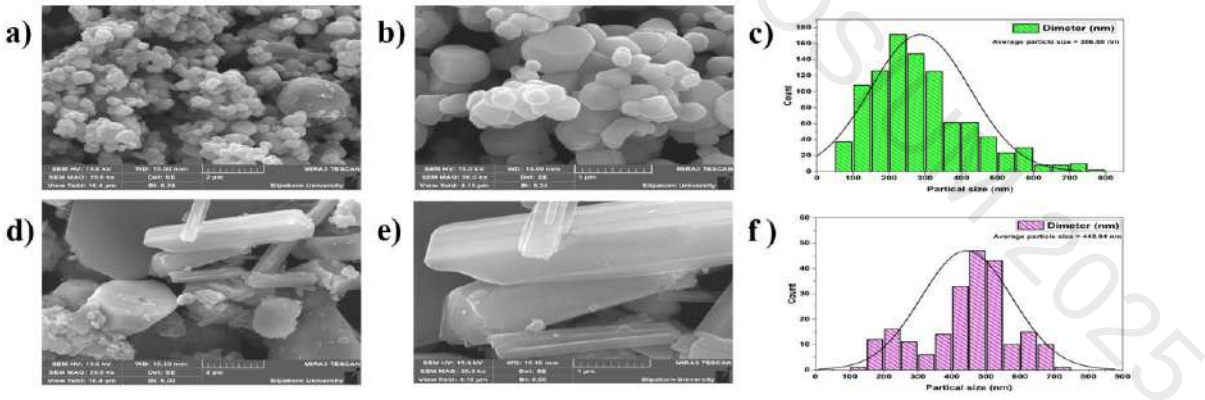


**Figure 3**. SEM images and particle size distribution of ZnO-NPs synthesized using *Andrographis paniculata* leaves (a–c) and *Garcinia mangostana* peels (d–f).

EDX results in Figure 4 show that ZnO-NPs synthesized from *Andrographis paniculata leaves* has a high Zn content (84.26%), indicating high purity and uniform crystallinity, which correlates with the formation of small, spherical particles. In contrast, ZnO from *Garcinia mangostana* peels contains lower Zn content (59.84%) and higher amounts of O and K. The presence of K in the structure may lead to substitution or interstitial incorporation, causing lattice strain. This structural distortion disrupts regular crystal growth and results in irregular morphologies, such as rods or plate-like structures.(Dappula et al., 2023)

**Figure 4.** EDX spectra of ZnO-NPs synthesized using a) *Andrographis paniculata leaves* and b) *Garcinia mangostana* peels extracts.

In Figure 5, film clarity was affected by PEG content and ZnO nanoparticle incorporation. Neat PLA (a) was highly transparent but brittle, while PLA/PEG blends at 96:4 (b) and 92:8 (c) improved flexibility. The 80:20 blend (d) exhibited poor formability and surface defects, likely due to excessive PEG reducing matrix compatibility. To ease processability, an 80:20:1 PLA:PEG:ZnO nanoparticle masterbatch was prepared and then mixed with neat PLA at 80:20 and 60:40 ratios to achieve final compositions of 96:4:0.2 and 92:8:0.4 (e–h). Films containing ZnO-NPs synthesized from *Andrographis paniculata* leaves (e, f) appeared more opaque than those with ZnO-NPs from *Garcinia mangostana* peels (g, h). Notably, film (h) was clearer than film (f) despite both having the same PEG ratio (92:8), indicating better dispersion and morphology of the *Garcinia mangostana* peels derived ZnO. In contrast, ZnO-NPs derived from *Andrographis paniculata* leaves may have agglomerated more under high PEG conditions, leading to increased film turbidity. The masterbatch improved processability and enhanced the dispersion of both ZnO-NPs and PEG, resulting in greater film uniformity and improved visual quality (Shin et al., 2022).

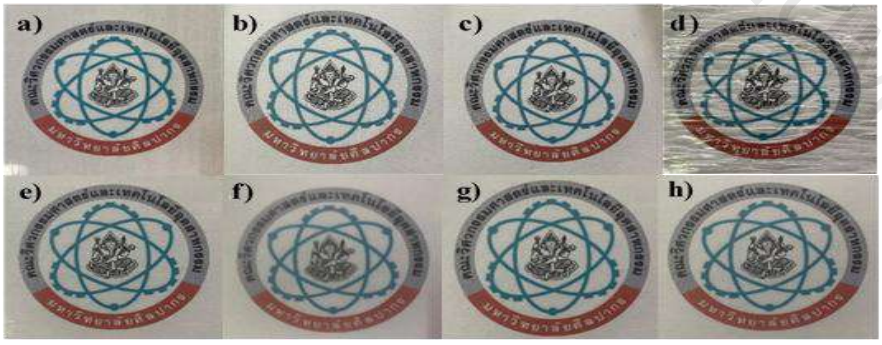


**Figure 5.** a) Neat PLA, b) PLA/PEG (96:4), c) PLA/PEG (92:8), d) PLA/PEG (80:20) , e) PLA/PEG/ZnO-NPs APL (96:4:0.2) , f) PLA/PEG/ZnO-NPs APL (92:8:0.4), g) PLA/PEG/ZnO-NPs GMP (96:4:0.2), h) PLA/PEG/ZnO-NPs GMP (92:8:0.4)

## CONCLUSIONS

This research successfully synthesized green zinc oxide nanoparticles (ZnO-NPs) through an eco-friendly process using hydroalcoholic extracts of *Andrographis paniculata leaves* and *Garcinia mangostana* peels, with each extract's unique phytochemicals influencing the nanoparticles size, shape, and elemental composition. ZnO-NPs from *Andrographis paniculata leaves* extracts were smaller and more spherical, while those from *Garcinia mangostana* peels extracts exhibited larger, rod-like structures. These nanoparticles were incorporated into biodegradable PLA/PEG blends via a masterbatch approach, which eased film processability and improved nanoparticle dispersion of ZnO-NPs and PEG within the polymer matrix. Optical assessments showed that films with *Garcinia mangostana* peels extracts derived ZnO had superior clarity, likely due to better nanoparticle dispersion and morphology. Overall, incorporating biosynthesized ZnO-NPs into PLA/PEG composites at ratios of 96:4:0.2 and 92:8:0.4 offers a promising and sustainable approach for developing active food packaging materials. Further studies will focus on evaluating the improved mechanical and structural properties of these films for packaging applications.

## ACKNOWLEDGEMENTS

The authors thank the Department of Materials Science and Engineering, Faculty of Engineering and Industrial Technology, Silpakorn University and Hub of Talent: Sustainable Materials for Circular Economy, National Research Council of Thailand (NRCT).

## REFERENCES

**Adaramola, F., Benjamin, G., Oluchi, O., & Fapohunda, S. (2018).** Antimicrobial and antioxidant activities of crude methanol extract and fractions of Andrographis paniculata leaf (Family: Acanthaceae) (Burm. f.) wall. Ex Nees. Jordan Journal of Biological Sciences, 11, 23-30.

**Cao, Y., Alijani, H. Q., Khatami, M., Bagheri-Baravati, F., Iravani, S., & Sharifi, F. (2021).** K-doped ZnO nanostructures: biosynthesis and parasiticidal application. Journal of Materials Research and Technology, 15, 5445-5451.

**Dappula, S. S., Kandrakonda, Y. R., Shaik, J. B., Mothukuru, S. L., Lebaka, V. R., Mannarapu, M., & Amooru, G. D. (2023).** Biosynthesis of zinc oxide nanoparticles using aqueous extract of Andrographis alata: Characterization, optimization and assessment of their antibacterial, antioxidant, antidiabetic and anti-Alzheimer's properties. Journal of Molecular Structure, 1273, 134264.

**Jaithon, T., Atichakaro, T., Phonphoem, W., T-Thienprasert, J., Sreewongchai, T., &T -Thienprasert, N. P. (2024).** Potential usage of biosynthesized zinc oxide nanoparticles from mangosteen peel ethanol extract to inhibit Xanthomonas oryzae and promote rice growth. Heliyon, 10(1), e24076.

**Shin, H., Thanakkasaranee, S., Sadeghi, K., & Seo, J. (2022).** Preparation and characterization of ductile PLA/PEG blend films for eco-friendly flexible packaging application. Food Packaging and Shelf Life, 34, 100966.

**Suttirak, W., & Manurakchinakorn, S. (2014).** In vitro antioxidant properties of mangosteen peel extract. J Food Sci Technol, 51(12), 3546-3558.

PPC & PETROMAT SYMPOSIUM 2025

# ECO-FRIENDLY PLA COMPOSITES MADE WITH EGGSHELL-SOURCED CALCIUM OXIDE AND D-LIMONENE FOR 3D PRINTING

*Pajaera Patanathabutr*[*,a,b], *Panisara Deelert* [a,b], *Nattariga Kewthong* [a,b], *Tawatchai Arthonkij* [a,b] *Nattakarn Hongsriphan* [a,b]

[a] Department of Materials Science and Engineering, Faculty of Engineering and Industrial Technology Silpakorn University
[b] Center of Excellence on Petrochemical and Materials Technology, Chulalongkorn University

Keywords: Calcium oxide, PLA composites, D-Limonene, 3D Printing

## ABSTRACT

The increasing problem of plastic waste from non-degradable polymers has prompted the development of biodegradable alternatives, such as polylactic acid (PLA)-based composites enhanced with additives like calcium oxide (CaO) derived from chicken eggshells, a byproduct of the food industry. This study investigates the synthesis of calcium oxide (CaO) from chicken eggshells and its incorporation into a polylactic acid (PLA)-based polymer composite. The composite formulation includes 5 phr of CaO and 5 phr of D-limonene, aiming to develop a material suitable for use as filament in 3D printing technology. CaO was synthesized by calcining pre-treated eggshells at 900°C for 3 hours. The microstructure, thermal behaviours, and mechanical properties of the PLA/CaO/D-limonene composites were analysed. A comparative analysis of 3 D-printed specimens and injection-moulded specimens revealed that CaO is well-dispersed within the polymer matrix of the 3 D-printed specimens, enhancing their tensile strength. Meanwhile, D-limonene improves the melt flow behaviours of the PLA/CaO composite, making it a promising alternative for use as a filament in 3D printing through fused deposition modelling (FDM) technology.

*** Patanathabutr_P@su.ac.th**

## INTRODUCTION

Recent advancements in 3D printing have enhanced its accessibility and sustainability by enabling the fabrication of complex structures with high precision and reduced material waste, supporting global decarbonization efforts. However, the accumulation of non-biodegradable plastic waste from 3D printing raises environmental concerns. Polylactic acid (PLA), a biodegradable thermoplastic derived from renewable resources such as corn starch or sugarcane, offers a greener alternative to petroleum-based polymers. Nonetheless, its brittleness and limited thermal stability hinder its broader use in fused deposition modeling (FDM) (Moshood, T. D., 2022). To overcome these limitations, functional fillers and plasticizers have been explored. Calcium oxide (CaO), traditionally derived from limestone, can be sustainably synthesized from calcium carbonate-rich waste like chicken eggshells, supporting circular economy practices. In PLA-based composites, CaO acts as an effective reinforcing filler, enhancing mechanical strength and thermal resistance, and crystallinity of the polymer matrix. D-limonene, a bio-based monoterpene extracted from citrus peel waste, serves as an eco-friendly plasticizer that enhances PLA's melt processability and thermal stability. This study aims to develop PLA composite filaments containing eggshell-derived

PPC & PETROMAT SYMPOSIUM 2025

CaO and D-limonene for FDM 3D printing, with comparative evaluation of their structural and mechanical properties in both injection-molded and 3D-printed forms.

## EXPERIMENTAL

*A. Materials*

Polylactic acid (PLA 4043D) were purchased from SMART BIO PLASTIC Co., Ltd., Eggshells waste from the omelet rice shop in Silpakorn University, Calcium oxide was purchased from ITALMAR (THAILAND) CO., LTD.

*B. CaO Synthesis from Chicken Eggshells and Characterization of CaO*

Chicken eggshells were processed to synthesize calcium oxide (CaO) through chemical precipitation, followed by direct calcination methods. In the chemical route, ground and dried eggshells were reacted with 1% HCl to form calcium chloride ($CaCl_2$), which was then precipitated with NaOH to obtain calcium hydroxide ($Ca(OH)_2$), followed by calcination at 900 °C for 3 hours to produce CaO. For comparison, direct calcination of eggshell powder at 700 °C, 800 °C, and 900 °C was conducted to convert calcium carbonate into CaO. The percentage yield was calculated based on the initial mass of dried eggshells. Energy Dispersive X-ray Spectroscopy (EDS) and X-ray Diffraction (XRD) analyses were used to evaluate the chemical composition, crystal structure, and crystallinity of the resulting CaO samples, as well as to compare them with commercial CaO.

*C. Composite compounding and 3D filament processing and Preparation of PLA composite FDM printed specimens and injection molding specimens*

PLA composites containing 5 phr of synthesized CaO, with and without 5 phr of D-limonene, were dried at 80 °C for 24 hours before compounding. The materials were processed using a twin-screw extruder using a twin-screw extruder (SHJ-25, China) equipped with a round-shaped die with a 2 mm diameter under a controlled temperature profile (140–180 °C) and a screw speed of 45 rpm to produce filaments with diameters between 1.5–1.75 mm, suitable for FDM 3D printing. These CaO/PLA filaments, along with neat PLA, were 3D printed into ASTM D638 dog-bone specimens using an FDM printer (Model 557E1, NTT Pro IIID). For comparison, similarly formulated PLA composites were also molded into ASTM D638 specimens using an injection molding machine (Model PS40E5ASE, NISSEI), ensuring consistent material preparation for mechanical testing.

*D. Characterization of CaO/PLA FDM specimens and injection molding specimens*

Neat PLA and CaO/PLA composites, with and without 5 phr D-limonene, were characterized using various analytical techniques. The melt flow index (MFI) was measured at 180 °C under a 2.16 kg load, with triplicate testing for each formulation. Thermal behavior was analyzed using Differential Scanning Calorimetry (DSC) with heating and cooling rates of 3 °C/min. Mechanical properties were assessed via tensile testing (Instron 5960, 50 kN load cell) according to ASTM D638 (Type I specimens, 50.2 mm gauge length, 50 mm/min crosshead speed). Fracture surface morphology was examined using a Scanning Electron Microscopy (SEM, TM3030, Hitachi) at accelerating voltages of 5–15 kV and magnifications ranging from 100× to 1200×.

## RESULTS AND DISCUSSION

PPC & PETROMAT SYMPOSIUM 2025

*A. Characterization of synthesized CaO*

The yield of calcium oxide (CaO) from chicken eggshells was evaluated using both direct thermal calcination and combined chemical-thermal methods. Direct calcination at 700 °C, 800 °C, and 900 °C produced CaO yields of 90.70% ± 1.28, 85.23% ± 1.21, and 63.54% ± 0.73, respectively. In contrast, the chemical route converting eggshells to calcium hydroxide ($Ca(OH)_2$) prior to calcination at an optimized temperature of 900 °C, yielded a significantly lower CaO content of 37.64% ± 1.34 but with no carbon impurities, confirming by Energy Dispersive X-ray Spectroscopy (EDS) as shown in Figure 1. All calcined samples contained calcium (Ca) and oxygen (O) as the main elements. carbon (C) content in raw chicken eggshells and samples calcined at lower temperatures (700–800 °C) indicated incomplete decomposition of organic and carbonate components. Higher temperature calcination at 900 °C confirmed a more complete thermal conversion to calcium oxide (CaO)

**Table 1.** EDS element analysis of calcium oxide from chicken eggshells by different methods.

| Samples | % element | | |
|---|---|---|---|
| | Ca | O | C |
| As received chicken eggshell | 35.31 | 56.28 | 8.40 |
| CaO calcination at 700 °C | 33.72 | 57.54 | 8.74 |
| CaO calcination at 800 °C | 37.11 | 53.24 | 9.66 |
| CaO calcination at 900 °C | 46.22 | 53.78 | 0.00 |
| $Ca(OH)_2$–CaO calcination at 900 °C | 63.07 | 36.93 | 0.00 |
| Commecial CaO powder | 54.20 | 45.80 | 0.00 |

XRD patterns of samples included untreated eggshell powder, thermally CaO from different thermal treated eggshells (700 °C, 800 °C, and 900 °C), CaO synthesized from calcium hydroxide ($Ca(OH)_2$) and calcined at 900 °C, and commercial CaO are shown in Figure 1. The structure and crystallinity of calcium oxide (CaO) derived from chicken eggshells were depends on phase transformations during different thermal treatment. Untreated eggshells exhibited characteristic diffraction peaks of calcium carbonate ($CaCO_3$), primarily in the calcite phase, consistent with previous studies (Alagarsamy et al., 2018). Progressive decomposition of $CaCO_3$ into CaO was observed with increasing calcination temperature. The sample calcined at 900 °C displayed sharp peaks at 2θ values of approximately 32.2°, 37.4°, 64.2°, and 67.6°, corresponding to crystalline CaO (Khalid et al., 2022). The $Ca(OH)_2$-derived sample also showed dominant CaO peaks, indicating successful conversion during calcination. Commercial CaO exhibited similar patterns, confirming high phase purity. Minor residual peaks in lower-temperature-calcined samples suggest incomplete decomposition or the presence of intermediate phases such as $Ca(OH)_2$. These results demonstrate that calcination at 900 °C effectively converts biogenic $CaCO_3$ in eggshells into crystalline CaO, with comparable quality to commercial products, supporting its viability as a sustainable and economical CaO source.

*B. Thermal and mechanical properties of synthesized CaO/PLA composites*

Figure 2 shows that the melt flow index (MFI) of CaO/PLA composites is lower than that of neat PLA. This reduction is attributed to the presence of CaO particles, which hindered the mobility of the molten PLA, leading to increased viscosity and reduced flowability. However,

PPC & PETROMAT SYMPOSIUM 2025

when D-limonene is incorporated into the formulation, the MFI of the CaO/PLA composites increased, indicating improved melt flow behavior and a reduction in viscosity. This enhancement is particularly advantageous for FDM 3D printing, as improved flowability enables smoother extrusion, better layer adhesion, and higher overall print quality. Therefore, D-limonene effectively offsets the negative impact of CaO on flow behavior, thereby making CaO/PLA composite more suitable for reliable 3D printing applications.

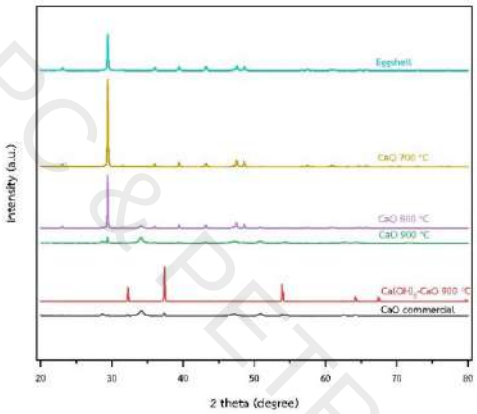


**Figure 1.** X-ray diffraction (XRD) patterns of untreated eggshells and CaO derived from eggshells under different conditions of treatment and commercial calcium oxide used for comparison.

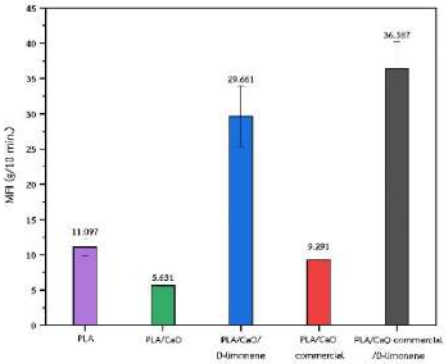


**Figure 2**. Melt flow index of neat PLA, PLA with synthesized CaO with and without D-limonene, PLA with commercial CaO, with and without D-limonene specimens

Table 2 shows that all PLA-based composites showed reduced glass transition temperatures ($T_g$) compared to neat PLA, indicating enhanced chain mobility. The addition of D-limonene further lowered $T_g$ and $T_{cc}$ due to its plasticizing effect. Neat PLA exhibited the highest $T_g$, reflecting its rigid structure. CaO incorporation also contributed to $T_g$ reduction, likely due to polymer–filler interactions that increase chain flexibility. The melting temperature ($T_m$) slightly increased with CaO addition, possibly due to its role as a nucleating agent. However, D-limonene had minimal effect on $T_m$, indicating its influence is limited to amorphous phase.

**Table 2.** Thermal Properties for of neat PLA, PLA with synthesized CaO with and without D-limonene, PLA with commercial CaO, with and without D-limonene specimens

| Samples | $T_g$ (°C) | $T_{cc}$ (°C) | $T_m$ (°C) | $X_c$(%) |
|---|---|---|---|---|
| neat PLA | 65.01 | 108.58 | 141.74 | 35.66 |
| 5phr synthesized CaO/PLA | 50.63 | 108.51 | 144.64 | 7.77 |
| 5phr synthesized CaO/PLA with 5 phr. D-limonene | 53.89 | 104.96 | 144.12 | 4.21 |
| 5phr commercial CaO/PLA | 46.49 | 97.99 | 139.87 | 9.01 |
| 5phr commercial CaO/PLA with 5 phr. D-limonene | 57.25 | 116.81 | 144.93 | 3.02 |

Tensile properties of PLA-based composite fabricated via FDM and injection moulding of formulations included neat PLA, PLA with synthesized CaO with and without D-limonene, PLA with commercial CaO, with and without D-limonene was shown in Figure 4. For FDM-printed specimens, the tensile strength values were 14.28±2.33, 15.43±2.89, 8.18±2.31, 9.55±1.63, and 13.87±1.31 MPa, respectively. Corresponding elongation at break values were 10.46±0.24%, 5.28±3.56%, 13.46±2.89%, 9.88±0.35%, and 12.57±4.76%, while

PPC & PETROMAT SYMPOSIUM 2025

tensile modulus values were 408.24±71.44, 730.50±44.18, 518.19±22.96, 743.03±10.43, and 620.20±17.25 MPa, respectively. While injection-moulded samples showed higher tensile strength and stiffness but lower elongation. The tensile strength values were 63.22±0.57, 18.02±3.23, 37.80±7.70, 27.96±3.06, and 34.16±2.93 MPa, with elongation values of 14.34±2.49%, 1.63±0.29%, 6.08±1.94%, 4.02±0.54%, and 5.53±0.63%, and tensile modulus values of 1110.13±30.64, 1494.76±26.00, 1341.55±86.70, 1295.39±32.28, and 1191.51±80.15 MPa, respectively. Injection-moulded specimens exhibited lower tensile strength but higher tensile modulus, indicating increased stiffness with reduced ductility. These results align with previous findings (Mishra, S. K. et al., 2021 and Pavon Vargas, C. P. et al., 2022) who reported that rigid fillers can improve stiffness due to rigid filler but may compromise strength due to filler agglomeration and stress concentration at the filler-matrix interface. Whie, the addition of D-limonene slightly reduced tensile strength in CaO/PLA composites but notably increased elongation at break, consistent with plasticizer-induced enhancement of polymer chain mobility (Arrieta, M. P.,2021). Overall, the results suggest that FDM-printed PLA composites, particularly those optimized with CaO and D-limonene, exhibit superior tensile properties, making them suitable for 3D printing FDM applications.

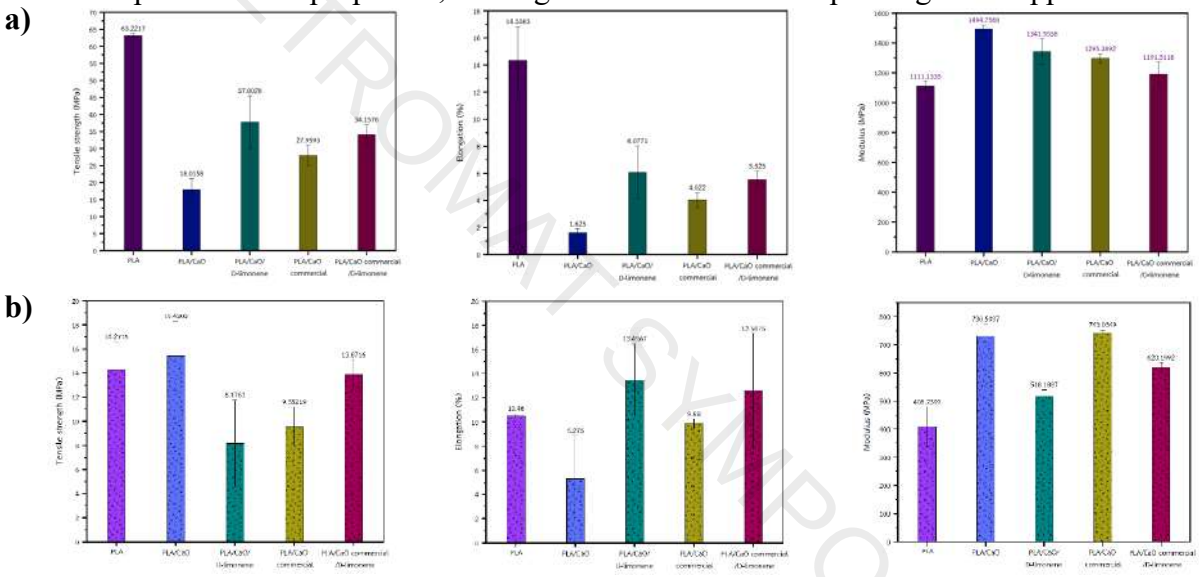


**Figure 4.** Tensile strength, elongation at break, and Tensile modulus of neat PLA, PLA with synthesized CaO with and without D-limonene, PLA with commercial CaO, with and without D-limonene specimens via a) 3D printing FDM and b) injection moulding.

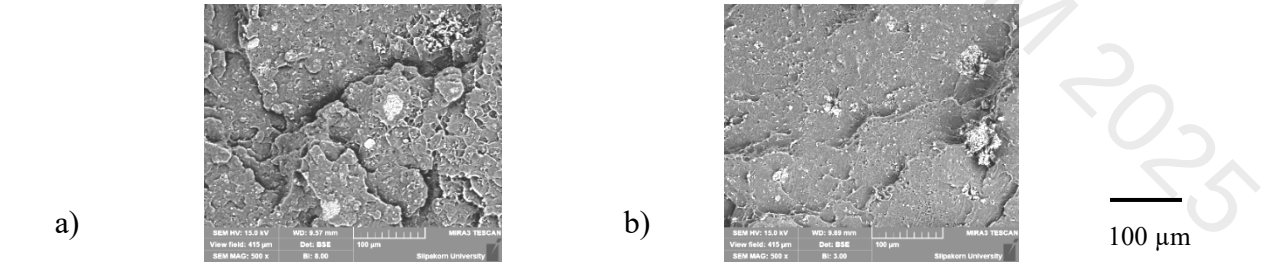


**Figure 5.** SEM analysis of fracture surface of PLA 3D printing FDM with CaO synthesized from eggshells a) without and b) with D-limonene

PPC & PETROMAT SYMPOSIUM 2025

Figure 5 revealed that PLA with 5 phr. synthesized CaO exhibited significant CaO agglomeration, indicating poor dispersion and weak interfacial bonding with the PLA matrix. The addition of D-limonene improved filler distribution, leading to more uniform particle dispersion and fewer interfacial voids. Although interlayer disturbances from FDM 3D printing remained, they were less pronounced in samples containing D-limonene, suggesting improved compatibility between the filler and polymer.

## CONCLUSIONS

This study successfully synthesized calcium oxide (CaO) from chicken eggshells via combined chemical and thermal methods, and subsequently incorporated the CaO into polylactic acid (PLA) composites using D-limonene as a plasticizer. Characterization results confirmed that the eggshell-derived CaO exhibited compositional properties comparable to those of commercial CaO. The incorporation of CaO enhanced the mechanical strength of the PLA composites, while D-limonene improved polymer chain mobility and melt flow, albeit with a slight reduction in tensile strength. The synergistic effects of CaO and D-limonene enabled tailored thermal and rheological properties suitable for 3D printing applications. Although injection moulding produced superior mechanical performance, fused deposition modelling (FDM) 3D printing offered greater design flexibility and material efficiency. Overall, this research demonstrates the potential of sustainable, bio-derived CaO fillers and natural D-limonene plasticizers in developing functional, eco-friendly PLA composites for FDM 3D printing, contributing to the advancement of biodegradable polymer technologies and circular economy initiatives.

## ACKNOWLEDGEMENTS

The authors thank the Department of Materials Science and Engineering, Faculty of Engineering and Industrial Technology, Silpakorn University and Hub of Talent: Sustainable Materials for Circular Economy, National Research Council of Thailand (NRCT).

## REFERENCES

**Alagarsamy, P., & Kandasamy, S. (2018).** Biomineralization of calcium carbonate in avian eggshells: A review. Journal of Materials Science, 53(5), 3397–3414.

**Arrieta, M. P. (2021).** Influence of plasticizers on the compostability of polylactic acid. Journal of Renewable Technologies, 2(1), 1–15.

**Khalid, M., Jikan, S. S., Adzila, S., & Badarulzaman, N. A. (2022).** Characterizations of calcium oxide from calcined eggshell waste. Key Engineering Materials, 908, 130–134.

**Mishra, S. K., Dahiya, S., Gangil, B., Ranakoti, L., & Agrawal, N. (2021).** Mechanical properties of fibre/filler based polylactic acid (PLA) composites: A brief review. Acta Innovations, 41, 5–18.

**Moshood, T. D., Nawanir, G., Mahmud, F., Mohamad, F., Ahmad, M. H., & AbdulGhani, A. (2022).** Biodegradable plastic applications towards sustainability: A recent innovations in the green product. Cleaner Engineering and Technology, 6, 100404.

**Pavon Vargas, C. P., Aldas, M., Samper, M., López, J., Rojas-Lema, S., & Cañadas, J. C. (2022).** Mechanical, dynamic-mechanical, thermal and decomposition behavior of 3D-printed PLA reinforced with $CaCO_3$ fillers from natural resources. Polymers, 14(13), 2646.

PPC & PETROMAT SYMPOSIUM 2025

# AN INFLUENCE OF ANIONIC SURFACTANT MOLECULAR STRUCTURES ON SURFACTANT-NANOPARTICLE INTERACTIONS FOR MITIGATING ADSORPTION ONTO SOLID SURFACES

*Piraya Bootkrut* [a], *Bor-Jier Shiau* [b], *Uthaiporn Suriyapraphadilok* [a], *Ampira Charoensaeng**, [a]

[a] The Petroleum and Petrochemical College, Chulalongkorn University, Bangkok, Thailand
[b] Mewbourne School of Petroleum and Geological Engineering, University of Oklahoma, Norman, Oklahoma, USA

Keywords: Adsorption, Enhanced oil recovery (EOR), Hydrophobic silica nanoparticle (SNP), Surfactant, Silica oxide, Alumina oxide

## ABSTRACT

Surfactant and silica nanoparticle (SNP) mixed system have gained significant attention for their potential in various applications, such as oil decontamination and oil recovery, due to reducing interfacial tension, improving surfactant efficiency, enhancing stability, wettability alteration, and reducing surfactant adsorption. The incorporation of hydrophobic silica nanoparticles extends adsorption at the solid properties, achieving, adsorption reduction, and promoting association in like-charged surfactant–silica nanoparticle systems. This study investigated the competitive adsorption behavior between surfactants and hydrophobic SNP systems to solid surfaces (i.e., silica and alumina oxide). A static adsorption experiment was conducted under controlled conditions. Two surfactants with different structure single, and double head were selected and solid surface with different charges were investigated. Single-head-head, Sodium dodecylbenzene sulfonate (SDBS) and twin head, Disodium dodecyl diphenyl oxide disulfonate (DSDDS) onto negatively charged silica oxide ($SiO_2$) and positively charged alumina oxide ($Al_2O_3$) were investigated. Results revealed that the SDBS had a higher affinity to adsorbed onto the SNP than DSDDS. Also, SDBS exhibited greater adsorption onto $Al_2O_3$ than $SiO_2$. For the twin head system, DSDDS showed lower adsorption across all media and even lower with SNP. The adsorption of the surfactant onto surface was characterized by Scanning Electron Microscopy (SEM) and Fourier Transform Infrared Spectroscopy (FTIR), providing comprehensive insights into the mechanisms.

***Ampira.C@chula.ac.th**

## INTRODUCTION

Surfactant-based enhanced oil recovery (EOR) has emerged as a promising technique for improving the recovery from reservoirs. However, one of the primary challenges limiting its widespread application is the adsorption of surfactants onto reservoir rock surfaces (e.g. sand, carbonate). This phenomenon significantly reduces the concentration of surfactants available for interfacial tension (IFT) reduction and wettability alteration, (Khandoozi et al., 2022). As a result, undesirable surfactant adsorption leads to higher costs and overall lower oil recovery (Christian, 2022).

The adsorption of surfactants onto reservoir rock surfaces is influenced by various factors, including the characteristics of surfactant, rock mineralogy, salinity, temperature, and pH of the reservoir fluids (Liu et al., 2021; Malozyomov et al., 2023). One of the primary factors influencing surfactant behavior at interfaces is their molecular structure. Variations in

PPC & PETROMAT SYMPOSIUM 2025

hydrophilic and hydrophobic groups, chain length, and functional groups can significantly alter surfactants interaction onto solid surfaces (Omari et al., 2021). Nanoparticles have found to be an additive in surfactant systems due to their ability to modify interfacial properties. When combined with surfactants, nanoparticles can mitigate the adsorption (Rattanaudom et al., 2023). To understand the molecular characteristics of surfactants, influence their interaction with nanoparticles. This research investigates for understanding of the structure-property relationships that govern surfactant adsorption behavior in surfactant-nanoparticle systems. The adsorption between surfactant nanoparticles under conditions was studied by advanced image techniques to prove surfactant adsorption by understanding the mechanisms of surfactant adsorption and employing effective mitigation strategies. The findings could lead to mitigating the surfactant losses by adsorption. Thus, enhancing the efficiency and economic feasible of surfactants for EOR.

## EXPERIMENTAL

*A. Materials*

Two anionic surfactants with distinct molecular architectures were employed in this study. Sodium Dodecylbenzene Sulfonate (SDBS, 95% purity) was purchased from Sigma-Aldrich). Disodium dodecyl diphenyl oxide disulfonate (DSDDS, 45% purity.) was supplied by Utica Chemical Company (Thailand). Adsorption media, silica oxide was purchased from MD ProSupply Co., Ltd. Aluminum oxide was purchased from Merck Ltd. Hydrophobic silica nanoparticle was obtained by Wacker Chemical Company, USA. The specific surface area, characterized by BET (Quantachrome, AS-3XR) of $SiO_2$, $Al_2O_3$ and SNP were 220,138, and 126 $m^2/g$, respectively. The chemical structures of the surfactants are shown in **Figure 1**

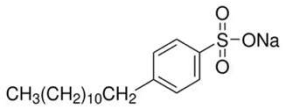


Structure of sodium dodecylbenzene sulfonate (SDBS)

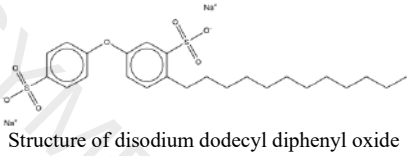

Structure of disodium dodecyl diphenyl oxide disulfonate (DSDDS) structure

**Figure 1** Chemical structure of surfactants in this study.

*B. Static adsorption of single surfactant systems onto solid surfaces*

The adsorption study of the single surfactant system on media was prepared at 50 mL by varying surfactant concentrations from 0.01 mM to 10 mM, with a fixed mass of the media 0.1 g. The samples were shaken for 24 hours to reach equilibrium at room temperature (25 ±2 °C) and controlled pH at 7.0±0.5. After equilibrium, the samples were centrifuged to separate the supernatant to determine the concentration. The initial and equilibrium surfactant concentrations were determined by UV–Vis spectroscopy (Thermo Scientific, GENESYS 40).

*C. Static adsorption study of surfactant-SNP systems onto solid surfaces*

The adsorption study of the surfactant-SNP systems was prepared by mixing the surfactant concentration at 2wt.% with 0.02wt.% of SNP then, stirred for 24 hours to ensure surfactant-SNPs dispersion. Surfactant-SNP solution at varying concentration were prepared

PPC & PETROMAT SYMPOSIUM 2025

for 50 mL ranging from 0.01 mM to 10 mM by dilution with DI water. A fixed mass of media (0.1 g for $SiO_2$, and 1.0 g for $Al_2O_3$) was added to each vial. The samples were shaken for 24 hours to ensure equilibrium at room temperature (25±2 °C) and controlled pH at 7.0±0.5. After equilibrium, they were centrifuged to separate the supernatant and solids, The initial and equilibrium surfactant concentrations were measured by UV–visible spectroscopy. The adsorption capacity of surfactant was calculated by the mass balanced equation:

$$Q = (C_0\text{-}C_e)/m \text{ x } V$$

Where Q is the adsorption capacity (mg/g), $C_0$ is the initial surfactant concentration (mg/L), $C_e$ is the equilibrium surfactant concentration in mg/L, V is the volume of the sample solution (mL), and m is the weight of the media or medium make consistent (g)

*D. Surface characterization by image techniques*

Surfactant adsorption was characterized by FTIR (Thermo Scientific, Nicolet iS5-iD7 (ATR)) and SEM (Thermo Scientific, Nicolet iS5-iD7 (ATR)), performing to confirm the adsorption between the surfactant and SNP. The sample analyzed was collected as the solid precipitate from the surfactant solution at equilibrium after reaching the maximum adsorption capacity in Region IV. The precipitate was frozen at -55 °C and then freeze-dried for 72 hours to remove residual moisture.

## RESULTS AND DISCUSSION

*A. Adsorption isotherm of surfactant onto solid surfaces*

The single surfactant adsorptions of SDBS and DSDDS onto the surface (including $SiO_2$, and $Al_2O_3$) were compared with and without SNP were investigated. **Figure 2**, The maximum adsorption capacities of SDBS alone onto $SiO_2$, $Al_2O_3$, and SNP were 6.94, 52.91, and 68.99 mg/g, respectively. While the DSDDS, the maximum adsorption capacities were 17.82 mg/g onto $Al_2O_3$ and 45.45 mg/g onto SNP. The adsorbed surfactant per unit area of the SDBS onto $SiO_2$, $Al_2O_3$ and SNP were 0.05, 0.67 and 1.07 mg/nm$^2$, respectively. For DSDDS, the adsorbed surfactant per unit area were 0.23 mg/nm$^2$ onto $Al_2O_3$ and 0.67 mg/nm$^2$ onto SNP. On the $SiO_2$ surface, DSDDS showed no significant adsorption. This could be because of combined like-charge repulsion from its dual-head structure (Yekeen et al., 2021). In contrast, SDBS adsorbed onto $SiO_2$ surface. The adsorption could occur despite the like charged silica surface because the benzene ring in SDBS interacted with the surface through π–π stacking. Hydrogen bonds could also form between the benzene ring and silanol (-OH) groups on the $SiO_2$ surface, further promoting adsorption (Thrower et al., 2009). On the $Al_2O_3$ surface, SDBS adsorbs greater than DSDDS because its single head group allows tighter, more efficient packing (Omari et al., 2021). In contrast, DSDDS has twin sulfonate heads that generate stronger mutual repulsion, preventing close packing and resulting in lower overall adsorption. On a hydrophobic SNP, both surfactants rely on tail-surface and tail-tail van der Waals forces (Liu et al., 2021). However, the molecules of SDBS have a simpler structure, allowing its C12 tail to lie flat and pack more tightly (Kamal et al., 2017). In contrast, the molecular structure of DSDDS, with its bulkier twin-ring head, limits how closely its tails can approach the hydrophobic surface of SNP (Gowtham V et al., 2024)

PPC & PETROMAT SYMPOSIUM 2025

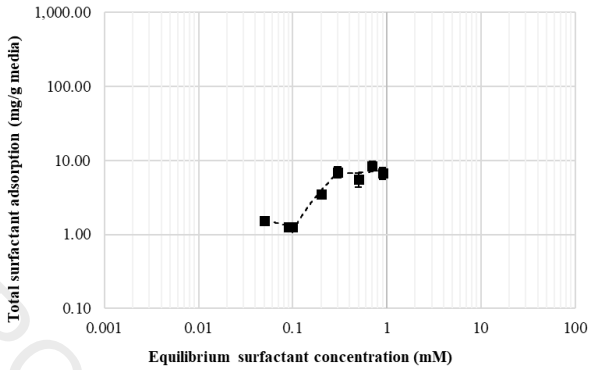


a. Adsorption isotherm of SDBS onto $SiO_2$ as media), pH = 7, T = 25±2°C.

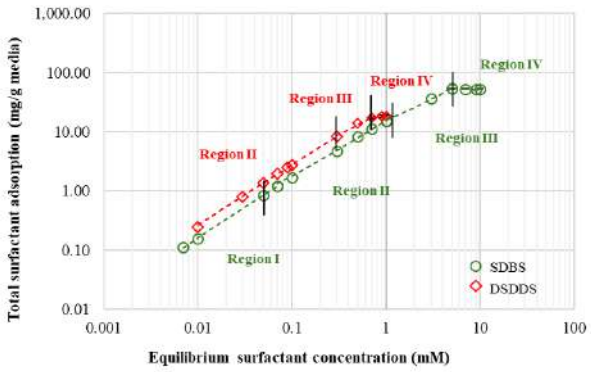


b. Adsorption isotherms of single surfactant system onto $Al_2O_3$ as media

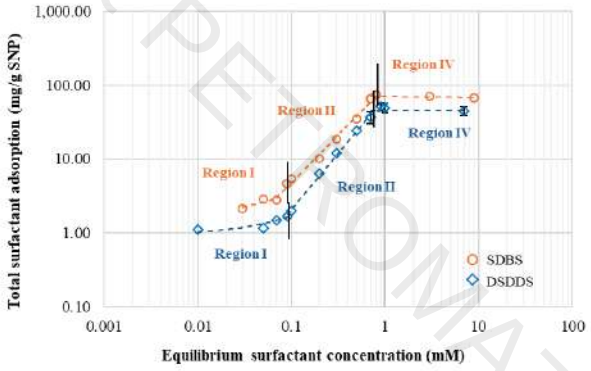


c. Adsorption isotherms of single SDBS and DSDDS onto hydrophobic silica nanoparticle (SNP), pH = 7, T = 25±2°C.

**Figure 2** Adsorption isotherm of single surfactants SDBS and DSDDS onto (a) $SiO_2$, (b) aluminum oxide ($Al_2O_3$), and (c) SNP.

*B. Adsorption isotherms of the surfactant-SNP systems onto solid surfaces*

The adsorption isotherms of the surfactant with and without SNP are shown in Figure 3(a) of SDBS, and Figure3(b) of DSDDS. According to the results, the addition of SNP was found to reduce the surfactant adsorption onto the solid surfaces for the SDBS system onto $SiO_2$ surface cannot be detected. About 84.28% for the SDBS onto $Al_2O_3$ surface. It is consistent with DSDDS-SNP system that adding SNP could mitigate the surfactant adsorption onto $Al_2O_3$ surface by 14.60%. However, the previous results showed that DSDDS did not adsorb onto $SiO_2$, and this remains true even in the presence of SNP.

The adsorption of the surfactant-SNP system onto $SiO_2$ showed that the surfactants did not adsorb, which could occur because the SNP-modified by surfactants could create negatively charged at the surface from surfactants adsorbed on the surface by hydrophobic interaction and head part were placed outward from surface, this created strong repulsive force between $SiO_2$ surface and surfactant modified SNP, prevent the surfactant adsorption onto $SiO_2$ surface.

For the $Al_2O_3$ as a media, the adsorption capacity of SDBS significantly reduced when increased SNP concentration, consistent with observed for DSDDS shown in Figure 3. The addition of SNP demonstrated that SNP effectively traps surfactant molecules in the bulk

PPC & PETROMAT SYMPOSIUM 2025

solution before they can adsorb onto solid surfaces. The plotted adsorption isotherm of the surfactant-SNP system (Figure 3) clearly showed that the presence of SNP reduced the free surfactant molecules in the bulk solution, leading to reduced adsorption on the media surface. There is a competitive adsorption of surfactant molecules onto the solid media surface (i.e., $SiO_2$ and $Al_2O_3$)

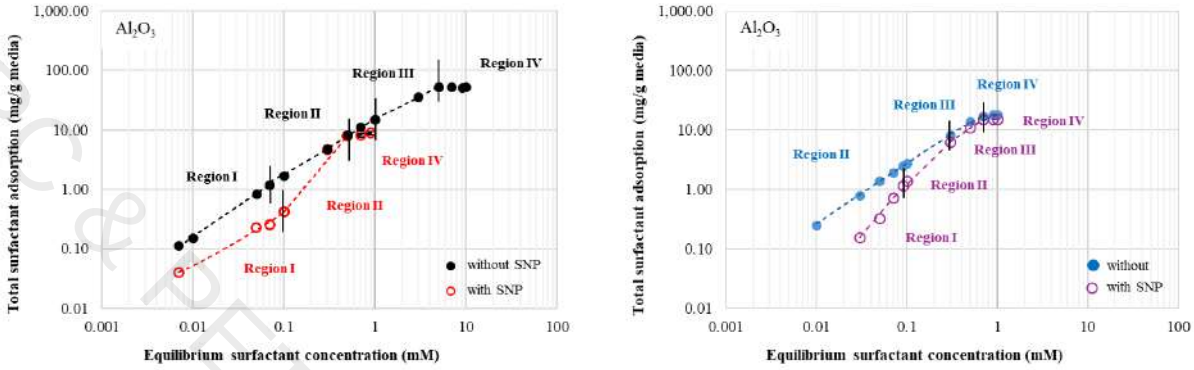


a. Adsorption isotherms of SDBS with and without SNP onto aluminum oxide ($Al_2O_3$) as media, pH = 7, T = 25±2°C.

b. Adsorption isotherms of DSDDS with and without SNP onto aluminum oxide ($Al_2O_3$) as media, pH = 7, T = 25±2°C.

**Figure 3** Adsorption isotherm of (a) SDBS, and (b) DSDDS with and without SNP onto aluminum oxide ($Al_2O_3$) as media.

*C. Surface Characterization for the surfactant-SNP systems onto the solid surface*

The surface characterization by FT-IR is shown in Figure 4-5. The FT-IR analysis showed critical peaks confirming SNP surface modification: the 2964 $cm^{-1}$ band indicates $Si–CH_3$ stretching, while the $CH_2$ stretching vibrations at 2925 and 2855 $cm^{-1}$ verify hydrophobic part of surfactant anchoring onto SNP for the SDBS–SNP systems (Chaieb et al., 2022). The stretching vibrations at 2959 and 2870 $cm^{-1}$ are attributed to the vibration of -CH of aromatic stretching and symmetric stretching vibration of $–CH_2$ of the surfactant tail, respectively. The band at 1244 $cm^{-1}$ indicates C-O-C stretching of the DSDDS' head part confirmed the adsorption of DSDDS–SNP systems (Singh et al., 2014). These IR spectra demonstrate an evidence adsorption of surfactant onto the SNP by hydrophobic interactions.

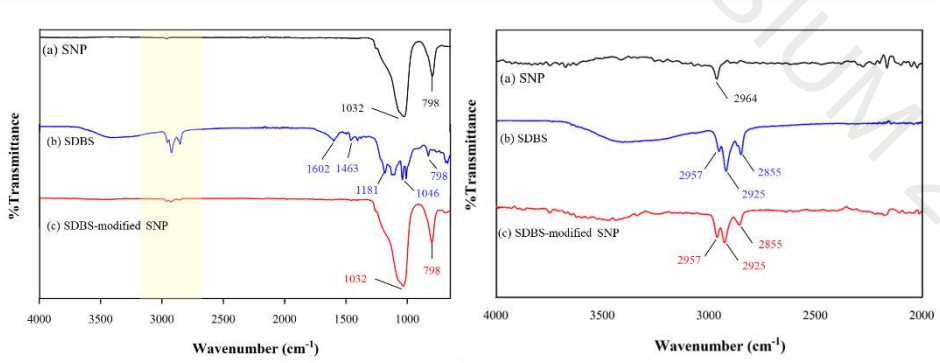


**Figure 4**. FT-IR Spectra of (a) SNP, (b) SDBS surfactant, (c) SDBS-modified SNP, and expanded spectrum in the 2000-4000 cm-¹ region.

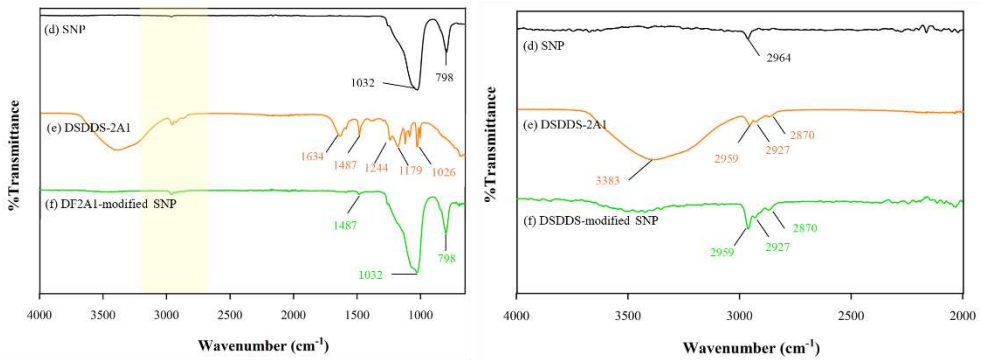


**Figure 5.** FT-IR Spectra of (d) SNP, (e) DSDDS surfactant, (f) DSDDS-modified SNP, and expanded spectrum in the 2000-4000 $cm^{-1}$ region.

Figure 6 shows the SEM image and corresponding EDAX results of bare SNP (Figure 6-a), SDBS-modified SNP (Figure 6-b), DSDDS-modified SNP (Figure 6-c). The SEM micrograph of the SNP appears as an irregular, highly textured, and porous aggregate. SNP exhibits a fluffy, clustered morphology. The major elements of the SNP composted carbon (C), oxygen (O), and silicon (Si). The SEM image of the SNP after adsorption by SDBS (Figure-6b) indicates that the surface appears noticeably smoother and less porous than that of bare SNP. EDAX results, major elements of SDBS-modified SNP, consisted of C, O, Si, sodium (Na), and sulfur (S). The presence of Na and S indicates the presence of sodium salt and sulfonate head groups in SDBS molecule. The SEM image of DSDDS-modified SNP (Figure-c) displays a denser, more clumped appearance. The pores and cavities appear partially filled, resulting in a slightly smoother surface compared to bare SNP. The results from EDAX show the element composition of C, O, and Si, Na and S, which are derived from the DSDDS sodium salt and sulfonate groups of the DSDDS. The appearances of Na and S in the SNP modified by surfactant directly indicate the presence of DSDDS on the surface.

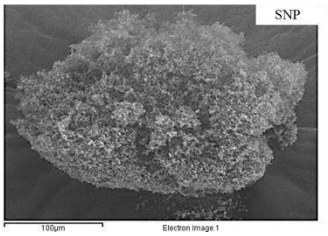


| EDAX Results | |
|---|---|
| Element | Weight% |
| C | 56.92 |
| O | 37.99 |
| Si | 5.09 |
| Totals | 100.00 |

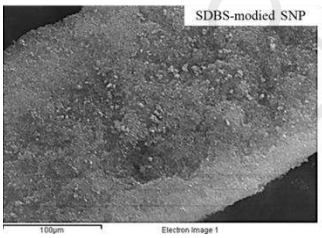


| EDAX Results | |
|---|---|
| Element | Weight% |
| C | 53.51 |
| O | 33.87 |
| Na | 0.37 |
| Si | 11.79 |
| S | 0.46 |
| Totals | 100.00 |

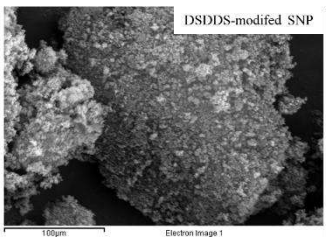


| EDAX Results | |
|---|---|
| Element | Weight% |
| C | 41.55 |
| O | 43.96 |
| Na | 0.53 |
| Si | 13.32 |
| S | 0.64 |
| Totals | 100.00 |

PPC & PETROMAT SYMPOSIUM 2025

**Figure 6** SEM image of (a) hydrophobic silica nanoparticle (SNP), (b) SDBS-modified SNP, (c) DSDDS modified SNP and EDAX results.

## CONCLUSIONS

This study investigated the adsorption behavior of single and double-head group, SDBS and DSDDS surfactants onto $SiO_2$ and $Al_2O_3$ surfaces with and without adding silica nanoparticles (SNP) as an additive. The adding SNP showed a significant reduction the surfactant adsorption SDBS onto $SiO_2$ and 84.28% for SDBS onto $Al_2O_3$ surface. These results are consistent with DSDDS, adding SNP has slightly mitigated DSDDS surfactant adsorption to 14.60% onto $Al_2O_3$ surface. The higher adsorption of only surfactant, and surfactant-SNP, SDBS compared to DSDDS it can be attributed to differences in their molecular structures. Corresponding to the characteristics by imaging technique of bare SNP and surfactant-modified SNP on the surface. Based on the results of the SNP and surfactant-modified SNP from FT-IR analysis, the IR spectra revealed that the surfactant system both SDBS and DSDDS, are anchored onto SNP by hydrophobic interactions, confirming the adsorption of surfactants onto SNP. In contrast, the SEM image shows a slightly smoother surface of SDBS-modified SNP and DSDDS-modified SNP than SNP, which does not conclusively prove the presence of a surfactant-coated layer. However, EDAX confirms surfactant adsorption by detecting new elements on the surface.

## ACKNOWLEDGEMENTS

The authors gratefully thanks the Petroleum and Petrochemical College, Chulalongkorn University. The development of environmentally corrosion inhibitors for sustainable industrial development (Fundamental Fund, DISF67630021) Chulalongkorn University and PTT Exploration and Production Public Company Limited for their financial support of this research

## REFERENCES

Chaieb, Z., Zizi, Z., & Benghalem, A. (2022). Synthesis, characterization and structural study of Fe(III) complex derived from sodium dodecyl benzene sulfonate. *Bulletin of the Chemical Society of Ethiopia*, *36*, 353-361. https://doi.org/10.4314/bcse.v36i2.9

Christian, A. P. (2022). Applications of Surfactants and Nanoparticles in Enhanced Oil Recovery Processes. In A.-J. Ali Ismail (Ed.), *Sedimentary Petrology* (pp. Ch. 3). IntechOpen. https://doi.org/10.5772/intechopen.97506

Gowtham V, M., Deodhar, S., Thampi, S. P., & Basavaraj, M. G. (2024). Association in Like-Charged Surfactant–Nanoparticle Systems: Interfacial and Bulk Effects. *Langmuir*, *40*(33), 17410-17422. https://doi.org/10.1021/acs.langmuir.4c01517

PPC & PETROMAT SYMPOSIUM 2025

Kamal, M. S., Hussein, I. A., & Sultan, A. S. (2017). Review on Surfactant Flooding: Phase Behavior, Retention, IFT, and Field Applications. *Energy & Fuels*, *31*(8), 7701-7720. https://doi.org/10.1021/acs.energyfuels.7b00353

Khandoozi, S., Sharifi, A., & Riazi, M. (2022). Chapter 3 - Enhanced oil recovery using surfactants. In A. Hemmati-Sarapardeh, M. Schaffie, M. Ranjbar, M. Dong, & Z. Li (Eds.), *Chemical Methods* (pp. 95 - 139). Gulf Professional Publishing. https://doi.org/https://doi.org/10.1016/B978-0-12-821931-7.00007-9

Liu, Z., Zhao, G., Brewer, M., Lv, Q., & Sudhölter, E. J. R. (2021). Comprehensive review on surfactant adsorption on mineral surfaces in chemical enhanced oil recovery. *Advances in Colloid and Interface Science*, *294*, 102467. https://doi.org/https://doi.org/10.1016/j.cis.2021.102467

Malozyomov, B. V., Martyushev, N. V., Kukartsev, V. V., Tynchenko, V. S., Bukhtoyarov, V. V., Wu, X., Tyncheko, Y. A., & Kukartsev, V. A. (2023). Overview of Methods for Enhanced Oil Recovery from Conventional and Unconventional Reservoirs. *Energies*, *16*(13), 4907. https://www.mdpi.com/1996-1073/16/13/4907

Omari, A., Cao, R., Zhu, Z., & Xu, X. (2021). A comprehensive review of recent advances on surfactant architectures and their applications for unconventional reservoirs. *Journal of Petroleum Science and Engineering*, *206*, 109025. https://doi.org/https://doi.org/10.1016/j.petrol.2021.109025

Rattanaudom, P., Alimin, A. A., Shiau, B.-J. B., Harwell, J. H., Suriyapraphadilok, U., & Charoensaeng, A. (2023). Experimental investigation of hydrophobic and hydrophilic silica nanoparticles on extended surfactant properties: Micro-emulsion, viscosity, and adsorption behaviors. *Geoenergy Science and Engineering*, *223*, 211582. https://doi.org/https://doi.org/10.1016/j.geoen.2023.211582

Singh, K., Devi, S., Bajaj, H., Ingole, P., Chaudhari, J., & Harshad, B. (2014). Optical Resolution of Racemic Mixtures of Amino Acids through Nanofiltration Membrane Process. *Separation Science and Technology*, *49*. https://doi.org/10.1080/01496395.2014.911023

Yekeen, N., Al-Yaseri, A., Idris, A. K., & Khan, J. A. (2021). Comparative effect of zirconium oxide (ZrO2) and silicon dioxide (SiO2) nanoparticles on the adsorption properties of surfactant-rock system: Equilibrium and thermodynamic analysis. *Journal of Petroleum Science and Engineering*, *205*, 108817. https://doi.org/https://doi.org/10.1016/j.petrol.2021.108817

PPC & PETROMAT SYMPOSIUM 2025

# Microwave-Assisted Acid-Base Reflux for Post-Synthesis Purification of CNTs Synthesized by CMD

*Suttida Pongsiripan*[a], *Phuwadej Pornaroontham*[a,b*]

[a] Department of Chemical Technology, Faculty of Science, Chulalongkorn University, Bangkok, Thailand
[b] Centre of Excellence on Petrochemical and Materials Technology, Chulalongkorn University, Bangkok, Thailand

Keywords: Carbon nanotube (CNTs), Microwave-assisted, Post-Synthesis Purification, Catalytic Methane Decomposition (CMD)

## ABSTRACT

Carbon nanotubes (CNTs) synthesized via catalytic methane decomposition (CMD) are often embedded with residual catalyst particles, particularly alumina ($Al_2O_3$), which is widely used in industry due to its high thermal stability—essential for CMD processes operating at temperatures around 1,000°C. However, residual catalysts can compromise the electrical, thermal, and mechanical properties of CNTs, making efficient post-synthesis purification critical. This study explores a microwave-assisted reflux process—offering rapid and uniform heating—to enhance the efficiency of acid-base treatments for catalyst removal, particularly of bimetallic catalyst residues supported by alumina. Initially, acid digestion using a mixed solution of nitric and sulfuric acids exhibited limited efficiency. Although NaOH under microwave-assisted reflux completely dissolved pure alumina, its performance on catalyst residues was hindered, likely due to CNT coverage restricting access to the catalyst surface. Applying base treatment before acid digestion (Base-Acid sequence) resulted in a 29.2% reduction of catalyst residue. In contrast, reversing the order (Acid-Base sequence) achieved a 46.2% reduction, as acid treatment partially removed surface metals and disrupted the outer structure, improving access for subsequent base dissolution of embedded alumina. This sequence offers a more effective strategy for purifying CMD-grown CNTs and may extend to other nanostructured carbon materials.

*** phuwadej.p@chula.ac.th**

## INTRODUCTION

Carbon nanotubes (CNTs) are nanomaterials with outstanding mechanical and electrical properties, including high thermal resistance, excellent electrical conductivity, and superior mechanical strength compared to conventional materials. These characteristics have drawn significant interest from various industries, especially the rapidly growing electric vehicle (EV) sector. One notable application of CNTs in this field is as reinforcement material for vehicle structures (Anvesh & Madhu, 2015), where replacing conventional steel with CNT-based composites can reduce vehicle weight, improve battery efficiency, and extend driving range.

In addition to structural applications, CNTs are increasingly used as additives in lithium-ion batteries (LiBs), a key component in EVs. While carbon black and graphite are commonly used (Jankowski et al., 2018), CNTs offer superior performance, particularly in cathodes, by enhancing energy density and battery longevity even at low loadings (Landi et al., 2009).

PPC & PETROMAT SYMPOSIUM 2025

Among the three main CNT synthesis methods—arc discharge, laser ablation, and chemical vapor deposition (CVD)—this study focuses on the CVD method due to its scalability for industrial production (Danafar et al., 2009). While conventional CVD processes typically utilize more reactive hydrocarbon sources such as ethylene or acetylene—allowing CNT growth at relatively lower temperatures—the present study employs methane as the carbon source, resulting in a methane-based CVD process, catalytic methane decomposition (CMD). Methane offers advantages in terms of cost and purity but requires a significantly higher reaction temperature, typically around 1000 °C, to initiate and sustain CNT growth. This elevated temperature necessitates the use of a thermally stable support, such as alumina, which can maintain structural integrity under such conditions. However, CNTs synthesized via CMD often contain residual catalysts, particularly alumina, which degrade material properties and reduce market value. Therefore, purification is essential to improve CNT quality and enhance commercial viability.

Acid digestion is widely used for catalyst removal due to its simplicity, but it faces challenges such as long processing time and limited effectiveness against thermally stable supports like alumina. To address this, this study proposes a microwave-assisted acid treatment, leveraging rapid and uniform internal heating to improve purification efficiency. Furthermore, mixed acid systems, such as nitric acid ($HNO_3$) combined with sulfuric acid ($H_2SO_4$), have been widely used to introduce oxidative species like nitronium ions ($NO_2^+$), which are known to disrupt graphitic structures and enhance catalyst accessibility by opening CNT tube ends (Shin et al., 2013). In parallel, sodium hydroxide (NaOH) treatment has been employed in post-synthesis processing to target catalyst supports (Orwat et al., 2016) These combined acid–base strategies offer a promising route for enhancing the structural purity of CNTs by facilitating effective removal of both metallic and support-derived residues, thereby improving CNT purity.

## EXPERIMENTAL

### *A. Materials*

The chemical reagents used in this study included nitric acid ($HNO_3$, 65%) and sulfuric acid ($H_2SO_4$, 98%), both of analytical reagent (AR) grade and purchased from Qrec (New Zealand), as well as sodium hydroxide (NaOH), also AR grade, obtained from LABSCAN (Ireland). Carbon nanotubes were synthesized in a vertical furnace using $FeMo/Al_2O_3$ as catalyst and methane ($CH_4$) as the carbon source at a temperature of 950°C for 60 minutes.

### *B. 1-step Purification*

A 0.3 g sample of carbon nanotubes (CNTs) was treated with a mixed acid solution consisting of sulfuric acid ($H_2SO_4$, 10 M) and nitric acid ($HNO_3$, 4 M) in a volume ratio of 3:1, with a total volume of 20 mL. The mixture was placed in a 100 mL PTFE (polytetrafluoroethylene) vessel and subjected to microwave heating under reflux at 100 °C for varying durations of 10, 20, and 30 minutes. After the reaction, the CNTs were filtered using a vacuum pump through a PTFE membrane and rinsed with deionized water until the filtrate reached a neutral pH (pH ≈ 7). The washed samples were then dried in an oven at 80 °C overnight and stored in a desiccator for later use.

PPC & PETROMAT SYMPOSIUM 2025

*C. 2-step Purification*

Two-step purification of carbon nanotubes (CNTs) was performed using both acid–base and base–acid sequences. For each procedure, 0.3 g of CNTs was treated with 20 mL of solution under microwave irradiation in a PTFE vessel. The acid treatment involved a mixed acid solution of sulfuric acid ($H_2SO_4$, 10 M) and nitric acid ($HNO_3$, 4 M) in a 3:1 volume ratio, heated at 100 °C for 30 minutes. The base treatment used sodium hydroxide (NaOH, 10 M) at 140 °C for 90 minutes. After each reaction, the samples were filtered using a vacuum pump through a PTFE membrane and rinsed thoroughly with deionized water until the filtrate reached a neutral pH (pH ≈ 7). The sequence of treatment varied: in the acid–base route, CNTs were treated with acid first, followed by base; in the base–acid route, the order was reversed. All treated samples were dried at 80 °C overnight and stored in a desiccator before undergoing structural and compositional analysis. The percentage of impurity removal for both 1-step and 2-step treatments was calculated using Equation (1) below

$$\%\ Removal = \frac{\Delta m}{m_0} \times 100 \quad (1)$$

where $\Delta m$ represents the change in mass (initial mass – final mass) and $m_0$ is the initial mass of the sample.

*D. Characterization*

Thermogravimetric analysis (TGA, Perkin Elmer 8000) was employed to quantify the residual catalyst content in carbon nanotubes after each treatment. The weight loss of the CNTs samples was recorded from 30 to 1000°C at a heating rate of 20°C/min under an oxygen atmosphere with a flow rate of 30 mL/min. In parallel, the surface morphology and structural features of the CNTs were observed using field emission scanning electron microscopy (FE-SEM, Hitachi S-4800) operated at 2 kV. Prior to imaging, all samples were dried at 105°C for 24 hours to remove residual moisture.

## RESULTS AND DISCUSSION

*A. Removal performance of 1-step Acid-treatment*

Based on thermogravimetric analysis (TGA) results shown in Figure 1a, the weight loss curves of the as-grown CNTs and acid-treated samples at 10 min, 20 min, and 30 min exhibited similar decomposition patterns, particularly in the temperature range of 500–650 °C, which corresponds to the thermal oxidation of carbon structures. Above 650 °C, the remaining mass is attributed to thermally stable residues such as metallic catalysts and support materials. The results indicate that increasing the acid treatment time ($H_2SO_4$/$HNO_3$ at a 3:1 ratio) under microwave-assisted heating at 100 °C from 10 to 30 minutes did not produce a significant change in the TGA profiles when compared to the as-grown CNTs. This observation is consistent with the calculated percentage of residue removal shown in Figure 1b, which ranged only from 2.0% to 4.8%. The slight improvement in residue removal may be due to the partial dissolution of metal catalysts such as Fe or Mo, which are known to dissolve in strong acid solutions. However, alumina ($Al_2O_3$), a common support material used in CNTs synthesis, remains largely undissolved due to its high chemical stability, resulting in limited removal efficiency under these conditions.

PPC & PETROMAT SYMPOSIUM 2025

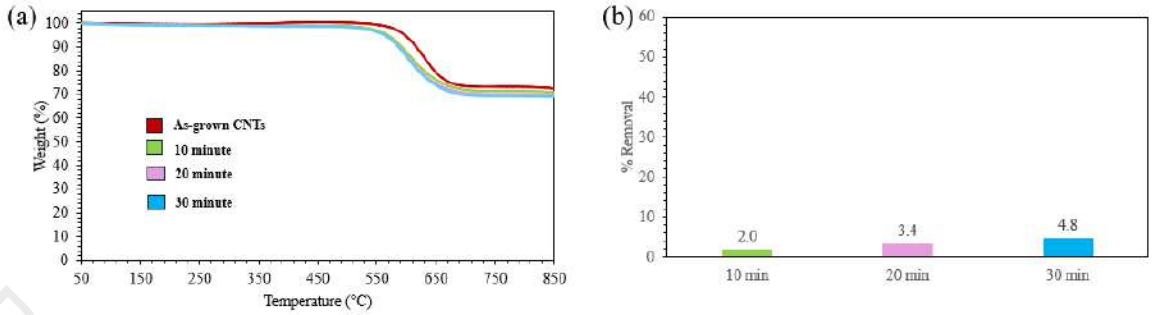


Figure 1. TGA curves of CNTs before and after purified using 1-step acid treatment (a), and percentage of residue removal after using 1-step acid treatment (b).

*B. Removal performance of 2-step Purification*

Based on the premise that acid treatment alone may be insufficient for the effective removal of catalysts from CNTs, a two-step purification strategy was developed. A key factor in this process is the sequence of acid and base application, which may influence the removal efficiency. Therefore, a comparative study between Acid–Base and Base–Acid sequences was conducted under identical time and temperature conditions.

According to the thermogravimetric analysis (TGA) and derivative thermogravimetry (DTG) results shown in Figure 2a, the as-grown CNTs exhibited a higher residual mass beyond 650 °C, corresponding to non-combustible catalyst residues such as metal oxides and supports. Comparing the treated samples, the Acid–Base sequence demonstrated a more pronounced weight loss and an earlier DTG peak shift, indicating greater catalytic residue removal and lower thermal stability. This behavior is attributed to the reduced nanotube diameter after purification, as smaller CNTs are known to oxidize at lower temperatures. The % removal analysis in Figure 2b supports these findings, showing that the Acid–Base method achieved a 46.2% removal rate, significantly higher than the 29.2% observed in the Base–Acid method.

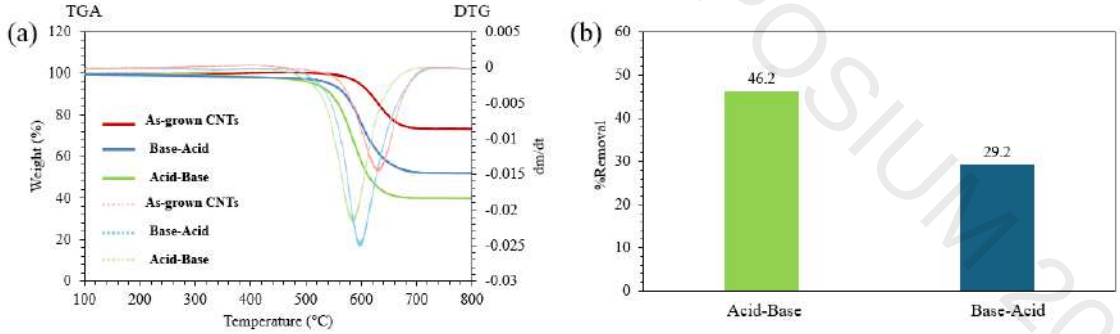


Figure 2 TGA and DTG curves of CNTs before and after purified using different treatment sequences (Acid–Base and Base–Acid) (a), percentage of residue removal after purification with different treatment sequences (b).

PPC & PETROMAT SYMPOSIUM 2025

*C. The surface morphology of carbon nanotubes*

The surface morphology of carbon nanotubes (CNTs) before and after purification was examined using field emission scanning electron microscopy (FE-SEM), as shown in Figure 3. The as-grown CNTs exhibited rough surfaces with numerous irregular particles attached along the tube walls, which are presumed to be residual catalyst particles and support materials. After purification, both the number and size of these surface particles were substantially reduced, indicating effective removal of impurities. The purified CNTs displayed a cleaner and more uniform surface, consistent with the measured percentage of catalyst removal. Specifically, the acid–base treatment eliminated nearly 50% of the residual catalyst content, whereas the base–acid sequence achieved only about 30% removal. In addition to surface cleanliness, a notable decrease in average tube diameter was observed following purification. The as-grown CNTs had an average diameter of approximately 52.2 nm, which was reduced to about 40.9 nm after base–acid treatment and further to 35.7 nm following acid–base treatment. This diameter reduction is attributed to the combined chemical and structural effects of oxidative acid and base treatments. During the acid step, oxygen-containing functional groups such as –COOH and –OH are introduced onto the CNT surface, weakening the graphitic structure and facilitating cap opening. In the subsequent base step, these defect-rich regions are selectively etched, resulting in partial exfoliation or thinning of the outer tube walls (Fan et al., 2010). This mechanism accounts for both the improved morphological quality and the observed diameter reduction.

The sequence of treatments also plays a critical role. When the base treatment is applied first, it acts as a mild cleaning step, removing loosely bound impurities and potentially defect-prone sites. This pre-cleaning reduces the number of reactive sites available for subsequent oxidative attack during the acid step, thereby limiting further exfoliation. As a result, base–acid treatment yields a lower percentage of catalyst removal, and a larger average CNT diameter compared to the acid–base approach. This explanation is further supported by the differential thermogravimetric (DTG) analysis. As shown in Figure 2a, the degradation peak temperature of the acid–base treated CNTs was approximately 586 °C, while that of the base–acid treated CNTs was higher, around 598 °C. This difference aligns with the proposed mechanism, as smaller-diameter CNTs are known to possess lower oxidation resistance and thus thermally degrade at lower temperatures (Singh et al., 2010).

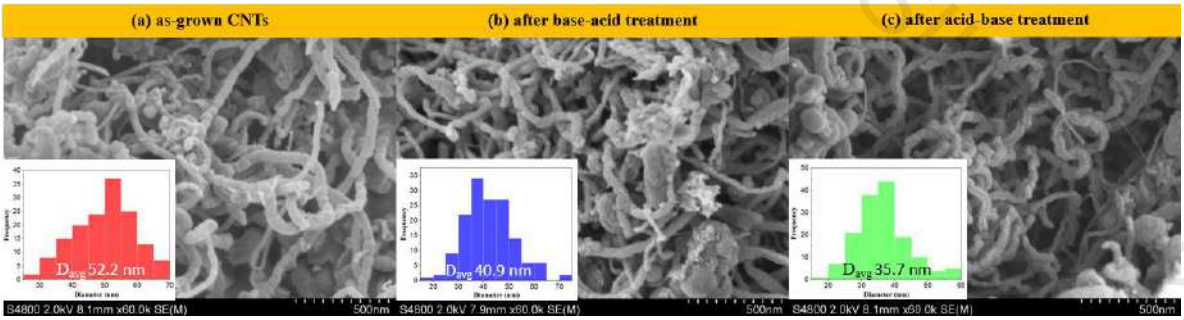


Figure 3. SEM image of as-grown CNTs (a), purified CNTs using Base-Acid treatment (b), and purified CNTs using Acid-Base treatment.

## CONCLUSIONS

This study highlights the effectiveness of a microwave-assisted acid–base reflux method for purifying carbon nanotubes (CNTs) synthesized via catalytic methane decomposition (CMD). The acid–base sequence showed greater catalyst residue removal than the base–acid method, achieving a 46.2% reduction, as confirmed by TGA. FE-SEM images revealed fewer and smaller surface particles after purification. Additionally, CNT diameter decreased from 52.2 nm to 35.7 nm using Acid-Base treatment, indicating wall thinning. This is explained by oxidative functionalization during acid treatment, which weakens tube walls and opens caps, followed by base treatment dissolving alumina and etching defect sites. DTG analysis further confirmed earlier thermal degradation, consistent with the reduced oxidation resistance of smaller-diameter CNTs. These results suggest that the acid–base process is an effective approach for enhancing CNT purity and structural quality.

## ACKNOWLEDGEMENTS

The author would like to express sincere gratitude to the Department of Chemical Technology, Faculty of Science, Chulalongkorn University for the financial support provided during this study.

## REFERENCES

**Anvesh, P., & Madhu, S. (2015)**. *Applications of carbon nanotubes (CNT) in automobiles-a review.* International Journal of Applied Engineering Research, 10(33), 2015.

**Danafar, F., Fakhru'l-Razi, A., Salleh, M. A. M., & Biak, D. R. A. (2009)**. *Fluidized bed catalytic chemical vapor deposition synthesis of carbon nanotubes*—A review. Chemical Engineering Journal, 155(1-2), 37-48.

**Fan, Q.-Q., Qin, Z.-Y., Liang, X., Li, L., Wu, W.-H., & Zhu, M.-F. (2010)**. *Reducing defects on multi-walled carbon nanotube surfaces induced by low-power ultrasonic-assisted hydrochloric acid treatment.* Journal of Experimental Nanoscience, 5(4), 337-347.

**Jankowski, P., Lindahl, N., Weidow, J., Wieczorek, W., & Johansson**, **P. (2018)**. I*mpact of sulfur-containing additives on lithium-ion battery performance: from computational predictions to full-cell assessments.* ACS Applied Energy Materials, 1(6), 2582-2591.

**Landi, B. J., Ganter, M. J., Cress, C. D., DiLeo, R. A., & Raffaelle, R. P. (2009)**. *Carbon nanotubes for lithium ion batteries.* Energy & Environmental Science, 2(6), 638-654.

**Orwat, K., Bernard, P., & Migdał-Mikuli, A. (2016).** *Obtaining and investigating amphoteric properties of aluminum oxide in a hands-on laboratory experiment for high school students.* Journal of Chemical Education, 93(5), 906-909.

**Shin, Y.-R., Jung, S.-M., Jeon, I.-Y., & Baek, J.-B. (2013).** *The oxidation mechanism of highly ordered pyrolytic graphite in a nitric acid/sulfuric acid mixture*. Carbon, 52, 493-498.

**Singh, D. K., Iyer, P. K., & Giri, P. (2010).** *Diameter dependence of oxidative stability in multiwalled carbon nanotubes*: Role of defects and effect of vacuum annealing. Journal of applied physics, 108(8).

PPC & PETROMAT SYMPOSIUM 2025

# The Effect of Coir Fiber Content on Anti-Dripping Property of Polyoxymethylene

*~~Peerawit Klinsrisuk~~* [a], *Somjate Patcharaphan* [b], *Sudsiri Hemsri* [a], *Chanchai Thongpin* *[a]

[a] Department of Materials Science and Engineering, Faculty of Engineering and Industrial Technology, Silpakorn University, Nakhon Pathom, Thailand
[b] Department of Materials Engineering, Faculty of Engineering, Kasetsart University, Bangkok, Thailand

Keywords: Polyoxymethylene, Coir fiber, Anti-dripping

## ABSTRACT

Polyoxymethylene, also known as POM or polyacetal, is an engineering plastic with excellent mechanical properties and abrasion resistance. POM has some drawbacks, including limited UV resistance, flammability, moisture absorption, and releasing formaldehyde during processing. In this work, the influence of coir fiber content on the flaming behavior of POM is our main interest. The coir fiber is used as a reinforcing filler ranging from 5 to 20 percent by weight (wt%). It can be seen that the tensile modulus and yield strength tend to increase with the increase of coir fiber content, while a dramatic decrease in impact strength is found. The flammability with regard to the anti-dripping of POM filled with various coir fiber concentrations is characterized by the horizontal burning test in accordance with UL94. It is found that the number of molten droplets significantly decreases with increasing coir fiber content. This reduction in dripping is attributed to the occurrence of the char layer which acts as a protective layer for inhibiting droplet formation.

*** chanchai@su.ac.th**

## INTRODUCTION

Polyoxymethylene (POM) is an engineering thermoplastic with excellent mechanical properties, good abrasion resistance, low moisture absorption, and resistance to chemicals such as alcohols, engine oils, brake fluids, coolants, and lubricants. With these properties, polyoxymethylene is used in automotive parts, electronic components, and machinery parts. A major disadvantage of polyoxymethylene is its high flammability [1]. At temperatures above 100ºC, in the presence of oxygen, polyoxymethylene undergoes depolymerization, resulting in the release of formaldehyde, which is a flammable gas. Formaldehyde can react with oxygen to form formic acid, which promotes the degradation of polyoxymethylene [2, 3]. Coir fiber has been widely used as a reinforcing filler for plastic materials due to its low density, acceptable mechanical, and thermal properties. During melt, thermoplastic containing coir fiber could give rise to less abrasion to the processing tools [4]. Another advantage of using coir fiber is its high lignin content in which it can promote char yield during thermal degradation due to its chemical structure composing of aromatic rings and hydroxyl groups. The char layer serves as a protective layer which can act as thermal and oxygen barrier [5]. This part of the research is therefore aimed to incorporate coir fiber into polyoxymethylene in order to achieve the flame retardance and retard flame spreading of polyoxymethylene.

PPC & PETROMAT SYMPOSIUM 2025

## EXPERIMENTAL

*A. Materials*

The polyoxymethylene (POM) homopolymer (DELRIN 500P NC010) and coir fibers were purchased from Global Connections Public Company Limited (Thailand) and Thong Mongkhon Fiber Factory (Thailand).

*B. Size reduction of coir fiber*

The received coir fibers were cut with a shredder, washed with acetone, and then dried subsequently sifted using 45 mesh sieves. Then the passed through fibers was sifted again using 100 mesh sieves in order to sift out the fibers shorter than 150 μm. The images of 500 fibers were captured then fibers length and diameter were analyzed using ImageJ program. The length and diameter were found to be 8.99 ± 0.13 mm and 146 ± 1.96 μm respectively.

*C. Composite preparation*

POM and coir fibers were dried in a hot oven at 80ºC overnight before processing. Composition of coir fibers in POM were varied from 0%, 5%, 10%, 15%, and 20% by weight. The mixtures were hand mixed in a plastic bag before feeding into a twin-screw extruder (SHJ-25, China). The mixing was carried out with temperature profile from feed zone to die from 130 to 200ºC with the screw speed of 120 rpm. The extrudate was passed through a cooling water bath and were subsequently pelletized and being dried in a hot air oven at 80ºC overnight. The specimens were fabricated using injection molding machine (ARBURG, ALL ROUNDER 500-320C, Germany) with nozzle temperature, injection pressure, and injection speed at 230 ºC, 1100 bar, and 30 ccm/s respectively. Mold temperature was set at 80 ºC with holding pressure of 700 bar and cooling time of 18 s.

*D. Characterization*

The flammability characteristics of POM/coir fiber composites were performed by horizontal burning test according to the UL-94 standard. Thermal stability was analyzed using a thermogravimetric analyzer (TGA/DSC1, Mettler Toledo, Switzerland). Approximately 5 to 6 mg of each sample was heated from 30 to 700ºC with the heating rate of 5 ºC/min under nitrogen. Melting and crystallization of POM in the composites were evaluated using differential scanning calorimeter (DSC, Mettler Toledo, Switzerland). A sample about 5 to 6 mg was heated and cooled with the rate of 10 ºC/min under nitrogen. Mechanical properties were assessed through tensile and Izod notched impact testing. Tensile tests were performed according to ASTM D638 (Type I) using a universal testing machine (Model 5960, Instron, USA) with a 50 kN load cell at a crosshead speed of 50 mm/min. In term of impact testing, a pendulum impact tester (Instron, USA) was used according to ASTM D256 with 2.75 Joule hammer. The tensile fractured surfaces of the composites were examined using a scanning electron microscope (SEM, TM3030, Hitachi, Japan).

PPC & PETROMAT SYMPOSIUM 2025

## RESULTS AND DISCUSSION

*A. Mechanical properties*

The Young's modulus and 0.2% offset yield stress of POM/coir fibers composites were increased with coir fibers contents, as shown in Fig. 1(a)-1(b), especially at the fiber content of 20 wt%, the increment were increased approximately 30% and 22% respectively. These improvements are attributed to the high Young's modulus of coir fiber compared to that of POM. These results have agreed well with those reported by Soćko, A. and J. Andrzejewski [6] In contrast, the elongation at break of the composites containing 20 wt% of coir fibers was decreased by approximately 57%, as depicted in Fig. 1(c). This reduction indicates the composites brittleness upon incorporation of coir fibers. This observation is consistent with the decrease in impact strength which was dropped by about 41%, as shown in Fig. 1(d).

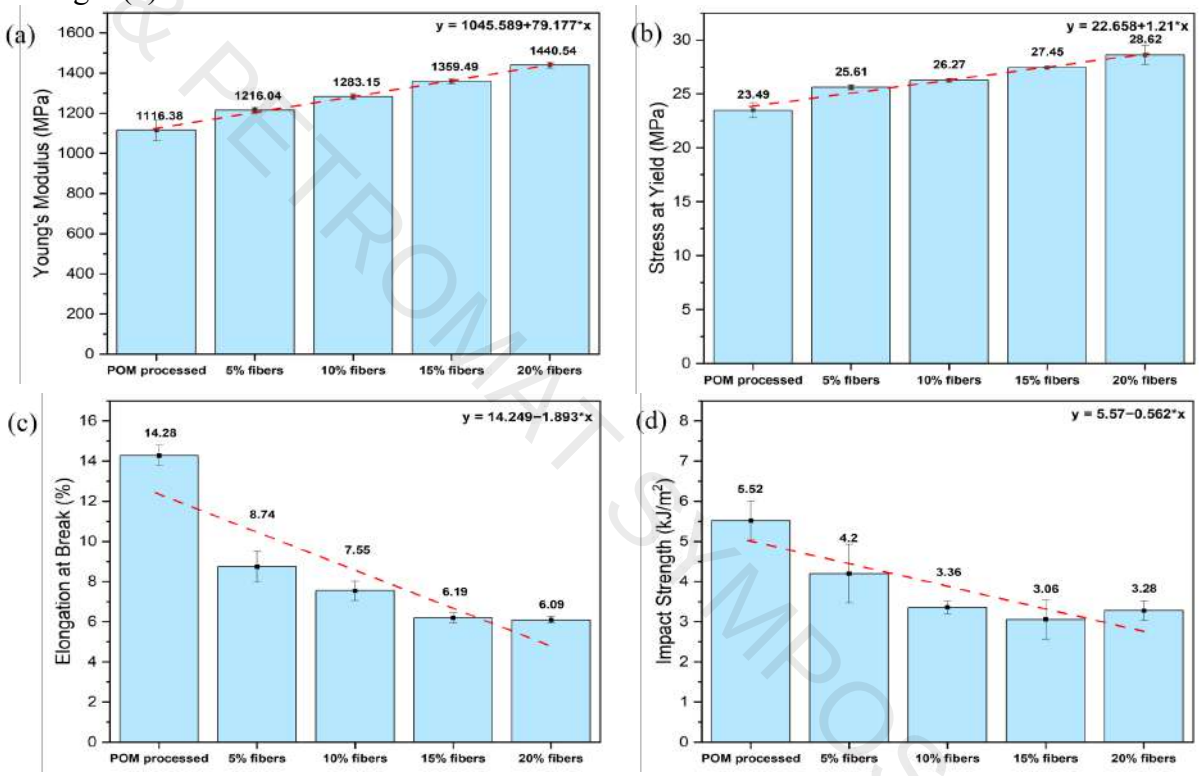


Fig. 1 (a) Young's modulus, (b) Yield strength, (c) Elongation at break, and (d) Impact properties of POM fill with various coir fiber contents.

Considering the SEM images of the tensile fractured surfaces, shown in Fig. 2 (a)- (b), exhibiting the debonding, occurring during tensioning, at the interface, indicating poor interfacial adhesion between coir fibers and the POM matrix. This incompatibility leads to poor stress transferring from matrix to fibers via interfacial shear stress (ISS) [7] and consequently generated stress concentration at the interface. These sites facilitated the initiation of microcracks which would be propagated leading to fracture at lower strain level, thereby reducing the elongation at break of the composite [7].

PPC & PETROMAT SYMPOSIUM 2025

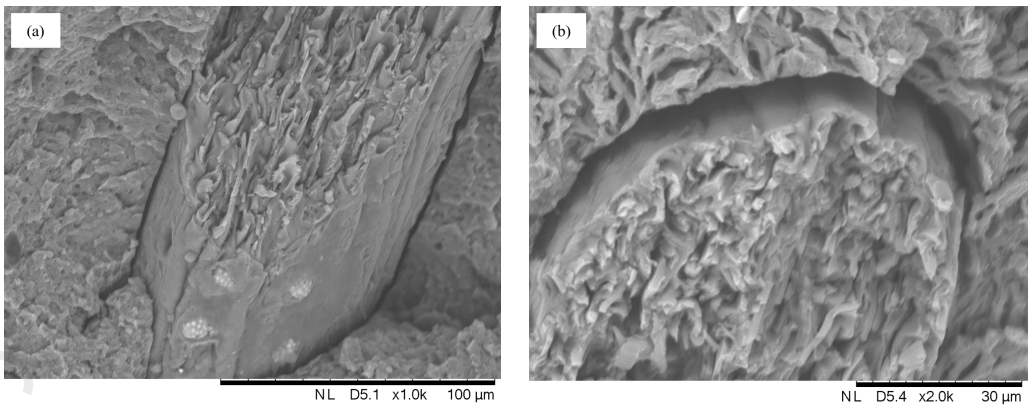


Fig. 2. SEM images of fracture surfaces of POM/Coir fiber composites (a) 1000 and (b) 2000 magnification.

Degree of crystallinity, $X_c$, and melt crystallization temperature, $T_c$, of POM in POM/coir fiber composites were evaluated from DSC on heating and cooling scans respectively. The values are listed in Table 1. The degree of crystallinity was found decreasing with increasing coir fiber contents. This is due to the crystallization obstruction by coir fibers during processing [8]. Then melted POM was crystallized upon cooling and crystallization temperature, $T_c$, of the POM in composite appeared at higher temperature than that of neat POM. This is caused by the presence of coir fiber in the melt acting as the cage which restricted POM chain mobility thereby the nucleation and growth of polymer chains is located in this location. This could facilitate the onset crystallization of melted POM in the fibers cages and hence $T_c$ appearing at higher temperature.

Table 1. Crystallization and melting characteristics of POM fill with various coir fiber contents.

| Sample | Degree of crystallinity $X_c$ (%) | Crystallization temperature (°C) |
|---|---|---|
| POM processed | 46.50 | 145.50 |
| 5% fibers | 44.65 | 147.83 |
| 10% fibers | 43.16 | 148.50 |
| 15% fibers | 43.83 | 149.33 |
| 20% fibers | 43.09 | 149.67 |

*B. Burning behavior*

The horizontal burning rate, number of dripping and UL94 rating of POM/coir fiber composites at various coir fiber contents are depicted in Table 2.

Table 2. Horizontal burning rate and dripping behavior of POM fill with various coir fiber contents.

| Sample | Horizontal burning rate (mm/min) | No. of dripping (drip) | UL94 rating |
|---|---|---|---|
| POM processed | 33.76 ± 0.78 | >100 | Burn out |
| 5% fibers | 38.44 ± 0.30 | 29.2 ± 1.79 | Burn out |
| 10% fibers | 40.90 ± 0.01 | 14.2 ± 1.79 | Burn out |
| 15% fibers | 43.75 ± 0.44 | 4.8 ± 1.30 | Burn out |
| 20% fibers | 45.13 ± 0.29 | 2.4 ± 0.55 | Burn out |

PPC & PETROMAT SYMPOSIUM 2025

The results showed that the composites containing 5, 10, 15, and 20 wt%, the burning rate was increased approximately 14%, 21%, 30%, and 34%, respectively. Thermal decomposition temperatures, $T_d$, of coir fibers and POM in POM/coir fiber composites were examine and presented in Fig. 3 (a) and (b). The decreasing $T_d$ of POM was also resulted from the releasing of acetic acid and vanillic acid during coir fiber degradation [9, 10] both of which could accelerate the degradation of POM hence caused the increased horizontal burning rate. Ditta et al. [11] also found a similar behavior of POM/organo clay composites. The acid sites on the surface of organo clay accelerated the thermal degradation of POM, causing a reduction in decomposition temperature.

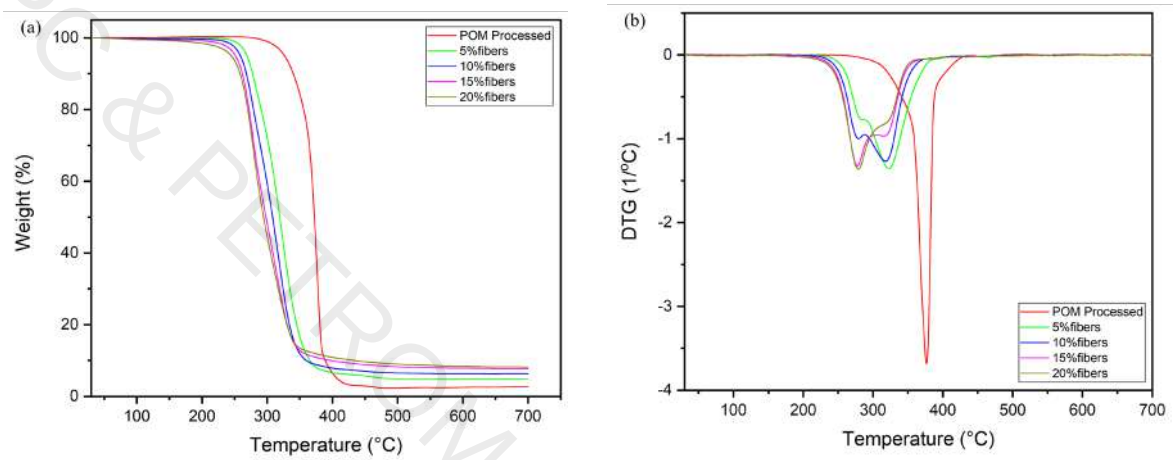


Fig. 3 (a) TGA and (b) DTG curves of POM fill with various coir fiber contents.

It seems that the incorporation of coir fiber accelerated burning rate of the POM/coir fiber composite specimens. It must be inevitably admitted that dripping of burning material caused flame spreading. It is therefore useful to investigate the dripping behavior of burning composites. The results in Table 2 elucidated a significant reduction in dripping behavior. It was observed that at fiber contents of 5, 10, 15, and 20 wt%, the numbers of dripping were reduced with coir fiber contents and the reduction is approximately 85%, 93 %, 98 %, and 99 %, respectively. The dripping reduction was due to the carbonaceous char layer being formed, during combustion, and coating on specimen surface, leading to inhibition of molten composite dripping [12] as shown in Fig. 4(a)-4(b). This observation is supported by TGA results in Fig. 3 (a) which revealed residue contents of 6.57%, 8.76%, 10.94%, and 12.29% with respect to coir fiber contents. This finding also agreed well with Khuntia et al [13]. As expected, coir fiber containing high lignin content which its aromatic structure could rearrange and condense at the temperature above 500°C and this is responsible for carbonaceous compound formation [14].

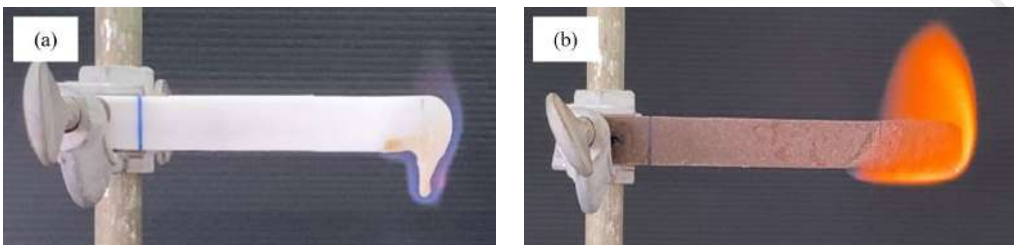


Fig. 4 Horizontal burning test of POM fill with (a) 0 wt% and (b) 20 wt% coir fiber.

PPC & PETROMAT SYMPOSIUM 2025

## CONCLUSIONS

From this part of the work, the incorporation of coir fiber showed an enhancement for Young's modulus and 0.2% offset yield stress. It is inevitable to avoid brittleness of POM/coir fiber composites that was evaluated by tensile elongation and Impact strength. SEM images investigated from tensile fractured surface indicated poor interfacial adhesion between coir fibers and the POM matrix. This adversely affected stress transferring from matrix to fibers and caused the brittleness displayed by elongation and impact properties. The presence of coir fiber limited mobility of melted POM chain resulting in shifting of $T_c$ to a higher temperature than neat POM. Poor interfacial bonding, large diameter led to low surface area of coir fiber inevitable caused obstruction of crystallization and hence reduce degree of crystallinity of POM in POM/coir fiber. The horizontal burning rate tended to increase with the increasing fiber content. However, the incorporation of coir fiber resulted in the formation of a protective carbonaceous char layer, which contributed to the reduction of flame dripping. The decreased molten dripping can reduced flame spreading.

## ACKNOWLEDGEMENTS

The author gratefully acknowledges the Department of Materials Science and Engineering, Faculty of Engineering and Industrial Technology, Silpakorn University, Nakornpathom, for facilities providing and financial support. The authors also would like to express their deepest gratitude for the Department of Materials Engineering, Faculty of Engineering, Kasetsart University, Bangkok, for allowing them to access crucial instruments especially injection molding machine.

## REFERENCES

1. **Lüft, S. and V. P.M** (2014)**.** Polyoxymethylene Handbook, 2014, 1-19.
2. **Harashina, H., Y. Tajima, and T. Itoh** (2006). Polymer Degradation and Stability, 2006, **91**, 1996-2002.
3. **Zhang, Q. and Y. Chen** (2011). Journal of Polymer Research, 2011, **18**, 293-303.
4. **Kneissl, L.M., et al.** (2023). Polymer Testing, 2023, **128**, 108234.
5. **Cayla, A., et al.** (2019). Materials, 2019, **12**.
6. **Soćko, A. and J. Andrzejewski** (2024). Journal of Composites Science, 2024, **8**.
7. **Huang, S., et al.** (2021). Journal of Materials Research and Technology, 2021, **13**, 1441-1484.
8. **Chen, J. and N. Yan** (2013). Composites Part B: Engineering, 2013, **54**, 180-187.
9. **Thomason, J.L. and J.L. Rudeiros-Fernández** (2021). Polymer Degradation and Stability, 2021, **188**, 109594.
10. **Brodin, I., E. Sjöholm, and G. Gellerstedt** (2010). Journal of Analytical and Applied Pyrolysis, 2010, **87**, 70-77.
11. **Ditta, A., et al.** (2016). Polymer Degradation and Stability, 2016, **131**, 122-131.
12. **Su, C., et al.** (2025). Polymer Degradation and Stability, 2025, **240**, 111445.
13. **Khuntia, T. and S. Biswas** (2020). Journal of Industrial Textiles, 2020, **51**, 1616-1640.
14. **Dorez, G., et al.** (2014). Journal of Analytical and Applied Pyrolysis, 2014, **107**, 323-331.

PPC & PETROMAT SYMPOSIUM 2025

# Preliminary condition of Prussian Blue-Doped Membrane Composition on Glyphosate Detection

*~~Chattrin Navapongsiri~~* [a], *Luxsana Dubas* [a,*]

[a] Department of Chemistry, Faculty of Science, Chulalongkorn University, Bangkok 10330, Thailand.

Keywords : Glyphosate, Prussian blue, Polyelectrolyte complexes, Colorimetric sensor

## ABSTRACT

Glyphosate (Gly), a widely used herbicide, poses environmental concern. In this study, a simple Gly indirect analysis method based on Prussian blue (PB) doped in polyelectrolyte complexes (PECs) membranes (PB-PECs) was developed. The analysis was based on the redox characteristics between PB and Prussian white (PW) and complex formation between iron (III) ions (excess amount) and glyphosate. PECs membrane of poly(diallyl dimethylammonium chloride) (PDADMAC) and poly(sodium-p-styrenesulfonate) (PSS) were utilized as a media because of the ion-exchange properties and simple preparation process. To achieve the best sensing conditions, the composition and fabrication condition of PECs were investigated. This study examined PECs membranes prepared with different mole ratios of PDADMAC:PSS (1:1, 1:2, and 2:1). Firstly, the suitable fabrication condition and composition were identified, and the membranes were characterized via ATR-FTIR. Then, preliminary sensing performance of chosen PB-PECs membranes was evaluated using Gly 0.01, 0.1 and 1.0 ppm. The blue intensity of regenerated PB was evaluated using Lab* color space. This method is simple to use, affordable, and provides lots of opportunities for on-site research.

***luxsana.l@chula.ac.th**

## INTRODUCTION

Nowadays, Glyphosate (Gly) [N-(phosphonomethyl) glycine] is one of the commonly used non-selective herbicides in agriculture and households[1]. Many studies have suggested that Gly residuals is hazardous to humans and residues in the water and soil[1, 2]. Maximum residue limits (MRLs) for Gly in drinking water set by the United States and the European Union (EU) are 0.70 ppm[3] and 0.10 ppb[4], respectively. Furthermore, Gly has an ability to chelate with metal ions ($Al^{3+}$, $Co^{2+}$, $Cu^{2+}$, $Fe^{2+}$, $Fe^{3+}$) forming a stable 1:1 Gly-metal complex[5]

These days, a variety of analytical methods have been developed to determine Gly including HPLC analysis with the pre-column derivatization[6]. Nevertheless, this approach is time-consuming and required expensive equipment. Furthermore, Gly in water was determined by measuring the increase of the Cu(II) oxidation signal following the formation of the Gly-Cu(II) complex in carbon electrodes with in situ electrodeposited copper, which provided a LOD of 5 μM[6]. Although, this method is easier and affordable, the sample preparation procedure was complicated[6]. To detect Gly, colorimetric sensors have been deeply investigated in recent years[1]. Two ligands, the colorless 4-(2-(3-chloropyridin-4-yl)vinyl)-N,N-dimethylaniline (BP-Cl) and the yellow 4-(3-chloropyridin-

PPC & PETROMAT SYMPOSIUM 2025

4-yl)buta-1,3-dien-1-yl)-N,N-dimethylaniline (CP-Cl), were used to detect Gly based on the complexation between Gly and BP-Cl or CP-Cl which giving different colors. LOD for BP-Cl and CP-Cl in this research were 1.23 mM and 0.847 mM[7], respectively. Unfortunately, this approach cannot perform in-field due to its complicated sample preparation procedure and sensor preparation[7].

A simple colorimetric analysis method for Gly analysis is still needed for in-field analysis.In this study, this analysis method is based on the complexation of Gly-metal ions and the redox properties of the dark blue colorimetric reagent Prussian blue (PB) [$KFe(III)Fe(II)(CN)_6$ ] was developed. PB can react with various reducing agents such hydrogen sulfide, hydrogen peroxide, or ascorbic acid producing a colorless product, Prussian white ([$KFe(II)Fe(II)(CN)_6$],PW)[8] (**eq.1)**.

$KFe(III)Fe(II)(CN)_6$ (aq) + reducing analyte (aq) + $K^+$ (aq) ⟶ $K_2Fe(II)Fe(II)(CN)_6$ (aq) **(eq. 1)**

Then, the oxidizing analytes such as hexacyanoferrate(III), Fe(III), or $K_2CrO_4$ can recreate the blue PB complexes through the oxidation process[8] as shown in eq. 2.

$K_2Fe(II)Fe(II)(CN)_6$ (aq) + oxidizing analyte (aq) ⟶ $KFe(III)Fe(II)(CN)_6$ (aq) + $K^+$ (aq) **(eq. 2)**

Based on the PB redox properties, PB-composite film was developed to detect ascorbic acid by changing its blue color to colorless[9].

Polyelectrolyte complexes (PECs) are polymers prepared by mixing the opposite charge of polyelectrolyte cations such as Poly(diallydimethyl ammonium chloride) (PDADMAC) and Polyelectrolyte anions, poly(sodium-p-styrenesulfonate) (PSS) [10]. For a variety of uses, polyelectrolyte complexes (PECs) have been researched to produce ion selective membranes. For example, a filter composed of poly(sodium-p-styrenesulfonate) (PSS) and poly(ethyleneimine) (PEI) can be used to create a nanofiltration membrane for wastewater desalination, providing high stability and ion selectivity[11]. PECs was also developed into a colorimetric sensor to detect $NH_3$ by adding colorimetric indicator into PECs membrane[12].

Therefore, this study aims to develop a colorimetric sensor PB-DOPED PECs membrane as an indirect measurement for Gly detection. Ascorbic acid was used to initially convert the PB in membrane sensors to PW. PW membranes were then submerged in the sample solutions, which had already been treated with a known excess amount of $Fe^{3+}$ to regenerate PB as shown in Figure 2. The sensors displayed high sensitivity and selectivity for glyphosate through color changes, based on the excess of $Fe^{3+}$ after Gly-$Fe^{3+}$ complex was formed in the solution.

PPC & PETROMAT SYMPOSIUM 2025

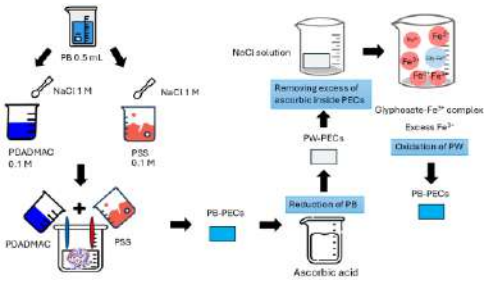


**Figure 2**. Schematic of fabrication and analysis method

## EXPERIMENTAL

*A. Materials and chemicals*

Potassium hexacyanoferrate(II) trihydrate, Sodium chloride, Ascorbic acid, Ferric(III) chloride, Glyphosate, Poly(sodium-p-styrenesulfonate) and Poly(diallyldimethylammoniumchloride) were analytical grade and used without further purification.

*B. PECs Preparation*

PB-doped PECs were made by mixing 20.0 mL of 0.10 or 0.20 M Poly(diallyldimethylammonium chloride) (PDADMAC) and 20.0 mL of 0.10 or 0.20 M Poly(sodium-p-styrenesulfonate) (PSS). After that, 0.50 mL of PB (mole ratio $Fe^{3+}$: $K_4Fe(CN)_6.3H_2O$ 1:1) prepared by mixing 1.00 mL of $1.184x10^{-3}$ M $K_4Fe(CN)_6.3H_2O$ and 1.00 mL of $1.184x10^{-3}$ M $Fe^{3+}$ was added to each PDADMAC and PSS solutions. PB Before mixing PDADMAC and PSS, NaCl with difference molar concentrations (0.00, 0.50 ,1.00 and 2.00 M) was added to each solution. After mixing, the PECs solution was stirred for 2 minutes and then centrifuged for 20 minutes at 4000 rpm. PECs were compressed into a membrane using a press machine and left to be air-dried. The sensing membrane was then cut into 1x2.5 $cm^2$ for further experiments**.** The PECs membrane was made in the same way as PB-doped PECs, except PB was not added to each PDADMAC and PSS.

*C. Characterization of PECs*

PECs with different mole ratios (PDADMAC:PSS, 1:1, 1:2 and 2:1) were studied using Attenuated Total Reflectance Fourier transform Infrared Spectrometer (ATR-FTIR).

*D. Identification of the suitable mole ratio of PDADMAC:PSS and NaCl concentration in PECs preparation process*

PB-doped PECs (1:1, 1:2 and 2:1) prepared using various NaCl concentration (0.00, 0.50, 1.00, 1.50 and 2.00 M) were prepared and then soaked in solution (2.00 mL ascorbic acid 6000 ppm and 1.00 mL NaCl 3 M) for 10 minutes. UV-Vis spectrophotometry was used to measure absorbance of PB at 720 nm, in order to verify the absence of Prussian Blue.

*E. Optimization of the soaking time in 1 M NaCl to leach ascorbic acid from PW-PECs*

PPC & PETROMAT SYMPOSIUM 2025

Due to the ascorbic acid could interfere with the detection, the soaking time in 1 M NaCl required for ascorbic acid to leach out from PECs was investigated. PECs 1:1 and PW-PECs 1:1 membranes were chosen for this study. After rinsing PECs membranes with 6.00 mL of 0.1 M NaCl, membranes were, firstly, soaked in 2.00 mL of 1 M NaCl for 5, 10, 15, 20 minutes and overnight. To check the residual, PECs membranes were then soaked in fresh 1 M NaCl for 10 minutes (after rinsing with 0.1 M NaCl). The content of ascorbic acid in these solutions were measured using UV-Vis spectrophotometry at 265 nm.

*F. Sensor performance toward Gly detection*

To investigate the sensing performance of the developed membrane, 1.00 mL $FeCl_3$ 600.0 ppm was firstly added into the 5.00 mL glyphosate solutions (0.01, 0.1 and 0.1 ppm) in NaCl 1.5 M and control (no Gly) solution, which was diluted from Gly $1.1x10^2$ ppm stock solution. PW membrane was then immersed into the standard solutions for ten minutes. The pictures of membranes were taken by smartphone (Samsung s20fe) for measuring Lab* color space with ImageJ program. (n = 3)

## RESULTS AND DISCUSSION

*A. Characterization of PECs*

The PB-DOPED PECs membrane with different mole ratio (PDAD:PSS / 1:1, 1:2 and 2:1) were investigated by ATR-FTIR show in **Figure 3**

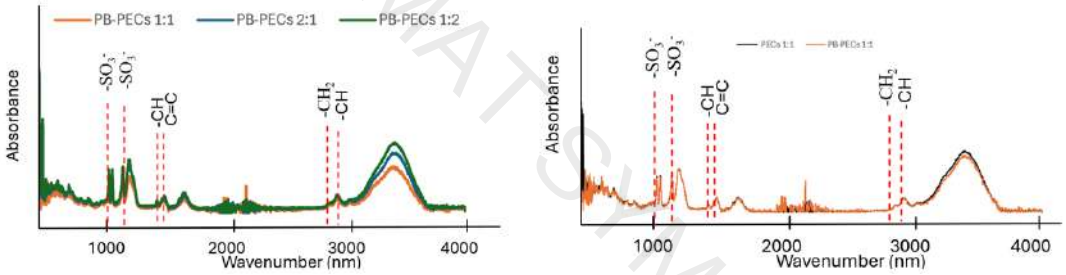


(a) (b)

**Figure 3:** FTIR spectra of (a) PB-DOPED PECs membrane with different mole ratios (PDADMAC:PSS / 1:1, 1:2 and 2:1) (b) PB-DOPED PECs membrane 1:1 and PECs 1:1 without PB. (n=6)

The sulfonate group of PSS was detected at 1000–1100 $cm^{-1}$ in the FTIR spectra of the PB-DOPED PECs membrane[13], where alkane and alkene groups of PDADMAC were detected at 1410 and 1472 $cm^{-1}$, respectively. The methylene group and the alkane group are seen in the PDADMAC characteristic bands at 2866 and 2926 $cm^{-1}$, respectively[14]. The nitrile group at 2074 $cm^{-1}$ and amide at 1500-1600 $cm^{-1}$ of PB were evidenced for PB[15]. PB can be inside PECs membrane and did not change the formation of PECs by comparing the FTIR spectrum **Figure 3 (b)**. The mole ratio of PECs can also be classified by intensity of FTIR spectra of sulfonate group, alkane and alkene group. **Figure 3 (a).**

*B. Fabrication of PECs and NaCl in PW process*

The NaCl concentrations in the PECs preparation process needs to be optimized because it decreases the physical crosslink of the PECs, resulting in a significant decrease in aggregation leading to a more coiled structure and providing the space in the PECs where the other molecule can go inside[12].

PPC & PETROMAT SYMPOSIUM 2025

PECs with NaCl 0.0 and 0.5 M after compressing, the smaller PEC membranes were obtained because too less or no NaCl in the system[10] which caused PECs to remain as colloids in the solution. On the other hand, PECs with NaCl 1.5 M required longer time for the membrane to dry and be ready for usage. However, PECs membranes prepared using more than 2.0 M NaCl were not suitable to perform the experiment due to the lengthy drying time period. PECs 2:1 (PDADMAC:PSS) prepared using all NaCl solutions became opaque when soaked in ascorbic acid (PW process) making them unsuitable for making colorimetric sensors. In conclusion, PECs membranes using 1.0 M NaCl were chosen to use in further experiments due to the acceptable performance of changing blue color (PB) to colorless (PW).

**Table 1:** PECs(1:1, 1:2 and 2:1)-NaCl (0.0, 0.5, 1.0, 1.5 and 2.0 M after soaking in 6000 ppm ascorbic acid with 3M NaCl. (n = 6)

| NaCl (M) | Air-dried |
|---|---|
| 0.0 | 4 days |
| 0.5 | 4 days |
| 1.0 | 4 days |
| 1.5 | 2-3 weeks |
| 2.0 | Not dried |

*C. Optimization of the soaking time in 1 M NaCl to leach ascorbic acid from PW-PECs*

The effect of ascorbic acid can interfere the sensor performance toward glyphosate detection. This investigation was necessary to find the optimal procedure to leach out ascorbic acid which might be inside and on the surface of PECs after PW process in both the NaCl concentration and soaking time.

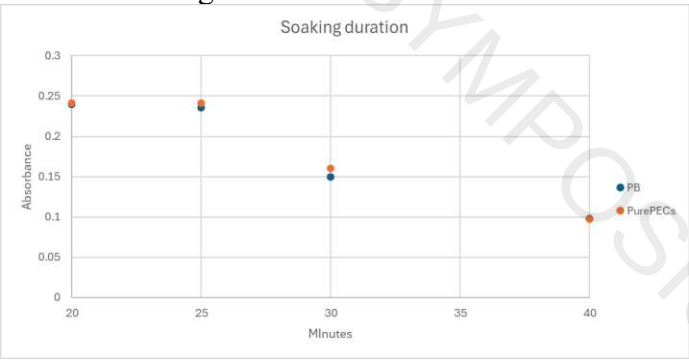


**Figure 4 :** The absorbance at 265 nm was recorded for PECs subjected to soaking in 1 M NaCl solution for varying durations (n=6)

From **Figure 4**, the soaking time in 1 M NaCl in total of 30 minutes is suitable for leaching ascorbic acid out of the membrane.

*D. Sensor performance toward Gly detection*

To evaluate the performance of our developed PECs membrane sensor, PW-doped PEC membranes prepared using optimized condition were dipped into the Gly-$FeCl_3$ solutions

(0.01, 0.1 and 1 ppm) for 10 minutes. To determine the color of membrane sensors, the b values of the Lab*color were evaluated from the photos of PECs membranes after being immersed into Gly-$FeCl_3$ solutions. ΔE values used to evaluate the color differences between two photos were also calculated using equation 3[18].

$$\Delta E = \sqrt{(L_2 - L_1)^2 + (a_2 - a_1)^2 + (b_2 - b_1)^2}$$ (eq. 3).

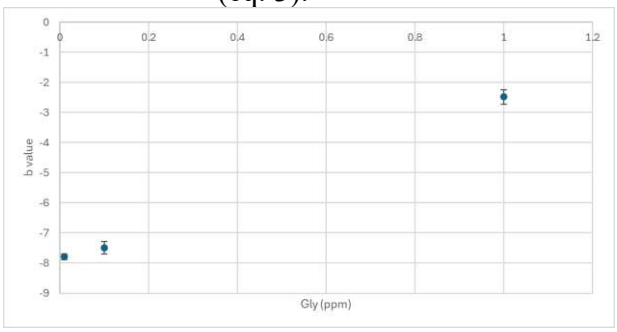


**Figure 5**: b value represents the blueness component of PECs soaked in different Gly concentrations.

In **Figure 5**, the b value in the Lab color space represents the blue-to-yellow axis. Negative b values indicate increased blueness of the PECs, suggesting that higher glyphosate concentrations result in more b values.

**Table 3:** Color difference value (ΔE) and standard diviation of PECs that soaked in sample**.**

| Gly (ppm) | ΔE | SD |
|---|---|---|
| 0.01 and control (0 ppm) | 2.3921 | 0.1544 |
| 0.01 and 0.1 | 0.6304 | 1.0187 |
| 0.01 and 1.0 | 5.5488 | 0.1888 |

ΔE calculated is more than 1 which indicates that the developed blue color of PECs dipping in the solutions with and without Gly is different[16]. As shown in **Table 3**, our developed sensors could separate between solution with Gly 0.01 ppm (10 ppb) which is lower than the MRLs in USA. Unfortunately, the developed PECs membrane could not distinquish between Gly 0.01 (10 ppb) and 0.1 ppm (100 ppb). To summary, this method provided the semi-quantitative Gly detetction.

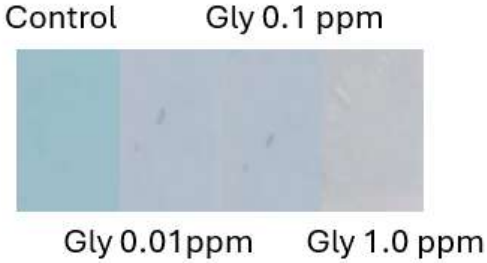


**Figure 5:** Picture of PECs at different Gly concentrations.

## CONCLUSIONS

In this study, three different mole ratios of PECs (1:1, 1:2 and 2:1) and varying molar of NaCl (0.00, 0.50, 1.00, 1.50 and 2.00M) were tested with the different concentrations of

PPC & PETROMAT SYMPOSIUM 2025

Gly. The results indicated that PECs at a 1:1 ratio with 1 M NaCl enabled semi-quantitative detection of Gly at concentrations of 0.01, 0.1, and 1 ppm. The method is simple, cost-effective, and offers significant potential for on-site analysis.

## ACKNOWLEDGEMENTS

This work was greatly supported by the Department of Chemistry, Faculty of Science, Chulalongkorn University

## REFERENCES

(1) Valle, A. L.; Mello, F. C. C.; Alves-Balvedi, R. P.; Rodrigues, L. P.; Goulart, L. R. Glyphosate detection: methods, needs and challenges. *Environmental Chemistry Letters* **2019**, *17* (1), 291-317. DOI: 10.1007/s10311-018-0789-5.
(2) Busse, M. D.; Ratcliff, A. W.; Shestak, C. J.; Powers, R. F. Glyphosate toxicity and the effects of long-term vegetation control on soil microbial communities. *Soil Biology and Biochemistry* **2001**, *33* (12), 1777-1789. DOI: https://doi.org/10.1016/S0038-0717(01)00103-1.
(3) Rubio, F.; Veldhuis, L. J.; Clegg, B. S.; Fleeker, J. R.; Hall, J. C. Comparison of a Direct ELISA and an HPLC Method for Glyphosate Determinations in Water. *Journal of Agricultural and Food Chemistry* **2003**, *51* (3), 691-696. DOI: 10.1021/jf020761g.
(4) Mörtl, M.; Németh, G.; Juracsek, J.; Darvas, B.; Kamp, L.; Rubio, F.; Székács, A. Determination of glyphosate residues in Hungarian water samples by immunoassay. *Microchemical Journal* **2013**, *107*, 143-151.
(5) Subramaniam, V.; Hoggard, P. E. Metal complexes of glyphosate. *Journal of Agricultural and Food Chemistry* **1988**, *36* (6), 1326-1329. DOI: 10.1021/jf00084a050.
(6) Pintado-Benzal, S.; Montoya, M.; Rodríguez-Amaro, R.; Mayen, M.; Mellado, J. Electrochemical Determination of Glyphosate in Waters Using Electrogenerated Copper Ions. *International journal of electrochemical science* **2012**, *7*, 2523-2530.
(7) Aydin, Z.; Keleş, M. A reaction-based system for the colorimetric detection of glyphosate in real samples. *Spectrochimica Acta Part A: Molecular and Biomolecular Spectroscopy* **2022**, *267*, 120501. DOI: https://doi.org/10.1016/j.saa.2021.120501.
(8) Ozeki, T.; Watanbe, I.; Ikeda, S. Study of the prussian blue/prussian white redox reaction by cyclic voltammothermometry. *Journal of Electroanalytical Chemistry and Interfacial Electrochemistry* **1987**, *236* (1), 209-218. DOI: https://doi.org/10.1016/0022-0728(87)88028-2.
(9) Koncki, R.; Lenarczuk, T.; Głąb, S. Optical sensing schemes for Prussian Blue/Prussian White film system. *Analytica Chimica Acta* **2000**, *424* (1), 27-35. DOI: https://doi.org/10.1016/S0003-2670(00)01144-2.
(10) Meka, V. S.; Sing, M. K.; Pichika, M. R.; Nali, S. R.; Kolapalli, V. R.; Kesharwani, P. A comprehensive review on polyelectrolyte complexes. *Drug discovery today* **2017**, *22* (11), 1697-1706.
(11) Huang, H.; Maman, N.; Bernstein, R. A mixed-charged polyelectrolyte complex nanofiltration membrane for mitigating scaling during high-recovery wastewater effluent desalination. *Desalination* **2023**, *565*, 116853. DOI: https://doi.org/10.1016/j.desal.2023.116853.

PPC & PETROMAT SYMPOSIUM 2025

(12) Saikaew, R.; Dubas, S. T. Effect of the composition stoichiometry and salt on the ammonia sensing properties of curcumin-loaded polyelectrolyte complex membranes. *Polymer Bulletin* **2022**, *79* (6), 4171-4181. DOI: 10.1007/s00289-021-03698-7.
(13) Salloum, D. S.; Schlenoff, J. B. Protein Adsorption Modalities on Polyelectrolyte Multilayers. *Biomacromolecules* **2004**, *5* (3), 1089-1096. DOI: 10.1021/bm034522t.
(14) Eneh, C. I.; Bolen, M. J.; Suarez-Martinez, P. C.; Bachmann, A. L.; Zimudzi, T. J.; Hickner, M. A.; Batys, P.; Sammalkorpi, M.; Lutkenhaus, J. L. Fourier transform infrared spectroscopy investigation of water microenvironments in polyelectrolyte multilayers at varying temperatures. *Soft Matter* **2020**, *16* (9), 2291-2300. DOI: 10.1039/c9sm02478f From NLM.
(15) Petroviciu, I.; Teodorescu, I.; Albu, F.; Vîrgolici, M.; Nagoda, E.; Medvedovici, A. Dyes and biological sources in nineteenth to twentieth century ethnographic textiles from Transylvania, Romania. *Heritage Science* **2019**, *7*. DOI: 10.1186/s40494-019-0255-0.
(16) Annisa, M.; Harsini, H.; Nuryanti, A. The comparison of two programmes to measure color difference (Î”E) from tooth sample photo. *Odonto : Dental Journal* **2023**, *10*, 257. DOI: 10.30659/odj.10.2.257-267.

PPC & PETROMAT SYMPOSIUM 2025

# Development of *Streptococcus pyogenes* point-of-care test kit in necrotizing fasciitis from blood sample

~~Paranee Phuking~~ [a], Piyachat Chuysinuan [b], Pitt Supaphol [*,a]

[a] The Petroleum and Petrochemical College, Chulalongkorn University, Bangkok, Thailand
[b] Laboratory of Organic Synthesis, Chulabhorn Research Institute, Bangkok, Thailand

Keywords: Electrospinning, Zeolitic imidazolate framework-8, L-pyrrolidonyl-β-naphthyl amide test, Hemoglobin removal, and *Streptococcus pyogenes*

## ABSTRACT

Necrotizing fasciitis (NF), an aggressive soft tissue infection caused by *S. pyogenes*, leads to amputation due to misdiagnosis and delayed treatment. Early detection of *S. pyogenes* in NF from wound exudate is crucial for mitigating patient disability and mortality. The L-pyrrolidonyl-β-naphthylamide (PYR) test is used to identify *S. pyogenes* based on a colorimetric change. However, red blood cells interfere with the results. In this study, a PYR test strip incorporating a zeolitic imidazolate framework-8 (ZIF-8) on electrospun polyacrylonitrile membrane (ZIF-8/PAN) as a hemoglobin separation pad was developed for presumptive *S. pyogenes* identification at point-of-care in NF from blood. The ZIF-8/PAN pad prepared using an initial zinc nitrate hexahydrate concentration of 400 mM, contained ZIF-8 on electrospun PAN mat up to 34.92 ± 2.64% with the fiber diameter of 1719.20 ± 251.00 nm. The ZIF-8/PAN demonstrated hemoglobin absorption at equilibrium of 52.35 ± 2.41 mg/g in 90 min. Furthermore, the bacterial distinguishing activity of the PYR test strip was evaluated. This test kit promises to enable earlier treatment of NF.

*** pitt.s@chula.ac.th**

## INTRODUCTION

NF is an aggressive soft tissue infection predominantly caused by *S. pyogenes* invasion through a wound. The ambiguous symptoms make diagnosis difficult and time-consuming, allowing amputation or mortality (Stevens & Bryant, 2017). The survival rate increases significantly when surgical intervention is performed within 24 hours of hospital admission (Guliyeva et al., 2024). To address these challenges, the development of rapid point-of-care *S. pyogenes* detection in wound exudate is required for fast diagnostic adjuncts. PYR test is a colorimetric method for rapid presumptive identification of *S. pyogenes* based on pyrrolidonyl arylamidase activity. (Kaufhold, Lütticken, & Schwien, 1989). While the PYR test provides a significant time advantage, a notable limitation of this test emerges in wound exudate analysis, where overlapping color between the positive PYR result and hemoglobin confounds the result interpretation

.

Immobilized-metal affinity chromatography (IMAC), based on differential binding affinity between electron donors of proteins and immobilized transition metal ions on the solid support, is a favorable technique for histidine-tagged protein fractionation due to high adsorption capacity and selectivity (Porath et al., 1975). Membrane system with a

PPC & PETROMAT SYMPOSIUM 2025

macroporous structure demonstrates rapid mass transfer and low pressure drop, resulting in high-throughput (Suen, Liu, & Chang, 2003). Electrospinning, a fabrication process utilizing electrostatic repulsion to produce nonwoven fibers, has been applied in an affinity membrane because of tunable morphology, high surface area, and porosity (Bhardwaj & Kundu, 2010). In previous work, iron oxide nanoparticle-immobilized PAN nanofiber was used for Congo Red dye removal in wastewater (Patel & Hota, 2016).

Moreover, the IMAC suffers from other drawbacks of complex ligand conjugation and metal ion leakage during isolation or elution steps, which reduce the purity of eluted proteins (Block et al., 2009). ZIF-8 is a coordinated network of 2-methylimidazole and zinc ion. The ZIF-8 has gotten attention in biomolecular adsorption and separation due to its high porosity, facile functionalization, and resistance to alkaline or aqueous solutions (Mousavi et al., 2024). In previous work, magnetic ZIF-8 nanocomposites demonstrated hemoglobin adsorption capacity of 6,222 mg/g within 10 min while retaining 96.3% of its binding efficiency over 10 reuse cycles. The stability of ZIF-8 was exhibited to overcome the metal leakage problems (Zheng et al., 2015).

In this study, in-situ growth of ZIF-8 on the electrospun PAN membrane as a hemoglobin removal pad was integrated into the PYR substrate-coated electrospun PAN membrane as a detection pad to indicate the presence of *S. pyogenes*. This test strip promised to provide point-of-care identification of *S. pyogenes* from blood for the assumption of NF.

## EXPERIMENTAL

### *A. Fabrication of electrospun PAN membrane*

PAN powder was dissolved in DMF at 60 ºC for 6 h to receive 12 wt% PAN solutions. The PAN solutions was injected at a constant flow rate of 1 mL/h through a 20G needle located at an angle of 45º from a vertical baseline under a high AC applied voltage of +12/-5 kV between the needle tip and the collector at a distance of 15 cm to obtain PAN nanofibers on the wire drum collector with different rotational speed of 50, 100, 200, and 300 rpm after 2 h. The electrospun PAN membrane was dried at 80 ºC for 24 h.

### *B. In-situ growth of ZIF-8 on electrospun PAN membrane*

3×3 $cm^2$ of electrospun PAN membrane was soaked in 1 M NaOH at 70 ºC for 15 min. The hydrolyzed electrospun PAN mat (H-PAN) was washed with water several times and dried in an oven at 80 ºC for 24 h. Next, the H-PAN mat was immersed in 100, 200, and 400 mM $Zn(NO_3)_2 \cdot 6H_2O$ in 2.5 mL of water for 1 h. The H-PAN mat and $Zn(NO_3)_2$ solution were added to 7.5 mL of MIM in water to achieve 1:80, 1:40, and 1:20 of $Zn^{2+}$:MIM molar ratio. Then, the mixture was sonicated at room temperature for 15 min. The ZIF-8 immobilized on the membrane (ZIF-8/PAN) was rinsed with water and dried at 80 ºC for 24 h.

### *C. Characterization*

Morphology was observed by a scanning electron microscope (Hitachi S-4800). Crystalline structure was characterized X-ray diffractometer (SmartLab, Rigaku) at 40 kV and 30 mA in

PPC & PETROMAT SYMPOSIUM 2025

the 2θ range of 5˚ to 45˚ for a 0.01˚ step increment, and the crystallite size was calculated using Debye–Scherrer's equation. The Hb adsorption kinetics and isotherms were analysed using UV-1700 (PharmaSpec, Shimadzu).

## RESULTS AND DISCUSSION

### *A. Yield of ZIF-8 on PAN membrane*

Yields of ZIF-8 coated on an electrospun PAN membrane, synthesized by different initial $Zn^{2+}$ concentrations of 100, 200, and 400 mM are 17.15 ± 2.29, 26.01 ± 1.77, and 34.92 ± 2.64%, respectively due to a greater amount of $Zn^{2+}$ for binding with MIM to form ZIF-8.

### *B. Morphology of ZIF-8/PAN membrane*

SEM images of the ZIF-8/PAN membranes are displayed in Figure 1. A rough surface occurs in all membranes caused by the growth of the ZIF-8 layer. Increasing the initial $Zn^{2+}$ concentration of 100, 200, and 400 mM increases the fiber diameter to 1587.10 ± 261.86, 1669.80 ± 194.77, and 1719.20 ± 251.00 nm, respectively (n=200).

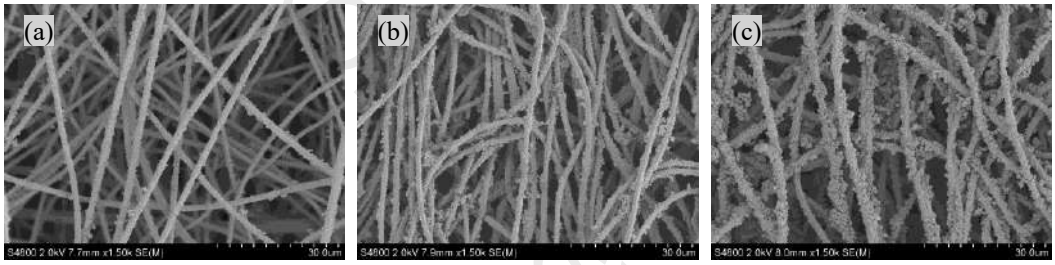


**Figure 1** SEM images of ZIF-8/PAN membranes, synthesized by different initial $Zn^{2+}$ concentrations of 100 (a), 200 (b), and 400 mM (c).

### *C. XRD pattern of the ZIF-8/PAN membrane*

All XRD patterns of ZIF-8/PAN membranes possess the same characteristic peaks as solidate nanocrystal structure of ZIF-8 powder on the plane (011), (002), (112), (022), (013), and (222) as illustrated in Figure 2, ensuring the ZIF-8 growth. Crystallite sizes were calculated from the strongest peak at 7.3˚. Increasing the initial $Zn^{2+}$ concentrations of 100, 200, and 400 mM increases the crystallite size of the ZIF-8/PAN membranes to 23.39 ± 4.37, 28.82 ± 0.92, and 36.61 ± 7.20 nm, respectively. However, these sizes are smaller than 41.15 ± 8.12 nm of the ZIF-8 powder.

PPC & PETROMAT SYMPOSIUM 2025

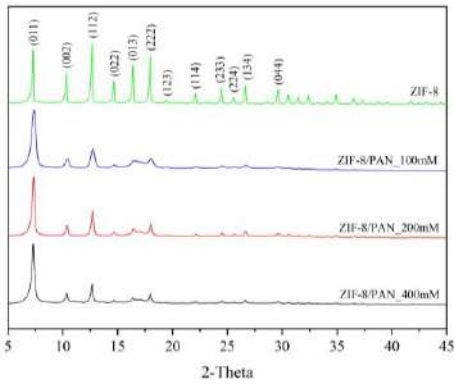


**Figure 2** XRD diffractograms of ZIF-8 and ZIF-8/PAN membranes

*D. Hb adsorption kinetics of ZIF-8/PAN membrane*

Adsorption kinetics of 0.15 mg/mL Hb in PBS pH 7.4 on ZIF-8/PAN membranes were analyzed using UV-Vis as shown in Figure 3(a). Amounts of adsorbed Hb on the ZIF-8/PAN membranes steeply increase in the first, and then gradually increase until they become constant, indicating a high adsorption rate at the beginning and then decrease due to saturation of Hb in the membrane. Figure 3(b) exhibits that all adsorption kinetics are fitted well with the pseudo-second-order kinetic model. The amount of adsorbed Hb at equilibrium ($q_e$) increases when the $Zn^{2+}$ concentration increases, caused by a higher yield of ZIF-8 provides more binding sites. However, the rate constant ($k_2$) decreases, correlated to a lower surface area and pore volume as presented in Table 1.

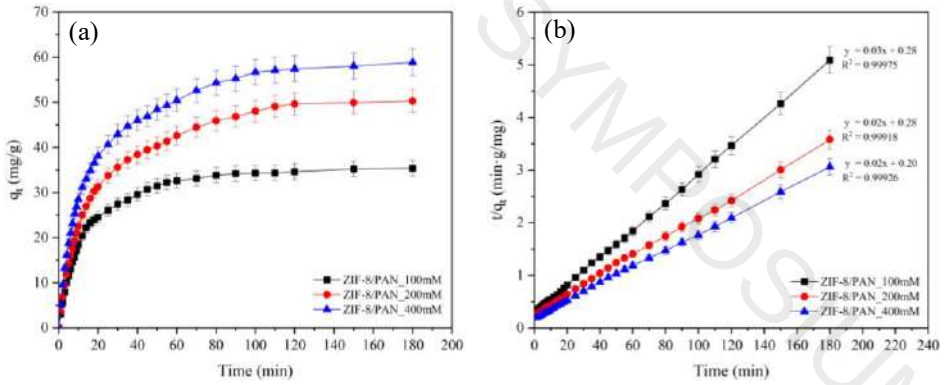


**Figure 3** Hb adsorption kinetics (a) and fitting curves with the pseudo-second-order kinetic model (b) of ZIF-8/PAN membranes.

**Table 1** Hb adsorption kinetic parameters of ZIF-8/PAN membranes.

| Sample | $q_e$ (mg/g) | $k_2$ (g/mg·min) | $R^2$ |
|---|---|---|---|
| ZIF-8/PAN_100mM | 38.03 ± 0.17 | 0.002 ± 4.940×10$^{-5}$ | 0.99975 |
| ZIF-8/PAN_200mM | 54.05 ± 0.38 | 0.001 ± 3.835×10$^{-5}$ | 0.99918 |
| ZIF-8/PAN_400mM | 61.90 ± 0.44 | 0.001 ± 4.224×10$^{-5}$ | 0.99926 |

PPC & PETROMAT SYMPOSIUM 2025

*E. Hb adsorption isotherm*

Hb adsorption on ZIF-8/PAN membranes for 90 min in simulated blood containing the various concentrations of Hb from 0.025 to 0.150 mg/mL in PBS pH 7.4 was illustrated in Figure 4(a). The increase in initial Hb concentration will increase the amount of adsorbed Hb on the ZIF-8/PAN membrane surface. All adsorption isotherms are fitted well with the Freundlich model, as displayed in Figure 4.22(b), assuming multilayers of Hb are adsorbed on heterogeneous sites of the membrane. The Freundlich constant ($K_F$) and the Freundlich exponent (n) increase for adsorption capacity and for intensity of adsorption, respectively, when the initial $Zn^{2+}$ concentration increases, as denoted in Table 2.

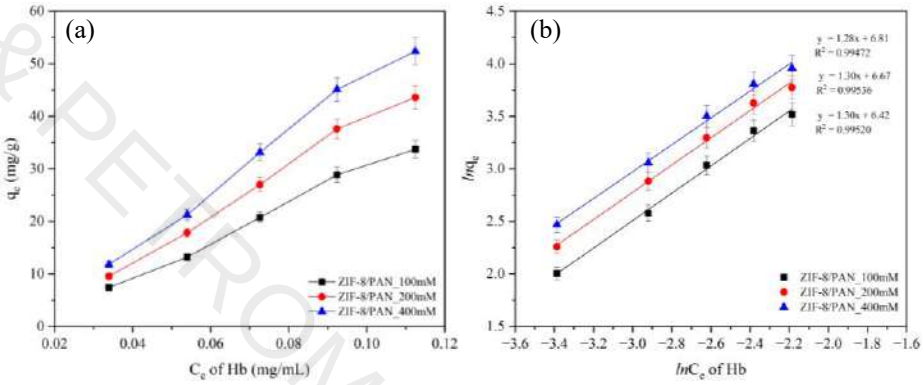


**Figure 4** Hb adsorption isotherms (a) and fitting curves with the Freundlich model (b) of ZIF-8/PAN membranes.

**Table 2** Fitting parameters of Hb adsorption on ZIF-8/PAN membranes.

| Sample | $K_F$ (mg/g)·(mL/mg)$^{1/n}$ | n | $R^2$ |
|---|---|---|---|
| ZIF-8/PAN_100mM | 522.44 ± 115.21 | 0.81 ± 0.06 | 0.99520 |
| ZIF-8/PAN_200mM | 641.24 ± 140.03 | 0.82 ± 0.06 | 0.99536 |
| ZIF-8/PAN_400mM | 746.84 ± 164.74 | 0.83 ± 0.06 | 0.99472 |

## CONCLUSIONS

In summary, ZIF-8 immobilized on an electrospun PAN membrane, synthesized by 400 mM of $Zn^{2+}$ concentration demonstrate rapid Hb adsorption rate and high Hb absorption at equilibrium of 52.35 ± 2.41 mg/g within 90 min. The ZIF-8/PAN membrane promises to be a hemoglobin removal pad for integrating with the PYR test strip as a point-of-care identification of *S. pyogenes* from blood for the assumption of NF.

## ACKNOWLEDGEMENTS

The author would like to sincerely thank the Petroleum and Petrochemical College, Chulalongkorn University, Center of Excellence on Petrochemical and Materials Technology (PETROMAT), and Chulabhorn Research Institute for the research grant that was conducted for this research.

PPC & PETROMAT SYMPOSIUM 2025

## REFERENCES

**Bhardwaj, N., & Kundu, S. C.** (2010) *Biotechnology Advances*, **28(3)**, 325-347.

**Block, H., Maertens, B., Spriestersbach, A., Brinker, N., Kubicek, J., Fabis, R., Labahn, J., & Schäfer, F.** (2009) *Methods in Enzymology.* pp. 439-473). Academic Press.

**Guliyeva, G., Huayllani, M. T., Sharma, N. T., & Janis, J. E.** (2024) *Plastic and Reconstructive Surgery*, **12(1)**, e5533.

**Kaufhold, A., Lütticken, R., & Schwien, U.** (1989) *Zentralblatt für Bakteriologie*, **272(2)**, 191-195.

**Mousavi, S. M., Fallahi Nezhad, F., Akmal, M. H., Althomali, R. H., Sharma, N., Rahmanian, V., Azhdari, R., Gholami, A., Rahman, M. M., & Chiang, W. H.** (2024) *Talanta*, **275**, 126097.

**Patel, S., & Hota, G.** (2016). *RSC Advances*, **6(19)**, 15402-15414.

**Porath, J., Carlsson, J. A. N., Olsson, I., & Belfrage, G.** (1975) *Nature*, **258(5536)**, 598-599.

**Stevens, D. L., & Bryant, A. E.** (2017) *New England Journal of Medicine*, **377(23)**, 2253-2265.

**Suen, S. Y., Liu, Y. C., & Chang, C. S.** (2003) *Journal of Chromatography B*, **797(1)**, 305-319.

**Zheng, J., Lin, Z., Lin, G., Yang, H., & Zhang, L.** (2015) *Journal of Materials Chemistry B*, **3(10)**, 2185-2191.

PPC & PETROMAT SYMPOSIUM 2025

# Enhancing the Rheological and Mechanical Performance of PHB Through PLA and PBS Blending for Sustainable 3D Printing Filaments

*Jitrawee Suk-em* *[a], *Kunanon Passarapark* [a], *Chuanchom Aumnate* [a,b]

[a] Metallurgy and Materials Science Research Institute, Chulalongkorn University, Bangkok, Thailand
[b] Center of Excellence in Responsive Wearable Materials, Metallurgy and Materials Science Research Institute, Chulalongkorn University, Bangkok, Thailand

Keywords : polyhydroxybutyrate, polylactic acid, polybutylene succinate, 3D printing, rheology

## ABSTRACT

Biodegradable polymers play a crucial role in mitigating the environmental impact of conventional plastics, as they decompose naturally and help reduce plastic waste and carbon emissions. Among them, polyhydroxybutyrate (PHB) is a biodegradable polymer produced by microorganisms. It is non-toxic, making it suitable for applications in agriculture, food packaging, and the medical field. However, its poor impact resistance and low melt strength hinder its use in flexible and high-performance applications, especially in extrusion-based 3D printing. This study focuses on developing alternative biodegradable 3D printing filaments by blending PHB with polylactic acid (PLA) and polybutylene succinate (PBS), with particular attention to their rheological behavior and processability. The PHB-based blends were prepared using a twin-screw extruder and 3D printed into test specimens to evaluate their mechanical and morphological properties. Rheological analysis revealed that increasing PLA and PBS content led to an increase in melt viscosity, indicating improved melt strength and enhanced flow stability, which is critical for consistent filament extrusion and 3D printing. Additionally, mechanical testing showed improvements in flexural modulus and strength with the addition of PLA and PBS. SEM micrographs confirmed partial compatibility among the immiscible phases, evidenced by the uniform dispersion of PLA and PBS within the PHB matrix.

*** jitrawee.s@chula.ac.th**

## INTRODUCTION

In recent years, increasing environmental concerns have accelerated the search for sustainable alternatives to conventional petroleum-based plastics. Among these alternatives, biodegradable polymers derived from renewable sources have garnered significant attention due to their ability to decompose into non-toxic byproducts, thereby reducing plastic waste and mitigating long-term environmental impacts. Additionally, their degradation process can contribute to lower net carbon emissions, aligning with global sustainability goals. Owing to their versatility and environmental compatibility, biodegradable polymers are now widely utilized in diverse fields such as food packaging, agriculture, and biomedical applications [1]. Polyhydroxybutyrate (PHB), a member of the polyhydroxyalkanoate (PHA) family, is a biodegradable polyester synthesized by microbial fermentation under nutrient-limited, carbon-rich conditions. Due to its biocompatibility, biodegradability, and non-toxic nature, PHB is particularly attractive for biomedical

PPC & PETROMAT SYMPOSIUM 2025

applications such as drug delivery, tissue engineering, and implants [2]. However, its high crystallinity and narrow processing window result in brittleness and poor processability, limiting its competitiveness with conventional polymers like polypropylene (PP) [3-4]. To overcome these limitations, PHB is often blended with other polymers to improve its mechanical and processing performance. Polylactic acid (PLA), derived from renewable sources such as cassava and corn, offers excellent processability and high melt strength, making it a suitable candidate for blending with PHB to improve printability and mechanical performance [5-7]. While PLA has good flexural properties, it is inherently brittle with low toughness and elongation at break [8]. Incorporating a more ductile polymer into the PHB/PLA blend has the potential to significantly enhance its mechanical performance. Polybutylene succinate (PBS), a biodegradable aliphatic polyester produced from succinic acid and 1,4-butanediol, exhibits favorable mechanical properties comparable to or exceeding those of polyethylene (PE) and PP, and superior to low-density polyethylene (LDPE), except in flexural modulus. PBS is also compatible with standard processing techniques, including extrusion and injection molding, and is suitable for filament production [9].

This study aims to develop and characterize biodegradable filaments based on PHB/PLA/PBS ternary blends for FFF 3D printing. PHB serves as the primary matrix, with PLA and PBS incorporated at varying concentrations (10–30 wt.%). Filaments were prepared using a twin-screw extruder and used to print test specimens. Rheological behavior, mechanical properties, and blend morphology were analyzed to evaluate their suitability for applications requiring printability, biodegradability, and enhanced mechanical performance.

## EXPERIMENTAL

*Materials*

PHB (Biomer® P263E), sourced from Biomer (Germany), was selected as the primary matrix material and maintained at a constant proportion of 60 wt.%. To modify the blend properties, PLA (Ingeo™ Biopolymer 4043D) from NatureWorks (USA), and bio-based PBS (BioPBS™ FD92PM) from PTT MCC Biochem (Thailand), were incorporated at varying concentrations ranging from 10 to 30 wt.%, as detailed in Table 1.

**Table 1** Composition of the PHB/PLA/PBS blends.

| Sample | PHB [wt.%] | PLA [wt.%] | PBS [wt.%] |
|---|---|---|---|
| 60/30/10 | 60 | 30 | 10 |
| 60/20/20 | 60 | 20 | 20 |
| 60/10/30 | 60 | 10 | 30 |

*Filament Preparation and 3D printing of specimens*

Prior to processing, virgin polymer pellets were dried in a hot-air oven at 60 °C for 12 hours to eliminate residual moisture. The dried pellets were then melt-blended using a co-rotating twin-screw extruder (Thermo PRISM DSR-28, L/D ratio 25:1). The extrudate was immediately cooled in a water bath and collected using a winding machine with adjustable speed to form continuous filaments. To maintain a consistent filament diameter within the

PPC & PETROMAT SYMPOSIUM 2025

range of 1.6-1.8 mm, extrusion was performed using a temperature profile of 100-165 °C and a screw speed of 30-50 rpm.
Flexural test specimens were 3D printed (Raise3D Pro2) from the prepared filaments, following ASTM D638 Type V dimensions (63.5×12.7×2 mm), with at least five specimens per composition. 3D printing parameters included a nozzle diameter of 0.4 mm, nozzle temperature of 210 °C, bed temperature of 50 °C, layer height of 0.2 mm, 100% infill density, and a print speed of 60 mm/s.

*Rheology*
Rheological measurements were performed using a parallel plate rheometer (HAAKE MARS 40, Thermo Scientific, Germany) equipped with 20 mm diameter plates and a 1 mm gap. Steady shear tests were conducted at 210 °C, over a shear rate range of 0.01 to 100 $s^{-1}$

*Mechanical Properties*
Flexural testing was carried out using a universal testing machine (Tinius Olsen, Model 5ST) at a crosshead speed of 50 mm/min and a support span of 32 mm, in accordance with ASTM D790. Each measurement was performed with a minimum of five replicates.

*Scanning electron microscopy (SEM)*
To investigate the phase morphology of the blend filaments, SEM was performed using a Hitachi SU3500 - Horiba X-maxN, operating at an accelerating voltage of 5 kV. Prior to imaging, the filaments were fractured under cryogenic conditions using liquid nitrogen, followed by immersion in acetone at room temperature for 30 minutes to selectively remove the PLA phase and enhance phase contrast.

## RESULTS AND DISCUSSION

*PHB/PLA/PBS blend filaments*
Fig. 1 shows 3D printing filaments produced from neat PHB, PLA, PBS, and their blends. All materials were successfully melt-extruded into uniform filaments (1.6–1.8 mm diameter), suitable for FFF printing. The PHB-based blends exhibited a characteristic brownish-yellow hue due to natural pigmentation of PHB.

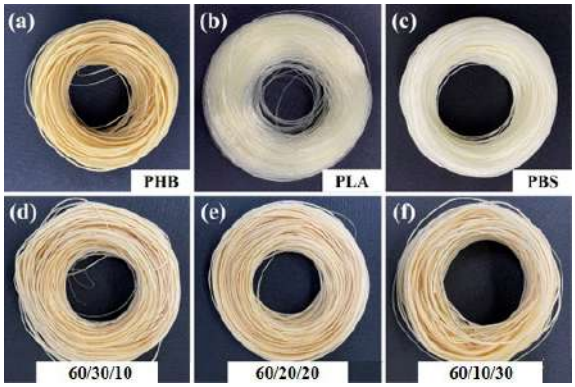


**Fig. 1** The appearance of the prepared filaments from neat polymers: (a) PHB, (b) PLA, (c) PBS, and PHB/PLA/PBS blends: (d) 60/30/10, (e) 60/20/20, and (f) 60/10/30.

PPC & PETROMAT SYMPOSIUM 2025

*Rheological Properties*

Fig. 2 presents the steady shear viscosity as a function of shear rate for neat PLA, PBS, PHB, and their blends at 210 °C, corresponding to the 3D printing temperature. Both PBS and PLA exhibited high initial viscosities that remained nearly constant up to a shear rate of approximately 10 $s^{-1}$, followed by a pronounced decrease at higher shear rate. This behavior indicates shear thinning characteristics, suggesting high melt strength and stability under shear.

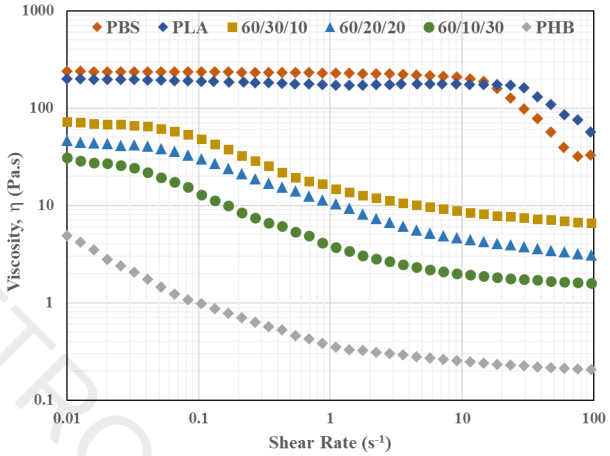


**Fig. 2** Steady shear viscosity of PHB, PLA, PBS, and blends as a function of shear rates.

In contrast, PHB exhibited the lowest viscosity across the entire shear rate range, with a continuous decline in viscosity even at low shear rates. This behavior reflects its low melt strength and poor flow stability, which can limit its suitability for processing techniques requiring dimensional stability during flow [4]. The PHB/PLA/PBS blends showed intermediate viscosity values between those of the individual polymers. At low shear rates (up to~ 0.05 $s^{-1}$), the blends maintained relatively constant viscosities, followed by a noticeable shear thinning response at higher shear rates. Among the blends, 60/30/10 formulation showed the highest viscosity, which increase with higher PLA content. This trend suggests that the blend benefits from the inherently high melt strength of PLA, contributing to improved rheological performance and processability [6,7].

*Mechanical properties*

The flexural modulus and flexural strength of 3D-printed PHB, PLA, PBS and all blends are shown in Fig. 3(b) and 3(c), respectively. The incorporation of PLA and PBS led to a significant enhancement in the mechanical properties across the blends. The 60/30/10 composition exhibited the greatest improvement, with the flexural modulus and flexural strength increasing by 23.5% and 33.6%, respectively. This enhancement is primarily attributed to the inherently high flexural properties of PLA [8,10]. Even at relatively small proportions, PLA contributed noticeably to the mechanical properties, as demonstrated in the 60/10/30 blend. The uniform dispersion of PLA within the PHB matrix likely facilitated more effective stress distribution. In contrast, increasing the PBS content to 20 wt.% and 30 wt.% resulted in reduced flexural modulus and flexural strength, likely due to the comparatively lower flexural properties of PBS [9].

PPC & PETROMAT SYMPOSIUM 2025

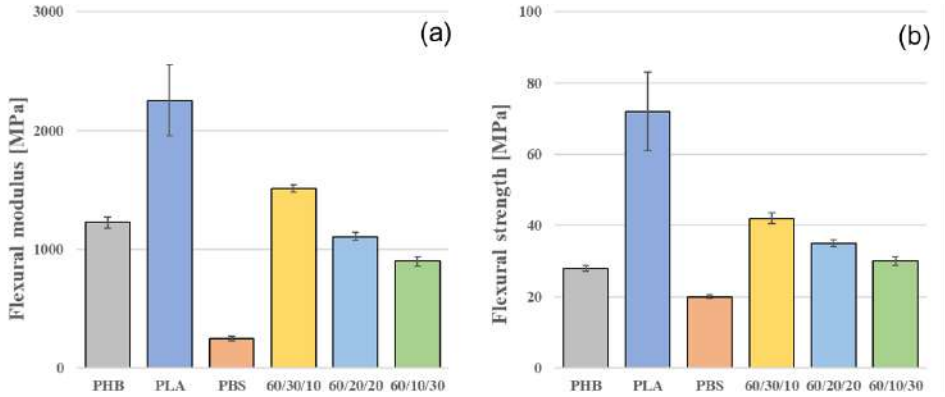


**Fig. 3** The flexural properties of the 3D-printed specimens made from PHB, PLA, PBS and the PHB/PLA/PBS blend filaments; flexural modulus (a) and flexural strength (b).

*Morphology*

Fig. 4 presents the phase morphologies of cryo-fractured surfaces of PHB/PLA/PBS blends with varying compositions, both before and after acetone etching. The results revealed clear phase separation among the PHB, PLA, and PBS components. PHB, serving as the continuous matrix, shows a roughly spherical morphology, while PLA and PBS appear as dispersed phases. This observation confirms that the PHB/PLA/PBS system is immiscible [11].

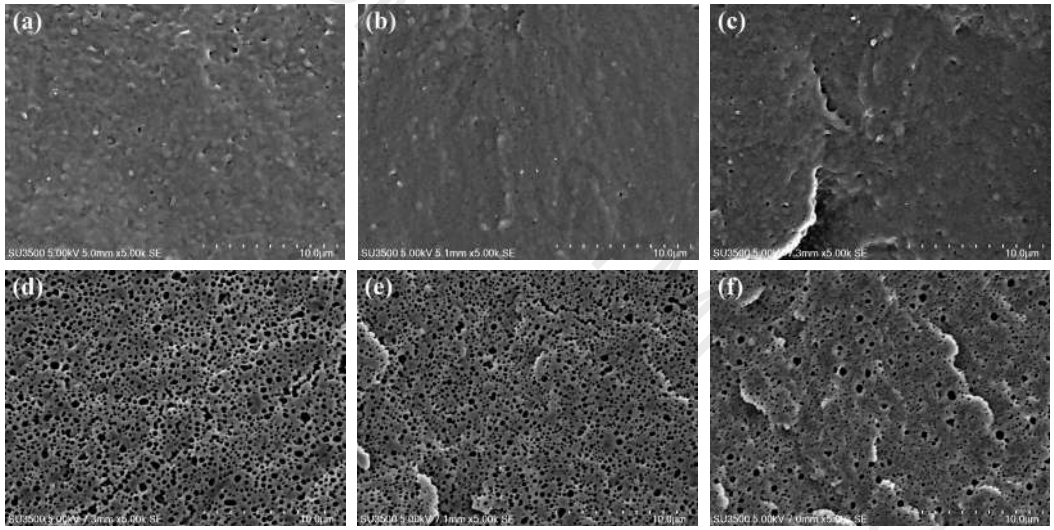


**Fig. 4** SEM images of cryo-fractured surfaces of PHB/PLA/PBS blends at 5000x; (a) 60/30/10; (b) 60/20/20; (c) 60/10/30 before etching; (d) 60/30/10; (e) 60/20/20; (f) 60/10/30 after etching.

Notably, an increasingly rough surface with sharper and larger droplets was observed as the PBS content increased. This trend is attributed to the detachment of PBS domains during fracturing, suggesting weak interfacial adhesion between PBS and the PHB matrix [12]. After acetone etching, which selectively removed PLA, a large number of cavities appeared on the fracture surface. These voids correspond to the removed PLA phase and were uniformly distributed throughout the PHB matrix, indicating good dispersion. However, as the PBS content increased, both the number and size of these cavities decreased, suggesting reduced PLA content and altered blend morphology with higher PBS loading.

## CONCLUSIONS

This study focuses on developing alternative biodegradable filaments, aiming to enhance the mechanical properties and processability of PHB-based materials specifically for 3D printing applications. PHB/PLA/PBS blend filaments were successfully fabricated using a twin-screw extrusion process. The incorporation of PLA and PBS significantly improved the melt strength of PHB, with PLA contributing notably to the improvement in flexural modulus and flexural strength. These improvements resulted in superior mechanical performance compared to neat PHB. Morphological analysis revealed distinct phase separation among PHB, PLA, and PBS, both dispersed phases uniformly distributed within the PHB matrix. Overall, the developed PHB/PLA/PBS blends demonstrate strong potential as alternative sustainable filament for 3D printing, particularly in applications requiring complex, customized shapes and biodegradability.

## ACKNOWLEDGEMENTS

This research project is supported by the National Research Council of Thailand (NRCT) and Chulalongkorn University (N42A670570), and Metallurgy and Materials Science Research Institute, Chulalongkorn University.

## REFERENCES

[1] **Colnik, M. Hrncic, M. K. Skerget, M. and Knez Z.** (2020) Chem. Ind. Chem. Eng. Q. 26 (4), 401−418.
[2] **Raju, N. N. Sankaranarayanan, M. and Bharathiraja, B.** (2024) J. Mol. Struct. 1303, 137511.
[3] **Dalton, B. Bhagabati, P. Micco, J. D. Padamati, R. B. and O'Connor, K.** (2022) Catalysts. 12, 319.
[4] **Kanabenja, W. Passornraprasit, N. Aumnate, C. Osswald, T. A. Aht-Ong, D. and Potiyaraj, P.** (2024) Addit. Manuf. 86, 104205.
[5] **Wang, X. Huang, L. Li, Y. Wang, Y. Lu, X. Wei, Z. Mo, Q. Zhang, S. Sheng, Y. Huang, C. Zhao, H. and Liu, Y.** J. Manuf. Process. 112, 161-178.
[6] **Aumnate, C. Soatthiyanon, N. Makmoon, T. Potiyaraj, P.** (2021) Cellulose. 28: 8509-8525.
[7] **Kanabenja, W. Passarapark, K. Subchokpool, T. Nawaaukkaratharnant, N. Román, A. J. Osswald, T. A. Aumnate, C. and Potiyaraj, P.** (2022) Addit. Manuf. 59, 103130.
[8] **Garcia-Campo, M. J. Boronat, T. Quiles-Carrillo, L. Balart, R. and Montanes, N.** (2018) Polym. 10, 3.
[9] **Barletta, M. Aversa, C. Ayyoob, M. Gisario, A. Hamad, K. Mehrpouya, M. and Vahabi, H.** (2022) Prog. Polym. Sci. 132, 101579.
[10] **Jaffur, B. N. Kumar, G. and Khadoo, P.** (2024) Int. J. Biol. Macromol. 278, 134907.
[11] **D'Anna, A. Arrigo, R. and Frache, A.** (2022) J. Polym. Environ. 30: 102–113.
[12] **Righetti, M. C. Cinelli, P. Aliotta, L. Bianchi, E. Tricoli, F. Seggiani, M. and Lazzeri, A.** (2021) Polym. Int. 71: 47-56.

PPC & PETROMAT SYMPOSIUM 2025

# THE PROPERTIES OF PLA/NATTO COMPOSITE FILMS

*Natrata Thitinardwong* [a]

[a]Department of Technopreneurship and Innovation Management Program, Graduate School, Chulalongkorn University, Bangkok 10330,Thailand.

Keywords :
Bioplastic, PLA (Polylactic acid), PLA/Natto composite

## ABSTRACT

Polylactic acid (PLA) film, a biodegradable alternative to petroleum-based plastics, has gained significant attention for sustainable packaging applications. However, its limited film-forming ability requires the use of plasticizers to improve processability. In this study, natto powder was incorporated into PLA at concentrations of 1wt%, 5wt%, and 10wt% to enhance its properties and investigate the resulting PLA/natto composites as a natural bio-based additive. The composites were prepared using a twin-screw extrusion process before being shaped into films. PLA/Natto composite films were fabricated by cast film extrusion with Natto contents of 1, 5, and 10 wt%. The films showed uniform thickness (0.2–0.4 mm) and stable formation, with color changing from transparent (neat PLA) to increasingly brown with higher Natto loading. Thermogravimetric analysis indicated that Natto enhanced the thermal stability of PLA, increasing degradation temperatures from 348 °C (PLA) to 380–392 °C (PLA/Natto), likely due to interactions between PLA chains and Natto particles. Mechanical testing demonstrated significant reinforcement: tensile strength increased from 12.2 MPa (PLA) to 28.6–37.1 MPa, and Young's modulus increased at 1 wt% Natto (1535 MPa) but slightly decreased at higher loadings, suggesting that excessive Natto caused particle agglomeration. Soil burial tests revealed accelerated biodegradation for PLA/Natto films, with weight loss increasing from 5.42% (1 wt%) to 10.24% (10 wt%), attributed to the hydrophilic and organic components of Natto promoting moisture absorption and microbial activity.These results indicate that Natto incorporation simultaneously improves thermal stability, mechanical performance, and biodegradability, with 5 wt% Natto providing optimal reinforcement without compromising film integrity, highlighting the potential of PLA/Natto composites for sustainable packaging applications.

***6581014520@student.chula.ac.th**

## INTRODUCTION

Polylactic acid (PLA) is a compostable, bio-based polymer that has gained widespread attention for sustainable packaging applications due to its biodegradability and derivation from renewable resources (Stefano Fiori, 2014). However, the inherently low surface energy of PLA films limits their processability (Dhathathreyan & R. Maheshwari ,2002) particularly in film formation and surface-related applications. To overcome these limitations, the incorporation of bio-based additives, or bio plasticizers, has been explored to enhance PLA's surface properties and overall performance.

PPC & PETROMAT SYMPOSIUM 2025

In this study, natto powder was introduced as a natural bio-based additive to develop PLA/Natto composites. Natto, containing beneficial microorganisms, offers two main advantages: it can improve the thermal stability of PLA and facilitate the biodegradation of the resulting films after their end-of-life. The research focuses on investigating the influence of natto powder on the thermal, structural, and surface properties of PLA films, aiming to provide a sustainable strategy for enhancing PLA's functionality in film applications.

## EXPERIMENTAL

### *A. Materials*

Natto powder was sourced from Gene Ferm Biotechnology Co.,Ltd. Polylactic acid Polylactic acid (PLA) pellets (grade 2003D) were obtained from Nature Works LLC (United States of America). The material has a melt flow index (MFI) of 6 g/10 min measured at 210°C, with a density of 1.24 g/cm³, both determined according to the ASTM D1238 standard. Methanol was obtained from RCI Lab Scan Co. (Thailand) and used as received without further purification.

### *B. Preparation of PLA/Natto composites*

PLA and Natto powder were blended at a weight ratio of 70:30 and vacuum-dried at 60°C for 24 hours to remove moisture. The dried mixture was then melt-compounded using a twin-screw extruder (Prism TSE 16TC, Thermo Electron Corporation, Germany) equipped with a 16 mm diameter screw and an L/D ratio of 25. The extrusion temperature profile was set as follows: feeding zone at 170°C. The screw speed was controlled at 50 rpm throughout the process. After extrusion, the strands were chopped into pellets, forming masterbatch chips ready for subsequent film casting.

### *C. Preparation of PLA/PLA/Natto Film Casting*

Natto powder was physically blended with polylactic acid (PLA) to prepare feeding pellets containing 1, 5, and 10 wt% of Natto. Prior to processing, the mixed pellets were vacuum-dried at 50 °C for 24 hours to eliminate moisture. The composite films were fabricated using a cast film and sheet extruder. During extrusion, the feeding zone temperature was maintained at 170 °C, while the die zone was set at 220 °C. The casting screw speed was controlled between 15 and 20 rpm to ensure uniform mixing and stable film formation. The resulting films had a thickness of 0.2–0.4 mm and a width of approximately 180 mm. The extruded films were collected and stored under controlled conditions for subsequent characterization.

## RESULTS AND DISCUSSION

### *A. Results of PLA/Natto Film Casting Process*

Natto powder was successfully blended with PLA at 1, 5, and 10 wt% and processed into composite films using a cast film extrusion system. The films exhibited uniform thickness in the range of 0.2–0.4 mm and a width of approximately 180 mm, indicating stable extrusion at controlled temperatures (170 °C feeding zone and 220 °C die zone). The addition of Natto affected the film appearance: neat PLA showed a transparent color, while films containing 1

PPC & PETROMAT SYMPOSIUM 2025

wt% appeared slightly yellowish, 5 wt% showed a brown shade, and 10 wt% exhibited a darker brown color due to increased filler content and reduced transparency.

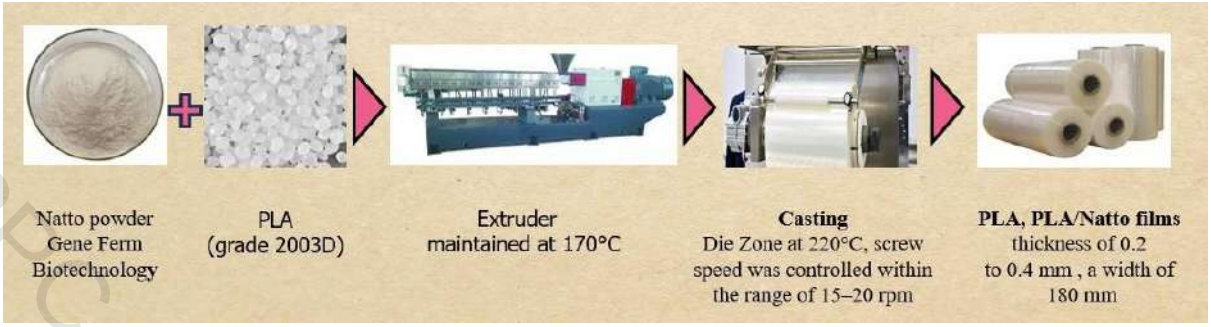


Figure 1. PLA and PLA/Natto Films Casting

*B.Thermal and decomposition characteristics PLA/Natto composite*

Thermogravimetric analysis (TGA) was performed to investigate the thermal stability and decomposition behaviour of neat PLA and PLA/Natto composite films using a TGA-5500 (USA). The TGA curves and characteristic thermal degradation parameters are presented in Table 1 and Figure 2. Neat PLA exhibited a single major decomposition stage, corresponding to polymer chain scission at elevated temperatures. In contrast, the PLA/Natto films showed a slight reduction in onset degradation temperature with increasing Natto content, indicating that the bio-based filler promoted earlier thermal decomposition.

Table 1: Thermal characteristics of the samples evaluated as determined by TGA

| Sample | $T_d$ (°C) |
|---|---|
| (a)PLA | 348 |
| (b)PLA /1wt%Natto | 380 |
| (c)PLA/5wt%Natto | 382 |
| (d)PLA/10wt%Natto | 392 |

The results show that pure PLA and PLA/Natto composites at 1 wt%, 5 wt%, and 10 wt% all exhibit a single-step thermal degradation pattern. Among the samples, PLA/Natto with 10 wt% demonstrated the highest thermal degradation temperature (Td) at 392°C, followed by PLA/Natto 5 wt% at 382°C, PLA/Natto 1 wt% at 380°C, and pure PLA at 348°C. These findings indicate that the incorporation of Natto enhanced the thermal stability of PLA, likely due to improved interactions between PLA chains and Natto particles, which help delay the onset of thermal decomposition.

PPC & PETROMAT SYMPOSIUM 2025

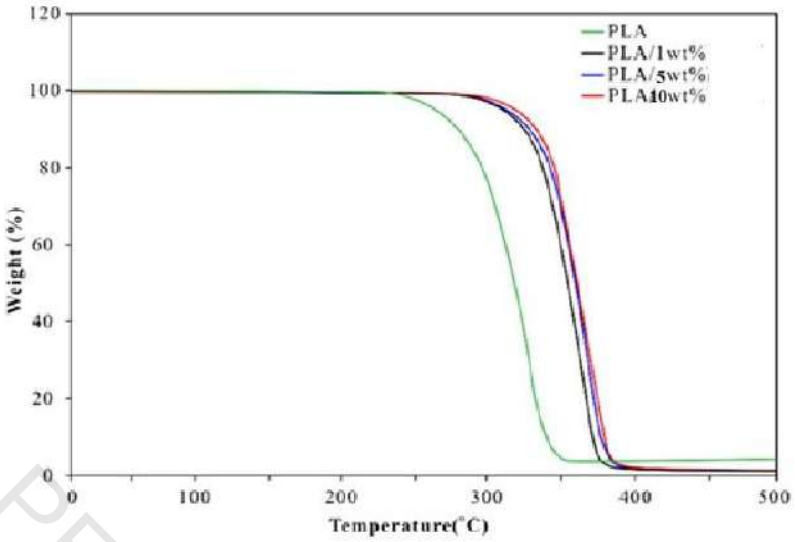


Figure 2. TGA analysis curves of PLA and PLA/Natto films

*B. Mechanical properties*

The incorporation of PLA/Natto composites enhanced the tensile strength of PLA. Each sample was tested in ten replicates, and the mean values were calculated. Pure PLA exhibited a tensile strength of 12.2 MPa. The addition of 1 wt% Natto increased the tensile strength to 28.6 MPa, while 5 wt% and 10 wt% Natto further raised the values to 32.0 MPa and 37.1 MPa, respectively. These results indicate a significant increase in tensile strength with increasing Natto content. Although all composite samples showed higher tensile strength than pure PLA, the improvement can be attributed to the reinforcing effect of the Natto particles within the PLA matrix. The mechanical properties of PLA and PLA/Natto composites are presented in Figure 3. The addition of Natto composite also influenced the Young's modulus of PLA, as presented in Figure 4. Pure PLA exhibited a Young's modulus of 1085 MPa. The incorporation of 1 wt% Natto significantly increased the stiffness of the material, resulting in a Young's modulus of 1535 MPa. When the Natto content increased to 5 wt% and 10 wt%, the Young's modulus slightly decreased to 1282 MPa and 1250 MPa, respectively, although both values remained higher than that of pure PLA. This behavior suggests that excessive Natto loading (10 wt%) may lead to particle agglomeration, which disrupts effective stress transfer within the PLA matrix and consequently reduces stiffness. Therefore, a Natto loading of 5 wt% is recommended to achieve the optimal improvement in mechanical reinforcement.

PPC & PETROMAT SYMPOSIUM 2025

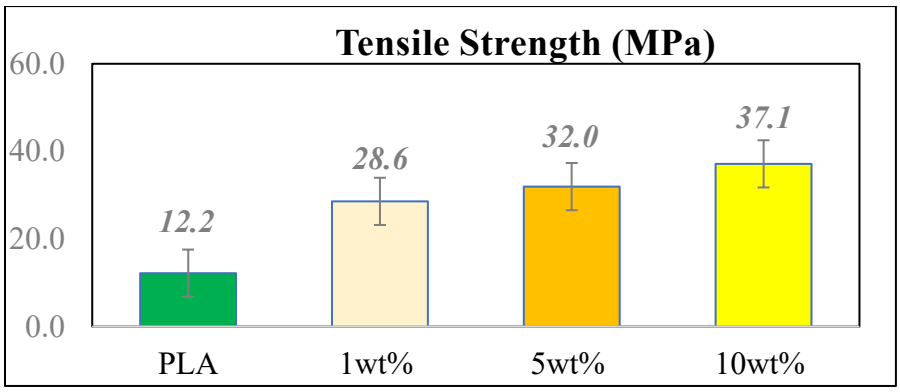


Figure 3. Tensile Strength PLA comparative to 1%,5% and 10% Natto composite

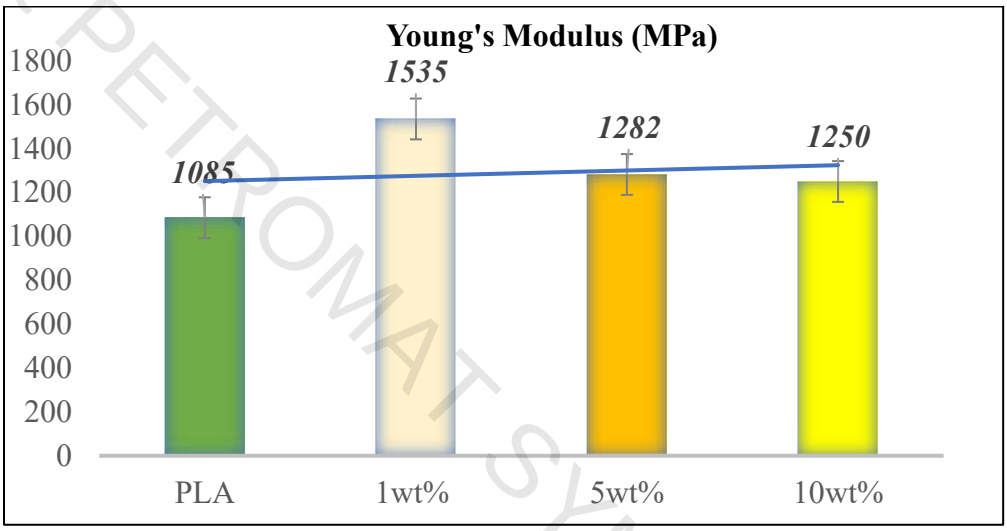


Figure 4. Young's Modulus PLA comparative to 1%,5% and 10% Natto composite

*C. Soil Burial Test and Percent Weight Loss of PLA and PLA/Natto Composite Films*

The biodegradation behavior of neat PLA and PLA/Natto composite films was evaluated according to ASTM D5988 for aerobic biodegradation in soil environments. Film specimens with dimensions of 20 mm × 20 mm and a thickness of approximately 0.20–0.25 mm were buried at a depth of 10 cm in controlled soil conditions, and the percent weight loss of each film was measured at defined time intervals.

Table 2: Soil Burial Test and Percent Weight Loss of PLA and PLA/Natto Composite Films

| Day/(%wt loss) | PLA | 1% | 5% | 10% |
|---|---|---|---|---|
| Day 0 | 0 | 0.15 | 0.38 | 0.42 |
| Day 30 | 0.18 | 0.28 | 0.42 | 0.54 |
| Day 60 | 0.24 | 3.29 | 4.05 | 6.22 |
| Day 120 | 0.30 | 5.42 | 8.76 | 10.24 |

PPC & PETROMAT SYMPOSIUM 2025

Neat PLA showed negligible degradation throughout the testing period, with only a 0.30% weight loss after 120 days. In contrast, PLA/Natto composite films exhibited significantly higher degradation rates, which increased with Natto content. After 120 days, the weight loss reached 5.42%, 8.76%, and 10.24% for films containing 1%, 5%, and 10 wt% Natto, respectively. The enhanced biodegradation is attributed to the hydrophilic nature and organic components of Natto powder, which promote moisture absorption and microbial colonization, thereby accelerating polymer chain breakdown. Visual inspection further confirmed more pronounced surface erosion and structural fragmentation in films with higher Natto content.

## CONCLUSIONS

PLA/Natto composite films were successfully fabricated via cast film extrusion with Natto contents of 1, 5, and 10 wt%. Incorporation of Natto improved the thermal stability of PLA, increased tensile strength and Young's modulus (with optimal reinforcement at 5 wt%), and accelerated biodegradation under soil burial conditions. Higher Natto loadings enhanced weight loss but slightly reduced stiffness, likely due to particle agglomeration. Overall, Natto acts as an effective biodegradable filler that simultaneously reinforces PLA mechanically, enhances thermal performance, and promotes environmentally friendly degradation, making PLA/Natto films promising for sustainable packaging

## REFERENCES

Aurich, T.; Mennig, G. (2001). *Polym. Compos., 22, 680.*
Dhathathreyan, A., & Maheshwari, R. (2002*). Surface energy, wettability, and water vapor permeability of Langmuir–Blodgett films of protein–polymer composites. Langmuir, 18, 5374–5380.*
Gassan, J.; Bledzki, A. K. (1997). *Compos. A, 28A, 1001.*
Hornsby, P. R.; Hinrichsen, E.; Tarverdi, K. (1997). *J. Mater. Sci., 32, 1009.*
Leaversuch, R. (2002). *Materials: Renewable PLA polymer gets green light for packaging uses. Plastic Technology.*
Maiza, et al. (2016). *Natural plasticizers improve thermal and mechanical properties of PLA.*
Marano, S.; Laudadio, E.; Minnelli, C.; Stipa, P. (2022). *Tailoring the barrier properties of PLA: A state-of-the-art review for food packaging applications. Polymers, 14(8), 1626.*
Mishra, S.; Tripathy, S. S.; Mishra, M.; Mohanty, A. K.; Nayak, S. K. (2002). *Reinforced Plastics and Composites, 21, 5570.*
Paul, M. A.; Alexandre, M.; Degee, P.; Henrist, C.; Rulmont, A.; Dubois, P. (2003). *Polymer, 44, 443.*
Stefano, F. (2014). *Industrial uses of PLA. Poly(lactic acid) Science and Technology: Processing, Properties, Additives and Applications, EPUB ISBN: 978-1-78262-34.*
Verma, S. K.; Prasad, A.; Katiyar, V. (2024). *State of art review on sustainable biodegradable polymers with a market overview for sustainability packaging. Materials Today Sustainability, 26, June 2024.*

PPC & PETROMAT SYMPOSIUM 2025

# SYNTHESIS OF ORGANIC ACIDS VIA OZONOLYSIS AND OXIDATION OF OLEFINS IN WATER ASSISTED BY LOW-FOAMING MICELLE

*Sutthida Iamsaard*[a,b], *Panuwat Padungros**[,b]

[a] Program in Petrochemistry and Polymer Science, Faculty of Science, Chulalongkorn University, Bangkok, Thailand, 10330
[b] Green Chemistry for Fine Chemical Production and Environmental Remediation Research Unit, Department of Chemistry, Faculty of Science, Chulalongkorn University, Bangkok, Thailand, 10330

Keywords: organic acids, olefins, low-foaming micelle, renewable resources

## ABSTRACT

Renewable resources are increasingly recognized as critical alternatives to produce monomers, which serve as key precursors in polymer synthesis. An example is azelaic acid, which can be synthesized from oleic acid derived from vegetable oils and serves as a bio-based monomer for polyester production. Conventional monomer synthesis from petroleum feedstock often involves heavy metal catalysts and harsh conditions, raising environmental concerns. Ozonolysis, wherein ozone ($O_3$) generated from oxygen ($O_2$) is bubbled through olefin substrates, enables efficient cleavage of carbon–carbon double bonds at low temperatures. However, the poor aqueous solubility of olefins necessitates the use of organic solvents. The organic solvents are flammable, toxic, and require substantial energy to cool the reaction mixture while carrying out the reaction. This study reports an alternative method for the synthesis of organic acids *via* ozonolysis and oxidation in aqueous media, assisted by a low-foaming micellar system (Coolade) instead of using organic solvents. The results show that organic acids (10 samples) were successfully synthesized with yields ranging from 45 to 91%. Product structures were confirmed by nuclear magnetic resonance spectroscopy (NMR). In conclusion, the research presents an effective, environmentally friendly approach for organic acid production using water-based ozonolysis assisted by a micellar medium.
***panuwat.p@chula.ac.th**

## INTRODUCTION

Dicarboxylic acids are of great significance to the polymer production industry. Typically, they are derived from petrochemical sources. For example, succinic acid is synthesized through the hydrogenation of maleic anhydride, which is obtained from benzene or butane.[1] Adipic acid is synthesized *via* the oxidation of cyclohexane or phenol and is widely used in the production of nylon-6 or nylon-6,6 fibers for the textile industry[2]. In addition, terephthalic acid, which is derived from *p*-xylene, an aromatic compound obtained from petroleum, is produced *via* the oxidation of *p*-xylene with oxygen in the presence of a catalyst. Terephthalic acid and ethylene glycol are monomers used in the synthesis of polyethylene terephthalate (PET)[3], a highly durable plastic used in packaging such as water bottles, food containers, and various other products.

However, improper disposal methods, such as incineration of these polymers contribute significantly to carbon dioxide emissions into the atmosphere, thereby worsening global warming. This has led to increasing efforts to use renewable resources from plants and

PPC & PETROMAT SYMPOSIUM 2025

animals as alternatives. One such example is the production of azelaic acid, a dicarboxylic acid possessing carboxylic groups at both ends. It serves as a monomer in the production of polyesters and polyamides. Azelaic acid can be synthesized from unsaturated fatty acids, such as oleic and linoleic acids, through oxidative cleavage of the double bonds. Several previous reports for the synthesis of azelaic acid require heavy metal catalysts and involve high temperature and pressure conditions,[4,5] making them environmentally unfriendly.

Nevertheless, ozonolysis, using ozone gas ($O_3$), offers an efficient way to cleave double bonds in oleic acid or olefin compounds at low temperatures. Ozone can be generated from oxygen gas, resulting in low production costs. Generally, ozonolysis relies on flammable and low-boiling point organic solvents to perform the reaction, requiring energy to cool the system in order to maintain constant reaction concentration while ozone gas is purged during the course of the reaction.[6] As a result, the use of water, being non-flammable and having a high boiling point, presents an attractive alternative as a reaction medium. However, oleic acid and most olefins have low water solubility, posing a challenge. To address this, chemical reactions carried out in aqueous systems have been continuously developed. One method involves using water in combination with micelles to prevent phase separation between water and hydrophobic substrates. Typically, micelles possess a hydrophobic head and a lipophilic hydrocarbon tail, which causes foaming when a stream of gas is purged into the micelle. The foam formation becomes a limitation during ozonolysis since ozone gas must be continuously bubbled into the solution, causing excessive foaming that overflows the reaction flask.[7] The research group of Lipshutz reported the development of a low-foaming micellar system named Coolade, (bis[4 - ( {2 - ( methoxycarbonyl)phenyl}amino)-4 - oxobutanoic acid] polyethylene glycol 1000), which is water-soluble and suitable for chemical reactions [8] (Figure 1). Therefore, the application of Coolade micelle in aqueous ozonolysis reactions is of great interest for ozonolysis in water.

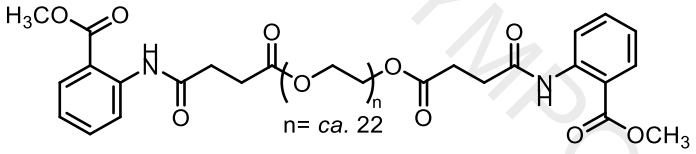


**Figure 1.** Structure of Coolade

In 2022, Padungros and co-workers reported the use of micelles in aqueous ozonolysis and reduction of olefinic compounds. Their study began by investigating various types of micelles, including anionic, cationic, and nonionic micelles. Although these micelles helped improve the dispersion of olefins in water, they also caused excessive foaming when ozone was bubbled continuously, resulting in a significant loss of the desired products. Foam reduction was successfully achieved using low-foaming Coolade micelle, which yielded carbonyl compounds in high amounts comparable to those obtained from reactions using organic solvents.[7]

Herein, this research aims to apply low-foaming Coolade micelles in the ozonolysis and oxidation of olefinic compounds in water to produce carboxylic acids. It is expected that this method will enable the efficient synthesis of carboxylic acids from olefins and contribute to

PPC & PETROMAT SYMPOSIUM 2025

the development of a broadly applicable synthetic method using substrates derived from renewable resources, as illustrated in Scheme 1.

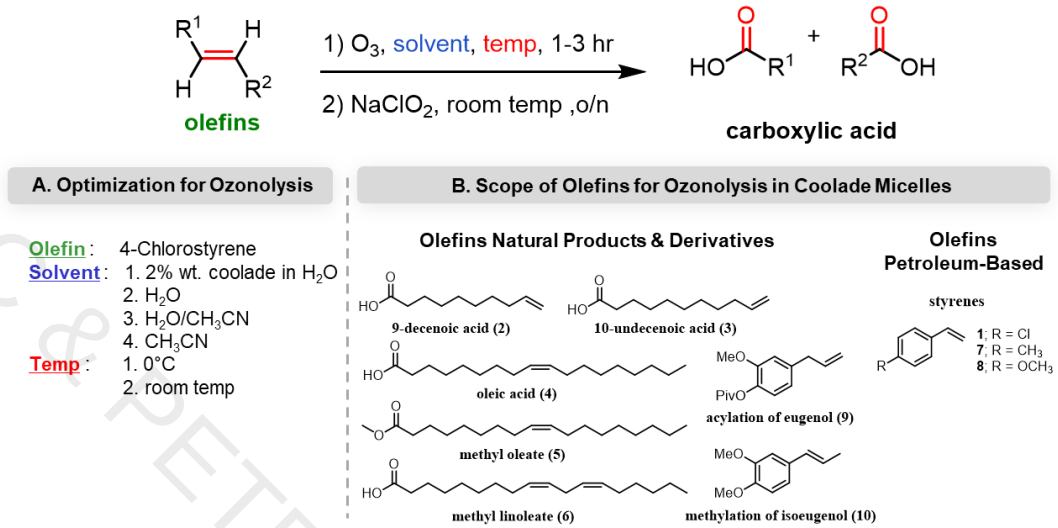


**Scheme 1.** A) Optimization for ozonolysis and B) Scope of olefins

## EXPERIMENTAL

*A. Materials*

All chemicals were purchased from Merck, Sigma-Aldrich, and Tokyo Chemical Industry (TCI). Solvents (A.R. grade) were purchased from RCI Labscan and used without purification, except for commercial grade hexanes and ethyl acetate, which were distilled prior to use. The progress of the reaction was monitored by performing TLC on silica gel 60 F254 0.2 mm precoated aluminum plates (Merck) and visualized on UV 254 nm or stained with iodine and 2,4-DNP. $^{1}H$ and $^{13}C$ NMR spectra were recorded on a JEOL NMR spectrometer (500 MHz and 126 MHz) using DMSO-$d_6$ (Merck) or $CDCl_3$ (Cambridge Isotope) as solvents. The chemical shift was reported in ppm (δ) unit.

*B.* Coolade solution

The Coolade solution (2 wt%) was prepared by dissolving 0.5 g of Coolade in 24.5 g of deionized water with stirring and gentle heating at 50–60 °C in a round-bottom flask. The solution was purged with argon for 3 hours and subsequently stored at 4 °C until use.

*C. Ozonolysis experiments (Tables 1 and 2)*

The olefins (0.2–1.0 mmol) were suspended in organic solvent or 2 wt% Coolade solution in a 10 mL round-bottom flask at the final concentration of olefin in a reaction mixture of 0.3 M. The biphasic mixture in Coolade was vigorously stirred for 30 min until a stable suspension or a turbid solution formed. In all reactions, ozone gas ($O_3/O_2$) generated from oxygen gas was used, with a flow rate of 500 mL/min using a household ozone disinfector as an ozone generator. The progress of the reaction was monitored using TLC, and upon complete consumption of the starting material, sodium chlorite ($NaClO_2$) was added as an oxidizing agent to convert the intermediate aldehyde/ozonide to the desired carboxylic acids at room temperature (27–30 °C), and left the mixture overnight (12–16 h.). Residual oxidants

PPC & PETROMAT SYMPOSIUM 2025

and any formed peroxides were subsequently quenched using sodium bisulfite ($NaHSO_3$). The reaction products were then extracted with an organic solvent for purification and structural confirmation of the carboxylic acid compounds by nuclear magnetic resonance spectroscopy (NMR).

## RESULTS AND DISCUSSION

*A. Optimization for ozonolysis*

The optimal conditions for the ozonolysis were studied using 4-chlorostyrene (**1**) as the model olefin due to its ease of monitoring by TLC. The parameters, including reaction medium and temperature, were investigated (Table 1). Ozonolysis at 0 °C using water as the reaction medium in combination with Coolade micelles provided acid 1**a** in 79% yield (Table 1, entry 1). Next, ozonolysis at room temperature and Coolade micelles gave acid **1a** in comparable yields (73%, entry 2). Using water alone, without Coolade micelles, as reaction medium gave acid **1a** in 62% yield (entry 3), which was a significantly lower yield. Employing a mixture of $CH_3CN$ and water (10:1) (entry 4) or $CH_3CN$ alone (entry 5) led to higher yields (77% and 84%, respectively); however, the requirement for cooling to prevent $CH_3CN$ evaporation limits their practicality. Thus, the Coolade micelle in water (entry 2) presents a more environmentally and operationally favourable option, as ozonolysis was carried out at room temperature, thereby eliminating the need for energy-intensive cooling. Thus, it was selected as the optimal conditions for ozonolysis with other olefinic substrates.

**Table 1.** Ozonolysis of 4-chlorostyrene (**1**) in different solvents and temperatures

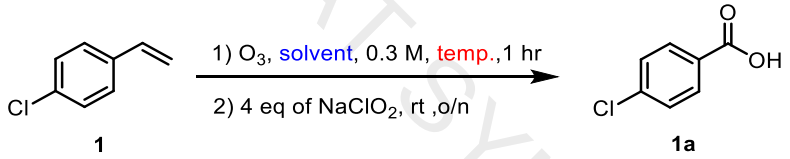


**1** **1a**

| entry | solvent or medium | temp (°C) | acid **1a** (yield) |
|---|---|---|---|
| 1 | 2 wt% Coolade in $H_2O$ | 0 | 79% |
| **2** | **2 wt% Coolade in $H_2O$** | **room temp** | **73%** |
| 3 | $H_2O$ | 0 | 62% |
| 4 | (10:1) $CH_3CN$: $H_2O$ | 0 | 77% |
| 5 | $CH_3CN$ | 0 | 84% |

*B. Scope of olefins for ozonolysis in Coolade micelle*

After establishing the optimal conditions, the method was applied to a variety of olefinic substrates (Table 2). The experiments were carried out according to the procedure described in the experimental section. As shown in Table 2, ozonolysis proceeded successfully for all olefins, including those aliphatic and aromatic alkenes which were derived from petrochemical (olefins **7** and **8**) and renewable resources (olefins **2**–**6** and **9**–**10**). Each olefin exhibited different reactivities, resulting in varying yields of carboxylic acid products (**2a**–**10a** and **4b**–**5b**), ranging from 45–91%, depending on the structural and intrinsic reactivity of the substrate.

PPC & PETROMAT SYMPOSIUM 2025

**Table 2.** Coolade-assisted ozonolysis of olefins in water

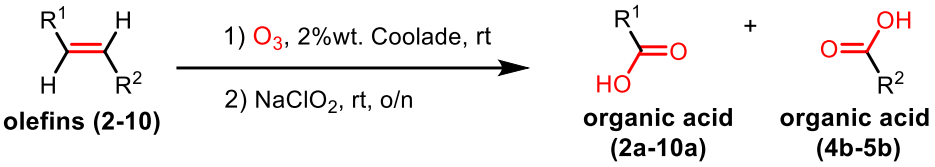


| entry | olefin | organic acid (yield) |
|---|---|---|
| 1 | 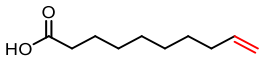 **2** | 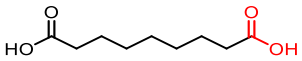 **2a** (85%) |
| 2 | 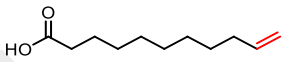 **3** | 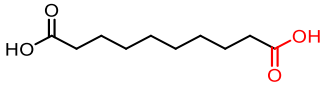 **3a** (87%) |
| 3 | 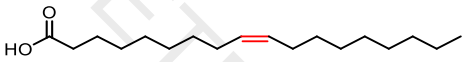 **4** | 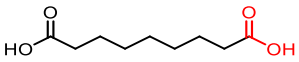 **4a** (74%) 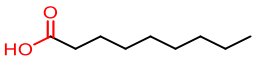 **4b** (91%) |
| 4 | 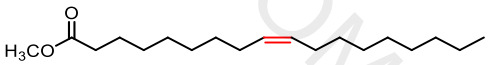 **5** | 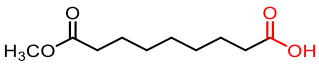 **5a** (91%) 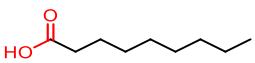 **5b** (89%) |
| 5 | 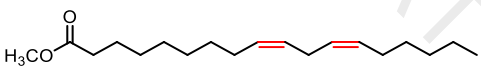 **6** | 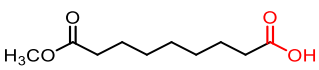 **6a** (90%) |
| 6 | 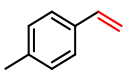 **7** | 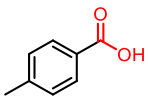 **7a** (67%) |
| 7 | 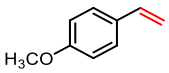 **8** | 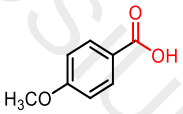 **8a** (68%) |
| 8 | 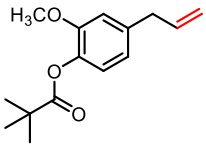 **9** | 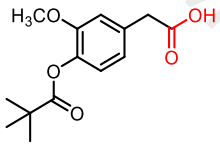 **9a** (45%) |
| 9 | 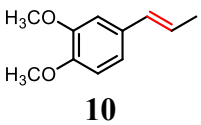 **10** | 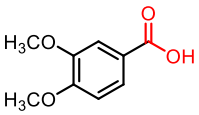 **10a** (68%) |

PPC & PETROMAT SYMPOSIUM 2025

## CONCLUSIONS

This study demonstrates the synthesis of organic acids *via* ozonolysis and subsequent oxidation of olefins derived from renewable bio-based sources. The ozonolysis reaction was performed under mild conditions, offering a distinct advantage over other conventional methods for double bond cleavage. Ozone exhibits high efficiency and stability in cleaving carbon–carbon double bonds in olefins. Moreover, the use of water as a reaction medium in combination with a low-foaming Coolade micellar system was successfully developed. Water is non-flammable and has a high boiling point; thus, it does not require energy-intensive cooling, allowing ozonolysis to proceed efficiently at room temperature. This approach avoids the use of hazardous and flammable organic solvents derived from petrochemical sources, aligning with the principles of green chemistry.

## ACKNOWLEDGEMENTS

This research is supported by the Thailand Science Research and Innovation Fund Chulalongkorn University (for PP). SI would like to thank the scholarship from the Petrochemistry and Polymer Science Program, Faculty of Science, Chulalongkorn University, for the M.Sc. scholarship.

## REFERENCES

1. Lee, J.; Han, M.; Choi, S.; Yi, J.; Lee, T.; Lee, S. Organic acids: succinic and malic acids. In Industrial Biotechnology and Commodity Products. *Elsevier* **2011**, *3*, 149–161.
2. Rahman, A.; Mupa, M.; Mahamadi, C. A mini review on new emerging trends for the synthesis of adipic acid from metal-nano heterogeneous catalysts. *Catalysis Letters* **2016**, *146*, 788–799.
3. Hayashi, A. Industrial development of terephthalic acid production in Japan. *In World Petroleum Congress* **1963**, *6*, 249–258.
4. Godard, A.; De Caro, P.; Thiebaud-Roux, S.; Vedrenne, E.; Mouloungui, Z. New environmentally friendly oxidative scission of oleic acid into azelaic acid and pelargonic acid. *Journal of the American Oil Chemists' Society* **2013**, *90*, 133–140.
5. Li, X.; Syong, J. C. P.; Zhang, Y. Sodium stannate promoted double bond cleavage of oleic acid by hydrogen peroxide over a heterogeneous $WO_3$ catalyst. *Green Chemistry* **2018**, *20*, 3619–3624.
6. Ackman, R. G.; Retson, M.; Gallay, L.; Vandenheuvel, F. Ozonolysis of unsaturated fatty acids: I. Ozonolysis of oleic acid. *Canadian Journal of Chemistry* **1961**, *39*, 1956–1963.
7. Buntasana, S.; Hayashi, J.; Saetung, P.; Klumphu, P.; Vilaivan, T.; Padungros, P. Surfactant-assisted ozonolysis of alkenes in water: mitigation of frothing using coolade as a low-foaming surfactant. *The Journal of Organic Chemistry* **2022**, *87*, 6525–6540.
8. Lee, N. R.; Cortes-Clerget, M.; Wood, A. B.; Lippincott, D. J.; Pang, H.; Moghadam, F. A.; Gallou, F.; Lipshutz, B. H. Coolade. a low-foaming surfactant for organic synthesis in water. *ChemSusChem* **2019**, *12*, 3159–3165.

PPC & PETROMAT SYMPOSIUM 2025

# TISSUE-ADHESIVE INJECTABLE HYDROGEL *VIA* THIOL-MICHAEL ADDITION FOR WOUND CLOSURE APPLICATIONS

*Nadine Fesya Shafira* [a] *and Nuttapol Risangud** [a,b]

[a)] The Petroleum and Petrochemical College, Chulalongkorn University, Bangkok, Thailand
[b)] Center of Excellence on Petrochemical and Materials Technology, Bangkok, Thailand

Keywords: Polydopamine, Click chemistry, Injectable hydrogel, Wound closure

## ABSTRACT

Injectable hydrogels with tissue-adhesive properties have attracted significant interest as advanced wound closure materials. They can seal wounds rapidly, conform to irregular geometries and promote tissue regeneration. In this study, we developed a tissue-adhesive injectable hydrogel based on dextran-vinyl sulfone (Dex-VS) and thiol-terminated polyethylene glycol (PEG-SH). Crosslinked *via* thiol-Michael addition reaction in the presence of polydopamine nanoparticles (PDA NPs). The degree of vinyl-sulfone substitution (%DS) was calculated by $^{1}$H NMR spectroscopy, yielding a %DS 15. The hydrogel exhibited a relatively reasonable gelation time, approximately 30 seconds to 5 minutes, depending on the solution used. Indeed, hydrogel incorporating catechol functional groups using PDA NPs exhibited enhanced adhesion to porcine skin, increasing adhesive strength from 0.96 ± 0.05 kPa to 1.22 ± 0.05 kPa. The cytotoxicity tests on the hydrogel revealed that the hydrogels were non-cytotoxic to fibroblasts (NIH3T3). These results demonstrate the feasibility of using this approach to fabricate injectable hydrogel hydrogels with promising adhesive and injectable properties, indicating their potential for further development as wound closure materials.
***nuttapol.r@chula.ac.th**

## INTRODUCTION

Traditional wound closure methods such as sutures, staples, and clips are still widely used in medical practice. While these methods effectively keep wound edges closed, their application often causes postoperative pain, slows the healing process, and requires additional procedures for removal. Furthermore, these conventional methods are less suitable for treating deep, moist wounds with irregular shapes. As an alternative to these limitations, injectable hydrogels have garnered increasing attention as a more innovative and functional approach to wound closure. Hydrogels are hydrophilic polymer networks capable of absorbing fluids and mimicking the mechanical properties of biological tissues. Due to these characteristics, hydrogels can serve as tissue adhesives and regenerative scaffolds with biodegradable properties. This study was inspired by the easy-to-use

PPC & PETROMAT SYMPOSIUM 2025

injectable hydrogels, the high effectiveness of the thiol-Michael addition reaction, and the mussel-inspired tissue adhesive that used PDA NPs. Through this approach, the developed hydrogel is designed to produce a hydrogel with favourable physicochemical properties, including gelation time, mechanical characteristics, adhesive properties and biocompatibility, positioning it as a compelling candidate for wound closure applications (Liang et al., 2024).

## EXPERIMENTAL

### *A. Materials*

Dextran (*M*w ~150 kDa), divinyl Sulfone (96% purity), dopamine Hydrochloride (99%), thiolated-Polyethylene Glycol (*M*w~1,500, ≥95%) were purchased from Sigma-Aldrich. Hydrochloric (HCl) was obtained from RCI Labscan, Dulbecco's Phosphate buffer saline (DPBS) was purchased from Thermo Fisher Scientific.

### *B. Synthesis dextran-divinyl sulfone (Dex-VS)*

Dextran (1 g) was dissolved in 50 mL of NaOH (0.1 M); subsequently, (1 mL, 9.69 mmol) of divinyl sulfone was rapidly injected into the solution and allowed to react for 1 minute. Then, 1 mL of HCl (5 M) solution was quickly added to the reaction mixture to terminate the reaction. The resulting mixture was transferred into a dialysis membrane and dialysed (MWCO = 3.5 kDa) against deionised (DI) water for 5 days to remove unreacted reagents. The purified solution was lyophilised to obtain the final product.

### *C. Polydopamine Polymerization*

Dopamine hydrochloride (0.4 gram, 2.11 mmol) was dissolved in 100 mL of NaOH (0.01 M) and stirred for 24 hours. Then, the mixture was centrifuged at 5,000 rpm for 20 mins, and the black precipitation was collected and washed three times with deionised water. Polydopamine was dried under a vacuum oven at 40°C for 12 hours and stored at 4°C prior to use.

### *D. Hydrogel Fabrications*

Three precursor solutions were prepared: (i) dextran-vinyl sulfone (Dex-VS) at 10 % w/v in DPBS, (ii) PEG-SH at 2.5 % w/v in DPBS, and (iii) polydopamine (PDA) at 2 % w/v, dispersed in deionised water and sonicated for 15 minutes at 45°C. The PDA solution was filtered using a 0.45 µm nylon membrane filter. These three solutions were then mixed to a final total volume of 100 µL. Initially, the Dex-VS solution was mixed with the PDA suspension, and the PEG-SH solution was added. The combined solution was incubated at 37°C, and gelation time was recorded. The code of resulting hydrogel is ascribed based on the polymer composition in 100 µL of hydrogel, e.g., Dex-VS4/PEG0.75/PDA0.6 contains Dex-VS (4 mg), PEG (0.75 mg), and PDA (0.6 mg). If PDA is not specified in the hydrogel formulation label, polydopamine was not included in that particular hydrogel composition.

### *E. Characterisations*

Proton Nuclear Magnetic Resonance ($^1$H-NMR, Bruker DPX-500 spectroscopy, USA) was used to analyse the degree of vinyl sulfone substitution. Fourier Transform Infrared

PPC & PETROMAT SYMPOSIUM 2025

Spectroscopy (FTIR, Thermo Scientific, Nicolet iS5, USA) was employed to identify the functional groups. A scanning electron microscope (SEM, Hitachi, S-4800, Japan) was employed to investigate the morphology of PDA NPs. The gelation time of the hydrogel was evaluated using the vial tilting method. In this procedure, the gelation time was considered complete when the solution no longer flowed upon tilting the tube. The tissue adhesive properties of the hydrogel were assessed through a lap shear test using a Universal Testing Machine (UTM, Instron, D638, USA) with porcine skin as a tissue model.

## RESULTS AND DISCUSSION

### *A. Dex-VS Characterizations*

Dextran was modified with divinyl sulfone to produce Dex-VS. The modification was carried out *via* a nucleophilic addition reaction, in which the hydroxyl groups (-OH) on the dextran backbone became reactive upon deprotonation under basic conditions, allowing them to react with the electrophilic vinyl groups (Yu & Chau, 2012). The successful functionalisation of Dex-VS was confirmed using FTIR and $^{1}$H-NMR spectroscopy, as depicted in Fig. 1. FTIR spectra (Fig. 1(a)) revealed a new peak at 1312 cm$^{-1}$, indicating the presence of sulfonyl groups (S=O) from divinyl sulfone. Meanwhile, the $^{1}$H-NMR spectra (Fig. 1(b)) displayed characteristic signals of vinyl protons in the 6.24-6.36 ppm range, supporting the successful conjugation. The degree of substitution (%DS) was determined by integrating the area under the vinyl proton peaks and comparing it with the area under the proton peaks of the dextran backbone (3.44-3.89 ppm). Based on this analysis, the DS of vinyl sulfone to dextran was calculated to be 15%, corresponding to the previous study (Sungkhaphan et al., 2022).

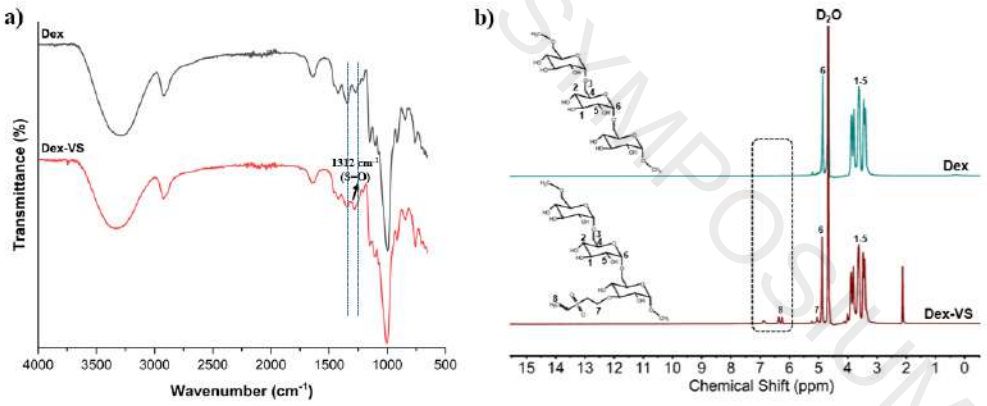


**Fig 1.** a) FTIR spectra of dextran and Dex-VS and b) $^{1}$H NMR Spectra of dextran and Dex-VS

### *B. Polydopamine Characterizations*

FT-IR spectroscopy affirmed the oxidative conversion of dopamine (DA) to polydopamine (PDA) (Fig. 2(a)). Pristine DA displayed a narrow O–H/N–H stretching band at 3329 cm$^{-1}$, primary-amine N–H bending at 1615 cm$^{-1}$, an aromatic C=C/N–H at 1497 cm$^{-1}$, and a phenolic C–O stretch at 1285 cm$^{-1}$. After polymerisation, these signals are largely extinguished, while the PDA spectrum exhibits (i) a broad, hydrogen-bonded O–

H/N–H envelope centred at about 3165 $cm^{-1}$ and (ii) new aromatic bands at 1568 $cm^{-1}$ and 1510–1470 $cm^{-1}$ that are characteristic of indole/indoline motifs. The simultaneous disappearance of monomer peaks and the emergence of indolic vibrations provide definitive evidence for the successful formation of the heterogeneous, π-conjugated PDA network. Furthermore, the morphology of polydopamine was observed *via* SEM, revealing uniform, nearly spherical PDA nanoparticles with a mean diameter of 288 nm, as represented in Fig. 2(b), corroborating the efficacy of the oxidative polymerisation (Mehwish et al., 2022).

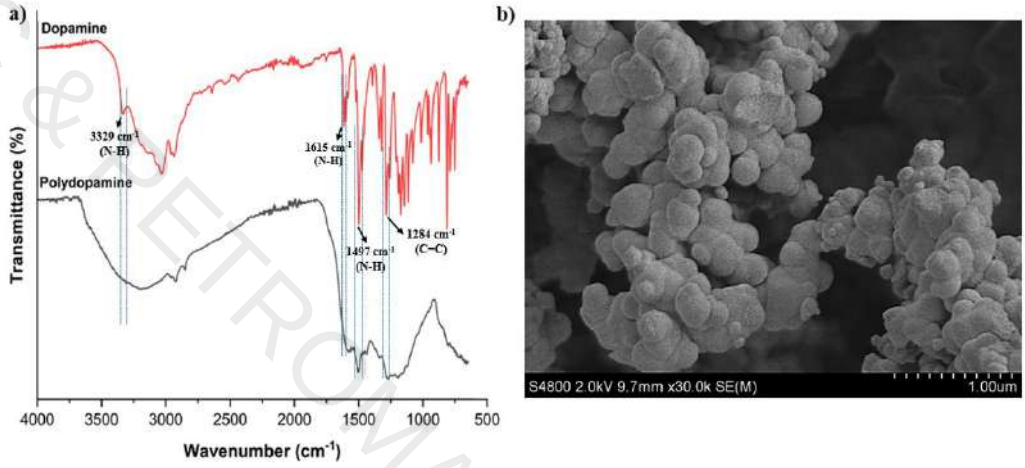


**Fig 2.** a) FTIR spectra of dopamine and PDA. b) SEM image of PDA.

*C. Hydrogel Formation*

The hydrogel solidified rapidly within approximately 30 seconds to 5 minutes, depending on the formulation, after initiating the thiol–Michael reaction and incorporating PDA. As illustrated in Fig. 3, the vinyl-sulfone precursor displays a distinct C═C stretching band at 1650 $cm^{-1}$, while PEG-SH shows a reasonably weak –SH stretching peak at about 2563 $cm^{-1}$. Polydopamine (PDA) is characterised by an indole/aromatic C═C vibration at 1568 $cm^{-1}$. Interestingly, no bands assignable to PDA appear in the hydrogel spectrum after thiol–Michael crosslinking, presumably because the PDA loading (< 1 wt %) falls below the detection threshold of ATR-FTIR. PDA incorporation verification should rely on more sensitive techniques such as UV–Vis spectroscopy, Raman microscopy, or XPS. However, in gelation ability, the disappearance of the –SH peak and the vinyl band is markedly attenuated, confirming the consumption of both functional groups; indeed, this observation still can affirm the effectiveness of thiol-Michael crosslinking to prepare the injectable hydrogel in this study.

PPC & PETROMAT SYMPOSIUM 2025

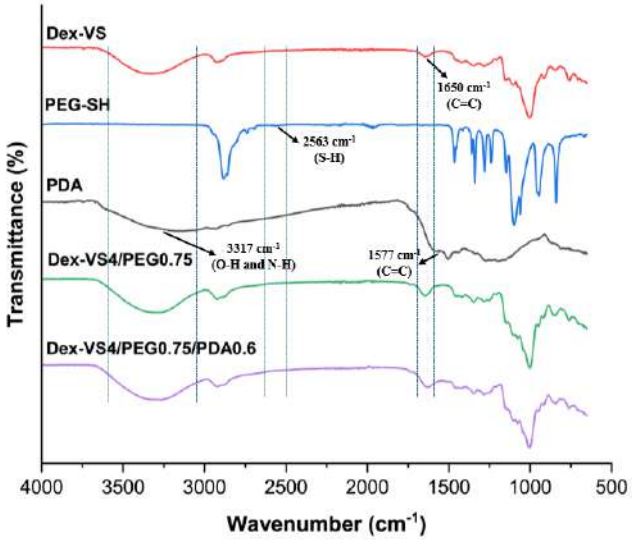


**Fig 3.** FTIR spectra of Dex-VS, PEG-SH, PDA and Dex-VS/PEG/PDA hydrogels

*D. Adhesive properties of hydrogels*

Tissue adhesion was quantified by performing lap-shear tests on fresh porcine skin substrates using a universal testing machine, as represented in Fig. 4(a). As illustrated in Fig. 4(b), native porcine skin provided a negligible adhesion baseline for comparison with the hydrogel formulations. Substituting PDA with an equivalent volume of water (Dex-VS4/PEG0.75) exhibited the lap-shear strength to 0.96 ± 0.05 kPa. Unsurprisingly, incorporating PDA further increased adhesion to 1.22 ± 0.05 kPa (Hydrogel Dex-VS4/PEG0.75/PDA0.6); this observation was attributed to the gain of catechol, phenolic, and amine groups on PDA that establish multiple hydrogen bonds and π–π interactions with the tissue surface. Also, the low-PDA formulation Dex-VS4/PEG0.75/PDA7x$10^{-5}$ exhibited a reduced lap-shear strength of 0.82 ± 0.02 kPa, indicating that the absence of PDA nanoparticle clusters compromises interfacial bonding and may even impede gel–tissue interactions (Han et al., 2018).

PPC & PETROMAT SYMPOSIUM 2025

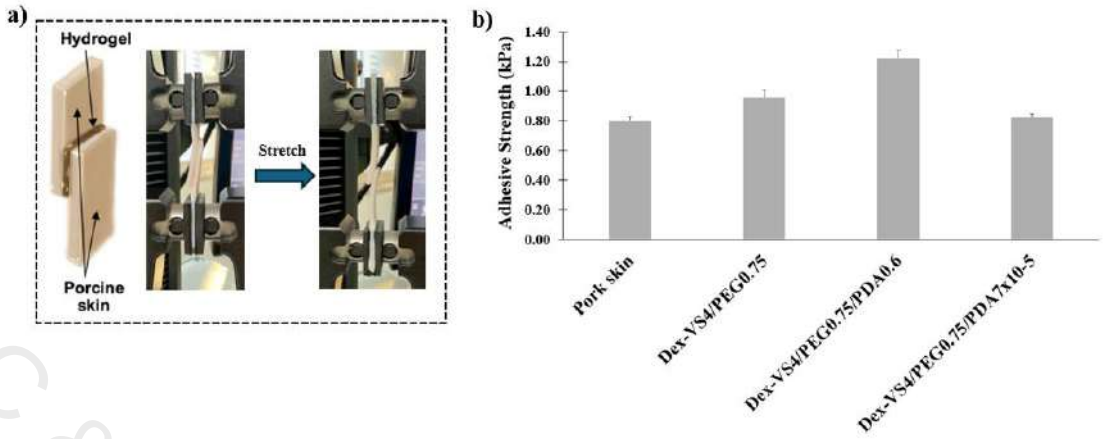


**Fig. 4** a) Schematic of the lap-shear test conducted on fresh porcine skin with a universal testing machine and b) lap-shear strength of hydrogels prepared from the different formulations

*E. Cytotoxicity of hydrogels*

Cell viability was evaluated using the MTT assay. The results showed that all hydrogels incorporated with and without PDA polydopamine exhibited cell viability of fibroblasts (NIH3T3) ranging from about 75 to 100% (Fig. 5). Indeed, all hydrogels demonstrated cell viability above 70%, indicating non-toxicity following the international standard ISO 10993:2009 (Xie et al., 2025).

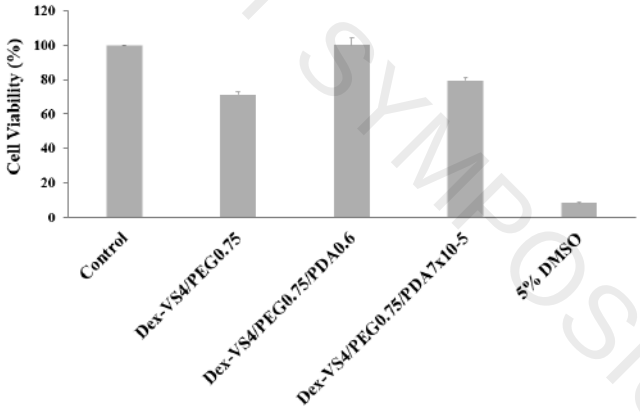


**Fig 5.** Cell viability profile of NIH3T3 cell cultured on hydrogels.

## CONCLUSIONS

Herein, tissue adhesive injectable hydrogel was successfully prepared *via* Michael addition between Dex-VS and PEG-SH, which revealed efficient gel formation under mild conditions. Indeed, incorporating PDA NPs enhanced adhesion to skin tissue without exhibiting cytotoxic effects, positioning it as a compelling candidate for wound closure applications.

PPC & PETROMAT SYMPOSIUM 2025

**ACKNOWLEDGEMENTS**

The authors express their gratitude to The Petroleum and Petrochemical College, Chulalongkorn University, for the ASEAN Scholarship. This research was also supported by the 90th Anniversary of Chulalongkorn University Scholarship, Thailand.

**REFERENCES**

Han, L., Wang, M., Li, P., Gan, D., Yan, L., Xu, J., Wang, K., Fang, L., Chan, C. W., Zhang, H., Yuan, H., & Lu, X. (2018). Mussel-Inspired Tissue-Adhesive Hydrogel Based on the Polydopamine-Chondroitin Sulfate Complex for Growth-Factor-Free Cartilage Regeneration. *ACS Appl Mater Interfaces*, *10*(33), 28015-28026. https://doi.org/10.1021/acsami.8b05314

Liang, X., Huang, C., Liu, H., Chen, H., Shou, J., Cheng, H., & Liu, G. (2024). Natural hydrogel dressings in wound care: Design, advances, and perspectives. *Chinese Chemical Letters*, *35*(10). https://doi.org/10.1016/j.cclet.2023.109442

Mehwish, N., Xu, M., Zaeem, M., & Lee, B. H. (2022). Mussel-Inspired Surface Functionalisation of Porous Albumin Cryogels Supporting Synergistic Antibacterial/Antioxidant Activity and Bone-Like Apatite Formation. *Gels*, *8*(10). https://doi.org/10.3390/gels8100679

Xie, Y., Li, G., Wu, J., Zhu, J., Cai, X., Zhao, P., Zhang, D., & Zhong, Y. (2025). Injectable self-healing alginate/PEG hydrogels crosslinked via thiol-Michael addition bonds for hemostasis and wound healing. *Carbohydr Polym*, *348*(Pt A), 122864. https://doi.org/10.1016/j.carbpol.2024.122864

PPC & PETROMAT SYMPOSIUM 2025

# SYNTHESIS OF TRIMETHYLSILYL CELLULOSE FROM BACTERIAL CELLULOSE IN IONIC LIQUID

*Nakamol Sansuktaweesub, Joshua Osorio, Panuwat Padungros**

Green Chemistry for Fine Chemical Production and Environmental Remediation Research Unit
Department of Chemistry, Faculty of Science, Chulalongkorn University, Bangkok 10330, Thailand

Keywords: trimethylsilyl cellulose, hexamethyldisilazane, ionic liquids, bacterial cellulose

## ABSTRACT

Nata de coco, a chewy and translucent dessert widely consumed in Southeast Asia, is a natural form of bacterial cellulose produced through the fermentation of coconut juice by *Acetobacter xylinum*. Its commercial production results in agricultural waste when the material is cut into uniform cubes. The Nata de coco waste may be converted into bacterial cellulose (BC) powder or fiber for various applications. However, the BC possesses a highly ordered structure stabilized by strong hydrogen bonding, resulting in high stability but poor solubility in organic solvents, which limits its direct use. To overcome this, the BC is chemically modified to disrupt the hydrogen bonding network and improve solubility and functionality. Trimethylsilyl cellulose (TMSC) is a hydrophobic derivative formed by the introduction of trimethylsilyl groups, which enhances solubility and enables further processing. In this study, microcrystalline bacterial cellulose (MCC-BC) was treated with hexamethyldisilazane (HMDS) in the ionic liquid, EMIMAc, at 70–80 °C, yielding hydrophobic TMSC with a 120.3° contact angle. In addition, Fourier transform infrared (FTIR) spectroscopy measurement confirmed the substitution of silyl groups. Using a mild silylating agent and the ionic liquid allows for a green, sustainable synthesis of trimethylsilyl cellulose from renewable bacterial cellulose.

***panuwat.p@chula.ac.th**

## INTRODUCTION

Cellulose is a polysaccharide composed of β-(1→4)-linked glucose units, characterized by a semicrystalline structure formed through extensive hydrogen bonding. Its multiple hydroxyl groups contribute to its hydrophilicity.[1] Bacterial cellulose (BC), synthesized by microorganisms such as Acetobacter, Rhizobium, and Agrobacterium, is a purer form of cellulose than plant-derived variants, which contain lignin and hemicellulose. BC has higher crystallinity and lower polymerization (2,000–6,000) compared to plant cellulose (13,000–14,000).[2] Due to its high surface area, porosity, and hydrophilicity, BC exhibits excellent water retention, mechanical strength, thermal stability, biocompatibility, and moldability, making it ideal for use in packaging, biomedicine, and pharmaceuticals.[3] A notable example is nata de coco, a chewy dessert derived from BC produced by fermenting coconut juice with *Acetobacter xylinum*.[4] Industrial production of nata de coco generates significant waste when cut into uniform cubes. The typical disposal method for this waste is incineration, which contributes to greenhouse gas emissions. Converting it into cellulose powder or fiber offers a sustainable alternative for use in food stabilizers and other cellulose-based products.[5]

PPC & PETROMAT SYMPOSIUM 2025

A key challenge in fabricating cellulose is its difficulty dissolving due to the strong hydrogen bonding contributing to its crystallinity. Effective solvents are required to penetrate through crystalline regions and disrupt the organized structure of cellulose, including hydrogen bonding networks and hydrophobic interactions. To overcome this, attempts to fabricate cellulose into a more practical form are of interest among researchers. Methods for dissolving cellulose have been developed over time by disrupting hydrogen bonds, making it soluble, and enabling it to dissolve in certain organic solvents.[6] Functionalization of cellulose by substituting the hydroxyl groups on the cellulose backbone has been widely studied, broadening cellulose's applications. Common examples of functionalized cellulose derivatives include cellulose acetate (CA), cellulose nitrate or nitrocellulose (NC), and the viscose process making rayon *via* formation of cellulose xanthate.

Yet another example of cellulose functionalization is trimethylsilyl cellulose (TMSC). Produced by replacing hydroxyl groups on cellulose with trimethylsilyl groups through silylation, the resulting enhanced solubility and processability of cellulose in organic solvents can be achieved (Scheme 1). Thus, TMSC is a valuable material in various applications, particularly in polymer science and materials engineering. Introducing trimethylsilyl groups increases the hydrophobic nature of TMSC, making it suitable for applications requiring water resistance.[7] TMSC is valued for forming ultrathin, smooth, and uniform films, outperforming other cellulose derivatives. Its solubility in various organic solvents, dependent on its degree of substitution, adds to its versatility. One of the most significant advantages of TMSC is that the trimethylsilyl group can be hydrolyzed under mild acidic conditions (*e.g.*, HCl vapor) and regenerated back into cellulose.[8] Compared to natural cellulose, the regenerated form of cellulose exhibits reduced crystallinity and altered arrangements, giving rise to further applications such as manufacturing textiles (rayon, lyocell), packaging films (cellophane), and specialty applications (medical sutures).[9]

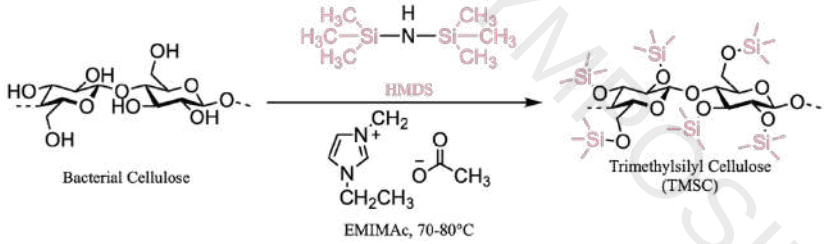


**Scheme 1.** Synthesis of trimethylsilyl cellulose from bacterial cellulose in EMIMAc

Solvents that can dissolve cellulose typically require specific conditions to disrupt the strong hydrogen bonding network and hydrophobic interactions within the cellulose structure. One of the potential solvents for cellulose dissolution is an ionic liquid. Ionic liquids (ILs) are molten salts with melting points below 100°C. They are considered greener solvents because they can be recycled, reducing waste generation and lowering environmental impact. Additionally, their low volatility limits air pollution and the emission of hazardous vapors, making them safer for both environmental and human health. ILs facilitate the dissolution of cellulose by disrupting its hydrogen bonding network. This effect is primarily driven by the anion, which interacts with the hydroxyl groups of cellulose, breaking the hydrogen bonds and improving its solubility.[10, 11] The synthetic methods of TMSC have been experimented on in different reaction media and silylating agents for cellulose dissolution and reaction

optimization. However, the synthesis requires petroleum-based organic solvents (dimethylacetamide; DMA) and inorganic salts (LiCl). Reactive silylating agents that produce hazardous by-products are also applied (chlorotrimethylsilane or trimethylsilyl chloride; TMSCl). In this research, we aimed to synthesize TMSC from microcrystalline bacterial cellulose (MCC-BC) using hexamethyldisilazane (HMDS) as the silylating agent, carried out in the ionic liquid 1-ethyl-3-methylimidazolium acetate (EMIMAc).

## EXPERIMENTAL

*A. Materials*

Microcrystalline bacterial cellulose was obtained from BioNext Company Limited, Thailand. 1-ethyl-3-methylimidazolium acetate (EMIMAc, purum, ≥ 98%w) was purchased from Proionic, Austria. 1,1,1,3,3,3-Hexamethyldisilazane (HMDS, > 96%(GC)) was purchased from TCI. Solvents (A.R. and commercial grades) were purchased from RCI Labscan and used without further purification. $^1$H NMR spectroscopy was conducted with a JEOL JNM-ECZ500R/S1 spectrometer operating at 500 MHz with $CDCl_3$ (Cambridge Isotope) as a solvent. The water contact angle (WCA) measurement was performed in a static mode using a contact angle goniometer (Rame-Hart instrument, model 200-F1, USA) with DROPimage Standard Software. The FTIR spectra were obtained from an ATR-FTIR spectrometer (Thermo Scientific Nicolet iS5 FT-IR Spectrometer). The number of scans was 64, with the resolution of 4 $cm^{-1}$ at room temperature.

*B. Synthesis of trimethylsilyl cellulose from bacterial cellulose in EMIMAc*

EMIMAc was preheated for 1 h at 70–80 °C. The bacterial cellulose powder (0.5 g) was dissolved in 18 mL of EMIMAc and left to dissolve completely in a 150-mL seal tube. After complete dissolution, the HMDS (6 mL) was added and allowed to react for 24 h. The crude TMSC was isolated by adding 200 mL of isopropyl alcohol. The white solid was collected and left to dry. The crude TMSC was redissolved in tetrahydrofuran (50 mL) overnight. The undissolved solids (unreacted BC) were filtered out, and the mother liquor was obtained. 50 mL of methanol was added to precipitate TMSC as a white solid.

*C. TMSC-coated paper preparation for Water contact angle (WCA) measurement*

0.1 g of TMSC was dissolved in 10 mL of THF. After completely dissolving, 2x5-cm filter paper was soaked into the mixture and left to dry. The reported contact angles were average values from three different locations on the TMSC-coated paper sample.

*D. Calculation of degree of substitution (DS) from $^1$H NMR spectra*

The degree of substitution (DS) is the average number of hydroxyl groups replaced by TMS groups per glucose unit in cellulose. Fully silylated cellulose has a degree of substitution (DS) of 3.0. The DS of TMSC was calculated from $^1$H NMR spectrum *via* the integration of the peak area under the proton from the TMS group (a) and protons from the anhydroglucose unit (b and c). [14]

**Equation 1.** Calculation of DS of TMSC from $^1$H NMR spectrum

$$DS = \frac{Area\ of\ TMS\ protons}{9} \times \frac{7}{Area\ of\ anhydroglucose\ protons}$$

PROCEEDINGS OF PPC & PETROMAT SYMPOSIUM 2025

*E. Calculation of degree of substitution (DS) from FTIR spectra*

The DS of TMSC was also calculated from FTIR spectra *via* the integration of the characteristic O–H stretching band at approximately 3400–3500 $cm^{-1}$ and C–H stretching band (around 2900 $cm^{-1}$) in polysaccharides.[13]

**Equation 2.1.** Calculation of the fraction of OH remaining in the product

$$Fraction\ of\ OH\ remaining = \frac{\left(\frac{Area\ of\ OH\ stretching}{Area\ of\ CH\ stretching}\right)_{TMSC}}{\left(\frac{Area\ of\ OH\ stretching}{Area\ of\ CH\ stretching}\right)_{Unmodified\ cellulose}}$$

$$= \frac{\left(\frac{Area\ of\ OH\ stretching}{Area\ of\ CH\ stretching}\right)_{TMSC}}{2.0}$$

2.0 represents the fraction of the literature value of the unmodified cellulose; therefore, 2.0 was used in this study for the calculation of degree of substitution (DS).

**Equation 2.2.** Calculation of DS of TMSC from the calculated fraction of OH remaining

$$DS = 3 \times (1 - fraction\ of\ OH\ remaining)$$

## RESULTS AND DISCUSSION

*A. Synthesis of TMSC from bacterial cellulose*

The resulting TMSC was synthesized *via* silylation with HMDS in EMIMAc and obtained as a white solid (Figure 1A). The hydrophobicity of TMSC was evaluated using a WCA measurement, resulting in an angle of 120.3°, indicating the hydrophobic nature of the TMSC-coated paper surface (Figure 1B).

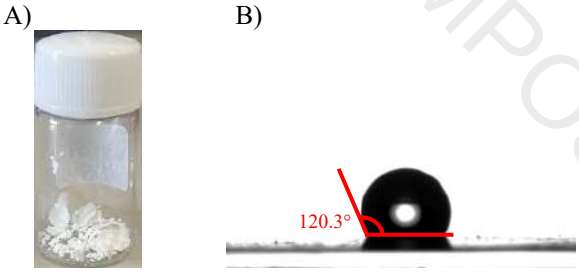


**Figure 1.** A) TMSC obtained as a white solid B) Contact angle of TMSC

The chemical structure of TMSC was further confirmed using Fourier transform infrared spectroscopy (FTIR). According to Figure 2, the FTIR spectrum showed the characteristic vibrations of O-Si$(CH_3)_3$ at 749 $cm^{-1}$, 836 $cm^{-1}$, and 1250 $cm^{-1}$. Moreover, low absorption of OH stretching at approximately 3400–3500 $cm^{-1}$ indicated the substitution of the trimethylsilyl groups at the hydroxyl positions.

PPC & PETROMAT SYMPOSIUM 2025

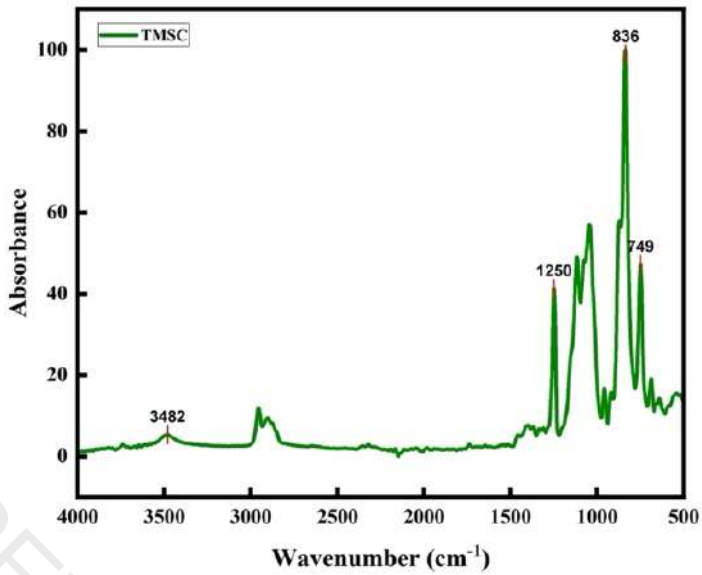


**Figure 2.** FTIR spectrum of TMSC

Next, the chemical structure of TMSC was also confirmed by $^{1}$H NMR in Figure 3. The intense signals at chemical shift (δ) 0.00–0.25 ppm indicated the protons from the $CH_3$ group in the trimethylsilyl groups. The peaks at 3.00–4.50 ppm were attributed to the protons on the anhydroglucose unit.[12]

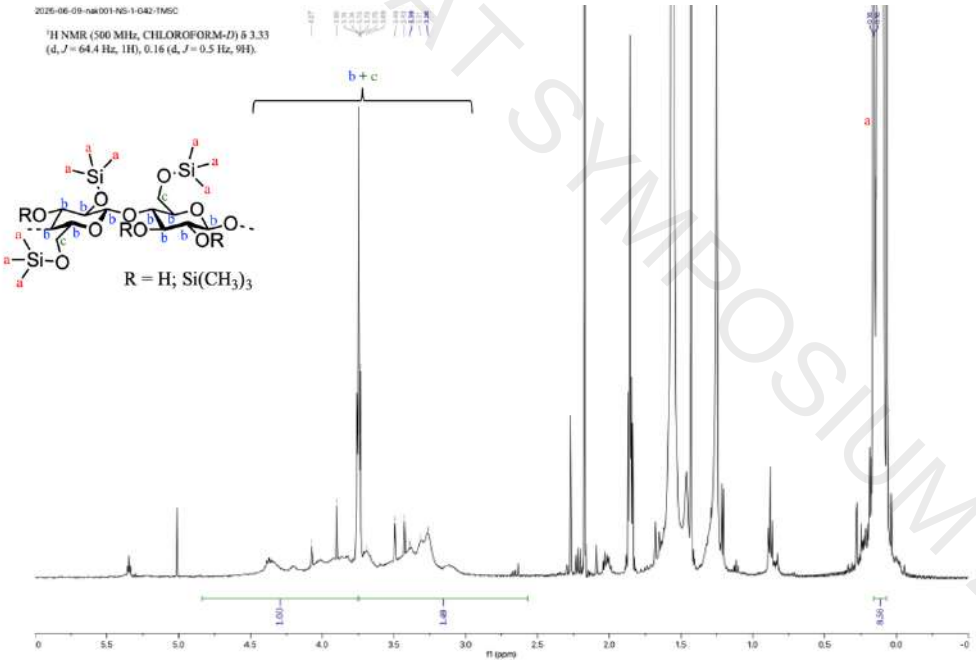


**Figure 3.** $^{1}$H NMR spectrum of TMSC in $CDCl_3$

*B. Calculation of degree of substitution (DS) from $^{1}$H NMR ($DS_{NMR}$) and FTIR ($DS_{FTIR}$)*
The DS of the synthesized TMSC (21% yield) was calculated from $^{1}$H NMR and FTIR spectra and summarized in Table 1.

PPC & PETROMAT SYMPOSIUM 2025

**Table 1.** Silylation of bacterial cellulose with HMDS in EMIMAc (70–80 °C, 24 h)

| entry | $n_{AGU}$ / $n_{TMSi}$ | yield | contact angle (°) | $DS_{NMR}$ | $DS_{FTIR}$ |
|---|---|---|---|---|---|
| 1 | 1:1.5 | 21% | 120.3 | 2.68 | 2.39 |

## CONCLUSIONS

TMSC was successfully synthesized from bacterial cellulose *via* silylation using HMDS in EMIMAc. The hydrophobicity of the product was confirmed by water contact angle analysis. FTIR and $^1$H NMR spectroscopy were used to validate the chemical structure of TMSC and to calculate the degree of substitution (DS).

## ACKNOWLEDGEMENTS

This research is supported by the Thailand Science Research and Innovation Fund Chulalongkorn University. The author would like to express sincere gratitude to Prof. Hathaikarn Manuspiya, Ph.D., and BioNext Co., Ltd., for kindly providing the bacterial cellulose used as a reactant in this study. Appreciation is also extended to the Department of Chemistry, Chulalongkorn University, for its support of the M.Sc. scholarship.

## REFERENCES

[1] Klemm, D.; Heublein, B.; Fink, H.-P.; Bohn, A. Cellulose: Fascinating Biopolymer and Sustainable Raw Material. *Angewandte Chemie International Edition* **2005**, *44*, 3358–3393.

[2] Park, J. K.; Jung, J. Y.; Khan, T. Bacterial cellulose. *Handbook of Hydrocolloid*s **2009**, 724–739.

[3] Srithammaraj, K.; Than-ardna, B.; Sain, M. M.; Manuspiya, H. A new design of colorimetric films using bacterial cellulose nanocrystals derived from nata de coco for sensing volatile organic compounds. *International Journal of Biological Macromolecules* **2024**, *275*, 133248–133248.

[4] Klemm, D.; Schumann, D.; Udhardt, U.; Marsch, S. Bacterial synthesized cellulose — artificial blood vessels for microsurgery. *Progress in Polymer Science* **2001**, *26*, 1561–1603.

[5] *Cello-gum นวัตกรรมจากเศษวุ้นมะพร้าวเหลือทิ้งสู่วัตถุดิบพันล้าน – จุฬาลงกรณ์มหาวิทยาลัย.* จุฬาลงกรณ์มหาวิทยาลัย. <https://www.chula.ac.th/highlight/143253/> Accessed 24.12.09.

[6] Kostag, M.; Gericke, M.; Heinze, T.; El Seoud, O. A. Twenty-five years of cellulose chemistry: innovations in the dissolution of the biopolymer and its transformation into esters and ethers. *Cellulose* **2019**, *26*, 139–184.

[7] Kostag, M.; Köhler, S.; Liebert, T.; Heinze, T. Pure Cellulose Nanoparticles from Trimethylsilyl Cellulose. *Macromolecular Symposia* **2010**, *294*, 96–106.

[8] Kontturi, E.; Spirk, S. Ultrathin Films of Cellulose: A Materials Perspective. *Frontiers in Chemistry* **2019**, *7*.

[9] Nagarajan, S.; Skillen, N. C.; Irvine, J. T. S.; Lawton, L. A.; Robertson, P. K. J. Cellulose II as bioethanol feedstock and its advantages over native cellulose. *Renewable and Sustainable Energy Reviews* **2017**, *77*, 182–192.

[10] Kraemer T., R.; Reyes, G.; Cartes, M.; Mejía, A.; Rojas, O. J. Ionic liquid interactions with cellulose and the effect of water. *Cellulose* **2024**, *31*, 6597–6610.

[11] Wang, H.; Gurau, G.; Rogers, R. D. Ionic liquid processing of cellulose. *Chemical Society Reviews* **2012**, *41*, 1519.

[12] Livazovic, S.; Li, Z.; Behzad, A. R.; Peinemann, K. V.; Nunes, S. P. Cellulose multilayer membranes manufacture with ionic liquid. *Journal of Membrane Science* **2015**, *490*, 282–293.

[13] Mormann, W.; Demeter, J.; Wagner, T. Partial silylation of cellulose with predictable degree of silylation–stoichiometric silylation with hexamethyldisilazane in ammonia. *Macromolecular Chemistry and Physics* **1999**, *200*, 693–697.

[14] Puspasari, T.; Pradeep, N.; Peinemann, K.-V. Crosslinked cellulose thin film composite nanofiltration membranes with zero salt rejection. *Journal of Membrane Science* **2015**, *491*, 132–137.

PPC & PETROMAT SYMPOSIUM 2025

# GRAPHITIC CARBON QUANTUM DOTS SPRAY-COATED INDIUM TIN OXIDE ELECTRODE FOR $Fe^{3+}$ DETECTION

*Bennui Firadao* [a], *Panpranot joongjai* [a]

[a] Center of Excellence on Catalysis and Catalytic Reaction Engineering, Department of Chemical Engineering, Faculty of Engineering, Chulalongkorn University, Bangkok, 10330, Thailand

Keywords: Graphitic carbon quantum dots, Indium tin oxide, Spray-coating, Electrochemical sensor, $Fe^{3+}$ ion detection

## ABSTRACT

Ferric ion ($Fe^{3+}$) contamination in water sources poses environmental and health risks, prompting the need for sensitive detection methods. In this study, graphitic carbon quantum dots (CQDs), CLS-3, were used to fabricate electrochemical sensors by spray-coating on indium tin oxide (ITO) glass. CQDs was dispersed in isopropyl alcohol (IPA), with and without Nafion to enhance film uniformity and adhesion. SEM analysis revealed distinct morphologies: CLS-3 spherical dot features dominate. Cyclic voltammetry was used to evaluate the detection performance using 5 mg/L $FeCl_3$. The highest oxidation peak current was observed with 4 mg CLS-3 in 5 mL IPA improved signals with 40 µL Nafion added, reaching $1.32 \times 10^{-6}$ A. Further validation was carried out over $Fe^{3+}$ concentrations ranging from 1.0 to 50.0 mg/L to determine linearity, detection limits, and repeatability. The findings confirm that CQDs-modified ITO electrodes offer a promising platform for $Fe^{3+}$ detection in aqueous environments).

***6572056721@student.chula.ac.th**

## INTRODUCTION

Stainless steel 304 pipes are widely used across petroleum, food, pharmaceutical, and other industries (Pal, Bhadauria, & Kumar, 2019). However, pitting corrosion can lead to the dissolution of $Fe^{2+}$ and $Cr^{3+}$ ions, which accumulate in the corrosion scale. $Fe^{2+}$ is largely oxidized to $Fe^{3+}$ by oxygen and chlorine, while residual $Fe^{2+}$ and $Cr^{3+}$ may equilibrate with unstable solids like $Fe(OH)_2$, $FeCO_3$, CrOOH, or $Cr_2O_3$. These metal ions can diffuse from the corrosion scale into bulk water, a process known as metal release (Cui et al., 2016). $Fe^{3+}$ in particular may cause water discoloration, poor taste, clogging, and promote bacterial growth (Lundquist et al., 2018). Moreover, it can generate reactive oxygen species (ROS), damaging biomolecules and contributing to diseases like Parkinson's (Huenchuguala & Segura-Aguilar, 2023). Hence, sensitive and selective $Fe^{3+}$ detection is critical.

Graphitic carbon quantum dots (CQDs), a zero-dimensional derivative of graphene, offer high water solubility, stable fluorescence, a tunable bandgap, low toxicity, and good biocompatibility (Abbas et al., 2020).Their unique HOMO-LUMO bandgap enables exceptional optical properties, making them a promising alternative to traditional fluorophores (Llaver et al., 2023). CQDs have been extensively used for $Fe^{3+}$ detection via fluorescence quenching (Zhang et al., 2019) though fluorescence methods face challenges like limited cell permeability and photobleaching (Rajasekar, Ranjitha, & Rajasekar, 2023).

PPC & PETROMAT SYMPOSIUM 2025

Electrochemical methods such as voltammetry offer low detection limits, high sensitivity, fast response, and portability, making them more practical than optical approaches (Sadak, Sundramoorthy, & Gunasekaran, 2017). Among electrode materials, indium tin oxide (ITO) stands out for its transparency, conductivity, chemical stability, and low cost (Aydın & Sezgintürk, 2017). Spray coating was employed in this study due to its low material usage, fast deposition rate, scalability, and compatibility with diluted CQDs solutions (Mohammad, Kumar, & Dutta, 2020).

In this work, low-cost CQDs were spray-coated onto ITO substrates to develop an electrochemical sensor for $Fe^{3+}$ detection in water environments.

## EXPERIMENTAL

*A. Electrode preparations*

Commercially available blue-luminescent graphitic carbon quantum dots (CQDs) from Crystallyte Co., Ltd. were used as precursor: CLS-3 (aqueous dispersion at 10 mg/mL). Each sample was diluted in 5 mL of isopropanol (IPA, Sigma-Aldrich) to enhance spray ability and surface wetting. For selected formulations, 40 µL Nafion™ PFSA 5% Dispersion (D520, The Chemours Company FC, LLC) was added as a polymeric binder to improve film adhesion and structural stability. All dispersions, both with and without Nafion, were homogenized by sonication at room temperature for 5 minutes to ensure uniform particle distribution. The prepared CQDs-based dispersions were then deposited onto indium tin oxide (ITO)-coated glass substrates (20 mm × 20 mm × 1.1 mm) using a spray-coating technique under ambient conditions. The spray parameters were optimized to achieve uniform film coverage and effective interaction with the conductive ITO surface.

*B. Electrode characterizations*

The morphological characteristics and surface elemental composition of the CQDs-coated ITO electrodes were analyzed using scanning electron microscopy coupled with energy-dispersive X-ray spectroscopy (SEM-EDX, Hitachi S-3400N). Structural transitions and optical properties were examined by ultraviolet–visible (UV–Vis) absorption spectroscopy (Lambda 650 spectrophotometer), while functional groups and chemical bonding were confirmed through Fourier-transform infrared spectroscopy (FT-IR, NICOLET 6700 spectrometer), providing comprehensive insight into the physical and chemical modifications of the electrode surface

*C. Electrochemical sensor measurements*

Electrochemical measurements were conducted using a electrode configuration comprising the CQDs-coated ITO glass as the working electrode, a platinum foil (0.1 mm thickness, 99.9999%, Alfa Aesar) as the counter electrode, and an Ag/AgCl reference electrode (Metrohm). The electrolyte solution consisted of 5 $mg \cdot L^{-1}$ $FeCl_3 \cdot 6H_2O$ (JT Baker) prepared in deionized water. Cyclic voltammetry (CV) was performed using a Multi Autolab/M204 electrochemical workstation (Metrohm AG) over a potential range from –1.2 V to +1.2 V at a scan rate of 100 $mV \cdot s^{-1}$. Each electrode condition was evaluated through five consecutive scan cycles to ensure measurement consistency, and the resulting peak currents were used for comparative analysis of electrochemical response.

PPC & PETROMAT SYMPOSIUM 2025

*D. Electrochemical sensor validation*

The performance of the CQDs-based electrochemical sensors was validated through a series of $Fe^{3+}$ solutions prepared at concentrations of 1.0, 1.5, 2.0, 2.5, 3.0, 3.5, 4.0, 4.5, and 5.0 $mg \cdot L^{-1}$ using $FeCl_3 \cdot 6H_2O$ diluted in deionized water. Cyclic voltammetry (CV) was employed to record electrochemical responses under a fixed potential range from –1.2 V to +1.2 V at a scan rate of 100 $mV \cdot s^{-1}$. For each concentration level and electrode, five scan cycles were performed. The peak current values were extracted, averaged, and plotted against the corresponding $Fe^{3+}$ concentrations to generate a calibration curve, from which the linearity was assessed using the coefficient of determination ($R^2$) (Kruekaew, 2018).

The limit of detection (LOD) and limit of quantification (LOQ) were calculated based on the standard deviation of the blank current response ($SD_{bl}$), determined from ten replicate CV scans (n = 10) of a blank solution (without $Fe^{3+}$) under identical CV conditions (–1.2 V to +1.2 V, 100 $mV \cdot s^{-1}$, 5 cycles). LOD and LOQ were calculated using the expressions $LOD = 3SD_{bl}/slope$ and $LOQ = 10SD_{bl}/slope$, where the slope was derived from the calibration curve. (Kruekaew, 2018)

For precision assessment, $Fe^{3+}$ solutions at concentrations of 1.0, 10.0, and 50.0 $mg \cdot L^{-1}$ were analyzed under the same CV conditions. Each measurement was repeated seven times (n = 7) for each electrode configuration, and the relative standard deviation (%RSD) (Kruekaew, 2018) was calculated to evaluate the repeatability and consistency of the electrochemical response.

## RESULTS AND DISCUSSION

*A. Electrode preparations*

Visual comparison of the CLS-3-coated electrodes, as shown in Figure a–d, reveals significant differences in film coverage and coloration depending on Nafion presence and CQD loading. The electrode in Figure a shows the lightest coloration and exhibits scattered particle distribution, indicating minimal surface interaction. In contrast, the sample in Figure b demonstrates darker coloration and more cohesive aggregation, attributed to Nafion's role in enhancing particle adhesion and dispersion stability. Figure c shows an increased particle presence relative to Figure a but still lacks uniform film coverage. The electrode in Figure d presents the darkest and most homogeneous film, suggesting that higher loading combined with Nafion significantly improves film uniformity and particle interaction during deposition.

(a) (b) (c) (d)

**Figure 1** CLS-3-coated ITO electrodes under various loading and binding conditions image: (a) 2 mg, (b) 2 mg with Nafion, (c) 4 mg, (d) 4 mg with Nafion.

PPC & PETROMAT SYMPOSIUM 2025

*B. Electrode characterizations*

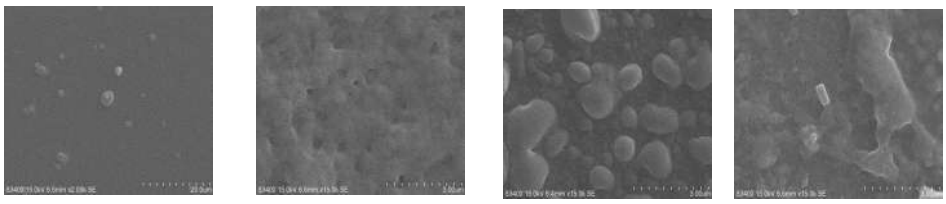

(a) (b) (c) (d)

**Figure 2** The morphology CLS-3 was investigated using scanning electron microscopy (SEM) under various loading and binding conditions: (a) 2 mg, (b) 2 mg with Nafion, (c) 4 mg, (d) 4 mg with Nafion.

The SEM images in Figure 2 show dot-like morphology typical of CQDs. At 2 mg without Nafion (Figure 2a), small, well-dispersed spherical dots are observed. With Nafion (Figure 2b), the film appears smoother and more uniform, indicating improved adhesion due to Nafion's binder effect. At 4 mg without Nafion (Figure 2c), larger and more aggregated dots form, suggesting increased particle accumulation. In contrast, 4 mg with Nafion (Figure 2d) shows dense, continuous films with enhanced surface coverage. The morphology remains predominantly spherical, confirming classical CQD characteristics.

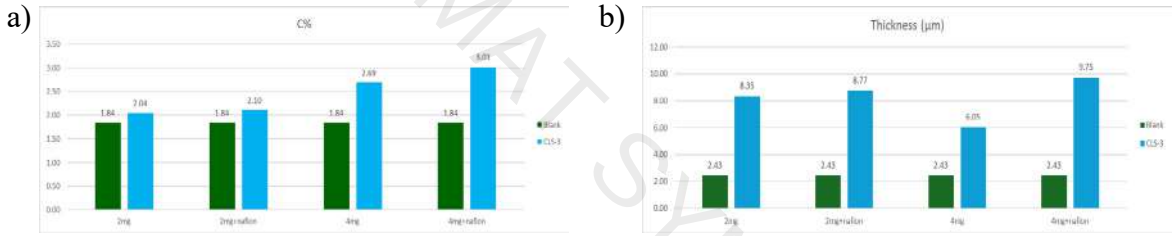


**Figure 3** Elemental analysis results of CQDs-modified electrodes obtained via energy-dispersive X-ray spectroscopy (EDX): (a) carbon content (wt%) and (b) film thickness (µm) for blank and CLS-3 samples at different loadings (2 mg and 4 mg) with and without Nafion

Elemental analysis and film thickness of CLS-3-modified electrodes were evaluated using energy-dispersive X-ray spectroscopy (EDX), as shown in Figure 3. Figure 3a indicates that the carbon content (wt%) of CLS-3-coated electrodes increased with both higher material loading and the presence of Nafion. The carbon percentage rose from 2.04 wt% to 3.01 wt%, confirming enhanced deposition and retention of carbonaceous material on the electrode surface. Figure 3b shows a similar trend in film thickness, where the presence of Nafion significantly improved the film build-up, increasing thickness from 8.35 µm (2 mg) to 9.75 µm.In all cases, the blank samples maintained a constant baseline thickness of ~2.43 µm, indicating that the increase is attributable solely to the CLS-3 layer. These results suggest that Nafion promotes uniform film formation and enhances material adherence, particularly at higher CQDs loadings.

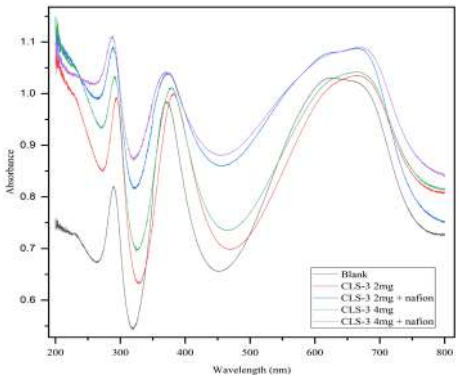


**Figure 4.** UV-Vis absorption spectra of blank and CLS-3 under various loading and binding conditions.

The UV-Vis spectra of blank and CQDs-modified electrodes exhibit prominent $\pi \rightarrow \pi^*$ transitions around 231 nm, indicative of aromatic C=C structures from $sp^2$ carbon networks. Peaks at ~291 nm are attributed to $n \rightarrow \pi^*$ transitions from lone-pair electrons on surface functional groups. A feature at ~380 nm appears in both blank and CQDs-coated electrodes, corresponding to transitions of the functional groups present in the GQDs(Ibarra, Kharissova, & Gomez, 2023). A broad absorbance near 675 nm, observed across all samples, may arise from nitrogen-containing moieties or surface trap states. The increase in absorbance with Nafion suggests better dispersion and tighter molecular packing of CLS-3 quantum dots, enabling stronger optical density and potential for improved photoresponse performance.

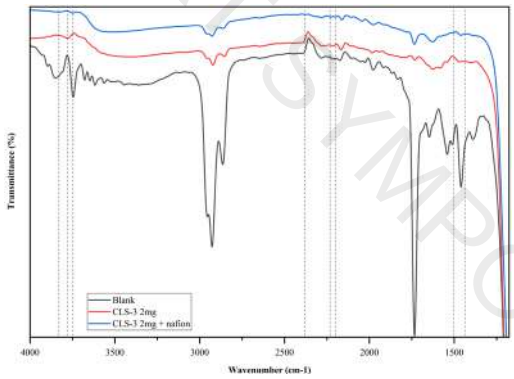


**Figure 5.** The FTIR spectra of blank, CLS-3 (2 mg), and CLS-3 (2 mg) with Nafion-coated electrodes.

Characteristic peaks associated with surface functional groups confirm the presence and interaction of CLS-3 and Nafion. The broad bands observed at 3829 $cm^{-1}$ and 3746 $cm^{-1}$ (only with Nafion), and at 3777 $cm^{-1}$ (without Nafion), correspond to O–H stretching vibrations, indicating the presence of hydroxyl groups, with slight shifts suggesting interactions with the Nafion matrix. Peaks at 2379 $cm^{-1}$, 2231 $cm^{-1}$, and 2197 $cm^{-1}$, all observed in Nafion-containing samples, may relate to C≡C triple bonds or alkynes, though their weak intensity suggests either symmetric substitution or conjugation effects. The C=C stretching vibration appears at 1505 $cm^{-1}$ in Nafion samples, while a distinct N–H bending vibration at 1433 $cm^{-1}$ (Yuan et al., 2014) is only seen in the sample without Nafion,

PPC & PETROMAT SYMPOSIUM 2025

indicating differences in chemical bonding environments. These spectral changes confirm that Nafion incorporation influences the chemical interactions and surface functionalities of CLS-3 films, enhancing molecular connectivity and film stability.

*C. Electrochemical sensor measurements*

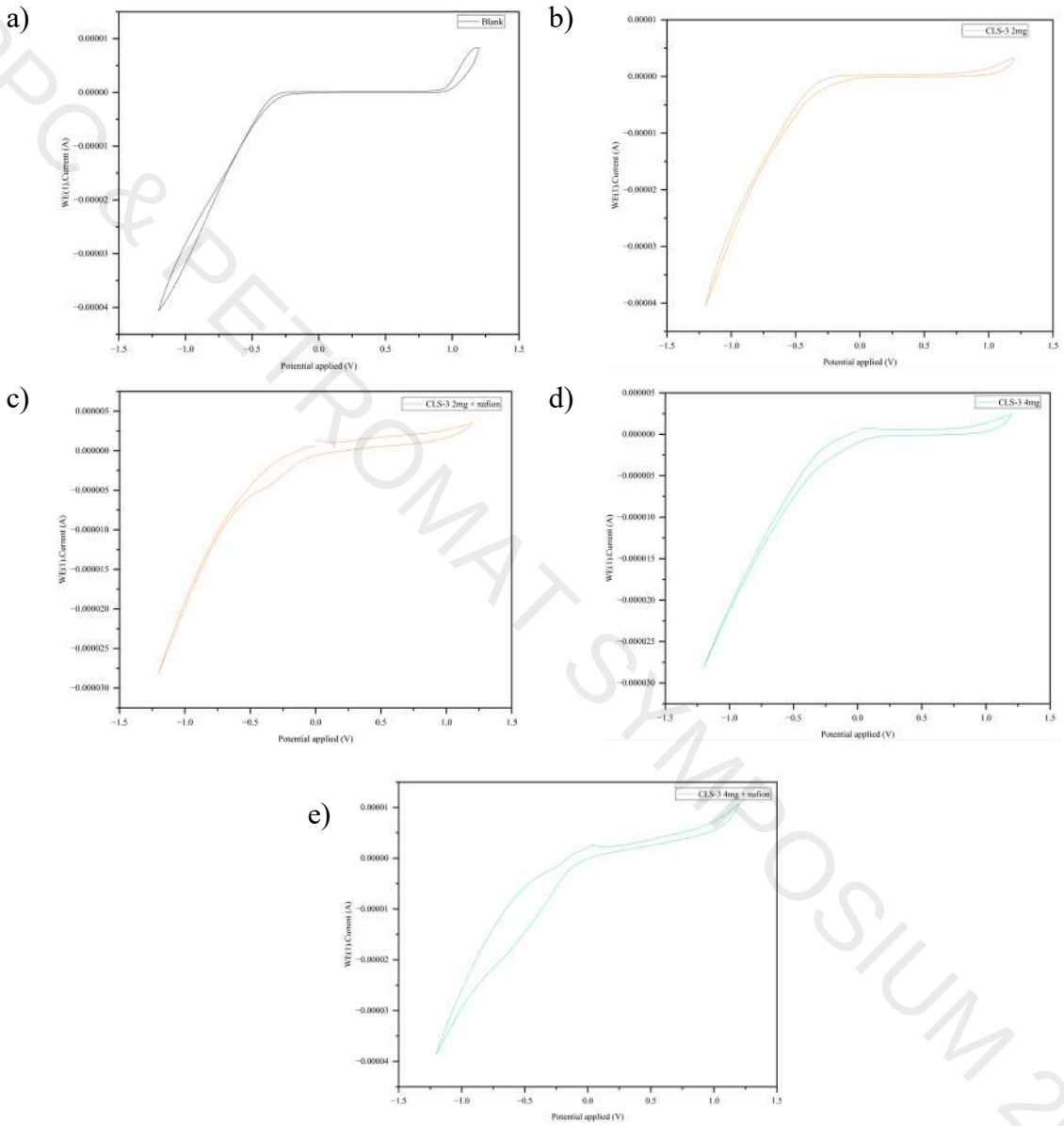


**Figure 6.** The cyclic voltammetry (CV) responses of (a) blank and CLS-3-modified electrodes under different conditions: (b) 2 mg, (c) 2 mg with Nafion, (d) 4 mg, (e) 4 mg with Nafion. in the potential window of –1.2 V to +1.2 V. at a scan rate of 100 $mV \cdot s^{-1}$ over five consecutive cycles.

The electrochemical response of an electrolyte solution containing 5 $mg \cdot L^{-1}$ $FeCl_3 \cdot 6H_2O$ was evaluated using cyclic voltammetry. The optimal scan cycle for reliable

data acquisition was identified as follows: the 2nd cycle was selected for the blank ITO-coated glass and all CLS-3-modified electrodes. The peak current increased progressively with both material loading and Nafion incorporation. The blank electrode (Figure 6a) exhibited the lowest peak current of $2.94 \times 10^{-8}$ A, indicating minimal electrochemical activity. The CLS-3 2 mg electrode (Figure 6b) showed a peak current of $1.24 \times 10^{-7}$ A, which increased to $6.52 \times 10^{-7}$ A upon addition of Nafion (Figure 6c), reflecting enhanced film conductivity and ion transport. A higher loading of 4 mg without Nafion (Figure 6d) produced a peak current of $2.16 \times 10^{-7}$ A, while the highest response of $1.32 \times 10^{-6}$ A was observed for the CLS-3 4 mg with Nafion electrode (Figure 6e). These results demonstrate that both increased CLS-3 loading and Nafion binder synergistically improve charge transfer kinetics and overall electrochemical performance.

These results indicate that both increased CQDs loading and the incorporation of Nafion significantly enhance the electron transfer kinetics and sensitivity of the electrode surface toward $Fe^{3+}$ detection. The improvement is attributed to the synergistic effect of higher active surface area and improved ionic conductivity provided by Nafion, as well as the intrinsic electrochemical properties of the CQDs.

*D. Electrochemical sensor validation*

Linear regression was used to analyze the relationship between current and $Fe^{3+}$ concentration. The coefficient of determination ($R^2$) indicated the strength of this correlation. The blank ITO electrode showed weak correlation with an $R^2$ of 0.4866, reflecting low electrochemical sensitivity. For CLS-3, the 2 mg electrode gave an $R^2$ of 0.2331. Adding Nafion improved it to 0.4677. At 4 mg loading, $R^2$ was 0.1471 without Nafion, but increased significantly to 0.786 with Nafion, showing strong linearity

The detection performance of each electrode was evaluated using the limit of detection (LOD) and limit of quantification (LOQ). These values were calculated from the calibration data of $Fe^{3+}$ solutions. The blank ITO electrode showed poor sensitivity, with an LOD of 178.21 $\mu g \cdot L^{-1}$ and LOQ of 594.05 $\mu g \cdot L^{-1}$. For CLS-3, the 2 mg loading had an LOD of 6.54 $\mu g \cdot L^{-1}$ and LOQ of 21.79 $\mu g \cdot L^{-1}$. With Nafion, the LOD increased slightly to 8.37 $\mu g \cdot L^{-1}$ and LOQ to 27.91 $\mu g \cdot L^{-1}$. At 4 mg loading, the LOD dropped to 2.90 $\mu g \cdot L^{-1}$ and further to 1.42 $\mu g \cdot L^{-1}$ with Nafion. The LOQ also improved to 9.67 and 4.74 $\mu g \cdot L^{-1}$, respectively.

The reproducibility of each electrode configuration was assessed through the calculation of the relative standard deviation (%RSD) values for blank and CLS-3-modified electrodes at $Fe^{3+}$ concentrations of 1, 10, and 50 $mg \cdot L^{-1}$. At 1 $mg \cdot L^{-1}$, the blank showed moderate repeatability (16.27%), while CLS-3 without Nafion had high %RSD (117.15% for 2 mg, 83.94% for 4 mg). Nafion improved precision, reducing %RSD to 72.66% (2 mg) and 13.26% (4 mg), the lowest among all.At 10 $mg \cdot L^{-1}$, %RSD increased across all samples, with the blank at 35.18%, and high variability observed for CLS-3: 87.78% (2 mg), 66.33% (2 mg with Nafion), 131.22% (4 mg), and 106.29% (4 mg with Nafion).At 50 $mg \cdot L^{-1}$, blank remained stable (16.40%), and the best repeatability was again seen with CLS-3 2 mg with Nafion (15.08%), while CLS-3 4 mg with Nafion showed high variation (103.72%). Overall, CLS-3 4 mg with Nafion at 1 $mg \cdot L^{-1}$ provided the most stable signal, and Nafion generally improved repeatability, especially at low concentration.

## CONCLUSIONS

This study successfully developed a low-cost electrochemical sensor for $Fe^{3+}$ detection using graphitic carbon quantum dots (CQDs, CLS-3) spray-coated onto indium tin oxide (ITO) electrodes. The inclusion of Nafion as a polymeric binder significantly improved film morphology, adhesion, and electrochemical performance. SEM analysis confirmed a dot-like morphology, while EDX showed increased carbon content and film thickness with both higher CQD loading and Nafion addition. UV-Vis and FTIR results revealed enhanced molecular interaction and packing upon Nafion incorporation.

Electrochemical measurements demonstrated that the highest oxidation peak current ($1.32 \times 10^{-6}$ A) was achieved with 4 mg CLS-3 and Nafion, highlighting the synergistic effect of material loading and binder on charge transfer kinetics. The electrode exhibited excellent linearity ($R^2 = 0.786$), low detection limit (1.42 $\mu g \cdot L^{-1}$), and improved repeatability (%RSD = 13.26% at 1 $mg \cdot L^{-1}$ $Fe^{3+}$). These findings confirm the potential of CLS-3/Nafion-modified ITO electrodes as a robust, sensitive, and cost-effective platform for $Fe^{3+}$ sensing in aqueous environments.

## ACKNOWLEDGEMENTS

This study was funded by the Program Management Unit for Human Resources & Institutional Development, Research and Innovation (PMU-B), Thailand. The authors express their sincere gratitude to the funding organization for its essential support, which greatly contributed to the successful completion of this research.

## REFERENCES

Abbas, A., Tabish, T. A., Bull, S. J., Lim, T. M., & Phan, A. N. (2020). High yield synthesis of graphene quantum dots from biomass waste as a highly selective probe for Fe(3+) sensing. Sci Rep, 10(1), 21262. https://doi.org/10.1038/s41598-020-78070-2

Aydın, E. B., & Sezgintürk, M. K. (2017). Indium tin oxide (ITO): A promising material in biosensing technology. TrAC Trends in Analytical Chemistry, 97, 309-315. https://doi.org/10.1016/j.trac.2017.09.021

Cui, Y., Liu, S., Smith, K., Hu, H., Tang, F., Li, Y., & Yu, K. (2016). Stainless steel corrosion scale formed in reclaimed water: Characteristics, model for scale growth and metal element release. Journal of Environmental Sciences, 48, 79-91. https://doi.org/https://doi.org/10.1016/j.jes.2015.12.035

Huenchuguala, S., & Segura-Aguilar, J. (2023). On the Role of Iron in Idiopathic Parkinson's Disease. Biomedicines, 11(11). https://doi.org/10.3390/biomedicines11113094

Ibarra, D., Kharissova, O., & Gomez, I. (2023). Synthesis of Graphene Quantum Dots Coupled to Au Nanoparticles: A Facile and Versatile Route Using Different Carbon Sources. C, 9(2), 45. https://www.mdpi.com/2311-5629/9/2/45

Kruekaew, S. (2018). DEVELOPMENT OF MODIFIED SCREEN-PRINTED GRAPHENE ELECTRODE WITH POLY-GLUTAMIC ACID AND GOLD NANOPARTICLES FOR DETERMINATION OF ARSENIC Srinakharinwirot University]. http://ir-ithesis.swu.ac.th/dspace/handle/123456789/481

PPC & PETROMAT SYMPOSIUM 2025

Llaver, M., Barrionuevo, S. D., Troiani, H., Wuilloud, R. G., & Ibañez, F. J. (2023). Highly selective and sensitive fluorescent determination of Fe3+ within alcoholic beverages with 1,5-diphenylcarbazone-functionalized graphene quantum dots. Talanta Open, 7. https://doi.org/10.1016/j.talo.2023.100202

Lundquist, N. A., Worthington, M. J. H., Adamson, N., Gibson, C. T., Johnston, M. R., Ellis, A. V., & Chalker, J. M. (2018). Polysulfides made from re-purposed waste are sustainable materials for removing iron from water. RSC Adv, 8(3), 1232-1236. https://doi.org/10.1039/c7ra11999b

Mohammad, T., Kumar, V., & Dutta, V. (2020). Spray deposited indium doped tin oxide thin films for organic solar cell application. Physica E: Low-dimensional Systems and Nanostructures, 117. https://doi.org/10.1016/j.physe.2019.113793

Pal, S., Bhadauria, S. S., & Kumar, P. (2019). Pitting Corrosion Behavior of F304 Stainless Steel Under the Exposure of Ferric Chloride Solution. Journal of Bio- and Tribo-Corrosion, 5(4), 91. https://doi.org/10.1007/s40735-019-0283-z

Rajasekar, M., Ranjitha, V., & Rajasekar, K. (2023). Recent advances in Fluorescent-based cation sensors for biomedical applications. Results in Chemistry, 5. https://doi.org/10.1016/j.rechem.2023.100850

Sadak, O., Sundramoorthy, A. K., & Gunasekaran, S. (2017). Highly selective colorimetric and electrochemical sensing of iron (III) using Nile red functionalized graphene film. Biosens Bioelectron, 89(Pt 1), 430-436. https://doi.org/10.1016/j.bios.2016.04.073

Yuan, X., Liu, Z., Guo, Z., Ji, Y., Jin, M., & Wang, X. (2014). Cellular distribution and cytotoxicity of graphene quantum dots with different functional groups. Nanoscale research letters, 9, 108. https://doi.org/10.1186/1556-276X-9-108

Zhang, Y., Yang, X., Pu, Y., Cheng, W., Lin, S., Shao, Z., & Liao, X. (2019). Selective, Sensitive and Label-Free Detection of Fe3+ Ion in Tap Water Using Highly Fluorescent Graphene Quantum Dots. Journal of Fluorescence, 29(3), 541-548. https://doi.org/10.1007/s10895-019-02365-5

PPC & PETROMAT SYMPOSIUM 2025

# Linking Thermoplastic Starch with Biodegradable Plastic: An approach to retard Retrogradation and improve Miscibility

*Pongsakorn Pandee* [a], *Suwabun Chirachanchai* [a,b,*]

[a)] The Petroleum and Petrochemical College, Chulalongkorn University
[b)] Center of Excellence in Bioresources to Advanced Materials (B2A-CE), The Petroleum and Petrochemical College, Chulalongkorn University, Bangkok, Thailand

**Keywords:** Thermoplastic starch, Mercaptosuccinic acid, thiol-containing compound, Polylactic acid (PLA)

## ABSTRACT

Thermoplastic starch (TPS) is a biodegradable material derived from renewable resources, but its poor mechanical properties and incompatibility with other polymers limit its broader applications. Blending TPS with polylactic acid (PLA) improves mechanical strength, yet phase separation occurs due to the polarity mismatch between hydrophilic TPS and hydrophobic PLA. In this study, a thiol-functionalized poly(butylene itaconate-co-lactic acid) was synthesized as a reactive compatibilizer to enhance compatibility between TPS and PLA. The synthesis involved polycondensation of dimethyl itaconate with 1,4-butanediol (PBI), followed by ring-opening polymerization of lactide (PBI-LA), and a thermal thiol-ene reaction with mercaptosuccinic acid (thiol-ene-PBI-LA). Structural confirmation of PBI, PBI-LA, and thiol-functionalized PBI-LA was achieved using FTIR and NMR spectroscopy. The resulting copolymer contains thiol and carboxyl groups that are expected to improve interfacial adhesion between TPS and PLA. Future work will investigate the compatibilizer's effect on phase dispersion, mechanical performance, and the overall processability and biodegradability of TPS/PLA blends. This approach offers a promising strategy for developing robust, compostable TPS-based materials.

* **csuwabun@chula.ac.th**

## INTRODUCTION

The growing need for sustainable materials has driven research into biodegradable polymers derived from renewable resources, particularly for applications where the environmental persistence of conventional plastics is a concern. Among the most promising candidates is thermoplastic starch (TPS), which offers low cost, biodegradability, and wide availability from sources such as cassava, corn, and potato. TPS can be processed using conventional melt-processing equipment, making it suitable for short-life applications such as packaging and agricultural films. However, TPS suffers from poor mechanical strength and high moisture sensitivity, which limits its broader utility. To address these shortcomings, TPS is often blended with polylactic acid (PLA), a biodegradable polyester known for its strength and rigidity. TPS/PLA blends combine the environmental benefits of starch with the mechanical performance of PLA (Martinez et al., 2022). However, their compatibility is hindered by the polarity mismatch between hydrophilic TPS and hydrophobic PLA, which results in weak interfacial adhesion, phase separation, and poor dispersion ultimately reducing overall blend performance (Mayekar et al., 2023). Various

PPC & PETROMAT SYMPOSIUM 2025

compatibilization strategies have been explored, including maleic anhydride-grafted PLA, which forms covalent bonds with starch (Maliger et al., 2006) and hydrophilic copolymers such as polyethylene glycol to bridge the two phases (Wang, Yu, & Ma, 2007). Yet, these methods often involve complex synthesis steps or compromise biodegradability. This study proposes a novel compatibilization method using a thiol-functionalized poly(butylene itaconate-co-lactic acid) (PBI-co-PLA) copolymer. The copolymer is synthesized from dimethyl itaconate and 1,4-butanediol, followed by ring-opening polymerization of lactide and a thermal thiol-ene reaction with mercaptosuccinic acid. The resulting thiol and carboxyl groups facilitate interfacial bonding with both TPS and PLA. When used as a reactive compatibilizer, this copolymer enhances phase dispersion and mechanical performance while preserving processability and biodegradability, enabling the development of robust, fully compostable TPS-based materials.

## EXPERIMENTAL

*A. Materials*

Native cassava starch (St) was purchased from E.T.C. Eaib Tong Chan, Co., Ltd. (Thailand). Glycerol (G) was purchased from Asian scientific, Co., Ltd. (Thailand). Ethylene Glycol (EG) was received from Ajax Finchem (Australia). Hydroquinone monomethyl ether (MeHQ) was obtained from Fluka Chemika, (Switzerland). Tin (II) 2-ethylhexanoate ($SnOct_2$), 1,4-Butandiol (BDO) and Mercaptosuccinic acid (MS) were bought from Sigma-Aldrich (USA). L-lactide was purchased from Department of Chemistry, Faculty of Science, Chiang Mai University (Thailand). Poly (lactic acid) (PLA) Luminy LX175 was received from Total-Corbion (the Netherlands). Dimethyl (DMIN) itaconate was bought from Tokyo Chemical Industry (TCI) (Thailand). N, N-Dimethylformamide, isopropanol, chloroform (CHCl3), methanol (MeOH), and acetone were purchased from RCI Lab Scan, Co., Ltd. (Thailand). Deuterated chloroform (CDCl3) was bought from Sigma-Aldrich (USA).

*B. Preparation of Thermoplastic starch (TPS) with Varying Plasticizer Types*

To evaluate the influence of different plasticizers on the structure and processability of thermoplastic starch (TPS) glycerol and ethylene glycol (EG). The starch content was fixed at 72 wt%, while each plasticizer was added at 28 wt% of the total formulation. Native starch was first oven-dried at 80 °C for 24 h to minimize moisture content. For each formulation, the plasticizer was manually mixed with the dried starch powder until a homogeneous mixture was obtained. The mixtures were then processed using a twin-screw extruder (Thermoscientific process 11). The screw speed was set at 20 rpm, and the temperature profile was 110, 120, 130, 140, 150, 160, 170, and 160 °C from hopper to die, respectively. The resulting TPS strands were subsequently pelletized using a rotating knife to produce uniform pellets with a diameter of approximately 2.5 mm. All samples were stored in a desiccator to prevent moisture uptake prior to downstream processing and characterization.

*C. Synthesis of PBI, PBI-LA, and thiol-ene-PBI-LA*

(PBI) was synthesized via melt polycondensation between DMIN and 1,4-butanediol in the presence of Sn $(Oct)_2$ as a catalyst, as described by (Ramirez-Suarez et al., 2024).

PPC & PETROMAT SYMPOSIUM 2025

Specifically, DMIN (50.00 g, 0.32 mol) and 1,4-butanediol (42.70 g, 0.47 mol) were added into a round bottle flask and magnetically stirred in an oil bath at 150 °C. The reaction continued for 24 hours to obtain a viscous product. The crude product was dissolved in chloroform, then precipitated in cold methanol. The precipitated product was washed with methanol several times. PBI was obtained after vacuum drying at 25 °C for 24 h. The PBI-LA was synthesized using a ring-opening polymerization (ROP). L-lactide (30.5 g, 200 mmol) was added into PBI (15 g, 8 mmol) in a round bottle flask and magnetically stirred under $N_2$ atmosphere in an oil bath at 130 °C for for 15 min. The $SnOct_2$ catalyst (0.90 g, 0.18 mmol, 100 mol equivalent of L-Lactide to 1 mol equivalent of $SnOct_2$) was added into the mixture and the reaction was continued under magnetic stirring for 24 h to obtain a viscous product. The crude product was dissolved in chloroform, then precipitated in cold methanol. The precipitated product was washed with methanol several times before filtering. The PBI-LA was obtained after vacuum drying at 40 °C for 24 h. After that, PBI-LA (10.00 g, 1.0 equiv.) was dissolved in 20 mL of dry DMF under a nitrogen atmosphere and stirred until completely dissolved. Afterward, MS (3.40 g, 10.0 equiv.) and AIBN (0.02 g, 0.5 equiv.) were added into the solution at room temperature. The mixture was then heated to 80 °C and stirred overnight to promote thermal thiol-ene radical addition between the vinyl groups on the copolymer and the thiol functionalities. The solution obtained was transferred into methanol for the precipitation. The crude product was dried under vacuum for 24 hours at 40 ºC. (see Scheme 1)

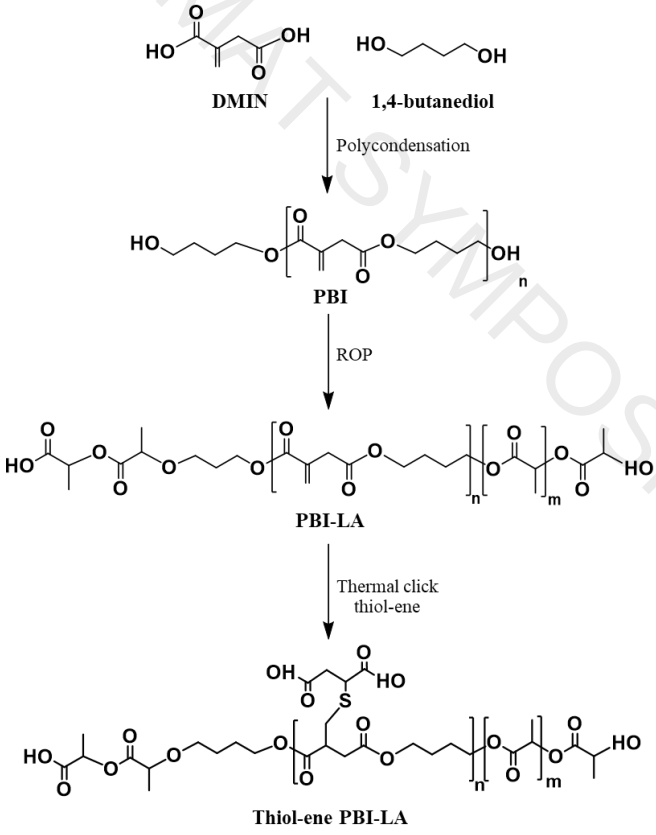


**Scheme 1.** Synthesis of Thiol-ene PBI-LA.

PPC & PETROMAT SYMPOSIUM 2025

*D. Characterizations*

The synthesized materials were characterized by various analytical techniques. Proton ($^{1}$H-NMR) and carbon ($^{13}$C-NMR) Nuclear Magnetic Resonance spectra were recorded using a Bruker AVANCE 500 MHz Ultra Shield Plus at 25°C. Fourier-transform infrared (FTIR) spectroscopy was conducted on a Bruker ALPHA FTIR in the wavenumber range of 4000-500 cm$^{-1}$. Viscoelastic properties were measured using a Discovery DMA 850 dynamic mechanical analyzer (DMA), with a heating rate of 5°C/min and a frequency set at 10 Hz.

## RESULTS AND DISCUSSION

*A. Rheological behaviour of TPS plasticised with glycerol and ethylene glycol.*

In TPS-G the storage modulus G′ (elastic component, blue ▲) exceeds the loss modulus G″ (viscous component, red ●) from 0.01 to roughly 80 rad s$^{-1}$, showing that the melt behaves mainly like an elastic solid and can recover its shape under deformation. Above 80 rad s$^{-1}$ G′ falls below G″, indicating the expected shift to more fluid-like behaviour at very short relaxation times. By contrast, TPS-EG displays G″ > G′ across the entire 0.01–300 rad s$^{-1}$ window, revealing a viscous-dominant melt that dissipates energy and offers little elastic recovery. These differences arise from the interactions between the plasticizer and starch molecules. Glycerol forms strong hydrogen bonds with the hydroxyl groups on starch chains, effectively disrupting the native crystalline structure while promoting the formation of a temporary network that enhances the material's ability to store mechanical energy. In contrast, ethylene glycol, with its smaller molecular size and weaker hydrogen-bonding capacity, is less effective at creating such a network, resulting in a melt that flows more easily but lacks structural strength. Therefore, glycerol was selected as the plasticizer for further studies due to its superior contribution to melt elasticity and overall structural stability.

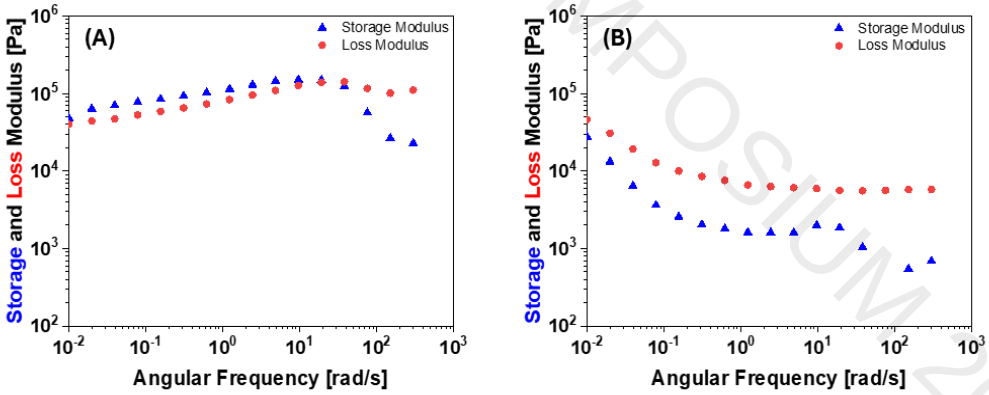


**Figure 2.** Rheological Properties of Thermoplastic Starch (TPS) Plasticized with Glycerol (TPS-G) (A) and Ethylene Glycol (TPS-EG) (B).

*B. Characterization of PBI, PBI-LA, and thiol-ene-PBI-LA*

PBI was synthesized by polycondensation of DMI and BDO while MeHQ was used as the vinyl stabilizer for itaconate group. The structure was qualitatively confirmed by FTIR

spectrum (Fig. 3 A). The peak at 1640 $cm^{-1}$ (C=C) corresponded to the vinyl group, while the peak at 1713 $cm^{-1}$ represented the C=O of itaconate. PBI-LA was synthesized via ring opening polymerization (ROP) of L-LA by using PBI as an initiator. PBI-LA structure was confirmed by FTIR spectrum (Fig. 3 A). FTIR peak observed at 1760 cm-1 correspond to C=O stretching of PLA. The change of peak intensity at 1640 $cm^{-1}$ (C=C) indicates that the addition of L-LA in PBI chain has occurred. The successful functionalization of PBI-LA via thiol-ene chemistry was confirmed by FTIR analysis (Fig. 3B). The characteristic peaks of MS at 2637 $cm^{-1}$ and 2540 $cm^{-1}$, corresponding to (S-H) stretching vibrations, were absent in the spectrum of thiol-ene PBI-LA, indicating the consumption of thiol groups during the thiol-ene reaction. Additionally, the peak at 1640 $cm^{-1}$, attributed to the C=C stretching of the vinyl group, also disappeared after the reaction. These spectral changes confirm that the thiol-ene reaction between the vinyl groups of PBI-LA and the thiol groups of MS proceeded successfully, resulting in covalent grafting and formation of a thiol-functionalized PBI-LA copolymer.

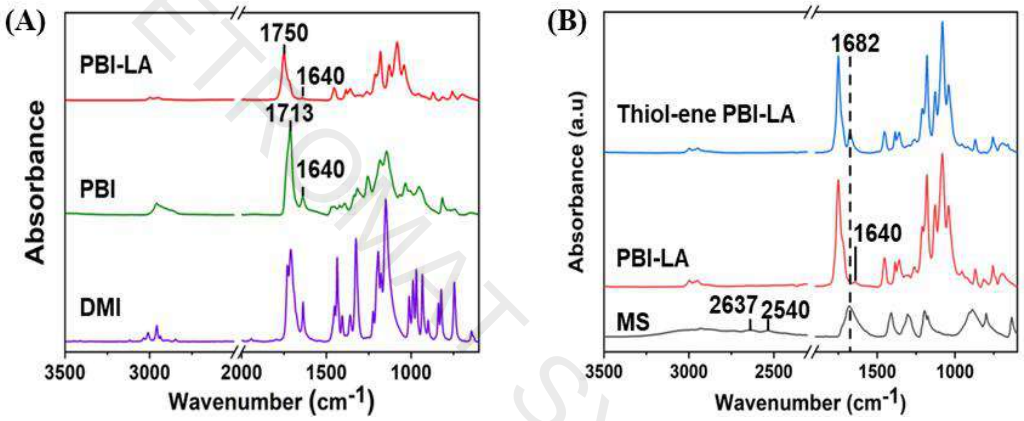


**Figure 3.** (a) TGA curves, (b) DSC curves of $EP_x$-$PEI_y$.

## CONCLUSIONS

This study outlines a promising approach to improve the miscibility between thermoplastic starch (TPS) and polylactic acid (PLA) through the design of a thiol-functionalized poly(butylene itaconate-co-lactic acid) (thiol-ene-PBI-LA) compatibilizer. The copolymer was synthesized via a multi-step process involving polycondensation, ring-opening polymerization, and thiol-ene functionalization, resulting in thiol and carboxyl groups capable of promoting interfacial adhesion with both TPS and PLA. Rheological evaluation demonstrated that TPS plasticized with glycerol exhibits superior viscoelastic properties compared to its ethylene glycol counterpart, supporting its selection for future blend formulations. FTIR analysis confirmed the successful synthesis and post-functionalization of the copolymer, validating its potential as a reactive compatibilizer for forthcoming TPS/PLA blend studies.

PPC PETROMAT SYMPOSIUM 2025

## ACKNOWLEDGEMENTS

The authors would like to express their gratitude to the Petroleum and Petrochemical College of Chulalongkorn University, and Center of Excellence in Bioresources to Advanced Materials (B2A-CE), The Petroleum and Petrochemical College, Chulalongkorn University, Bangkok, Thailand.

## REFERENCES

**Maliger, R., McGlashan, S., Halley, P., & Matthew, L.** (2006). Compatibilization of starch–polyester blends using reactive extrusion. *Polymer Engineering & Science*, *46*(3), 248-263.

**Martinez, K., Arias-Tapia, M., Useche, J., & Escobar Macías, D.** (2022). Thermoplastic Starch (TPS)/Polylactic Acid (PLA) Blending Methodologies: A Review. *Journal of Polymers and the Environment*, *30*. https://doi.org/10.1007/s10924-021-02207-1

**Mayekar, P. C., Limsukon, W., Bher, A., & Auras, R.** (2023). Breaking It Down: How Thermoplastic Starch Enhances Poly(lactic acid) Biodegradation in Compost─A Comparative Analysis of Reactive Blends. *ACS Sustainable Chemistry & Engineering*, *11*(26), 9729-9737. https://doi.org/10.1021/acssuschemeng.3c01676

**Ramirez-Suarez, J. H., Käfer, F., Ober, C. K., & Goddard, J. M.** (2024). Synthesis of Itaconate-Based Biopolyesters with Improved Polycondensation Control. *ACS Applied Polymer Materials*, *6*(19), 12207-12216.

**Wang, N., Yu, J., & Ma, X.** (2007). Preparation and characterization of thermoplastic starch/PLA blends by one-step reactive extrusion. *Polymer international*, *56*(11), 1440-1447.

PPC & PETROMAT SYMPOSIUM 2025

# DEVELOPMENT OF FILM FORMING WOUND DRESSING CONTAINING CYCLODEXTRIN- HERBAL DRUG COMPLEX

*G.D.D. Kavindi Karunathilaka* [a], *Pairayaphak Ngamplang* [a], *Chasuda Choipang* [a] *Piyachat Chuysinuan* [b], *Pitt Supaphol** [a]

[a] The Petroleum and Petrochemical College, Chulalongkorn University
[b] Chulabhorn Research Institute, Talat Bang Khen, Bangkok 10210, Thailand

Keywords: Mangosteen, Cyclodextrin, Wound dressing, Inclusion complex

## ABSTRACT

Film forming systems are novel drug delivery platform used as wound dressing primarily include film forming polymer, solvent and therapeutic drug which facilitate antibacterial properties to inhibit microbial infections that can compromise the whole immune system. Alpha mangosteen, known as the most abundant xanthone, therapeutically active agent in mangosteen pericarp extract (*Garcinia mangostana Linn*), exhibits potent biological properties, such as antibacterial, anti-inflammatory, antifungal and antioxidant activities that promotes the accelerated wound healing and control of infections. Yet, the poor water solubility and stability limits its potential benefits in drug delivery. Addressing the identified drawbacks, cyclodextrin the cyclic oligosaccharide gaining attention and popular for enhance the hydrophilicity of insoluble drugs by encapsulation phenomena. In this study mangosteen pericarp extract encapsulated in Beta-cyclodextrin (β-CD) through a coprecipitation method to enhance its solubility and stability by forming a host–guest inclusion complex by following molecular dynamic simulation. Concentration of alpha mangosteen in mangosteen pericarp extract identified by the HPLC analysis, phase solubility by UV-vis and inclusion complex characterized by FTIR, DSC and SEM for confirming the encapsulation. Enhance stability of the encapsulated alpha mangosteen confirmed by the thermogram and modified inclusion complex will further be used to test film forming wound dressing application.
***Pitt.s@chula.ac.th**

## INTRODUCTION

Wound dressings at present have been improved to provide biological properties such as antimicrobial, antiviral and antifungal contrast to traditional wound dressings which facilitated the covering of the wound bed (Krishnan K and Thomas, 2019). Plant derived herbal drugs gain much attention to use with wound dressing materials to improve and accelerate the healing property. Mangosteen pericarp extract is an interesting herbal medicinal extract containing antibacterial, antiviral and anticancer properties utilized in several ailments in traditional medicine due to its bioactive compounds, particularly

PPC & PETROMAT SYMPOSIUM 2025

xanthones such as α, β, and γ mangosteens (Tsai, 2016). Due to its pharmaceutical effect proves the therapeutic value for wound healing, yet the water insolubility is the major problem of mangosteen extract which limits its biological activity for wound healing and low bioavailability, lower stability and hydrophobicity contribute to limiting the drug delivery function. As a remedial action for poor water solubility, formation of host-guest inclusion complex with cyclodextrin (CDs) molecules, is an abundant technique which can reduce the limitation by their structure. CDs are cyclic oligosaccharides connect α-D-glucopyranose units with α-1, 4 glycosidic links and α, β, γ CDs composed of six, seven and eight units respectively. The truncated structure of CDs contains hydrophilic outer surface and hydrophobic inner cavities which trap the hydrophobic guest molecules alongside change their limited solubility and stability facilitating to use in pharmaceutical industry (Garg, 2021).

Film forming wound dressing is a dosage form drug delivery system, with high clinical potential of healing minor skin injuries. The system contains drug for the relevant wound type in a solution with film forming polymer to form a film when it contacts with therapeutic site. Ease of appliance, feasible skin adhesion, wound moist absorbance, painless removal, drug release in a sustained manner with close contact to skin are the benefits of film forming wound dressings (Bakhrushina, 2023).

The purpose of this study is to prepare the mangosteen extract/β-CD inclusion complex which can increase the hydrophilicity, stability of mangosteen extract and to develop new film forming wound dressing loaded with inclusion complex that can increase wound healing. Furthermore, the inclusion complex loaded wound dressing compared with drug loaded wound dressing by evaluating their physical and biological properties.

## EXPERIMENTAL

### *A. Materials*

β-CD (>98.0%) was purchased from Tokyo Chemical Industry Co.Ltd.(USA). Alpha mangosteen (>97.0%) was purchased from Tokyo Chemical Industry Co.Ltd. PVP K90 (Mw 360,000) was purchased from Tokyo Chemical Industry Co.Ltd.(USA). Ethanol (AR grade) was purchased from RCI Labscan limited (Thailand).

### *B. Formation of Mangosteen/β-CD inclusion complexes (ICs)*

Following the co-precipitation technique, 1M of β-CD dissolved in DI water separately and magnetically stirred at 55 $^{o}$ C. 1M of mangosteen extract dissolved in 1:3 (v/v) ethanol/deionized water and filtered solution was added dropwise to the fully dissolved CD solution. Then, the solution was magnetically stirred in 550 rpm at room temperature overnight and kept in the refrigerator to precipitate for 3 hour. Solution was vacuum filtered, and the powder dried in an oven at 40 $^{o}$C for 24 hour.

PROCEEDINGS OF PPC & PETROMAT SYMPOSIUM 2025

*C. Fabrication of PVP Film*

10% (w/v) of PVP was dissolved in 30% ethanol solution and stirred magnetically until fully dissolved. After that, different concentrations of ICs, (1%, 2%, 3%) are added to the PVP solution and stirred at 550 rpm overnight. Finally, the mixture was poured into the petri-dish and dried in an oven for 24 hour.

*D. Instrument and characterization.*

HPLC analysis was done to identify the alpha mangosteen content of mangosteen extract and phase solubility results gained from UV-vis spectrometry. Chemical structure of the ICs and films were characterized by Fourier transform infrared spectroscopy (FTIR). ATR-FTIR spectra were carried out in the wavenumber range 500-4000 $cm^{-1}$ for 64 scans. The thermal behaviour of β-CD, mangosteen extract, and ICs were studied via Differential scanning colorimetry (DSC) heated from 30 °C to 400°C at a heating rate of 10 °C/min in a nitrogen atmosphere. The morphology of mangosteen extract, β-CD and inclusion complex were observed by Field Emission Scanning Electron Microscopy.

## RESULTS AND DISCUSSION

*A. HPLC analysis*

The linear standard calibration curve of α mangosteen was constructed by HPLC with the peak area ratios and compared with the chromatogram of mangosteen extract which showed the peak for α mangosteen at same retention time, 6.54 minutes. Percentage of α mangosteen in mangosteen extract was calculated from the area under the peak at standard retention time and obtained 40.7% at 316nm wavelength.

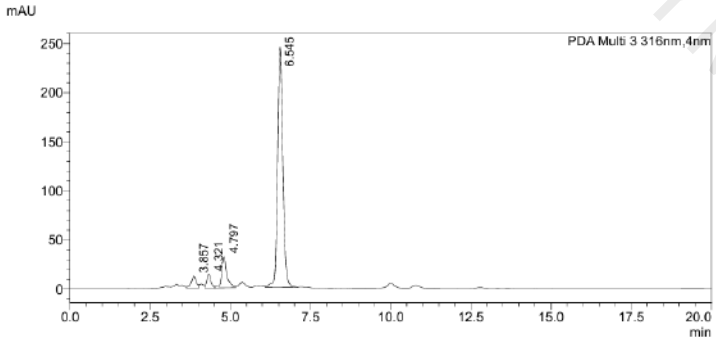


**Figure 1.** HPLC chromatography of mangosteen extract.

*B. Phase solubility*

Phase solubility studies were performed to investigate the interaction of mangosteen extract with β-CD at varied concentrations as reported by Higuchi and Connors. The dissolved α-mangosteen of mangosteen extract in the solution was determined by measuring absorbance at 316 nm with a UV-VIS spectrophotometer and calculated according to the standard curve of α-mangosteen. Phase solubility of mangosteen in aqueous solution linearly increased with β-CD concentration which provides an $A_L$ type phase solubility plot and

PPC & PETROMAT SYMPOSIUM 2025

confirmed the formation of inclusion complex with molar ratio of 1:1. The apparent stability constant ($K_S$) of the IC was calculated to be 874.658 $M^{-1}$ from the slope value of the diagram and complexation efficiency (CE) was 3.12 X $10^{-4}$ indicating stable complex.

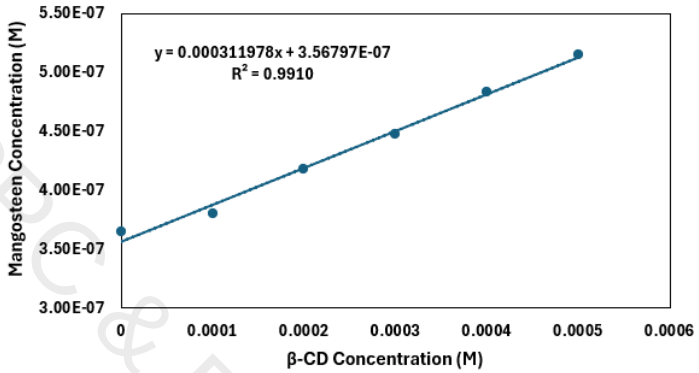


**Figure 2**. Phase solubility diagram

*C. FTIR characterization*

Figure 3 depicts the FTIR spectra of β-CD and β-CD ICs almost shared same peaks and both FTIR spectra shows 3280, 3287 $cm^{-1}$ correspond to O-H stretching. The strong peak at 1021 $cm^{-1}$ in β-CD relevant to C-O stretching vibration which depicts at 1017 $cm^{-1}$ in β-CD ICs. Both spectrum attributes H-O-H bending at 1643, 1645 $cm^{-1}$ for β-CD and 1:1 β-CD ICs respectively. The peak at 1448 $cm^{-1}$ of the mangosteen spectra associated with C=C stretching of the π-π bonding of aromatic rings and 1637,1602 $cm^{-1}$ associates to C=O stretching of aromatic ketone in tricyclic xanthone structure which was overlapped after the inclusion formation confirmed the successful complexation.

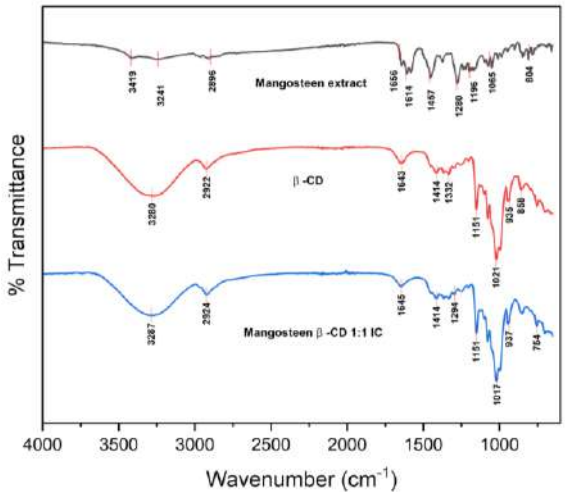


**Figure 3.** FTIR spectra of mangosteen extract, β-CD and mangosteen β-CD ICs.

From Figure 4 in PVP, 3419 $cm^{-1}$ peak attributes to O-H stretching vibration and 2952 $cm^{-1}$ relates to the C-H stretching vibrations of PVP pyrrole ring (Koczkur, 2015). The characteristic strong peak at 1645 $cm^{-1}$ occurs due to the C=O stretching vibration. 1287, 1075 $cm^{-1}$ peaks in PVP spectra exhibit the C-N vibration of PVP (Safo, 2019). Apart from

PVP, the other four films which contain PVP with mangosteen extract and ICs of 1.0, 2.0, 3.0 % hold similar peaks with PVP for O-H stretching vibration, C-H stretching vibration, C=O stretching vibration and C-N vibration at 1284, 1287, 1282 and 1289 $cm^{-1}$ respectively. Around 1024 to 1028 $cm^{-1}$ a new peak appears in 1.0, 2.0 and 3.0 % inclusion samples which did not occur in PVP and PVP with mangosteen extract film could be due to the C-O stretching vibration of β-CD.

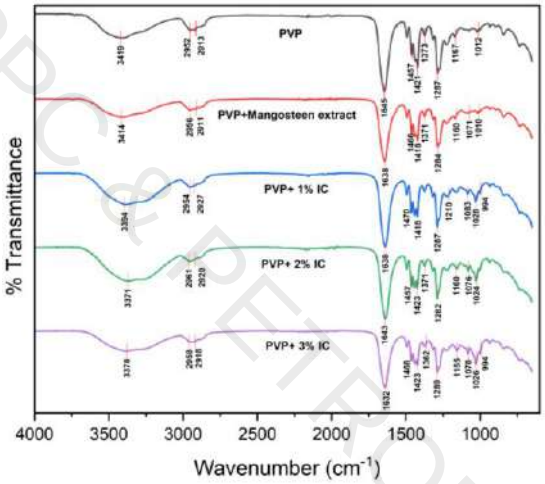


**Figure 4.** FTIR spectra of PVP, PVP-mangosteen extract, PVP with 1.0%, 2.0% and 3.0% ICs.

*D. DSC analysis*

Mangosteen showed a sharp endothermic peak at 159 °C corresponding to its melting point shown in Figure 5. Compared to that β-CD corresponds to dehydration peak at 109 °C and degradation at 296 °C. ICs of β-CD with mangosteen extract depicted the shifted dehydration peak of 107 °C and melting peak of mangosteen extract completely disappeared. Degradation temperature of ICs shifted 304-318 °C more broader peak than β-CD, which confirms the enhanced stability of the inclusion system.

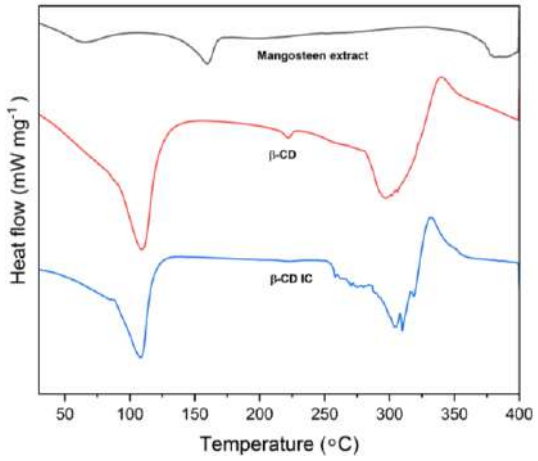


**Figure 5.** DSC thermogram of mangosteen extract, β-CD, mangosteen β-CD ICs

PPC & PETROMAT SYMPOSIUM 2025

*E. Morphology study of ICs*

To analyse surface morphology and texture of ICs, FE-SEM was used with 500X magnification for the investigation. According to the references (Ngamplang, 2025), morphology of β-CD depicts as block like large particles. Contrast to that small irregular cube like morphology shown by the mangosteen β-CD ICs that confirmed the inclusion formation by morphology difference.

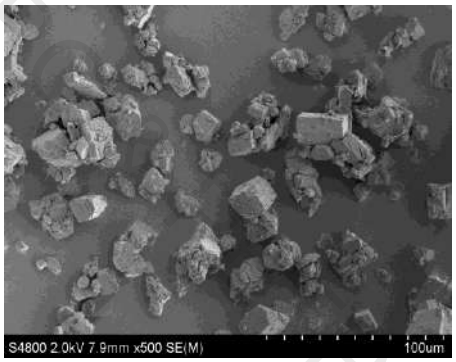


**Figure 6.** Morphology of mangosteen β-CD ICs.

## CONCLUSIONS

The present work demonstrates the inclusion complex formation between mangosteen extract and β-CD by coprecipitation method in 1:1 molar ratio. The major active compound for wound healing in mangosteen extract, α-mangosteen identified by HPLC chromatography. By utilizing the UV-vis spectrometry, $A_L$ type phase solubility diagram was achieved and confirmed the mangosteen solubility linearly increased with increasing β -CD concentration. FTIR spectroscopy of ICs confirmed by peaks which were shifted and overlapped the mangosteen functional groups after entrapped in CD cavity. The FTIR of PVP film with ICs showed the successful combination of PVP and ICs and DSC thermogram of ICs also confirmed the inclusion formation by disappearance of mangosteen melting point and increasing the degradation temperature by enhancing the stability. Investigated surface morphology of the ICs by FE-SEM provide irregular cube like structure which was difference from the referred β-CD morphology and altogether confirm the formation of mangosteen β-CD 1:1 inclusion complex.

## ACKNOWLEDGEMENTS

The author would like to acknowledge The Petroleum and Petrochemical College Chulalongkorn University (Thailand) for ASEAN and non-ASEAN scholarship program. Along with Chulabhorn Research Institute for the research grant and assistance in this research work.

PPC & PETROMAT SYMPOSIUM 2025

## REFERENCES

Bakhrushina, E.O., Shumkova, M.M., Sergienko, F.S., Novozhilova, E.V., and Demina, N.B. (2023). Spray Film-Forming systems as promising topical in situ Systems: A review. Saudi Pharmaceutical Journal, 31(1), 154-169.

Garg, A., Ahmad, J., and Hassan, M.Z. (2021). Inclusion complex of thymol and hydroxypropyl-β-cyclodextrin (HP-β-CD) in polymeric hydrogel for topical application: Physicochemical characterization, molecular docking, and stability evaluation. Journal of Drug Delivery Science and Technology, 64, 102609.

Koczkur, K.M., Mourdikoudis, S., Polavarapu, L., and Skrabalak, S.E. (2015). Polyvinylpyrrolidone (PVP) in nanoparticle synthesis. Dalton transactions, 44(41), 17883-17905.

Krishnan K, A., and Thomas, S. (2019). Recent advances on herb-derived constituents-incorporated wound-dressing materials: A review. Polymers for Advanced Technologies, 30(4), 823-838.

Ngamplang, P., Choipang, C., Chaiarwut, S., Chuysinuan, P., and Supaphol, P. (2025). Development of poly (vinyl alcohol)/carboxymethyl chitosan hydrogels loaded with encapsulated tea tree oil for wound care application. Journal of Drug Delivery Science and Technology, 107.

Tsai, S.-Y., Chung, P.-C., Owaga, E.E., Tsai, I.-J., Wang, P.-Y., Tsai, J.-I., Yeh, T.-S., and Hsieh, R.-H. (2016). Alpha-mangostin from mangosteen (Garcinia mangostana Linn.) pericarp extract reduces high fat-diet induced hepatic steatosis in rats by regulating mitochondria function and apoptosis. Nutrition & Metabolism, 13, 1-10.

PPC & PETROMAT SYMPOSIUM 2025

# Session 4-Energy Landscape Transformation: Renewable Generation, Storage, and Conversion (Energy)

# COMPARATIVE ANALYSIS OF WOOD PELLETS AND TORREFIED WOOD PELLETS AS FEEDSTOCKS IN THE 3-STAGE GASIFICATION PROCESS FOR SYNGAS PRODUCTION IN POWER GENERATION

*~~Panida Thepkhun~~[a]*, Warunyu Phondet[a], Chatuphon Uthaisri[a], Thanita Sonthisawate[a], Niramai Traiyawong[a], Phattacharee Jaiaun[a], Napaporn Klaijieam[a], Manoo Boonsae[a]*

[a] Expert Center of Innovative Clean Energy and Environment, Thailand Institute of Scientific and Technological Research, Pathum Thani, Thailand

Keywords: gasification, biomass, torrefied-biomass, syngas

## ABSTRACT

Torrefaction has been recognized as an effective thermochemical pretreatment that has improved the fuel properties of biomass, rendering it more coal-like. This study compared wood pellets (WP) and torrefied wood pellets or black pellets (BP) as feedstocks in a three-stage gasification process at a pilot-scale facility for electricity generation. The system was operated to produce syngas with a heating value of 4–6 MJ/Nm³ to support a 200 kW power generator. Syngas from WP comprised $H_2$ (6.07–7.21%), CO (10.61–13.55%), and $CH_4$ (4.63–12.07%), while that from BP contained $H_2$ (3.98–10.71%), CO (6.81–14.29%), and $CH_4$ (0.38–9.49%). A significant difference in equivalence ratio (ER) was observed, 0.38 for WP and 0.08 for BP, influenced by oxygen content and feed rate. WP showed a 21.03% lower feed rate than BP. Char discharge rates were 18.49 kg/hr for WP and 30.07 kg/hr for BP, corresponding to char-to-feed ratios of 9.47% and 12.72%, respectively. Consequently, WP demonstrated higher cold gas efficiency, with a higher generated tar content than BP, 11.42%. Wastewater from the synthesis gas cleaning system and the treatment was also monitored.

***panida_s@tistr.or.th**

## INTRODUCTION

Biomass has been increasingly used as a renewable energy source because it has helped improve energy security, reduced dependence on fossil fuels, and minimized environmental impact. Among the technologies available, gasification was one of the most efficient. Gasification was a thermochemical process that converted solid fuel under a restriction of oxygen into combustible gases. The process involved three zones with different temperature profiles and conditions: pyrolysis, oxidation, and reduction [McKendry, 2002; Slivka, et al., 2011]. This process converted biomass into syngas, a fuel gas mainly made of hydrogen ($H_2$), carbon monoxide (CO), methane ($CH_4$), and carbon dioxide ($CO_2$), through heating in a low-oxygen environment [Basu, P., 2013]. However, raw biomass had some limitations. It often contained high moisture content (20–40% by weight), which reduced efficiency because extra energy was needed to dry it. Also, when biomass was broken down during heating, it produced tar, a sticky substance that could damage equipment and reduce performance in engines used for power generation. Tar and other impurities like dust and ash have been removed before using syngas. These contaminants could clog engines and shorten their lifespan if not properly cleaned. One effective method to solve these problems was torrefaction. This was a mild thermal treatment where biomass was heated to 200–300°C in

PPC & PETROMAT SYMPOSIUM 2025

a low-oxygen atmosphere [Chen et al. 2010]. Torrefied biomass became drier, lighter, and more energy-dense [Nunes and Matias, 2020]. It was also more resistant to moisture and biological decay [Fisher et al., 2018; Pelaez-Samaniego et al., 2014]. Therefore, comparing regular wood pellets (WP) and torrefied wood pellets or black pellets (BP) in gasification was important [Raut et al., 2016]. This study compared the influence of both fuel types in a three-stage gasification system at pilot scale, with a maximum feed rate of 7 tons/day, to supply syngas to a 200 kW internal combustion generator.

## EXPERIMENTAL

*A. Raw material and property analysis*

The gasification tests were carried out using commercial wood pellets (WP) and torrefied wood pellets or black pellets (BP) with a diameter of approximately 0.8 cm. The raw materials were analyzed for their basic properties using proximate [ASTM D7582] and ultimate analysis methods [ASTM D5373; ASTM D4239] as shown in Table 1.

**Table 1.** Raw materials properties – dry basis

| Raw materials | Proximate analysis (%) | | Ultimate analysis (%) | |
|---|---|---|---|---|
| Wood pellet (WP) | Moisture (as-received) | 8.21 | H | 5.82 |
| | Volatile | 76.98 | C | 48.61 |
| | Fixed carbon | 20.06 | N | 0.58 |
| | Ash | 2.96 | O | 41.91 |
| | | | S | 0.10 |
| | LHV | 4,252 kcal/kg | | |
| Torrefied-wood Pellet (BP) | Moisture (as-received) | 7.29 | H | 5.51 |
| | Volatile | 64.72 | C | 56.23 |
| | Fixed carbon | 31.79 | N | 0.50 |
| | Ash | 3.49 | O | 34.22 |
| | | | S | 0.04 |
| | LHV | 5,034 kcal/kg | | |

The properties analysis showed that BP had a significantly lower amount of volatile matter, which decreased by 15.93%. On the other hand, the fixed carbon and net calorific value increased by 58.47% and 18.39%, respectively. The ultimate analysis also revealed that BP contains higher carbon levels, while hydrogen and oxygen were reduced.

*B. 3-stage Gasification System*

A pilot-scale three-stage gasification reactor, with a maximum fuel input capacity of 7 tons per day, was developed as shown in Figure 1. The system consisted of five main components. First, the fuel conveyor and drying unit utilized waste heat from the exhaust to reduce the moisture content of biomass to 5–8%, maintaining a drying temperature of 50–60°C. The core component, a downdraft gasifier, operated through three distinct thermal zones: pyrolysis (400–600°C), oxidation (800–1,100°C), and reduction (500–800°C). The reactor was internally lined with refractory insulation to minimize heat loss. At the same time,

PPC & PETROMAT SYMPOSIUM 2025

biomass was fed from the top, and air was introduced in controlled amounts to maintain sub-stoichiometric combustion.

**Figure 1.** The 3-stage Gasification Demonstration Plant

Residual ash and char were discharged from the bottom. The resulting syngas underwent a multi-stage cleaning process, beginning with a twin cyclone separator to remove coarse particles, followed by a water scrubber at 32°C and a chiller scrubber at 10°C to eliminate fine particles and tar, and the gas then passed through a secondary cyclone for final purification. Wastewater from the cleaning stages was treated via coagulation and flocculation processes, enabling water reuse within the system. Finally, cleaned syngas was tested using a start-up flare, stored in a 20 $m^3$ tank, and supplied to a 200 kW gas engine generator after passing through a fine dust pre-coat filter. The flare also functioned as an emergency gas release unit.

## RESULTS AND DISCUSSION

*A. Operating conditions*

The operation of the 3-stage gasification reactor began with woodchip as the initial feedstock to stabilize the system temperature. Once steady-state conditions were achieved, the target fuels (WP and BP) were introduced for comparative analysis. The operating conditions and syngas composition were shown in Table 2 and Figure 2. It was observed that BP required a higher feeding rate but produced a lower volume of syngas compared to the WP. Additionally, the BP resulted in a higher biochar yield in absolute quantity and as a proportion of the input feedstock.

**Table 2.** Operating conditions and syngas composition of WP and BP

| Raw materials | Feed rate (kg/hr) | Syngas ($Nm^3$/hr) | Biochar (kg/hr) | Tar (mg/$Nm^3$) |
|---|---|---|---|---|
| WP | 195 | 507 | 18.49 | 211.50 |
| BP | 236 | 429 | 30.07 | 187.33 |

PPC & PETROMAT SYMPOSIUM 2025

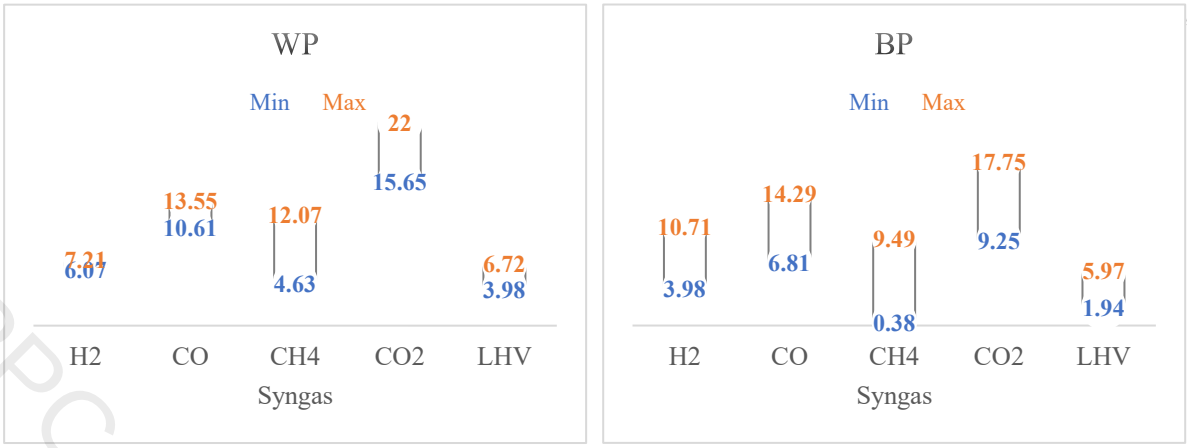


**Figure 2.** Gas composition (%) and LHV (MJ/Nm$^3$)

The Equivalence Ratio (ER) was defined as the ratio of the actual fuel-to-oxidizer quantity supplied in a reaction to the amount required for stoichiometric (theoretically complete) combustion. The average ER during the tests was 0.38 for the WP and 0.08 for the BP pellets. Different fuel properties primarily influence the variation in the required ER during gasification of various fuels. The BP had higher fixed carbon content, lower volatile matter, and greater heating value than the WP, which altered their combustion behavior [Bridgwater, 2012]. These characteristics reduced their reactivity, required lower ER values to maintain optimal gasification conditions, and avoided complete combustion. In contrast, conventional pellets with higher volatile content could sustain gasification at higher ER levels. These differences in fuel composition and thermal behavior directly impacted the air-to-fuel ratio required for efficient syngas production.

*B. Biochar Properties*

The biochar yield obtained from gasification using WP and BP was 9.48% and 12.74%, respectively. The biochar produced during syngas generation through the gasification process was carbon-rich and could be applied as a soil amendment to improve soil fertility. In this study, the resulting biochar was analysed and compared with the criteria for organic fertilizers specified in the Royal Gazette by the Department of Agriculture, Thailand.

**Table 3.** Biochar characteristics

| **Analysis criteria** | **Biochar** | |
|---|---|---|
| *Fertilizer analysis* | WP | BP |
| Total Nitrogen, % (≥ 1.0%) | 0.51 | 0.44 |
| Total Phosphorus ($P_2O_5$), % (≥ 0.5%) | 0.95 | 0.84 |
| Total Potassium ($K_2O$), % (≥ 0.5%) | 2.44 | 2.60 |
| Organic matter, % (≥ 20%) | 20.33 | 19.15 |
| C/N ratio, (≤ 20:1) | 23:1 | 25:1 |
| *Approximate analysis* | | |
| Net calorific value, kcal/kg | 6,076 | 6,339 |
| Volatile matter, % | 8.91 | 10.57 |
| Ash content, % | 18.13 | 16.77 |
| Fixed carbon, % | 72.96 | 72.66 |

PPC & PETROMAT SYMPOSIUM 2025

The comparison results, as shown in Table 3, indicated that, from the perspective of its use as an organic fertilizer, specific properties did not meet the required criteria, specifically, total nitrogen, organic matter content, and the C/N ratio. These parameters were indicative of the nutrient availability necessary for plant growth. Therefore, from this standpoint, biochar was more suitable for use solely as a soil amendment. Conversely, biochar appeared more appropriate when considering its potential as a fuel due to its high calorific value, exceeding 6,000 kcal/kg, and significantly higher fixed carbon content than raw biomass.

*C. Water quality within the syngas cleaning*

The water used in the 3-stage gasification system was operated in a closed-loop recirculating configuration. Water from the storage pond was supplied to the gas cleaning unit, or wet scrubber, where it was used to clean the synthetic gas. After passing through the wet scrubber, the water underwent treatment via the membrane filter press to remove suspended solids before being recirculated back to the storage pond for reuse. The analysis of water pollution was conducted by examining the water quality at two points in the system: (1) water exiting the wet scrubber before treatment, and (2) water after treatment. The results were shown in Table 4.

**Table 4.** Wastewater characteristics

| Parameter | Before treatment | | After treatment | |
|---|---|---|---|---|
| | **WP** | **BP** | **WP** | **BP** |
| pH | 7.4 | 7.5 | 7.6 | 7.7 |
| BOD, mg/L | 328 | 124 | 228 | 123 |
| COD, mg/L | 1161 | 674 | 668 | 339 |
| Total Suspended Solid (TSS), mg/L | 150 | 167 | <5.0 | <5.0 |
| Total Dissolved Solids (TDS), mg/L | 641 | 552 | 630 | 506 |
| Phenols, mg/L | 58 | 24.9 | 53 | 24.1 |
| Oil and grease, mg/L | 39 | 13 | 6 | 8 |

The results showed that WP contained higher contamination levels in the syngas cleaning water than BP, particularly COD, phenols, and oil and grease. The membrane filter press performed effectively in removing TSS. Furthermore, the overall treatment process reduced BOD, COD, and oil and grease levels. However, the system remained ineffective in reducing TDS and phenols, indicating the need for additional treatment processes if the water was to be discharged from the system.

## CONCLUSIONS

Using BP as fuel in syngas production helped address key limitations of biomass, particularly tar formation. Although the gasification system in this study already included a syngas cleaning unit and generated relatively low tar levels, the inherently lower volatile matter in BP further reduced tar production. However, this characteristic led to a higher feed rate, resulting in lower system efficiency than wood pellets (WP). Despite this, BP offered clear

PPC & PETROMAT SYMPOSIUM 2025

environmental benefits, especially regarding wastewater quality, as reduced tar content led to lower contamination levels during syngas cleaning. BP was therefore a suitable alternative fuel for gasification systems with limited cleaning efficiency. It could also be used as a substitute for coal in combustion due to its higher energy content and cleaner combustion characteristics.

## ACKNOWLEDGEMENTS

The authors would like to acknowledge Thailand Science Research and Innovation (TSRI) for funding support for this study.

## REFERENCES

**ASTM D4239,** *Standard Test Method for Sulfur in the Analysis Sample of Coal and Coke Using High-Temperature Tube Furnace Combustion*. American Society for Testing and Materials.
**ASTM D5373,** *Standard Test Methods for Determination of Carbon, Hydrogen and Nitrogen in Analysis Samples of Coal and Carbon in Analysis Samples of Coal and Coke*. American Society for Testing and Materials.
**ASTM D5865,** *Standard Test Method for Gross Calorific Value of Coal and Coke. ASTM D7582, Test Methods for Proximate Analysis of Coal and Coke by Macro Thermogravimetric Analysis*. American Society for Testing and Materials.
**Basu, P.** (2013). *Biomass Gasification, Pyrolysis, and Torrefaction – Practical Design and Theory.* Elsevier Inc.
**Bridgwater, A. V.** (2012). *Review of fast pyrolysis of biomass and product upgrading*. Biomass and Bioenergy, **38**, 68–94.
**Chen, Q., Zhou, J.S., Liu, B., Mei, Q. and Lou, Z.Y.** (2010). *Influence of Torrefaction Pretreatment on Biomass Gasification Technology*. Chinese Science Bulletin. **56 (14)**, 1449-1456.
**Fisher, E.M., Dupont, C., Darvell, L.I., Commandre, J.M., Saddawi, A., Jones, J.M., Grateau, M. Nocquet, T. and Salvador, S.** (2018). *Combustion and gasification characteristics of chars from raw and torrefied biomass*, http://hal.archives-ouvertes.fr/hal-01688420, 7 June 2020.
**McKendry, P.** (2002). *Energy production from biomass (part 3): gasification technologies*. Bioresource Technology, **83**, 55 – 63.
**Nunes, L.J.R., Matias, J.C.O.** (2020). *Biomass torrefaction as a key driver for the sustainable development and decarbonization of energy production*. Sustainability, **12,** 922.
**Pelaez-Samaniego, M.R., Yadama, V., Garcia-Perez, M., Lowell, E. and McDonald, A.G.** (2014). *Effect of Temperature during Wood Torrefaction on the Formation of Lignin Liquid Intermediates.* Journal of Analytical and Applied Pyrolysis. **109**, 222-233.
**Raut, M.K., Basu, P. and Acharya, B.** (2016). *The effect of torrefaction pre-treatment on the gasification of biomass*. International Journal of Renewable Energy & Biofuels, **2016**, Article ID 823723.
**Slivka, R.M., Chinn, M.S. and Grunden, A.M.** (2011). *Gasification and synthesis gas fermentation: an alternative route to biofuel production*. Biofuels, **2 (4)**, 405-419.

PPC & PETROMAT SYMPOSIUM 2025

# A STUDY OF TAR FROM 3-STAGE GASIFICATION TECHNOLOGY USING WOOD AND TORREFIED PELLETIZED FEEDSTOCK

*Thanita Sonthisawate*[*,a], Panida Thepkhun[a], Chatuphon Uthaisri[a], Niramai Traiyawong[a], Waranyu Phondet[a], Phattacharee Jaiaun[a], Napaporn Klaijieam[a], Manoo Boonsae[a], Piyanan Sreesiri[a]

[a] Expert Center of Innovative Clean Energy and Environment, Thailand Institute of Scientific and Technological Research, Pathum Thani, Thailand

Keywords: Gasification, Pelletized wood, Torrefied pellet, Tar

## ABSTRACT

Tar is a byproduct of biomass thermal decomposition, particularly formed under pyrolysis reaction conditions (200–500 °C). The quantity and chemical composition of tar are influenced by several variables such as feedstock, reaction temperature, and the air supply to the system. This study aims to investigate the tar produced through a 3-stage gasification, a thermochemical process that converts solid biomass into combustible gas for thermal or electrical energy production. This process contributes to enhancing energy resilience and supports the valorization of agricultural residues and other locally available biomass resources. Pyrolysis-GC/MS analysis was used to characterize tar from pelletized wood and torrefied pellets, purchased from 2 different companies. The results indicate a substantial variation in chemical composition between the two feedstocks. The tar from wood pallets was predominantly composed of phenol (49%), followed by aldehyde (14%), aliphatics (6%), heterocyclic (6%), and acids (6%). For torrefied pellets were primarily composed higher of phenol (69%), along with notable proportions of alicyclic (7%) and aldehyde compounds (6%). Under the operation of the 3-stage gasification, the measured tar yields for wood and torrefied pellets were 0.478 g/Nm³ and 0.069 g/Nm³, respectively. The tar composition of the 2 feedstocks prominently comprised of PAHs with 48% and 68%, consecutively.

***thanita@tistr.or.th**

## INTRODUCTION

As the world continues to search for cleaner and more sustainable energy sources, biomass has gained increasing attention due to its renewable nature and potential to reduce greenhouse gas emissions. Unlike fossil fuels, biomass is considered carbon-neutral due to the released carbon during combustion is part of a short-term carbon cycle (McKendry, 2002; Demirbaş, 2005). One promising way to utilize biomass effectively is through gasification; a thermal process that converts solid biomass into a gaseous fuel known as syngas. This syngas is mainly consisting of carbon monoxide (CO), hydrogen ($H_2$), methane ($CH_4$), and carbon dioxide ($CO_2$), which can be used for generating electricity, heat, or as a raw material for synthetic fuels (Basu, 2010).

In recent years, wood pellets have become a popular choice for gasification due to their compact size, consistent shape, and relatively low moisture content. However, these pellets can still have drawbacks, such as low thermal stability and high oxygen content, which may

lower the efficiency of gas production. To address this, a process called torrefaction has been introduced as a pretreatment technique. This involves heating biomass at moderate temperatures (typically between 200–300°C) in the absence of oxygen, which improves its energy density, moisture resistance, and grindability (Van der Stelt *et al.*, 2011 ;Wannapeera and Worasuwannarak, 2012). Although torrefied pellets show promise, it is still necessary to understand how this treatment affects gasification outcomes, particularly in terms of gas composition and byproducts like tar. Tar is a sticky, tarry substance made up of complex hydrocarbons that form during gasification. If not properly managed, it can condense in pipelines or equipment, leading to blockages and increased maintenance costs(Devi *et al.*, 2003; Milne *et al.*, 1998). Therefore, studying how much tar is produced and what it's made of is crucial when evaluating biomass gasification systems.

This study focuses on comparing the performance of conventional wood pellets with torrefied pellets when used in a 3-stage gasifier. The goal is to measure and compare the quality and quantity of syngas like CO, $H_2$, $CH_4$, and $CO_2$ from each feedstock, as well as the amount and composition of tar generated. Through this comparative approach, the findings may help improve the design and operation of cleaner, more efficient systems for converting biomass into useful energy.

## EXPERIMENTAL

### *A. Materials*

Two types of biomass feedstock were used in this study: conventional wood pellets and torrefied pellets, both with an approximate diameter of 0.8 cm. These materials were subjected to preliminary chemical and physical characterization, including moisture content, volatile matter, fixed carbon, and ash content, along with ultimate analysis and calorific value determination. The analyses were conducted in accordance with standard ASTM methods: D7582 for proximate analysis, D5373 and D4239 for elemental analysis, and D5865 for calorific value measurement. The results are summarized in Table 1. The calorific value of the torrefied pellets was found to be higher than that of the untreated wood pellets. This can be attributed to thermal pretreatment during torrefaction, which leads to a reduction in volatile content and an increase in fixed carbon. As a result, torrefied biomass tends to have greater energy density and combustion potential.

### *B. Pyrolysis Gas Chromatography Mass Spectrometry (Py-GC/MS)*

For qualitative analysis of tar composition derived from pyrolysis, a Pyrolysis-Gas Chromatography/Mass Spectrometry (Py-GC/MS) system was employed. The system consisted of three key components: a pyrolyzer (Frontier, Model PY-3030D), which thermally decomposes solid samples into volatile compounds; a gas chromatograph (Agilent, Model 7890B) that separates these compounds based on their solubility and affinity within the separation column; and a mass spectrometer (Agilent, Model 5977A) that identifies the compounds by their mass-to-charge (m/z) ratios. The operating conditions are detailed as follows. The pyrolyzer operated at 500ºC for 0.20 min of hold time. The oven temperature program was controlled; the initial temperature started at 40ºC for 3 min and then heated to 200ºC with the 5ºC/min heating rate, the final temperature reached 350ºC with the 10ºC/min heating rate and 10 min of hold time. The mass spectra scanned from 20 to 800 m/z.

**Table 1.** Proximate and ultimate analysis of wood and torrefied pellets.

| | Wood pallet | | Torrefied pellets | |
|---|---|---|---|---|
| Proximate analysis, wt.% | As received | Dry basis | As received | Dry basis |
| Moisture | 7.05 | - | 9.03 | - |
| Volatile matter | 76.91 | 82.74 | 50.46 | 55.47 |
| Fixed carbon | 13.46 | 14.48 | 35.66 | 39.20 |
| Ash | 2.58 | 2.78 | 4.85 | 5.33 |
| Ultimate analysis, wt.% | As received | Dry basis | As received | Dry basis |
| Hydrogen, H | 6.58 | 6.23 | 5.33 | 4.75 |
| Carbon, C | 45.86 | 49.34 | 58.09 | 63.86 |
| Nitrogen, N | 0.34 | 0.37 | 0.57 | 0.63 |
| Oxygen, O | 44.58 | 41.22 | 31.16 | 25.43 |
| Sulfur, S | 0.06 | 0.06 | - | - |
| Heating value, kcal/kg | 3,890 | 4,190 | 5,030 | 5,520 |

### *C. 3-stage Gasification*

This study employed a 3-stage gasification (downdraft) system (Figure 1a) capable of processing up to 5-8 kg of biomass per hour. The system comprises 3 zones: The 1st Pyrolysis Zone – Biomass is thermally decomposed at 400–600°C in an oxygen-free environment, producing volatile gases, liquid tar, and char. The 2nd Oxidation Zone – This is the most critical stage, where partial combustion occurs at temperatures between 800–1,100°C. Limited air (20–40% of the stoichiometric requirement for complete combustion) is introduced, producing CO, $CO_2$, $H_2$, $CH_4$, and $H_2O$. The 3rd Reduction Zone – The final stage involves endothermic reactions that convert remaining $CO_2$ and char into additional syngas. The temperature in this zone is lower, typically around 500–800°C. The product gas produced from the gasification was analyzed by the ETG MCA100 SYN P analyzer. The tar was collected by tar collector system with a steady flow rate of 5 L/min for 30 minutes (Figure 1b). The tar was absorbed by the isopropanol which further evaporated out to get the amount of tar. The composition of tar was observed by the GC/MS.

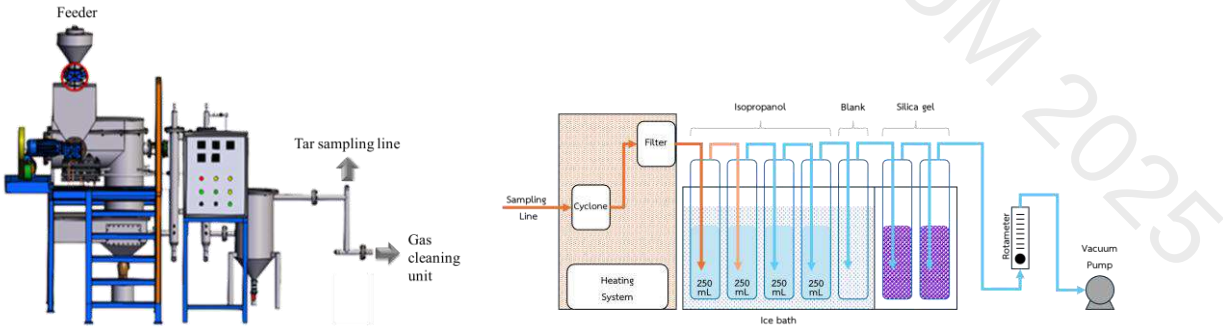


(a) (b)

Figure 1. (a) 3-stage Gasification and (b) Tar collector system.

PPC & PETROMAT SYMPOSIUM 2025

## RESULTS AND DISCUSSION

### *A. Pyrolysis Gas Chromatography Mass Spectrometry (Py-GC/MS)*

To differentiate the chemical composition of tars produced from various feedstocks, Py-GC/MS analysis was performed at 500°C on samples derived from wood pellets and torrefied pellets. In this study, the classification of tar was divided into 13 groups: as alicyclic, aliphatics, aromatics, esters, furans, heterocyclic, naphthalenes, polycyclic aromatic hydrocarbons (PAHs), phenols, amine, acids, aldehydes, and others. The compositions from wood and torrefied pellets contained 43 and 45 compounds, respectively. Both wood and torrefied materials shared similar compositions, dominated by phenols, accounting for 49% and 69%, respectively. This composition was classified as a primary tar. Normally, Primary tar compounds are formed during pyrolysis by decomposition of biomass building blocks and consists of acids, sugars, alcohols, ketones, aldehydes, phenols, catechols, guaiacols, syringols, furans and oxygenates, that pyrolyzed at temperature lower than 500°C (Milne *et al.*, 1998; Rios *et al.*, 2018).

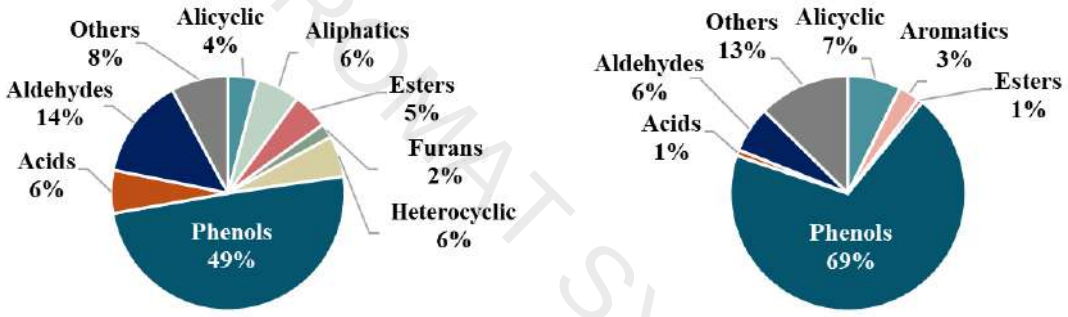


Figure 2. Tar compounds from Py-GC/MS of (a) wood pallet and (b) torrefied pallet.

### *B. 3-stage Gasification*

The 3-stage gasifier was controlled to produce syngas with a heat content of 4 MJ/Nm$^3$. The operated conditions for using wood pellets as a feedstock were identified with an average Equivalent Ratio (ER) of 0.20 and the syngas composition averaged out of 5.31% $CH_4$, 13.81% CO, and 6.91% $H_2$. However, for torrefied pellets, the operated condition was attained with a lower ER ratio of 0.12 and the syngas compositions consisted of 3.43% $CH_4$, 15.30% CO, and 8.54% $H_2$. In terms of ER, typically, the gasification of biomass should lie between 0.2 and 0.3 (Basu, 2010). However, for torrefied, it has higher heating value (higher energy density) with increased fixed carbon and reduced volatile content. This provided enough thermal energy with less oxidizing agents, and as a result the amount of air demand could be reduced. Moreover, the decreasing of oxygen-to-carbon (O/C) ratio (carbon-rich feedstock) required less air to avoid complete combustion to maintain syngas production. The lower reactivity by structural changing from torrefaction of the biomass proceeds more slowly. By those effects lead to a reduction in the optimal ER for torrefied feedstocks compared to raw biomass as well as lower feed rate of feedstock (Prins et al., 2006; Phanphanich and Mani, 2011; Chen *et al.*, 2015; Eling *et al.*, 2024).

PPC & PETROMAT SYMPOSIUM 2025

**Table 2.** Yield of syngas, char, and tar produced from, wood pallet and torrefied pellets.

| | Wood pallet | Torrefied pellets |
|---|---|---|
| Feed rate, kg/h | 6.31 | 4.91 |
| Equivalent ratio | 0.20 | 0.12 |
| Gas volume, $Nm^3/h$ | 23.90 | 25.49 |
| Calorific Value or CV, $MJ/Nm^3$ | 4.26 | 3.93 |
| Char, kg/hr | 0.88 | 1.29 |
| Tar, $g/Nm^3$ | 0.479 | 0.069 |

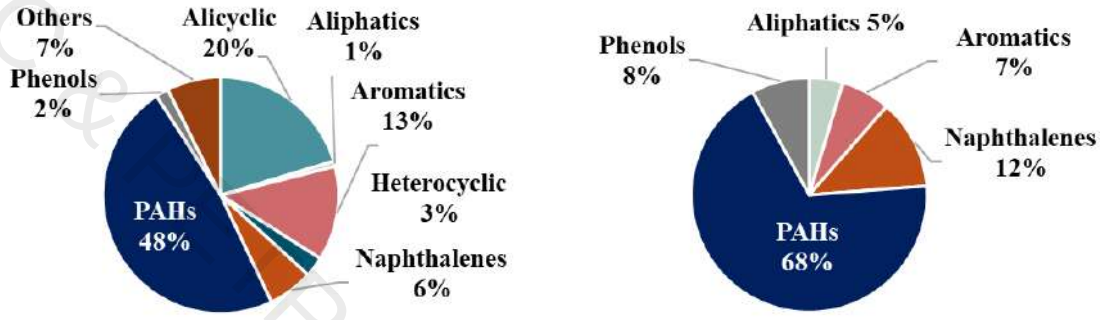


(a) (b)

Figure 3. Tar compounds from 3-stage gasification of (a) wood pallet and (b) torrefied pallet.

The amount of tar generated from several downdraft gasifiers were ranging from 0.060-32.3 $g/Nm^3$ (Rios *et al.*, 2018). In this study, tar produced from the 3-stage gasifier, were relatively low as 0.479 $g/Nm^3$ of wood pallet and 0.069 $g/Nm^3$ of torrefied pallet. The latter exhibited lower tar owing to their lower volatile matter compared to the former one. This aligned with the recent studied (Eling *et al.*, 2024), revealed and confirmed that torrefaction process leads to loss of surface and bound moisture, lowering of volatile matter content and depolymerisation of lignin. For the tar composition, wood pellets contained a wide range of compounds up to 108 different chemical species compared to 9 in torrefied pellets. The highest composition found from both materials were PAHs with 48% and 68%, consecutively. Due to the higher reaction temperature during the partial oxidation (the 2$^{nd}$ zone) and the reduction (the 3$^{rd}$ zone), light PAHs (2-3 rings PAHs as naphthalene, indene, biphenyl, anthracene) and heavy PAHs (> 4 rings as toluene, xylenes, ethylbenzene (excluding benzene)) were normally found around reaction temperature 800-900 °C (Nicolaou, 2016). Moreover, according to the potential evolution pathways of cellulose, hemicellulose, and lignin during biomass torrefaction, as the temperature further increases the aromatization and condensation may undergo formed PAHs (Wang *et al.*, 2025).

## CONCLUSIONS

This study highlights the impact of feedstock properties on gasification performance and tar characteristics using a 3-stage gasifier. Both wood pellets and torrefied pellets demonstrated effective syngas production. However, torrefied pellets yielded higher CO and $H_2$ concentrations at a lower equivalent ratio (ER), primarily due to their increased carbon content and reduced volatile matter. The lower ER requirement for torrefied

PPC & PETROMAT SYMPOSIUM PROCEEDINGS 2025

feedstocks indicates greater energy density, minimizing the need for oxidizing agents and supporting partial oxidation conditions. Tar generation was substantially reduced when using torrefied pellets (0.069 g/Nm³) compared to wood pellets (0.479 g/Nm³), corresponding with their lower volatile content and altered biomass structure. Furthermore, higher PAH concentrations were observed in torrefied pellet tars, likely due to the thermal decomposition pathways enhanced during high-temperature stages of gasification. These findings suggest that torrefied pellets offer advantages in syngas quality and tar mitigation, making them promising candidates for cleaner thermochemical conversion processes. The results provide valuable insight into feedstock optimization and tar behavior, which are critical for advancing efficient and sustainable biomass gasification technologies.

## ACKNOWLEDGEMENTS

The authors would like to express their grateful acknowledgment to the Thailand Science Research and Innovation (TSRI) for the financial support (Project no.198303).

## REFERENCES

**Basu, P.** (2010). *Biomass Gasification and Pyrolysis: Practical Design and Theory*. Academic Press.

**Chen, W. H., Peng, J., and Bi, X. T.** (2015) Renew. Sust. Energ. Rev., 44, 847–866.

**Demirbaş, A.** (2005) Prog. Energ. Combust., 31 **(2)**, 171–192.

**Devi, L., Ptasinski, K. J., and Janssen, F. J. J. G.** (2003) Biomass Bioenerg., 24 **(2)**, 125–140.

**Eling, J., Okot, D. K., Menya, E., and Atim, M.R.** (2024) Biomass Bioenerg., 184, 107210.

**McKendry, P.** (2002) Bioresource Technol., 83 **(1)**, 47–54.

**Milne, T. A., Evans, R. J., and Abatzoglou, N.** (1998). Biomass gasifier "tars": Their nature, formation, and conversion. NREL/TP-570-25357, National Renewable Energy Laboratory.

**Nicolaou, P.** (2016). *Removal, Utilization and Separation of Tars from Syngas.* MS Delft: Delft University of Technology.

**Phanphanich, M., and Mani, S.** (2011) Bioresource Technol., 102 **(2)**, 1246–1253.

**Prins, M. J., Ptasinski, K. J., and Janssen, F. J. J. G.** (2006) Energy, 31 **(15)**, 3458–3470.

**Rios, M. L. V. González, A. M., Lora, E. E. S., Olmo, O. A. A.,** (2018) Biomass Bioenerg., 108, pp. 345–370.

**Van der Stelt, M. J. C., Gerhauser, H., Kiel, J. H. A., and Ptasinski, K. J.** (2011) Biomass Bioenerg., 35 **(9)**, 3748–3762.

**Wang, Y., Guo, S., Qin, Y., Wang, W., Vassilev, S. V., He, C., Wei, Y., and Vassileva, C. G.** (2025) Energy, 318, 134912

**Wannapeera, J., and Worasuwannarak, N.** (2012) Enrgy. Proced., 14, 1126–1132.

PPC & PETROMAT SYMPOSIUM 2025

# A UTILIZATION OF GASIFICATION CHAR FROM STERILIZED MEDICAL WASTE FOR $H_2S$ REMOVAL IN BIOGAS PURIFICATION

*~~Napaporn Klaijieam~~* [a], *Panida Thepkhon* [a], *Niramai Traiyawong* [a], *Thanita Sonthisawate* [a], *Chatuphon Uthaisri* [a], *Manoo Boonsae* [a], *Warunyu Phondet* [a], *Phattacharee Jaiaun* [a]

[a)] Expert Center of Innovative Clean Energy and Environment, Thailand Institute of Scientific and Technological Research, Pathum Thani 12120, Thailand

Keywords: Gasification char, Waste Utilization, Biogas cleaning, Sterilized medical waste

## ABSTRACT

This study focuses on the utilization of char derived from a 3-stage gasification process using sterile waste mixed with wood chips as fuel for hydrogen sulfide ($H_2S$) adsorption in biogas. Conducted at the laboratory scale, the research aims to determine the factors influencing and the efficiency of the adsorption system. The char, with particle sizes of 1.18–2.36 mm, exhibited a fixed carbon content of 63.35%, an iodine number of 1,097.61 mg/g, a surface area of 72.78 $m^2/g$, and a pore size of 5.1 nm, indicating substantial physical adsorption potential. Major mineral components include CaO (18.947%), $K_2O$ (5.089%), $Fe_2O_3$ (2.924%), $Al_2O_3$ (1.585%), and MgO (1.495%), which promote the formation of metal sulfides and sulfates on the carbon surface. According to international biochar standards (e.g., ANZBI, EBC, IBI), such char contains heavy metals exceeding the limits (Cu, Hg, Zn), making them unsuitable for soil amendment. In addition, the raw material does not meet the accepted agricultural classification, despite its $H_2S$ adsorption potential. The adsorption experiments were conducted in an acrylic-packed column (ID 4.4 cm, height 50.0 cm) using biogas containing 1,000 $ppm_v$ $H_2S$. The experiment was designed using response surface methodology (RSM) to identify optimal conditions. Biogas flow rates (0.6–1.0 L/min) and adsorbent weights (60–140 g) were varied. The optimal conditions for $H_2S$ removal efficiency were found to be 140 g of char at 0.8 L/min flow rate. The breakthrough time, when outlet $H_2S$ exceeded 80% of inlet concentration, was 145 minutes.

[*] **napaporn_pa@tistr.or.th**

## INTRODUCTION

The COVID-19 pandemic has led to a significant surge in infectious waste, particularly in July 2021, when the recorded volume reached 294 tons per day, representing a 94% increase. (Department of Health, 2021). The majority of this waste consists of single-use materials, creating a pressing challenge for waste management systems. In response, the Thailand Institute of Scientific and Technological Research (TISTR) has implemented a demonstration-scale 3-stage gasification system at the Lamtakhong Research Station in Nakhon Ratchasima. This system processes up to 7 tons of sterilized medical waste and biomass per day, converting them into energy through thermal decomposition. The

PPC & PETROMAT SYMPOSIUM 2025

gasification process produces syngas (comprising hydrogen and carbon monoxide), valuable byproducts (char), as well as waste (i.e. ash and wastewater). Notably, char, which was primarily composed of carbon, exhibits a porous structure and a surface area suitable for adsorption applications. Given these structural and chemical properties, this research aimed to study the utilization of char derived from gasification of sterilized medical waste mixed with wood chips as an adsorbent for hydrogen sulfide ( $H_2S$) removal in biogas purification. Laboratory-scale experiments are conducted to evaluate the adsorption efficiency and key influencing factors. The findings will also support Thailand's long-term goal of improving waste-to-energy solutions and minimizing environmental impacts and promote circular economy principles

## EXPERIMENTAL

*A. Material*

The char obtained from a 3-stage gasification using sterilized medical waste mixed with wood chips was sieved to obtain particle sizes ranging from 1.18 to 2.36 mm and then dried at 105°C for 2 hours to remove residual moisture.

*B. Characterization of Adsorbent Material*

The adsorbent was characterized for its physicochemical and structural properties. Proximate analysis was conducted to determine moisture content, ash, volatile matter, and fixed carbon, along with bulk density and iodine number for surface activity. BET analysis was used to evaluate specific surface area, pore volume, and pore diameter. XRF were applied to identify crystalline phases and elemental composition, respectively. Functional groups were examined using FTIR spectroscopy (4000–400 cm. Surface morphology was observed via SEM after gold coating.

*C. Experimental Setup and Design*

A packed column adsorption system was designed using an acrylic column with an outer diameter of 5.0 cm, an inner diameter of 4.4 cm, and a height of 50.0 cm. The packed bed contained a 49.0 cm layer of the prepared adsorbent, supported by a mesh screen at the base. The setup was schematized in Figure 1. The study employed a central composite design (CCD) under response surface methodology (RSM) to determine optimal operating conditions. Two primary variables were investigated: biogas flow rates of 0.6, 0.7, 0.8, 0.9, and 1 L/min and adsorbent weights of 60, 80, 100, 120, and 140 g. Table 1 shows the range levels of each factor (variable) studied. As a result, the complete design matrix of the experiments was shown in Table 3. For two variables, 4 factorial points, 4 axial points, and 5 replicates at the center points were employed, as calculated from equation 1 (Ismail et al., 2020):

$$N = 2^n+2n+n_c = 2^2+2*2+5 = 13 \quad (1)$$

In the above equation, N was the total number of experiments, n was the number of factors, and $n_c$ was the number of replicates of center points.

**Table 1** Design of experiments: factors and levels in CCD

| Independent variables | Factor code | Level of factors | | | | |
|---|---|---|---|---|---|---|
| | | -1.414 | -1 | 0 | 1 | 1.414 |
| Biogas flow rate (L/min) | $X_1$ | 0.6 | 0.7 | 0.8 | 0.9 | 1 |
| Adsorbent weight (g) | $X_2$ | 60 | 80 | 100 | 120 | 140 |

*D. Biogas Purification Procedure*

The biogas used in the experiments contained 1,000 $ppm_v$ $H_2S$, 60% $CH_4$, and 40% $CO_2$. The adsorption performance was assessed based on the concentration of $H_2S$ at the outlet, which was measured using a biogas analyzer (Geotech Biogas 5000). The experimental steps included system leakage testing, loading the packed column with char adsorbent, adjusting biogas flow rates according to the experimental design, and monitoring adsorption efficiency. Statistical analysis, including analysis of variance (ANOVA) and response surface plots, was performed to identify the optimal adsorption conditions.

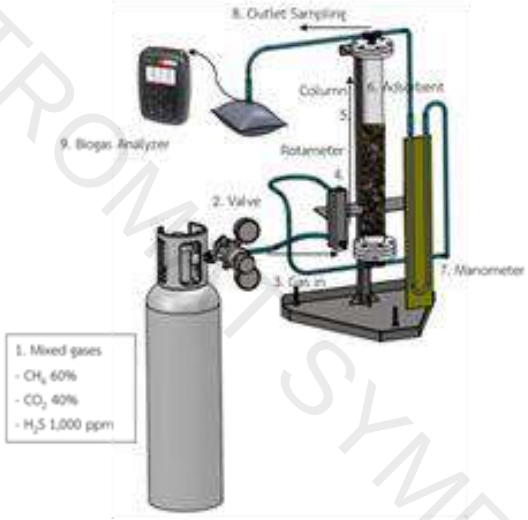


**Figure 1** Schematic diagram of the $H_2S$ adsorption unit used in the experimental setup

## RESULTS AND DISCUSSION

*A. Characterization of Adsorbent Material*

The physicochemical characterization of the char demonstrated a high fixed carbon content (63.35 wt%) and a high iodine number, indicating its potential as an effective $H_2S$ adsorbent. The high CaO content (18.9 wt%), which was a basic oxide, enhanced the surface alkalinity of the material. This increased alkalinity facilitated the adsorption of acidic gases such as $H_2S$, as summarized in Table 2, may contribute to the formation of metal sulfides and sulfates on the char surface during $H_2S$ adsorption (Hervy et al., 2018). Despite the heavy metal contents of Cu, Hg, and Zn exceeding international biochar standards (e.g., ANZBI, EBC, IBI), thereby rendering the material unsuitable for soil amendment, the high carbon content and the presence of these inorganic oxides align with

PPC & PETROMAT SYMPOSIUM 2025

the findings of Pelaez-Samaniego et al. (2020), who emphasized the role of carbon structure and surface oxides in enhancing $H_2S$ adsorption mechanisms.

**Table 2** Summary of physical and chemical properties, major oxides (XRF), and metals content of the gasification char

| Physical and Chemical | | | Major oxides (XRF) | | | Metals content | | |
|---|---|---|---|---|---|---|---|---|
| Properties | Unit | Result | Composition | Unit | Result | Metals | Unit | Result |
| Moisture | Wt %. | 10 | CaO | Wt %. | 18.947 | Cd | mg/kg | ND |
| Ash | Wt %. | 14.05 | $SiO_2$ | Wt %. | 5.089 | Hg | mg/kg | ND |
| Volatile matter | Wt %. | 11.91 | $K_2O$ | Wt %. | 2.924 | Ni | mg/kg | 69.9 |
| Fixed carbon | Wt %. | 63.35 | $Fe_2O_3$ | Wt %. | 1.585 | Cr | mg/kg | 28.8 |
| True density | g/cm³ | 1.8 | $Al_2O_3$ | Wt %. | 1.495 | Pb | mg/kg | 1.74 |
| Iodine number | mg/g | 1097.6 | MgO | Wt %. | 1.273 | Cu | mg/kg | 213 |
| BET surface area | m²/g | 72.78 | $Na_2O$ | Wt %. | 0.973 | Zn | mg/kg | 1299 |
| Pore size | nm | 5.1 | $P_2O_5$ | Wt %. | 0.907 | | | |

Figure 2 illustrated the FTIR spectra of the char, which revealed a broad O–H stretching band at 3421 $cm^{-1}$ and a C–O stretching peak at 1086 $cm^{-1}$, attributed to moisture content or presence of hydroxyl, phenol or ether groups that enhanced $H_2S$ adsorption. Peaks at 2922–2851 $cm^{-1}$ (aliphatic C–H) and 1627 $cm^{-1}$ (aromatic C=C). These oxygen-containing groups increased surface polarity and provided acid-base and redox active sites, which were favorable for $H_2S$ removal. Overall, the presence of these functional groups confirmed the char's suitability as an $H_2S$ adsorbent. (Pelaez-Samaniego et al., 2020).

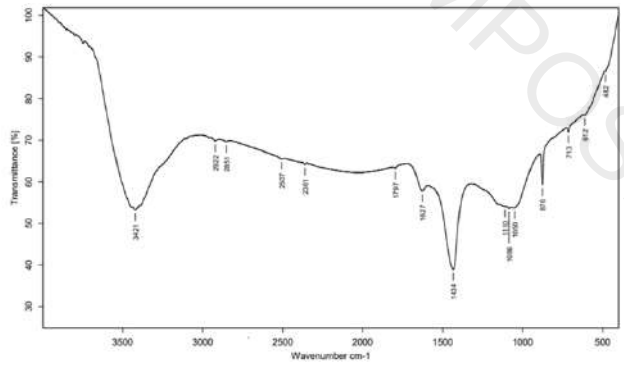


**Figure 2** FTIR spectra of the gasification char

*B. Responses obtained from adsorption test*

The $H_2S$ adsorption time results using gasification char are shown in Table 3. The optimal conditions consisted of a biogas flow rate ($x_1$) of 0.8 L/min and an adsorbent weight ($x_2$) of 140 g. Under these conditions, the system yielded a maximum adsorption time of 145

minutes at 80.15% $H_2S$ removal efficiency. The model-predicted value of 141.90 minutes closely matched the observed value. Some deviations between the actual and predicted values may result from experimental variations such as slight inconsistencies in biogas flow, char packing, or environmental conditions during trials which are common in lab-scale setups. However, these deviations are within an acceptable range, and the high coefficient of determination ($R^2$ = 0.9137) confirms that the model is both reliable and accurate in predicting $H_2S$ removal efficiency.

**Table 3** Actual variable levels and codes from CCD experimental design, and results for $H_2S$ adsorption

| Run No. | Uncoded variables | | Coded variables | | Breakthrough time (min) | |
|---|---|---|---|---|---|---|
| | Biogas flow rate, (L/min) | Adsorbent weight, (g) | $X_1$ | $X_2$ | Actual | Predicted |
| 1 | 0.7 | 80 | -1 | -1 | 35 | 25.87 |
| 2 | 0.9 | 80 | 1 | -1 | 29 | 50.54 |
| 3 | 0.7 | 120 | -1 | 1 | 85 | 70.87 |
| 4 | 0.9 | 120 | 1 | 1 | 74 | 100.54 |
| 5 | 0.6 | 100 | -1.141 | 0 | 120 | 53.23 |
| 6 | 1 | 100 | 1.141 | 0 | 47 | 107.56 |
| 7 | 0.8 | 60 | 0 | -1.141 | 50 | 46.90 |
| 8 | 0.8 | 140 | 0 | 1.141 | 145 | 141.90 |
| 9 | 0.8 | 100 | 0 | 0 | 39 | 36.52 |
| 10 | 0.8 | 100 | 0 | 0 | 39 | 36.52 |
| 11 | 0.8 | 100 | 0 | 0 | 44 | 36.52 |
| 12 | 0.8 | 100 | 0 | 0 | 39 | 36.52 |
| 13 | 0.8 | 100 | 0 | 0 | 39 | 36.52 |

ANOVA results (Table 4) showed that adsorbent weight ($X_2$), the interaction between biogas flow rate and adsorbent weight ($X_1X_2$), and the quadratic effect of biogas flow rate ($X_1^2$) significantly influenced $H_2S$ adsorption time ($p < 0.05$) (Saleh et al., 2024).

**Table 4** Analysis of variance (ANOVA) suitable for $H_2S$ adsorption

| Source of Variation | Coefficient | P-value | Remarks |
|---|---|---|---|
| Constant | 44.14 | <0.00002 | significant |
| $X_1$ | -1.75 | 0.4438 | not significant |
| $X_2$ | 13.25 | <0.0004 | significant |
| $X_1X_2$ | 15.75 | <0.0039 | significant |
| $X_1^2$ | -6.62 | <0.0038 | significant |
| $X_2^2$ | -2.12 | 0.2172 | not significant |

*C. Biogas Purification Results*

Figure 3(a) (3D plot) illustrated the effects of biogas flow rate and absorbent weight on $H_2S$ breakthrough time, showing that lower flow rates and higher absorbent weights prolonged

PPC & PETROMAT SYMPOSIUM 2025

breakthrough time, while higher flow rates reduced it. This finding was consistent with the research conducted by Rahman et al. (2019). A nonlinear relationship and interaction effect between the variables were observed. Figure 3(b) (contour plot) confirmed this trend, with green-yellow regions indicating longer breakthrough times at low flow rates and high absorbent weights, and blue regions representing faster breakthrough at higher flow rates, highlighting enhanced adsorption under these conditions.

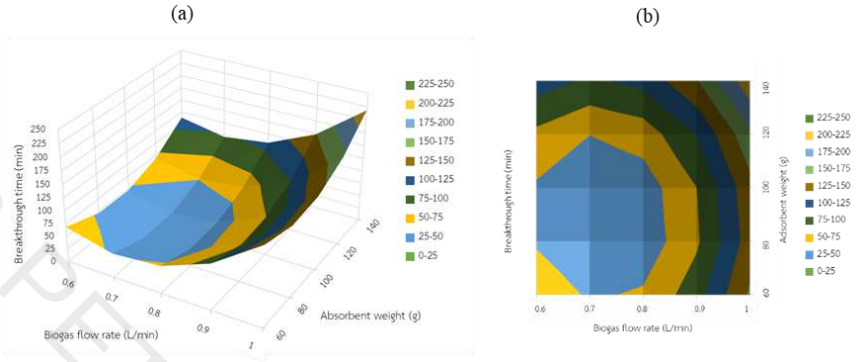


**Figure 3**(a) 3D plot showing the effects of biogas flow rate and adsorbent weight on $H_2S$ breakthrough time. (b) Contour plot confirming the interaction, indicating longer breakthrough at low flow rates and high adsorbent weights.

Figure 4(a) showed the breakthrough curve of $H_2S$ adsorption at 0.8 L/min and 140 g adsorbent, achieving 100% removal for 75 minutes and declining to 80.15% at 145 minutes before reaching equilibrium. Figures 4(b, d) showed SEM images of the char surface before adsorption, characterized by uniform pores. After adsorption (Figure 4(c, e)), the SEM images revealed partially destroyed or blocked pores due to reaction byproducts, indicating reduced adsorption capacity, which was consistent with research by Pelaez-Samaniego et al. (2020).

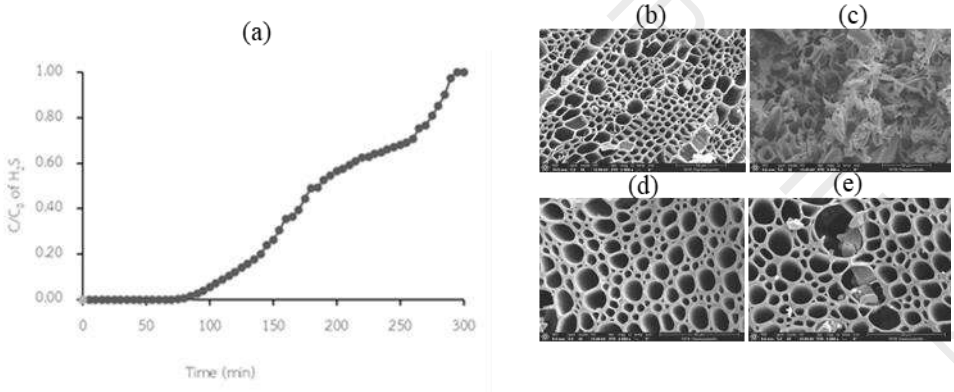


**Figure 4** (a) Breakthrough curve of $H_2S$ adsorption**,** SEM images of gasification char before (left) and after (right) $H_2S$ adsorption at different magnifications: (b) 2000x before adsorption; (c) 2000x after adsorption; (d) 4000x before adsorption; (e) 4000x after adsorption.

## CONCLUSIONS

waste and biomass as an effective adsorbent for $H_2S$ removal from biogas. The char's physicochemical properties, including its surface area and pore structure, enabled it to adsorb $H_2S$ effectively. RSM employing CCD was applied to determine the optimal operating conditions, identifying a biogas flow rate of 0.8 L/min and an adsorbent weight of 140 g, achieving a breakthrough time of 145 minutes and an $H_2S$ removal efficiency of 80.15%. The results highlighted the importance of integrating statistical design with process engineering to optimize adsorptive systems. Overall, this research supports sustainable biogas purification and promotes circular economy practices.

## ACKNOWLEDGEMENTS

The authors would like to acknowledge Thailand Science Research and Innovation (TSRI) for funding support for this study.

## REFERENCES

**Asquer, C. et al. (**2019). *Biomass ash characterisation for reuse as additive in composting process*. Biomass and Bioenergy, 123, pp 186–194.

**Hervy, M. et al.** (2018). *$H_2S$ removal from syngas using wastes pyrolysis chars.* Chemical Engineering Journal, 334(2018), pp 2179–2189.

**Ismail, M. N. bin, et al.** (2020). *Biomass-based activated carbon from Areca catechu for dye wastewater treatment*. Journal on Technical and Vocational Education (JTVE), 5(1).

**Kaewalin Pathomravee.** (2016). *Hydrogen sulfide removal from biogas using potassium permanganate-impregnated activated carbon (Master's thesis*, Chemical Engineering, Prince of Songkla University, Songkhla, Thailand).

**Köseog˘lu, E., & Akmil-Basar, C.** (2015). *Preparation, structural evaluation and adsorptive properties of activated carbon from agricultural waste biomass*. Advanced Powder Technology, 26, 811–818.

**Pelaez-Samaniego, M. R. et al.** (2020). *Chars from wood gasification for removing $H_2S$ from biogas.* Biomass and Bioenergy, 142(2020), pp 105754.

**Rahman, A. A. A. et al.** (2019). *Adsorption of Hydrogen Sulphide by Commercialized Rice Husk Biochar (RHB) & Hydrogel Biochar Composite (RH-HBC).* International Journal of Recent Technology and Engineering, 8(4), pp 6874-6870.

**Saleh, A. M., et al.** (2024). *Application of Response Surface Methodology (RSM) for optimization of hydrogen sulphide adsorption using coconut shell activated carbon xerogel: Effect of adsorption pressure and hydrogen sulphide flowrate.* Annales de Chimie - Science des Matériaux, 48(4), 509-518.

**Sawalha, H. et al.** (2020). *Removal of hydrogen sulfide from biogas using activated carbon synthesized from different locally available biomass wastes - a case study from Palestine.* Bioengineered, 11(1), pp 607–618.

**Sharifi, S. H., & Shoja, H.** (2018). *Optimization of process variables by response surface methodology for methylene blue dye removal using Spruce sawdust/MgO nanobiocomposite.* Journal of Water and Environmental Nanotechnology, 3(2), 157–172.

PPC & PETROMAT SYMPOSIUM 2025

# SULFONATED POLY(ETHER ETHER KETONE)/SULFONATED BETA ZEOLITE (S-PEEK/S-BETA) COMPOSITE PROTON EXCHANGE MEMBRANE FOR VANADIUM REDOX FLOW BATTERY

*Intan Elvina* [a,b], *Anuvat Sirivat* [a,b]

[a] The Petroleum and Petrochemical College, Chulalongkorn University, Bangkok, Thailand
[b] Conductive and Electroactive Polymers Research Unit, Chulalongkorn University, Bangkok, Thailand

Keywords: Sulfonated poly(ether ether ketone) (S-PEEK); Sulfonated beta zeolite (S-BETA); Proton exchange membrane (PEM); Vanadium redox flow battery (VRFB).

## ABSTRACT

Energy storage is an important key towards success in the shift to renewable energy. Vanadium redox flow battery (VRFB) is one of the promising storage systems that comes up with high capacity and long lifespan among other technologies. One of the paramount and important components that determines flow battery performances is the proton exchange membrane (PEM). Poly(ether ether ketone) (PEEK), a high-performance polymer, is a promising candidate to be developed as a PEM. Aiming to enhance the proton conductivity of the PEM, PEEK as the matrix phase was sulfonated to S-PEEK by reacting with concentrated $H_2SO_4$. Beta zeolite, an aluminosilicate mineral with high surface area and Si/Al ratio expected to improve both proton conductivity and thermomechanical stabilities, was prepared by reacting the Beta zeolite with 3-(mercaptopropyl)trimethoxy silane (MPTMS) as thiol precursor, followed by reacting with $H_2O_2$ 30%. The successful incorporation of S-BETA into S-PEEK matrix phase was characterized by the FTIR, STA, XRD, and FE-SEM techniques. S-BETA was loaded into S-PEEK at various volume fractions and cast in a petri dish. The 8% v/v incorporation of S-BETA zeolite into S-PEEK matrix exhibited the highest proton conductivity of $3.25\times10^{-2} \pm 1.9\times10^{-2}$ S.cm$^{-1}$ relative to the pristine S-PEEK and other composite membranes, as well as the improvement in the $V^{4+}$ ionic selectivity of $4.15\times10^{5} \pm 1.4\times10^{5}$ cm$^2$.sec$^{-1}$.

***anuvat.s@chula.ac.th**

## INTRODUCTION

Energy storage is an important key towards the success of the shift to renewable energy. Renewable sources, such as solar, wind, hydropower, biomass and waste, geothermal and wave and tidal, are expected to become alternatives to replace fossil fuels as the main share for producing electricity. Solar and wind are two stochastic power sources, in which power production can be partially predicted; they are projected to dominate the growth of new renewable energy power by supplying 46% and 70% of electricity in 2030 and 2050, respectively (Kumi, 2023). The dependency of these sources on the environment accounts for the fluidity of the energy produced and is one of the biggest obstacles in using it as a reliable energy source. The integration between the generating section and storage in the electricity grid is needed to achieve the system that can provide a stable power.

PPC & PETROMAT SYMPOSIUM 2025

One of the storage technologies that can comes up with high capacity and long lifespan is the flow battery or redox flow battery (RFB). In this battery, the energy is stored in electrolytes placed in two vessels, and the energy conversion is taken place in a stack with many cells (Doetsch *et al*., 2020). All-vanadium redox flow batterie (VRFB), which uses
vanadium with different oxidation states as catholytes ($V^{4+}$, $V^{5+}$) and anolytes ($V^{2+}$, $V^{3+}$), is the most common and promising RFB energy storage.

Proton exchange membrane (PEM) is one of the paramount and important components that determines VRFB performances. Several requirements that must be met as an ideal membrane for VRFBs are high proton conductivity, low water and vanadium permeability, low area resistance, good chemical stability, and inexpensiveness (Schwenzer *et al*., 2011
).
Just as the membrane functions as a separator to prevent electrolyte mixing, the membrane must also be semi-permeable for proton transport. These two properties, unfortunately, are intimately related. Once the membrane has good proton transfer, it is accompanied by high electrolyte ions cross-over which can lead to low energy efficiency.
Over the decades, developments in polymer membranes for VRFBs are aimed at finding a replacement for perfluorosulfonic acid-based membranes which include structural modifications as well as blending of materials into composites. PEEK, poly(ether ether ketone), is one of the auspicious materials that is expected to become an alternative by some modifications such as sulfonation and a mixing with other materials such as zeolite to form a composite membrane. Impregnation of zeolite, an aluminosilicate mineral, is expected to improve both proton conductivity and thermomechanical stabilities (Changkhamchom *et al*., 2019). Beta zeolite, which has a Si/Al ratio of 300 and a surface
area of 620 $m^2/g$, can be expected to provide improved proton transport, and its sulfonation can increase proton conductivity even more.

As the matrix phase in this work, S-PEEK was successfully prepared by reacting PEEK with concentrated $H_2SO_4$ at various reaction times. The S-BETA as the dispersed phase was successfully prepared by reacting the Beta zeolite with 3-(mercaptopropyl)trimethoxy silane (MPTMS) as thiol precursor, followed by reacting with $H_2O_2$ 30%. The incorporation of S-BETA into S-PEEK at various concentrations was then investigated for the correlation between S-BETA concentration and the membrane properties for VRFB.

## EXPERIMENTAL

### *A. Materials*

Poly(ether ether ketone) (PEEK; polyoxy-1,4-phenyleneoxy-1,4-phenylenecarbonyl-1,4-phenylene) was purchased from Sigma-Aldrich. Concentrated sulfuric acid ($H_2SO_4$, 98%) was purchased from RCL Labscan. Beta ($H^+$) zeolite (Si/Al ratio 300, surface area 620 $m^2/g$) was purchased from Zeolyst International. 3-(mercaptopropyl)trimethoxy silane (MPTMS, 96%) was purchased from TCI. Hydrogen peroxide ($H_2O_2$, 30%, AR grade) was purchased from Chem-supply. Vanadium (IV) sulphate oxide hydrate ($VOSO_4.xH_2SO_4$, 97%) was purchased from TCI. Magnesium sulphate 7-hydrate ($MgSO_4{\cdot}7H_2O$, AR grade) was purchased from Kemaus.

### *B. Membrane Preparation*



PPC & PETROMAT SYMPOSIUM 2025

PEEK pellet was dried overnight before use. 2.5 g of PEEK was dissolved in 50 mL of $H_2SO_4$ 98% and stirred for 30 minutes at room temperature. The solution was then continuously stirred at 60°C for 30 minutes, 1 hour, 2 hours, 3 hours, 5, and 7 hours (referred to as S-PEEK-a, S-PEEK-b, S-PEEK-c, S-PEEK-d, S-PEEK-e, S-PEEK-f respectively). Afterwards, the polymer solution was poured into an excess amount of ice, filtered for the precipitate, and then washed with DI water. The S-PEEK precipitate polymer was dried at 70°C for 24 hours. Beta zeolite powder was grinded and dried overnight. 2 g of Beta zeolite, 6 g of 3-(mercaptopropyl)trimethoxy silane (MPTMS, 96%) were added to a flask with 20 mL of toluene and stirred for 24 hours at 70°C with reflux. The mixture was then washed with toluene and DI water to obtain the BETA-SH and then dried at 80°C for 12 hours. Subsequently, the BETA-SH powder was added to a beaker containing $H_2O_2$ 30% at ratio 1:10 (mass:volume) and stirred at room temperature for 12 h. The mixture was then washed with DI water and dried at 80°C for 12 h. S-PEEK membranes were prepared by the dissolved 7% v/v of S-PEEK polymer in DMSO. The polymer solution was then cast in a petri dish and dried at 70°C for 24 hours to form the S-PEEK membrane. As for the composite membranes, various concentrations of S-BETA zeolite (0.4%, 0.8%, 2%, 4%, and 8%v/v) were added to the polymer solution. Then, each solution was cast in a petri dish and dried at 70°C for 24 hours to form the S-PEEK/S-BETA zeolite composite membrane.

*C. Characterization of S-BETA and S-PEEK*

A FT-IR spectrometer (Thermo Nicolet, Nexus 670) was used to observe the presence of sulfonic acid group in S-BETA, S-PEEK, and S-PEEK-f/S-BETA zeolite composite membranes. The characteristic peaks of BETA and S-BETA zeolite were observed by using x-ray diffraction (XRD) (Rigaku, Smartlab).

*D. Degree of Sulfonation (DS) and Ion Exchange Capacity (IEC)*

In order to determine the degree of sulfonation, the S-PEEK polymer was dissolved in N,N-dimethylformamide (DMF) for 24 hours. Subsequently, the solution was titrated with NaOH 0.1 N using a phenolphthalein indicator. The titrant consumed during titration was then used to determine the DS by following the equation (1):

$$DS = \frac{0.288 \times M_{NaOH} \times V_{NaOH}}{W - (0.081 \times M_{NaOH} \times V_{NaOH})} \quad (1)$$

where $M_{NaOH}$ is the molarity of NaOH (N), $V_{NaOH}$ is the NaOH solution volume (mL), and W is the dry weight of the membrane (g).

Ion exchange capacity (IEC) is the ability of a membrane in providing path for protons transport. Titration method was used to examine the IEC value in this work. The S-PEEK and S-PEEK-f/S-BETA membranes were immersed in a 0.1 M HCl solution for 24 hours and then washed with DI water. The membranes were then immersed in a 50 mL 1 M HCl solution for 12 hours. The amount of $H^+$ was determined by titration using a 0.01 M NaOH solution and phenolphthalein as indicator. The IEC value was then calculated by following the equation (2):

PPC & PETROMAT SYMPOSIUM 2025

$$IEC_{cation-membrane}(meq.g^{-1}) = \frac{V_{NaOH} \times N_{NaOH}}{W_d} \quad (2)$$

where $V_{NaOH}$ is the volume of NaOH solution (mL), $N_{NaOH}$ is the normality of NaOH used for titration (meq./mL), $W_d$ is the dry weight mass of the membranes (g).

*E. Proton Conductivity (σ)*

The proton conductivity of the membrane was calculated by measuring the membrane capacitance using a Keysight E4980A LCR Meter and Anton Paar Rheometer at a potential of 1 V and in the frequency range of 20 Hz - 1 MHz. The membranes were fully hydrated by immersing in DI water for 1 hour. They were then wiped out of excess water and cut into a diameter 2.5 cm before measurement. The ionic conductivity (σ) of the membranes was calculated by following the equation (3):

$$\sigma = \frac{d}{RS} \quad (3)$$

where R (Ohm) is the membrane resistance which was obtained from the linear extrapolation of the Nyquist plot onto the real impedance axis (Z'), d (cm) is the membrane thickness, and S ($cm^2$) is the membrane surface area.

*F. Vanadium ($V^{4+}$) Permeability (P) and Ion Selectivity (S)*

Ion selectivity (S) is the ratio of proton conductivity (σ) to the permeability of $V^{4+}$ ions. This parameter represents the balance between the amount of proton transfer and the $V^{4+}$ ions permeate through the membrane. The dialysis cell consisted of two reservoirs, which were the A cell filled with Vanadium solution and the B cell filled with blank solution, separated by the membrane which was used to determine the $V^{4+}$ permeability. The $V^{4+}$ concentration was measured by using a UV-Vis Spectrometer at 760 nm, and the permeability of the membrane was calculated by following the equation (4):

$$V_B \frac{dC_B(t)}{dt} = A\frac{P}{L}(C_A - C_B(t)) \quad (4)$$

where $V_B$ represents the volume of the B cell, $C_B(t)$ represents the $V^{4+}$ concentration as a function of time in the B cell, $C_A$ represents the $V^{4+}$ concentration in the A cell, A represents the area of the membrane, L represents the thickness of the membrane, $dC_B(t)/dt$ is the slope obtained from the UV-Vis measurement, and P represents the permeability of the $V^{4+}$ ions.

## RESULTS AND DISCUSSION

*A. Characterization of S-BETA and S-PEEK*

FT-IR spectra of BETA zeolite before and after sulfonation are shown in Figure 1a. The characteristic peaks at the wavenumbers of 1063 $cm^{-1}$ and 786 $cm^{-1}$ in the BETA zeolite spectrum can be assigned to the vibration of Si-O-Si bond in the framework of BETA zeolite. The characteristic peak at the wavenumber of 1055 $cm^{-1}$ in the S-BETA zeolite spectrum belongs to the Si-O-Si bond denoting the chemical framework of zeolite remaining. The peak at the wavenumber of 802 $cm^{-1}$ in the S-BETA spectra is assigned to the S-O bond signifying the success of BETA zeolite sulfonation (Mansour *et al*, 2022).

PPC & PETROMAT SYMPOSIUM 2025

The XRD pattern of the S-BETA in Figure 1b shows the characteristic peaks at 2 = 8.2°, 14.8°, 22.7°, 25.7°, and 27.2° indicating that the sulfonation process preserved the crystal structure of the Beta zeolite.

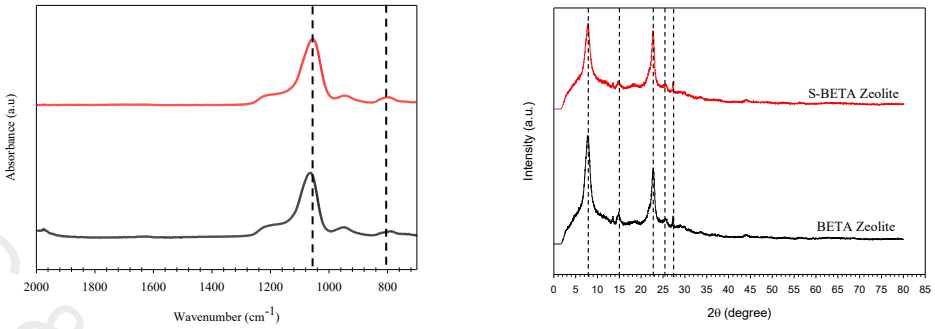


**a.** **b.**

Figure 1 (a) FTIR spectra of BETA and S-BETA zeolite, (b) XRD spectra of BETA and S-BETA zeolite.

The success of PEEK sulfonation can be seen in Figure 2. The broad peak in S-PEEK-f and S-PEEK-f/S-BETA-8% spectra at wavenumber around 3500 $cm^{-1}$ can be assigned for the -OH vibration of -$SO_3H$ functional group. The wavenumbers of 788 and 1064 $cm^{-1}$ in S-PEEK-f/S-BETA-8% spectra can be assigned for the symmetrical and anti-symmetrical Si-O-Si stretching vibrations, respectively.

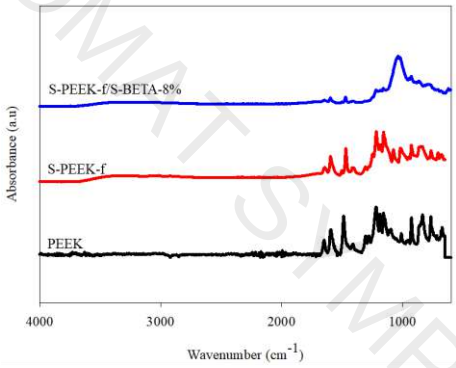


Figure 2 FTIR spectra of PEEK, S-PEEK and S-PEEK-f/S-BETA membranes.

*B. Degree of Sulfonation (DS) and Ion Exchange Capacity (IEC)*

DS of the S-PEEK was influenced by the reaction time, in which the longer the reaction time resulted in higher DS value as shown in Table 1. This is also in line with the IEC value. The presence of sulfonic acid groups provided the more ions $H^+$ therefore the ability of exchanging was higher with the highest DS value.

*C. Proton Conductivity (σ)*

Table 1 shows the proton conductivity values of S-PEEK membranes at various DS and composite membranes at various zeolite concentrations. By increasing the DS value, or providing more sulfonic acid groups, more protons were transported especially via the hopping mechanisms (Grotthuss mechanism) therefore enhancing the proton conductivity. Incorporation of S-BETA zeolite to the S-PEEK matrix phase provided the highest proton

PPC & PETROMAT SYMPOSIUM 2025

conductivity value at concentration 8%(v/v). The sulfonation modification in BETA zeolite enhanced the hydrophilicity of the zeolite which further improved the proton transport.

*D. Vanadium ($V^{4+}$) Permeability (P) and Ion Selectivity (S)*

Table 1. Degree of sulfonation, ion exchange capacity, proton conductivity, and $V^{4+}$ ion selectivity of S-PEEK and S-PEEK/S-BETA zeolite composite membranes.

| Membrane | DS (%) | IEC (meq.g$^{-1}$) | σ (S.cm$^{-1}$) | S (S.sec.cm$^{-3}$) |
|---|---|---|---|---|
| S-PEEK-b | 34.01 ± 0.008 | 1.02 ± 0.13 | $2.75\times10^{-4} \pm 4.9\times10^{-5}$ | $6.22\times10^{4} \pm 1.1\times10^{4}$ |
| S-PEEK-c | 40.04 ± 0.008 | 1.15 ± 0.02 | $4.46\times10^{-4} \pm 6.3\times10^{-5}$ | $3.32\times10^{4} \pm 2.3\times10^{3}$ |
| S-PEEK-f | 76.98 ± 0.01 | 1.35 ± 0.04 | $6.09\times10^{-3} \pm 2.4\times10^{-3}$ | $3.60\times10^{5} \pm 1.8\times10^{5}$ |
| S-PEEK-f/S-BETA-0.8% | 34.01 ± 0.008 | 1.57 ± 0.16 | $2.58\times10^{-3} \pm 1.1\times10^{-3}$ | $1.79\times10^{5} \pm 1.7\times10^{4}$ |
| S-PEEK-f/S-BETA-4% | 34.01 ± 0.008 | 2.15 ± 0.12 | $3.31\times10^{-3} \pm 3.4\times10^{-3}$ | $1.53\times10^{5} \pm 8.2\times10^{3}$ |
| S-PEEK-f/S-BETA-8% | 34.01 ± 0.008 | 2.21 ± 0.06 | $3.25\times10^{-2} \pm 1.9\times10^{-2}$ | $4.15\times10^{5} \pm 1.4\times10^{5}$ |

With the enhancement of proton conductivity in the S-PEEK membranes from increasing DS value, the permeability of $V^{4+}$ ions increased as well. In line with this, the $V^{4+}$ permeability of the composite membranes also increased by increasing the zeolite concentration due to the sulfonation modification and the dispersion of large amounts of zeolite into the S-PEEK matrix, rather than blocking ions from passing, instead forming voids. However, the composite membranes possessed an improvement in ion selectivity (S) than the pristine S-PEEK membranes as shown in Table 1.

## CONCLUSIONS

The sulfonation modification of PEEK polymer was successfully carried out by reacting with concentrated sulfuric acid, as well as the sulfonation of BETA zeolite was done by reacting with MPTMS and $H_2O_2$. The proton conductivity and ion selectivity of S-PEEK and S-PEEK/S-BETA composite membranes were increased by increasing the DS value and the zeolite concentration. The S-PEEK-f/S-BETA-8%v/v zeolite composite membrane showed the highest proton conductivity at $3.25\times10^{-2} \pm 1.9\times10^{-2}$ S.cm$^{-1}$ and the ion selectivity at $4.15\times10^{5} \pm 1.4\times10^{5}$ cm$^2$.sec$^{-1}$.

## ACKNOWLEDGEMENTS

The authors appreciatively acknowledge financial support from the Conductive and Electroactive Polymers Research Unit, the Petroleum and Petrochemical College of Chulalongkorn University, the ASEAN & NON-ASEAN Scholarship of Chulalongkorn University, and the National Research Council of Thailand (NRCT).

## REFERENCES

**Changkhamchom, S. and Sirivat, A.** (2019). Polymer-Plastics Technology and Materials, 58**(17)**, 1900-1913.

**Doetsch, C. and Pohlig, A.** (2020). Future Energy (pp. 263-277).

**Kumi, E. N.** (2023). *Energy storage technologies. In Pumped Hydro Energy Storage for Hybrid Systems* (pp. 1-21).

PPC & PETROMAT SYMPOSIUM 2025

# SYNTHESIS OF POROUS CARBON MATERIALS FROM POLYBENZOXAZINE DERIVED FROM PEI AS ZINC-AIR BATTERY CATALYST SUPPORT

*Kangpeng Chen [a], Thanyalak Chaisuwan*[a, b]*

[a] The Petroleum and Petrochemical College, Chulalongkorn University, Bangkok, Thailand
[b] Center of Excellence on Petrochemical and Materials Technology, Bangkok, Thailand

Keywords: Polybenzoxazine; Porous carbon; Transition metal doping; Zinc–air battery

## ABSTRACT

A nitrogen-rich benzoxazine precursor was synthesized via a sol-gel method using formaldehyde, polyethyleneimine (PEI), and bisphenol A. Transition metal elements were introduced into the precursor, followed by thermal polymerization and carbonization, to obtain porous carbon-based electrocatalysts. The resulting material exhibits a high specific surface area of 339 $m^2/g$ and hierarchical pore distribution. Electrochemical evaluations demonstrate that the catalyst shows excellent oxygen evolution reaction (OER) performance with an OER overpotential of 1.48V at 10 $mA/cm^2$. The developed material offers a promising, cost-effective alternative to precious metal-based catalysts and exhibits great potential as a cathode electrocatalyst in rechargeable zinc-air batteries.
***thanyalak.c@chula.ac.th**

## INTRODUCTION

Zinc-air batteries have gained widespread attention due to their high theoretical energy density, low cost, and environmental friendliness, making them promising candidates for next-generation energy storage systems. However, the practical application of ZABs is still hindered by sluggish kinetics of the oxygen reduction reaction (ORR) and oxygen evolution reaction (OER) at the air cathode (Fu et al., 2017; Li & Dai, 2014). The conventional use of noble metal-based catalysts such as Pt, $IrO_2$, and $RuO_2$ faces challenges including high cost, aggregation, and poor durability, which restrict their large-scale application (Yang et al., 2021). Developing low-cost, abundant, and efficient bifunctional electrocatalysts is crucial. Nitrogen-doped carbon materials are promising due to their adjustable surface chemistry, high conductivity, and many active sites. Introducing nitrogen heteroatoms can modify the electronic structure, improving catalytic activity for both ORR and OER.(Singh et al., 2019).
Polybenzoxazine, a thermosetting resin with high nitrogen content and good carbon yield, has emerged as an attractive precursor for preparing heteroatom-doped porous carbon materials (Tiwari et al., 2022). Furthermore, the coordination of transition metals (e.g., Co, Fe) with nitrogen atoms within the carbon matrix can form M–N–C active sites, which exhibit remarkable bifunctional catalytic performance (Zhang et al., 2022).

## EXPERIMENTAL

*A. Synthesis of PEI-based benzoxazine (PEI-BZ)*

PPC & PETROMAT SYMPOSIUM 2025

PEI-BZ was synthesized via a sol–gel method using bisphenol A, polyethyleneimine (PEI), and formaldehyde at a molar ratio of 12:1:48. Bisphenol A was first dissolved in ethanol under stirring at room temperature, followed by the sequential addition of formaldehyde and dropwise addition of PEI. The mixture was stirred for 1 hour to form benzoxazine precursors, then transferred into vials and heated at 95 °C for 24 hours to complete gelation. The final product was a yellowish gel-like PEI-BZ material.

*B. Synthesis of FeNi-doping BZ (FeNi@BZ)*

The previously prepared PEI-BZ gel was first dried in an oven to remove residual solvents. $Fe(NO_3)_3 \cdot 9H_2O$ and $Ni(NO_3)_2 \cdot 6H_2O$ were then dissolved at a 1:1 weight ratio in a mixed solvent of 10g deionized water and 10g ethanol. After complete dissolution and homogenization of the metal precursors, 2 g of the dried PEI-BZ gel was added to the solution. After stirring for 30 minutes at room temperature to promote ion adsorption, the mixture was left undisturbed for 12 hours to enhance metal incorporation.

*C. Preparation of FeNi-doping nitrogen-rich porous carbon (FeNi@NC)*

The FeNi-doped PBZ composite was thermally cured in stages: 160 °C for 1 h, 190 °C for 1 h, and 210 °C for 2.5 h to complete ring-opening polymerization. The cured sample was then carbonized under nitrogen by heating to 800 °C over 2.5 h and holding for another 2.5 h. After cooling to room temperature under nitrogen, the resulting FeNi@NC was collected for ZABs applications.

## RESULTS AND DISCUSSION

*A. Characterization of the PEI-based benzoxazine monomer and polybenzoxazine*

Fig. 1a shows the FTIR spectra of the PEI-based benzoxazine monomer (PEI@BZ) and its polymer (PEI@PBZ). The absorption bands at 1230 and 1110 $cm^{-1}$ correspond to the C–O–C and C–N–C stretching vibrations, confirming the presence of the benzoxazine ring. A characteristic peak at 935 $cm^{-1}$, assigned to the oxazine ring, disappears after polymerization, indicating complete ring-opening and successful monomer curing.

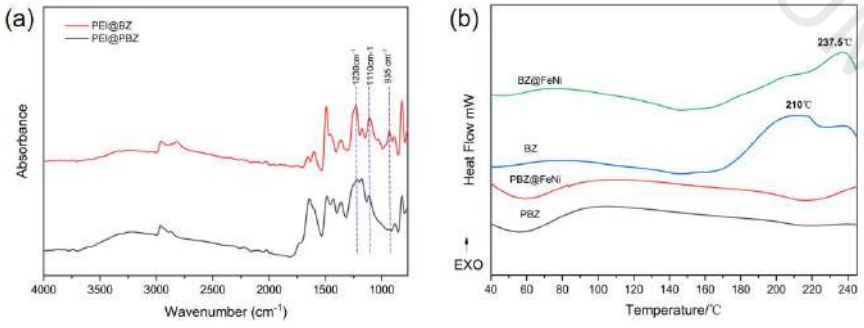


Fig. 1 (a) FT-IR spectrum of PEI@BZ and PEI@PBZ, (b) DSC thermograms of BZ, PBZ, BZ@FeNi and PBZ@FeNi

PPC & PETROMAT SYMPOSIUM 2025

DSC analysis was employed to investigate the curing behavior and thermal properties of BZ monomer and its polymer. The undoped monomer began polymerization at approximately 160 °C, with a maximum exothermic peak near 210 °C. After FeNi doping, the onset temperature remained unchanged, but the exothermic peak shifted to 237.5 °C, suggesting increased difficulty in ring-opening polymerization. In the DSC curves of both PBZ and PBZ@FeNi, the exothermic peaks disappeared, indicating complete polymerization into polybenzoxazine, as shown in Fig. 1b.

*B. Characterization of the morphology and microstructure of porous and transition metal-doped carbon materials*

To investigate the effects of different transition metals (Fe, Co, Ni, FeNi, and FeCo) on the pyrolysis behavior of polybenzoxazine, X-ray diffraction (XRD) analysis was performed. As shown in Fig. 2, the XRD results are presented below. For nitrogen-rich porous carbon (NC), two broad diffraction peaks were detected at 2θ =24° and 43.5°, indicating the (002) and (100) planes of amorphous carbon with some degree of graphitization (Thubsuang et al., 2020). With the introduction of Fe or Co, sharper diffraction peaks are observed at 26° and 43°, indicating an enhanced degree of graphitization promoted by Fe and Co elements. For the Co@NC, additional reflections appear at 31° and 37°, which can be attributed to $Co_3O_4$. In the Fe@NC, characteristic peaks at 33°, 35.5°, and 44.5° correspond to iron oxides and metallic Fe species, suggesting that these components facilitate structural ordering during pyrolysis (Maldonado-Hódar et al., 2000). In contrast, the Ni@NC sample exhibits no significant differences from the undoped counterpart. No distinct peaks associated with nickel species are detected, and the carbon structure remains predominantly amorphous. This indicates that Ni exerts a negligible catalytic effect on the graphitization process under identical thermal treatment conditions.

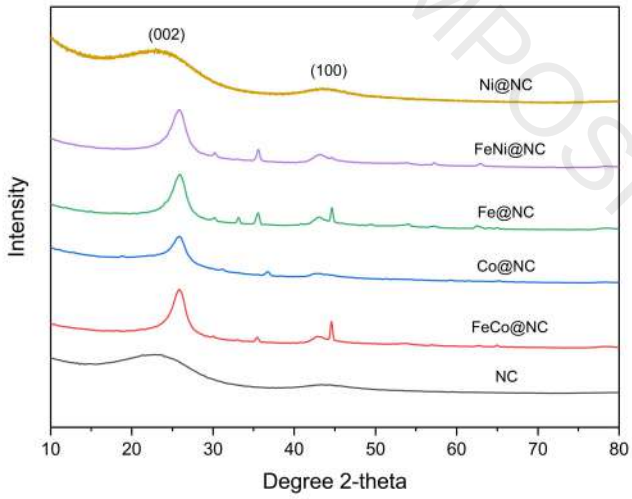


Fig. 2 XRD patterns of nitrogen-rich carbon (NC) and NC doped with transition metals: Co@NC, Fe@NC, Ni@NC, FeCo@NC, and FeNi@NC.

PPC & PETROMAT SYMPOSIUM 2025

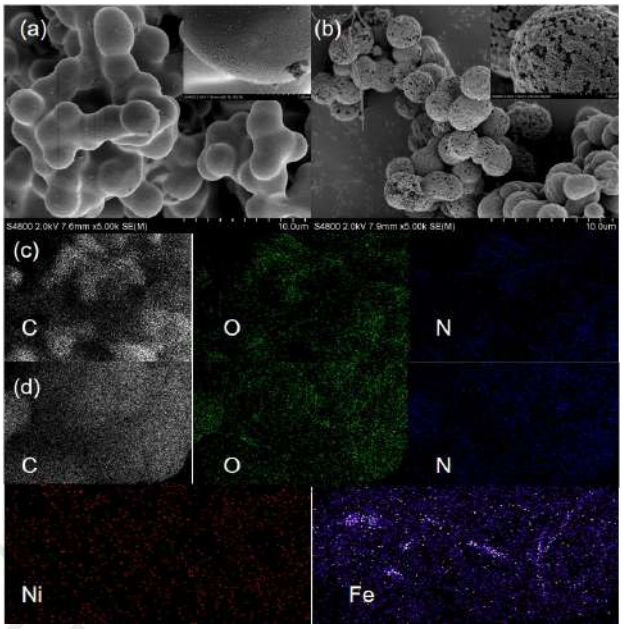


Fig. 3 (a) SEM image of nitrogen-rich carbon (NC); (b) SEM image of FeNi-doped nitrogen-rich carbon (FeNi@NC); (c) Energy-dispersive X-ray spectroscopy (EDX) spectrum of NC; (d) EDX spectrum of FeNi@NC

The surface features and nanostructures of the porous carbons were analysed through SEM. Shown in Fig. 3a and 3b, the FeNi@NC sample exhibits a characteristic "peanut shell"-like morphology with a broader pore size distribution compared to NC. This suggests that the co-doping of Fe and Ni facilitates the development of a more expanded and heterogeneous porous structure. Additionally, as shown in Fig. 3c and 3d, the nitrogen content in FeNi@NC is higher than that in NC, indicating that the coordination interaction between Fe, Ni, and nitrogen species during pyrolysis enhances nitrogen retention within the carbon framework.

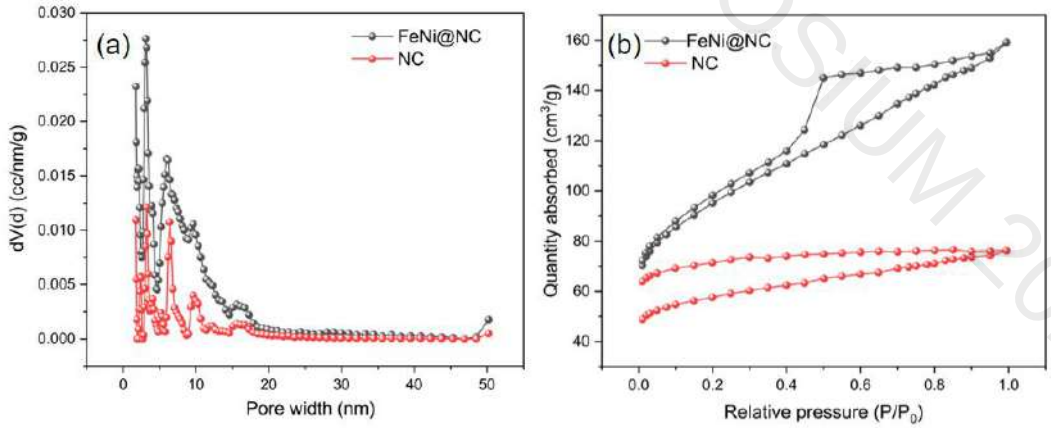


Fig. 4 (a) Pore size distribution curves of FeNi@NC and NC; (b) Nitrogen adsorption–desorption isotherms of FeNi@NC and NC.

PPC & PETROMAT SYMPOSIUM 2025

This observation is further supported by the nitrogen adsorption–desorption measurements. As shown in the pore size distribution curves (Fig. 4a), FeNi@NC exhibits a broader mesoporous structure with a 3.09 nm average pore size compared to NC with a 1.88 nm average pore size. The isotherm profiles (Fig. 4b) also reveal a distinct difference in pore characteristics: FeNi@NC displays a typical type IV isotherm with a clear hysteresis loop, indicative of mesoporosity, whereas NC shows a curve closer to type I, characteristic of microporous materials. Despite the enhanced mesoporosity, the specific surface area of FeNi@NC (339 $m^2/g$) is lower than that of NC (422 $m^2/g$). This decrease can be attributed to the expansion of pore structure, which tends to reduce surface area, as well as the partial blockage of pores by metal species during the doping process.

*C. OER performance of transition metal-doped catalysts*

The OER performance of the catalysts was evaluated by linear sweep voltammetry (LSV) in $O_2$-saturated 1.0 M KOH solution. As shown in Fig. 5, FeNi@NC delivers a lower overpotential of 1.48 V at a current density of 10 $mA \cdot cm^{-2}$, significantly lower than that of NC (1.62 V), indicating improved catalytic activity. This enhancement is mainly attributed to the synergistic interaction between Fe and Ni, which modulates the electronic structure of the active sites and facilitates the adsorption and conversion of oxygen intermediates. Moreover, the nitrogen-doped carbon matrix provides a conductive and porous framework that further supports charge transfer and mass diffusion during the OER process.

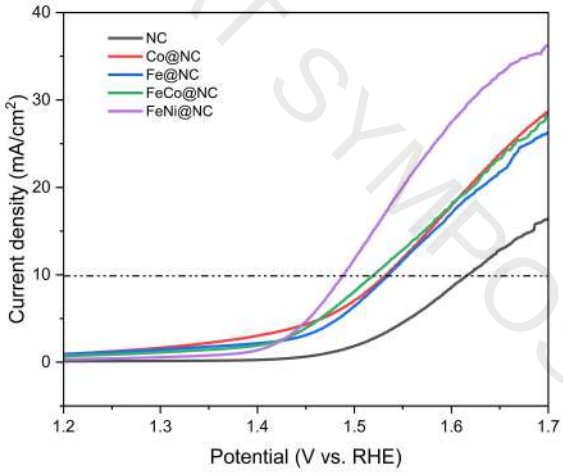


Fig. 5 The OER performance of NC and transition metal-doped NC samples in $O_2$-saturated 1.0 M KOH.

## CONCLUSIONS

In this study, FeNi@NC was successfully prepared via a sol-gel-derived PEI-based benzoxazine precursor followed by thermal curing and carbonization. The resulting material exhibited a high surface area and well-developed mesoporous structure. LSV measurement indicated that FeNi@NC delivered excellent OER activity with a low

PPC & PETROMAT SYMPOSIUM 2025

overpotential of 1.48V at 10 mA $cm^{-2}$ ($E_{10}$) and favorable kinetics, attributed to the synergistic effect of Fe and Ni, nitrogen doping, and the conductive porous structure. These results confirm that FeNi@NC is a promising electrocatalyst for Zn–air batteries.

## ACKNOWLEDGEMENTS

This work was financially supported by the Graduate Scholarship Program for ASEAN or Non-ASEAN Countries, Chulalongkorn University, and the Petroleum and Petrochemical College, Chulalongkorn University. The author gratefully acknowledges The Petroleum and Petrochemical College, Chulalongkorn University, for providing research facilities and technical support.

## REFERENCES

Fu, J., Cano, Z. P., Park, M. G., Yu, A., Fowler, M., & Chen, Z. (2017). Electrically rechargeable zinc–air batteries: progress, challenges, and perspectives. *Advanced Materials*, *29*(7), 1604685.

Li, Y., & Dai, H. (2014). Recent advances in zinc–air batteries. *Chemical Society Reviews*, *43*(15), 5257-5275.

Maldonado-Hódar, F. J., Moreno-Castilla, C., Rivera-Utrilla, J., Hanzawa, Y., & Yamada, Y. (2000). Catalytic Graphitization of Carbon Aerogels by Transition Metals. *Langmuir*, *16*(9), 4367-4373. https://doi.org/10.1021/la991080r

Singh, S. K., Takeyasu, K., & Nakamura, J. (2019). Active sites and mechanism of oxygen reduction reaction electrocatalysis on nitrogen-doped carbon materials. *Advanced Materials*, *31*(13), 1804297.

Thubsuang, U., Chotirut, S., Thongnok, A., Promraksa, A., Nisoa, M., Manmuanpom, N., Wongkasemjit, S., & Chaisuwan, T. (2020). Facile preparation of polybenzoxazine-based carbon microspheres with nitrogen functionalities: Effects of mixed solvents on pore structure and supercapacitive performance. *Frontiers of Chemical Science and Engineering*, *14*(6), 1072-1086. https://doi.org/10.1007/s11705-019-1899-8

Tiwari, I., Sharma, P., & Nebhani, L. (2022). Polybenzoxazine-an enticing precursor for engineering heteroatom-doped porous carbon materials with applications beyond energy, environment and catalysis. *Materials Today Chemistry*, *23*, 100734.

Yang, M., Shu, X., Pan, W., & Zhang, J. (2021). Toward Flexible Zinc–Air Batteries with Self-Supported Air Electrodes. *Small*, *17*(48), 2006773.

Zhang, H., Guang, H., Li, R., Lu, X., Xu, H., Wang, D., Xiao, L., Zhang, J., An, M., & Yang, P. (2022). Doping engineering: modulating the intrinsic activity of bifunctional carbon-based oxygen electrocatalysts for high-performance zinc–air batteries. *Journal of Materials Chemistry A*, *10*(41), 21797-21815.

PPC & PETROMAT SYMPOSIUM 2025

# EFFECT OF ACID DOPING ON POLYANILINE SYNTHESIS FOR HIGH-PERFORMANCE SUPERCAPACITOR APPICATIONS

*Orawee Jirachaisakul* [a,b], *Manop Panapoy* [a], *Nattawut Chaiyut* [a], *Bussarin Ksapabutr* [*, a]

[a] Department of Materials Science and Engineering, Faculty of Engineering and Industrial Technology, Silpakorn University, Nakhon Pathom, Thailand
[b] Center of Excellence on Petrochemical and Material Technology, Chulalongkorn University

Keywords: Polyaniline, Acid doping, Supercapacitor

## ABSTRACT

Efficient energy storage has become of key interest in the development of renewable and sustainable energy systems. Supercapacitors have emerged as promising energy storage devices owing to their high power density, rapid charge-discharge capability, and long cycle life. Polyaniline (PANI) is widely used as an electrode material because of its high electrochemical performance, short synthesis time, and low production cost. The morphology of PANI can be influenced by the type of doping acid used during the synthesis. In this work, the effect of different doping acids on the in-situ polymerization of PANI was investigated. The obtained PANI was characterized using Raman spectroscopy, Fourier-transform infrared spectroscopy (FTIR), X-ray diffraction (XRD), scanning electron microscopy (SEM), and cyclic voltammetry (CV). The results revealed that PANI synthesized using HCl exhibited the maximum specific capacitance. These findings highlight the crucial role of acid doping in enhancing the electrochemical properties of PANI in high-performance supercapacitor applications.

*** ksapabutr_b@su.ac.th**

## INTRODUCTION

In recent years, renewable energy has garnered significant attention owing to the limitations of fossil fuels and their negative impacts such as global warming and the release of toxic chemicals (Lima et al., 2024). Electrochemical energy storage systems have become increasingly important for addressing the challenges of supplying renewable energy. Among these, supercapacitors have attracted considerable interest as energy storage devices owing to their high-power density, large energy storage capacity, and wide range of applications including portable electronics, solar energy systems, and electric vehicles (Thongkam et al., 2023; Wang et al., 2020). The performance of supercapacitors depends on the properties of the electrode materials, which presents a challenge in the development of high-performance devices. Conductive polymers have emerged as promising electrode materials, with polyaniline (PANI) being one of the most extensively studied owing to its excellent electrical conductivity, flexibility, multiple intrinsic redox states, pseudocapacitive behavior, easy synthesis, and low cost (Qiu et al., 2018). However, the capacitance of PANI is significantly influenced by its morphology, combination with other materials, and doping (Gawli et al., 2016). Acid doping can alter the morphology, including the surface area and pore size distribution, thereby affecting the electrochemical properties of PANI (Zhou et al., 2021). This study investigated the effects of different acid dopants on the electrical properties of polyaniline for use as an electrode material. Four doping acids

PPC & PETROMAT SYMPOSIUM 2025

were used: sulfuric acid ($H_2SO_4$), phosphoric acid ($H_3PO_4$), nitric acid ($HNO_3$), and hydrochloric acid (HCl). The doped PANI samples were characterized and evaluated by electrochemical measurements to assess their performance as supercapacitor electrodes.

## EXPERIMENTAL

### *A. Materials*

Aniline monomer was purchased from Loba Chemie Pvt. Ltd. (India). Ammonium persulfate ($(NH_4)_2S_2O_8$) was obtained from Ajax Finechem Pty. Ltd. (Poland). Nitric acid ($HNO_3$), phosphoric acid ($H_3PO_4$), sulfuric acid ($H_2SO_4$), and hydrochloric acid (HCl) were purchased from Carlo Erba™ (German). All reagents were employed without any additional purification.

### *B. Synthesis of Polyaniline (PANI)*

PANI was synthesized by dissolving 0.1 mL the aniline monomer in 25 mL of 1 M $H_2SO_4$ with stirring for dissolution. Simultaneously, 0.25 g of $(NH_4)_2S_2O_8$ was dissolved in 25 mL of 1 M $H_2SO_4$ solution under continuous stirring until a homogeneous solution was obtained. $(NH_4)_2S_2O_8$ solution was then added to the aniline monomer solution. The mixture was continuously stirred in an ice bath for 4 h. After polymerization, the resulting dark-green PANI precipitate was washed repeatedly with ethanol until a neutral pH was reached to remove the excess acid and oligomer of PANI. The washed PANI was then dried in an oven at 80°C for 24 h. The same procedure was repeated using $H_3PO_4$, $HNO_3$, and HCl. Therefore, the PANI samples obtained using different doping acids were denoted as PANI-$H_2SO_4$, PANI-$H_3PO_4$, PANI-$HNO_3$, and PANI-HCl.

### *C. Characterization of PANI*

Raman spectra were obtained using a Senterra Raman microscope (Bruker Optics, Inc.). The surface functional groups of the samples were identified using Fourier-transform infrared spectroscopy (FTIR, Vertex 70, Bruker) from 500 to 4000 $cm^{-1}$. The crystalline phases of the samples were analyzed using an X-ray diffractometer (XRD-6100, Shimadzu). Field-emission scanning electron microscopy (FESEM, MIRA3 Tescan) was used to examine the surfaces and morphologies of the samples.

### *D. Preparation of Electrode and Electrochemical test*

The electrode was prepared by blending PANI, poly(vinylidene difluoride), and acetylene black in a weight ratio of 80:5:15. The components were mixed with dimethylformamide (DMF) to form a slurry, which was then applied to a stainless-steel mesh (1 cm diameter) and dried overnight at 70°C. Electrochemical characterization was performed using a three-electrode setup, with Ag/AgCl as the reference electrode and a platinum wire as the counter electrode. A 1.0 M $H_2SO_4$ solution was used as the electrolyte. Cyclic voltammetry (CV) was conducted using an electrochemical workstation (EA163, eDAQ).

## RESULTS AND DISCUSSION

FTIR and Raman analyses were conducted to investigate the chemical structure of PANI synthesized with different acids. The FTIR spectra of PANI-$H_2SO_4$, PANI-HCl, PANI-$H_3PO_4$, and PANI-$HNO_3$ are shown in Fig. 1(a). The spectra of the four different

PPC & PETROMAT SYMPOSIUM 2025

types of PANI exhibited characteristic peaks at approximately 1574 $cm^{-1}$ and 1480 $cm^{-1}$, corresponding to the C=C/C=N stretching vibrations of the quinoid and benzenoid rings, respectively. The peaks around 1296 $cm^{-1}$ and 1240 $cm^{-1}$ are associated with the C-N stretching vibration of the quinoid and benzenoid rings, respectively (Jisha et al., 2020; Kupfer et al., 2015). The peaks located at 1123 $cm^{-1}$ and 796 $cm^{-1}$ indicate C-H in-plane and C-H out-of-plane bending, respectively (Wang et al., 2017). This indicates the presence of characteristic absorption peaks associated with PANI generated during polymerization in solutions of $H_2SO_4$, $H_3PO_4$, $HNO_3$, and HCl with the same concentration. The Raman spectra of PANI synthesized with different acid types are shown in Fig. 1(b). Bands were observed at 818 $cm^{-1}$ (N-H stretching) (Thongkam et al., 2023), 1172 $cm^{-1}$ (C-H bending vibration of the quinoid ring), 1330 $cm^{-1}$ ($C\text{-}N^{\bullet+}$ stretching of the polarons), 1495 $cm^{-1}$ (C=N stretching of the quinoid ring), and 1599 $cm^{-1}$ (C=N stretching of the benzenoid ring) (Li et al., 2023; Wang et al., 2017). The results of the delocalized polarons indicate the presence of the emeraldine salt form in the PANI, which contributes to the enhanced capacitance through rapid redox reactions (Zhou et al., 2021). PANI-HCl demonstrated the highest intensity among the various doping acids tested. This may be attributed to the small size of $Cl^-$ ions, which allows for greater intercalation during the reaction process, leading to a more ordered polymer structure. Additionally, it is a strong acid with excellent protonation ability, which enhances the charge storage capacity and improves electrochemical properties (Wang et al., 2022).

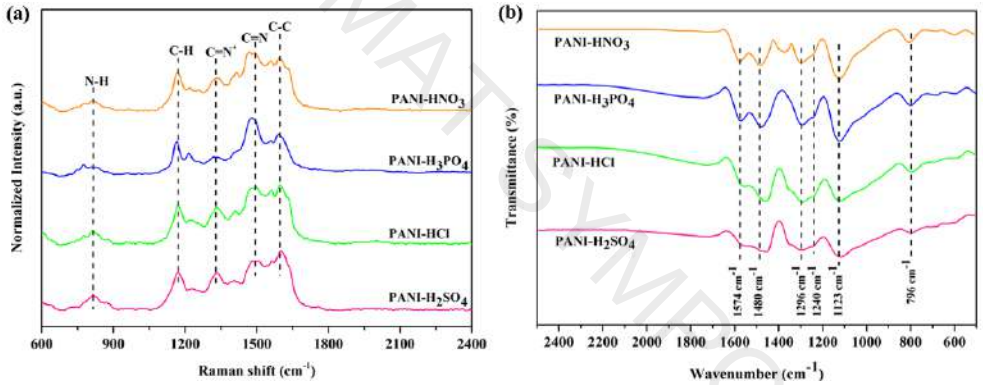


Fig. 1 (a) FTIR spectra and (b) Raman spectra of PANI-$H_2SO_4$, PANI-HCl, PANI-$H_3PO_4$, and PANI-$HNO_3$.

The nanostructures of PANI-$H_2SO_4$, PANI-HCl, PANI-$H_3PO_4$, and PANI-$HNO_3$ were further confirmed by XRD. As shown in Fig. 2, XRD peaks are observed at approximately 20.3° and 25.1°, corresponding to the (020) and (200) planes, respectively, indicating the presence of the emeraldine form (Zhou et al., 2021). In addition, the presence of the characteristic peak of PANI signifies the extent of π-conjugation within the polyaniline structure, while the sharpness of the peak indicates the degree of order in the π-conjugated system (Ajekwene and Kurian, 2018). A slight shift in the peaks was observed, which was attributed to the variation in dopant ions that induced changes in the lattice orientation of polyaniline and its internal crystallinity (Han et al., 2020). The DSC curves obtained under a nitrogen atmosphere showed an endothermic peak at approximately 75°C, which was attributed to the presence of moisture and PANI oligomers (Matoetoe et al.,

PPC & PETROMAT SYMPOSIUM 2025

2015; Ajekwene and Kurian, 2018). PANI-HCl exhibited a higher peak intensity than PANI doped with other acids (Karbownik et al., 2021).

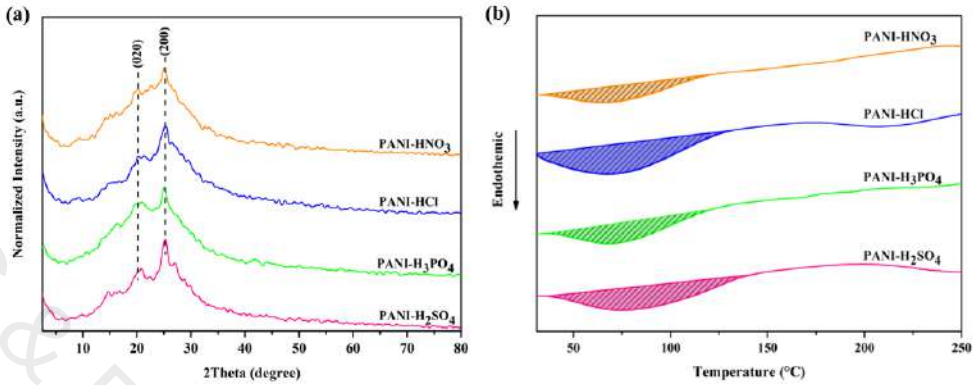


Fig. 2 (a) XRD patterns and (b) DSC thermograms of PANI-$H_2SO_4$, PANI-HCl, PANI-$H_3PO_4$, and PANI-$HNO_3$.

The morphologies of the PANI-$H_2SO_4$, PANI-HCl, PANI-$H_3PO_4$, and PANI-$HNO_3$ samples were investigated using SEM. As shown in Fig. 3(a), the SEM images of PANI-$H_2SO_4$ displayed a network of nanofibers with a range of sizes (Zhou et al., 2021). Fig. 3(b) illustrates the presence of uniformly distributed coral-like nanostructures in PANI-HCl (Li et al., 2023). Fig. 3(c) shows that PANI-$H_3PO_4$ contains distributed porous structures with some stacked sheet-like structures. As shown in Fig. 3(d), nanorod structures and several clustered formations are observed in the PANI-$HNO_3$ sample. These structural differences facilitate the diffusion of ions and molecules through the material in the electrolyte solution during the redox process, resulting in an efficient electrode (Sidheekha et al., 2022; Zhou et al., 2021).

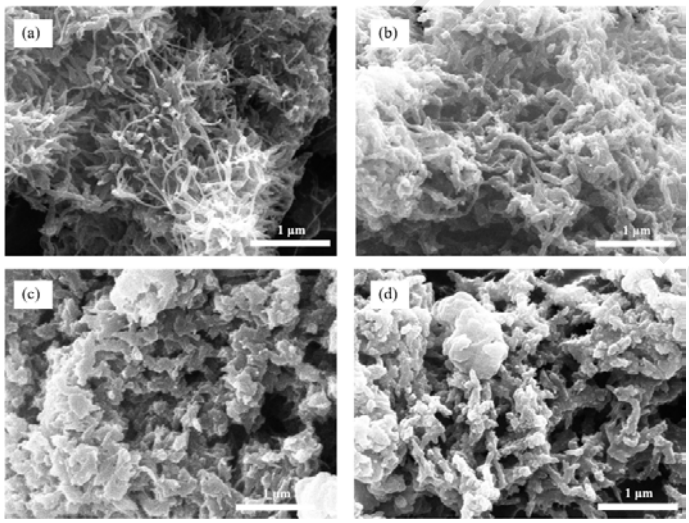


Fig. 3 SEM images of (a) PANI-$H_2SO_4$, (b) PANI-HCl, (c) PANI-$H_3PO_4$, and (d) PANI-$HNO_3$.

PPC & PETROMAT SYMPOSIUM 2025

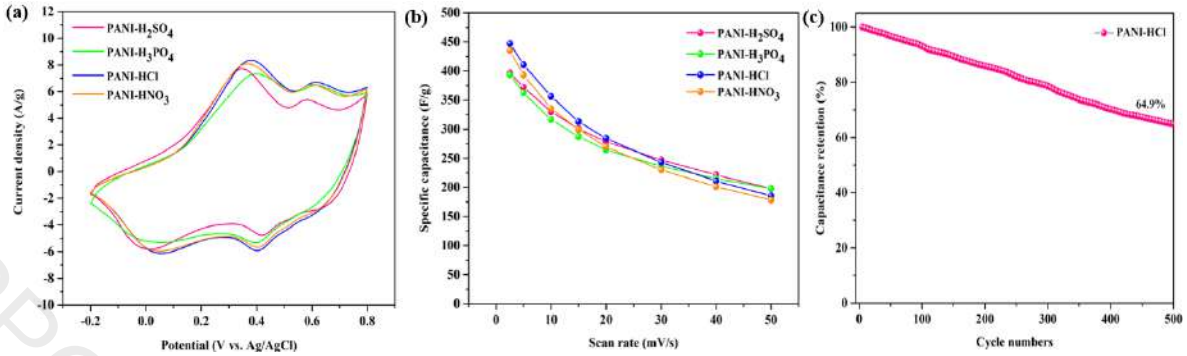


Fig. 4. (a) CV curves, (b) specific capacitance at different scan rates of PANI-$H_2SO_4$, PANI-$H_3PO_4$, PANI-HCl, and PANI-$HNO_3$, and (c) %capacitance retention versus number of cycles.

The pseudocapacitive behavior of PANI-$H_2SO_4$, PANI-$H_3PO_4$, PANI-HCl, and PANI-$HNO_3$ was studied within the potential window of -0.2 V to +0.8 V in 1 M $H_2SO$ electrolyte at a scan rate of 10 $mV \cdot s^{-1}$, as shown in Fig. 4(a). All synthesized PANI samples exhibited two anodic (~0.3 V/~0.6 V) and two cathodic (~0.0 V/~0.4 V) peaks during the redox process, indicating the reversible transition from the leucoemeraldine to the emeraldine state of PANI (Bhandari and Khastgir, 2015; Sidheekha et al., 2022). Among the investigated samples, the PANI-HCl electrode exhibited the largest enclosed area, indicating higher current values and distinct redox peaks compared to the other doping agents (Liu et al., 2016) because of its well-ordered structure and high crystallinity. This demonstrates the significant role of the doping agent in enhancing specific capacitance. As illustrated in Fig. 4(b), the PANI-HCl electrode exhibited the highest specific capacitance, and the specific capacitance of all samples decreased with increasing scan rate, which was attributed to the limited ion diffusion at higher scan rates. Furthermore, after 500 charge-discharge cycles at a scan rate of 30 $mV \cdot s^{-1}$, a capacitance retention of 64.9% was observed, as shown in Fig. 4(c). Charge storage in PANI occurs through rapid surface redox reactions. During repeated charge and discharge processes, the swelling and shrinkage of the electrode materials lead to physical deformation of the electrode structure and loss of electrochemical stability (Zhou et al., 2021; Thongkam et al., 2023).

## CONCLUSIONS

The type of doping agent used in the synthesis of PANI was found to have a notable effect on the resulting morphologies, leading to improved electrochemical properties of the resulting PANI. Specifically, the well-organized coral-like nanostructures observed in PANI-HCl may facilitate enhanced ion transport and a higher density of electric charges at the highest specific capacitance value of 356.20 $F \cdot g^{-1}$ at 10 $mV \cdot s^{-1}$.

## ACKNOWLEDGEMENTS

The authors thank the Department of Materials Science and Engineering, Faculty of Engineering and Industrial Technology, Silpakorn University. The authors also thank the Hub of Talent: Sustainable Materials for Circular Economy, National Research Council of Thailand (NRCT).

PPC & PETROMAT SYMPOSIUM 2025

## REFERENCES

**Lima, J. V., Lemos, H. G., Silva, R. A., Rossato, J. H., Boratto, M. H. & Graeff, C. F.** (2024). Journal of Alloys and Compounds Communications, **3,** 100007.
**Thongkam, K., Chaiyut, N., Panapoy, M. & Ksapabutr, B.** (2023). Journal of Metals, Materials and Minerals, **33,** 1675-1675.
**Wang, Q., Li, J., Wang, D., Niu, J., Du, P., Liu, J. & Liu, P.** (2020). Electrochimica Acta, **349,** 136348.
**Qiu, M., Zhang, Y. & Wen, B.** (2018). Journal of Materials Science: Materials in Electronics, **29,** 10437-10444.
**Gawli, Y., Banerjee, A., Dhakras, D., Deo, M., Bulani, D., Wadgaonkar, P., Shelke, M. & Ogale, S.** (2016). Scientific reports, **6,** 21002.
**Zhou, C., He, S., Yang, H., An, J., Yang, L., Yan, P. & Zhang, H.** (2021). Electrochimica Acta, **390,** 138818.
**Jisha, P., Suma, M., Murugendrappa, M. & Raj, K.** (2020). International Journal of Polymer Analysis and Characterization, **25,** 176-187.
**Kupfer, V., Pereira da Silva, C., de Campos Domingues, N., Pereira Moises, M. & Wellington Rinaldi, A.** (2015). Int. J. Innov. Sci. Eng. Technol, **3,** 2348-7968.
**Wang, W., Yang, F., Chen, C., Zhang, L., Qin, Y. & Knez, M.** (2017). Advanced Materials Interfaces, **4,** 1600806.
**Li, B., Li, Y. & Ma, P.** (2023). Organic Electronics, **114,** 106749.
**Wang, D., Si, Y., Cai, T., Hu, H. & Xing, W.** (2022). Highlights in Science, Engineering and Technology, **13,** 62-67.
**Ajekwene, K. K. & Kurian, T.** (2018). Int. J. Res. Advent Technol, **6,** 2321-9637.
**Han, J.-J., Zhang, N., Liu, D.-L., Ma, H., Han, T. & Sun, D.-D.** (2020). Ionics, **26 ,**1029-1038.
**Matoetoe, M., Okumu, F., Maphale, C. & Fatoki, O. S.** (2015). Asian Journal of Chemistry, **27(4)**, 1411-1416.
**Karbownik, I., Rac-Rumijowska, O., Rybicki, T., Suchorska-Woźniak, P. & Teterycz, H.** (2021). IEEE Access, **9,** 74017-74027.
**Sidheekha, M. P., Nufaira, K., Shabeeba, A., Rajan, L. & Ismail, Y. A.** (2022). Materials Today: Proceedings, **51,** 2286-2292.
**Bhandari, S. & Khastgir, D.** (2015). Polymer, **81,** 62-69.
**Liu, W.-f., Yang, Y.-z., Liu, X.-g. & Xu, B.-s.** (2016). New Carbon Materials, **31,** 594 -599.

PROCEEDINGS OF PPC & PETROMAT SYMPOSIUM 2025

# Optimizing Electrolyte Composition with Nano-Silica for High-Performance Rechargeable Zinc-Ion Batteries

*Nonthakan Saikhwa* [a], *Napat Kiatwisarnkij* [b], *Panyawat Wangyao* [b], *Jiaqian Qin*[*c,d]

[a] Defense Engineering and Technology, Chulalongkorn University, Bangkok, Thailand
[b] Department of Metallurgical Engineering, Faculty of Engineering, Chulalongkorn University, Bangkok, Thailand
[c] Center of Excellence on Petrochemical and Materials Technology
[d] Center of Excellence on Advanced Materials for Energy Storage, Department of Materials Science Faculty of Science Chulalongkorn University, Bangkok, Thailand

Keywords: Zinc-ion batteries, Electrolyte additives, Nano-silica ($SiO_2$), Zinc deposition, Dendrite suppression

## ABSTRACT

Battery Energy Storage Systems (BESS) are becoming increasingly vital for powering electronic devices such as smartphones, computers, and electric vehicles. While lithium-ion batteries currently dominate the market, they face significant challenges, including high costs, toxicity, environmental concerns, and limited lithium availability particularly in countries like Thailand. These limitations have spurred interest in alternative technologies. Rechargeable zinc-ion batteries have emerged as a promising alternative due to their lower cost, improved safety, and the abundance of zinc resources. However, their widespread adoption is hindered by issues such as electrode corrosion, hydrogen evolution reactions (HER), and dendrite formation, which compromise performance and lifespan. This study focuses on optimizing the electrolyte composition of zinc-ion batteries by incorporating nano-$SiO_2$ as an additive. nano-$SiO_2$ helps regulate water activity, reducing the amount of free water and thereby minimizing side reactions like HER and corrosion. Experimental results demonstrate that symmetric zinc-ion batteries enhanced with nano-$SiO_2$ achieve a cycle life exceeding 300 hours at a current density of 5 mA $cm^{-2}$. Additionally, full-cell batteries deliver a discharge capacity of 160 mAh $g^{-1}$ at 1 A $g^{-1}$, significantly outperforming those without nano-$SiO_2$, which achieve only 125 mAh $g^{-1}$
*** jiaqian.q@chula.ac.th**.

## INTRODUCTION

Among the different types of Energy Storage Systems (ESS), Battery Energy Storage Systems (BESS) have gained significant attention, with batteries playing a crucial role in the operation of electronic devices such as smartphones, computers, and electric vehicles. Lithium-ion batteries currently dominate the market due to their high energy density and low self-discharge rates. However, challenges such as high costs, toxicity, environmental impact, and limited availability of lithium pose substantial barriers to widespread adoption, particularly in countries like Thailand, which lacks significant lithium resources. In response to these limitations, rechargeable zinc-ion batteries have emerged as a promising alternative. These batteries offer numerous advantages, including lower cost, enhanced safety, and

improved environmental compatibility (Alawi et al., 2025). Zinc, the primary material used in these batteries, is abundant, inexpensive, and exhibits fewer environmental risks. Thailand possesses ample zinc resources. Despite these advantages, challenges such as electrode corrosion, hydrogen evolution reactions (HER), and dendrite formation during cycling continue to hinder the performance and longevity of zinc-ion batteries (Yang et al. 2022).

To mitigate these challenges, various strategies have been proposed, including modifications to the anode, cathode, separator, and electrolyte. Among these, electrolyte modification has garnered particular attention due to its direct influence on interfacial reactions and zinc deposition behavior. (Huang et al. 2023) investigated the use of nano-$SiO_2$ as an additive in electrolytes, showing that nano-$SiO_2$ helps regulate water activity, thereby minimizing parasitic reactions such as hydrogen evolution and surface corrosion, and improving battery stability and cycling performance.

Inspired by this approach, this study also explores the incorporation of nano-$SiO_2$ as an electrolyte additive. However, unlike previous studies, the current work examines the effect of nano-$SiO_2$ under different electrolyte formulations and testing conditions. The hygroscopic nature of nano-$SiO_2$ is expected to suppress dendrite formation, enhance charge-discharge efficiency, extend cycle life, and mitigate degradation mechanisms, contributing to improved performance in rechargeable zinc-ion batteries.

## EXPERIMENTAL

### *A. Preparation of electrolytes*

The electrolyte was prepared by dissolving Zinc sulfate ($ZnSO_4$) in deionized water (DI water) to obtain a 2M $ZnSO_4$ solution, followed by continuous stirring at room temperature until complete dissolution. The solution was then aliquoted into five beakers, and nano-$SiO_2$ (average primary particle size ~20 nm, XF NANO INC., China) was incorporated in varying concentrations: (1) pristine, (2) 0.05 wt% nano-$SiO_2$, (3) 0.10 wt% nano-$SiO_2$, (4) 0.15 wt% nano-$SiO_2$, and (5) 0.20 wt% nano-$SiO_2$. Each mixture was ultrasonicated for 1 hour at room temperature to enhance additive dispersion, followed by magnetic stirring for 12 hours to ensure homogeneity. The final electrolyte solutions were transferred into sealed glass vials for subsequent use.

### *B. Electrochemical Measurements*

The symmetric batteries (Zn||Zn half-cells) were assembled using CR2032 coin cells. Each cell contained two 0.05 mm zinc foils functioning as electrodes, along with a glass microfiber separator (GF/C, 47 mm) and a nano-$SiO_2$-based electrolyte. A total of 100 μL of electrolyte was used in each cell. The deposition/dissolution performance was evaluated using a BTS battery tester (Neware, China) at current densities of 1 and 5 mA $cm^{-2}$. In Zn||Cu cells, zinc foil functioned as the counter electrode, while copper foil served as the working electrode, tested at a current density of 1 mA $cm^{-2}$ with a capacity of 0.5 mAh $cm^{-2}$. The cathode was prepared by mixing Vanadium pentoxide ($V_2O_5$), conductive carbon, and Polyvinylidene

PPC & PETROMAT SYMPOSIUM 2025

fluoride (PVDF) in a ratio of 7:2:1 to create a uniform slurry. This slurry was then applied to graphite paper using a doctor blade technique, resulting in a coating thickness of 120 µm. After the drying process, the coated electrode was punched into 14 mm discs for further use. Electrochemical performance of Zn||$V_2O_5$ full cells was systematically investigated, analyzing rate and cycling performance from 0.2 to 1.6 V to validate the electrocatalytic potential of nano-$SiO_2$ electrolyte additive. Comprehensive electrochemical analyses, including cyclic voltammetry (CV), electrochemical impedance spectroscopy (EIS), and Tafel plot measurements, were conducted utilizing a CHI 660E potentiostat (Chenhua, China) to elucidate intrinsic electrochemical kinetics and provide mechanistic insights into the zinc plating/stripping behavior.

*C. Material Characterization*

Morphological characterization of the materials and zinc dendrites was conducted using high-resolution imaging techniques, specifically a JSM-IT800 scanning electron microscope (SEM).

## RESULTS AND DISCUSSION

To determine the optimal concentration of nano-silica for improving Zn plating behavior, electrolytes with varying nano-$SiO_2$ concentrations were investigated. As shown in Figure 1(a), the electrolyte containing 0.15 wt% nano-$SiO_2$ exhibited the lowest overpotential at all current densities, indicating more efficient and uniform Zn deposition. Moreover, this composition demonstrated the longest cycling stability, maintaining a consistent voltage profile for over 150 hours under current densities of 1, 3, and 5 mA $cm^{-2}$. The voltage–current relationship shown in Figure 1(b) further corroborates these findings, as the 0.15 wt% sample consistently displayed the lowest overpotential across all tested current levels. These results suggest that 0.15 wt% nano-$SiO_2$ is the optimal concentration for enhancing Zn plating/stripping reversibility. Overall, the electrochemical performance strongly depends on nano-$SiO_2$ concentration, with insufficient or excessive amounts leading to suboptimal results.

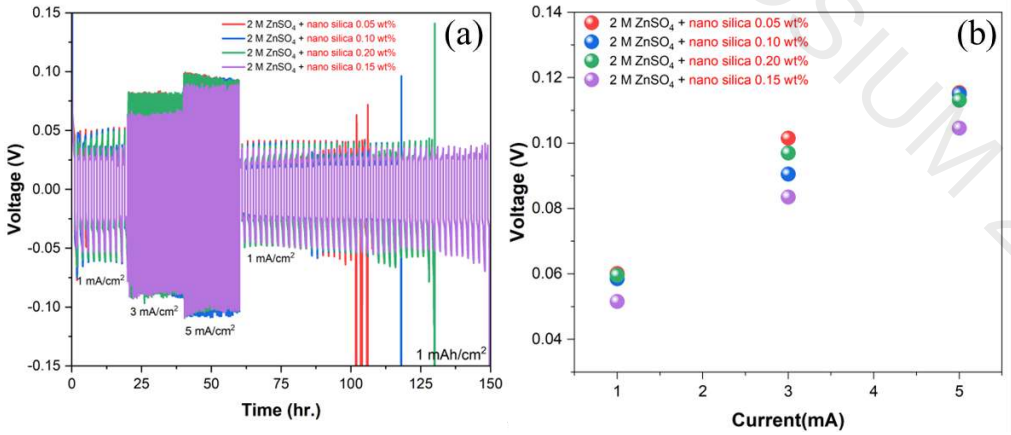


Figure 1 (a) Voltage profiles of Zn//Zn cells with various nano-silica concentrations at 1, 3, and 5 mA $cm^{-2}$. (b) Average overpotentials extracted from (a), showing the lowest values for 0.15 wt% nano-silica.

PPC & PETROMAT SYMPOSIUM 2025

To comprehensively evaluate the effects of the nano-$SiO_2$ 0.15 wt% additive on zinc anode behavior, morphological characteristics and electrochemical performance were examined. Figures 2a–2d present SEM images of Zn anodes after 400 cycles in symmetric cells with different electrolytes. Figures 2a and 2b show top-view images, while Figures 2c and 2d display cross-sectional views. The anode without the nano-$SiO_2$ 0.15 wt% additive (Figures 2a and 2c) shows a rough surface with visible dendrites and by-products, whereas the anode with the additive (Figures 2b and 2d) exhibits a smoother surface with minimal dendrite formation and fewer by-products. These results indicate that the nano-$SiO_2$ 0.15 wt% additive effectively suppresses dendrite growth and mitigates side reactions during cycling.

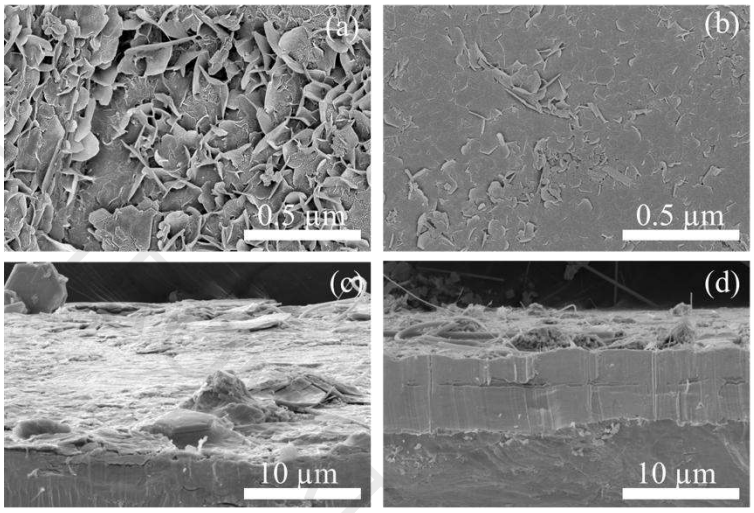


Figure 2 SEM images of Zn anodes after 400 cycles in symmetric cells in electrolytes with and without nano-$SiO_2$ 0.15 wt% **.** (a, b) Top-view images and (c, d) cross-sectional images of Zn anodes cycled without (a, c) and with (b, d) the nano-$SiO_2$ 0.15 wt% additive.

To evaluate the influence of nano-$SiO_2$ as an electrolyte additive on the zinc plating/stripping behavior, symmetric Zn/Zn cells were employed. The overpotential (ΔV), defined as the voltage difference between the deposition and dissolution processes, was utilized as a key electrochemical indicator. A lower overpotential (ΔV) signifies improved reaction kinetics and more uniform zinc deposition (Shang et al.2022). Figure 3a illustrates the voltage profiles of symmetric cells under different electrolytes. The Zn||Zn battery with the nano-$SiO_2$ additive electrolyte exhibited a lifespan of over 450 hours and a lower overpotential of 60 mV at a current density of 1 mA $cm^{-2}$ and capacity of 1 mAh $cm^{-2}$. In contrast, The Zn||Zn battery without the nano-$SiO_2$-additive electrolyte experienced a short circuit after approximately 360 hours, with an overpotential of 72 mV. At a higher current density of 5 mA $cm^{-2}$ and capacity of 1 mAh $cm^{-2}$ (Figure 3b) the Zn||Zn battery with the nano-$SiO_2$ additive electrolyte remained stable for over 300 hours and showed an overpotential of 127 mV, while The Zn||Zn battery without the nano-$SiO_2$ additive electrolyte short-circuited after 240 hours and exhibited a higher overpotential of 149 mV.

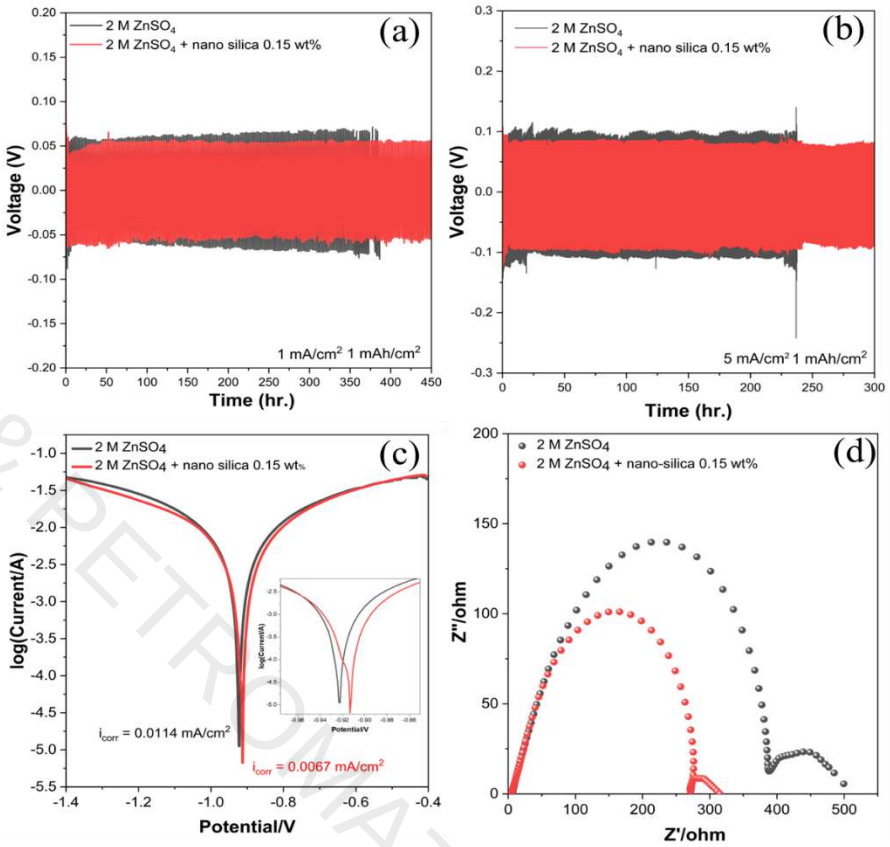


Figure 3 Electrochemical characterization of Zn||Zn symmetric cells in electrolytes with and without nano-$SiO_2$: (a) voltage profiles at 1 mA $cm^{-2}$ and 1 mAh $cm^{-2}$, (b) voltage profiles at 5 mA $cm^{-2}$ and 1 mAh $cm^{-2}$, (c) Tafel plots in different electrolytes, and (d) electrochemical impedance spectra (EIS).

To investigate the corrosion-inhibiting effect of the nano-$SiO_2$-additive, Tafel curve measurements were conducted on Zn electrodes in different electrolytes, as shown in Figure 3c. The Tafel plots reveal that the corrosion current density ($i_{corr}$) of the Zn electrode with the nano-$SiO_2$-additive electrolyte decreased significantly from 0.0114 to 0.0067 mA $cm^{-2}$, indicating that the additive can effectively inhibit the corrosion reaction. To further elucidate the electrochemical behavior of Zn||Zn batteries with and without the nano-$SiO_2$-additive electrolyte, electrochemical impedance spectroscopy (EIS) measurements were conducted to examine changes in the batteries' internal resistance and charge transfer (Figure 3d). The addition of nano-$SiO_2$ effectively reduced the internal resistance of the Zn||Zn batteries, decreasing from 380 Ω (without the nano-$SiO_2$-additive electrolyte) to 270 Ω (with the nano-$SiO_2$-additive electrolyte). These electrochemical results further support and confirm the findings from the SEM analysis.

PPC & PETROMAT SYMPOSIUM 2025

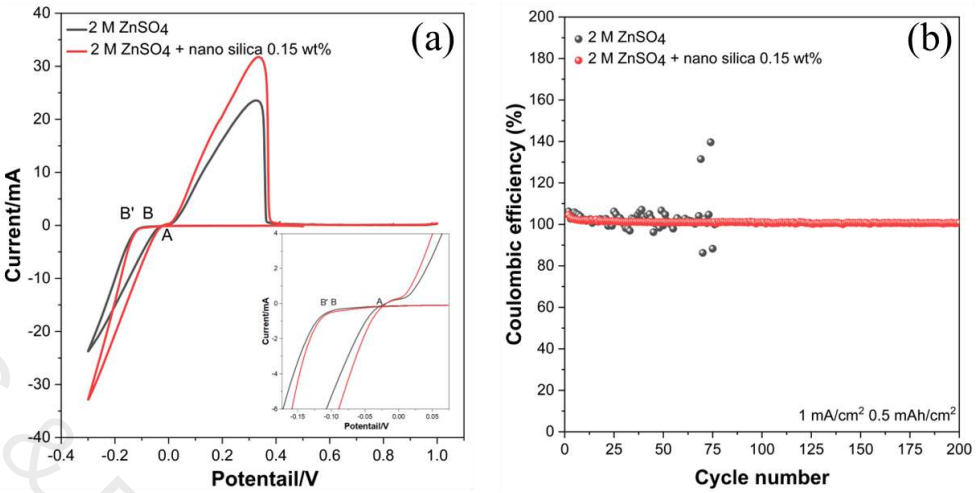


Figure 4 (a) Cyclic voltammograms (the first cycle) for Zn nucleation on Cu at a scan rate of 5 mV $s^{-1}$ in electrolytes with and without nano-$SiO_2$.(b) Coulombic efficiency of Zn||Cu cells operated at 1 mA $cm^{-2}$ capacity of 0.5 mAh $cm^{-2}$ in electrolytes with and without nano-$SiO_2$

To evaluate the zinc plating/stripping behavior in the presence of the nano-$SiO_2$ additive, cyclic voltammetry (CV) and Coulombic efficiency (CE) measurements were conducted using Zn||Cu half-cells. CV analysis was employed to investigate the redox behavior and nucleation overpotential, while CE measurements were used to assess the long-term stability and reversibility of the plating/stripping process. From Figure 4a, the CV curves of Zn||Cu half-cells with different electrolytes are presented. The battery with the nano-$SiO_2$-additive electrolyte exhibits broader redox peaks and a lower nucleation overpotential compared to the electrolyte without the nano-$SiO_2$-additive. This reduction in overpotential indicates facilitated Zn nucleation and enhanced charge transfer kinetics, which contribute to more uniform zinc deposition and reduced risk of dendrite formation (Lin et al. 2025). Furthermore, as shown in Figure 4b, the battery with the nano-$SiO_2$-additive electrolyte maintained stable Coulombic efficiency up to 200 cycles, whereas the battery without nano-$SiO_2$-additive electrolyte failed after approximately 75 cycles.

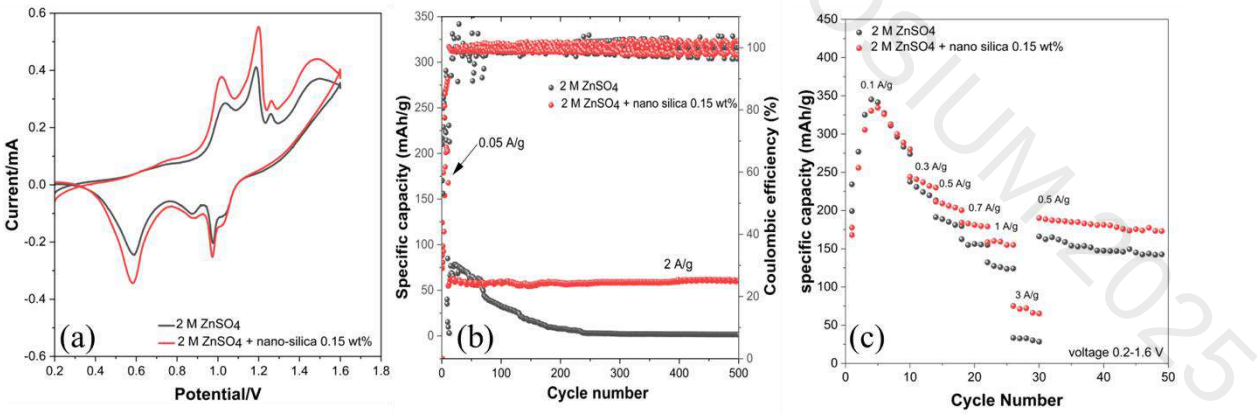


Figure 5 Electrochemical performance of full-cell batteries in electrolytes with and without nano-$SiO_2$ :(a) Cyclic voltammetry (CV) curves (the third cycle) measured at a specific scan rate 0.1 mV $s^{-1}$; (b) Cycling stability tested at current densities of 0.05 A $g^{-1}$ and 2 A $g^{-1}$ (c) Rate performance evaluated under current densities ranging from 0.1 to 3 A $g^{-1}$

To evaluate the overall electrochemical performance and practical applicability of the system under realistic conditions, a full-cell battery was assembled using $V_2O_5$ as the cathode, Zn foil as the anode, and different electrolytes. Figure 5a shows the CV curves of the full batteries with different electrolytes. Notably, the battery with the nano-$SiO_2$-additive electrolyte displays a larger CV curve area, while the overall shape remains like the battery without the nano-$SiO_2$-additive electrolyte. This suggests improved capacitive behavior or greater charge storage capability, without significantly affecting the redox mechanism (Mohanty et al., 2023). To further investigate battery stability, long-term cycling tests were conducted using different electrolytes. As shown in Figure 5b, the battery with the nano-$SiO_2$-additive electrolyte exhibits excellent cycling stability, maintaining stable capacity over 500 cycles. In contrast, the battery without the nano-$SiO_2$-additive electrolyte shows a rapid capacity decline after 80 cycles. This highlights the role of the nano-$SiO_2$-additive electrolyte in significantly enhancing the long-term durability of the battery. Figure 5c further illustrates the rate performance of the full batteries with different electrolytes under various current densities. The battery with the nano-$SiO_2$-additive electrolyte consistently delivers higher specific capacities across all rates, and after returning to the current density of 0.5 A $g^{-1}$, it recovers most of its original capacity. These results confirm the beneficial effect of the nano-$SiO_2$-additive electrolyte in improving both rate capability and structural stability.

## CONCLUSIONS

This study explores the effectiveness of nano-$SiO_2$ as an electrolyte additive to enhance the performance of rechargeable zinc-ion batteries. The optimized incorporation of nano-$SiO_2$ significantly improves zinc plating and stripping behavior by reducing overpotential, suppressing dendrite formation, and mitigating corrosion reactions. In symmetric Zn||Zn cells, the presence of nano-$SiO_2$ extended cycling life and markedly reduced internal resistance compared to control electrolytes without the additive. Zn||Cu half-cells exhibited enhanced Coulombic efficiency and a notably lower nucleation overpotential, indicating more uniform and stable zinc deposition. Furthermore, full-cell configurations employing $V_2O_5$ cathodes and nano-$SiO_2$-enhanced electrolytes demonstrated larger cyclic voltammetry (CV) curve areas, reflecting improved capacitive behavior and charge storage capability. The system also showed superior rate capability across a range of current densities and maintained stable capacity retention over 500 charge–discharge cycles. These findings confirm that strategic electrolyte engineering using nano-silica additives offers a scalable and effective pathway to developing high-performance, long-lasting zinc-ion batteries, making them viable candidates for next-generation energy storage applications.

## ACKNOWLEDGEMENTS

This work was supported by the Thailand Science Research and Innovation Fund Chulalongkorn University and National Research Council of Thailand (NRCT) and Chulalongkorn University (N42A660383).

PPC & PETROMAT SYMPOSIUM 2025

## REFERENCES

**Alawi, M. J., Gamal, H., Rashad, M., Alziyadi, M. O., & Shalaby, M. S.** (2025). *Zinc-Ion Batteries: Drawbacks, Opportunities, and Optimization Performance for Sustainable Energy Storage*. pp. 1–15. Journal of Alloys and Compounds, Elsevier.

**Yang, J., Yin, B., Sun, Y., Pan, H., Sun, W., Jia, B., Zhang, S., & Ma, T.** (2022). *Zinc Anode for Mild Aqueous Zinc-Ion Batteries: Challenges, Strategies, and Perspectives*. pp. 1–42. Nano-Micro Letters, Springer.

**Huang, J., Peng, Q., Liu, K., & Fang, G.** (2023). *Silica-based electrolyte regulation for stable aqueous zinc-manganese batteries.* pp. 434–442. Journal of Central South University, Springer.

**Shang, Y., & Kundu, D.** (2022). *Understanding and Performance of the Zinc Anode Cycling in Aqueous Zinc-Ion Batteries and a Roadmap for the Future*. pp. 1–20. Batteries & Supercaps, Wiley.

**Lin, C., Ou, S., Liu, B., Niu, Y., Wang, X., Lin, H., Li, R., An, M., Zhang, X., & Yuan, Z.** (2025). *Enhanced electrochemical performance of zinc-ion batteries using functionalized nano-chitin separators*. pp. 1–12. Advanced Composites and Hybrid Materials, Springer.

**Mohanty, R., Parida, K., & Parida, K.** (2023). *Redox mediator-enhanced charge storage in dimensionally tailored nanostructures towards flexible hybrid solid-state supercapacitors*. pp. 4521–4535. Nanoscale Advances, Royal Society of Chemistry

PPC & PETROMAT SYMPOSIUM 2025

# Mn-DOPED $NiCo_2S_4$ SUPPORTED ON REDUCED GRAPHENE OXIDE AS BIFUNCTIONAL CATALYSTS IN RECHARGEABLE ZINC-AIR BATTERIES

***Chatthakarn Banyongponglert*** [a], ***Nisit Tantavichet*** *, [a]

[a)]**Department of Chemical Technology, Faculty of Science, Chulalongkorn University**

Keywords: Zinc-air batteries (ZABs); Bifunctional catalyst; Oxygen reduction reaction (ORR); Oxygen evolution reaction (OER)

## ABSTRACT

Rechargeable zinc-air batteries (RZABs) are promising electrochemical energy conversion and storage devices due to their high theoretical energy density, low cost, the abundance of oxygen, the affluence of zinc, and safety. However, the slow reactions on the air cathode limit the efficiency of the RZABs. Therefore, developing high-performing bifunctional catalysts to improve both the oxygen reduction reaction (ORR) and the oxygen revolution reaction (OER) is very important. $NiCo_2S_4$/rGO is reportedly used as the electrode material for energy storage devices including a catalyst for air cathode in RZABs. In this work, we focus on improving the electrochemical performance of $NiCo_2S_4$/rGO by doping it with manganese (Mn) to modify its electronic structure and enhance the electrocatalytic activities and stabilities of the ORR and OER.The results demonstrate that doping $NiCo_2S_4$/rGO with Mn can enhance electrocatalytic activities of the ORR and OER of RZABs.

* Nisit.T@chula.ac.th

## INTRODUCTION

Nowadays electrical energy is being used more and more , and with the increased global focus on environmental friendliness, the use of renewable energy sources has been increasing to generate electricity instead of using fossil fuels. The potential of using renewable energy is increasing gradually (Díaz et al., 2024). However, since renewable energy cannot consistently produce electricity, energy storage devices are needed to store energy for use when production is not possible. It is well-known that oxygen reduction reaction (ORR) and oxygen evolution reaction (OER) play a vital role in energy storage devices, especially metal-air batteries. In RZABs, ORR/OER bifunctional catalyst is necessary to achieve high performance and stability. Normally, platinum is almost universally known as the best catalyst for ORR, while iridium and rudium oxides are known for their great electrocatalytic activities for OER. However, certain shortcomings, such as high price, scarcity and poor stability, have prohibited RZABs extensive applications (Zheng et al., 2021).

PPC & PETROMAT SYMPOSIUM 2025

The purpose of this study is to improve the electrochemical performance of $NiCo_2S_4$/rGO by doping it with manganese (Mn) to modify its electronic structure and enhance the electrocatalytic activities and stabilities of both the ORR and OER.

## EXPERIMENTAL

*A. Chemicals*

Graphite, Nickel nitrate hexahydrate ($Ni(NO_3)_2.6H_2O$), Cobalt nitrate hexahydrate ($Co(NO_3)_2.6H_2O$), Thiourea ($CH_4N_2S$), Manganese chloride tetrahydrate ($MnCl_2.4H_2O$), Nafion (5%wt.) were purchased from sigma Aldrich. Hydrogen peroxide ($H_2O_2$), Potassium permanganate ($KMnO_4$), Hydrochloric acid (HCl), ethanol were purchased from Qrec. All chemical were commercially available and used directly after purchase without further purification.

*B. Preparation of Graphene oxide (GO)*

GO was synthesised by the modified hummer method, when ref. 2 g graphite was stirred in $H_2SO_4$ for 2 h. After that, 6 g $KMnO_4$ was gradually added with stirring while maintaining temperature below 20 °C, and stirred for 2 h. 90 ml deionized water was slowly added to the mixture while adding 10 ml $H_2O_2$ solution followed by 150 ml deionized water. The suspension was centrifuged, washed in HCl and water until pH 5-7, and dried overnight at 60 °C (Tumnantong et al., 2020).

*C. Synthesis of $NiCo_2S_4$/rGO composites*

60 mg GO was dispersed in 60 ml ethylene glycol and sonicate for 1 h. Then 0.5 mmol $Ni(NO_3)_2.6H_2O$, 1 mmol $Co(NO_3)_2.6H_2O$ were added and stirred at 80 °C for 2 h, subsequently, then 4 mmol thiourea was added into the solution. The solution was transferred to a teflon-lined stainless steel autoclave heated at 180 °C for 7 h . After cooling, the sample was washed with DI water and ethanol, and dried at 60 °C for 24 h to obtain the NCS-rGO product.

*D. Synthesis of Mn doped $NiCo_2S_4$/rGO composites*

For the synthesis of Mn doped $NiCo_2S_4$/rGO composites, the process was similar to that of $NiCo_2S_4$/rGO composites, except varied amounts of $MnCl_2.4H_2O$, including 0.25 mmol (assigned as 0.5Mn-NCS/rGO following the mole ratio of Mn:Ni) and 0.5 mmol (1Mn-NCS-rGO), were added to the process above.

*E. Characterizations*

The morphology and physical structure and the element composition distribution of these catalyst were characterized by field scanning electron microscopy and energy dispersive spectroscopy (FESEM/EDS). The phase of composition of the samples was analyzed by X-ray diffractometer (XRD).

PPC & PETROMAT SYMPOSIUM 2025

*F. Electrochemical measurements*

All electrochemical analysis for the ORR and OER was carried out in 0.1 M KOH solution using a Gamry Potentiostat (type 1010E), with an Ag/AgCl as the reference electrode, a Platinum (Pt) electrode as the counter electrode and a 5 mm diameter glassy carbon rotating disk electrode (RDE) as the working electrode. To prepare the catalyst ink, 6 mg of catalyst was dispersed in 700 µL ethanol, 300 µL DI water and 60 µL Nafion (5 wt.%) and sonicated for 60 min. The as-prepared catalyst ink was dropped onto the GC surface using micropipette and then dried under ambient conditions.

## RESULTS AND DISCUSSION

*A. Structural properties*

Fig. 1 shows the XRD pattern of $NiCo_2S_4$/rGO, where the diffraction peaks at 16.8°, 24.7° , 31.98° , 38.10° 55.42° corresponding to the (111), (220), (311), (400), (440) planes, respectively matches the $NiCo_2S_4$ (JCPDS Card no. 00-043-1477), indicating the formation of $NiCo_2S_4$ (Abdel-Salam et al., 2022). The XRD patterns of the Mn-doped samples exhibit similar profiles to that NCS-rGO, which no distinct peaks corresponding to Mn observed. This may be due to the low doping amount of Mn, which was below the detection limit of the XRD.

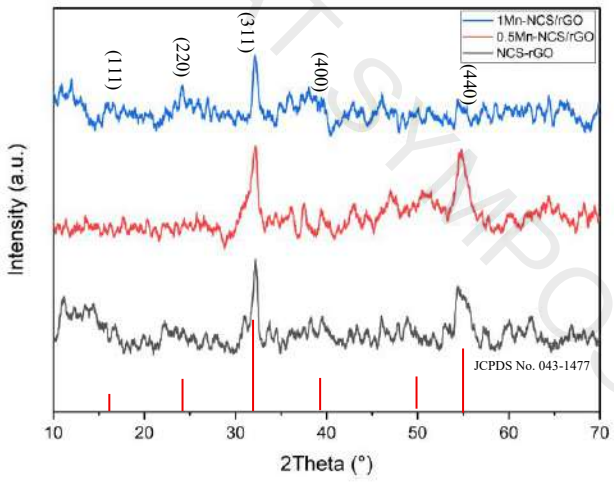


**Fig. 1** XRD diffraction patterns of the NCS-rGO and Mn-doped NCS-rGO

Fig. 2 (a-c) show the morphologies of undoped and Mn doped $NiCo_2S_4$-rGO. The SEM images indicated that NCS-rGO and Mn doped $NiCo_2S_4$-rGO had relatively similar morphologies and had good distribution of NiCoS on reduced graphene oxide. The EDS elemental analysis results show the content of Mn in 0.5Mn-NCS/rGO and 1Mn-NCS/rGO were 0.03 and 0.11 %wt., respectively.

PPC & PETROMAT SYMPOSIUM 2025

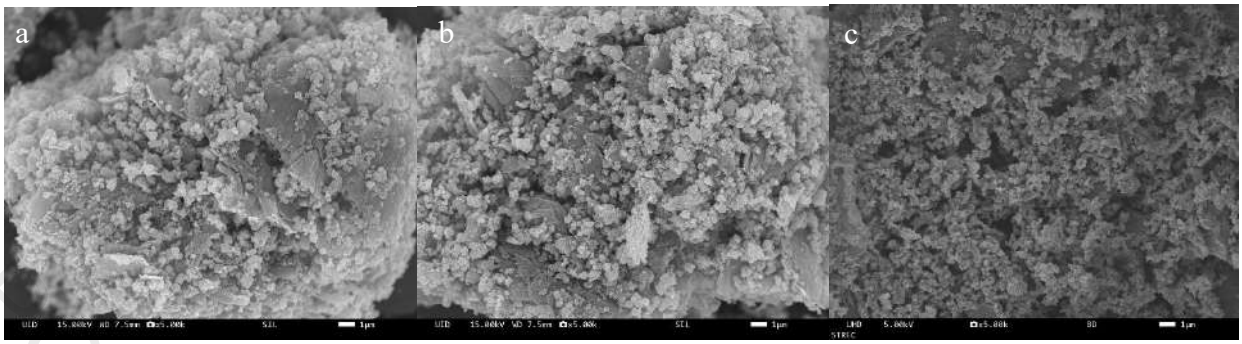


**Fig. 2** SEM images of (a) NCS-rGO, (b) 0.5Mn-NCS/rGO (c) 1Mn-NCS/rGO

*B. ORR and OER performance*

The electrochemical catalytic performance of these catalysts was measured with linear sweep voltammetry (LSV) at a scan rate of 5 $mV.s^{-1}$ at various the rotation speeds from 425 to 2500 rpm. Fig. 3 exhibit the comparison of the electrocatalytic performances for ORR and OER of NCS-rGO, 0.5Mn-NCS/rGO and 1Mn-NCS/rGO, and the corresponding onset potential ($E_{onset}$ ), half-wave potentials ($E_{1/2}$) for ORR, where $E_{onset}$ is defined as the potential at which the oxygen reduction reaction (ORR) becomes discernible and the reaction begins to proceed; more positive onset potential indicates enhanced ORR activity and a lower activation barrier. Fig. 3a shows that the onset potentials ($E_{onset}$) of NCS-rGO, 0.5Mn-NCS/rGO and 1Mn-NCS/rGO are 0.82 V, 0.84 V, 0.86 V, respectively. The half-wave potentials ($E_{1/2}$) of NCS-rGO, 0.5Mn-NCS/rGO and 1Mn-NCS/rGO are 0.60 V, 0.64 V, 0.65 V, respectively. As a result, both the onset potentials ($E_{onset}$) and half-wave potentials ($E_{1/2}$) values of 0.5Mn-NCS/rGO and 1Mn-NCS/rGO are higher than NCS-rGO, which indicating that 0.5Mn-NCS/rGO and 1Mn-NCS/rGO exhibit superior ORR performance. For the OER (Fig. 3b), the potentials of the catalysts were evaluated at a current density of 10 $mA.cm^{-2}$. The potentials of NCS-rGO, 0.5Mn-NCS/rGO and 1Mn-NCS/rGO are 1.67 V, 1.52 V and 1.52 V, respectively. These results clearly show that 0.5Mn-NCS/rGO and 1Mn-NCS/rGO require a lower overpotential than NCS-rGO, confirming their enhanced OER activity.

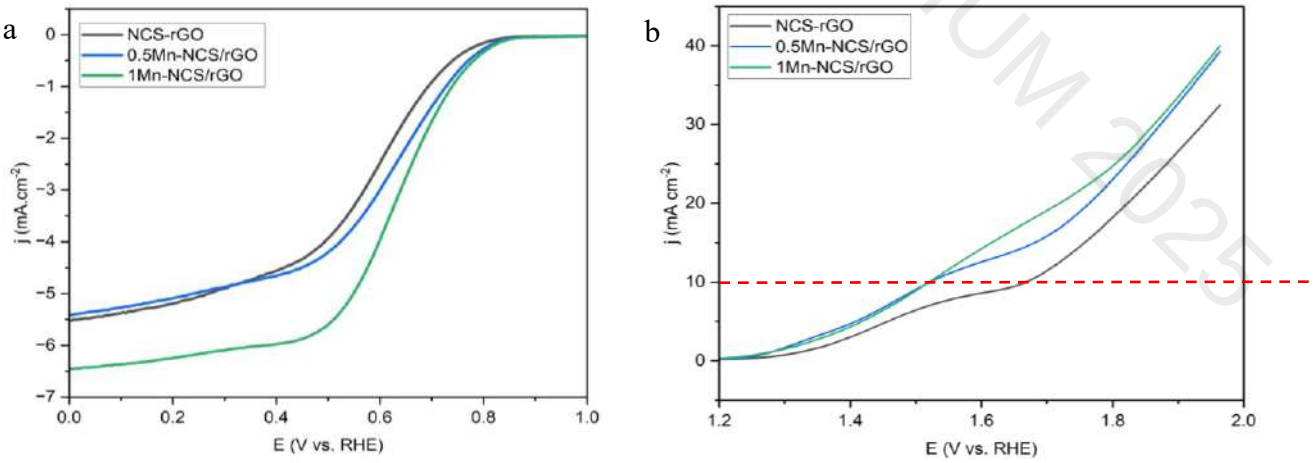


**Fig. 3** (a) ORR at 1600 rpm (b) OER at 1600 rpm

In summary, Mn-doped $NiCo_2S_4$/rGO was synthesized via a one-step solvothermal method. Mn incorporation was found to enhance the electrocatalytic performance of the $NiCo_2S_4$/rGO toward both the oxygen reduction reaction (ORR) and the oxygen evolution reaction (OER). As a result, the ORR half-wave potential increased from 0.60 V to 0.65 V, while the OER potential at a current density of 10 $mA \cdot cm^{-2}$ decreased from 1.67 V to 1.52 V. Although the amount of Mn incorporated was relatively low, a significant improvement in performance as observed compared to undoped $NiCo_2S_4$/rGO when the Mn content reached an optimal level.

## ACKNOWLEDGEMENTS

This Research is funded by Center of Excellence on Advanced Materials for Energy Storage, Chulalongkorn University, Bangkok, Thailand.

## REFERENCES

**Tumnantong, D., Poompradub, S., & Prasassarakich**, P. (2020). Poly(methyl methacrylate)-graphene emulsion prepared via RAFT polymerization and the properties of NR/PMMA-graphene composites. *European Polymer Journal*, *139*, 109983. https://doi.org/https://doi.org/10.1016/j.eurpolymj.2020.109983

**Díaz, C., Jaramillo, D., Sierra, L., López, B. L., Zheng, X., Moreno-Zuria, A., Mohamedi, M., & Palacio, R.** (2024). Nanoparticles of NiO and CoO simultaneously dispersed on a mesoporous carbonaceous support as bifunctional electrocatalysts for ORR and OER reactions and Zn-air battery performance. *Applied Catalysis A: General*, *682*, 119805. https://doi.org/https://doi.org/10.1016/j.apcata.2024.119805

**Zheng, X., Mohammadi, N., Moreno Zuria, A., & Mohamedi, M.** (2021). Advanced Zinc–Air Batteries with Free-Standing Hierarchical Nanostructures of the Air Cathode for Portable Applications. *ACS Applied Materials & Interfaces*, *13*(51), 61374-61385. https://doi.org/10.1021/acsami.1c22371

**Abdel-Salam, A. I., Attia, S. Y., El-Hosiny, F. I., Sadek, M. A., Mohamed, S. G., & Rashad, M. M.** (2022). Facile one-step hydrothermal method for NiCo2S4/rGO nanocomposite synthesis for efficient hybrid supercapacitor electrodes. Materials Chemistry and Physics, 277, 125554. https://doi.org/https://doi.org/10.1016/j.matchemphys.2021.125554

PPC & PETROMAT SYMPOSIUM 2025

# Effect of Diverse Cation-Anion Salt Combinations on Methane Hydrate Formation

*Teerapat Pongpuak* [a], *Kan Jeenmuang* [b], *Phuwadej Pornaroontham* [c], *Santi Kulprathipanja* [a], *Pramoch Rangsunvigit* *, [a]

[a] The Petroleum and Petrochemical College, Chulalongkorn University, Bangkok, Thailand
[b] Department of Chemical and Biomolecular Engineering, National University of Singapore, Singapore 117575, Singapore
[c] Department of Chemical Technology, Faculty of Science, Chulalongkorn University, Bangkok, 10330, Thailand

Keywords: Methane hydrate; Salt inhibition; Hydrate formation kinetics; Seawater-based storage

## ABSTRACT

This study explores the effects of various cation salts on methane hydrate formation under moderate conditions (277.2 K and 8 MPa), with 1.0 wt% methionine serving as a kinetic promoter. Four salts, NaCl, KCl, $CaCl_2$, and $MgCl_2$ were investigated across three concentrations (0.20, 0.40, and 0.60 mol%) to assess their influence on formation kinetics and storage capacity. The findings reveal a clear correlation between cation charge density and ionic radius on hydrate inhibition. Divalent salts ($Ca^{2+}$, $Mg^{2+}$) significantly suppressed hydrate formation, attributed to strong electrostatic fields that create strongly hydration shells and limit water availability for cage formation. Methane uptake decreased by up to 98%, and the normalized initial formation rate at 30 minutes after induction ($NR_{30}$) dropped by more than 95% compared to the salt-free system. In contrast, monovalent salts ($Na^+$, $K^+$) exhibited weaker inhibitory effects, maintaining relatively higher uptake and shorter $t_{90}$ (time to reach 90% of total methane uptake), due to its lower charge density and diffuse hydration shell. Morphological analyses supported these trends, showing slower growth and altered nucleation in divalent salt systems. These results provide mechanistic insights into how cation properties modulate hydrate behavior and offer guidance for designing hydrate-based energy storage systems, particularly under saline or seawater-based conditions.

***pramoch.r@chula.ac.th**

## INTRODUCTION

Natural gas continues to play an important role in the shift toward cleaner energy. As demand rises, efficient, safe, and cost-effective storage and transport methods are increasingly important. Traditional options such as pipelines, Compressed Natural Gas (CNG), and Liquefied Natural Gas (LNG) face limitations related to infrastructure, safety, or high energy costs. Solidified Natural Gas (SNG), formed via gas hydrates, offers a promising alternative technology. SNG using gas hydrates has emerged as a promising alternative. Gas hydrates are crystalline compounds where gas molecules are trapped within hydrogen-bonded water cages, offering a volumetric storage up to 160 times the gas volume at STP (Sloan and Koh, 2007). They are stable, non-explosive, environmentally benign, and form under moderate pressure and temperature conditions without requiring extreme cooling (Veluswamy *et al*., 2018; Xia *et al*., 2022). These advantages make hydrate-based systems attractive for long-term, safe, and compact gas storage.

PPC & PETROMAT SYMPOSIUM 2025

One practical challenge in hydrate-based storage systems is the reliance on deionized (DI) water, which can become prohibitively expensive at industrial scales, especially considering that hydrates are composed of over 85 mol% water. Seawater presents a more economical and sustainable alternative due to its abundance and accessibility, but the presence of dissolved salts and ions can interfere with hydrate formation. The influences by which individual ions suppress formation kinetics remain poorly understood. This study addresses that gap by systematically examining how different salts commonly found in seawater influence methane hydrate formation kinetics. Methionine, a hydrophobic amino acid, is employed as a kinetic promoter to overcome the inhibition. The findings aim to support the development of cost-effective, seawater-based SNG technologies by identifying the ionic factors that most significantly impact hydrate behavior.

## EXPERIMENTAL

*A. Chemicals*

1. Ultra-high purity methane (from Thai-Japan Gas Company, 99.9 %)
2. Methionine (from Sigma-Aldrich, amino acid reagent grade > 98 % (HPLC)
3. Potassium chloride (from Supelco, Inc, ≥99.5 %)
4. Calcium chloride dihydrate (from Supelco, Inc, 99.0-102.0 %)
5. Magnesium chloride hexahydrate (from Supelco, Inc, 99.0-102.0 %)
6. Sodium chloride (from RCI Labscan Limited, 99 %)
7. Deionized water

*B. Experimental Apparatus*

The experimental setup for methane hydrate formation is shown in Figures 1(a). A stainless-steel crystallizer (CR), designed for up to 20 MPa, contains two sapphire windows for visual observation, Figures 1(b). Gas is supplied from a 50 $cm^3$ reservoir (R), with both CR and R immersed in a water-glycol cooling bath regulated by an external refrigerator (LCB-R20, Labtech). Pressure is monitored using a pressure transmitter (Cole Parmer, 0-21 MPa, 0.13% accuracy) and an analog pressure gauge. A T-type thermocouple (accuracy of ± 0.1 °C) measures internal temperature. Data are recorded every 10 seconds by a data logger (AI210, Wisco) connected to a PC. A video camera (C-B3, Optika) captures hydrate morphology throughout the experiment.

*C. Experimental Procedure*

Aqueous solutions were prepared by dissolving methionine and the desired salt in a small amount of water, then diluted to 35 $cm^3$. The solution and a magnetic stir bar were added to the stainless-steel crystallizer, which was then connected to the gas line and thermocouple. The crystallizer was placed in a glycol-water bath and cooled to 277.2 K using an external chiller. The system was purged three times to eliminate residual air before introducing methane to a final pressure of 8 MPa. Stirring was initiated at 550 rpm to ensure uniform mixing. Temperature and pressure were continuously recorded, and hydrate formation was visually monitored by capturing images every 60 seconds through a sapphire window.

PPC & PETROMAT SYMPOSIUM 2025

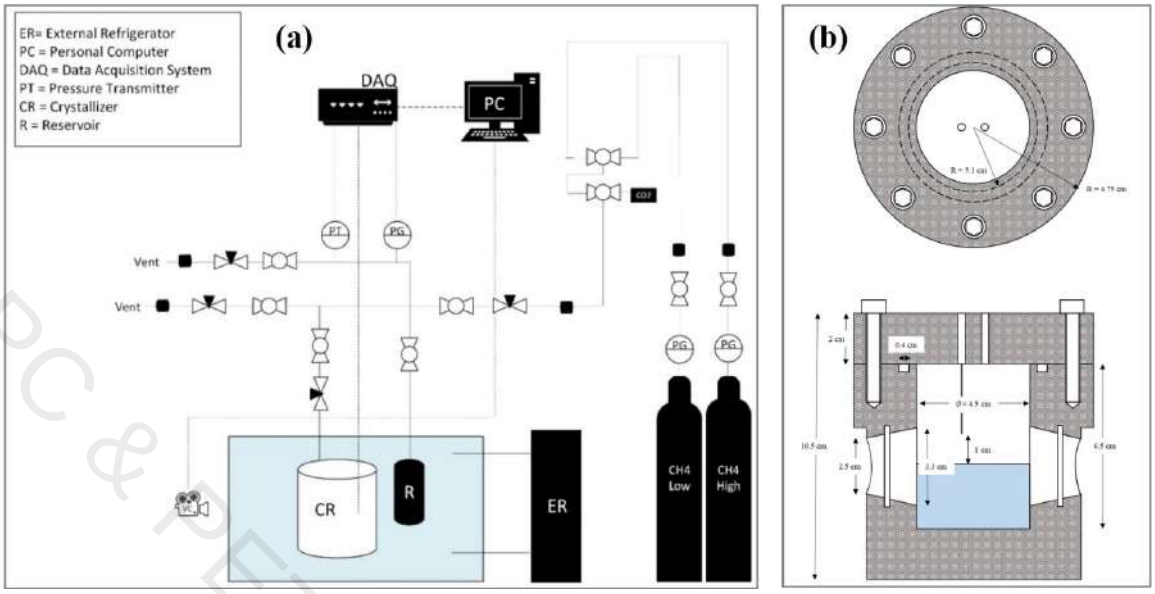


**Figure 1** Schematic of gas hydrate (a) experimental apparatus and (b) cross-section of a crystallizer.

## RESULTS AND DISCUSSION

### *A. Influence of Salt Ion on Methane Hydrate Formation*

This study examined the effect of salt ions, specifically sodium ion ($Na^+$), the most abundant cation in seawater, on methane hydrate formation using NaCl as the representative salt. As shown in the hydrate methane uptake profiles, Figure 2(a), increasing NaCl concentration from 0.20 to 0.60 mol% progressively inhibited hydrate formation. The slope of the uptake curves, representing the normalized rate of hydrate formation during the first 30 minutes after nucleation ($NR_{30}$), decreased significantly with increasing salt concentration, showing reductions of approximately 44%, 67%, and 80% at 0.20, 0.40, and 0.60 mol%, respectively, compared to the salt-free condition. In contrast, the time to reach 90% completion of hydrate formation ($t_{90}$) increased from 40.11 (salt-free system) to 143.39 minutes at the highest concentration, indicating slower growth kinetics. Methane uptake also decreased from 127.05 mmol/mol in the salt-free system to 96.11 mmol/mol at 0.60 mol% of NaCl, along with a reduction in water-to-hydrate conversion from 73.05% to 55.26%, respectively. The morphology observation (Figure 2(b)) supported the kinetic trends, showing that high NaCl concentrations resulted in delayed nucleation and disrupted early hydrate formation and growth, as evidenced by the appearance of sparse and patchy hydrate structures, Figure 2 (b2)-i.

PPC & PETROMAT SYMPOSIUM 2025

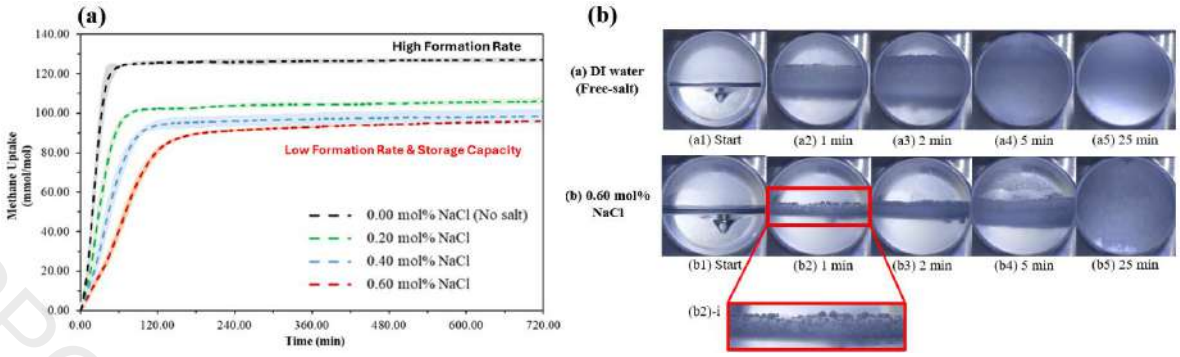


**Figure 2** (a) Methane uptake profiles at different NaCl concentrations. (b) Visual morphology showing hydrate formation of 0.60 mol% NaCl compared to salt-free system.

*B. Comparative Analysis of Cationic Effects on Methane Hydrate Formation*

The comparative influence of four cations commonly found in seawater ($Na^+$, $K^+$, $Ca^{2+}$, and $Mg^{2+}$) on methane hydrate formation, evaluated through $NR_{30}$ (Figure 3(a)) and final methane uptake (Figure 3(b)). The results clearly showed that monovalent cations ($Na^+$ and $K^+$) caused less inhibition than divalent cations ($Ca^{2+}$ and $Mg^{2+}$) across all concentrations. Between NaCl and KCl, the $NR_{30}$ values were comparable, with KCl showing only a slightly higher rate, especially at 0.40 and 0.60 mol%. This difference was minimal and not prominent. In contrast, $CaCl_2$ and $MgCl_2$ significantly reduced the $NR_{30}$, dropping by over 99% at 0.60 mol% compared to the salt-free system, indicating complete suppression of early-stage hydrate growth. Methane uptake followed a similar trend, with all salts showing a concentration-dependent decline, which was particularly pronounced in divalent systems. At 0.40 mol%, methane uptake in $CaCl_2$ and $MgCl_2$ systems was reduced by more than half compared to monovalent salts. At 0.60 mol%, hydrate formation was nearly halted, with final methane uptake approaching zero. These findings highlight the distinct impact of ionic valency on both hydrate formation rate and methane uptake under identical experimental conditions.

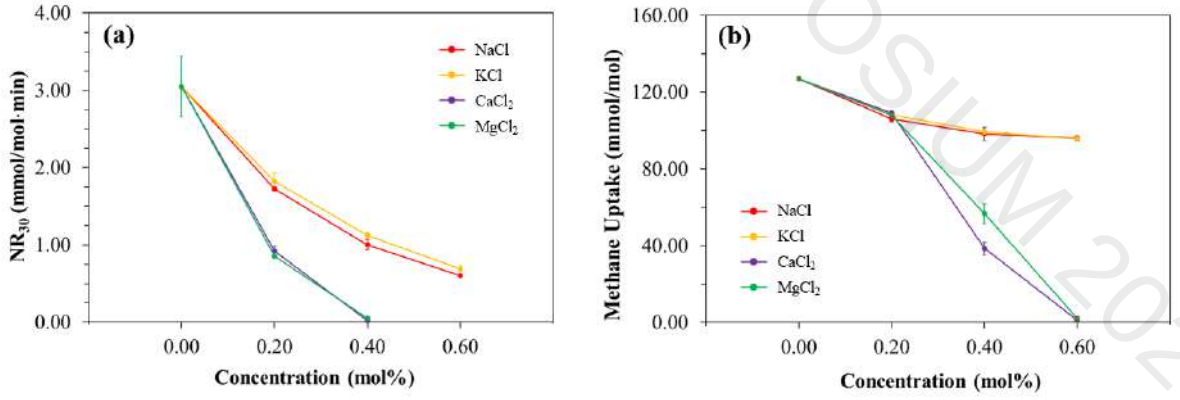


**Figure 3** Scatter plots comparing hydrate formation parameters (a) $NR_{30}$ and (b) methane uptake during methane hydrate formation at 277.2 K and 8.0 MPa in the presence of 1.00 wt% methionine and four salts at varying concentrations.

*C. Mechanistic Insights into Salt-Inhibition of Methane Hydrate Formation*

The mechanism underlying the differing effects of the four salts lies in their chemical behavior upon dissolution. In water, salts dissociate into cations and anions, which form hydration shells through electrostatic interactions with surrounding water molecules. The strength and structure of these hydration shells are influenced by the ions' charge density and ionic radius. These structured shells interfere with the natural hydrogen-bonding network of water, thereby disrupting with the molecular arrangement required for hydrate formation. As shown in Figure 4, inhibition increased with cation charge density, $K^+$ (11 C/mm$^3$) ≈ $Na^+$ (24 C/mm$^3$) < $Ca^{2+}$ (52 C/mm$^3$) < $Mg^{2+}$ (120 C/mm$^3$). Stronger hydration shells, especially in $Ca^{2+}$ and $Mg^{2+}$ systems, disturbed water structure more severely and suppressed hydrate formation. Additionally, salt ions may transiently interact with forming hydrate cages, attracting water molecules and introducing structural distortions. These disruptions lead to weakened cage stability and potential disintegration due to steric and electrostatic mismatches (Tung et al., 2012). The reduction of such structures suggests that salts inhibit both the nucleation and growth phases of hydrate formation, ultimately lowering the storage capacity and efficiency of methane encapsulation (Xu et al., 2021).

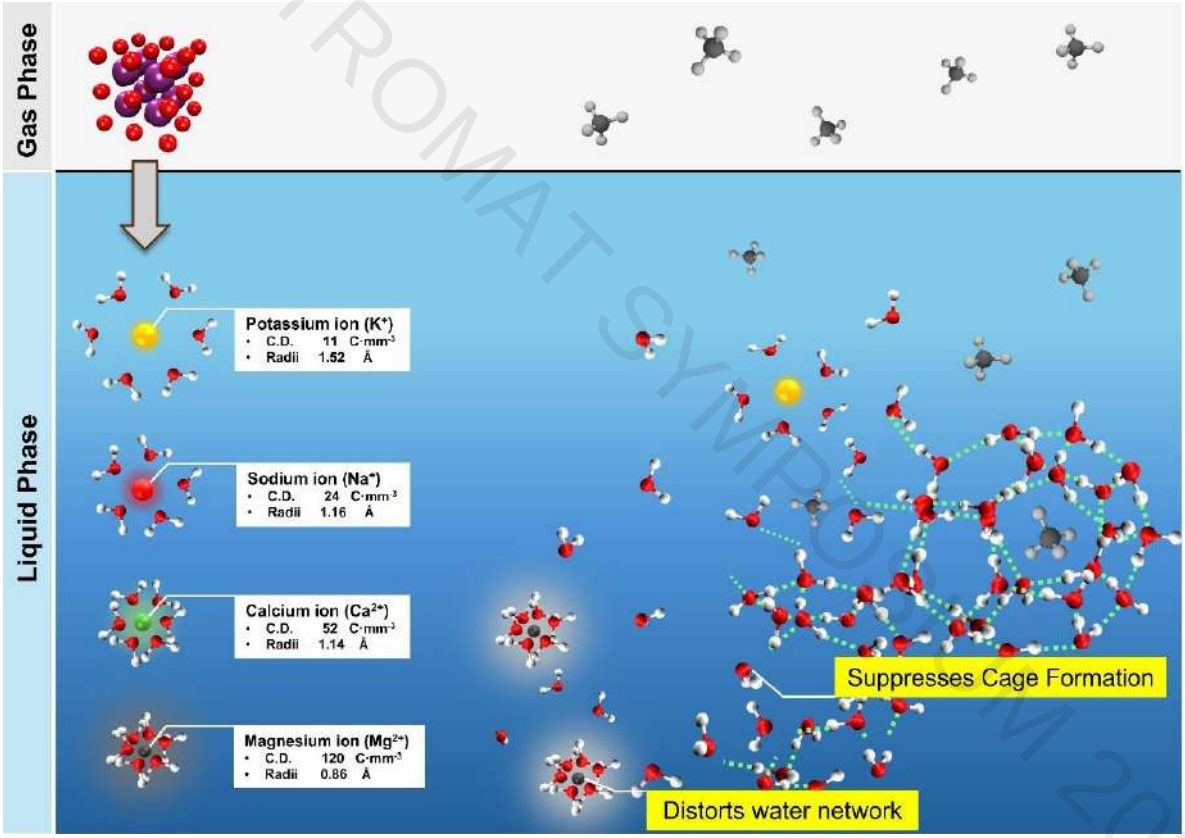


**Figure 4** Schematic illustration of the effects of different cations ($K^+$, $Na^+$, $Ca^{2+}$, and $Mg^{2+}$) on methane hydrate formation through their interactions with water molecules.

PPC & PETROMAT SYMPOSIUM 2025

## CONCLUSIONS

This study demonstrated the significant influence of cationic salts on methane hydrate formation under 277.2 K and 8 MPa with 1.0 wt% methionine. Inhibition increased with cation charge density, following the trend $K^+ \approx Na^+ < Ca^{2+} < Mg^{2+}$. Divalent cations, particularly $Ca^{2+}$ and $Mg^{2+}$, formed strong hydration shells that severely suppressed hydrate nucleation and growth, reducing methane uptake and $NR_{30}$ by up to 98%. In contrast, monovalent cations caused only minor inhibition. These findings confirm that ion-specific properties, especially charge density and hydration structure, critically govern hydrate formation behavior.

## ACKNOWLEDGEMENTS

The author would like to acknowledge the Petroleum and Petrochemical College (PPC), Chulalongkorn University, for providing research facilities and academic support. Special thanks go to Prof. Pramoch Rangsunvigit for his guidance and encouragement throughout this work.

## REFERENCES

**Sloan and Koh, C.** (2007). Clathrate hydrates of natural gases, thrid edition. 1-730.

**Veluswamy, H. P., Kumar, A., Seo, Y., Lee, J. D. and Linga, P.** (2018). A review of solidified natural gas (SNG) technology for gas storage via clathrate hydrates. Applied Energy, 216, 262-285.

**Xia, Z., Zhao, Q., Chen, Z., Li, X., Zhang, Y., Xu, C. and Yan, K.** (2022). Review of methods and applications for promoting gas hydrate formation process. Journal of Natural Gas Science and Engineering, 101, 104528.

**Tung, Y.-T., Chen, L.-J., Chen, Y.-P. and Lin, S.-T. (2012).** Molecular Dynamics Study on the Growth of Structure I Methane Hydrate in Aqueous Solution of Sodium Chloride. The Journal of Physical Chemistry B, 116(48), 14115-14125.

**Xu, J., Du, S., Hao, Y., Yang, X. and Zhang, J. (2021).** Molecular simulation study of methane hydrate formation mechanism in NaCl solutions with different concentrations. Chemical Physics, 551, 111323.

PPC & PETROMAT SYMPOSIUM 2025

# Effect of Viscoelastic Silica Gel in Generating Foam for Enhanced Oil Recovery (EOR)

*Pemika Sathitwong*[a], *Ampira Charoensaeng*[a,b], *Bor-Jier Shiau*[c], *Uthaiporn Suriyapraphadilok* [a,b]

[a] The Petroleum and Petrochemical College, Chulalongkorn University, Bangkok, Thailand
[b] Center of Excellence on Petrochemical and Materials Technology, Bangkok, Thailand
[c] Mewbourne School of Petroleum and Geological Engineering, University of Oklahoma, Norman, Oklahoma, USA

Keywords: Silica Nanoparticle, Surfactant, Foam Flooding, Enhanced Oil Recovery (EOR)

## ABSTRACT

Gas-foam flooding is a promising technique for Enhanced Oil Recovery (EOR). However, foam instability under harsh reservoir conditions remains a significant challenge. This research focuses on enhancing foam stability by incorporating a viscoelastic silica-based gel into a surfactant-stabilized foam system. The viscoelastic silica gel was prepared from 1 wt.% hydrophilic silica nanoparticles dispersed in 1.8 wt.% synthetic brine composed of 17.03 wt.% NaCl, 0.58 wt.% KCl, 1.22 wt.%, $CaCl_2$, and 0.05 wt.% $MgCl_2$. The pH, a key factor influencing gel strength, was adjusted to 7 using HCl and NaOH. This neutral condition promotes gelation while ensuring compatibility with field infrastructure. Sodium Cocoyl Isethionate (SCI), in fumed form, was directly incorporated at 2 wt.% into the silica gel. The combination of viscoelastic silica gel and SCI produced synergistic effects, reinforcing foam lamellae and improving resistance to coalescence and liquid drainage. The resulting viscoelastic foam demonstrated enhanced thermal stability, with foam half-lives of 53 minutes at 25 °C and 91 minutes at 60 °C. Foam propagation and structure were evaluated using a micromodel with in-situ nitrogen co-injection. This integrated system significantly improves foam durability and performance, offering a practical and scalable solution for enhancing oil recovery under demanding reservoir conditions.

* **uthaiporn.s@chula.ac.th**

## INTRODUCTION

Enhanced Oil Recovery is the process of recovering the remaining oil that is trapped in the reservoir by the injection of water or chemicals. Oil displacement and volume sweep efficiency are improved during the enhanced oil recovery process. EOR utilizes advanced techniques, including surfactant and/or polymer flooding and gas-foam flooding, to further boost oil extraction. The foam flooding process has been considered by researchers as one of the most effective ways to increase oil recovery by reducing the gas relative permeability, increasing the gas viscosity, and improving the sweep efficiency (Farajzadeh et al., 2010). However, conventional surfactant-stabilized foams often face challenges such as foam drainage, non-uniform bubbles, and low stability of foam. Silica nanoparticles can adsorb at the gas-liquid interface, creating a protective coating over bubbles, therefore improving foam stability by inhibiting bubble coalescence and minimizing liquid outflow (Rezaei et al., 2021). Viscoelastic fluids exhibit both viscous and elastic properties, allowing the viscoelastic foam to resist deformation and maintain its structure under

PPC & PETROMAT SYMPOSIUM 2025

carrying stresses. By incorporating viscoelastic agents like silica nanoparticles into the foam, it is possible to create a more stable and durable structure that can effectively sweep oil from the reservoir. When the foam exhibits viscoelastic properties, the film around the gas bubbles can stretch and recover their shape, which helps in maintaining bubble integrity, while silica nanoparticles adsorb at the gas-liquid interface, forming a reinforced network that prevents film rupture and reduces bubble coalescence.

## EXPERIMENTAL

*A. Viscoelastic silica gel preparation*

A 1.8 wt.% synthetic brine solution was prepared, consisting of 17.03 wt.% NaCl, 0.58 wt.% KCl, 1.22 wt.% $CaCl_2$, and 0.05 wt.% $MgCl_2$ dissolved in deionized water. Hydrophilic silica nanoparticles were dispersed into the brine at the desired concentration by sonication for 30 minutes twice, followed by continuous stirring with a magnetic stirrer for 24 hours. The pH of the mixture was then adjusted to 7 using HCl and NaOH. The viscoelastic properties were characterized by measuring the storage modulus (G') and loss modulus (G") using a rheometer (Anton Paar, Model MCR 702e).

*B. Surfactant screening*

A preliminary surfactant screening was conducted using the handshake method, in which 3 mL of a 2 wt.% surfactant solution was placed into a 15 mL vial. Surfactants demonstrating superior foam half-life were selected for further evaluation using a foam column. For this test, 50 mL of the surfactant solution was introduced into a vertical glass column fitted with a porous glass diffuser at the bottom. Nitrogen gas was injected from the base at a rate of 250 mL/min for 30 seconds, with the flow regulated by a needle valve equipped with a gas flow meter. Foam performance was evaluated at both 25 °C and 60 °C.

*C. Viscoelastic foaming agent preparation*

The viscoelastic foaming agent was formulated by blending the viscoelastic silica gel with the 2 wt.% selected surfactant under continuous magnetic stirring for 24 hours. The resulting mixture was subsequently evaluated for foamability and foam stability at 25 °C and 60 °C to assess its effectiveness as a viscoelastic foaming system.

*D. Micromodel experiment*

Micromodel chips with etched pore structures resembling a sandstone reservoir were used to simulate porous media. In-situ foam was generated by alternately injecting either the surfactant solution or the viscoelastic foaming agent along with nitrogen gas. Foam quality was set at 80%, with a gas injection rate of 1 mL/min and a liquid injection rate of 0.25 mL/min. The oil phase is Isopar L, which was dyed by Oil Red O prior to injection into the micromodel. The oil was aged in the micromodel at 25°C before injecting the displacing phase. Along with the flooding process, the 1.8 wt.% brine was used to flood into the micromodel chip with the injection rate of 0.25 mL/min. This experiment wasdesigned to evaluate the displacement efficiency and flow behavior of the viscoelastic foam compared to conventional surfactant-only foam. Parameters such as oil recovery, breakthrough time, and foam mobility were visually monitored and analyzed using microscopy (Leica, Model DM2700M).

PPC & PETROMAT SYMPOSIUM 2025

## RESULTS AND DISCUSSION

### *A. Viscoelastic silica gel*

To prepare the viscoelastic silica gel, the concentration of silica nanoparticles (SNP) was varied between 1 and 2 wt.%. A 1.8 wt.% synthetic brine, consisting of 17.03 wt.% NaCl, 0.58 wt.% KCl, 1.22 wt.% $CaCl_2$, and 0.05 wt.% $MgCl_2$, was used to promote effective gel formation. The pH of the mixture was adjusted using NaOH to achieve optimal gelation conditions. The viscoelastic behavior of the resulting gels was characterized using rheological measurements, which are essential for evaluating their foam-stabilizing potential. Initially, amplitude sweep tests were conducted to determine the Linear Viscoelastic Region (LVR). Frequency sweep tests were then performed within the LVR to investigate the frequency-dependent viscoelastic properties of the silica gel.

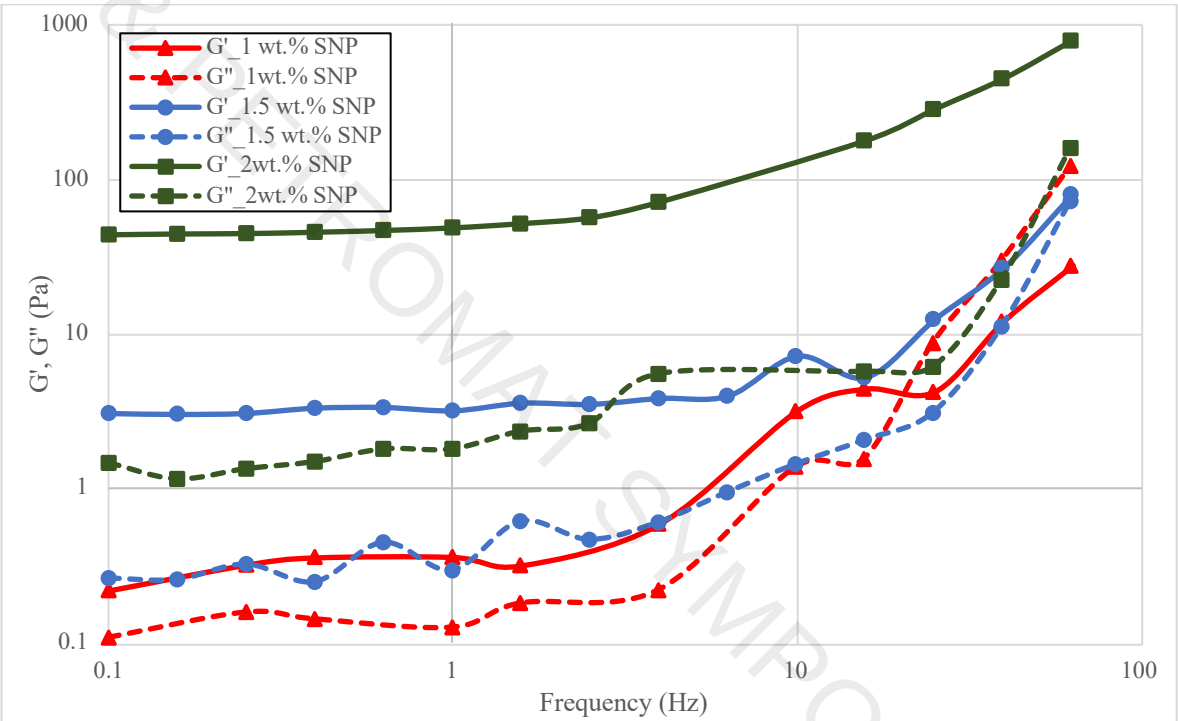


**Figure 1:** Storage modulus (G′) and loss modulus (G″) of silica gel at different silica nanoparticle (SNP) concentrations (1, 1.5, and 2 wt.%) in 1.8 wt.% brine at 25 °C as a function of frequency.

As shown in Figure 1, rheological measurements conducted at 25 °C reveal that all silica gel samples comprising, 1, 1.5, and 2 wt.% SNPs in 1.8 wt.% brine, demonstrate viscoelastic behavior. In each case, the storage modulus (G′), representing the elastic or solid-like nature of the material, exceeds the loss modulus (G″), which reflects its viscous or liquid-like response, particularly at low frequencies. This dominance of G′ over G″ at low deformation rates indicates that the gels behave primarily as elastic solids, suggesting the development of a well-defined internal network structure within the system. (Ilyin et al., 2016).

PPC & PETROMAT SYMPOSIUM 2025

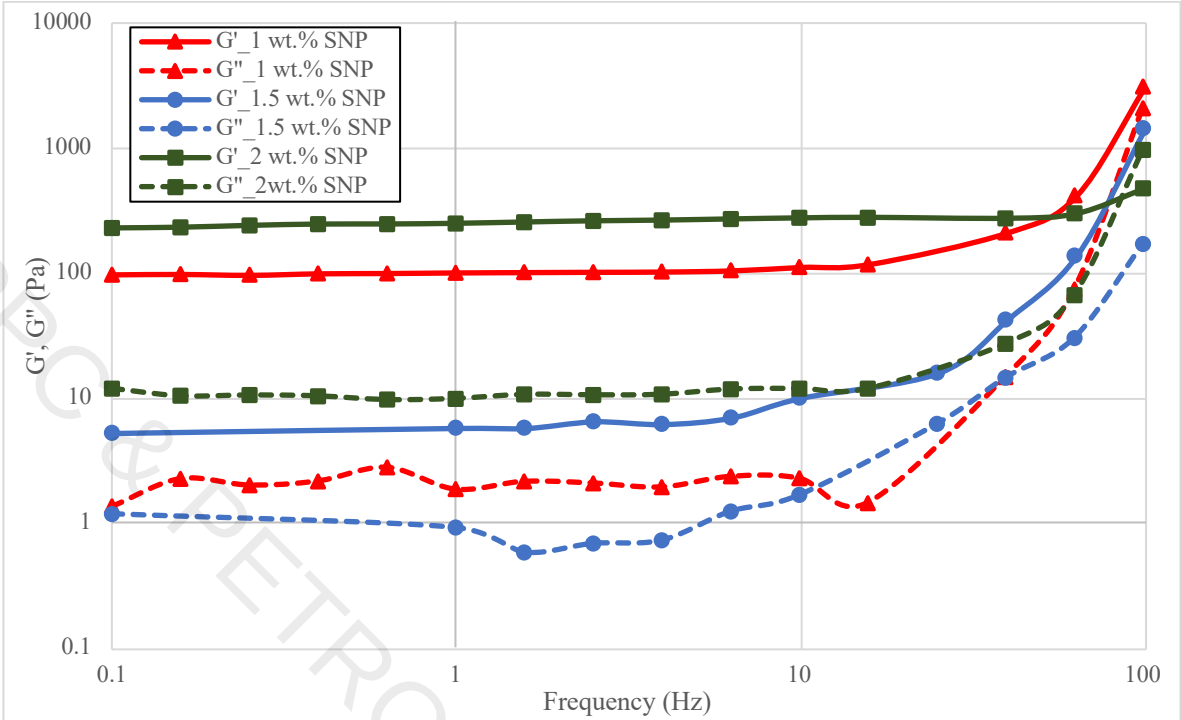


**Figure 2:** Storage modulus (G′) and loss modulus (G″) of silica gel at different silica nanoparticle (SNP) concentrations (1, 1.5, and 2 wt.%) in 1.8 wt.% brine at 60 °C as a function of frequency.

At 60°C, as shown in Figure 2, all samples exhibit a storage modulus (G') that remains consistently higher than the loss modulus (G") across most of the frequency spectrum. This behavior highlights the dominance of the elastic, solid-like properties over the viscous, liquid-like characteristics, indicating that the gel network persists even under elevated temperature conditions. Such results confirm the stability of the viscoelastic structure when subjected to thermal stress.

From a practical standpoint, including considerations like cost-effectiveness, manageable viscosity, and ease of dispersion, the 1 wt.% silica nanoparticle (SNP) concentration was chosen for preparing the viscoelastic foaming agent. This level achieves adequate gel strength and thermal resistance necessary for foam stabilization, while minimizing complications related to high viscosity and processing difficulties encountered at higher SNP concentrations.

*B. Surfactant screening*

The surfactant screening was conducted to identify the most effective surfactant for foam generation and stabilization. The foam ability and foam stability of selected surfactant, Sodium Cocoyl Isethionate (SCI), were evaluated using a foam column.

**Table 1:** Foam ability and foam stability of Sodium Cocoyl Isethionate at 25°C and 60°C in foam column

| | **25°C** | **60 °C** |
|---|---|---|
| **Initial foam height (cm)** | 23.50 | 28.37 |
| **Foam half-life (min)** | 129.28 | 46.62 |

PPC & PETROMAT SYMPOSIUM 2025

Sodium Cocoyl Isethionate (SCI) demonstrated consistent foam generation at both temperatures, indicating its capability to produce foam under ambient and elevated thermal conditions. At 25°C, the initial foam height was measured at 23.50 cm, while at 60°C, a higher foam height of 28.37 cm was observed. This increase is likely associated with the reduced viscosity of the solution and thermal expansion of gas at elevated temperatures, which facilitate foam formation.

In terms of stability, the foam at 25°C exhibited a half-life of 129.28 minutes, reflecting strong stability under room temperature conditions. However, at 60°C, the foam half-life dropped considerably to 46.62 minutes. This decline is likely a result of accelerated water evaporation and weakened lamellae at higher temperatures, leading to faster foam breakdown. These findings underscore the thermal sensitivity of SCI-based foam, particularly regarding its long-term stability.

*C. Viscoelastic foaming agent*

The viscoelastic foaming agent was formulated by blending viscoelastic silica gel, formed using 1 wt.% silica nanoparticles (SNP) in 1.8 wt.% brine, with 2 wt.% Sodium Cocoyl Isethionate (SCI). The foamability and stability of the resulting viscoelastic foam were assessed to evaluate the impact of the gel network on enhancing the structural integrity of the surfactant-based foam.

**Table 2:** Foam ability of the surfactant foam in compare with the viscoelastic foam at 25°C and 60°C in foam column

| | **25°C** | **60 °C** |
|---|---|---|
| **Surfactant foam (cm)** | 23.50 | 28.37 |
| **Viscoelastic foam (cm)** | 26.00 | 37.57 |

**Table 3:** Foam stability of the viscoelastic foam in compare with the surfactant foam at 25°C and 60°C in foam column

| | **25°C** | **60 °C** |
|---|---|---|
| **Surfactant foam (min)** | 129.28 | 46.62 |
| **Viscoelastic foam (min)** | 53.96 | 91.65 |

At 25°C, the viscoelastic foam achieved an average foam height of approximately 26.0 cm with the standard deviation of 1.37, compared to 23.50 cm with the standard deviation of 1.32 for the surfactant-only foam under identical conditions. This enhancement in foam height indicates that the addition of viscoelastic silica gel significantly improves the foam generation capability of the system. The increased foamability is likely due to the elevated bulk viscosity and elasticity imparted by the gel network, which contributes to better stabilization of gas bubbles during foam formation and reduces bubble coalescence in the early stages (Pu et al., 2017). The viscoelastic foam exhibited a shorter foam half-life of 53.96 minutes with the standard deviation of 20.54, compared to the surfactant-only foam, which had a longer half-life of 129.28 minutes with the standard deviation of 9.86. This indicates that the viscoelastic foam collapsed more rapidly. One possible explanation is that

PPC & PETROMAT SYMPOSIUM 2025

the dense gel phase in the viscoelastic system may suppress the Marangoni effect, which is crucial for restoring the interfacial film during local thinning. As a result, the reduced interfacial mobility compromises the foam's ability to resist rupture, leading to decreased stability over time. (Moradpour et al., 2024).

The foam ability of the viscoelastic foam was greater than the of the surfactant foam at 60°C. The initial foam height of the viscoelastic foam reached 37.57 cm, compared to 28.37 cm for the surfactant foam. The presence of the silica nanoparticles and the gel matrix likely contribute to increased elasticity and viscosity, improving the efficiency of gas trapping and leading to higher foam volume. At 60°C, the viscoelastic foam demonstrated significantly superior performance. The foam half-life was recorded at 91.65 minutes for the viscoelastic foam, nearly double that of the surfactant foam, which was only 46.62 minutes. This improvement contrasts with the behavior observed at room temperature, where the viscoelastic foam exhibited lower stability due to excessive viscosity interrupting drainage and elasticity.

*D. Viscoelastic foam flooding*

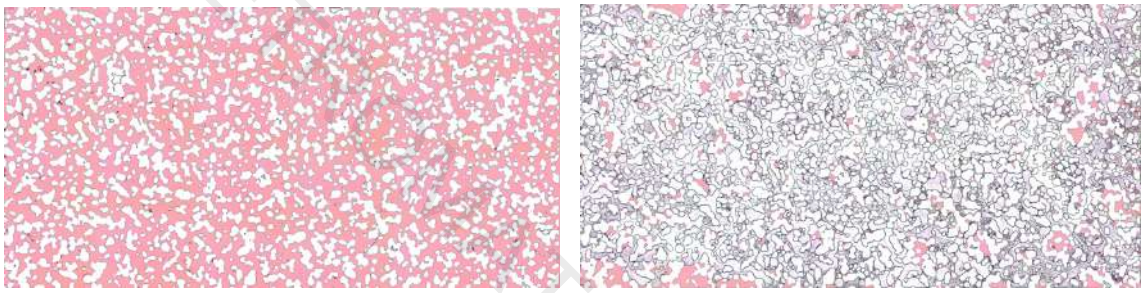

*(a)* *(b)*

**Figure 3:** Viscoelastic foam flooding observed in micromodel experiment: a) Micromodel chip saturated with Isopar L oil and b) Micromodel chip after the viscoelastic foam, generated by 1 wt.% SNP with 1.8 wt.% brine and 2 wt.% SCI, flooding at 25°C,

The viscoelastic foam flooding experiment was conducted using formulation consisting of 1 wt.% Silica nanoparticles (SNP) with 1.8 wt.% brine and 2 wt.% Sodium Cocoyl Isethionate (SCI) as the surfactant, Figure 3. The foam quality was set at 80%, calculating using a gas flow rate of 1 ml/min and a foaming agent rate of 0.25 ml/min. The breakthrough time was recorded at 4.30 minutes, which was substantially longer than in surfactant foam flooding. This extended breakthrough time reflects the viscoelastic foam's high apparent viscosity and improved mobility control, allowing it to displace oil and delay gas channeling more evenly. The oil recovery achieved from viscoelastic foam flooding was 92.90%, demonstrating excellent displacement efficiency. The strong elastic and cohesive structure of the foam enable deeper penetration into the porous network and better access to previously unswept zones, resulting in higher recovery factory (Yin et al., 2024).

## CONCLUSIONS

This study demonstrated that the integration of viscoelastic silica gel with Sodium Cocoyl Isethionate (SCI) significantly enhances foam stability and performance under high-temperature conditions typical of oil reservoirs. The rheological evaluation confirms the viscoelastic nature of the silica gels, which remained stable at 60°C. Although the viscoelastic foam performed less effectively than the surfactant-only foam at room

PROOF PETROMAT SYMPOSIUM 2025

temperature, it exhibited superior foam stability and structural resilience at elevated temperatures.

Micromodel flooding experiments validates the enhanced oil recovery potential of the viscoelastic foam system, with an oil recovery rate of 92.90% and delayed breakthrough, highlighting its effectiveness in improving sweep efficiency and mobility control. These findings indicate that the combined viscoelastic-surfactant system offers a promising strategy to overcome foam instability challenges in Enhanced Oil Recovery (EOR) applications.

## ACKNOWLEDGEMENTS

The author would like to express sincere gratitude to the USAC Research Group for their valuable support and guidance throughout the course of this research. This study was supported by a full scholarship from The Petroleum and Petrochemical College (PPC), Chulalongkorn University. Research funding was granted by the Thailand Science Research and Innovation Fund Chulalongkorn University (DISF67630023). Special thanks were also extended to PTT Exploration and Production Public Company Limited (PTTEP) for research collaboration and instrumental support, and Prof. Anuvat Sirivat for consultation of viscoelastic property measurement.

## REFERENCES

Farajzadeh, R., Andrianov, A., & Zitha, P. L. J. (2010). Investigation of Immiscible and Miscible Foam for Enhancing Oil Recovery. *Industrial & Engineering Chemistry Research*, *49*(4), 1910-1919. https://doi.org/10.1021/ie901109d

Ilyin, S., Arinina, M., & Kulichikhin, V. (2016). Sol–gel transition and rheological properties of silica nanoparticle dispersions. *Colloid Journal*, *78*, 608-615. https://doi.org/10.1134/S1061933X16050070

Moradpour, N., Yang, J., & Tsai, P. A. (2024). Liquid foam: Fundamentals, rheology, and applications of foam displacement in porous structures. *Current Opinion in Colloid & Interface Science*, *74*, 101845. https://doi.org/https://doi.org/10.1016/j.cocis.2024.101845

Pu, W.-f., Wei, P., Sun, L., Jin, F.-y., & Wang, S. (2017). Experimental investigation of viscoelastic polymers for stabilizing foam. *Journal of Industrial and Engineering Chemistry*, *47*, 360-367. https://doi.org/https://doi.org/10.1016/j.jiec.2016.12.006

Rezaei, A., Derikvand, Z., Parsaei, R., & Imanivarnosfaderani, M. (2021). Surfactant-silica nanoparticle stabilized N2-foam flooding: A mechanistic study on the effect of surfactant type and temperature. *Journal of Molecular Liquids*, *325*, 115091. https://doi.org/https://doi.org/10.1016/j.molliq.2020.115091

Yin, D., Li, Q., Zhao, D., & Huang, T. (2024). Modified silica nanoparticles stabilized foam for enhanced oil recovery. *Frontiers in Energy Research*, *12*. https://doi.org/10.3389/fenrg.2024.1386538

PROCEEDINGS OF PPC & PETROMAT SYMPOSIUM 2025

# DEVELOPMENT OF ZINC-ION BATTERIES USING MILD ELECTROLYTES TOWARD THE DEVELOPMENT OF WEARABLE DEVICES

*Borin Khun* [a], *Stephan Thierry Dubas* *[a,b]

[a] The Petroleum and Petrochemical College, Chulalongkorn University, Bangkok, Thailand
[b] Center of Excellence on Petrochemical and Materials Technology, Bangkok, Thailand

PPC & PETROMAT SYMPOSIUM 2025

Keywords: Zinc-ion battery, Electrolytes, Composite electrodes, Potassium acetate (KAc)

## ABSTRACT

The performance of poly (diallyl dimethylammonium chloride) (PDAD)–poly (styrene sulfonate) (PSS) / carbon black (CB) / manganese dioxide ($MnO_2$) composite electrodes used in zinc-ion batteries was explored using mild electrolytes for potential applications in wearable devices. As zinc-ion batteries gain attention for their safety and suitability for human-related applications, selecting mild and safe electrolytes is essential to replace the commonly used Potassium electrolyte (KOH). A series of six electrolytes, namely sodium chloride (NaCl), sodium acetate (NaAc), potassium chloride (KCl), potassium acetate (KAc), zinc chloride ($ZnCl_2$), and zinc acetate (ZnAc) were used to investigate their effect on the discharge behaviour and current efficiency of the batteries. The composite electrodes were prepared via co-precipitation and compression and used as cathodes with zinc-plate anodes in a full-cell configuration. Among the tested electrolytes, KCl and KAc exhibited the most promising performance. KCl offered stable current output with moderate discharge behaviour, while KAc demonstrated superior discharge characteristics and balanced power density, likely due to minimized side reactions. These results suggest that potassium-based electrolytes, particularly KAc, hold potential as safe and efficient candidates for advancing zinc-ion batteries in wearable electronics.

***stephan.d@chula.ac.th**

## INTRODUCTION

The increasing demand for flexible, lightweight, and biocompatible energy storage systems has driven the exploration of alternative battery chemistries suitable for wearable electronics [1]. Among these, aqueous zinc-ion batteries (ZIBs) have emerged as promising candidates due to their inherent safety, low toxicity, environmental friendliness, and cost-effectiveness [2]. In recent years, research attention has focused on optimizing electrode materials and electrolyte compositions to improve the energy density, cycling stability, and ionic conductivity of ZIBs. While manganese dioxide ($MnO_2$) has been widely investigated as a cathode material due to its high capacity and environmental benignity [3, 4], its performance is heavily influenced by the type of electrolyte used. Electrolytes not only govern ionic conductivity but also affect electrolyte interactions, swelling behavior, and charge transfer efficiency.

In this study, a composite electrode composed of poly (diallyldimethylammonium chloride) (PDAD), poly (styrene sulfonate) (PSS), 80 phr CB, and 80 phr $MnO_2$ was developed and evaluated using six biocompatible electrolytes: NaCl, NaAc, KCl, KAc, $ZnCl_2$, and ZnAc

to investigate their effects on discharge behavior and overall battery performance. The morphology of the synthesized $MnO_2$, CB, and polyelectrolyte complex (PEC) composite membranes was characterized by field-emission scanning electron microscopy (FE-SEM), while electrochemical performance was assessed using a battery testing system. This work aims to identify effective and safe electrolyte systems for enhancing the applicability of zinc-ion batteries (ZIBs) in wearable energy storage technologies.

## EXPERIMENTAL

*A. Preparation of composite PEC2:1 with Carbon black (CB) and $MnO_2$*

The composites of polyelectrolyte complex (CPECs) were prepared by 0.2 M of PDADMAC and 0.1M of PSS in 20 mL of $H_2O$ with 2 M of NaCl separately. CB N550 and $MnO_2$ fillers were put into PSS beakers as 80/80 per-hundred resin (phr, resin = PEC), sonicated for 30 minutes, and then mixed with PDADMAC solutions under stirring for 20 min. The precipitates were separated by centrifugation at 4000 rpm for 40 min and compressed together with 0.1 mm aluminum as a spacer at 70 °C for 6 minutes.

*B. Electrolyte Up-take of CPEC2:1*

The swelling behaviour of composite electrodes, PEC2:1-80CB-80$MnO_2$ composites, were precisely cut into uniform squares of 1 cm × 1 cm, and each was weighed to determine the initial dry mass ($W_0$). These membrane pieces were then individually immersed in 1 M KOH and six different 1 M salt solutions: NaCl, NaAc, KCl, KAc, $ZnCl_2$, and ZnAc. After immersion, the samples were gently blotted to remove surface moisture and immediately weighed to obtain the swollen mass ($W_1$). Each swelling experiment was performed in triplicate to ensure data reliability and reproducibility.

$$\text{Swelling Percentage (\%)} = (W_1 - W_0)/W_0 \times 100$$

*C. Battery testing of CPEC2:1-80CB-80$MnO_2$*

Zinc ion battery testing of CPEC 2:1-80CB-80$MnO_2$ was tested by using 1 M KOH and six different 1M salt concentrations: sodium chloride (NaCl), sodium acetate (NaAc), potassium chloride (KCl), potassium acetate (KAc), zinc chloride ($ZnCl_2$), and zinc acetate (ZnAc) to study the performance of discharge.

## RESULTS AND DISCUSSION

*A. Preparation of composite PEC2:1 with CB and $MnO_2$*

The compression of the polyelectrolyte complex composite contains 80 PHR of Carbon black to provide conductivity and $MnO_2$ to provide electron storage capability. The amount of filler makes the compression process more difficult as the viscosity of the mixture increases, and therefore, higher NaCl (2M) is used to plasticize the complex and allow compression molding. After compression and drying, the composite appears as a plate-sheet like in Fig.1a, then the dried composite was cut into pieces of 1 cm* 3.5 cm (Figure 1b) for battery testing.

PPC & PETROMAT SYMPOSIUM 2025

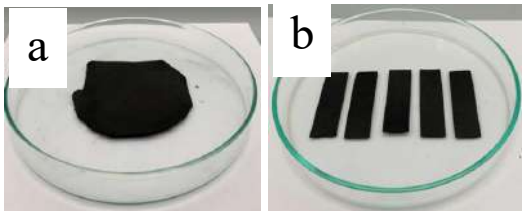


*Figure 1. a, the composite after compression and drying; b, pieces of the composite used as electrodes*

The morphology of electrode materials in the composite was examined using Field Emission Scanning Electron Microscopy (FE-SEM), as shown in Figures 2a and 2b.

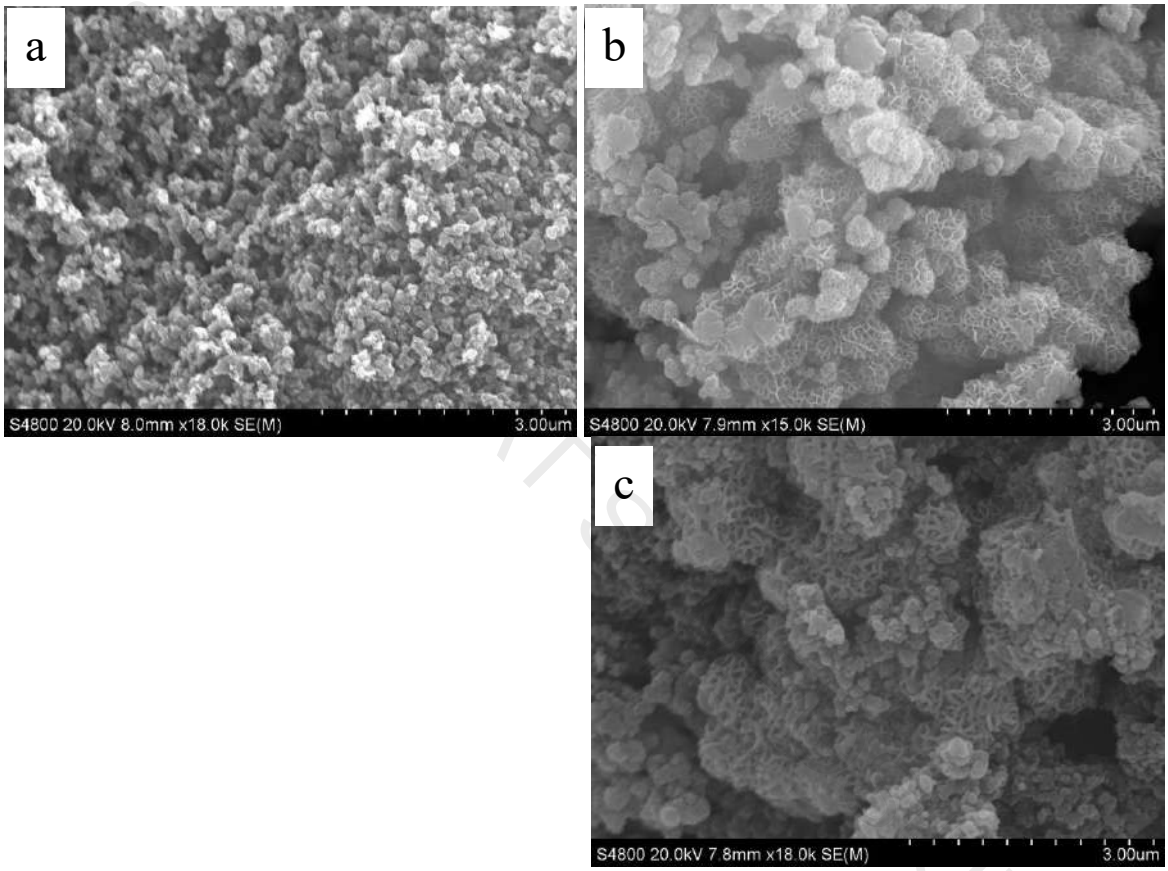


*Figure 2 Field Emission Scanning Electron Microscopy (FE-SEM) images of a, CB; b, MnO2; c, composite*

The FE-SEM image of carbon black (CB) (Figure 2a) reveals a dense, granular structure composed of fine agglomerated particles with an average size of approximately 0.1 µm. These particles exhibit a relatively smooth surface with minimal porosity, indicating that CB primarily functions as a conductive additive rather than providing structural porosity. In contrast, Figure 2b displays the surface morphology of manganese dioxide ($MnO_2$), which shows a distinct flower-like nanostructure composed of interconnected nanosheets with an average particle size of approximately 0.65 µm. This hierarchical morphology is known to facilitate improved surface area and ion diffusion pathways, which are beneficial for redox activity in battery applications [5] [6].

The composite electrode PEC2:1-80CB-80$MnO_2$ (Figure 2c) demonstrates a uniform distribution of both CB and $MnO_2$ particles embedded within the polyelectrolyte complex matrix. The presence of flower-like $MnO_2$ structures interspersed with CB clusters suggests successful incorporation and physical blending of the fillers.

*B. Electrolyte Up-take of CPEC2:1*

When CB is used at 80 PHR in the PEC, it is known to provide electrical conductivity due to percolation of the electrical charges through the PEC network. This percolation is dependent on the degree of swelling of the matrix, which depends on the degree of hydration. This water content can be observed for each salt, as it is expected that different salts will have different uptake. The swelling behavior of PEC2:1-80CB-80$MnO_2$ varied with different 1 M salt electrolytes (Figure 3). Zinc salts ($ZnCl_2$ and ZnAc) showed the highest uptake (~48-49%), likely due to strong electrostatic interactions between divalent $Zn^{2+}$ and the $–SO_3^-$ groups in the PEC, the more hydration, enhancing water absorption, and forming ionic bridges [7].
Monovalent salts (NaCl, KCl, NaAc, KAc) displayed lower uptake (30-34%), with acetate salts swelling slightly more than chlorides due to their larger, more polarizable anions. The positively charged PDAD-rich matrix further enhanced swelling with acetate ions.
Notably, KOH showed the lowest electrolyte uptake at 27.35%, indicating limited water absorption by the composite in alkaline conditions. This can be attributed to the high ionic strength and basicity of KOH, which may dehydrate the matrix or reduce polymer chain mobility through increased ionic shielding. These findings suggest that both cation valency and anion type critically influence electrolyte absorption and ion transport efficiency in Zn-ion battery systems.

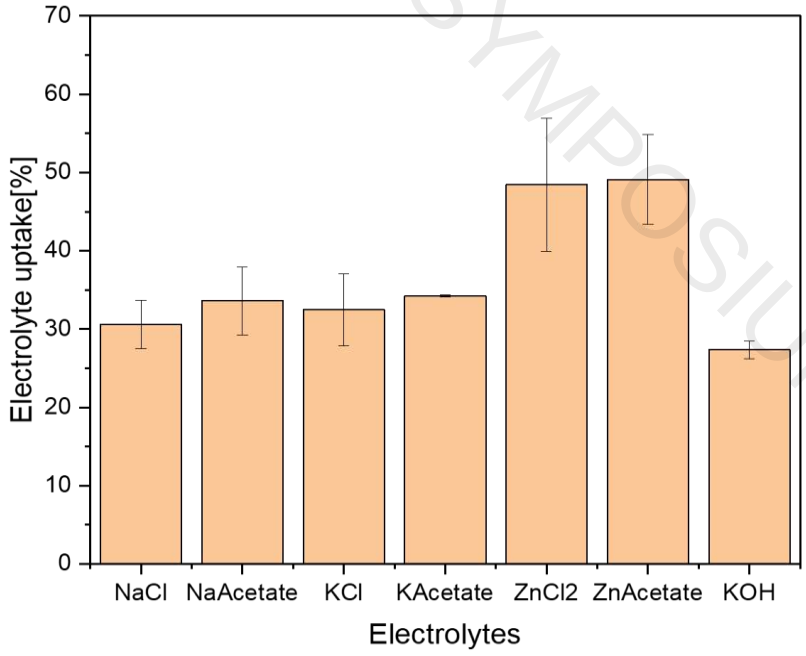


*Figure 3 Electrolyte uptake of composite PEC2:1-80CB-80$MnO_2$*

*C. Battery testing of CPEC2:1-80CB-80$MnO_2$*

PPC & PETROMAT SYMPOSIUM 2025

The polarization and power density curves for each system are presented in Figure 4. Among all tested systems, KOH delivered the highest power output, reaching 4.0 mW/cm² at 8.1 mA/cm². This performance is attributed to KOH's high ionic conductivity and alkaline environment, which enhance redox kinetics and reduce internal resistance [8].

Following KOH, the potassium acetate (KAc) and potassium chloride (KCl) systems delivered the highest maximum power density, reaching approximately 2.8-3.1 (mW/cm²). This performance can be attributed to the favorable ionic mobility of potassium ions, which possess a moderate hydration radius, allowing effective interaction with the polyelectrolyte complex (PEC) matrix and promoting ion diffusion within the electrode system.

Sodium-based electrolytes (NaCl and NaAc) showed moderate performance, with power density values between 1.2 and 2.2 mW/cm². Although their electrolyte uptake was lower than potassium salts (30.6% and 33.6%, respectively), they still allowed sufficient ionic mobility to support respectable electrochemical output.

In contrast, zinc-based electrolytes ($ZnCl_2$ and ZnAc) exhibited the highest electrolyte uptake values (48.4% and 49.1%, respectively, as shown in Figure 3). However, these systems yielded the lowest power density outputs, measured at approximately 1.5 mW/cm² and 1.75 mW/cm². This relationship suggests that while $Zn^{2+}$ ions induce much more swelling of the membrane, leading to loss of conductivity of electrodes, they may also form strong ionic crosslinks with negatively charged sites on the PEC [9], thereby hindering ion transport and increasing internal resistance.

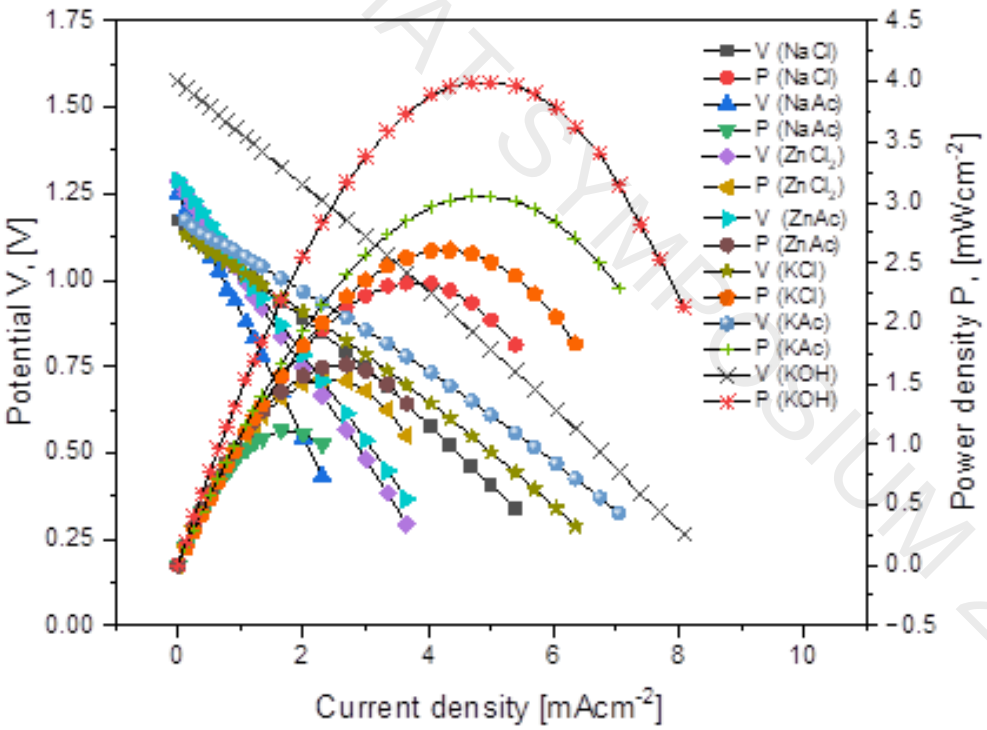


*Figure 5 The polarization and power density curves of NaCl, NaAc, KCl, KAc, ZnCl2, ZnAc and KOH electrolytes*

## CONCLUSIONS

PPC & PETROMAT SYMPOSIUM 2025

This study demonstrated the critical role of electrolyte selection in determining the discharge performance of zinc-ion batteries (ZIBs) intended for wearable applications. By evaluating six different biocompatible electrolytes, NaCl, NaAc, KCl, KAc, $ZnCl_2$, and ZnAc, with composite electrodes composed of PDAD-PSS, carbon black, and $MnO_2$, significant differences in electrochemical behaviour were observed. Among the tested systems, potassium-based electrolytes, particularly potassium acetate (KAc) and potassium chloride (KCl), exhibited the most favourable characteristics, including superior power density and discharge performance following the KOH. These results suggest that the ionic mobility and compatibility of potassium ions with the polyelectrolyte matrix contribute to more efficient ion transport and reduced internal resistance. In contrast, zinc-based electrolytes, despite exhibiting high electrolyte uptake, resulted in poor performance due to excessive swelling and increased ionic crosslinking. The findings highlight the importance of tailoring electrolyte chemistry to enhance the safety, efficiency, and suitability of ZIBs for integration into wearable electronic devices.

## ACKNOWLEDGEMENTS

The authors gratefully acknowledge the ASEAN and Non-ASEAN Scholarship Board of The Petroleum and Petrochemical College, Chulalongkorn University, for their financial support.

## REFERENCES

1. Ahmed, A., et al., *Enhancing high ionic conductivity of polyacryamide/hemp cellulose nanofibers for utilizing as quasi solid electrolyte composites in flexible rechargeable zinc-ion battery with high-safety.* Materials Today Sustainability, 2025. **30**: p. 101088.
2. Zhang, T., et al., *Wearable flexible zinc-ion batteries based on electrospinning technology.* Journal of Energy Chemistry, 2024. **98**: p. 562-587.
3. Xiao, X., et al., *Rational Design of Flexible Zn-Based Batteries for Wearable Electronic Devices.* ACS Nano, 2023. **17**(3): p. 1764-1802.
4. Jiang, Z., et al., *Flexible fiber-shape Zn-MnO2 battery for wearable electronic devices.* Journal of Energy Storage, 2024. **98**: p. 113010.
5. Zhu, X., et al., *Superior-Performance Aqueous Zinc-Ion Batteries Based on the In Situ Growth of MnO2 Nanosheets on V2CTX MXene.* ACS Nano, 2021. **15**(2): p. 2971-2983.
6. Zheng, W., et al., *Tailoring hierarchical MnO2 nanostructures on self-supporting cathodes for high-mass-loading zinc-ion batteries.* Chemical Science, 2024. **15**(48): p. 20303-20314.
7. Schlenoff, J., A. Rmaile, and C. Bucur, *Hydration Contributions to Association in Polyelectrolyte Multilayers and Complexes: Visualizing Hydrophobicity.* Journal of the American Chemical Society, 2008. **130**: p. 13589-97.
8. Qu, X., et al., *High-performance flexible zinc–air batteries enabled by carboxymethyl cellulose/graphene oxide composite hydrogel electrolytes.* New Journal of Chemistry, 2025. **49**(18): p. 7376-7383.

PPC & PETROMAT SYMPOSIUM 2025

9. Praphakar, R.A., et al., *Zn2+cross-linked sodium alginate-g-allylamine-mannose polymeric carrier of rifampicin for macrophage targeting tuberculosis nanotherapy.* New Journal of Chemistry, 2017. **41**(19): p. 11324-11334.

PPC & PETROMAT SYMPOSIUM 2025

# DEVELOPMENT OF ZIF-8 ZEOLITE COMPOSITE CATHODES FOR ZINC IONS BATTERIES

*Natthakan Rattanaphong[a,c], Pisut Wijitsettakun[a,c], Alissa Dubas[b], Kulsinee Potisen[b], Stephan Thierry Dubas *[a,c]*

[a] The Petroleum and Petrochemical College, Chulalongkorn University, Bangkok, Thailand
[b] Chulalongkorn University Demonstration Secondary School, Bangkok, Thailand
[c] Center of Excellence on Petrochemical and Materials Technology, Bangkok, Thailand

Keywords: Zinc-ion battery, Polyelectrolyte complexes, membranes, ZIF-8

**Abstract**
The escalating demand for safe, flexible energy storage solutions for wearable electronics necessitates innovations in zinc-ion battery (ZIB) design. In this study, we introduce a novel approach by incorporating zinc-imidazolate-based metal-organic framework (MOF), ZIF-8, into polyelectrolyte complex (PEC) cathodes. The cathode matrix is composed of poly(styrene sulfonate)/poly(diallyl dimethylammonium chloride) (PSS/PDADMAC), manganese dioxide ($MnO_2$), carbon black, and varying contents of ZIF-8 (0–20 phr). The incorporation of ZIF-8 enhances both ion transport and storage dynamics while preserving mechanical flexibility. Cross-sectional SEM reveals a uniform dispersion of ZIF-8 nanopores within the PEC, forming hierarchical ion-diffusion networks. Electrolyte uptake in 6 M KOH decreases with ZIF-8 addition due to reduced hydrophilic matrix content, yet electrical conductivity improves owing to reduced swelling and strengthened percolation pathways. Electrochemical testing demonstrates a current density increase from 12 mA/cm² (without ZIF-8) to 28 mA/cm² at 10 phr ZIF-8, with only a minor loss in specific capacity due to lower $MnO_2$ content per gram. These findings establish ZIF-8 as a multifunctional filler that decouples ion-storage from rate performance, offering a promising strategy for high-performance, flexible ZIBs tailored for wearable applications.

***stephan.d@chula.ac.th**

## INTRODUCTION

The rapid proliferation of wearable electronics—from medical monitors to smart textiles—demands energy storage systems that harmonize safety, flexibility, and high energy density [2,9]. Aqueous zinc-ion batteries (ZIBs) have emerged as frontrunners in this space, taking advantage of zinc's low toxicity, abundance, and compatibility with biocompatible electrolytes [4,10]. However, conventional rigid electrodes struggle to meet the requirements for mechanical flexibility, and low-capacity retention during dynamic deformation remains a bottleneck [3,11]. To address these limitations, polyelectrolyte complex (PEC) membranes—self-assembled networks of oppositely charged polymers such as poly (styrene sulfonate) (PSS) and poly (diallyl dimethylammonium chloride) (PDADMAC)—offer an interesting alternative to traditional carbon felt [7,12]. Their tunable swelling behavior, intrinsic ion conductivity, and adhesive properties enable the fabrication of robust, bendable electrodes. Yet, without the integration of strategic material fillers, PECs suffer from limited

PPC & PETROMAT SYMPOSIUM 2025

active sites and sluggish ion diffusion, constraining their electrochemical performance [13]. Integrating metal-organic frameworks (MOFs) into PEC matrices presents a promising solution. MOFs like ZIF-8 (zinc imidazolate framework-8) possess ultrahigh surface areas (>1,000 $m^2/g$) and molecular-sieving pores (~3.4 Å), which can pre-concentrate $K^+$ ions and accelerate desolvation kinetics [6,14]. Recent studies have confirmed ZIF-8's efficacy in stabilizing zinc anodes and suppressing dendrite formation [15], but its role in PEC-based cathodes remains largely unexplored, particularly for wearable ZIBs. When combined with manganese dioxide ($MnO_2$), a high-capacity cathode material, and carbon black (CB), which ensures percolation conductivity, ZIF-8's nanoporous structure can create hierarchical ion highways within the PEC, enhancing ion transport and capacity without compromising flexibility [16]. However, excessive MOF loading can disrupt conductive networks and decrease mechanical integrity, necessitating careful optimization of the ZIF-8/PEC interface. Cathodes utilizing polyelectrolyte complexes were therefore formed from PSS and PDADMAC. These complexes incorporated $MnO_2$ at 40 parts per hundred resins (phr) as the active cathode material and carbon black (CB) at 80 phr to ensure percolation conductivity. Crucially, ZIF-8 was added as a multifunctional filler across a range of 0 to 20 phr. The electrostatic crosslinks inherent in the PEC matrix provide essential ductility and mechanical strength, while the micropores of the ZIF-8 nanoparticles enhance ion accessibility within the cathode structure. The cells employed a 6 M potassium hydroxide (KOH) aqueous electrolyte and were tested using custom-designed 3D-printed housings. Although further development will require milder electrolytes for practical applications, the use of 6 M KOH is standard for performance benchmarking [17]. ZIF-8's dual role extends beyond porosity. It is hypothesized that the $Zn^{2+}$-coordinated sites within the ZIF-8 structure may also suppress the dissolution of $MnO_2$ during battery cycling, thereby significantly improving the long-term cycling stability of the cathode [18]. This study evaluates the impact of ZIF-8 incorporation by correlating its content (0–20 phr) with key performance metrics: electrolyte uptake (via swelling dynamics in 6 M KOH), electronic conductivity (via four-point probe), discharge performance (via capacity in mA h/$cm^2$ under various current densities), and longevity (via cycle life testing).

## EXPERIMENTAL

### A. *Preparation of composite PEC with Carbon black (CB) $MnO_2$ and ZIF-8*

The composites of polyelectrolyte complex (CPECs) were prepared by mixing 0.1 M of PDADMAC and 0.1M of PSS in 20 mL of $H_2O$ with 2 M of NaCl separately. CB N550 and $MnO_2$ fillers were added to PSS at 80/40 phr. by taking the PEC as matrix and various amounts of ZIF-8, sonicated for 30 minutes, and then mixed with PDADMAC solutions under stirring for 20 min. The precipitates were separated by centrifugation at 4000 rpm for 40 min and compressed together with 0.3 mm aluminum as a spacer at 70 °C for 6 minutes. The ZIF-8 particles were prepared by mixing a 1:15 ratio of zinc acetate with 2-imidazole in a beaker under fast stirring. the precipitate was centrifuged at 4000 rpm and dried in an oven at 60 °C.

PPC & PETROMAT SYMPOSIUM 2025

B. *Electrolyte Uptake*

The swelling behavior of composite electrodes, PEC with 80 phr CB 40 phr $MnO_2$, and various contents of ZIF-8 from 0 to 20 phr., was precisely cut into uniform squares of 1 cm × 1 cm, and each was weighed to determine the initial dry mass ($W_0$). These membrane pieces were then individually immersed in 6 M KOH. After immersion, the samples were gently blotted to remove surface moisture and immediately weighed to obtain the swollen mass ($W_1$). Each swelling experiment was performed in triplicate to ensure data reliability and reproducibility.

Swelling Percentage (%) = $(W_0 - W_1)/W_0 \times 100$

C. *Battery testing*

Zinc ion battery testing of CPEC with various contents was tested using 6M KOH in a home-built cell using a zinc plate as anode and our composite PEC as cathode, while Celgard was used as a separator. The NEWARE battery testing unit was used to measure the maximum current, power density, and specific capacity.

## RESULTS AND DISCUSSION

*A. Preparation of composite PEC with various Zif-8 content*

The polyelectrolyte complex (PEC) composite membranes were engineered to include 80 phr of carbon black (CB) for electronic conductivity and 40 phr of $MnO_2$ as the active cathode material, with ZIF-8 added as a tunable porosity-enhancing filler. The high CB loading ensures the formation of percolative electron pathways throughout the polymer matrix, which is essential given the typically insulating nature of polymer electrolytes. However, increasing filler content significantly raises the viscosity of the precursor mixture, complicating processing. To mitigate this, a high concentration of NaCl (2 M) was employed to temporarily plasticize the PEC and facilitate compression molding. The resulting films were mechanically robust and could be formed into flexible sheets approximately 300 microns thick, suitable for battery assembly

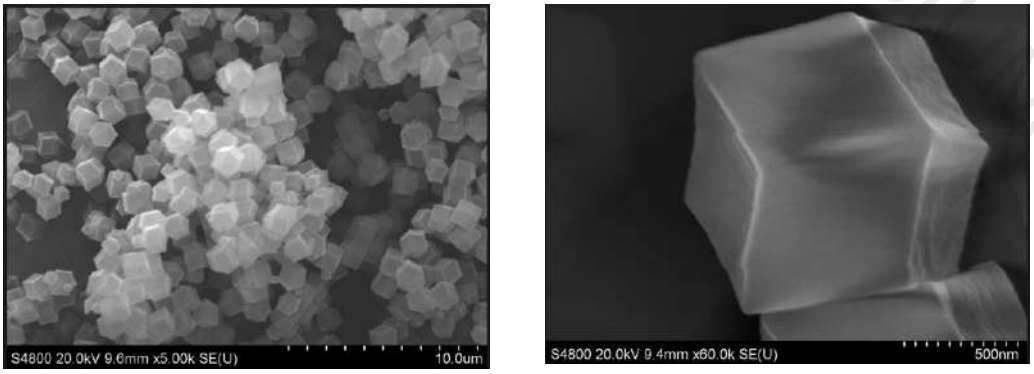


*Figure 1. Scanning electron image of the synthesized ZIF-8*

PPC & PETROMAT SYMPOSIUM 2025

The FE-SEM image of the sample confirmed the formation of composite electrodes with uniform filler distribution. The ZIF-8 particles synthesized in water showed a characteristic cubic morphology, as visualized via FE-SEM (Figure 1). $MnO_2$ appeared as nanosheet-like clusters with high surface area, while the CB displayed a dense, granular structure, consistent with its role as a conductive additive rather than a source of porosity. The observed morphology supports the hypothesis that the composite achieves a multiscale architecture where electronic and ionic transport can coexist efficiently

*B. Electrolyte Uptake*

Swelling behavior is a critical metric for PEC-based battery materials, as it directly impacts ionic conductivity and mechanical integrity. Figure 2 illustrates the swelling percentage of the composites in 6 M KOH as a function of ZIF-8 loading. The swelling decreased progressively from 37% in the ZIF-8-free system to only 17% at 10 phr ZIF-8. This trend is attributed to two primary factors: the reduction of the hydrophilic PEC matrix content and the physical barrier imposed by the ZIF-8 particles, which restrict polymer chain mobility and water absorption. Interestingly, while reduced swelling might seem detrimental from a conventional electrolyte uptake standpoint, in this context, it is actually beneficial. High water content can lead to over-swelling and disrupt the percolating CB network, diminishing electrical conductivity. By reducing excess swelling, ZIF-8 helps maintain the structural integrity and continuity of the conductive network, which is critical for achieving high power densities. Thus, the decreased swelling is not merely a side effect but an engineered feature that contributes to enhanced electrode stability and performance.

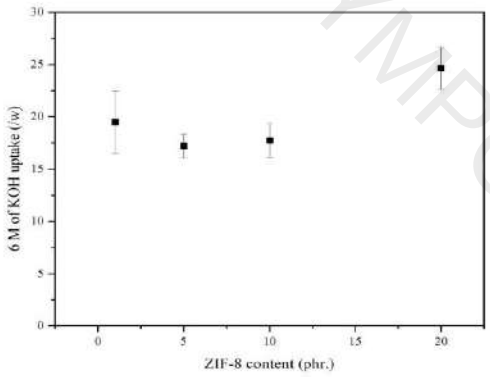


*Figure 2 Electrolyte uptake of composite PEC1:1-80CB-40$MnO_2$ with vary ZIF-8 content phr.)*

*C. Battery testing of ZIF-8 composite PEC*

The electrochemical performance of the composite electrodes was assessed in custom-built zinc-ion cells, with a particular focus on current density and capacity. Figure 3 shows that the current density increased markedly from 12 mA/cm² for the control sample to 28 mA/cm²

PPC & PETROMAT SYMPOSIUM 2025

upon incorporating 10 phr of ZIF-8. This substantial improvement highlights the dual role of ZIF-8: while it does not conduct electrons, its highly porous structure promotes more efficient ion transport, thereby minimizing polarization under load. Additionally, as supported by the electrolyte uptake data, reduced swelling helps preserve percolation pathways for electronic conduction. Beyond 10 phr, however, a performance decline was observed. This suggests that there is an optimal filler loading threshold. At higher ZIF-8 concentrations, particle aggregation becomes more likely, potentially disrupting the uniform conductive and ionic pathways within the matrix. Furthermore, excessive MOF content may reduce the proportion of electrochemically active $MnO_2$, contributing to diminished performance.

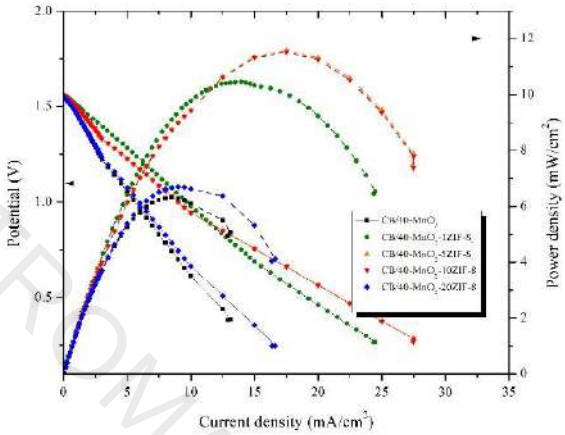


*Figure 3 Current–Voltage (I–V) and Power Density Curves of CB/40-$MnO_2$ Composites with Varying ZIF-8 Content (phr.)*

Figure 4 examines specific capacity across the same compositions. While the current density improved significantly, capacity remained relatively stable, with only a slight decrease at higher ZIF-8 contents. This trade-off is understandable given the fixed volume of the electrode: as more inert ZIF-8 is introduced, it replaces some active $MnO_2$ content. Nonetheless, the capacity retention despite reduced $MnO_2$ loading suggests that ZIF-8 facilitates more efficient utilization of the remaining active material—possibly by accelerating ion diffusion or suppressing parasitic reactions during cycling. Overall, the electrochemical results underline the effectiveness of ZIF-8 as a multifunctional additive that enhances rate capability without a proportional loss in capacity. This is especially promising for applications in wearable devices, where fast charging and stability under mechanical deformation are more critical than absolute energy density.

PPC & PETROMAT SYMPOSIUM 2025

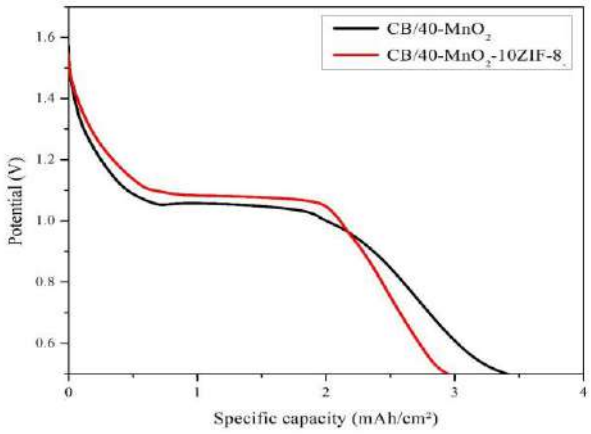


*Figure 4 Specific capacity of the CB/$MnO_2$ and the CB/$MnO_2$/ZIF-8 10 phr at 1 mA/cm$^2$.*

The second useful metric for the evaluation of the performance of the cell is to look at the capacity which represents the amount of electron storage capacity of the cell. It can be seen in figure 4 that the capacity performance of the cell was maintained while with a slight loss of performance which is possibly explained by the lower content of the $MnO_2$ due to the adjunction of the ZIF-8.

## CONCLUSIONS

This study highlights the strategic incorporation of ZIF-8 into polyelectrolyte complex (PEC)-based cathodes as a powerful route to enhance the performance of aqueous zinc-ion batteries (ZIBs) for wearable applications. The inclusion of ZIF-8 significantly reduces electrolyte uptake by limiting excessive swelling of the hydrophilic PEC matrix. This suppression of swelling helps preserves the integrity of the conductive carbon black network, leading to a notable increase in electronic conductivity. The most striking outcome is a 220% improvement in current density—from 12 mA/cm² to 28 mA/cm²—demonstrating that ZIF-8 enhances rate performance without significantly compromising storage capacity. Moreover, the stable specific capacity despite reduced $MnO_2$ content indicates that the hierarchical porous architecture of ZIF-8 facilitates more efficient ion transport and possibly suppresses $MnO_2$ dissolution. These improvements are particularly relevant for flexible and wearable energy systems, where mechanical resilience and high charge/discharge rates are essential. Overall, this work establishes a clear link between rational composite design and functional performance, providing a solid foundation for the development of next-generation flexible energy storage systems.

## ACKNOWLEDGEMENTS

The authors gratefully acknowledge the Petroleum and Petrochemical College, Chulalongkorn University, for their financial support.

PPC & PETROMAT SYMPOSIUM 2025

## REFERENCES


1. Ahmed, A., et al., *Enhancing high ionic conductivity of polyacryamide/hemp cellulose nanofibers for utilizing as quasi solid electrolyte composites in flexible rechargeable zinc-ion battery with high-safety.* Materials Today Sustainability, 2025. **30**: p. 101088.
2. Zhang, T., et al., *Wearable flexible zinc-ion batteries based on electrospinning technology.* Journal of Energy Chemistry, 2024. **98**: p. 562-587.
3. Xiao, X., et al., *Rational Design of Flexible Zn-Based Batteries for Wearable Electronic Devices.* ACS Nano, 2023. **17**(3): p. 1764-1802.
4. Jiang, Z., et al., *Flexible fiber-shape Zn-MnO2 battery for wearable electronic devices.* Journal of Energy Storage, 2024. **98**: p. 113010.
5. Zhu, X., et al., *Superior-Performance Aqueous Zinc-Ion Batteries Based on the In Situ Growth of MnO2 Nanosheets on V2CTX MXene.* ACS Nano, 2021. **15**(2): p. 2971-2983.
6. Zheng, W., et al., *Tailoring hierarchical MnO2 nanostructures on self-supporting cathodes for high-mass-loading zinc-ion batteries.* Chemical Science, 2024. **15**(48): p. 20303-20314.
7. Schlenoff, J., A. Rmaile, and C. Bucur, *Hydration Contributions to Association in Polyelectrolyte Multilayers and Complexes: Visualizing Hydrophobicity.* Journal of the American Chemical Society, 2008. **130**: p. 13589-97.
8. Praphakar, R.A., et al., *Zn2+cross-linked sodium alginate-g-allylamine-mannose polymeric carrier of rifampicin for macrophage targeting tuberculosis nanotherapy.* New Journal of Chemistry, 2017. **41**(19): p. 11324-11334.
9. Wang, Y., et al., Recent advances in flexible zinc-ion batteries for wearable electronics. Energy Storage Materials, 2024. 66: p. 418-438.
10. Kim, H., et al., Aqueous rechargeable Zn batteries: progress and perspectives. Journal of Materials Chemistry A, 2020. 8(5): p. 2473-2505.
11. Wu, X., et al., Flexible and durable ZIBs based on freestanding polyelectrolyte films. Advanced Functional Materials, 2023. 33(12): p. 2211267.
12. Schlenoff, J.B., et al., Hydrated polyelectrolyte multilayers and complexes: from physics to applications. Macromolecules, 2022. 55(9): p. 3501-3515.
13. Chen, R., et al., Design of conductive polymer composites for advanced energy storage devices. Progress in Polymer Science, 2023. 139: p. 101498.
14. Liu, T., et al., Metal–organic frameworks as ionic sieves for zinc ion batteries. ACS Applied Materials & Interfaces, 2021. 13(21): p. 24829–24838.
15. Xue, W., et al., ZIF-8 coating on zinc anode suppresses dendrite formation in aqueous zinc-ion batteries. Journal of Power Sources, 2023. 562: p. 232700.
16. Tang, B., et al., Interface engineering in ZIBs: role of MOF-derived structures in performance enhancement. Journal of Energy Chemistry, 2024. 99: p. 23–35.


PROCEEDINGS OF PPC & PETROMAT SYMPOSIUM 2025

# Unravelling the Pd Size on Partial Hydrogenation of Mesoporous Carbon Plate-Supported Pd and Activated Carbon-Supported Pd Catalysts for Biodiesel Upgrading

*Muhammad Habib Nurain[a], Apanee Luengnaruemitchai[a]*, Takehisa Mochizuki[b,c], Shih-Yuan Chen[b,c]*, Li Yu Wang[d], Chia-Min Yang[d]*

a) The Petroleum and Petrochemical College, Chulalongkorn University, Pathumwan, Bangkok, 10330, Thailand.
b) Energy Catalyst Technology Research Group, Energy Process Research Institute (EPRI), National Institute of Advanced Industrial Science and Technology (AIST), Japan.
c) Synthetic Fuel Production and Evaluation Research Team (FPET), Integrated Research Center for CCUS Implementation, National Institute of Advanced Industrial Science and Technology (AIST), Japan.
d) Department of Chemistry, National Tsing Hua University, Hsinchu 300044, Taiwan

Keywords: SO-BDF, partial hydrogenation, palladium, mesoporous carbon platelet (MCP), activated carbon (AC)

## ABSTRACT

Soybean oil-derived biodiesel (SO-BDF), rich in polyunsaturated fatty acid methyl esters (poly-FAME), is prone to oxidation, leading to the formation of deposits, which can damage diesel engine vehicles. To mitigate this, two palladium (Pd) catalysts—one supported on mesoporous carbon plates (MCP) with an ordered mesoporous structure, and the other on activated carbon (AC) with a disordered microporous structure—were synthesized for the partial hydrogenation of SO-BDF. This process converts poly-FAME into partially hydrogenated fatty acid methyl esters (H-FAME), thereby increasing the content of monounsaturated fatty acid methyl esters (mono-FAME). Pd/MCP and Pd/AC, with varying Pd loadings were prepared using the impregnation method, and evaluated for H-FAME synthesis. The reactions were conducted at 80 °C and 0.5 MPa $H_2$ under stirring at 1000 rpm using 110 g of SO-BDF and the Pd/SO-BDF mass ratio was maintained at $3 \times 10^{-5}$. The prepared catalysts exhibited high activity in H-FAME synthesis. Among them, 1 wt.% Pd/MCP and 0.5 wt.% Pd/AC showed the highest performance, achieving 51wt% *cis*-mono-FAME with 71% Poly-FAME conversion and 83% selectivity within 10 minutes, and 61 wt% *cis*-mono-FAME with 86% poly-FAME conversion and 85% selectivity in 30 minutes, respectively. These differences likely stem from variations in Pd nanoparticle size and metal dispersion, which influence poly-FAME hydrogenation kinetics.

*** apanee.l@chula.ac.th, sy-chen@aist.go.jp**

## INTRODUCTION

In recent years, the adoption of biodiesel fuels has faced several issues, especially oxidation stability (OS) and cold flow property (CFP). Low OS is caused by the high presence of poly-FAMEs. These poly-FAMEs readily react with oxygen to form undesirable compound like aldehydes, ketones, peroxides and acids [(Chen *et al*., 2016; Tang *et al*., 2008)]. These undesirable compounds, at high concentrations may alter biodiesel properties, making them much less desirable for fuel use and to resolve this issue, several solutions have been proposed. The first solution is the addition of additives such as antioxidant to improve the OS; however, the added antioxidant or chemical compound may have positive or negative

PPC & PETROMAT SYMPOSIUM 2025

effects on other fuel properties. The second and a novel solution is through partial hydrogenation. Through partial hydrogenation, poly-FAMEs can be converted into mono-FAMEs and saturated fatty acid methyl esters (sat-FAMEs) counterparts, leading to improved OS. The partially hydrogenated biodiesel is enriched in mono-FAMEs, which enhance OS without compromising CFP. Na Rungsi *et al.* (2018) investigates the influence of MCM-41 support structure on Pd catalyst activity in the partial hydrogenation of SO-BDF under mild conditions (100ºC and 0.4 MPa). Chen *et al.* (2020) found that the prepared Pd/SBA-15 catalyst treated under nitrogen at 400°C for 3 h. The type of reactor plays a critical role in the partial hydrogenation of BDF and batch-type reactor is preferable compared to a continuous flow type reactor (Numwong *et al*. (2012). Efremenko (2003) have noted an interesting property of carbon for metal catalyst support is carbon's ability to transfer π-electron from carbon to metal active sites, thus enriching the active phase with electrons which improves the selectivity towards the intermediate product. Overall, carbon-supported Pd as a catalyst for hydrogenation of organic chemical compound are well-research; however, the effect of Pd nanoparticle size on carbon-supported Pd for partial hydrogenation of biodiesel is still lacking. Therefore, in this study, the effect of Pd particle size on carbon supported Pd catalysts on partial hydrogenation of biodiesel catalyst will be investigated.

## EXPERIMENTAL

### A. Catalyst Synthesis

The Pd/mesoporous carbon platelet (MCP) was synthesized by incipient wetness impregnation method and was prepared by Prof. Yang's research group (Li-Yu Wang *et. al.*(2025)). The catalysts with various Pd loadings are denoted as 0.25wt%Pd/MCP, 0.5wt% Pd/MCP, 1wt%Pd/MCP, 2.5wt%Pd/MCP, and 5wt%Pd/MCP. For the Pd/AC catalyst, approximately ~2 g of $HNO_3$-treated activated carbon was dispersed in 25 mL of deionized water and then sonicated for 10 min to ensure thorough mixing. The impregnation solution was prepared by dissolving *y* g of $Pd(NH_3)_4Cl_2 \cdot H_2O$ in 9.38 mL deionized water where *y* is the amount of Pd precursor needed to obtain the desired Pd loading. The $HNO_3$ treated activated carbon suspension was combined with $Pd(NH_3)_4Cl_2 \cdot H_2O$ solution and stirred vigorously at approximately 500 rpm for 30 min. Subsequently, the mixture was dried in an oven at 80°C for 12 h. The dried 1wt%Pd/AC was then reduced at 200ºC for 1 h under a hydrogen gas stream at a flow rate of approximately 100 mL/min (Gao *et al*., 2024). The catalysts with various Pd loadings are denoted as 0.25wt%Pd/AC, 0.5wt% Pd/AC,1wt%Pd/AC, 2.5wt%Pd/AC, and 5wt%Pd/AC.

### B. Partial Hydrogenation of Biodiesel

The partial hydrogenation of SO-BDF was carried out in a 300 mL stainless steel semi-batch reactor. The process starts by mixing 110 g of SO-BDF with y gram of Pd/MCP or Pd/AC catalysts. The system was purged with nitrogen for 15 min and subsequently purging with hydrogen gas. The reaction was carried out at a temperature of 80ºC, hydrogen partial pressure of 0.5 MPa for 60 min, and stirring rate of 1000 rpm. The samples were taken every 5 min. FAME composition was identified using a Hewlett Packard gas chromatograph 7890B equipped with a flame ionization detector (GC-FID), Agilent 7693A ALS (Automatic Liquid

PPC & PETROMAT SYMPOSIUM 2025

Sampler) and HP-88 (100 m x 0.25 mm) fused-silica capillary column coated with a 0.2 µm film.

C. Catalyst Characterization

X-ray diffraction (XRD) patterns were recorded using a Rigaku TTRAX III diffractometer with Cu Kα radiation (wavelength of 1.5405 Å), operated at 40 kV and 30 mA to identify the bulk phase and crystallinity. Diffractograms were obtained within a 2θ range of 10-80° at a scan rate of 5° $min^{-1}$. Brunaeur-Emmett-Teller surface areas ($S_{BET}$) were determined using a Quantachrome Autosorb-1MP instrument, where 50 mg of catalyst samples were degassed at 150°C for 12 h. The analysis was performed over a relative pressure ($P/P_0$) range of 0.05 to 0.30, and the total pore volume was calculated at $P/P_0$ = 0.95. CO-Chemisorption was done on the Pd/MCP catalyst using an Ohkura Riken R6015, assuming a 1:1 ratio of Pd atoms and CO molecules. Prior to measurements, samples were reduced in a flow of $H_2$ (50 mL $min^{-1}$) at 300 °C for 4 h and then purged with He (50 mL $min^{-1}$) while cooling to 50 °C. For the chemisorption measurements, the reduced samples were exposed to a sequence of 5 vol% CO/He pulses at 50 °C until no more CO was adsorbed.

## RESULTS AND DISCUSSION

A. Partial Hydrogenation of Biodiesel

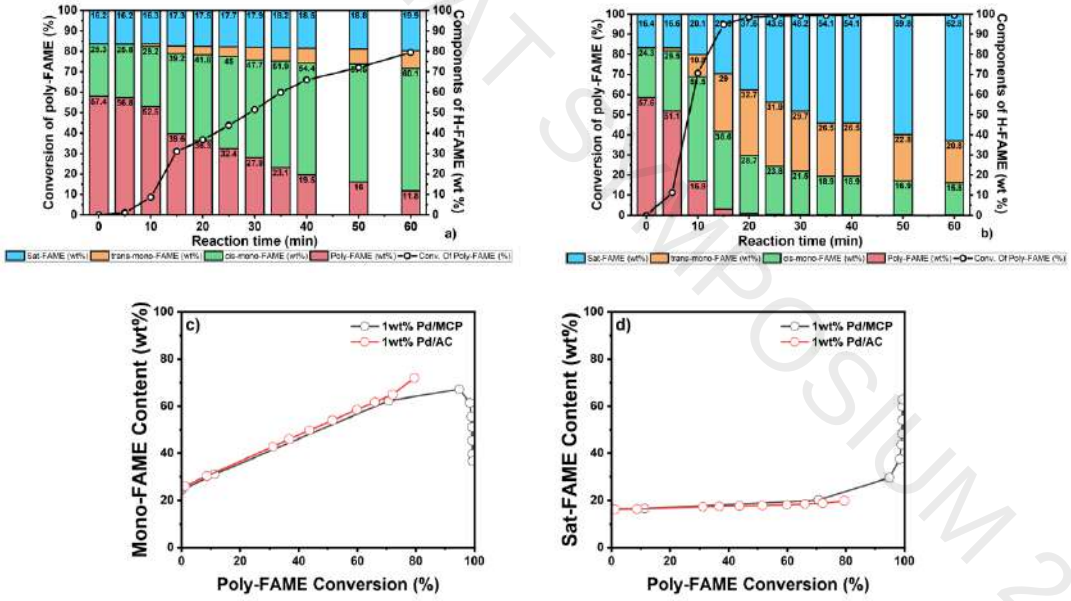


**Figure 1.** poly-FAME conversion as a function of reaction time of (a) 1wt%Pd/AC and (b) 1wt%Pd/MCP, (c) mono-FAME and (d) sat-FAME content over poly-FAME conversion.

Figure 1 displays the catalytic performance of 1wt% Pd/AC and 1wt%Pd/MCP catalysts at 80°C, 0.5MPa $H_2$ pressure, a stirring rate of 1000 rpm and a Pd/SO-BDF mass ratio of $3 \times 10^{-5}$. Figure 1(a) shows that the poly-FAME conversion gradually rise over the course of partial hydrogenation, reaching a maximum of 79% after 60 min of partial hydrogenation. In contrast, 1wt%Pd/MCP achieved a higher poly-FAME conversion of 99% within 25 min

PPC & PETROMAT SYMPOSIUM 2025

(Fig. 1(b)). Figure 1(c) shows the plot between mono-FAME content profiles and poly-FAME conversion. For the H-FAME obtained from 1wt%Pd/MCP, the mono-FAME content starts to drop as it was converted into sat-FAME suggesting that less poly-FAME was being converted to mono-FAME, as shown in Figure 2(d).

Table 1 shows the FAME composition obtained from Pd catalysts with different Pd loadings. For the Pd/MCP catalysts, after a 10 min-reaction time, the 1wt%Pd/MCP achieved the highest activity, yielding 51.5wt% *cis*-mono-FAME and 70.7% poly-FAME conversion.
Compared to other Pd/MCP catalysts under the same reaction conditions, a clear trend in catalytic activity was observed: 1wt%Pd/MCP > 0.5wt%Pd/MCP > 2.5wt%Pd/MCP > 0.25wt%Pd/MCP > 5wt%Pd/MCP. Interestingly, for the Pd/AC catalysts, after 30 min if reaction, the 0.5wt%Pd/AC achieved the highest level of *cis*-mono-FAME at 61.2% and an 86%poly-FAME conversion. Among the Pd/AC catalysts, the catalytic activities are ranked as 0.5wt%Pd/AC > 1wt%Pd/AC > 2.5wt%Pd/AC > 5wt%Pd/AC > 0.25wt%Pd/AC. In terms of overall poly-FAME conversion efficiency, only 1wt%Pd/MCP achieved 99% conversion within 25 min of hydrogenation, while 0.5wt%Pd/AC only achieved 92% conversion after 60 min of hydrogenation, suggesting the superior performance of 1wt% Pd/MCP catalyst.

The initial rate of partial hydrogenation of SO-BDF for all catalysts. was calculated at 20% poly-FAME conversion. Table 1 shows a comparison of initial rate of partial hydrogenation of SO-BDF for both Pd/MCP and Pd/AC catalysts with different Pd loadings. For Pd/MCP, the initial rate of reaction improves as Pd loading increases until 1wt% Pd loading (0.03617 mol/g.min). After that, the initial rate gradually lowered until 5wt% Pd/MCP showed an initial rate of 0, as it did not reach 20% poly-FAME conversion even after 60 min. This suggests an optimum particle size for this reaction and 1%Pd/MCP provides a balance of active sites and electronic properties, leading to maximized initial reaction rate for the Pd/MCP catalysts. For Pd/AC catalysts, the initial rate increased from 0.25wt% Pd until 5 wt% Pd (0.03877 mol/g.min), suggesting a different trend compared to the Pd/CMP catalysts.

**Table 1.** FAME composition obtained from Pd/MCP and Pd/AC with different Pd loadings

| Pd Loading (wt%) | poly-FAME (wt%) | *cis*-mono-FAME (wt%) | *trans*-mono-FAME (wt%) | sat-FAME (wt%) | poly-FAME conversion (%) | cis-mono-FAME Selectivity (%) | Initial rate*$10^3$ (mol/gcat.min) |
|---|---|---|---|---|---|---|---|
| 0.25wt%Pd/MCP | 55.9 | 25.8 | 0.5 | 16.4 | 3.4 | 98.0 | 0.9 |
| 0.5wt%Pd/MCP | 41.9 | 37.8 | 3.0 | 16.5 | 27.6 | 91.9 | 12.2 |
| 1wt%Pd/MCP | 16.9 | 51.5 | 10.8 | 20.1 | 70.7 | 82.7 | 36.2 |
| 2.5wt%Pd/MCP | 55.6 | 25.8 | 0.6 | 16.5 | 3.6 | 97.5 | 8.9 |
| 5wt%Pd/MCP | 57.4 | 24.4 | 0.2 | 16.6 | 0.8 | 99.2 | 0 |
| 0.25wt%Pd/AC | 51.0 | 31.4 | 1.3 | 17.0 | 11.3 | 95.8 | 0.9 |
| 0.5wt%Pd/AC | 7.7 | 61.2 | 10.5 | 20.3 | 86.7 | 85.2 | 7.8 |
| 1wt%Pd/AC | 27.9 | 47.7 | 6.3 | 17.9 | 51.5 | 88.4 | 16.6 |
| 2.5wt%Pd/AC | 42.5 | 36.3 | 2.8 | 17.5 | 28.7 | 92.9 | 21.7 |
| 5wt%Pd/AC | 43.9 | 35.2 | 2.6 | 17.3 | 24.0 | 92.9 | 38.8 |

Note:

- FAME composition obtained from Pd/MCP samples at 10 min.
- FAME composition obtained from Pd/AC samples at 30 min.

The physicochemical properties of the synthesized Pd catalysts are shown in Table 2. The $S_{BET}$ of the MCP support has significantly higher surface area (1518 $m^2g^{-1}$) than AC support (672 $m^2g^{-1}$). Generally, the incorporation of Pd nanoparticles will reduce the surface area and

PPC & PETROMAT SYMPOSIUM 2025

pore volume of the support. However, an increase in surface area was observed for both 0.5wt%Pd/AC and 1wt%Pd/AC. The average pore size of Pd catalysts are approximately 3.6-3.9 nm. Aside from pore size, porosity or pore volume plays a crucial role in the kinetics of partial hydrogenation and MCP has a higher pore volume (1.2 mL/g) compared to AC (0.6 mL/g), which could affect the catalytic performance in the partial hydrogenation.

Table 2. Physicochemical properties of Pd/MCP and Pd/AC catalysts

| Support | Pd Loading (wt%) | $S_{BET}$ ($m^2g^{-1}$) | Pore diameter (nm) | Pore Volume (ml $g^{-1}$) | Pd Crystallite Size (XRD) (nm) | Pd Size (CO-Chemisorption) (nm) |
|---|---|---|---|---|---|---|
| MCP | Blank | 1518 | 3.7 | 1.2 | - | - |
| | 0.25 | 1424 | 3.7 | 1.1 | - | 5.9 |
| | 0.5 | 1460 | 3.6 | 1.1 | - | 6.3 |
| | 1 | 1339 | 3.6 | 1.1 | - | 8.0 |
| | 2.5 | 1316 | 3.6 | 1.0 | 8.0 | 11.0 |
| | 5 | 1335 | 3.6 | 1.0 | 19.0 | 13.0 |
| AC | Blank | 672.8 | 3.7 | 0.6 | - | - |
| | 0.25 | 585.0 | 3.7 | 0.5 | - | - |
| | 0.5 | 736.9 | 3.8 | 0.7 | - | - |
| | 1 | 726.1 | 3.7 | 0.7 | - | - |
| | 2.5 | 642.9 | 3.7 | 0.6 | 7.0 | - |
| | 5 | 685.3 | 3.9 | 0.7 | 12.0 | - |

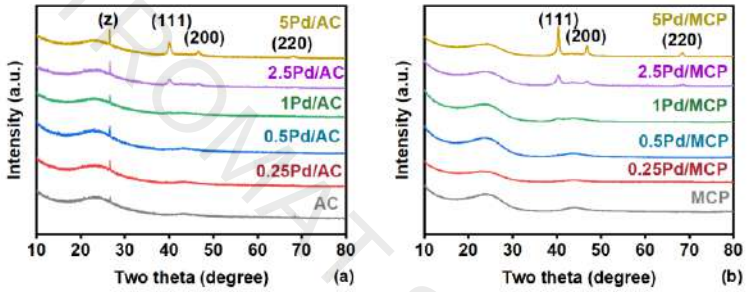


**Figure 2**. Representative wide-angle XRD patterns of reduced (a) Pd/AC and (b) Pd/MCP

Figure 2 compares the XRD patterns of the reduced Pd/AC and Pd/MCP catalysts. A broad, diffuse peak observed around 2θ = 20-30° (centered around 23-25°) corresponds to the (002) reflection of graphitic carbon. From Fig. 2(a), one peak denoted as Z was identified as an impurity present in most commercial activated carbon. Aside from the impurity in Pd/AC catalyst, both Pd/AC and Pd/MCP possess three distinct Pd crystalline peaks namely Pd(111), Pd(200), and Pd(220) at 2θ = 40.2º, 46.8º, and 68.3º, respectively. The crystallinity of the Pd increased with higher Pd loading, and the Pd peaks signal became stronger, especially for 2.5wt% and 5wt%Pd loadings. It suggests that Pd loading influences the formation of Pd nanoparticle, which in turn influences the catalytic performance during partial hydrogenation.

## CONCLUSIONS

In conclusion, this study successfully presented the influence of Pd loading on Pd/MCP and Pd/AC on the partial hydrogenation of SO-BDF. Pd loading is a crucial parameter, while increasing Pd loading can enhance activity, excessive loading can lead to particle growth, reduced dispersion, pore blocking, and decreased activity. It was found that 0.5wt% Pd/AC achieved 61wt% *cis*-mono-FAME content and 86% poly-FAME conversion after 30 min. For the Pd/MCP catalyst, 1wt% Pd/MCP achieved 51wt% *cis*-mono-FAME content with 71% poly-FAME conversion within 10 min of hydrogenation. Aside from the Pd loading,

PPC & PETROMAT SYMPOSIUM 2025

the carbon support structure with higher surface area played a role in the partial hydrogenation of BDF. The 1wt%Pd/MCP has better initial rate compared to 1wt%Pd/AC catalyst.

## ACKNOWLEDGEMENTS

Nurain, M.H. is grateful to Chulalongkorn University's Graduate Scholarship Programme for ASEAN and Non-ASEAN Countries. Chen, S.-Y. and Mochizuki, T. acknowledge AIST for providing financial support. Wang, L.-Y., Yang, C.-M. are grateful to the National Science and Technology Council providing financial support. Luengnaruemitchai, A. acknowledges financial support from the Thailand Science Research and Innovation Fund Chulalongkorn University.

## REFERENCES

Chen, S.-Y., Attanatho, L., Mochizuki, T., Abe, Y., Toba, M., Yoshimura, Y., Kumpidet, C., Somwonhsa, P., & Lao-ubol, S. (2016). Upgrading of palm biodiesel fuel over supported palladium catalysts. *Comptes Rendus. Chimie*, *19*(10), 1166-1173. https://doi.org/10.1016/j.crci.2015.12.005

Chen, S.-Y., Chang, A., Rungsi, A. N., Attanatho, L., Chang, C.-L., Pan, J.-H., Suemanotham, A., Mochizuki, T., Takagi, H., Yang, C.-M., Luengnaruemitchai, A., & Chou, H.-H. (2020). Superficial Pd nanoparticles supported on carbonaceous SBA-15 as efficient hydrotreating catalyst for upgrading biodiesel fuel. *Applied Catalysis A: General*, *602*. https://doi.org/10.1016/j.apcata.2020.117707

Efremenko, I. (2003). Carbon-supported palladium catalysts. Molecular orbital study. *Journal of Catalysis*, *214*(1), 53-67. https://doi.org/10.1016/s0021-9517(02)00103-3

Gao, X., Qiu, F., Xie, H., Chen, X., Wu, C., Chen, Y., Liang, J., & Wang, L. (2024). Efficient catalytic hydrogenation of acrylic rosin over high-activity Pd/C catalyst under mild conditions. *Reaction Kinetics, Mechanisms and Catalysis*, *137*(3), 1721-1739. https://doi.org/10.1007/s11144-024-02615-z

Wang, L.-Y., Chen, S.-Y., Pan, J.-H., Nurain, M.H., Chen, K.-C., Mochizuki,T., Takagi, H., Luengnaruemitchai, A., Nuwong, C., Yoshimura, Y., Yang, C.-M. Mesoporous carbon plate–supported Pd catalysts for the selective hydrogenation of commercial biodiesel fuel. *Fuel (submitted manuscript).*

Na Rungsi, A., Luengnaruemitchai, A., Wongkasemjit, S., Chollacoop, N., Chen, S.-Y., & Yoshimura, Y. (2018). Influence of silica sources on structural property and activity of Pd-supported on mesoporous MCM-41 synthesized with an aid of microwave heating for partial hydrogenation of soybean methyl esters. *Applied Catalysis A: General*, *563*, 80-90. https://doi.org/10.1016/j.apcata.2018.06.028

Numwong, N., Luengnaruemitchai, A., Chollacoop, N., & Yoshimura, Y. (2012). Partial hydrogenation of polyunsaturated fatty acid methyl esters over Pd/activated carbon: Effect of type of reactor. *Chemical Engineering Journal*, *210*, 173-181. https://doi.org/10.1016/j.cej.2012.08.034

Tang, H., Wang, A., Salley, S. O., & Ng, K. Y. S. (2008). The Effect of Natural and Synthetic Antioxidants on the Oxidative Stability of Biodiesel. *Journal of the American Oil Chemists' Society*, *85*(4), 373-382. https://doi.org/10.1007/s11746-008-1208-z

PPC & PETROMAT SYMPOSIUM 2025

# Session 5-Carbon & Sustainability Solutions for a Net-Zero Future (Carbon)

# A NEW DESIGN OF PHOTO-RESPONSIVE METAL-ORGANIC FRAMEWORKS FOR $CO_2$ CAPTURE

*Teerapat Rodcharoen* [a], *Bhumin Than-ardna* [a,b,*]

[a)] The Petroleum and Petrochemical College, Chulalongkorn University
[b)] Center of Excellence on Petrochemical and Materials Technology

Keywords: Smart Materials, Photo-Responsive Metal-Organic Frameworks, $CO_2$ Capture, Environmental Sustainability

PPC & PETROMAT SYMPOSIUM 2025

## ABSTRACT

Rising Carbon Dioxide ($CO_2$) levels enhance the greenhouse effect, leading to higher global temperatures and changes in precipitation patterns. These changes result in more severe storms, extended droughts, and faster melting of ice sheets, which have a wide range of effects on ecosystems, agriculture, and public health. Traditional methods for $CO_2$ capture, e.g., amine scrubbing, are effective but energy-intensive, with operational and environmental drawbacks. To address these limitations, this research studies the potential of photo-responsive metal-organic frameworks (PMOFs) for $CO_2$ capture by integrating azo ligand with nitrogen-donor ligand due to their ability to improve surface area, tunable pore environments, and possible responsiveness to light stimuli. The synergistic effect of Azo and nitrogen-donor ligand in Zn-based MOFs results in a remarkable surface area of 433.81 $m^2/g$ and a pore volume of 0.135 $cm^3/g$. In addition, it exhibits a significant $CO_2$ capture capacity of 3.67 mmol/ g at 273 K and 1 bar. This study shows that upon UV light irradiation, the cis isomerization of azobenzene groups effectively shelters the amines, reducing $CO_2$ adsorption capacity by 30.79%. This PMOFs demonstrates promising potential for addressing one of the most pressing environmental challenges of our time.

***bhumin.t@chula.ac.th**

## INTRODUCTION

The continuous burning of fossil fuels is causing atmospheric $CO_2$ to reach historic highs. In 2024, energy-related emissions increased by 0.8% to 37.8 Gt, raising the mean concentration to almost 422 ppm (Cheng *et al.*, 2021). This elevated $CO_2$ baseline underpins current extremes in temperature, intensification of storm phenomena, accelerated sea-level rise, and progressive acidification of marine environments. A viable strategy for mitigating this challenge involves the deployment of carbon capture and storage (CCS), a technology designed to selectively isolate $CO_2$ emissions from power-generation facilities and sequester them securely.

Amine scrubbing is the process used to capture $CO_2$ from flue-gas streams by chemically binding it to aqueous alkanolamine solvents, which are subsequently regenerated through heating to release the concentrated $CO_2$, but regenerating the rich solvent by heating to 100-150 °C incurs an energy penalty of 20-30 % of a plant's output and leads to solvent degradation, corrosion, and bulky absorber–stripper equipment. In contrast, metal organic frameworks (MOFs) are solid adsorbents featuring highly tunable pore environments and open metal sites that can selectively uptake $CO_2$ and then release it with a mild temperature swing or a simple pressure change, eliminating corrosive liquids and reducing regeneration energy (Lin *et al.*, 2021). Zeolitic imidazolate framework-8 (ZIF-8) is recognized as one of the most thoroughly investigated MOFs and has been extensively explored for a multitude of

applications, including the removal of heavy metal pollutants from aqueous solutions, drug delivery systems, and $CO_2$ capture.

Recent progress in materials science has led to the development of photo-responsive metal-organic frameworks (PMOFs) that incorporate light-sensitive elements to facilitate the dynamic regulation of $CO_2$ adsorption and desorption processes. These materials utilize light as an external stimulus to lower the energy expenditure associated with regeneration, thereby offering a sustainable and scalable method for $CO_2$ capture (Jiang *et al.*, 2019). However, recent studies have not yet revealed that $Zn^{2+}$ is included in the development of light-responsive ligands for photo-responsive MOFs remain limited, particularly in the case of using 2-(4-hydroxyphenylazo) benzoic acid (HABA) as a ligand on PMOFs to investigate the effect of light on $CO_2$ capture performance. Consequently, this study aims to design and synthesize PMOFs that utilize $Zn^{2+}$ as the central metal ion, coordinated with 2-aminoterephthalic acid as nitrogen-donor ligands to establish active sites for $CO_2$ adsorption. Additionally, 2-(4-hydroxyphenylazo) benzoic acid will be incorporated as a photo-responsive organic ligand to enhance light-induced modulation of adsorption properties.

## EXPERIMENTAL

### *A. Materials and chemicals*

Zinc nitrate hexahydrate ($Zn(NO_3)_2.6H_2O$, 98.5%) was obtained from Q-Rec. 2-aminoterephthalic acid (BCD-$NH_2$, 99%) and 2-(4-hydroxyphenylazo) benzoic acid (HABA, ≥99.5%) were obtained from Sigma-Aldrich. Dimethylformamide (DMF) was purchased from RCI Labscan Ltd. All chemicals were used as received without any further purification.

### *B. Preparation of photo-responsive MOFs*

**Synthesis of Zn[BCD-$NH_2$]-MOF (single-ligand MOFs)**

Zinc nitrate hexahydrate ($Zn(NO_3)_2 \cdot 6H_2O$, 0.40 mmol) and 2-aminoterephthalic acid (BCD-$NH_2$, 0.4 mmol) were dissolved in N,N-dimethylformamide (DMF, 12 mL) and ultrasonicated for 15 min to obtain a homogeneous solution. The mixture was transferred to a tightly capped 20 mL glass vial and heated in a convection oven at 120 °C for 48 h. After cooling to room temperature, the resulting brown solid was isolated by centrifugation, washed with fresh DMF (4 × 10 mL), and dried under dynamic vacuum at 60 °C overnight.

**Synthesis of Zn[HABA][BCD-$NH_2$]-MOF (mixed-ligand MOFs).**

For the mixed-ligand framework, $Zn(NO_3)_2 \cdot 6H_2O$ (0.40 mmol), BCD-$NH_2$ (0.13 mmol), and 2-(4-hydroxyphenylazo)benzoic acid (HABA, 0.26 mmol) were co-dissolved in DMF (12 mL), followed by 15 min of ultrasonication. The solution was transferred to a capped 20 mL glass vial and heated at 120 °C for 48 h. Upon cooling, a brown precipitate was collected by centrifugation, washed four times with DMF, and vacuum-dried at 60 °C overnight to remove residual solvent.

### *C. $CO_2$ adsorption evaluation*

$CO_2$ adsorption capacity was conducted on Autosorb-IQ-MP (Quantachrome). The free space was determined by using Helium (99.999%), assuming that Helium couldn't be adsorbed at the investigated temperature. The adsorption isotherm of $CO_2$ at 273.15 and 298.15 K in a water-mixed ethylene glycol bath with refrigerator equipment. The concentration of $CO_2$ was

PPC & PETROMAT SYMPOSIUM 2025

monitored by a $CO_2$ sensor, and the amount of $CO_2$ adsorbed per unit mass of solid sorbent was subsequently calculated by the following expression (Than-ardna *et al.*, 2025):

$$q_e = \frac{1}{m}\int_0^t Q(C_{in} - C_{out})dt$$

*D. Characterization of photo-responsive MOFs*

The crystal structure of the MOFs was determined by X-ray diffraction (XRD) on a 3 kW Rigaku SmartLab instrument (Japan) equipped with Cu-Kα radiation (λ = 1.542 Å), operating at 40 kV and 30 mA. The morphological analysis and elemental composition of the samples were observed via scanning electron microscopy by using a Hitachi S4800 field emission SEM (FE-SEM) operated at an accelerating voltage of 2 kV, coupled with an energy-dispersive X-ray spectroscope (EDX) at an accelerating voltage of 20 kV for elemental analysis. The functional groups in the sample were analyzed by using a Thermo IS5 FTIR with ID7 Diamond ATR spectrometer in transmission mode at the range of 4000 to 650 $cm^{-1}$, with 256 scans. The photo-switch behavior of the sample was examined by using a PerkinElmer Lambda 950 in the wavelength region of 200-800 nm. The isothermal adsorption-desorption curves of the prepared MOFs were measured by using a Quantachrome Autosorb gas sorption analyzer (USA) under liquid nitrogen conditions at 77 K. The BrunauerEmmett-Teller (BET) method was employed to determine the specific surface area of the samples.

## RESULTS AND DISCUSSION

*A. The chemical structure and functional group of photo-responsive MOFs*

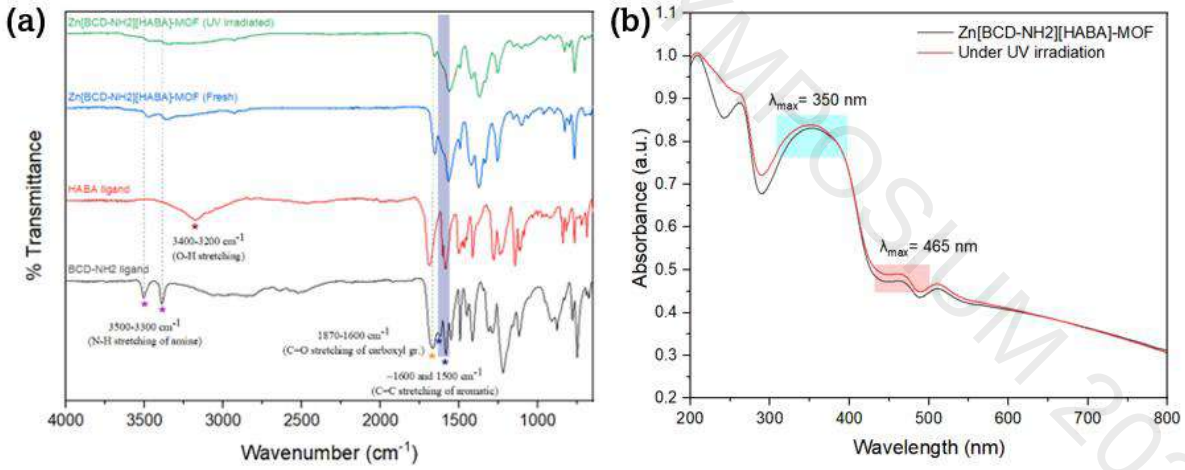


**Fig. 1** The FTIR spectra of the BCD-$NH_2$ ligand, HABA ligand, and the mixed-ligand MOF (a). UV-vis absorption spectrum of mixed-ligand MOF with different UV irradiation conditions (b).

Figure 1a depicts the UV-vis absorption spectrum used to probe the photo-responsive behavior of the mixed-ligand Zn[BDC-$NH_2$][HABA] MOF. In the unirradiated state, a pronounced $\pi \rightarrow \pi^*$ transition appears at 350 nm alongside a weaker $n \rightarrow \pi^*$ feature at 465 nm, both characteristic of the trans-form of the HABA linker. Exposure to 365 nm light

attenuates the 350 nm band while amplifying the 465 nm shoulder. These changes confirm reversible trans-to-cis photo-isomerization occurring within the framework.

The chemical structures and functional groups of the MOF samples were investigated via FTIR spectroscopy, as illustrated in Fig. 1a. The free BDC-$NH_2$ ligand exhibits two distinct N-H stretching bands at 3450 and 3370 $cm^{-1}$, while the free HABA ligand presents a broad phenolic O-H absorption between 3400-3200 $cm^{-1}$. Upon formation of the mixed-ligand MOF, these features merge into a single broad band at 3430 $cm^{-1}$, indicating that both the amine and hydroxyl groups remain protonated yet form hydrogen bonds within the Zn-O-carboxylate framework. Concurrently, the intense C=O stretches at 1688 $cm^{-1}$ (BDC-$NH_2$) and 1680 $cm^{-1}$ (HABA) in the free ligands are greatly attenuated and supplanted by a strong asymmetric ($COO^-$) band at 1585 $cm^{-1}$ in the MOF, confirming deprotonation and coordination of the carboxylate groups to $Zn^{2+}$. Following various UV irradiation treatments, the FTIR spectra of the MOF exhibit no appreciable changes relative to the fresh materials, demonstrating that exposure to UV light does not alter their underlying chemical framework.

*B. Morphology and Elemental Analysis of photo-responsive MOFs*

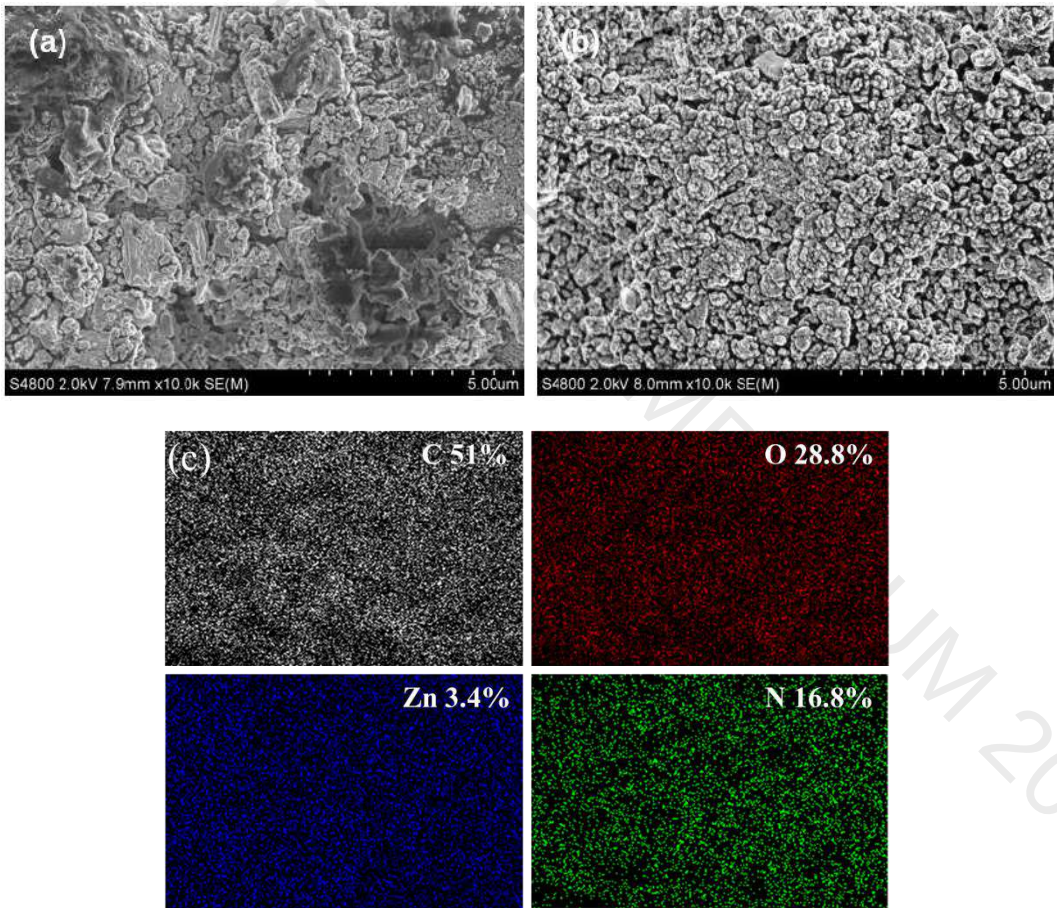


**Fig. 2** SEM images of the Zn[BCD-$NH_2$]-MOF (a) and Zn[BCD-$NH_2$][HABA]-MOF (b). The element mapping of C, O, Zn, and N atoms of Zn[BCD-$NH_2$][HABA]-MOF (c).

The MOFs morphology was investigated by SEM. Zn[BDC-$NH_2$]-MOF did not form well-defined, single crystals; instead, it grew as highly aggregated, irregularly shaped clusters (Fig. 2a), with average crystal sizes around 0.426 μm. Upon incorporating HABA as a co-

ligand alongside BDC-$NH_2$, neither the crystal morphology nor the average size changed significantly (Fig. 2b). Moreover, EDX elemental mapping of the Zn[BDC-$NH_2$][HABA]-MOF confirmed the presence and uniform distribution of carbon, oxygen, zinc, and nitrogen.

*C. Crystal structure of photo-responsive MOFs*

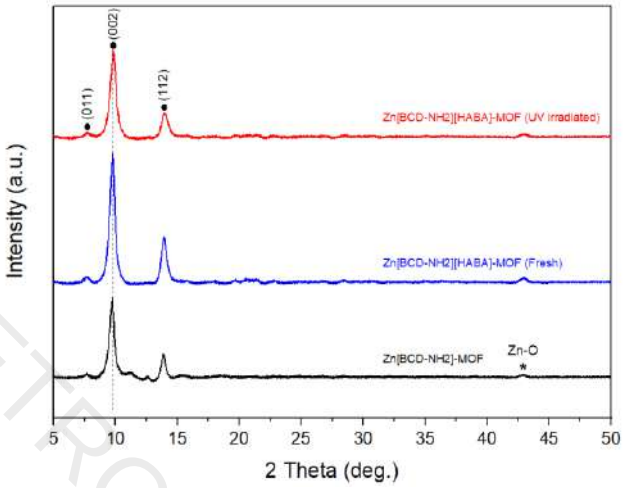


**Fig. 3** The XRD pattern of the Zn[BCD-$NH_2$]-MOF and the mixed-ligand MOF with different conditions.

The crystallographic structures of the MOF samples were analyzed by powder X-ray diffraction (XRD) in JCPDS No. 96-432-6738 (Fig. 3). In the Zn[BCD-$NH_2$]-MOF, distinct reflections appear at 7.7°, 9.8°, 13.9°, and 42.9°, which can be indexed to the (011), (002), and (112) planes of the lattice and the characteristic Zn-O linkage, respectively. In addition, minor peaks at approximately 11.2° and 12.6°, also assignable to the (002) and (112) planes, are observed. When HABA is introduced as a co-ligand, these weak high-angle reflections disappear, reflecting the partial replacement of BCD-$NH_2$ sites by azo functionalities, and the main diffraction peak becomes more intense. In addition, upon UV irradiation, Zn[BCD-$NH_2$][HABA]-MOF retains essentially the same peak positions but shows a smaller relative decrease in intensity, indicating low-level defect formation within the MOF structure.

*D. Gas adsorption properties of photo-responsive MOFs*

**Table 1** Textural properties of the MOFs sample

| MOFs sample | BET surface area ($m^2/g$) | Total volume ($cm^3/g$) | Pore diameter (nm) | $CO_2$ uptake (mmol/g) | |
|---|---|---|---|---|---|
| | | | | 273.15 K | 298.15 K |
| Zn[BCD-$NH_2$]-MOF | 101.31 | 0.154 | 6.08 | 1.26 | - |
| Zn[BCD-$NH_2$][HABA]-MOF | 433.81 | 0.348 | 3.21 | 3.67 | 2.32 |

PPC & PETROMAT SYMPOSIUM 2025

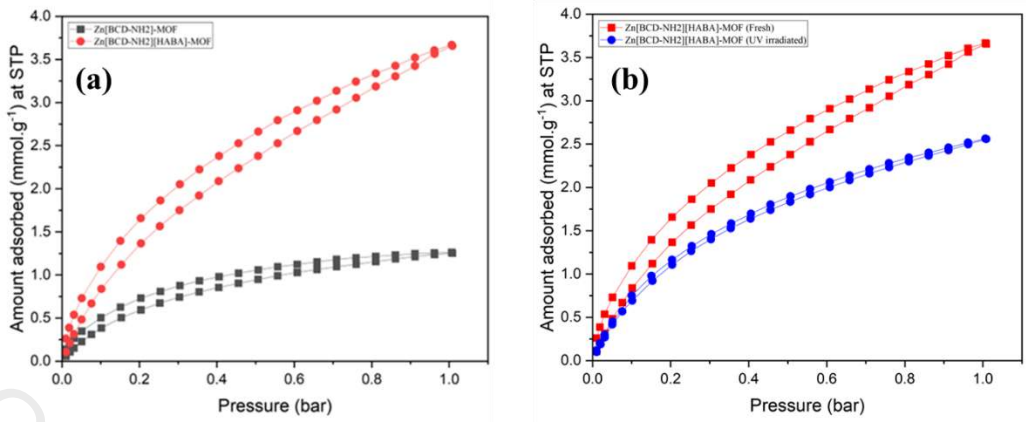


**Fig. 4** $CO_2$ adsorption-desorption isotherms of the Zn[BCD-$NH_2$]-MOF and photo-responsive MOFs (a), and photo-responsive MOFs with different UV irradiation conditions (b).

Table 1 presents the calculated surface area and pore size of the MOF samples. Incorporation of HABA as a co-ligand significantly increases the specific surface area and total pore volume while reducing the average pore diameter relative to the HABA-free framework. This modification enables $CO_2$ uptake to rise from 1.26 mmol/g to 3.67 mmol/g at 273.15 and 1 bar. After 2 h UV irradiation at 365 nm, however, this uptake capacity decreases to 2.54 mmol/g, an approximate 30.8% reduction, because partial trans to cis isomerization of the azo moiety hides the active site within the framework, thereby demonstrating the light-responsive gas capture capability of HABA-functionalized MOFs.

## CONCLUSIONS

In this study, photo-responsive MOF structures were synthesized by incorporating HABA into Zn[BCD-$NH_2$] frameworks, yielding a crystalline architecture with enhanced micropore volume. The amount of $CO_2$ sorption measurements at 273.15 K and 1 bar reveal that this topological modification increases uptake from 1.26 to 3.67 mmol/g. Under 365 nm irradiation, partial trans to cis photoisomerization of the HABA moieties causes a reversible 30.8% decline in uptake to 2.54 mmol/g, implying a photomechanical gating mechanism. To further develop this material for practical $CO_2$ capture applications, future studies should systematically optimize the molar ratio of HABA to BCD-$NH_2$, carry out cyclic sorption-desorption experiments under alternating UV and visible light to assess structural and functional stability, determine the isosteric heat of adsorption for both azo isomers through variable-temperature isotherms, and evaluate mixed-gas selectivity under simulated flue gas conditions.

## ACKNOWLEDGEMENT

The authors gratefully acknowledge the full scholarship and academic support provided by the Petroleum and Petrochemical College (PPC), Chulalongkorn University. This research is supported by the 90$^{th}$ Anniversary of Chulalongkorn University, Rachadapisek Sompote Fund. This research project is supported by grants for development of new faculty staff, Ratchadaphiseksomphot Fund, Chulalongkorn University.

PPC & PETROMAT SYMPOSIUM 2025

## REFERENCES

**Cheng, C.-Y., Kuo, C.-C., Yang, M.-W., Zhuang, Z.-Y., Lin, P.-W., Chen, Y.-F., Yang, H.-S., & Chou, C.-T**. (2021). CO2 Capture from Flue Gas of a Coal-Fired Power Plant Using Three-Bed PSA Process. *Energies*, *14*(12), 3582. https://www.mdpi.com/1996-1073/14/12/3582

**Jiang, Y., Tan, P., Qi, S.-C., Liu, X.-Q., Yan, J.-H., Fan, F., & Sun, L.-B**. (2019). Metal–Organic Frameworks with Target-Specific Active Sites Switched by Photoresponsive Motifs: Efficient Adsorbents for Tailorable CO2 Capture. *Angewandte Chemie International Edition*, *58*(20), 6600-6604. https://doi.org/https://doi.org/10.1002/anie.201900141

**Lin, J.-B., Nguyen, T. T. T., Vaidhyanathan, R., Burner, J., Taylor, J. M., Durekova, H., Akhtar, F., Mah, R. K., Ghaffari-Nik, O., Marx, S., Fylstra, N., Iremonger, S. S., Dawson, K. W., Sarkar, P., Hovington, P., Rajendran, A., Woo, T. K., & Shimizu, G. K. H**. (2021). A scalable metal-organic framework as a durable physisorbent for carbon dioxide capture. *Science*, *374*(6574), 1464-1469. https://doi.org/doi:10.1126/science.abi7281

**Than-ardna, B., Hiranphinyophat, S., Matsumoto, M., Meeyoo, V., & Kitiyanan, B**. (2025). Synthesized structure of Mg-MOF-74 decorated on ZIF-8 as solid adsorbent for CO2 capture. *Resources Chemicals and Materials*, *4*(3), 100116. https://doi.org/https://doi.org/10.1016/j.recm.2025.100116

PPC & PETROMAT SYMPOSIUM 2025

# DESIGN AND DEVELOPMENT OF NOVEL MIXED-LIGAND METAL-ORGANIC FRAMEWORKS FOR SELECTIVE $CO_2$ CAPTURE

*Suphawadee Siriphutthanon*[a], *Bhumin Than-ardna*[a,b,*]

[a)] The Petroleum and Petrochemical College, Chulalongkorn University
[b)] Center of Excellence on Petrochemical and Materials Technology

Keywords: Metal-Organic Frameworks, $CO_2$ adsorption

## ABSTRACT

The industrial emission of carbon dioxide ($CO_2$) from the flue gas has been a major contributor to global warming, emphasizing the need for efficient $CO_2$ capture technologies. Metal-organic frameworks (MOFs) have emerged as highly promising materials for $CO_2$ capture due to their porous structures, high adsorption capacities, and excellent $CO_2/N_2$ selectivity. In this study, we report a strategy to enhance the performance of MOF by combining nitrogen and oxygen donor ligands to improve structure stability, along with the incorporation of amine functional group (-$NH_2$) in ligands to interact with $CO_2$ and increase $CO_2$ adsorption capacity. The synthesized MOF exhibits the $CO_2$ capture performance of 2.56 mmol/g and the $CO_2/N_2$ selectivity of 12.53% at 273 K and 1 bar. The surface area and pore sizes are 238.63 $m^2/g$ and 3.06 nm, respectively. Moreover, comprehensive characterization using X-ray diffraction (XRD), field emission scanning electron microscopy (FE-SEM), Fourier-transform infrared spectroscopy (FT-IR), and simultaneous thermal analysis (STA) confirms the structural, morphological, chemical, and thermal properties of the material. These results demonstrate that the synthesized MOF is a promising candidate for $CO_2$ adsorption applications.

***bhumin.t@chula.ac.th**

## INTRODUCTION

Carbon dioxide ($CO_2$) is greenhouse gas and plays a fundamental role in regulating the Earth's climate. A significant portion of $CO_2$ emissions arises from human activities, particularly the combustion of fossil fuels such as coal and petroleum for energy production (Tedesco, 2022). The increasing concentration of $CO_2$ in the atmosphere disrupts natural temperature balance of the planet and is a major driver of global warming. In response to this environmental challenge, the Intergovernmental Panel on Climate Change (IPCC) has proposed the goal of achieving net-zero greenhouse gas emissions resulting from human activities (Fletcher & Smith, 2024). One of the most promising strategies for limiting atmospheric $CO_2$ levels is Carbon Capture and Storage (CCS), a technology that encompasses post-combustion, pre-combustion, and oxy-fuel combustion methods. Among these, post-combustion $CO_2$ capture is particularly advantageous due to its feasibility for retrofitting existing power generation systems and industrial facilities (Rezaei *et al.*, 2023). From various techniques, solid adsorption has emerged as a compelling alternative owing to its lower energy requirements and the potential for selective adsorption of $CO_2$. Metal-organic frameworks (MOFs) have emerged as highly promising types of adsorbents due to their unique properties, such as high porosity, large surface area, tunable structures, and the ability to

PPC & PETROMAT SYMPOSIUM 2025

incorporate functional groups. These characteristics make MOFs excellent candidates for effective $CO_2$ adsorption (Osman *et al.*, 2021).

MOFs are composed of metal ions or clusters coordinated to organic linkers, forming highly porous structures with tunable physicochemical properties. MOFs are characterized by large surface areas (up to 10,000 $m^2/g$), adjustable pore sizes ranging from 3 to 100 Å, and the potential for chemical functionalization (Gulbalkan *et al.*, 2024). However, MOFs are employed for $CO_2$ capture from flue gas, which contains approximately 8-10% $CO_2$, 67-72% $N_2$, and 18-20% $H_2O$. Therefore, $CO_2/N_2$ selectivity, along with thermal and moisture stability, are essential performance criteria for MOF adsorbents (Xiao *et al.*, 2024).

This study focuses on the development of MOFs with enhanced $CO_2$ adsorption capacity and improved $CO_2/N_2$ selectivity while maintaining high structural integrity. To achieve this, nitrogen and oxygen donor ligands are incorporated, as they are expected to form stronger coordination bonds with metal centers, thereby enhancing the stability of framework in accordance with the Hard and Soft Acids and Bases (HSAB) theory. Furthermore, the adsorption sites from these donor ligands are anticipated to strengthen interactions between the framework and $CO_2$ molecules, resulting in improvement of adsorption efficiency.

## EXPERIMENTAL

*A. Synthesis of Co-MOF-1 and Co-MOF-2*

**Co-MOF-1** was synthesized through a solvothermal method with a single organic ligand. A solution of 2.5 mmol 4,4′-oxybis(benzoic acid) ($H_2OBA$) in *N,N*-dimethylformamide (DMF) was prepared, while 2.5 mmol of cobalt(II) nitrate hexahydrate [$Co(NO_3)_2 \cdot 6H_2O$] was dissolved in deionized water. The two solutions were mixed and stirred. The resulting mixture was then transferred to a 100 mL Teflon-lined autoclave and heated at 130 °C for 24 hours. After natural cooling to room temperature, the solid product was collected, washed with methanol to remove residual reactants, and dried at 80 °C for 24 hours.

**Co-MOF-2** was prepared under similar solvothermal conditions but employed a mixed-ligand strategy. A solution containing 2.5 mmol of $H_2OBA$ and 2.5 mmol of 3,5-diamino-1,2,4-triazole (DATz) in DMF was prepared and mixed with the same cobalt precursor solution described above. The remaining steps, including stirring, thermal treatment, washing, and drying, were carried out following the same procedure as used for Co-MOF-1.

*B. Characterization*

The crystalline structures of Co-MOF-1 and Co-MOF-2 were characterized using X-ray diffraction (XRD) performed on a Rigaku SmartLab diffractometer equipped with CuKα radiation (λ = 1.5406 Å). Diffraction patterns were collected over a 2θ range of 5° to 40° with a step increment of 0.02° and a scan rate of 2°/min. The morphological features of the synthesized materials were observed using a Hitachi S-4800 field emission scanning electron microscope (FE-SEM). Fourier-transform infrared (FT-IR) spectroscopy was conducted using a Thermo Scientific Nicolet iS10 instrument in transmission mode, scanning from 4000 to 525 $cm^{-1}$ with 256 scans to identify functional groups present in the frameworks.

PPC & PETROMAT SYMPOSIUM 2025

Thermal stability and decomposition behavior were determined using a Netzsch STA409 thermogravimetric analyzer (STA) under a nitrogen atmosphere. The samples were heated from 25 °C to 800 °C at a constant rate of 10 °C/min. Surface area and porosity were evaluated by nitrogen adsorption-desorption isotherms at 77 K, analyzed with an Autosorb-IQ-MP-MP-MP (3STAT) analyzer (Quantachrome). The Brunauer–Emmett–Teller (BET) method was employed to calculate the specific surface area, while the Barrett–Joyner–Halenda (BJH) method was applied to the desorption branch of the isotherms to determine pore size distribution. Additionally, gas adsorption measurements for $CO_2$ and $N_2$ were carried out to measure the adsorption performance of the samples. The measurements were conducted using the BET analyzer within a pressure range of 0 to 1 bar at 0 °C.

*C. $CO_2/N_2$ Selectivity*

$CO_2/N_2$ selectivity of samples was determined based on the Ideal Adsorbed Solution Theory (IAST), originally developed by Myers and Prausnitz. The selectivity was calculated using Equation (1) (Yulia *et al.*, 2022).

$$S_{ads} = \frac{(q_1/q_2)}{(p_1/p_2)} \quad (1)$$

Where $q_i$ and $p_i$ denote the adsorption capacity and partial pressure of component i in a binary gas mixture.

## RESULTS AND DISCUSSION

The crystallinity of synthesized samples was characterized by X-ray diffraction (XRD), as presented in Figure 1a. The Co-MOF-1, synthesized using only the oxygen donor ligand $H_2OBA$, exhibited distinct diffraction peaks at 2θ of 14.8°, 20.2°, 21.6°, 24.8°, 29.8°, 32.5°, and 39.2°. In contrast, the introduction of the nitrogen donor ligand DATz into the mixed-ligand system (Co-MOF-2) resulted in a significantly altered diffraction pattern, with a characteristic peak observed at 2θ of 5.3°. This notable shift in the XRD pattern indicated a considerable structural transformation induced by the presence of both ligands. These results are further supported by the morphological differences observed in Figure 1b. While Co-MOF-1 exhibited a cubic crystal shape, Co-MOF-2 displayed an elongated, tetragonal-like morphology, reinforcing the structural impact of nitrogen donor ligand incorporation.

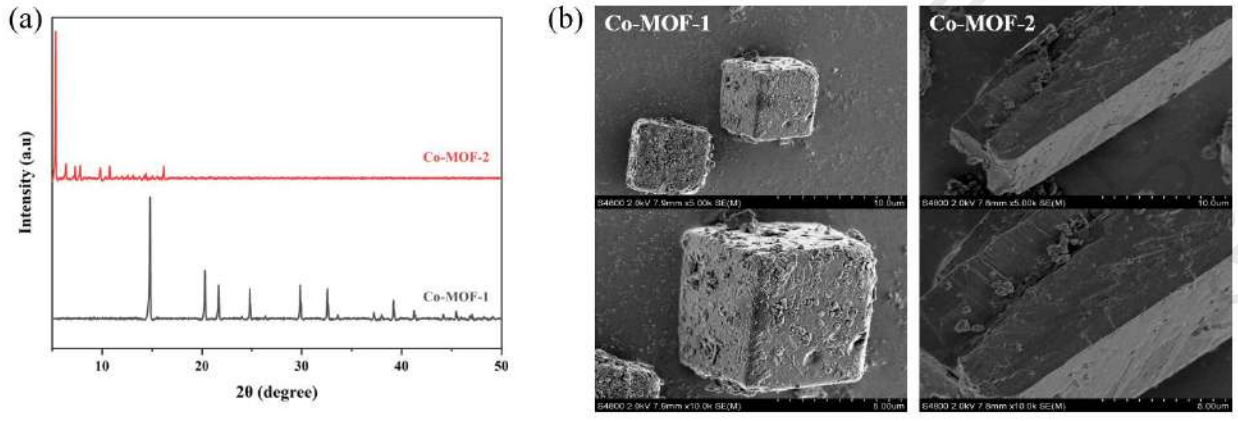


**Figure 1.** (a) XRD patterns and (b) FE-SEM images of Co-MOF-1 and Co-MOF-2.

The functional groups of the synthesized Co-MOF were examined using Fourier transform infrared (FT-IR) spectroscopy, as illustrated in Figure 2a. For Co-MOF-1, a prominent absorption band appeared at 1563 $cm^{-1}$, corresponding to the C=O stretching vibration of the carboxyl group. This band was shifted to a lower wavenumber relative to the $H_2OBA$ ligand (1675 $cm^{-1}$), indicating deprotonation and coordination of the oxygen donor ligand to cobalt ions (Wang *et al.*, 2020). In the case of Co-MOF-2, which incorporated the DATz ligand, a characteristic C=N stretching vibration from the triazole ring was detected at 1596 $cm^{-1}$. This peak also showed a shift to lower wavenumber compared to the DATz ligand (1624 $cm^{-1}$), confirming the coordination of nitrogen donor sites to the metal centers (Nabipour *et al.*, 2024). Moreover, the C-O stretching band of $H_2OBA$ was observed at 1244 $cm^{-1}$, supporting the successful integration of both oxygen and nitrogen donor ligands into the Co-MOF-2 framework. Furthermore, thermogravimetric analysis (Figure 2b) revealed that Co-MOF-2 remained structure to 368 °C, whereas Co-MOF-1 began to decompose at 253 °C. This improved thermal stability highlights the advantageous effect of incorporating multiple ligand types on the framework.

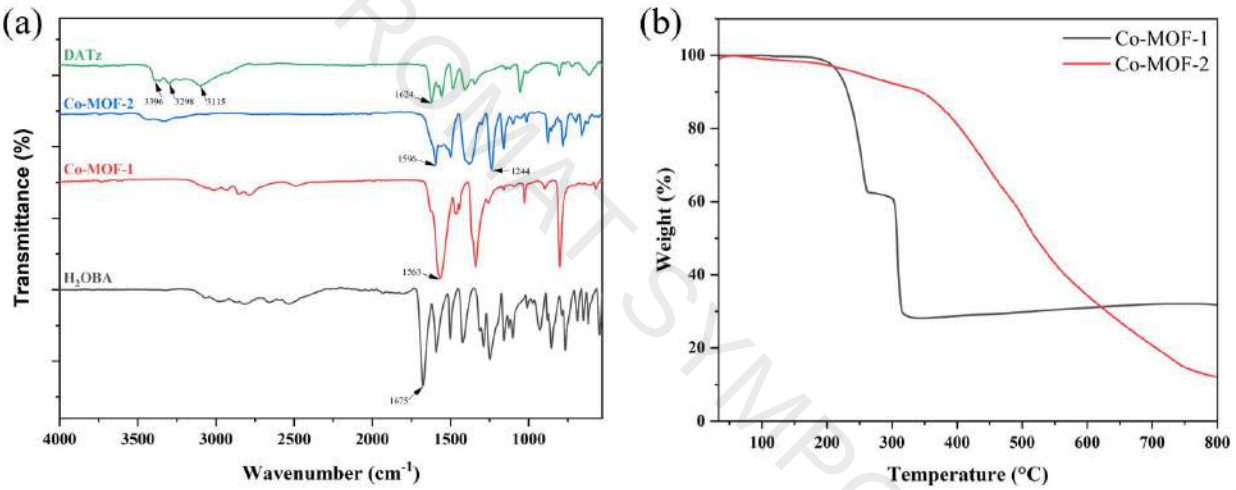


**Figure 2.** (a) FT-IR spectra and (b) STA profiles of Co-MOF-1 and Co-MOF-2.

Table 1 summarizes the adsorption characteristics of the synthesized MOFs. Co-MOF-1 exhibited a BET surface area of 42 $m^2/g$ and a pore volume of 0.045 $cm^3/g$. In contrast, the introduction of the nitrogen donor ligand DATz into the framework (Co-MOF-2) substantially enhanced both parameters, resulting in a BET surface area of 235 $m^2/g$ and a pore volume of 0.124 $cm^3/g$. The mixed-ligand strategy effectively tuned the textural properties of framework, thereby increasing the available surface area and providing more accessible sites for $CO_2$ adsorption.

This improvement was reflected in the $CO_2$ adsorption capacity of Co-MOF-2, which reached 2.56 mmol/g at 0 °C and 1 bar, significantly higher than the 0.24 mmol/g from Co-MOF-1. The enhanced $CO_2$ adsorption performance can be attributed to the synergistic effect of incorporating both nitrogen and oxygen donor ligands. Specifically, the DATz ligand introduced additional adsorption sites such as amine groups ($-NH_2$) and triazole rings. The nitrogen atom in the amine group, possessing a lone pair of electrons, acts as a Lewis base and interacts strongly with the

carbon atom of $CO_2$, which behaves as a weak Lewis acid (Nabipour *et al.*, 2024; Peng *et al.*, 2023), These interactions complement the functional groups provided by $H_2OBA$, including carbonyl (C=O) and ether (C-O) moieties, which further contribute to the adsorption process (Parmar *et al.*, 2019). Furthermore, Co-MOF-2 exhibited a $CO_2/N_2$ selectivity of 12.53% at 0 °C and 1 bar, indicating the potential of the mixed-ligand MOFs for effective gas separation applications.

**Table 1.** Adsorption properties of Co-MOF-1 and Co-MOF-2.

| MOFs | Surface area ($m^2/g$) | Pore volume ($cm^3/g$) | Pore Diameter (nm) | $CO_2$ uptake (mmol/g) |
|---|---|---|---|---|
| Co-MOF-1 | 42 | 0.045 | 3.832 | 0.24 |
| Co-MOF-2 | 238 | 0.1250 | 3.061 | 2.56 |

## CONCLUSIONS

The mixed-ligand MOF (Co-MOF-2) demonstrated superior $CO_2$ adsorption performance compared to the single-ligand framework (Co-MOF-1), with uptake capacities of 2.56 mmol/g and 0.24 mmol/g, respectively, at 0 °C and 1 bar. This enhancement was attributed to the increased surface area and adsorption sites from functional groups in mixed-ligands of Co-MOF-2, which provided more available sites for $CO_2$ adsorption. Furthermore, Co-MOF-2 exhibited a notable $CO_2/N_2$ selectivity of 12.53% at 0 °C, strong potential for gas separation applications. The incorporation of both nitrogen and oxygen donor ligands not only enhanced the $CO_2$ adsorption capacity but also improved thermal stability. Co-MOF-2 retained its structural integrity at higher temperatures compared to Co-MOF-1. These findings highlight the effectiveness of the mixed-ligand approach in developing MOFs with enhanced $CO_2$ adsorption capabilities and structural robustness.

## ACKNOWLEDGEMENTS

The authors gratefully acknowledge the full scholarship and academic support provided by the Petroleum and Petrochemical College (PPC), Chulalongkorn University. This research is supported by the 90th Anniversary of Chulalongkorn University, Rachadapisek Sompote Fund. This research project is supported by grants for development of new faculty staff, Ratchadaphiseksomphot Fund, Chulalongkorn University.

## REFERENCES

**Fletcher, W. D., & Smith, C. B.** (2024). Chapter 2 - Dealing with global warming. In W. D. Fletcher & C. B. Smith (Eds.), *The Global Climate Crisis (Second Edition)* (pp. 9-16). Elsevier. https://doi.org/https://doi.org/10.1016/B978-0-443-27322-3.00014-1

**Gulbalkan, H. C., Aksu, G. O., Ercakir, G., & Keskin, S.** (2024). Accelerated Discovery of Metal–Organic Frameworks for CO2 Capture by Artificial Intelligence. *Industrial & Engineering Chemistry Research*, *63*(1), 37-48. https://doi.org/10.1021/acs.iecr.3c03817

PPC & PETROMAT SYMPOSIUM 2025

**Nabipour, H., Hu, Y., & Rohani, S.** (2024). Development of novel microporous guanazole complex for CO2 adsorption. *Separation and Purification Technology*, *351*, 127996. https://doi.org/https://doi.org/10.1016/j.seppur.2024.127996

**Osman, A. I., Hefny, M., Abdel Maksoud, M. I. A., Elgarahy, A. M., & Rooney, D. W.** (2021). Recent advances in carbon capture storage and utilisation technologies: a review. *Environmental Chemistry Letters*, *19*(2), 797-849. https://doi.org/10.1007/s10311-020-01133-3

**Parmar, B., Patel, P., Pillai, R. S., Kureshy, R. I., Khan, N.-u. H., & Suresh, E.** (2019). Efficient catalytic conversion of terminal/internal epoxides to cyclic carbonates by porous Co(ii) MOF under ambient conditions: structure–property correlation and computational studies [10.1039/C8TA10631B]. *Journal of Materials Chemistry A*, *7*(6), 2884-2894. https://doi.org/10.1039/C8TA10631B

**Peng, J., Fu, C., Zhong, J., Ye, B., Xiao, J., Duan, C., & Lv, D.** (2023). Efficient Selective Capture of Carbon Dioxide from Nitrogen and Methane Using a Metal-Organic Framework-Based Nanotrap. *Molecules*, *28*(23).

**Rezaei, S., Liu, A., & Hovington, P.** (2023). Emerging technologies in post-combustion carbon dioxide capture & removal. *Catalysis Today*, *423*, 114286. https://doi.org/https://doi.org/10.1016/j.cattod.2023.114286

**Tedesco, S. A.** (2022). Chapter 2 - Nitrogen, carbon dioxide, argon, neon, krypton, and xenon. In S. A. Tedesco (Ed.), *Geology and Production of Helium and Associated Gases* (pp. 33-59). Elsevier. https://doi.org/https://doi.org/10.1016/B978-0-323-90988-4.00004-9

**Wang, S., Xie, X., Xia, W., Cui, J., Zhang, S., & Du, X.** (2020). Study on the structure activity relationship of the crystal MOF-5 synthesis, thermal stability and N2 adsorption property. *39*(1), 171-177. https://doi.org/doi:10.1515/htmp-2020-0034 (High Temperature Materials and Processes)

**Xiao, C., Tian, J., Chen, Q., & Hong, M.** (2024). Water-stable metal–organic frameworks (MOFs): rational construction and carbon dioxide capture [10.1039/D3SC06076D]. *Chemical Science*, *15*(5), 1570-1610. https://doi.org/10.1039/D3SC06076D

**Yulia, F., Zulys, A., Saha, B. B., Mabuchi, T., Gonçalves, W., & Nasruddin.** (2022). Bio-metal-organic framework-based cobalt glutamate for CO2/N2 separation: Experimental and multi-objective optimization with a neural network. *Process Safety and Environmental Protection*, *162*, 998-1014. https://doi.org/https://doi.org/10.1016/j.psep.2022.04.076

PPC & PETROMAT SYMPOSIUM 2025

# In-situ construction of UiO-66 on bacterial cellulose membranes for enhanced $CO_2$ separation

*Nongnapat Budsrijaroen* [a], *Bhumin Than-ardna*[a], *Hathaikarn Manuspiya*[a,b,*]

[a] The Petroleum and Petrochemical College, Chulalongkorn University, Bangkok, Thailand
[b] Center of Excellence on Petrochemical and Materials Technology, Bangkok, Thailand

Keywords: Bacterial cellulose (BC), MOFs, UiO-66, Superhydrophobic membrane

## ABSTRACT

The increasing levels of atmospheric $CO_2$ pose a significant challenge to climate stability while developing efficient carbon capture technologies remains a critical need. In this study, bacterial cellulose (BC), a mechanically robust and biodegradable biopolymer, is employed as a substrate for the *in situ* growth of amino-functionalized UiO-66 (UiO-66 -$NH_2$), a member of the metal-organic frameworks (MOFs) family known for their excellent
$CO_2$ capture capability. The effect of mixed-linker ratios on MOF integration within the BC matrix is systematically investigated. Additionally, the composite membrane is modified with hydrophobic polydimethylsiloxane (PDMS) to improve gas separation performance. The results show that the UiO-66-$NH_2$@BC composite membrane exhibits improved $CO_2$ adsorption capacity, attributed to the presence of amine groups. Upon PDMS coating, the PDMS/UiO-66-$NH_2$@BC membrane demonstrates enhanced surface hydrophobicity, as confirmed by water contact angle measurements, and increased $CO_2$ adsorption. These findings present a novel strategy for constructing composite membranes for efficient $CO_2$ capture and separation applications.

***hathaikarn.m@chula.ac.th**

## INTRODUCTION

The rising concentration of atmospheric carbon dioxide ($CO_2$), predominantly from fossil fuel combustion, remains a primary contributor to global climate change. Membrane-based separation technologies have gained attention for their energy efficiency and scalability [1]. However, many commercial membranes rely on petroleum-based polymers, raising concerns about sustainability. Therefore, developing biodegradable, high-performance alternatives is critical.

Bacterial cellulose (BC), produced by *Acetobacter xylinum*, is a biodegradable nanofiber with excellent mechanical strength and flexibility [2]. In this study, BC is synthesized using crude glycerol, a low-cost by-product of biodiesel production, which adds value to industrial waste and reduces production costs, supporting circular economy principles. BC's flexibility and abundant hydroxyl groups provide an ideal metal-organic framework (MOF) growth scaffold. These hydroxyl sites promote uniform MOF dispersion, while strong hydrogen bonding among BC fibers imparts mechanical robustness to the composite aerogels, allowing significant deformation without damage. To test this, we

PPC & PETROMAT SYMPOSIUM 2025

developed a rapid, facile, in-situ growth method for integrating MOFs into BC membranes with hierarchical structures, overcoming the challenge of fabricating flexible, processable MOF-based membranes.

UiO-66, recognized for its exceptional chemical and thermal stability as well as its robust resistance under gas separation conditions, was selected as the metal-organic framework (MOF) for this study. Functionalization with amine groups (UiO-66-$NH_2$) further enhances its $CO_2$ affinity by promoting selective adsorption through strong interactions with $CO_2$ molecules [3]. The primary objective of this project is to develop a sustainable, high-performance composite membrane by incorporating amine-functionalized UiO-66 into a biodegradable bacterial cellulose (BC) scaffold. Membrane performance is further optimized through hydrophobic surface modification, aiming to improve durability and selectivity in humid gas separation environments.

To enhance stability under humid conditions, the membranes were coated with polydimethylsiloxane (PDMS), a hydrophobic and $CO_2$-philic polymer that reduces water uptake and improves selective $CO_2$ transport [4,5]. The resulting PDMS/ UiO-66-$NH_2$@BC composite membranes demonstrate significantly enhanced $CO_2$ capture performance, presenting a promising sustainable solution for practical gas separation applications.

## EXPERIMENTAL

### *A. Materials and Chemicals*

The bacterial cellulose (BC) pellicles were produced using a static fermentation technique with *Acetobacter xylinum* as the bacterial strain and crude glycerol as the carbon source. Zirconium(IV) oxychloride octahydrate, hydrochloric acid, N, N-dimethylformamide, 2-aminoterephthalic acid, terephthalic acid, ethanol, polydimethylsiloxane (SYLGARD184) and n-hexane.

### *B. Production of bacterial cellulose from crude glycerol*

BC sheets were grown at the air-liquid interface was removed after 14 days in aseptic condition. Rinsed thoroughly with distilled water, boiled in 2% (w/v) NaOH 80 °C for 1 hr After boiling, the pellicle was removed and washed repeatedly in distilled water until the neutral pH was reached. BC was oven dried at 70 °C for 24 hrs and the dry weight was noted.

### *C. Preparation of BC membrane*

The purified BC pellicles were blended into a paste, then mixed with deionized water and homogenized for 5 minutes. The suspension was cast into a Petri dish lined with a Teflon patch and placed in an oven at 100°C. Once 70% of the water had evaporated, another Teflon patch, a plastic Petri dish, and a flask were placed on top to prevent shrinkage. Drying was completed at 70 °C for 24 hours.

### *D. Synthesis of UiO-66-$NH_2$*

$ZrOCl_2 \cdot 8H_2O$ was dissolved in a DMF/HCl solution (15:1 mL). 3 different linker mixtures of BDC and BDC-$NH_2$ were prepared with BDC-$NH_2$ molar fractions of 0, 0.50 and 1, producing UiO-66, UiO-66-$NH_2$-50 and UiO-66-$NH_2$-100, respectively. The solution was stirred for 15 minutes, sonicated for 30 minutes, then transferred to an autoclave and

heated at 120 °C for 24 hours. The resulting mixture was centrifuged, washed three times with DMF/EtOH, and dried overnight in a preheated oven to obtain MOF particles.

*E. Synthesis of MOFs@BC composite membrane*

BDC and BDC-$NH_2$ were dissolved in DMF (solution A), and $ZrOCl_2 \cdot 8H_2O$ was dissolved in a DMF/HCl mixture (solution B). The BC paste was submerged in solution B and stirred for 10 minutes. While stirring, solution A was added and mixed for another 10 minutes. The mixture was then reacted at 80 °C for 3 hours. The resulting UiO-66-$NH_2$@BC was washed three times with DMF/EtOH and dried overnight in a preheated oven.

*F. Hydrophobic modification*

Hydrophobic modification was synthesized UiO-66-$NH_2$@BC was soaked in 40 mL n-hexane solution of PDMS main agent and curing agent (w/w 10:1) for 10 min. Subsequently, the membrane sample was cured in the preheating oven for 3 hours. The resulting sample was denoted as PDMS/UiO-66-$NH_2$@BC.

*G. Characterization*

X-ray diffraction (XRD) was performed using a Rigaku SmartLab diffractometer, scanning 2θ angles from 5° to 80°. Fourier transform infrared spectroscopy (FTIR) was conducted on a Thermo Scientific Nicolet iS5 using ATR iD7 mode over the range of 4000-400 $cm^{-1}$. Surface morphology and microstructure were examined via field-emission scanning electron microscopy (FE-SEM, Hitachi S-4800) at 2.0–5.0 kV and 5000x–50000x magnification. Samples were sputter-coated with platinum under vacuum for 250 seconds. The $CO_2$ adsorption capacity of all samples were evaluated through BET. The pressures of $CO_2$ gas were up to 1 bar and the adsorption temperature at 273 K was applied during the adsorption measurement. Before performing each adsorption experiment, all samples were degassed at 80°C for 12 hours. The measurement of the surface wettability of the samples was conducted utilizing a contact angle meter (DPA 10, Krus).

## RESULTS AND DISCUSSION

*A. FT-IR analysis and XRD pattern of UiO-66-$NH_2$@BC membranes*

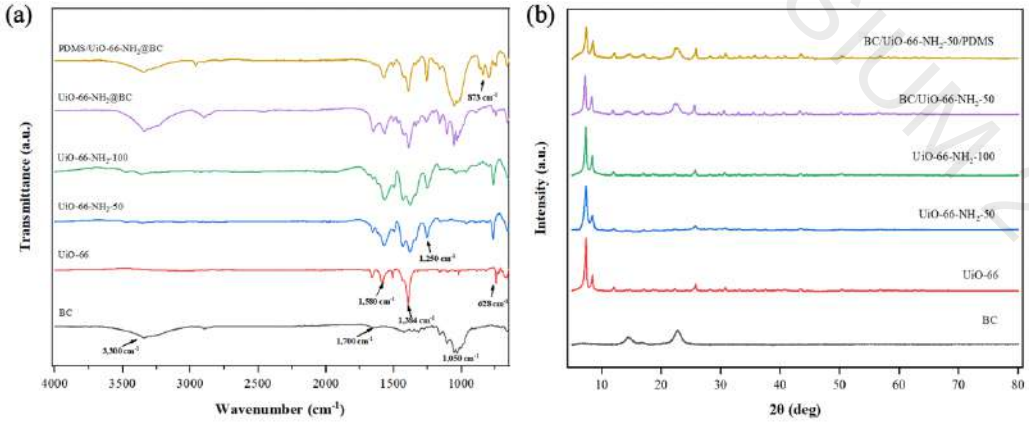


**Fig 1.** (a) FT-IR spectra of UiO-66-$NH_2$@BC membranes (b) XRD patterns of UiO-66-$NH_2$@BC membranes

FTIR analysis was performed to investigate the interactions between UiO-66 based materials and the bacterial cellulose (BC) membrane. The BC spectrum showed broad absorption bands around 3300 $cm^{-1}$ and 1050 $cm^{-1}$, corresponding to -OH and C-O stretching vibrations, respectively, and a peak near 1700 $cm^{-1}$ attributed to C=O stretching. In the pure UiO-66 spectrum, peaks at 1580 $cm^{-1}$ and 1384 $cm^{-1}$ were assigned to the asymmetric and symmetric stretching of carboxylate groups, while the band at 628 $cm^{-1}$ indicated Zr-O bonding. For UiO-66-$NH_2$, an additional peak at 1250 $cm^{-1}$ confirmed the presence of amine groups. Upon incorporating PDMS into UiO-66-$NH_2$@BC, a new peak emerged at 873 $cm^{-1}$, corresponding to the Si-C-H stretching vibration. These results indicate the successful incorporation of UiO-66-$NH_2$ and PDMS into the BC matrix, as evidenced by the characteristic functional group vibrations in the FTIR spectra.

The XRD patterns of the materials, which allowed determining their crystallinity. UiO-66 and UiO-66-$NH_2$ demonstrate similar characteristic peaks with two sharp peaks at 7.2˚ and 8.3˚ which indexed well to the (111) and (200) crystal planes [5]. The main XRD peaks of BC at 2θ = 14.9˚, 16.0˚, and 22.8˚, which were ascribed to the crystallographic planes of cellulose I crystalline structure. The distinctive peaks of BC and UiO-66-$NH_2$ appeared in UiO-66-$NH_2$@BC, which confirmed the successful growth of UiO-66-$NH_2$ on BC. Moreover, the distinctive peaks of composite membrane have no significant change after treatment with PDMS, demonstrating that its structure was not affected.

*B. Physical Morphology of UiO-66-$NH_2$@BC by SEM analysis*

The membrane morphology was characterized visually and by scanning electron microscopy (SEM). A noticeable color change in the bacterial cellulose (BC) from white to light yellow (Fig. 2a, 2e) indicated a uniform distribution of UiO-66-$NH_2$ particles on the BC. SEM images revealed that the BC fibers were densely packed with smooth surfaces and no visible particle attachment prior to MOF incorporation (Fig. 2b).

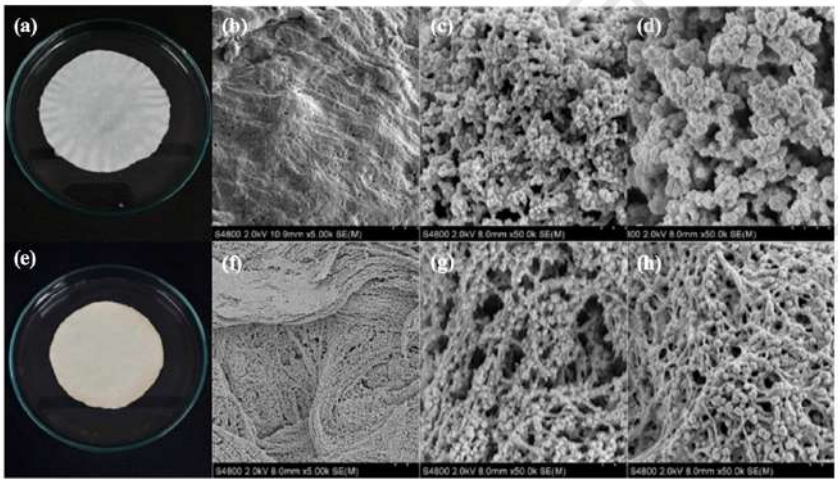


**Fig 2.** Optical view and SEM images of BC (a, b), UiO-66 (c), UiO-66-$NH_2$(d) UiO-66-$NH_2$@BC (e, f, g), and PDMS/UiO-66-$NH_2$@BC (h)

PPC & PETROMAT SYMPOSIUM 2025

UiO-66 and UiO-66-$NH_2$ particles displayed spheroidal structures. As shown in Fig. 2c,2d. UiO-66-$NH_2$ particles were uniformly and compactly distributed on the BC fibers, maintaining their morphology throughout the composite synthesis (Fig. 2f, 2g). After PDMS modification, a continuous PDMS layer encapsulated the MOF particles on the fiber surface (Fig. 2h), confirming successful coating.

*C. Surface Area Analysis and $CO_2$ adsorption by composite membranes*

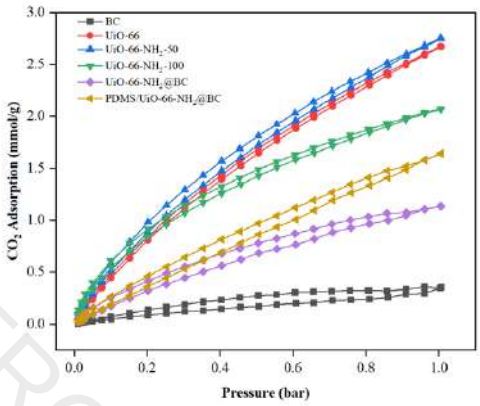


**Fig 3.** Isotherms for $CO_2$ adsorption capacities of UiO-66-NH2@BC

The $CO_2$ adsorption capacities of UiO-66s based crystals and composite membranes were measured at 273 K up to 1 bar (Fig. 3). The BC membrane showed low uptake (0.17 mmol/g) due to limited porosity and few active sites. Pristine UiO-66 adsorbed 2.69 mmol/g, benefiting from -OH groups on Zr nodes. UiO-66-$NH_2$-100 had reduced uptake (2.07 mmol/g) because excessive -$NH_2$ groups caused pore blockage. UiO-66-$NH_2$-50 achieved the highest uptake (2.75 mmol/g), balancing porosity and functional groups. UiO-66-$NH_2$@BC showed 1.13 mmol/g uptake, while PDMS/UiO-66-$NH_2$@BC improved to 1.64 mmol/g, highlighting the role of PDMS in enhancing $CO_2$ affinity.

*D. Superhydrophobicity performance*

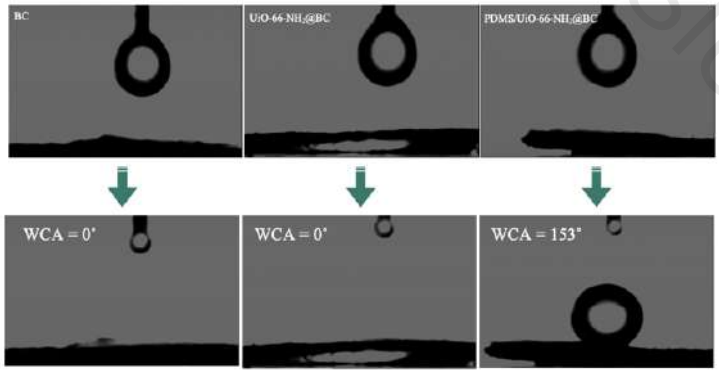


**Fig 4.** WCA of BC, UiO-66-$NH_2$@BC and PDMS/UiO-66-$NH_2$@BC

PPC & PETROMAT SYMPOSIUM 2025

Fig 4. shows the water contact angle (WCA) of the samples. Both bacterial cellulose (BC) and UiO-66-$NH_2$@BC absorbed water droplets quickly, indicating strong hydrophilicity. After coating with polydimethylsiloxane (PDMS), the WCA of PDMS/UiO-66-$NH_2$@BC reached 153º, demonstrating superhydrophobicity.

## CONCLUSIONS

The synthesis of UiO-66-$NH_2$ MOF crystals on bacterial cellulose (BC) substrate successfully produced the UiO-66-$NH_2$@BC composite, which was then coated with polydimethylsiloxane (PDMS) to modify surface properties. XRD and FTIR analyses confirmed the MOF's successful formation and structural integrity within the composite. Notably, the UiO-66-$NH_2$-50 sample showed the highest $CO_2$ uptake of 2.75 mmol/g. After immobilization on BC, the composite exhibited a $CO_2$ adsorption capacity of 1.13 mmol/g, which increased to 1.64 mmol/g upon PDMS coating. The resulting PDMS/ UiO-66-$NH_2$@BC composite membranes demonstrate significantly enhanced $CO_2$ capture performance, presenting a promising sustainable solution for practical gas separation applications.

## ACKNOWLEDGEMENTS

The authors would like to express their gratitude to the Petroleum and Petrochemical College, Chulalongkorn University, and the DPST scholarship for support and financial assistance.

## REFERENCES

**Bernardo, P., Drioli, E., & Golemme, G.** (2009). Membrane gas separation: A review /state of the art. Ind. Eng. Chem. Res., 48(10), 4638–4663.

**Yang, F., Hanna, M. A., & Sun, R.** (2012). Value-added uses for crude glycerol. Biotechnol. Biofuels, 5, 13.

**Biswas, S., & Van Der Voort, P.** (2013). A general strategy for the synthesis of functionalized UiO-66 frameworks. Eur. J. Inorg. Chem., 12, 2154–2160.

**Meng, H., & Park, C. B. (2012).** Hydrophobic modification of cellulose-based materials for $CO_2$-selective membranes. J. Membr. Sci., 417–418, 101–110.

**Dai Q., Liu J., Zheng, J., Fu B. (2023).** Immobilization of UiO-66-$NH_2$ into bacterial cellulose aerogels for efficient particulate matter filtration. Sustainability, 15, 13382.

PPC & PETROMAT SYMPOSIUM 2025

# SIMULATION AND OPTIMIZATION OF WAX PRODUCTION FROM MULTILAYER PLASTIC PACKAGING WASTES VIA PD-MCM-41 CATALYZED PYROLYSIS

*Phailin Thipkonglas* [a], *Jitima Preechawong* [a], *Jirasuta Chungprempree* [a], *Aung Kyaw Moe* [a], *Pisitpong Intarapong* [b], *Manit Nithitanakul* [a]

[a] The Petroleum and Petrochemical College, Chulalongkorn University, Bangkok, Thailand
[b] King *Mongkut's University of Technology Thonburi*

PPC & PETROMAT SYMPOSIUM 2025

## ABSTRACT

Catalytic pyrolysis offers a promising solution for converting multilayer plastic packaging waste (MPPWs) into valuable hydrocarbon products. This study investigates the pyrolysis of MPPWs containing ultra-thin aluminum layer and complex and chemical bonds, using Pd-MCM-41 catalysts (0.2% - 1.0% Pd loading) with varying acidities (0.84–1.50 mmol/g) to optimize wax production, specifically aiming for a high paraffin-to-olefin ratio. Experiments were conducted in a batch reactor at 500 °C for 4 hours under nitrogen atmosphere, yielding wax, gas, and char. The catalyst with 1.0%Pd and 1.50 mmol/g acidity achieved the highest paraffin-to-olefin ratio (2.11), indicating wax quality involved. Complementary, Aspen Plus simulations were performed at 400 °C, 500 °C, and 600 °C. At 400 °C, 1.0% Pd-MCM-41, paraffin yield reached 2.94 g and olefin yield 1.39 g, at 600 °C, yields declined to 2.22 g and 1.05 g respectively, showing that lower temperatures favor wax formation while higher temperatures enhance gas production. These findings highlight the influence of catalyst acidity and operating temperature in tailoring product distributions and support the use of Pd-MCM-41 for sustainable valorization of plastic waste into industrial grade wax.

***manit.n@chula.ac.th**

## INTRODUCTION

As the global population continues to expand and urbanization accelerates, the demand for plastics has seen an unprecedented rise. This growth is driven by versatility of materials, low cost, and indispensable applications in many industries, including packaging, construction, automotive, and electronics (Vadera, 2021). Consequently, global plastic production has surged dramatically, from approximately 1.5 million tons in 1950 to around 460 million tons in 2019, with projections indicating a potential doubling or even quadrupling by 2050 (Dokl et al., 2024). One of the most widely used is multilayer plastic packaging, consisting of multiple layers of such as polyethylene (PE), polypropylene (PP), polyethylene terephthalate (PET), polyvinyl chloride (PVC), ethylene vinyl alcohol (EVOH), aluminum, and even paper, each chosen for specific functional properties such as oxygen or moisture barrier, mechanical strength, printability, or heat sealability, enhancing product protection, extending shelf life and allowing for customized functional properties that a single material cannot provide. However, the complex, inseparable composition of multilayer packaging presents significant challenges for traditional mechanical recycling methods. As a result, a substantial portion of multilayer plastic waste is currently incinerated or landfilled (Ciawi et al., 2025). Chemical recycling technologies, such as pyrolysis, are emerging as promising solutions to address these challenges. Pyrolysis is a thermochemical decomposition process that converts plastic waste into valuable products by providing high temperatures in the absence of oxygen. By employing catalysts, this method significantly enhances the selectivity towards desired

liquid pyrolysis products with favorable paraffin content, compared to non-catalytic thermal pyrolysis (Dai et al., 2022). MCM-41 with the incorporation of palladium metals (Pd) successfully enhances the catalyst acidity, crucial for facilitating cracking and secondary reactions that influence product selectivity (Choi et al., 2022). Beyond the scope of direct experimental testing, Aspen Plus simulation was utilized as a predictive tool to determine the wax product composition, optimize the process condition and offer the understanding of how catalyst properties and operating conditions influence the valorization of plastic waste (Motta et al., 2024). Especially, the specific role and optimal use of advanced catalysts such as Pd-MCM-41 with multilayer plastic packaging waste (MPPWs) feedstock, along with the integration of robust simulation and optimization strategies, are not yet fully explored or established in the current literature. In this research, Pd-MCM-41 catalysts with various Pd-loading were studied for upgrading the wax quality. Furthermore, Aspen Plus simulation was employed for prediction of the obtained wax products with the influence of catalyst acidity and operating temperature in pyrolysis process.

## EXPERIMENTAL

*A. Catalyst Preparation*

Pd-MCM-41 catalysts were prepared by wet impregnation, aiming for various palladium loadings ranging from 0.2, 0.4, 0.6, 0.8, and 1.0 wt.%. For each desired Pd loading conditions, a calculated amount of $PdCl_2$ dissolved in 0.1 M hydrochloric acid (HCl) solution. $PdCl_2$/HCl mixture slowly dropped onto the 6 g of MCM-41 support and impregnated overnight to ensure thorough dispersion. Lastly, the catalysts were calcined at 500 °C for 4 hours to convert the palladium precursor into active form and remove any residual organic matter.

*B. Characterization*

The acidity of catalysts was determined by Ammonia Temperature-Programmed Desorption, (NH3-TPD). The scanning electron microscopy (SEM) images of Pd-MCM-41 catalysts were examined by Hitachi field emission scanning electron microscopy (Model S-4300) at accelerating voltage of 2-20 kV, after platinum sputter coating. The crystallization of catalysts was determined by using X-ray diffraction with a Rigaku X-ray diffractometer (Model SmartLab 3kV, Japan). Measurements were conducted over a 2θ range of 2-10 deg, with a step size of 0.01 deg and scan speed 0.5 deg/min.

*C. Simulation for Plastic Pyrolysis*

The Aspen Plus simulation of catalytic pyrolysis of MPPWs using Pd-MCM-41 catalysts effectively modeled the conversion of a 10 g feedstock (assumed 7 g plastic + 3 g aluminum) under varying temperatures (400, 500, and 600 °C) with various acidity of prepared catalysts. Utilizing the RYield reactor as decomposition and pyrolysis reactor, the simulation incorporated literature-informed yield distributions of wax, gas and char products.

$$Wax\ yield\ (\%) = \frac{Total\ wax\ mass\ (g)}{Plastic\ feed\ mass\ (g)} \times 100$$

$$Gas\ yield\ (\%) = 100 - wax\ yield\ (\%) - 30\%\ of\ Al\ char$$

PPC & PETROMAT SYMPOSIUM 2025

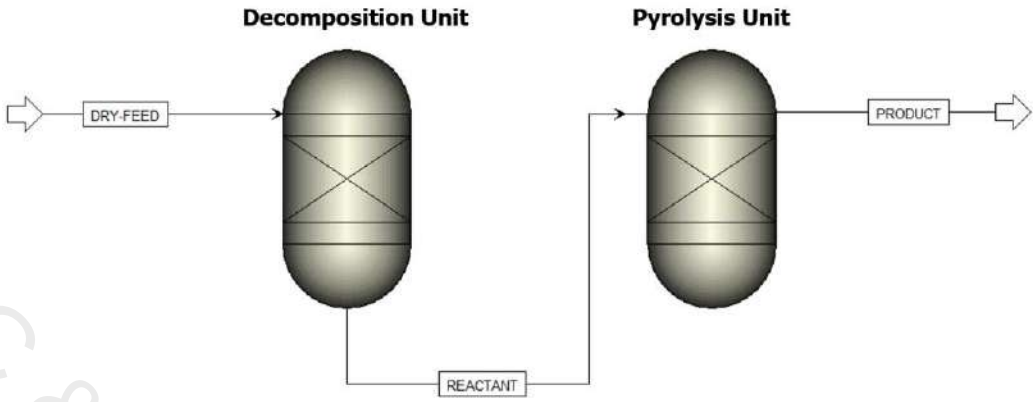


**Figure 1** The flowsheet for the catalytic pyrolysis process in Aspen Plus.

## RESULTS AND DISCUSSION

*A. Characterization of Catalyst*

$NH_3$-TPD profiles show that bare MCM-41 exhibits a flat line with a slight increase starting around 300°C. This indicates that bare MCM-41 has negligible acidity, consistent with its nature as a pure silica material, which typically lacks acidic sites, as shown in table 4.2. The introduction of palladium to the MCM-41 support significantly enhances its acidity. All Pd-MCM-41 catalysts demonstrate higher ammonia desorption compared to the bare support and indicate the generation of new acid sites. The observed desorption peaks predominantly in the low-to-medium temperature range which means the formation of weak to moderate strength acid sites, with 1.0% Pd-MCM-41 exhibiting the highest ammonia desorption among all conditions. It shows a broad peak is observed around 400 °C, with the highest intensity, resulting in the highest acidity at 1.5 mmol/g which is beneficial for catalytic cracking reactions. On the other hand, there was a slight decrease to 0.8% Pd, which may be due to structural changes. As observed in these catalysts, weak to moderate strength acid sites are particularly effective for cracking reactions at moderate temperatures, which are suitable for the typical operating conditions of pyrolysis.

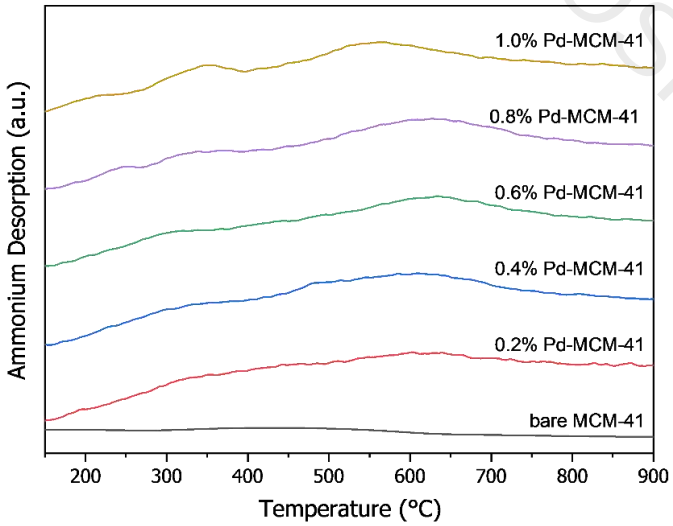


**Figure 2** $NH_3$-TPD profiles of MCM-41 and Pd-MCM-41 with various Pd loading.

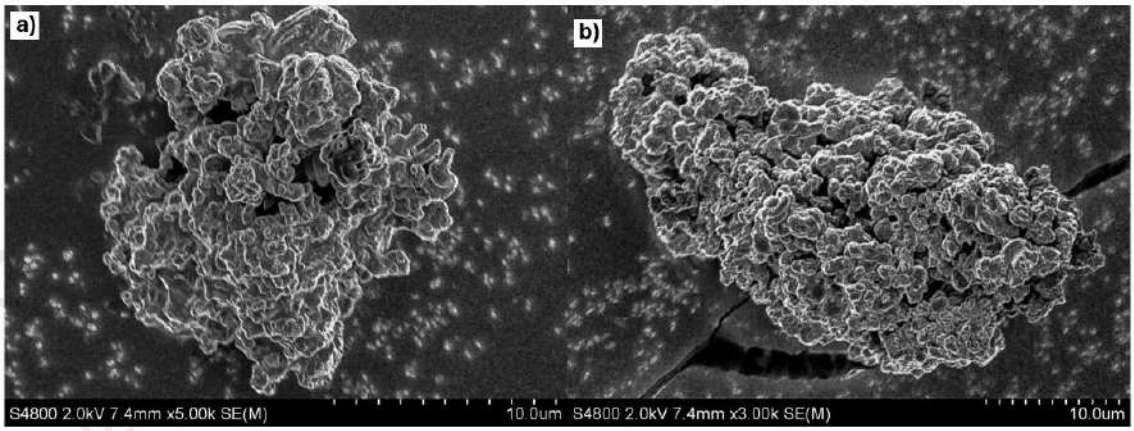


**Figure 3** SEM images of catalysts: a) MCM-41, b) Pd-MCM-41.

*B. Simulation for Catalytic Pyrolysis*

The Aspen Plus simulation was further utilized to predict the composition of the wax product under the conditions of batch reactor at 500°C for 4 hours under nitrogen atmosphere. As a result, 0.2% and 0.4% Pd-MCM-41 catalysts, with lower Pd loadings and likely lower effective acidity, exhibit lower paraffin contents (22% and 23%, respectively) and lower paraffin/olefin ratios (1.25 and 1.36). This suggests that at these lower loadings, the number of active sites is insufficient to drive extensive olefin saturation. In contrast, 1.0% Pd-MCM-41 catalyst yielded the highest simulated paraffin content (27%) and the highest paraffin-to-olefin ratio (2.15). The simulation results suggest that higher Pd loadings in Pd-MCM-41 catalysts, under the specified conditions, optimize the wax product for higher paraffin content. The decrease in olefin content with increasing Pd loading indicates a shift toward saturated hydrocarbons, likely due to enhanced hydrogenation catalyzed by Pd sites. This corresponds to the intended research goal of tailoring wax composition for multilayer plastic packaging pyrolysis, providing a basis for catalyst optimization.

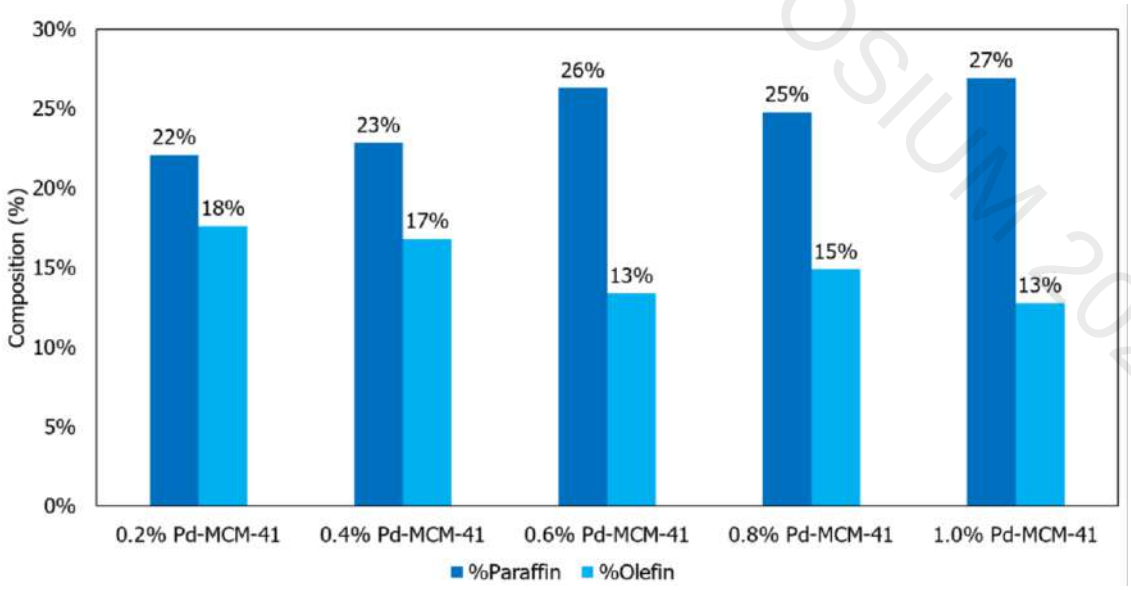


**Figure 4** The simplified components for Aspen Plus simulation.

Further simulations were conducted using Aspen Plus to investigate the influence of operating temperature. The percentage of wax products decreased significantly as the pyrolysis temperature increased. It is highest at 400 °C (63%), drops to 59% at 500 °C, and further declines to 52% at 600 °C. This trend is typical for pyrolysis processes, where lower temperatures favor the formation of heavier, less cracked liquid fractions, while higher temperatures provide more energy for further bond scission, converting these heavier components into lighter ones as shown in the percentage of gaseous products. The operation temperature at 400 °C showed the lowest gas yield (7%), increased to 11% at 500 °C, and then surged to 18% at 600 °C. This direct relationship indicated that at higher temperatures, the increased thermal energy led to more extensive cracking reactions, producing a larger quantity of non-condensable gases such as methane, ethane, propane, butane. This is a well-established principle in pyrolysis kinetics, where higher temperatures accelerate cracking rates, shifting the product spectrum towards lighter, more volatile compounds.

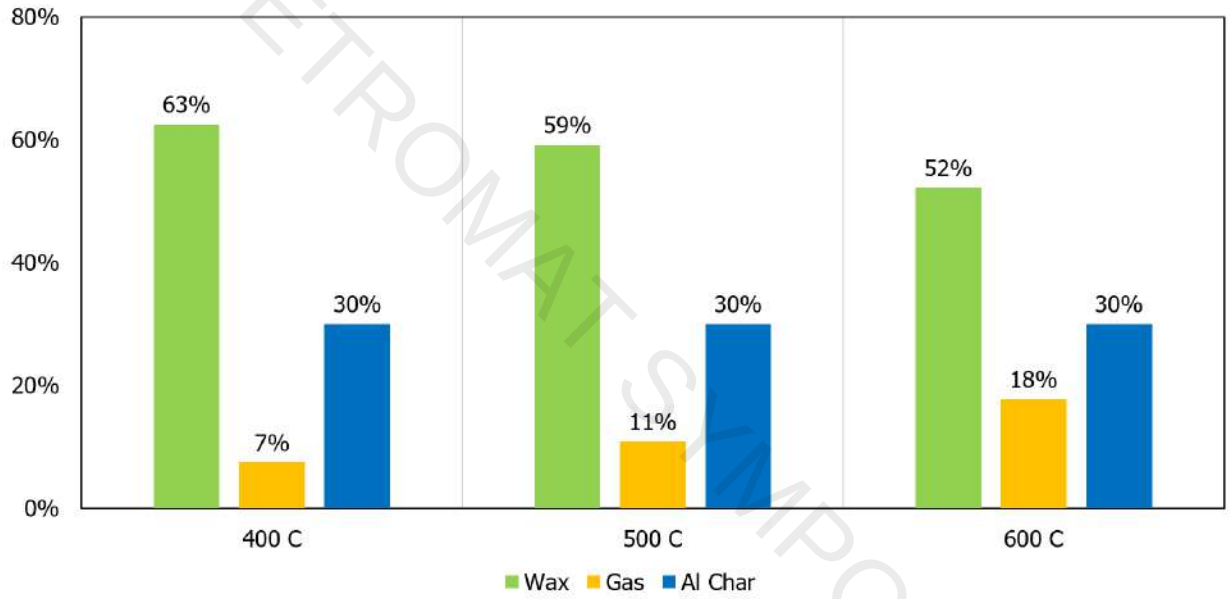


**Figure 5** Simulated wax product composition at varying temperatures via 1.0% Pd-MCM-41.

## CONCLUSIONS

The simulation of catalytic pyrolysis of multilayer plastic packaging waste demonstrated that catalyst acidity significantly affects the composition of the obtained wax product. Furthermore, the simulation of pyrolysis product composition at varying temperatures revealed a significant impact of operating temperature on overall product distribution. This simulation serves as a valuable tool for understanding and optimizing the valorization of challenging multilayer plastic waste.

## ACKNOWLEDGEMENTS

The authors would like to sincerely thank the Petroleum and Petrochemical College (PPC), Chulalongkorn University for supporting this research.

PPC PETROMAT SYMPOSIUM 2025

## REFERENCES

**Choi, I.-H., Lee, H.-J., Rhim, G.-B., Chun, D.-H., Lee, K.-H., & Hwang, K.-R.** (2022). Catalytic hydrocracking of heavy wax from pyrolysis of plastic wastes using Pd/Hβ for naphtha-ranged hydrocarbon production. *Journal of Analytical and Applied Pyrolysis*, *161*, 105424. https://doi.org/https://doi.org/10.1016/j.jaap.2021.105424

**Ciawi, Y., Tonyes, S., & Dwipayanti, N. M. U.** (2025). Multilayer packaging recycling: challenges, current practices, and future prospects. *2*, 1-12. https://doi.org/10.20935/AcadEnvSci7521

**Dai, L., Zhou, N., Lv, Y., Cheng, Y., Wang, Y., Liu, Y., Cobb, K., Chen, P., Lei, H., & Ruan, R.** (2022). Pyrolysis technology for plastic waste recycling: A state-of-the-art review. *Progress in Energy and Combustion Science*, *93*, 101021. https://doi.org/https://doi.org/10.1016/j.pecs.2022.101021

**Dokl, M., Copot, A., Krajnc, D., Fan, Y., Vujanović, A., Aviso, K., Tan, R., Kravanja, Z., & Čuček, L.** (2024). Global projections of plastic use, end-of-life fate and potential changes in consumption, reduction, recycling and replacement with bioplastics to 2050. *Sustainable Production and Consumption*, *51*. https://doi.org/10.1016/j.spc.2024.09.025

**Motta, I. L., Marchesan, A. N., Guimaraes, H. R., Chagas, M. F., Bonomi, A., Maciel, M. R. W., & Maciel Filho, R.** (2024). Co-pyrolysis of Lignocellulosic Residues and Plastics: a Simulation Approach to Predict Product Yields.

**Vadera, S.** (2021). A Critical Analysis of Rising Global Demand of Plastics and its Adverse impact on Environment Sustainability. *Journal of Environmental Pollution and Management*, *3*. https://doi.org/10.18875/2639-7269.3.105

PPC & PETROMAT SYMPOSIUM 2025

# Parametric Study on CNTs Growth by Catalytic Methane Decomposition Using Natural Mineral–Based Metal Catalysts

*Bayu Setiawan* [a], *Phuwadej Pornaroontham* [b,c], *Boonyarach Kitiyanan* [a,c,*]

[a] The Petroleum and Petrochemical College, Chulalongkorn University, Bangkok, Thailand
[b] Department of Chemical Technology, Faculty of Science, Chulalongkorn University, Bangkok, Thailand
[c] Centre of Excellence on Petrochemical and Materials Technology, Chulalongkorn University, Bangkok, Thailand

Keywords: Response surface methodology, CNTs, Methane, Decarbonization.

## ABSTRACT

Catalytic methane decomposition (CMD) offers an economical pathway for producing carbon nanotubes (CNTs) by converting methane, a potent greenhouse gas, into solid carbon. This study focuses on CNTs synthesis using a transition metal-based catalyst supported on natural mineral-based materials, which is abundant. The catalyst was prepared using incipient wetness impregnation and thermally activated prior to experiment. Experiments conducted in a fixed-bed vertical reactor explored the effects of reaction temperature and time on quantity and quality of deposited carbon. Response Surface Methodology (RSM) was employed to optimize both carbon deposition and the structural integrity of CNTs, as assessed by Raman spectroscopy ($I_D/I_G$ ratio). The results reveal a synergistic interplay between temperature and time, achieving an optimal carbon deposition of approximately 150% (relative to catalyst weight), along with CNTs exhibiting an $I_D/I_G$ ratio of 0.6. These findings present valuable insights for advancing practical CNT production methods to meet industrial demands.

*** boonyarach.k@chula.ac.th**

## INTRODUCTION

In the current era of decarbonization and sustainable energy, the conversion of greenhouse gases into value-added materials is a compelling research focus. Carbon nanotubes (CNTs), renowned for their exceptional mechanical, electrical, and thermal properties, are pivotal in advancing technologies in electronics, composite materials, and energy storage (Shah & Tali, 2016). Traditional CNTs production methods, such as arc discharge, plasma jet, and conventional chemical vapor deposition (CVD), often rely on hydrocarbon feedstocks that can contribute to COx emissions.

Catalytic methane decomposition (CMD) emerges as a promising alternative pathway. This process not only produces CNTs but also converts a potent greenhouse gas into solid carbon, thereby bolstering efforts toward carbon circularity and environmental sustainability (Raza et al., 2022).

This study focuses on the influence of operating condition on CNTs synthesis through methane decomposition using a transition metal-based catalyst supported on a natural mineral. Due to the uniqueness of its composition, the natural mineral possesses not only inertness and thermal stability but also abundance, considering the catalyst will be removed and disintegrated from CNTs during purification steps. The catalyst was prepared via

PPC & PETROMAT SYMPOSIUM 2025

incipient wetness impregnation and thermally activated to improve the dispersion of active sites. Operating parameters, including reaction temperature and time, were varied in a fixed-bed vertical reactor to assess their impact on carbon deposition and CNTs structural properties. Response Surface Methodology (RSM) was employed to elucidate the synergistic effects of these parameters, providing insights into achieving the best achievable CNTs quality among the designated conditions.

## EXPERIMENTAL

### *A. Materials*

High-purity reagents were employed in this study. The 2 transition metal precursors were obtained from a reputable chemical supplier, and a proprietary natural mineral-based support material was sourced from an established vendor. Methane ($CH_4$) gas (99.99% purity) was supplied by Labgaz Thailand Co., Ltd. Additionally, nitrogen ($N_2$, 99.9% purity) and hydrogen ($H_2$, 99.95% purity) gases were procured from Air Liquide.

### *B. Catalyst Preparation*

A metal precursor solution was prepared by dissolving the required amount of compound in deionized water under continuous stirring. This solution was then gradually introduced onto the support material to ensure uniform distribution and thorough wetting. The impregnated support was subsequently dried and calcined under controlled conditions to obtain the final catalyst.

### *C. Response Surface Methodology (RSM)*

A Response Surface Methodology (RSM) approach was employed to optimize and reveal the influence of main effects and interaction to the process parameters. The experimental design was defined by selecting factors, response, and a quadratic model. Levels of each variable were set, and experiments were executed as per the generated run matrix. The results were input into the software for statistical analysis. Diagnostic checks were conducted to validate model assumptions, and a Box-Cox transformation was applied if necessary. ANOVA and fit statistics were used to evaluate model adequacy, and only terms with p-values < 0.05 were retained in the final model. The RSM method is exhibited in Figure 1.

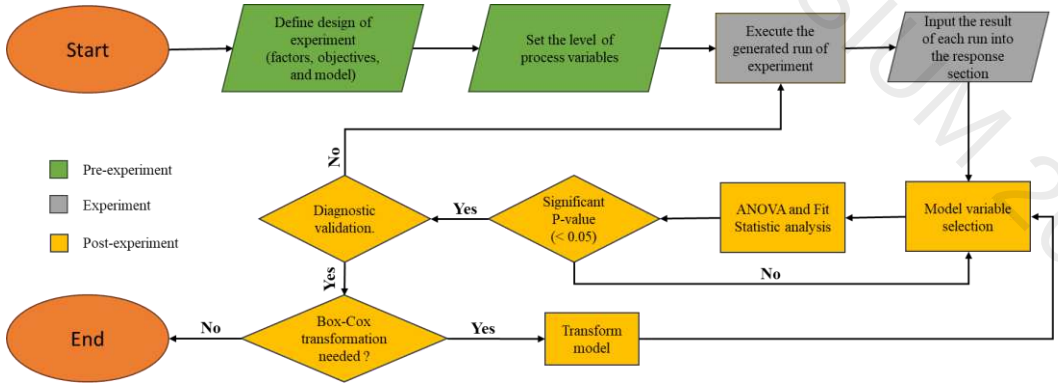


Figure 1. Response surface methodology flowchart.

*D. Catalytic Performance Test*

The catalytic performance of the prepared catalyst for CNTs production was evaluated in a vertical reactor using 0.10 g of the prepared catalyst. Through several sequence steps with operation conditions corresponding to the design of the experiment, the synthesized CNTs were collected and examined.

*E. Characterization of Synthesized CNTs*

Raman spectroscopy (Horiba iHR-550) was conducted to assess the quality of synthesized CNTs within the range of 100–2500 $cm^{-1}$ wavenumbers using a 532 nm wavelength laser

## RESULTS AND DISCUSSION

A $3^k$ factorial Design of Experiments (DOE) was employed to assess the combined influence of reaction temperature (A) and time (B) on both deposited carbon ($y_1$) and the quality of synthesized CNTs ($y_2$). Both reaction temperature (800, 875, and 950°C) and reaction time (30, 60, and 90 min) were coded at levels: –1, 0, and +1. Furthermore, to enhance the robustness of the data, each experimental condition was replicated in two blocks, as illustrated in Table 1.

Table 1. Design of experiment

| Standard Order* | Coded Level | | Actual Level | | Response | |
|---|---|---|---|---|---|---|
| | A (°C) | B (min) | A (°C) | B (min) | $y_1$ (%) | $y_2$ ($I_D/I_G$) |
| 1 | –1 | –1 | 800 | 30 | 71.17 | 0.78 |
| 2 | –1 | –1 | 800 | 30 | 65.94 | 0.80 |
| 3 | –1 | 0 | 800 | 60 | 82.09 | 0.77 |
| 4 | –1 | 0 | 800 | 60 | 83.81 | 0.75 |
| 5 | –1 | 1 | 800 | 90 | 102.79 | 0.87 |
| 6 | –1 | 1 | 800 | 90 | 101.09 | 0.85 |
| 7 | 0 | –1 | 875 | 30 | 73.38 | 0.62 |
| 8 | 0 | –1 | 875 | 30 | 72.05 | 0.62 |
| 9 | 0 | 0 | 875 | 60 | 102.19 | 0.57 |
| 10 | 0 | 0 | 875 | 60 | 104.55 | 0.55 |
| 11 | 0 | 1 | 875 | 90 | 120.61 | 0.70 |
| 12 | 0 | 1 | 875 | 90 | 120.70 | 0.69 |
| 13 | 1 | –1 | 950 | 30 | 86.64 | 0.82 |
| 14 | 1 | –1 | 950 | 30 | 82.92 | 0.80 |
| 15 | 1 | 0 | 950 | 60 | 134.06 | 0.68 |
| 16 | 1 | 0 | 950 | 60 | 132.94 | 0.70 |
| 17 | 1 | 1 | 950 | 90 | 156.94 | 0.74 |
| 18 | 1 | 1 | 950 | 90 | 151.24 | 0.77 |

***randomized**

PPC & PETROMAT SYMPOSIUM 2025

**A. Deposited Carbon Response ($y_1$)**

Based on ANOVA findings indicate that the model, which incorporates factors A, B, their interaction (AB), and the quadratic terms ($A^2$, $B^2$, and $AB^2$), robustly accounts for variations in the deposited carbon response. According to Equation 1, temperature (Factor A) and reaction time (Factor B) each positively affect the deposited carbon, while their combined interaction further boosts the output in a synergistic manner. The quadratic terms reveal non-linear dynamics, such as the deposited carbon follows a U-shaped trend with increasing temperature, whereas it follows an inverted U-shape with prolonged reaction time, suggesting that excessive reaction durations may reduce deposited carbon due to carbon encapsulation. Moreover, the negative coefficient for the $AB^2$ term indicates that extending reaction time at a constant temperature eventually results in diminishing returns.

$$y_1 = 103.01 + 25.28A + 25.11B + 8.98AB + 5.39A^2 - 6.15B^2 - 8.18AB^2 \quad (1)$$

Diagnostic tests (Figure 2) reveal that the residuals are normally distributed and homoscedastic (randomized pattern), with no undue influence from any single run, confirming the model's stability.

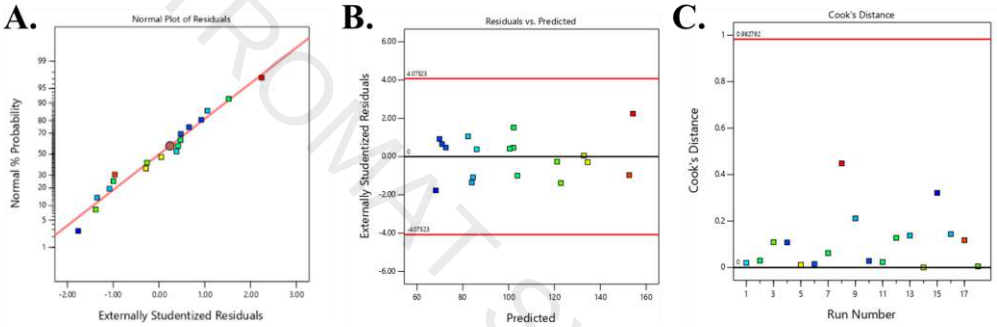


**Figure 2.** Y1's model diagnostic test plots: normal plot of residuals (A), residuals vs predicted pattern (B), cook's distance (C).

**B. Quality of CNTs Response ($y_2$)**

Figure 3A shows that CNTs, which were synthesized at 30 minutes, have different qualities depending on the temperature. At 875°C ($I_D/I_G$ = 0.62) exhibits superior graphitization compared to those produced at 800°C ($I_D/I_G$ = 0.78) and 950°C ($I_D/I_G$ = 0.82). The higher defect level at 800°C likely results from insufficient energy to drive rapid CNT formation, while the increased defects at 950°C are attributed to excessive carbon deposition and irregular layer growth that compromise structural integrity.

In comparison, when the reaction was run at fixed temperature (800°C), reaction time variation appears to have a lesser positive effect on quality, as indicated in Fig. 3B. Although extending the reaction time from 30 to 60 minutes slightly elevates the quality, further extension to 90 minutes results in a marked deterioration of CNT quality. Prolonged reaction time leads to denser CNTs, which restricts the newly formed CNTs from growing properly due to mutual blockage.

PPC & PETROMAT SYMPOSIUM 2025

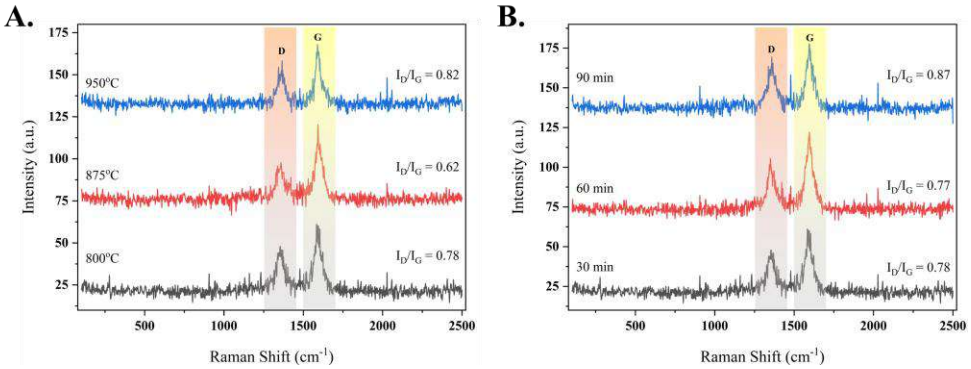


**Figure 3.** Raman spectra of synthesized CNTs through: temperature variation at 30 min (A) and time variation at 800°C (B).

Regarding CNTs quality,as measured by the $I_D/I_G$ ratio, ANOVA indicates that factors A, B, their interaction (AB), and the quadratic terms ($A^2$, $B^2$, and $A^2B$) significantly influence quality changes.

$$y_2 = 0.5677 - 0.0255A + 0.0371B - 0.0331AB + 0.1520A^2 + 0.0871B^2 - 0.0330A^2B \quad (2)$$

The statistical model (Equation 2) predicts how reaction temperature (A) and reaction time (B) affect the $I_D/I_G$ ratio, where lower values correspond to higher quality CNTs. Specifically, temperature has a dual effect, in which its linear term (A) decreases defects and improves quality, while the quadratic term ($A^2$) shows that very high temperatures eventually offset this benefit. Reaction time, on the other hand, has a predominantly negative impact, as indicated by its positive linear coefficient (B), meaning that longer durations tend to worsen quality, however, the quadratic term ($B^2$) suggests that at some point, the negative effects may plateau before intensifying again due to curvature effects. The interaction terms (AB and $A^2B$) imply that moderate temperature increases can counteract the adverse effects of extended reaction time, although this balance is lost when excessive heat prevails. Model diagnostics (Figure 4) confirm that the residuals are normally distributed and exhibit constant variance.

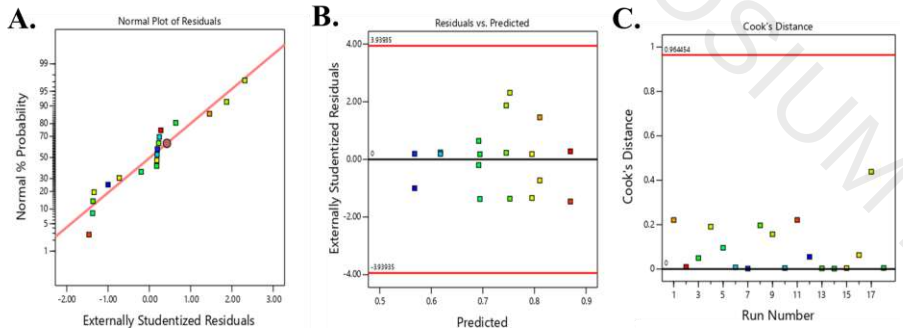


**Figure 4.** Y2's model diagnostic test plots: normal plot of residuals (A), residuals vs predicted pattern (B), cook's distance (C).

The 3D-surface plot depicts the influence of these both operating condition to deposited carbon (Fig. 5A) and the quality of synthesized CNTs (Fig. 5B).

PPC & PETROMAT SYMPOSIUM 2025

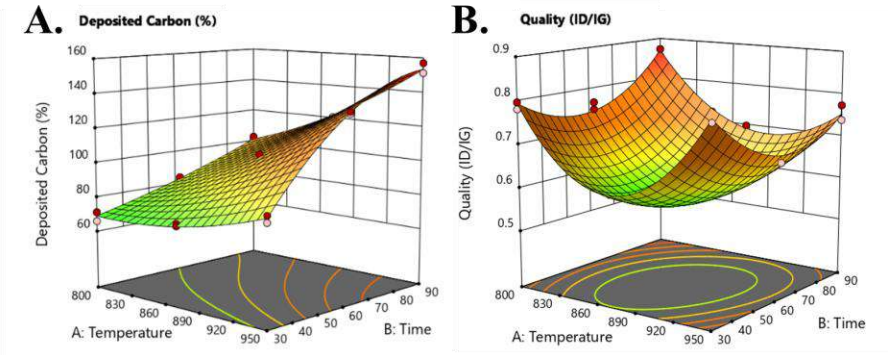


**Figure 5.** 3D-surface plot of deposited carbon (A) and CNTs quality (B) response.

The final stage of the study focused on model validation through confirmation runs, where predicted results were compared with experimental data. Three randomized conditions were selected and tested (Table 3) to assess the model's predictive accuracy and precision.

Table 3. Validation runs of model.

| Temp. | Time | Deposited Carbon (%) | | | Quality ($I_D/I_G$) | | |
|---|---|---|---|---|---|---|---|
| | | Predicted | Observed | %error | Predicted | Observed | %error |
| 850 | 70 | 102.18 | 100.70 | 1.45 | 0.62 | 0.62 | 0.16 |
| 825 | 45 | 78.83 | 75.60 | 4.10 | 0.65 | 0.63 | 3.59 |
| 900 | 40 | 89.36 | 87.05 | 2.58 | 0.60 | 0.62 | 2.80 |

## CONCLUSIONS

Operating conditions significantly impact CNTs growth, affecting both deposited carbon and quality. The findings highlight a synergistic effect of parameters such as reaction temperature and time, providing insights for further optimization of CNTs synthesis using transition metal-based catalysts on natural mineral supports.

## ACKNOWLEDGEMENTS

The author would gratefully acknowledge the support provided by Chulalongkorn University through the ASEAN and Non-ASEAN Countries Scholarship Program and The Petroleum and Petrochemical College.

## REFERENCES

**Raza, J., Khoja, A. H., Anwar, M., Saleem, F., Naqvi, S. R., Liaquat, R., Hassan, M., Javaid, R., Qazi, U. Y., & Lumbers, B.** (2022). *Methane decomposition for hydrogen production: A comprehensive review on catalyst selection and reactor systems*. Renewable and Sustainable Energy Reviews, **168**, 112774.

**Shah, K. A., & Tali, B. A.** (2015). *Synthesis of carbon nanotubes by catalytic chemical vapour deposition: A review on carbon sources, catalysts and substrates*. Materials Science in Semiconductor Processing, **41**, 67–82.

PPC & PETROMAT SYMPOSIUM 2025

# IN-SITU GROWTH OF MIL-125 IN BACTERIAL CELLULOSE-BASED AEROGELS FOR $CO_2$ CAPTURE

*Hasitha Erandani Jayasinghe Jayasinghe Koralalage* [a], *Bhumin Than-ardna* [a,b], *Hathaikarn Manuspiya** [a,b]

[a)] *The Petroleum and Petrochemical College, Chulalongkorn University*
[b)] *Center of Excellence on Petrochemical and Materials Technology*

Keywords: MIL-125, bacterial cellulose, aerogel, $CO_2$ adsorption

## ABSTRACT

The urgent need to mitigate anthropogenic $CO_2$ emissions has intensified research on effective adsorbent materials. One promising strategy is the in-situ growth of MIL-125, a titanium-based metal-organic framework, within bacterial-cellulose (BC) aerogels. BC is a natural biopolymer that offers a highly pure, three-dimensional nanofibrillar network with excellent mechanical stability, making it an ideal scaffold for designing ultralight, high-surface-area aerogels. Integrating MIL-125 into this network (MIL-125@BC) creates a hybrid adsorbent that combines the tunable porosity of MOFs and $CO_2$ affinity with the low density and structural robustness of aerogel. The synthesis of MIL-125@BC was successfully proved with FTIR, XRD, and FE-SEM while preserving a $CO_2$ adsorption of 3.21 mmol/g at 273 K compared to pristine MIL-125 (3.89mmol/g,273K).

## INTRODUCTION

The demand for fossil fuels and deforestation have been elevating the atmospheric carbon dioxide concentration, with an annual emission of 38.8 GT contributing to the greenhouse effect resulting in global warming, changes in weather patterns, increased sea level, and drastic changes in human lifestyles (Liu et al., 2024). Furthermore, fossil fuels are depleted continuously due to the high energy demand for electricity, transportation, construction, and manufacturing, resulting in a lack of raw materials for future manufacturing industries. Continuous population growth and economic development contribute to the necessity of recovering carbon dioxide from the atmosphere. Consequently, carbon capture, storage (CCS), and utilization (CCU) have emerged as key factors in achieving net zero emissions by 2050 (Obobisa, 2022).

The major outcome of accelerating $CO_2$ accumulation is global warming, resulting in rising sea levels. Despite the increasing world population, the land area has decreased due to melting glaciers (Ekwurzel et al., 2017). Post-combustion $CO_2$ capture has become the most accessible way to reduce $CO_2$ accumulation in the atmosphere. Hence, $CO_2$ capture has become an emerging field via the implementation of developing research strategies.

Among the $CO_2$ capture materials, MOFs depict a promising interest with their high selectivity for $CO_2$, high pore volume, stability across multiple cycles, easy synthesis on a large scale, and high potential due to modifiability. However, further attention is required on MOF as a $CO_2$ adsorption material due to its particulate nature and low mechanical strength.



PPC & PETROMAT SYMPOSIUM 2025

The polymers have been emerging as a principal matrix material to address the above limitation. $CO_2$ capture materials are immobilized in the polymer matrix, acting as a scaffold to increase mechanical strength while limiting the accumulation of particulate matter in the environment. Polyethyleneimine, polyacrylonitrile, nylon, and cellulose have been exhibiting properties of a matrix material. Nitrogen-containing polymers promote increased $CO_2$ capture, while cellulose ensures promising properties such as biodegradability, post-modifiability, extensive availability, and non-toxicity.
The primary aim of this research is to investigate the $CO_2$ adsorption ability of MIL-125 immobilized bacterial cellulose (BC) aerogel (MIL-125@BC) as a $CO_2$ adsorbent material.

## EXPERIMENTAL

*A. Materials*
Titanium butoxide (MW=340.32 g/mol, Assay= 99%, Sigma Aldrich) (TBOT), Benzene 1,4-dicarboxylic acid ($H_2BDC$) (MW=166.13 g/mol, Assay= 98%, Sigma Aldrich), Methanol (≥99.0%, RCL Labscan), DMF (99.8%, RCL Labscan), DI water. All the chemicals were used as received without any purification.

*B. Procedure*

*1) Synthesis of BC aerogel*

1.00 g of BC was mixed with 10.00 ml of deionized water and stirred for 5 minutes using vortex mixing followed by sonication for 30 minutes in an ice bath. The temperature was controlled between 30 °C- 50°C. Then the resulting was transferred into 1 $cm^3$ molds and frozen for 24 hours at -40 °C. After, samples were freeze-dried at -54 °C for 48 hours. Finally, the samples were stored and characterized for future modifications (Gupta et al., 2018).

*2) Synthesis of MIL 125*

18.00 mmol of $H_2BDC$ was dissolved in 54.00 ml of DMF and 4.50 mmol of TBOT was dissolved in 6.00 ml of methanol for 30 minutes separately. Then the titanium solution was transferred to the $H_2BDC$ solution at the ambient temperature followed by stirring for 30 minutes. Next, the mixture was refluxed at 130 °C for 48 hours. Finally, the precipitation was separated by centrifugation and washed with DMF twice, followed by methanol to remove unreacted titanium and organic linkers. The resultant white powder was dried at 80°C for 24 hours and stored for further characterization (Sun et al., 2024).

*3) Synthesis of MIL 125@BC composite*

14.40 mmol of $H_2BDC$ was dissolved in 32.00 ml of DMF and 3.60 mmol of TBOT was dissolved in 4.8 ml of methanol for 30 minutes separately. Then the titanium solution was transferred to the $H_2BDC$ solution followed by stirring for 15 minutes. Concurrently, the 0.20 g of cellulose was introduced into the solution and stirred for 15 minutes. Next, the mixture was refluxed at 130 °C for 48 hours. The precipitation was separated by centrifugation and washed with DMF followed by methanol Finally, the precipitation was washed with DI water to remove the methanol. Then the resulting was mixed with 10.00 ml of DI water, transferred into 1 $cm^3$ molds, and frozen for 24 hours at -40 °C. After, samples



PPC & PETROMAT SYMPOSIUM 2025

were freeze-dried at -54 °C for 48 hours. Finally, the samples are stored and characterized for future modifications.

*C. Characterization*

The BC, MIL-125, and MIL-125@BC were characterized using Thermo Scientific Nicolet iS5 (FTIR) equipped with ATR iD 7 mode with 256 scans. The Rigaku Smart Lab X-ray diffractometer with Cu-Kα radiation was used to investigate the structure of materials. The diffraction was measured from 0° to 50° step degree of 0.01° per 25s. X-ray diffraction (XRD) was performed by Rigaku Ultima IV (Japan) with an X-ray tube rating 40 KV and 40 mA having CuKα radiation (λ = 0.154 nm). The morphology of the material was investigated using a Field Emission Electron Microscope (FE-SEM). The $CO_2$ adsorption capacity of BC, MIL-125, and MIL-125@BC were analyzed by the $CO_2$ adsorption isotherm using Brunauer−Emmett−Teller (BET) utilizing a three-station specific surface area analyzer. $CO_2$ adsorption−desorption was measured at 273 K. The samples were dried at 80°C for 72 hours before each characterization.

## RESULTS AND DISCUSSION

The in-situ fabrication of MIL-125 on BC fibers at 130 °C followed by freeze-drying was a promising method to enhance the mechanical stability of MIL-125 contributing cellulose as a scaffold. The cellulose aerogel exhibits a density of 0.0134 g/cm$^3$ while MIL-125@BC resulted in a density of 0.1373 g/cm$^3$. The scaffold was successfully proved by XRD, FTIR, and FE-SEM.

Figure 1 The BC aerogel (a), MIL-125@BC composite (b), MIL-125 (c)

*A. XRD analysis*

As shown in Figure 2a, the XRD pattern of BC displayed characteristic diffraction peaks at 14.5°, 16.8°, and 22.8°, corresponding to a crystallinity index of 79.28% and an average crystallite size of 44.88 nm. In contrast, the MIL-125 powder exhibited high-intensity diffraction peaks at 6.8°, 9.5°, 9.7°, 11.6°, 14.9°, 15.4°, 16.6°, 17.9°, 18.0°, and 19.5°, indicative of a well-crystallized framework with a calculated crystallinity of approximately 68% (Anwar et al., 2021; Qiao et al., 2021). The MIL-125@BC composite exhibited an XRD pattern closely resembling that of pure MIL-125, albeit with reduced peak intensities. Notably, the characteristic BC peaks were absent, suggesting that the BC matrix was effectively coated by MIL-125, and further confirming the successful in-situ synthesis and structural integration of the MOF on the cellulose scaffold.



PROCEEDINGS OF PPC & PETROMAT SYMPOSIUM 2025

*B. FTIR analysis*

Figure 2b presents the FTIR spectra of BC, MIL-125, and MIL-125@BC. Pristine BC exhibited broad O–H stretching bands around 3330 $cm^{-1}$, along with asymmetric and symmetric C–H stretching at 2914 $cm^{-1}$ and 2848 $cm^{-1}$, respectively, which are characteristic of cellulose (Abol-Fotouh et al., 2020). In the spectrum of MIL-125@BC, these features were significantly diminished or absent, indicating the successful deposition of MIL-125 on the BC matrix and the reduced accessibility of hydroxyl groups. Additional BC-specific bands, C–O stretching at C3 and C6 (1054 $cm^{-1}$), C–C stretching at C6 (1034 $cm^{-1}$), C–H bending (1356 $cm^{-1}$), β-1,4-glycosidic linkage (807 $cm^{-1}$), and C–O–H out-of-plane bending (659 $cm^{-1}$), also exhibited reduced intensities in the MIL-125@BC spectrum. MIL-125 exhibited prominent peaks at 1651 $cm^{-1}$ (C=O stretching), 1502 $cm^{-1}$ (C=C stretching), 1378 $cm^{-1}$ (O–C–O bonding), and 744 $cm^{-1}$ (Ti–O stretching), consistent with previously reported data (Hao et al., 2022). These bands were preserved in MIL-125@BC, supporting the successful in-situ formation of MIL-125 on the cellulose substrate.

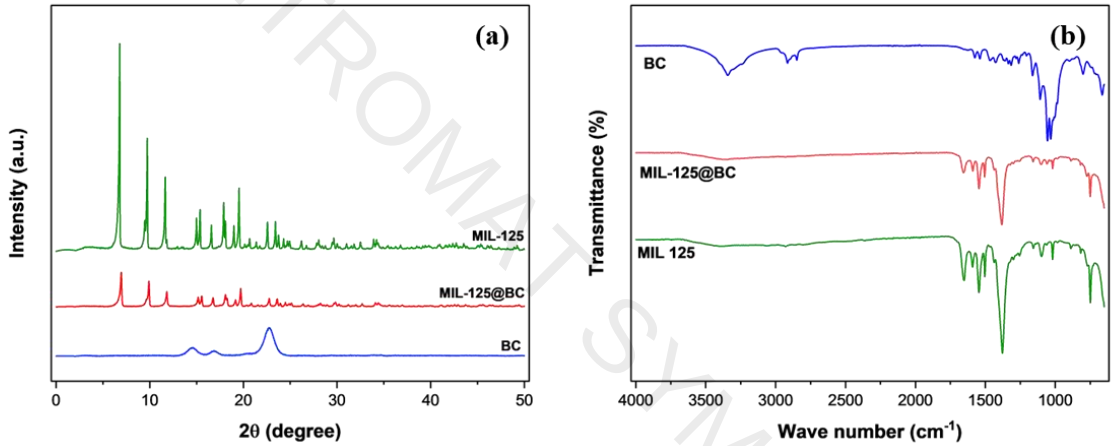


Figure 2 XRD (a) and FTIR (b) of BC aerogel, MIL-125 and MIL-125@BC composite

*C. SEM analysis*

The surface morphology of the materials was investigated using SEM, as shown in Figure 3. Figure 3a reveals the fibrillar network of cellulose within the aerogel, highlighting extensive fiber entanglement and partial agglomeration. This nanofibrous structure provides an effective scaffold for MOF integration. Figure 3b illustrates the morphology of MIL-125 synthesized in situ on the BC matrix. The MIL-125 particles exhibit a columnar structure, consistent with previous reports (Qiao et al., 2021). Notably, the particle size of MIL-125 appears smaller when grown on BC fibers, suggesting that the presence of the cellulose matrix during synthesis influences nucleation and growth, leading to greater dispersion and reduced aggregation of MIL-125 crystals.

PPC & PETROMAT SYMPOSIUM 2025

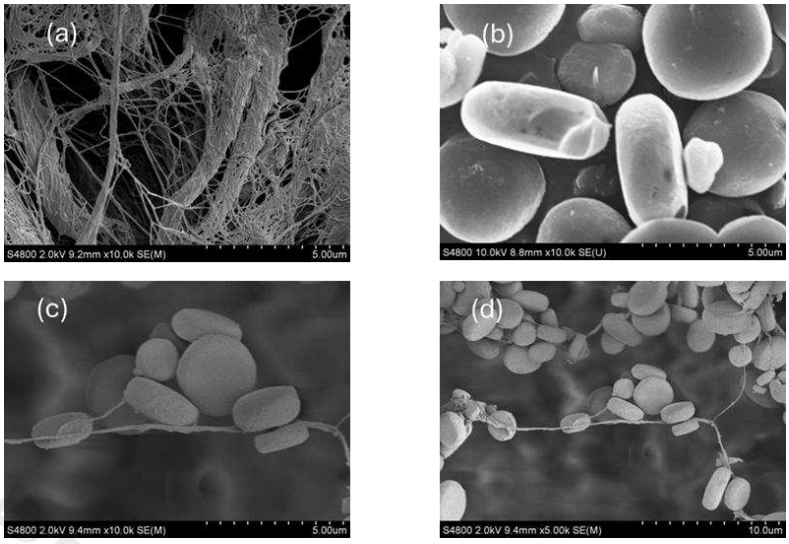


Figure 3 The FE-SEM images of (a) BC aerogel, (b) MIL-125, (c) MIL-125@BC composite with 10.0k magnification, (d) MIL-125@BC with 5.0k magnification.

*D. $CO_2$ adsorption*

The $CO_2$ adsorption capacities of BC, pristine MIL-125, and the MIL-125@BC composite were evaluated at 273 K. Pristine BC exhibited a low $CO_2$ uptake of 0.24 mmol/g, consistent with its limited surface area and non-porous nature. In contrast, MIL-125 demonstrated a significantly higher $CO_2$ adsorption capacity of 3.89 mmol/g, attributed to its intrinsic microporosity and large surface area. For the MIL-125@BC composite, the $CO_2$ uptake was measured at 3.21 mmol/g. While this value is slightly lower than that of pristine MIL-125, it remains substantially higher than that of BC alone, confirming the functional contribution of the MOF. The observed reduction in $CO_2$ capacity can be ascribed to the decrease in crystallinity and surface area of MIL-125 upon incorporation into the BC matrix, as evidenced by the XRD analysis in Figure 2a. These structural changes likely reduced the number of accessible active sites for $CO_2$ adsorption(Ghorbani, Ghahramaninezhad, & Shahrak, 2020).

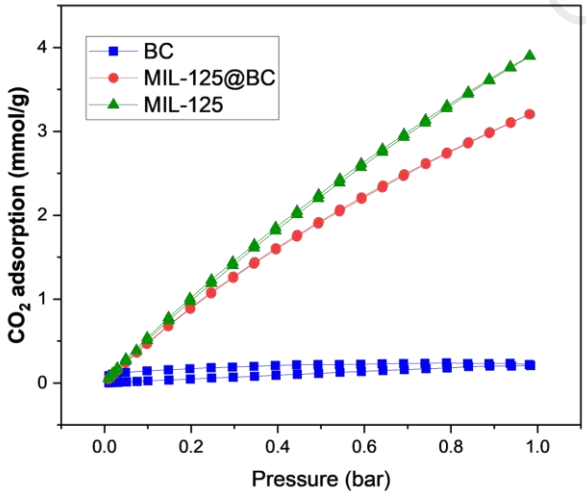


Figure 4 The $CO_2$ adsorption of BC, MIL 125, and MIL-125@BC composite.

## CONCLUSION

The successful synthesis of MIL-125, BC aerogel, and the MIL-125@BC composite aerogel was confirmed by FTIR, XRD, and FE-SEM analyses. Although the incorporation of BC led to a moderate reduction in $CO_2$ adsorption capacity compared to pristine MIL-125, the composite retained significant adsorption performance while benefiting from enhanced structural stability. BC served as an effective scaffold, providing mechanical reinforcement and facilitating the uniform dispersion of MIL-125 particles within the aerogel matrix. These findings demonstrate that BC is a promising matrix material for fabricating MOF-based composite aerogels, enabling structural robustness without compromising adsorption efficiency. The in-situ integration of MIL-125 onto the BC network presents a viable approach for the development of durable and functional materials for gas adsorption applications.

## ACKNOWLEDGEMENTS

The author would like to acknowledge The Petroleum and Petrochemical College, Chulalongkorn University, Bangkok, Thailand, and ASEAN and NON-ASEAN graduate scholarship program, Chulalongkorn University, Bangkok, Thailand.

## REFERENCES

Abol-Fotouh, D., Hassan, M., Shokry, H., Roig, A., Azab, M., & Kashyout, A. (2020). Bacterial nanocellulose from agro-industrial wastes: low-cost and enhanced production by Komagataeibacter saccharivorans MD1. Sci Rep 10: 3491. In.

Anwar, B., Bundjali, B., Sunarya, Y., & Arcana, I. M. (2021). Properties of bacterial cellulose and its nanocrystalline obtained from pineapple peel waste juice. *Fibers and Polymers*, *22*, 1228-1236.

Ekwurzel, B., Boneham, J., Dalton, M. W., Heede, R., Mera, R. J., Allen, M. R., & Frumhoff, P. C. (2017). The rise in global atmospheric CO2, surface temperature, and sea level from emissions traced to major carbon producers. *Climatic Change*, *144*(4), 579-590.

Ghorbani, H., Ghahramaninezhad, M., & Shahrak, M. N. (2020). The effect of organic and ionic liquid solvents on structure crystallinity and crystallite size of ZIF-8 for CO2 uptake. *Journal of Solid State Chemistry*, *289*, 121512.

Gupta, P., Singh, B., Agrawal, A. K., & Maji, P. K. (2018). Low density and high strength nanofibrillated cellulose aerogel for thermal insulation application. *Materials & Design*, *158*, 224-236.

Hao, D., Fu, B., Zhou, J., & Liu, J. (2022). Efficient particulate matter removal by metal-organic frameworks encapsulated in cellulose/chitosan foams. *Separation and Purification Technology*, *294*, 120927.

Liu, Z., Deng, Z., Davis, S. J., & Ciais, P. (2024). Global carbon emissions in 2023. *Nature Reviews Earth & Environment*, *5*(4), 253-254.

Obobisa, E. S. (2022). Achieving 1.5 C and net-zero emissions target: The role of renewable energy and financial development. *Renewable Energy*, *188*, 967-985.

Qiao, X., Liu, Y., Yang, Y., Wang, H., Ma, J., Wang, D., Gao, N., Li, L., Liu, W., & Wang, H. (2021). Synthesis optimization of metal-organic frameworks MIL-125 and its adsorption separation on C8 aromatics measured by pulse test and simulation calculation. *Journal of Solid State Chemistry*, *296*, 121956.



PPC & PETROMAT SYMPOSIUM 2025

Sun, Y., Ji, H., Sun, Y., Zhang, G., Zhou, H., Cao, S., Liu, S., Zhang, L., Li, W., & Zhu, X. (2024). Synergistic effect of oxygen vacancy and high porosity of nano MIL-125 (Ti) for enhanced photocatalytic nitrogen fixation. *Angewandte Chemie International Edition*, *63*(3), e202316973.

PPC & PETROMAT SYMPOSIUM 2025

# A Study on Biodiesel Production with Pretreated Anion Exchange Membrane as a Catalyst in a Batch Reactor

*Kittiporn Laita*[a], *Palang Bumroongsakulsawat*[*a]

[a]Center of Excellence in Catalysis and Catalytic Engineering, Chulalongkorn University, Bangkok, Thailand

Keywords: Biodiesel, Transesterification, Anion-exchange membrane, Palm oil

**ABSTRACT:**

Heterogeneous base catalysts are gaining more attention in biodiesel production field due to ease of separation from transesterification product mixtures and interesting catalytic stability which not only simplify the product purification systems but also reduce both operating costs and waste generated. Anion exchange membrane (AEM) shares similarities with anion exchange resins in terms of structure which have been proven to catalyze the transesterification reaction. Therefore, AEM is expected to be able to catalyze the transesterification reaction with the same mechanism as the resins. This study aims to explore the catalytic potential of AEM pretreated to adsorb methoxide for biodiesel synthesis. The reaction was conducted in a batch setup by mixing palm oil, methanol and the pretreated AEM under controlled temperature. Key operating parameters such as oil-to-methanol molar ratio and reaction time were varied to study their influence on biodiesel yields. Additionally, the reusability of AEM over multiple cycles were assessed. Following the biodiesel testing standard EN14103, preliminary results confirmed the presence of fatty acid methyl ester (FAME) in the final mixture, demonstrating the potential of AEM as a heterogeneous catalyst for biodiesel production.

***Palang.B@chula.ac.th**

## INTRODUCTION

Biodiesel is a renewable and biodegradable liquid fuel produced via the transesterification of triglycerides with short-chain alcohols, typically methanol. The fuel offers several advantages over conventional fossil diesel, including reduced greenhouse gas emissions and compatibility with existing diesel engines. However, the conventional process often relies on homogeneous alkaline catalysts, such as sodium or potassium hydroxide, which lead to not only complications in product purification and catalyst recovery, but also wastewater generation and more importantly unrecyclable salts. [1].

To overcome these limitations, heterogeneous catalysts have been investigated as a cleaner and more reusable alternative due to ease of separating the catalysts from biodiesel product. A possible method involves the use of anion-exchange membranes (AEMs), which contain fixed cationic sites, such as quaternary ammonium cations, capable of exchanging anions like hydroxide or methoxide. Due to structural similarity to anion-exchange resins, this type of

PPC & PETROMAT SYMPOSIUM 2025

membranes is hypothesized to have the potential to act as heterogeneous basic catalysts under mild conditions. Shibasaki-Kitakawa et al. proposed a mechanism of anion-exchange resins-catalyzed transesterification reaction as followed 1) free methanol react with adsorbed hydroxides at the fixed positive sites to form adsorbed methoxides and protons, 2) the adsorbed methoxides attack triglycerides resulting in fatty acid methyl ester (FAME) produced and negatively charge diglycerides, 3) the produced diglycerides deprotonate the sites and further react with another adsorbed methoxide forming another FAME [2].

This work investigates the catalytic potential of anion-exchange membranes for biodiesel production via transesterification of palm oil with methanol in a conventional stirred batch reactor. The objective is to evaluate whether AEMs can effectively catalyze the reaction without addition of homogeneous basic catalysts, under various oil-to-methanol molar ratios and reaction times.

## EXPERIMENTAL

### *A. Anion-exchange membrane preparation*

FUMASEP FAA PK130 anion-exchange membranes purchased from FUELCELL STORE were cut and weigh to 0.06 gram (approximately 2% of palm oil mass). The membranes were initially shipped with chloride ions as counterions, to exchange the chloride ions to methoxide ions, firstly, the AEMs were submerged into 1 M NaOH aqueous solution for 1 hour to exchange the chloride ions with hydroxide ions ($OH^-$) then each piece was carefully rinsed with deionized water to remove leftover NaOH and $Na^+$ ion, and submerged in 99.99% methanol for an hour to convert surface-bounded hydroxide ions to methoxide ions. The conversion of adsorbed hydroxide ions to surface-bounded methoxide ions are as shown by the following equations in Figure 1 [3]. The asterisk symbol means that the ions are being adsorbed to the fixed positive site of the AEMs, in this case, quarternary ammonium.

$$*Cl^- + Na^+OH^- \rightarrow *OH^- + Na^+Cl^- \quad (1)$$

$$*OH^- + CH_3OH \leftrightharpoons *CH_3O^- + H_2O \quad (2)$$

Figure 1 Equation for ion-exchanging process; (1) Exchanging adsorbed chloride ions with hydroxide ions in bulk 1 M NaOH aqueous solution, and (2) Reaction of surface-bounded hydroxide ion and free methanol resulting in adsorbed methoxide ion and free water.

### *B. Biodiesel production via catalytic transesterification in batch reactor*

The reaction was carried out in a batch reactor, stirred with a magnetic stirrer bar. A hotplate was employed to maintain the reaction temperature at approximately 64°C. An ice-cooled cold source

PPC & PETROMAT SYMPOSIUM 2025

was installed at the top of the reactor to prevent methanol losses. For each experiment, 3 grams of palm oil were used and the amount of methanol added was determined by the oil-to-methanol molar ratios of 1:20 and 1:54. The amount of AEMs were kept at 2% of palm oil mass for every experiment, as stated above. The reaction times were controlled at 1 and 2 hours. After the desired reaction time was reached, the sample was collected and heated to approximately 70°C for 2 hours to evaporate the remaining methanol.

*C. Biodiesel yield analysis with gas chromatography*

According to the EN14103 biodiesel testing standard, 250 mg of oily phase after methanol evaporation was collected and mixed with 50 mg of internal standard (methyl heptadecanoate) and were diluted with n-heptane to reach a final volume of 5 mL. The mixture was carefully stirred and transferred to a 1.5 mL vial. The gas chromatography system equipped with flame ionization detector (GC-FID) was programmed to inject 1 µL of the sample into the ZB-5HT column. The GC-FID settings are as shown in Table 1.

Table 1 Gas chromatography with flame ionization detector setting for the biodiesel analysis in this work.

| | |
|---|---|
| Column type | ZB-5HT |
| Injection volume | 1 µL |
| Injection temperature | 250 °C |
| Carrier gas | Helium |
| Column temperature | 150 °C |
| Detector temperature | 250 °C |

After data acquisition was completed, FAME yield was calculated using the following equation.

$$\%FAME\ yield = \left[\frac{A_{FAME}}{A_{std}} \times \frac{m_{std}}{m_{sample}}\right] \times 100\%$$

$A_{FAME}$ and $A_{std}$ are the total areas under FAME and the internal standard peaks. $m_{sample}$ and $m_{std}$ are the mass of the added oily phase sample and mass of the internal standard added to the mixture, respectively.

*D. Experimental design*

To study the effects of reaction time and oil-to-methanol molar ratio on biodiesel yield, a two-levels two-factors experimental design with one repetition table was constructed and shown in Table 2. The first independent variable was reaction time, and the second independent variable

PPC & PETROMAT SYMPOSIUM 2025

was oil-to-methanol molar ratio while FAME yield was the only response. The results were analysed statistically using linear regression and ANOVA in RStudio software.

Table 2 $2^2$ factorial design table for this work.

| **$2^2$ factors design of experiment** | | **Oil-to-methanol molar ratio** | |
|---|---|---|---|
| | | 1:20 | 1:54 |
| **Reaction time** | 1 hour | %FAME yield | %FAME yield |
| | 2 hours | %FAME yield | %FAME yield |

## RESULTS AND DISCUSSION

*A. Anion-exchange membrane-catalyzed transesterification reaction*

A blank control experiment conducted without presence of the AEMs under 1:54 oil-to-methanol molar ratio and 2 hours reaction time revealed negligible biodiesel formation. This confirmed that the AEM was responsible for catalyzing the transesterification reaction. A 2x2 factorial design with one repetition was employed to investigate the effects of reaction time and oil-to-methanol molar ratio on biodiesel yield, a total of eight runs were completed. The results are shown in Table 3. One outlier was detected using Grubb's test (with "outliers" library in RStudio) and was excluded from the analysis (1:54 oil-to-methanol molar ratio, 1 hour reaction time with 19.01% yield). The bar chart shown in Figure *2* illustrates average biodiesel yield obtained with 2 levels of oil-to-methanol molar ratio (ie. 1:54 and 1:20) and 2 levels of reaction time (1 hour and 2 hours) ranging from 3.03% to 6.32%. Statistical analysis indicated that neither reaction time (p-value: 0.217), oil-to-methanol molar ratio (p-value: 0.947) or interaction between both factors (p-value: 0.707) were not statistically significant at 95% confidence level within the tested factor levels. For the yield results, it seems possible that these relatively low yields are due to immiscibility between palm oil and methanol, promoting mass transfer resistance hence reducing effective contact of the reactants with the active sites over the AEMs surfaces. In terms of slightly increased yields observed at a longer reaction time, a possible explanation for this might be from methanol swelling of the AEMs, which creates free volume and facilitates diffusion of the reactants to the internal active sites [4].

PPC & PETROMAT SYMPOSIUM 2025

Table 3 Results of $2^2$ factorial design

| $2^2$ factorial design of experiment | | Oil-to-methanol molar ratio | | | |
|---|---|---|---|---|---|
| | | 1:20 (1) | 1:20 (2) | 1:54 (1) | 1:54 (2) |
| **Reaction time** | 1 hour | 3.03% | 3.07% | 3.64% | 19.17% |
| | 2 hours | 4.98% | 3.48% | 4.20% | 6.32% |

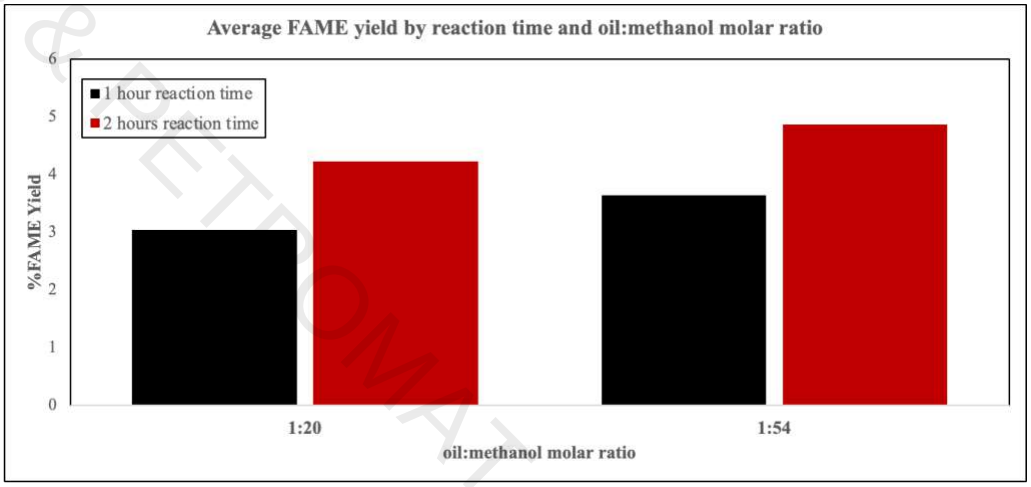


Figure 2 Biodiesel yield by reaction time and oil-to-methanol molar ratio.

*B. Catalytic stability*

After a 2-hour reaction time, the used AEMs pieces were collected and shown in Figure 3. The yellowish particulate component of the AEMs was broken apart, for some revealing the polymeric backbone of the membrane as white-long straight line. This indicated that the AEMs, particularly FUMASEP FAA PK130, were disintegrating as the reaction progress. As the root cause remains unclear, it might have resulted from loss of mechanical strength of the AEMs due to methanol swelling and mechanical stresses generated from agitation. Future studies should explore alternative membrane materials with enhanced methanol resistance and mechanical strength for improved long-term stability or alternative reactor design that causes less mechanical stress to the AEMs, for example, flow reactor.

PPC & PETROMAT SYMPOSIUM 2025

Figure 3 Photographs of the AEMs after 2-hour transesterification, showing signs of disintegration.

## CONCLUSIONS

This study confirms that anion-exchange membranes have the ability to catalyze biodiesel production via catalytic transesterification in a conventional stirred batch reactor. Although the biodiesel yields were small and statistically insignificant across tested factors and levels, the catalytic role of AEMs was verified. Future work should investigate effects of longer reaction time, improved membrane treatment methods, addition of co-solvent to improve palm oil and methanol miscibility, higher mechanical strength membranes, and flow reactor design that may causes lower mechanical stresses to the AEMs to improve biodiesel production performance.

## ACKNOWLEDGEMENT

The author gratefully acknowledges the guidance and support of Assoc. Prof. Palang Bumroongsakulsawat, who provided guidance and inspiration as the research advisor throughout this study. Special thanks are extended to the M.A.C. team for their kindness and ongoing support.

## REFERENCES

1. Prasongtham, N., *Separation of organic and inorganic compounds in solid waste obtained from biodiesel production process*. 2015, Chulalongkorn University.
2. Shibasaki-Kitakawa, N., et al., *Biodiesel production using anionic ion-exchange resin as heterogeneous catalyst.* Bioresource Technology, 2007. **98**(2): p. 416-421.
3. Jamal, Y., A. Rabie, and B. Boulanger, *Determination of methanolysis rate constants for low and high fatty acid oils using heterogeneous surface reaction kinetic models.* Reaction Kinetics, Mechanisms and Catalysis, 2015. **vol (114)**: p. 63-74.
4. Rios, L.A., P.P. Weckes, H. Schuster, and W.F. Hoelderich, *Resin catalyzed alcoholysis of epoxidized fatty esters: Effect of the alcohol and the resin structures.* Applied Catalysis A: General, 2005. **284**(1–2): p. 155-161.

PPC & PETROMAT SYMPOSIUM 2025

# THE EFFECT OF CALCIUM TO ALUMINUM RATIO IN LAYERED DOUBLE HYDROXIDES FOR $CO_2$ ADSORPTION

*Sitinjak Ebennezer[a], Bhumin Than-Ardna[a,b], Boonyarach Kitiyanan*[,a,b]*

[a] The Petroleum and Petrochemical College, Chulalongkorn University, Bangkok, Thailand
[b] Center of Excellence on Petrochemical and Materials Technology, Bangkok, Thailand

Keywords : Layered Double Hydroxide, $CO_2$ Adsorption

## ABSTRACT

Calcium layered double hydroxides (Ca-LDHs) have emerged as promising materials for $CO_2$ capture due to their high density of alkaline adsorption sites. In this study, Ca-LDHs with different molar ratios of calcium (Ca) to Aluminum (Al), 1:1, 2:1, and 3:1, were synthesized via co-precipitation. The Ca/Al ratio with 3:1 sample exhibited the highest crystallinity, with a crystal size of 52.6 nm and a D-spacing of 0.78 nm, based on X-ray diffraction (XRD). Field-emission scanning electron microscopy (FE-SEM) revealed well-defined plate-like particles and energy-dispersive X-ray spectroscopy (EDX) confirmed a high calcium content of 23 wt% in the 3:1 ratio sample. Fourier-transform infrared spectroscopy (FTIR) indicated subtle shifts in O–H and H–O–H stretching bands as the calcium content increased, indicating changes in the hydrogen bonds between the layers. Of all synthesized samples, the Ca/Al ratio with 3:1 LDH delivered the highest $CO_2$ uptake (0.69 mmol/g at 0 °C and 1 atm), which is attributed to its superior crystallinity and optimal distribution of basic sites. Moreover, temperature-programmed desorption (TPD-$CO_2$) analysis and Brunauer-Emmett-Teller (BET) measurements were conducted to understand the basicity content and surface area. This enhanced $CO_2$ adsorption efficiency highlights the potential of Ca-LDHs for practical $CO_2$ capture applications

***boonyarach.k@chula.ac.th**

## INTRODUCTION

The rapid increase in atmospheric carbon dioxide ($CO_2$) levels due to anthropogenic activities is a major contributor to climate change, leading to global warming and environmental degradation. Addressing this issue requires effective carbon capture technologies that can mitigate $CO_2$ emissions from industrial sources such as power plants, cement production, and other $CO_2$-intensive processes.

Layered double hydroxides (LDHs) have emerged as promising materials for $CO_2$ capture due to their unique structural properties and high surface area. LDHs consist of positively charged metal hydroxide layers intercalated with anions, which can be tailored to enhance their $CO_2$ adsorption capacity. Among various types of LDHs, calcium-based LDHs (Ca-LDHs) have shown superior performance in $CO_2$ capture due to their higher surface basicity and favourable interaction with $CO_2$ molecules. Calcium-based LDHs are particularly advantageous for several reasons. Firstly, calcium is abundant and cost-effective, making Ca-LDHs economically viable for large-scale applications (Zheng et al.,

2023). Secondly, Ca-LDHs exhibit strong basic site (Narayanappa & Kamath, 2019), which facilitates the adsorption of $CO_2$ through acid-base interactions. Additionally, the presence of calcium in the LDH structure enhances the thermal stability and regeneration efficiency of the material, allowing for effective cyclic $CO_2$ capture and release.

The interaction between Ca-LDHs and $CO_2$ is expected to involve the formation of carbonate species within the interlayer regions and on the surface of the LDH particles. This interaction is influenced by the ratio of calcium to aluminum in the LDH structure, which affects the material's crystallinity, surface area, and overall adsorption capacity. Studying the Ca:Al ratio is crucial to optimizing the synthesis and performance of Ca-LDHs for $CO_2$ capture, as it determines the balance between structural stability and adsorption efficiency.

In this research, we investigate the synthesis, characterization, and $CO_2$ capture performance of calcium-based LDHs with varying Ca:Al ratios. By understanding the impact of the Ca:Al ratio on the material's properties and interactions with $CO_2$, we aim to develop an efficient and sustainable carbon capture technology that can contribute to mitigating climate change.

## EXPERIMENTAL

*A. Layered Double Hydroxide Synthesis*

Calcium–aluminum chloride layered double hydroxide (CaAlCl LDH) was synthesized via a coprecipitation method (Benes et al., 2023). First, three aqueous solutions of calcium and aluminum were prepared in deionized water and designated as Solution A1, A2, and A3, with varying calcium concentrations and a constant aluminum concentration: A1 with Ca = 0.005 mol, A2 with Ca = 0.01 mol, and A3 with Ca = 0.015 mol, while Al was kept constant at 0.005 mol in all solutions. Separately, Solution B was prepared by dissolving 0.45 M sodium hydroxide (NaOH) and 0.4 M sodium chloride (NaCl) in 75 mL of a deionized water and ethanol mixture (3:1 v/v). Solution B was preheated to 80 °C. Each Solution A was then added dropwise to the preheated Solution B under continuous stirring. The resulting mixtures were maintained at 80 °C in flasks equipped with reflux condensers and nitrogen inlets. After aging for 1 hour at the reaction temperature, the resulting white dispersions were filtered, washed thoroughly with ethanol until a neutral pH was achieved, and dried at 80 °C for 12 hours. The final products were obtained as white powders of CaAlCl LDH.

*B. Characterization*

Powder X-ray Diffraction (XRD spectra were recorded on the Rigaku, Smart Lab,X-ray Diffractometer with Nickel (Ni) filtered Cu Kα radiation (λ=0.156406 nm) at a current of 30 mA and voltage of 40 kV. The sample was recorded in the 2θ=0-50º with the scanning step 0.02º per 25 s. The crystal phase was identified using the QUALX 2.0 program. Infra-red (IR) Spectra were obtained on FT-IR Thermo Scientific, Nicolet iS5. The IR spectra of samples were scanned at a wavenumber range of 650 to 4000 $cm^{-1}$ with resolution 4.0 $cm^{-1}$, and the number scans was 64 s. The image of elemental analyses of samples were obtained on the field emission scanning electron microscopy energy dispersive spectroscopy (FE-SEM EDX) Hitachi/S-4800. Nitrogen adsorption–desorption isotherms were measured at 77 K using a Quantachrome Autosorb-iQ-MP analyzer to determine specific surface area, pore size, and pore volume. The specific surface area was determined by calculating the area of desorbing $N_2$ using the multipoint Brunauer-Emmet-Teller (BET) equation. The basic properties of the samples were investigated via Micromeritics. Additionally, $CO_2$

PPC & PETROMAT SYMPOSIUM 2025

adsorption capacity was measure using the same BET instrument under static conditions at 1 atm and 0 ºC.

## RESULTS AND DISCUSSION

Powder X-ray diffraction (XRD) was employed to analyze the crystalline structure of the layered double hydroxides (LDHs). Figure 1A shows the characteristic diffraction patterns of samples A1, A2, and A3. The diffraction peaks observed for all samples correspond well with the standard hydrocalumite phase, as confirmed by comparison with the reference pattern (PDF No. 00-900-9354). A summary of the peak positions and corresponding assignments is provided in Table 1

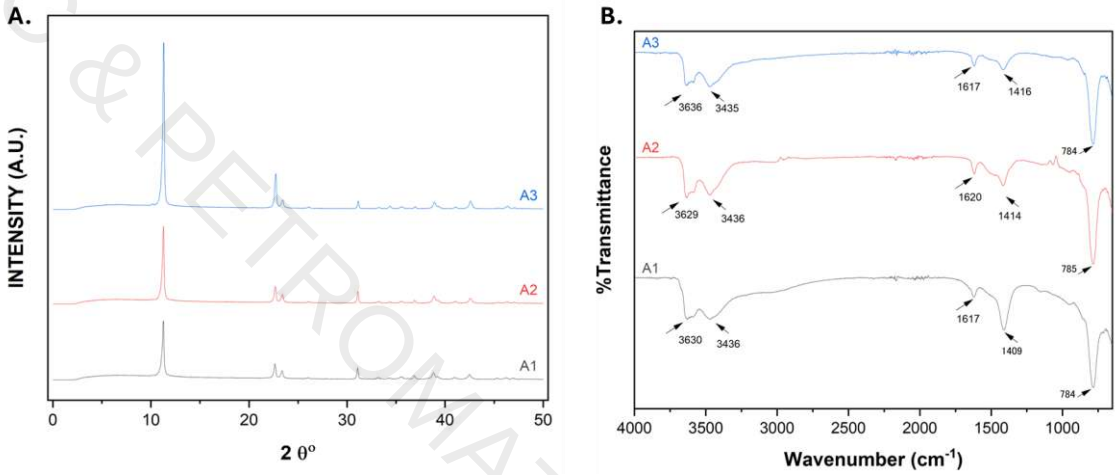


Figure 1. A. X-Ray diffraction of Calcium alumina chloride LDH, B. IR spectra of Calcium-aluminum Chloride Layered Double Hydroxide

Table 1. XRD Analysis of Samples A1–A3: Peak Positions, Crystal Sizes, and D-Spacings

| Sample | Peak | Crystal size (nm) | D-spacing (nm) |
|---|---|---|---|
| A1 | 11.24 | 52.6 | 0.78 |
| A2 | 11.3 | 36.9 | 0.78 |
| A3 | 11.28 | 57.6 | 0.78 |

Table 1. Following data and Calculation of crystal size and D-Spacing by Scherrer equation

XRD analysis reveals that increasing the calcium content in the LDH structure significantly influences its crystallographic features. A progressive increase in peak intensity indicates enhanced crystallinity and improved long-range ordering of the layered structure. A slight shift in peak positions is also observed, suggesting subtle changes in the lattice parameters, possibly due to variations in layer charge density or the ionic radius effect. The crystallite size varies across the samples, with the largest observed in A3, implying that higher Ca content may promote crystal growth. Despite these structural changes, the interlayer spacing (d-spacing) remains constant at 0.78 nm, indicating that the interlayer architecture is stable and unaffected by changes in the Ca/Al molar ratio.

PPC & PETROMAT SYMPOSIUM 2025

Figure 1B presents the IR spectra of the LDH samples. All spectra exhibit a broad absorption band in the range of 3300–3700 cm-1, corresponding to the stretching vibrations of lattice water and –OH groups, characteristic of CaAlCl-type LDHs. A distinct peak observed between 1400–1416 $cm^{-1}$ is attributed to the stretching vibrations of intercalated carbonate species, suggesting the presence of minor carbonate contamination. Additionally, a peak in the 1600–1621 $cm^{-1}$ region is assigned to the H–O–H bending vibrations of interlayer water molecules. The stretching and deformation vibrations of M–OH (metal–hydroxide) bonds are evident as peaks in the 780–785 $cm^{-1}$ region.

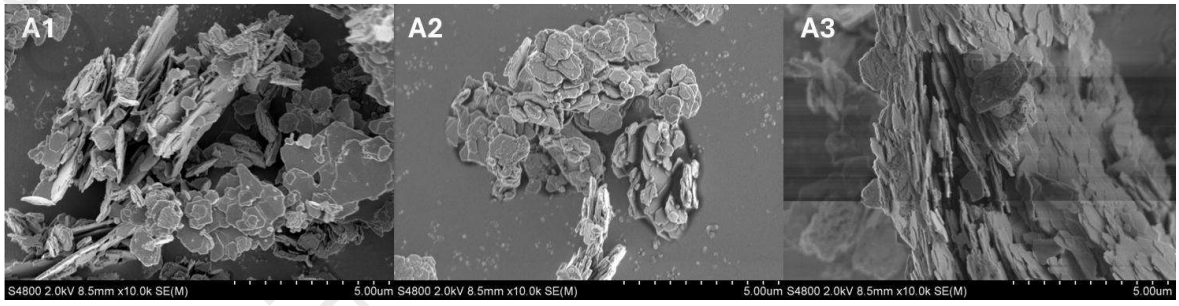


Figure 2 Morphology of LDH

The morphological evolution of LDH samples with varying Ca:Al molar ratios (A1 = 1:1, A2 = 2:1, A3 = 3:1) is evident from SEM analysis (Figure 2). Sample A1 (Ca:Al = 1:1) displays a compact, uniform platelet-like morphology, indicative of well-formed layered double hydroxides with high crystallinity. As the Ca:Al ratio increases to 2:1 in Sample A2, the structure becomes more disordered, characterized by loosely packed platelets and signs of agglomeration, suggesting that excess calcium disrupts the regular stacking of LDH layers. In Sample A3 (3:1), the morphology appears increasingly irregular, with loosely arranged and aggregated particles, implying that a high calcium content hinders the formation of well-defined LDH platelets. These observations highlight the critical role of the Ca:Al ratio in governing the structural integrity and self-assembly behavior of LDH materials.

Table 2. EDX analysis result for the composition of LDH

| Element | Weight(%) | | | Atomic(%) | | |
|---|---|---|---|---|---|---|
| | A1 | A2 | A3 | A1 | A2 | A3 |
| Ca | 17.94 | 19.74 | 23.02 | 8.79 | 9.83 | 11.93 |
| Al | 8.48 | 9.21 | 9.23 | 6.16 | 6.81 | 7.24 |
| Cl | 7.73 | 7.7 | 9.73 | 4.28 | 4.34 | 5.65 |
| O | 65.85 | 63.34 | 57.92 | 0.77 | 79.02 | 75.18 |

The EDX analysis of the LDH (Table 2) confirms the presence of Ca, Al, Cl, and O across the three analyzed regions (A1–A3). Calcium content shows a progressive increase from 17.94% to 23.02% by weight, suggesting localized enrichment consistent with the calcium-rich phases identified in the XRD patterns. Aluminium content varies moderately, supporting the presence of alumina-based components, while chlorine is consistently detected, implying possible chloride incorporation within the structure or surface

adsorption. Oxygen is the dominant element, comprising over 61% by weight, which is consistent with the presence of oxides and hydroxides and aligns with FTIR evidence of metal–oxygen and hydroxyl functional groups. These elemental distributions corroborate the structural and bonding information obtained from FTIR and XRD, confirming the formation of complex calcium–aluminate–oxide phases in the LDH samples.

Table 3. Surface area analysis, basicity and $CO_2$ adsorption of LDH

| Sample | SBET($m^2g^{-1}$) | Pore Size (nm) | Total pore volume ($cc^2g^{-1}$) | $CO_2$ Adsorption ($mmol.g^{-1}$) | Basicity ($mmol{\cdot}g^{-1}$) |
|---|---|---|---|---|---|
| A1 | 28.78 | 3.059 | 0.203 | 0.26 | 9.063 |
| A2 | 25.06 | 3.826 | 0.174 | 0.15 | 8.184 |
| A3 | 18.58 | 3.412 | 0.247 | 0.69 | 7.497 |

Table 3 presents the BET result, $CO_2$ adsorption capacity and Basicity. Sample A1 exhibits the highest BET surface area (28.78 $m^2/g$) but has a relatively smaller pore volume (0.203 cc/g) and pore size (3.059 nm), which may limit gas diffusion. A2 shows a slightly lower surface area (25.06 $m^2/g$) but a larger pore size (3.826 nm), though its total pore volume remains the lowest (0.174 cc/g), suggesting fewer accessible adsorption sites. In contrast, A3, despite having the lowest surface area (18.58 $m^2/g$), presents a balanced pore size (3.412 nm) and the highest total pore volume (0.247 cc/g). This combination enhances gas accessibility and storage, explaining A3's superior $CO_2$ adsorption capacity.

The superior $CO_2$ adsorption performance of the A3 sample (Ca:Al = 3:1) in CaAlCl-LDHs, despite its lowest BET surface area and total basicity, can be attributed to the presence of fewer but stronger and more accessible basic sites, as well as a well-developed pore architecture. This is supported by Pérez-Barrado et al. (2015), who demonstrated that CaAl-based LDHs possess stronger basic sites than MgAl analogs, and that these sites are more catalytically active even at lower total basicity. Furthermore, You et al. (2024) emphasized that the acid–base properties of LDHs are highly tunable through metal composition, where increasing divalent cation content (e.g., $Ca^{2+}$) enhances the strength of Lewis and Brønsted base sites while reducing overall acidity. These strong basic sites, particularly Ca–OH and CaO species, are known to facilitate $CO_2$ chemisorption, especially under humid conditions (Zheng et al., 2023). Additionally, the high pore volume and moderate pore size of A3 likely improved gas diffusion and accessibility to active sites, aligning with findings by Megías-Sayago et al. (2019), who reported that pore volume and structure can be factors in determining the efficiency of $CO_2$ capture in LDH-based materials. Together, these factors explain the counterintuitive yet enhanced $CO_2$ uptake observed in the A3 sample.

## CONCLUSIONS

This study successfully synthesized and characterized calcium–aluminum chloride layered double hydroxides (CaAlCl LDHs) with varying Ca:Al molar ratios (A1 = 1:1, A2 = 2:1, A3 = 3:1) to evaluate their performance in $CO_2$ Adsorption. Structural and surface analyses revealed that increasing the calcium content significantly influenced the crystallinity, morphology, and porosity of the materials. The A3 sample (Ca:Al = 3:1)

PPC & PETROMAT SYMPOSIUM 2025

exhibited the highest crystallinity and crystal size (57.6 nm), along with the largest total pore volume (0.247 cc/g), despite having the lowest BET surface area (18.58 $m^2/g$). Interestingly, A3 also demonstrated the highest $CO_2$ adsorption capacity (0.69 mmol/g), outperforming A1 and A2, which had higher surface areas but lower pore volumes and $CO_2$ uptake. Although A3 had the lowest basicity (7.497 mmol/g), its superior performance suggests that $CO_2$ capture is more strongly influenced by pore accessibility, crystallinity, and the nature of basic sites rather than their total quantity. These findings highlight the importance of optimizing the Ca to Al ratio to balance structural order, porosity, and chemical functionality. The A3 sample emerges as the most effective candidate for $CO_2$ capture, offering valuable insights into the design of LDH-based adsorbents where pore volume and site accessibility play a more critical role than surface area alone.

**ACKNOWLEDGEMENTS**

The Author would like to express to gratitude to the Scholarship Program for ASEAN and Non-ASEAN Countries Chulalongkorn University and The petroleum and Petrochemical College to fully supporting us on this research.

**REFERENCES**

Benes, H., Konefal, M., Bujok, S., Mrozek, O., Pavlova, E., Smrzova, D., & Ecorchard, P. (2023). Intercalation of Ionic Liquids into LDH Structures for Microwave-Accelerated Polymerizations. Inorg Chem, 62(36), 14694-14703. https://doi.org/10.1021/acs.inorgchem.3c02021

Megias-Sayago, C., Bingre, R., Huang, L., Lutzweiler, G., Wang, Q., & Louis, B. (2019). CO(2) Adsorption Capacities in Zeolites and Layered Double Hydroxide Materials. Front Chem, 7, 551. https://doi.org/10.3389/fchem.2019.00551

Narayanappa, A. N., & Kamath, P. V. (2019). Interaction of Pristine Hydrocalumite-Like Layered Double Hydroxides with Carbon Dioxide. *ACS Omega*, *4*(2), 3198-3204. https://doi.org/10.1021/acsomega.9b00083

Pérez-Barrado, E., Pujol, M. C., Aguiló, M., Llorca, J., Cesteros, Y., Díaz, F., Pallarès, J., Marsal, L. F., & Salagre, P. (2015). Influence of acid–base properties of calcined MgAl and CaAl layered double hydroxides on the catalytic glycerol etherification to short-chain polyglycerols. Chemical Engineering Journal, 264, 547-556. https://doi.org/10.1016/j.cej.2014.11.117

Santamaría, L., Korili, S. A., & Gil, A. (2023). Layered double hydroxides for CO2 adsorption at moderate temperatures: Synthesis and amelioration strategies. *Chemical Engineering Journal*, *455*. https://doi.org/10.1016/j.cej.2022.140551

You, X., Chen, L., He, S., & Zhang, G. (2023). Solid Acid–Base Catalysts Based on Layered Double Hydroxides Applied for Green Catalytic Transformations. Catalysts, 14(1). https://doi.org/10.3390/catal14010028

Zheng, S., Song, C., Curria, M. C., Ren, Z. J., & White, C. E. (2023). Ca-Based Layered Double Hydroxides for Environmentally Sustainable Carbon Capture. *Environ Sci Technol*, *57*(45), 17212-17224. https://doi.org/10.1021/acs.est.3c03742

PPC & PETROMAT SYMPOSIUM 2025

# SIMULATION OF $CO_2$ DISSOLUTION IN FORMATION BRINE UNDER SUPERCRITICAL CONDITION: UTILIZING SUPCRTBL THERMODYNAMICS DATABASE AND PITZAR-DUAN SUN ACTIVITY MODEL

*Usulludin* [a], *Ampira Charoensaeng* [a,b], *Bor-Jier Shiau* [c], *Astra Agus Pramana* [d], *Uthaiporn Suriyapraphadilok* [*,a,b]

[a] The Petroleum and Petrochemical College, Chulalongkorn University, Bangkok, Thailand
[b] The Center of Excellence on Petrochemical and Materials Technology (PETROMAT), Bangkok, Thailand
[c] Mewbourne School of Petroleum and Geological Engineering, The University of Oklahoma, Norman, OK, USA
[d] Department of Petroleum Engineering, Universitas Pertamina, Jakarta, Indonesia

Keywords: Brine, CCS , Pitzer-Duan Sun, Reaktoro, SUPCRTBL

## ABSTRACT

Accurate modeling of $CO_2$ dissolution in formation brines is critical for evaluating the efficiency and safety of geological carbon storage (GCS). This study presents a simulation-based investigation of $CO_2$ solubility under supercritical conditions (T > 304.13 K, P > 7.38 MPa) using the literature data collected from 70 formation brine samples, with total dissolved solids (TDS) in the 2736–143,000 mg/L range. The geochemical simulation framework Reaktoro was employed, integrating the SUPCRTBL thermodynamic database with a combined Pitzer–Duan Sun activity model to capture the interactions between brine components and the behavior of dissolved $CO_2$. Results showed that SUPCRTBL predicts the solubility with an accuracy ($R^2$ = 0.91, average error = 0.0299 mol/L) compared to PHREEQC. Sensitivity analyses confirmed that $CO_2$ solubility decreases with increasing temperature and increases with increasing pressure. Additionally, higher total dissolved solids (TDS) concentrations lead to reduced solubility due to the salting-out effect. The findings support the use of Reaktoro with SUPCRTBL for high-fidelity modeling of $CO_2$ behavior in subsurface brine systems, contributing to improved GCS site assessment and design.

***uthaiporn.s@chula.ac.th**

## INTRODUCTION

Geological carbon storage is regarded as an effective method for reducing anthropogenic $CO_2$ in the atmosphere by injecting captured $CO_2$ into geological formations, such as deep saline aquifers (Khojastehmehr et al., 2025; Mutailipu et al., 2024). The dissolution of $CO_2$ into the brine significantly affects $CO_2$ migration and storage capacity, both during the injection process and in the long-term post-injection period. Many studies have been conducted to elucidate these issues, utilizing experimental and simulation approaches to ensure the accurate measurement and prediction of CO2 solubility in subsurface formations (Aydin & Akin, 2023; Ji et al., 2024). Some studies focus on experimental analyses of the effects of brine composition, temperature, and pressure on solubility, while simulations help model $CO_2$ dissolution under varying conditions. These approaches are fundamentally guided by thermodynamic principles governing gas-aqueous phase interactions, particularly Le Chatelier's Principle and Henry's Law (Aydin & Akin, 2023; Fernandez-Prini, 1982). In the

PPC & PETROMAT SYMPOSIUM 2025

simulation study of gas solubilities in brine solutions, it is essential to accurately calculate the activity of the dissolved gas species, particularly in geological $CO_2$ storage. For subsurface formation brines, often high-salinity and multicomponent electrolytes, the Pitzer activity model is widely used to account for complex ion interactions (e.g., $Na^+$, $K^+$, $Ca^{2+}$, $Mg^{2+}$, $Cl^-$, $SO_4^{2-}$) at elevated ionic strengths. While the Duan-Sun model remains popular for $CO_2$ solubility calculations (0–260°C, 0–200 MPa, 0–4.5 molal salts), the Pitzer approach offers improved accuracy for hypersaline conditions typical of deep aquifers (Pitzer, 1973). Some software is designed with the capability to model geochemical interactions, such as PHREEQC and Reaktoro (Khojastehmehr et al., 2025; Leal, 2015; Parkhurst & Appelo, 2013).

This simulation study integrates the Pitzer and Duan-Sun activity models within Reaktoro's thermodynamics framework to accurately predict $CO_2$ solubility in formation brines. The approach utilizes Pitzer's precision for high salinity conditions while preserving Duan-Sun's broader pressure-temperature applicability on $CO_2$ solubility.

## METHODOLOGY

*A. Simulator and Thermodynamics Database*

This research employs Reaktoro v2.0, an open-source computational framework developed in C++ and Python by ETH Zurich for modeling chemical reactive processes. This simulator utilizes the Law of Mass Action (LMA) or Gibbs Energy Minimization (GEM) method to determine the system's equilibrium state. PHREEQC, a well-known scientific software for geochemical modeling, has benefited from the development of various thermodynamic databases over the past few decades. Reaktoro is compatible with the databases used by PHREEQC (Parkhurst & Appelo, 2013). Additionally, SUPCRTBL 2016 databases contain thousands of chemical species, including aqueous species, gases, and minerals. These thermodynamic databases include parameters for equations of state, enabling the computation of standard molal thermodynamic properties over a range of pressures from 1 to 500 MPa and temperatures from 0 to 1000 °C (Leal, 2015; Zimmer et al., 2016).

*B. Simulation Dataset*

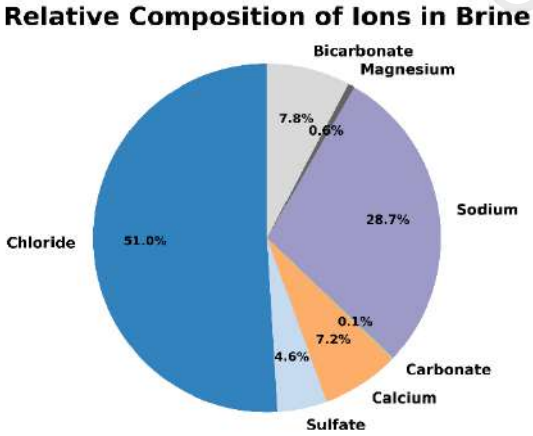


**Figure 1: a)** Relative composition of ions in brine for all 70 data samples.

PPC & PETROMAT SYMPOSIUM 2025

The dataset is collected from Ji et al. (2024), which contains 70 formation brine samples and experimental $CO_2$ dissolution. Figure 1a illustrates the relative composition of brines, particularly those dominated by 51% of chloride and 28.7% of sodium ions, with carbonate and magnesium as minor constituents (~0.7%).

*C. Simulation Procedure*

The simulation workflow begins by importing the 70 formation brine compositions. Next, the corresponding experimental conditions are programmed into Reaktoro for each sample. Furthermore, the simulation (1) initializes the geochemical system using SUPCRTBL/PHREEQC databases for species properties, (2) applies the activity model as a combination of Pitzer and Duan Sun, and (3) determines the equilibrium state through Gibbs Energy Minimization (GEM). The automated workflow iteratively calculates CO2 solubility in each brine sample under supercritical conditions (T > 304.13 K, P > 7.38 MPa), validating results against the experimental dataset from Ji et al. (2024).

A sensitivity analysis was performed to evaluate the effects of temperature and pressure on $CO_2$ solubility in three different brine TDS concentrations: low = 2736.1 mg/L, medium = 11049.9 mg/L, and high salinity = 143000.0 mg/L. For each selected sample, temperature and pressure were varied independently across their observed ranges, while the other variable remained constant. Equilibrium calculations produced the dissolved $CO_2$, offering insight into $CO_2$ behavior under various subsurface conditions.

## RESULTS AND DISCUSSION

*A. Dataset Analysis*

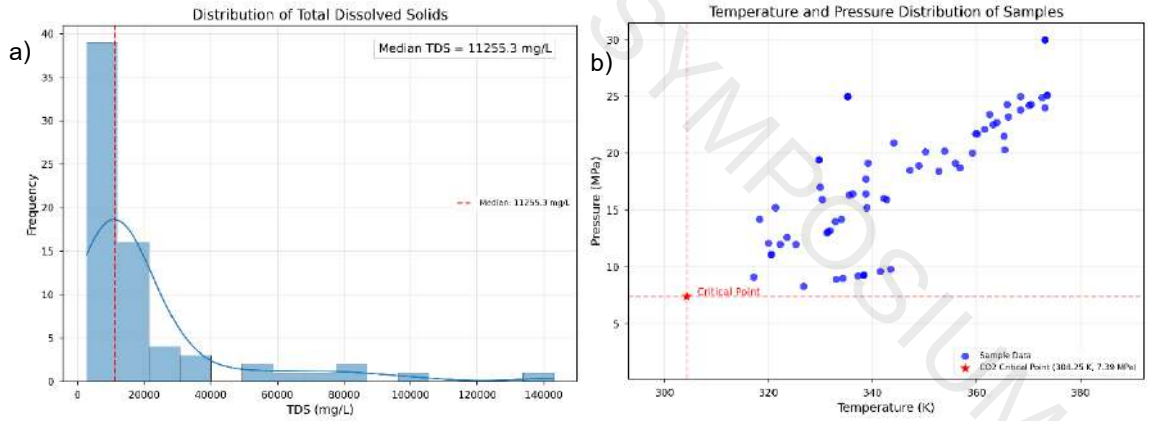


**Figure 2:** Total dissolved solids (TDS) and ions correlation.

Analysis of the brine samples revealed a median total dissolved solids (TDS) concentration of 11,255.3 mg/L, which falls within the high-salinity range of produced waters that exceed 10,000 mg/L TDS (Able & Trembly, 2020). All samples exhibited temperature and pressure conditions that exceeded the critical point of $CO_2$ (304.25 K, 7.39 MPa). These analyses reveal the formation conditions of the brine, and the geochemical composition of the samples aligns with the characteristics of formation brine, as established by Ji et al. (2024).

PROCEEDINGS PETROMAT SYMPOSIUM 2025

*B. Simulation Result and Validation*

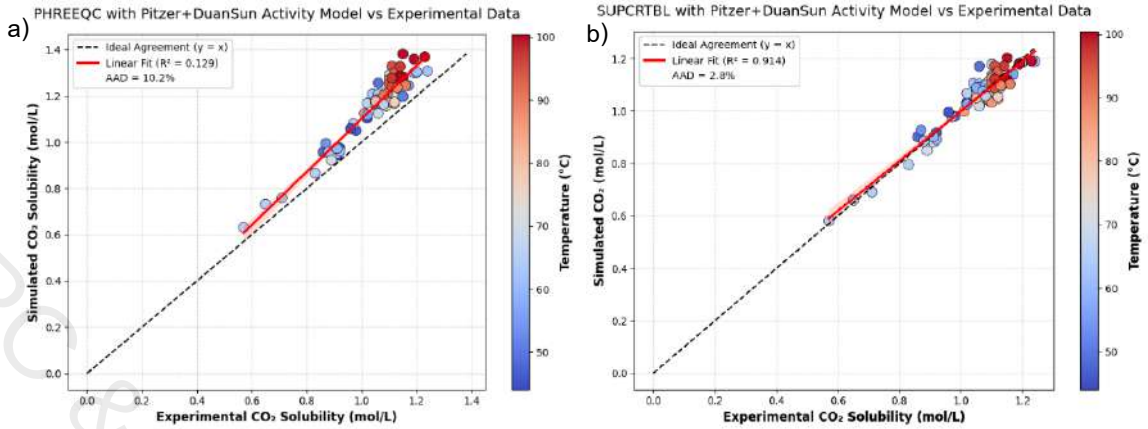


**Figure 3:** Simulation results and validation using: **a)** PHREEQC database + PitzerDuanSun activity model, **b)** SUPCRTBL database + PitzerDuanSun activity.

The simulations demonstrate that SUPCRTBL (Figure 3b) provides significantly more accurate results than PHREEQC (Figure 3a) for predicting $CO_2$ solubility in brine under high-pressure, high-temperature conditions. With SUPCRTBL, the model closely matched the experimental data, exhibiting an average error of 0.0299 mol/L. The $R^2$ score of 0.9141 indicates a strong correlation. The relative error was only 2.84%, suggesting that the predictions were reliable. In contrast, PHREEQC showed considerably larger errors, with an average error of 0.1084 mol/L, while the $R^2$ score of 0.1288 was notably low, indicating a poor fit to the actual data. The relative error of 10.25% was also significantly greater. Therefore, SUPCRTBL, along with the Pitzer and Duan Sun activity models, is much more effective for calculating $CO_2$ solubility in saline brines under supercritical conditions.

*C. Sensitivity Analysis*

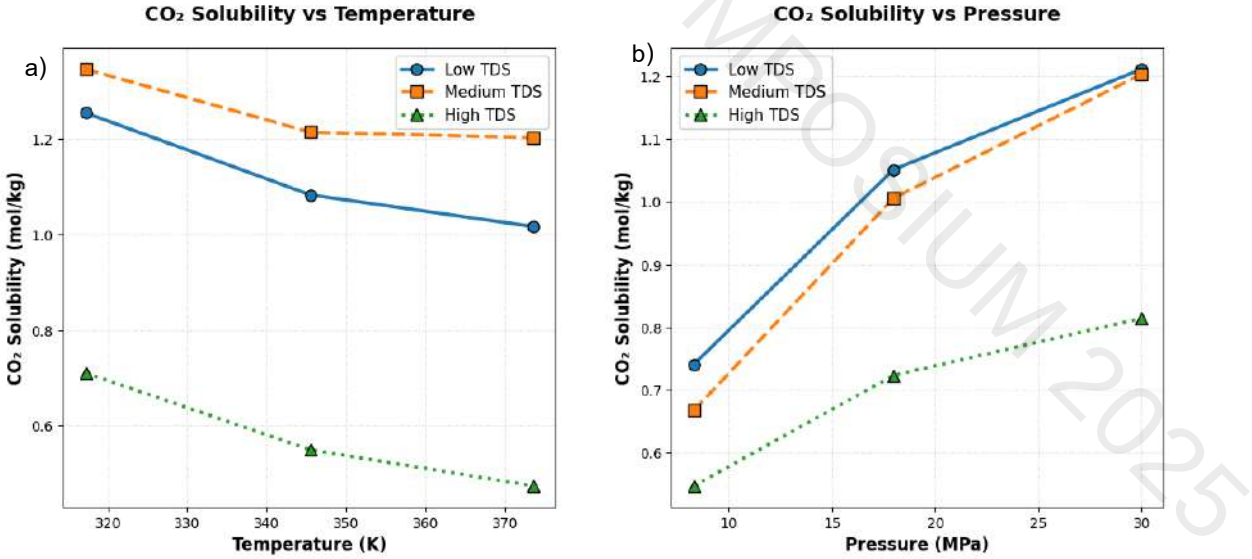


**Figure 4: a)** Temperature sensitivity at different TDS levels of brine. **b)** Pressure sensitivity at different TDS levels of brine.

The results demonstrate an inverse relationship (Le Chatelier's Principle, (Fernandez-Prini, 1982)), between temperature and $CO_2$ solubility across all tested sample types. As the temperature rises from 317.2 K to 373.6 K at constant pressure from the original sample, $CO_2$ solubility decreases significantly, showing reductions of approximately 33%, 11%, and 19% at maximum, mid, and minimum TDS concentrations, respectively. The mid TDS sample exhibits lower $CO_2$ solubility due to its higher pressure compared to the other samples: 30 MPa (others at 18.4 and 9 MPa). This finding is consistent with the pressure-solubility relationship (Henry's Law, (Mutailipu et al., 2024)), which reveals a strong positive correlation, with $CO_2$ solubility increasing nearly linearly across the tested pressure range (8.3-30 MPa). The pressure enhances $CO_2$ solubility by 47.1%, 44.4%, and 27.4% at minimum, mid, and maximum TDS concentrations, respectively.

Furthermore, the concentration of TDS from both pressure and temperature sensitivity analyses consistently influences the window of $CO_2$ solubility at different temperatures and pressures. Those two plots show that when the tested concentration of TDS is at its maximum, the $CO_2$ solubility is at its lowest. This can also be explained as the salting-out effect (Aydin & Akin, 2023) caused by soluble salts in the brine. This occurs because dissolved ions compete with $CO_2$ molecules for hydration, effectively inhibiting the $CO_2$ from entering the brine.

## CONCLUSIONS

This research successfully demonstrated the simulation of $CO_2$ solubility in formation brines under supercritical conditions using the Reaktoro framework integrated with both the SUPCRTBL thermodynamic database and a combined Pitzer–Duan Sun activity model. The results indicated that the SUPCRTBL database provided significantly accurate predictions compared to PHREEQC, showing a lower average error (0.0299 mol/L vs. 0.1084 mol/L) and a higher correlation to the experimental dataset ($R^2 = 0.91$ vs. 0.13). Sensitivity analyses revealed the negative and positive relationships of temperature and pressure, respectively, on $CO_2$ solubility, consistent with thermodynamic principles. Furthermore, high salinity decreased solubility due to the salting-out effect. These findings validate the robustness of the integrated simulation approach and offer valuable insights for carbon storage modeling in real formation brine.

## RECOMMENDATION

To extend this work, future studies could integrate SUPCRTBL with flow simulations and reactive transport models to account for coupled processes like mineral dissolution/precipitation, further optimizing GCS strategies for high-salinity reservoirs.

## ACKNOWLEDGEMENTS

The authors would like to acknowledge scholarship support received from the Petroleum and Petrochemical College and Chulalongkorn University through the ASEAN and Non-ASEAN Scholarship. Funding for this study was received from the Thailand Science Research and Innovation Fund, Chulalongkorn University (DISF67630023).

PPC & PETROMAT SYMPOSIUM 2025

## REFERENCES

**Able, C. M., & Trembly, J. P. (2020)**. Advanced supercritical water-based process concepts for treatment and beneficial reuse of brine in oil/gas production. *Desalination*, *481*, 114334. https://doi.org/https://doi.org/10.1016/j.desal.2020.114334

**Aydin, H., & Akin, S. (2023)**. CO2 Dissolution in the reservoir brine: An experimental and simulation-based approach. *Geothermics*, *113*, 102774. https://doi.org/https://doi.org/10.1016/j.geothermics.2023.102774

**Fernandez-Prini, R. (1982)**. Le Châtelier's principle and the prediction of the effect of temperature on solubilities. *Journal of Chemical Education*, *59*(7), 550. https://doi.org/10.1021/ed059p550

**Ji, Z., Wang, H., Wang, M., Lv, W., Wang, S., Kou, Z., He, C., & Wang, L. (2024)**. Experimental and modeling study of CO2 solubility in formation brines at in-situ conditions. *Journal of Cleaner Production*, *438*, 140840. https://doi.org/https://doi.org/10.1016/j.jclepro.2024.140840

**Khojastehmehr, M., Bazargan, M., & Masihi, M. (2025)**. CO2REAKT: A framework for predicting CO2 solubility in saline and acidic solutions using Reaktoro. *Fuel*, *388*, 134427. https://doi.org/https://doi.org/10.1016/j.fuel.2025.134427

**Leal, A. M. M. (2015)**. *Reaktoro: An open-source unified framework for modeling chemically reactive systems*. In https://reaktoro.org

**Mutailipu, M., Song, Y., Yao, Q., Liu, Y., & Martin Trusler, J. P. (2024)**. Solubility and interfacial tension models for CO2–brine systems under CO2 geological storage conditions. *Fuel*, *357*, 129712. https://doi.org/https://doi.org/10.1016/j.fuel.2023.129712

P**arkhurst, D. L., & Appelo, C. A. J. (2013)**. *Description of input and examples for PHREEQC version 3—A computer program for speciation, batch-reaction, one-dimensional transport, and inverse geochemical calculations* (U.S. Geological Survey Techniques and Methods, book 6, chap. A43, Issue. https://pubs.usgs.gov/tm/06/a43/

**Pitzer, K. S. (1973)**. Thermodynamics of electrolytes. I. Theoretical basis and general equations. *The Journal of Physical Chemistry*, *77*(2), 268-277. https://doi.org/10.1021/j100621a026

**Zimmer, K., Zhang, Y., Lu, P., Chen, Y., Zhang, G., Dalkilic, M., & Zhu, C. (2016)**. SUPCRTBL: A revised and extended thermodynamic dataset and software package of SUPCRT92. *Computers & Geosciences*, *90*, 97-111. https://doi.org/https://doi.org/10.1016/j.cageo.2016.02.013

PPC & PETROMAT SYMPOSIUM 2025

# EFFECT OF PRETREATMENT CONDITIONS ON SILICA EXTRACTION FROM BAGASSE ASH FOR USE AS $CO_2$ ADSORBENTS

*Chayanit Krainara*[a,b], *Thongthai Witoon*[a,b*]

[a)] Center of Excellence on Advanced Adsorbents and Catalysts for Carbon Capture and Utilization, Department of Chemical Engineering, Faculty of Engineering, Kasetsart University, Bangkok 10900, Thailand
[b)] Center of Excellence on Petrochemical and Materials Technology, Department of Chemical Engineering, Faculty of Engineering, Kasetsart University, Bangkok 10900, Thailand

Keywords: Sugarcane bagasse ash, Silica extraction, Calcination, Acid leaching, $CO_2$ adsorption

## ABSTRACT

The utilization of sugarcane bagasse ash (SCBA) as a silica precursor for $CO_2$ capture offers a sustainable approach to waste valorization and greenhouse gas mitigation. In this study, a modified extraction method was developed, combining acid pretreatment and thermal processing to obtain high-purity silica. Acid washing with 1 M HCl effectively removed metal oxides, while calcination at 700 °C eliminated residual hydrocarbons. Under optimal conditions, the silica achieved a purity of 98.42% and a yield of 41.51%. Silica supports were synthesized at various hydrothermal temperatures (130 °C, 160 °C, and 180 °C) to investigate the effect of synthesis temperature on structural properties. With increasing temperature, surface area decreased, whereas pore volume and pore size increased. The silica synthesized at 180 °C exhibited the most favorable textural characteristics, with a BET surface area of 132.64 $m^2 g^{-1}$ and a pore volume of 1.21 $cm^3 g^{-1}$. After functionalization with 50 wt% polyethylenimine (PEI), the adsorbents were tested for $CO_2$ capture in a fixed-bed system. The silica synthesized at 180 °C showed the highest $CO_2$ adsorption capacity (3.01 mmol $g^{-1}$), along with excellent cyclic stability and regenerability. These results demonstrate the promise of SCBA-derived silica as a cost-effective support for amine-based adsorbents in scalable carbon capture applications.

*** fengttwi@ku.ac.th**

## INTRODUCTION

Silica is a widely utilized material across numerous industrial applications, including catalysts, adsorbents, nanomaterials, and composites, due to its high specific surface area, thermal stability, and tunable porous structure (Iler, 1979). Conventionally, silica is synthesized from processed raw materials such as sodium silicate and tetraethyl orthosilicate (TEOS), which are derived from high-purity quartz sand. However, the reliance on non-renewable resources has led to increasing interest in identifying alternative, sustainable sources of silica.

Sugarcane bagasse ash (SCBA), a waste byproduct generated in large quantities from the sugar and biomass industries, represents a promising alternative. With global sugarcane production reaching approximately 1.6 billion tons annually, the resultant bagasse and subsequent combustion yield SCBA rich in silica up to 50 wt%, depending on the origin (Norsuraya et al., 2016). Despite this potential, direct extraction of silica from SCBA often results in low-purity products, typically around 40.2%, due to the presence of metallic and organic impurities (Megawati et al., 2018).

PPC & PETROMAT SYMPOSIUM 2025

To overcome these limitations, pretreatment of SCBA prior to extraction has been widely studied. Acid leaching, particularly with hydrochloric acid, has been shown to effectively remove metal oxides (Affandi et al., 2009), while high-temperature calcination promotes the decomposition of residual organic matter (Bezerra et al., 2013). Together, these processes play a crucial role in enhancing the purity of extracted silica and are necessary for obtaining silica suitable for advanced applications.

This study further refines the pretreatment strategy for SCBA to not only improve the purity but also increase the extraction yield of silica compared to previous reports. Key parameters such as acid concentration, leaching duration, and calcination temperature were systematically investigated to optimize the removal of impurities. The resulting high-purity silica was then employed in the synthesis of mesoporous supports for carbon dioxide ($CO_2$) adsorption applications.

Functionalized silica, particularly when modified with amine-containing polymers like polyethylenimine (PEI), has demonstrated enhanced $CO_2$ capture performance due to chemisorption mechanisms that enable selective and reversible interactions with $CO_2$ molecules (Choi et al., 2009). While previous studies have focused on the type and amount of amine loading, there remains a lack of understanding of how the synthesis conditions of the silica support, particularly hydrothermal temperature, influence its internal structure and, consequently, its $CO_2$ adsorption performance.

Therefore, this research aims to investigate the influence of synthesis temperature on the structural and adsorption properties of SCBA-derived silica after PEI functionalization. Silica supports were synthesized at varying hydrothermal temperatures and evaluated for their textural properties and $CO_2$ adsorption capacity in a fixed-bed adsorption system. This study provides insight into the relationship between synthesis parameters and material functionality, highlighting the potential of SCBA-derived silica as a cost-effective platform for scalable carbon capture technologies.

## EXPERIMENTAL

1. Pre-treatment of Sugarcane Bagasse Ash

Sugarcane bagasse ash (SCBA) was subjected to two primary pre-treatment approaches to enhance its suitability for high-purity silica extraction: high-temperature calcination alone, and acid pre-treatment combined with thermal calcination via conventional heating. In the first approach, 5 grams of SCBA were calcined at 600 °C and 800 °C for 2 hours. The resulting ash was subsequently analyzed for elemental composition to assess the effectiveness of thermal decomposition of organic and inorganic matter. In the second approach, SCBA underwent acid pre-treatment using hydrochloric acid (HCl) followed by calcination. Specifically, 10 grams of SCBA were mixed with 100 mL of HCl solutions at varying concentrations (0.5, 1.0, 1.5, and 2.0 M), and the suspensions were stirred at 300 rpm and heated at 90 °C under reflux for 1 hour. The solid residues were filtered, thoroughly washed with deionized water, dried at 100 °C, and then calcined at 600, 700, 800, or 900 °C for 2 hours. These procedures aimed to investigate the influence of acid strength, treatment duration, and calcination temperature on impurity removal and silica content.

2. Silica Extraction from Pre-treated SCBA

The pre-treated and calcined SCBA was used as a precursor for silica extraction. Ten grams of each sample were mixed with 100 mL of 1 M sodium hydroxide (NaOH) and heated under reflux at 90 °C with continuous stirring for 1 hour. The resulting slurry was filtered, and the filtrate containing dissolved silicate species was retained for silica synthesis, while the solid residues were dried for analysis.

3.Synthesis of Monodisperse Silica Supports

PROCEEDINGS PPC & PETROMAT SYMPOSIUM 2025

To synthesize the silica support, the filtrate was acidified with 2 M HCl until the pH reached 6, promoting the precipitation of silica. The solution was then transferred to a Teflon-lined autoclave and subjected to hydrothermal treatment at 130, 160, or 180 °C for 22 hours. The resulting solid was collected by filtration, washed with deionized water, dried at 60 °C for 12 hours and at 100 °C for another 24 hours. The dry silica was ground into powder and calcined at 600 °C for 4 hours to yield Si-130, Si-160, and Si-180 samples, corresponding to the respective synthesis temperatures.

4.Surface Functionalization with Amine Groups

The prepared silica supports were functionalized with amine groups via the impregnation method. One gram of polyethyleneimine (PEI) was dissolved in 10 mL of methanol and stirred at room temperature for 15 minutes. Then, 1 gram of each silica sample was added to the PEI solution and stirred for 3 hours under ambient conditions. The solvent was evaporated, and the samples were dried at 70 °C for 6 hours to obtain amine-functionalized adsorbents.

5. $CO_2$ Adsorption Performance Testing

The $CO_2$ adsorption capacity of the functionalized silica materials was evaluated using a fixed-bed adsorption column. The adsorbents (1.5 grams) were initially pre-treated at 100 °C under a nitrogen flow (50 $cm^3$/min) to remove residual moisture. Once cooled to 75 °C, the gas stream was switched to a $CO_2/N_2$ mixture (5 $cm^3$/min $CO_2$ and 45 $cm^3$/min $N_2$), and the breakthrough curves were recorded using a gas chromatograph equipped with a thermal conductivity detector (GC-TCD). Desorption was performed by reheating to 100 °C under nitrogen flow. Each material was tested for three adsorption–desorption cycles to assess regenerability.

## RESULTS AND DISCUSSION

**Table 1.** XRF results of SCBA and treated SCBA.

| Sample | Composition (%) | | | | | | | | | | | |
|---|---|---|---|---|---|---|---|---|---|---|---|---|
| | $SiO_2$ | $K_2O$ | CaO | $Fe_2O_3$ | $Al_2O_3$ | Cl | MgO | $P_2O_5$ | $TiO_2$ | MnO | $SO_3$ | Other |
| SCBA | 56.80 | 6.16 | 5.76 | 3.22 | 2.27 | 1.09 | 0.66 | 1.61 | 0.39 | 0.16 | 0.19 | 0.13 |
| AH-0.5-60-700 | 87.45 | 2.42 | 1.55 | 4.23 | 2.60 | - | 0.64 | - | 0.92 | 0.92 | - | 0.08 |
| AH -1-60-700 | 90.27 | 1.97 | 1.43 | 1.77 | 1.67 | - | 0.26 | 1.48 | 0.83 | 0.05 | - | 0.07 |
| AH -1.5-60-700 | 90.97 | 2.05 | 1.30 | 1.67 | 1.83 | - | 0.38 | 0.61 | 0.87 | 0.05 | - | 0.08 |
| AH -2-60-700 | 91.79 | 1.99 | 1.16 | 1.51 | 1.70 | - | - | 0.61 | 0.80 | 0.05 | - | 0.08 |

As shown in Figure 1, the XRD analysis revealed that the raw sugarcane bagasse ash (SCBA) exhibited prominent crystalline silica peaks in the form of quartz, with major diffraction peaks appearing at 2θ = 20.8°, 26.6°, 36.5°, 42.5°, 50.2°, and 54.9°. Additional peaks corresponding to orthoclase ($KAlSi_3O_8$) and calcium carbonate ($CaCO_3$) were also observed, indicating the presence of minor components such as $K_2O$ and $Al_2O_3$, consistent with the elemental composition data shown in Table 1. Upon calcination at 600 °C (H-600), the $SiO_2$ peaks became noticeably sharper, signifying an increase in crystallinity. However, new peaks appeared at 2θ = 35.5°, 39.5°, and 40.5°, corresponding to the formation of $Fe_2O_3$, $K_2O$, and CaO, respectively. Additionally, the peak intensity of $CaCO_3$ decreased, indicating partial decomposition of carbonate phases at this temperature.When the calcination temperature was increased to 800 °C (H-800), more pronounced phase transformations occurred. New crystalline phases such as $CaSiO_5$ and $KAlSiO_4$ emerged, indicating solid-state reactions between silica and metal oxides such as Ca, K, and Al. These changes are supported by the XRF results shown in Table 1, which revealed elevated levels of $K_2O$ and $Al_2O_3$ in the SCBA samples. Furthermore, the increasing intensity of $Fe_2O_3$ and CaO peaks at higher temperatures suggests enhanced aggregation of metal oxides, contributing to the formation of complex mineral structures.

PROCEEDINGS PETROMAT SYMPOSIUM 2025

Although moderate calcination can enhance the crystallinity of silica, excessive thermal treatment such as calcination at 800 °C can induce the formation of undesirable mixed phases. This phenomenon reduces the overall purity of the extracted silica and may limit its applicability in advanced applications. These findings are consistent with previous work by Frías et al. (2007), who reported that excessive calcination of biomass ash can trigger redistribution of metallic elements, resulting in secondary phases that compromise both purity and functional performance.

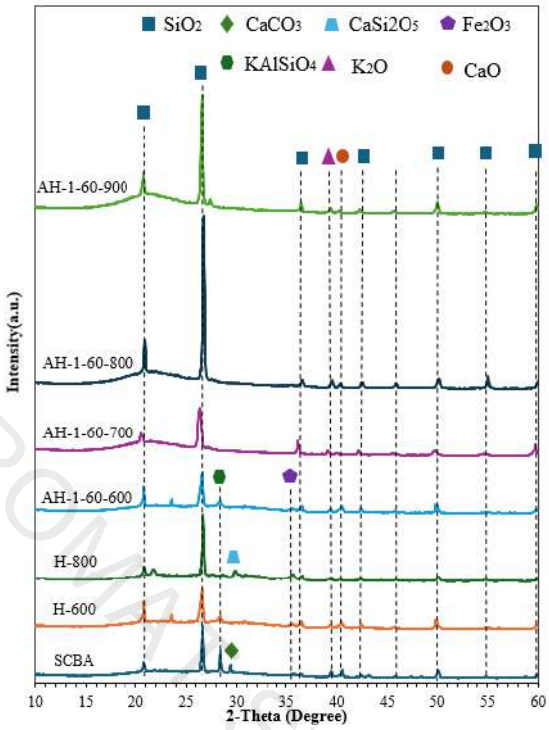


**Figure 1.** XRD patterns of raw sugarcane bagasse ash (SCBA), SCBA samples subjected to high-temperature calcination at 600 °C and 800 °C, and SCBA samples pretreated with acid followed by calcination at various temperatures ranging from 600 °C to 900 °C.

To investigate the effect of hydrochloric acid (HCl) concentration on the pre-treatment efficiency of sugarcane bagasse ash (SCBA) prior to silica extraction, SCBA samples were treated with HCl at concentrations of 0.5, 1.0, 1.5, and 2.0 M, followed by calcination at 700 °C. XRF analysis showed that increasing acid concentration significantly enhanced the removal of $Fe_2O_3$, which dropped from 4.23 wt% at 0.5 M to 1.30 wt% at 1.5 M, before slightly rising at 2.0 M, possibly due to saturation. In contrast, $K_2O$ showed only a slight decrease, indicating higher resistance to acid leaching. The optimal condition was found to be 1.0 M HCl, which yielded the highest silica purity (90.27 wt%) while maintaining effective removal of major impurities.

This phase of the study investigated how calcination temperatures (600–900 °C) after acid pre-treatment affect the composition and stability of SCBA. The optimal temperature was found to be 700 °C, which achieved high $SiO_2$ purity (90.27 wt%) while minimizing undesirable phase formation. Although 800 °C showed sharper $SiO_2$ peaks, it also promoted unwanted secondary phases. TGA results confirmed that organic components were sufficiently removed by 700 °C, and XRD patterns indicated improved crystallinity without significant mineralogical complexity. Therefore, 700 °C is considered the most effective calcination condition following acid treatment.

PPC & PETROMAT SYMPOSIUM 2025

**Table 2.** Physicochemical properties of silica supports synthesized at different temperatures before and after PEI impregnation, and their $CO_2$ adsorption performance and regenerability.

| Synthesis Temp. (°C) | BET Surface Area ($m^2/g$) | | Total Pore Volume ($cm^3/g$) | | Pore Diameter (nm) | | $CO_2$ Adsorption Capacity (mmol/g) | Regener-ability (%) |
|---|---|---|---|---|---|---|---|---|
| | Before | After | Before | After | Before | After | | |
| 130 | 226.97 | 8.38 | 0.914 | 0.052 | 16.11 | 25.13 | 1.389 | 94.31 |
| 160 | 174.87 | 10.67 | 1.086 | 0.108 | 24.84 | 40.73 | 1.948 | 99.38 |
| 180 | 132.64 | 12.83 | 1.216 | 0.165 | 36.68 | 51.45 | 3.011 | 99.57 |

As shown in Table 2, the synthesis temperature plays a significant role in determining the physicochemical properties of silica supports. An increase in synthesis temperature from 130 °C to 180 °C resulted in a decrease in BET surface area from 226.97 $m^2/g$ to 132.64 $m^2/g$. This reduction is attributed to accelerated silica precursor condensation and the formation of larger particles. In contrast, the total pore volume and average pore diameter increased with temperature. The highest pore volume (1.216 $cm^3/g$) and pore diameter (36.68 nm) were observed at 180 °C, suggesting the formation of a more open pore network that may facilitate functional group dispersion.
After PEI impregnation, all samples exhibited reduced surface areas due to pore blockage. Nevertheless, the sample synthesized at 180 °C retained the highest BET surface area (12.83 $m^2/g$), pore volume (0.165 $cm^3/g$), and pore diameter (51.45 nm), indicating that the structural openness was largely preserved. These properties are advantageous for $CO_2$ diffusion and interaction with amine groups. This structural benefit translated into improved $CO_2$ adsorption performance. The 180 °C sample achieved the highest adsorption capacity at 3.011 mmol/g, significantly higher than the 1.389 mmol/g observed at 130 °C. In terms of regenerability, the 180 °C sample showed excellent stability across cycles, maintaining 99.57% of its initial capacity after three adsorption–desorption cycles. Meanwhile, the 160 °C and 130 °C samples exhibited regenerability values of 99.38% and 94.31%, respectively. In summary, silica synthesized at 180 °C provided the optimal balance between porosity, surface characteristics, and functional performance, making it a highly promising support for PEI-based $CO_2$ capture materials.

## CONCLUSIONS

This study demonstrates the potential of sugarcane bagasse ash (SCBA) as a sustainable silica precursor for $CO_2$ adsorbent applications. A combined approach involving acid pre-treatment and thermal calcination was developed to improve the purity and structural quality of extracted silica. Among various conditions investigated, pre-treatment with 1.0 M HCl followed by calcination at 700 °C yielded silica with the highest purity (90.27 wt%) while minimizing the formation of undesirable secondary phases. XRD and TGA analyses confirmed that this condition offered an optimal balance between crystallinity, thermal stability, and phase composition.

Subsequent synthesis of silica supports at varying hydrothermal temperatures (130–180 °C) revealed that higher synthesis temperatures enhanced pore volume due to increased interparticle voids, while reducing the specific surface area. Silica synthesized at 180 °C provided the most favorable textural properties for PEI loading, resulting in the highest $CO_2$ adsorption capacity of 3.01 mmol/g and excellent regenerability across multiple adsorption–desorption cycles.

PPC & PETROMAT SYMPOSIUM 2025

Overall, the findings highlight the importance of optimizing both the purification and synthesis conditions to produce high-performance, amine-functionalized silica adsorbents from agricultural waste. This approach not only contributes to sustainable material development but also supports scalable carbon capture technologies.

**ACKNOWLEDGEMENTS**

This work was financially supported by the Kasetsart University Research and Development Institute (KURDI) under grant number FF(KU)31.68, and by the Hub of Talent: Sustainable Materials for Circular Economy, National Research Council of Thailand (NRCT).

**REFERENCES**

Affandi, S., Setyawan, H., Winardi, S., Purwanto, A., & Balgis, R. (2009). A facile method for production of high-purity silica xerogels from bagasse ash. *Advanced Powder Technology*, *20*(5), 468–472.

Choi, S., Drese, J., & Jones, C. (2009). Adsorbent materials for carbon dioxide capture from large anthropogenic point sources. *ChemSusChem, 2*(9), 796–854.

Frías, M., Villar-Cociña, E., & Valencia-Morales, E. (2007). Characterisation of sugar cane straw waste as pozzolanic material for construction: Calcining temperature and kinetic parameters. *Waste Management, 27*(4), 533–538.

Iler, R.K. (1979). *The Chemistry of Silica: Solubility, Polymerization, Colloid and Surface Properties, and Biochemistry.* Wiley.

Megawati, M., Fardhyanti, D., Putri, R., Fianti, O., Simalango, A., & Akhir, A. (2018). Synthesis of silica powder from sugar cane bagasse ash and its application as adsorbent in adsorptive-distillation of ethanol-water solution. *MATEC Web of Conferences, 237*, 02002.

Norsuraya, S., Fazlena, H., & Norhasyimi, R. (2016). Sugarcane bagasse as a renewable source of silica to synthesize Santa Barbara Amorphous-15 (SBA-15). *Procedia Engineering, 148*, 839–846.

PPC & PETROMAT SYMPOSIUM 2025

# Exploring the impact of cobalt and $H_2$ to CO ratios on catalytic performance of FeKAl and FeCoKAl catalysts in CO hydrogenation to light olefins

*Napaphut Dolsiririttigul [a], Thanapha Numpilai [b], Kajornsak Faungnawakij [c], Metta Chareonpanich [a,d], Thongthai Witoon [a,d,*]*

[a] Center of Excellence On Advanced Adsorbents and Catalysts for Carbon Capture and Utilization, Department of Chemical Engineering, Faculty of Engineering, Kasetsart University, Bangkok 10900, Thailand
[b] Department of Environmental Science, Faculty of Science and Technology, Thammasat University, Pathumthani 12120, Thailand
[c] National Nanotechnology Center (NANOTEC), National Science and Technology Development Agency (NSTDA), Pathum Thani 12120 Thailand
[d] Center of Excellence on Petrochemical and Materials Technology, Department of Chemical Engineering, Faculty of Engineering, Kasetsart University, Bangkok 10900, Thailand

Keywords: CO hydrogenation, light olefins, Fe-based catalyst, cobalt promotion, syngas conversion

## ABSTRACT

The conversion of syngas to light olefins is a promising alternative to conventional steam cracking, enabling petrochemical production from non-petroleum resources. This work investigates the performance of FeKAl compared with cobalt-modified (FeCoKAl) for CO hydrogenation. Cobalt was introduced to enhance hydrogen dissociation and to modify the redox behavior and carbide formation of Fe-based catalysts, aiming to improve activity and stability. Catalytic testing under varying $H_2$/CO ratios (1:1 to 7:1) revealed that FeKAl exhibited maximum light olefin productivity at a 3:1 ratio, while the incorporation of cobalt significantly enhanced CO conversion and light olefin space–time yield (STY), especially at low $H_2$/CO ratios. Moreover, FeCoKAl maintained superior stability during long-term operation, effectively reducing carbonaceous deposits and suppressing the re-oxidation of $Fe_5C_2$, which contributes to deactivation. Catalyst stability, evaluated as the percentage retention of light olefin STY after 96 h, clearly reflects this enhancement: at an $H_2$/CO ratio of 3:1, FeKAl retained only 14.9% of its initial activity, whereas FeCoKAl preserved 92.5%. Similarly, at 5:1, the stability of FeCoKAl reached 96.2%, outperforming FeKAl (77.5%). These results, visualized in the accompanying figure, emphasize the synergistic role of cobalt and optimized $H_2$/CO ratio in prolonging catalyst lifetime. Characterization confirmed that cobalt promoted the formation of active iron carbide phases while minimizing wax and carbon fiber accumulation. These findings highlight the critical interplay between metal composition and syngas ratio in tuning catalyst performance and support the role of cobalt in maintaining high olefin productivity under CO hydrogenation conditions.

***fengttwi@ku.ac.th**

## INTRODUCTION

Light olefins such as ethylene, propylene, and butene are vital petrochemical building blocks used in the production of plastics, rubbers, detergents, and solvents. Traditionally obtained via steam cracking of petroleum-derived hydrocarbons, their production faces challenges from volatile oil prices, fossil fuel depletion, and the need to reduce $CO_2$ emissions (Numplirai et al., 2021). As a sustainable alternative, synthesis gas (syngas)

PPC & PETROMAT SYMPOSIUM 2025

derived from biomass, municipal waste, or natural gas offers a promising route for light olefin production. Fischer–Tropsch synthesis (FTS) using iron-based catalysts has attracted attention due to their low cost, tolerance to varying $H_2$/CO ratios, and inherent water–gas shift (WGS) activity. However, conventional Fe catalysts often show low selectivity toward light olefins and suffer from deactivation due to carbon deposition or phase transformation of iron carbides (Ding et al., 2023; Tian et al., 2019). Incorporating alkali promoters like potassium enhances olefin selectivity by increasing surface basicity and promoting iron carburization (Ma et al., 2024). Additionally, cobalt has been introduced to improve hydrogen activation and modify metal-support interactions. Although Co is typically linked to paraffin formation, its cooperative effect with Fe in olefin production remains underexplored. This study investigates FeKAl and Co-modified FeCoKAl catalysts for CO hydrogenation to light olefins, focusing on the role of Co addition and feed $H_2$/CO ratio. The effects on activity, selectivity, iron phase evolution, adsorption behavior, and catalyst stability are systematically evaluated. The insights aim to inform catalyst design strategies for efficient and selective syngas-to-olefin conversion.

## EXPERIMENTAL

*A. Catalyst preparation*

FeKAl and FeCoKAl catalysts were synthesized using a sequential wet impregnation method. Initially, $Al_2O_3$ was impregnated with an aqueous $KNO_3$ solution to achieve a K/Fe molar ratio of 0.75. The slurry was stirred at 60 °C for 4 h, dried overnight at 100 °C, and then calcined at 400 °C for 4 h. Subsequently, FeKAl was prepared by impregnating the K-modified support with $Fe(NO_3)_3 \cdot 9H2O$ to achieve an Fe content of 12.4 wt%, followed by drying at 110 °C and calcination at 400 °C. For FeCoKAl, both $Fe(NO_3)_3 \cdot 9H_2O$ and $Co(NO_3)_2 \cdot 6H_2O$ were co-impregnated to yield a Co/Fe molar ratio of 0.2. A Co-only catalyst (CoKAl) was also prepared by replacing Fe nitrate with cobalt nitrate under the same procedure. All catalysts were labeled based on their composition.

*B. Catalyst characterization*

The physicochemical properties of the catalysts were investigated using various techniques. Powder X-ray diffraction (XRD) was used to identify crystalline phases. The reducibility of the metal species was evaluated using $H_2$ temperature-programmed reduction ($H_2$-TPR), while hydrogen adsorption properties were examined by $H_2$-TPD. $CO_2$-TPD was conducted to analyze surface basicity. X-ray photoelectron spectroscopy (XPS) was employed to determine the oxidation states and surface composition of Fe, Co, K, and Al. Transmission electron microscopy (TEM) provided insights into morphology, crystallite dispersion, and carbon deposition after reaction.

*C. Catalytic testing*

Catalytic performance for CO hydrogenation was tested in a fixed-bed stainless steel reactor at 20 bar and 340 °C, using a total gas flow rate of 60 mL $min^{-1}$ and varying $H_2$/CO molar ratios (1:1 to 7:1). Prior to reaction, 0.5 g of catalyst was reduced in situ under $H_2$ flow at 400 °C for 5 h. The product gases were analyzed using gas chromatography equipped with both TCD and FID detectors. Space–time yields (STY), conversion, and selectivity were calculated based on standard formulas. Long-term stability tests were carried out over 96 h under selected $H_2$/CO conditions (Witoon et al., 2022).

PPC & PETROMAT SYMPOSIUM 2025

## RESULTS AND DISCUSSION

### *A. Catalyst Characterization*

XRD analysis (Fig. 1) of the spent catalysts after 12 h reaction revealed significant phase evolution. For FeKAl catalysts, iron carbide ($Fe_5C_2$) was detected as the primary active phase, with the presence of wax peaks and $Fe_3O_4$ in FeKAl-3 and FeKAl-5, suggesting catalyst oxidation and carbon deposition at lower $H_2$:CO ratios. In contrast, FeCoKAl catalysts maintained predominantly $Fe_5C_2$ with minimal $Fe_3O_4$ or wax signals, especially under $H_2$:CO = 5:1, implying improved phase stability with Co addition.

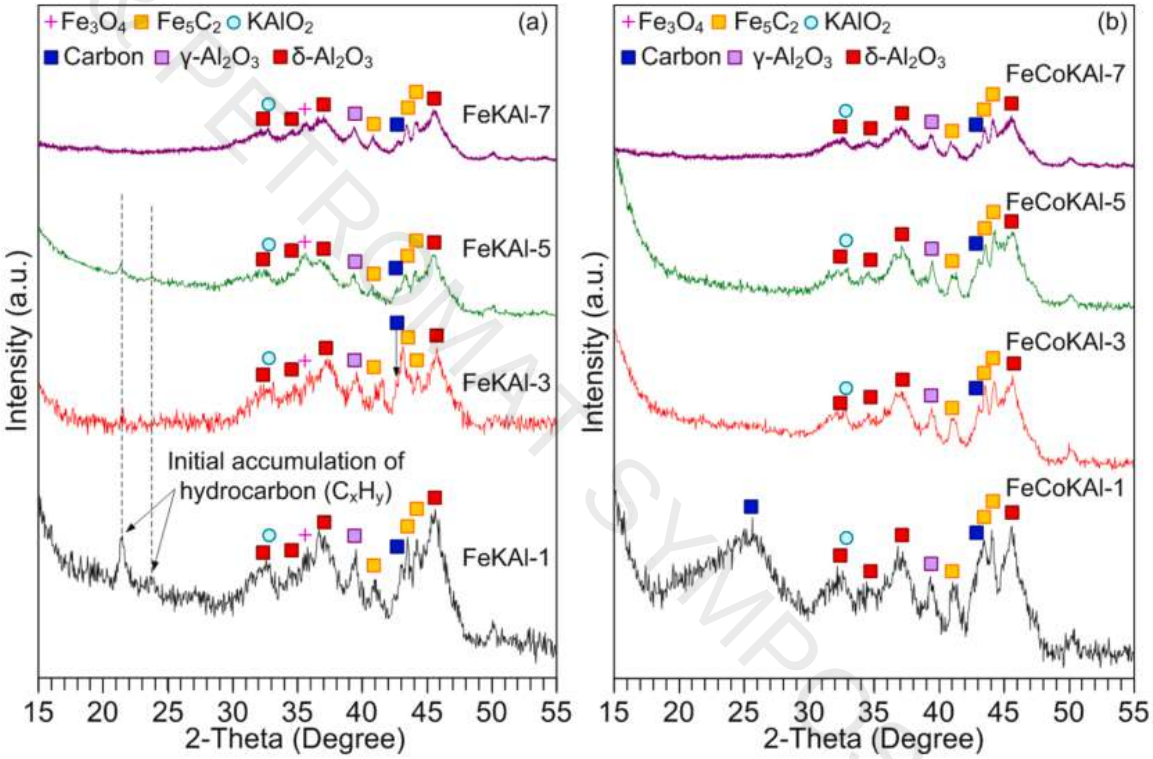


**Figure 1.** XRD analysis of FeKAl (a) and FeCoKAl (b) catalysts after undergoing reaction conditions of 360 °C for 12 h across varying $H_2$ to CO ratios.

$H_2$-TPD and $CO_2$-TPD analyses (Fig. 2) further clarified surface properties. FeCoKAl showed higher desorption in the moderate hydrogen adsorption region (β peak), implying more available active sites at the Fe-Co interface. The $CO_2$-TPD profile revealed a shift of α desorption peak to lower temperatures in FeCoKAl, suggesting weaker $CO_2$ adsorption and altered surface basicity.

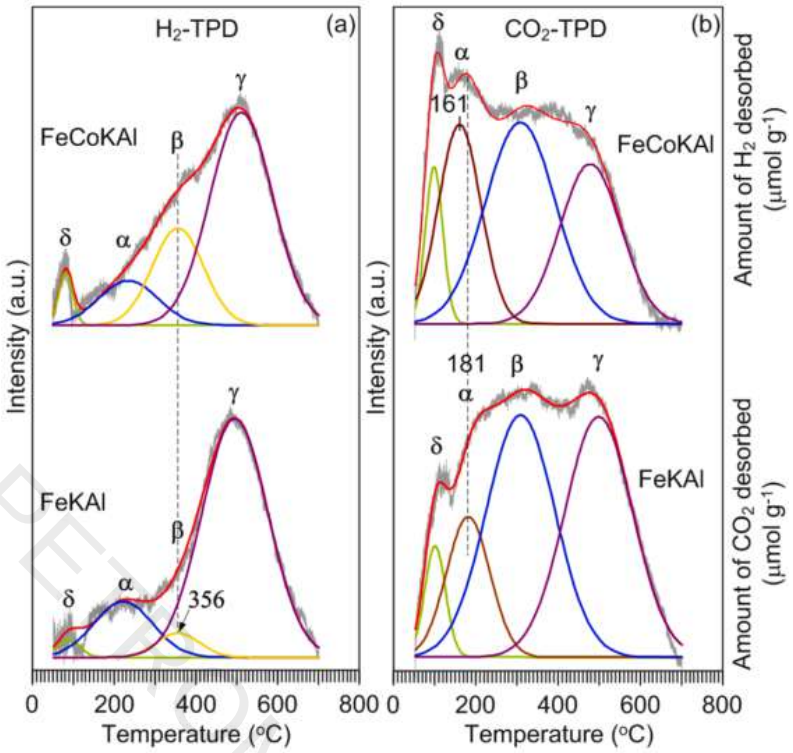


**Figure 2.** $H_2$-TPD (a) and $CO_2$-TPD (b) profiles of pre-reduced FeKAl and FeCoKAl catalysts.

*B. Catalyst activity*

Catalytic performance trends (Fig. 3) under different $H_2$:CO ratios (1:1 to 7:1) and temperatures (300-380 °C) showed optimal STY of light olefins at $H_2$:CO = 3:1 and 340 °C for both catalysts. FeKAl achieved the highest STY at 18.1 mmol $g^{-1}$ $h^{-1}$, while FeCoKAl reached 17.8 mmol $g^{-1}$ $h^{-1}$ with enhanced stability. At higher $H_2$:CO ratios (5:1 and 7:1), the STY of olefins declined due to excessive hydrogenation to paraffins, while lower ratios (1:1) favored carbon deposition, limiting overall productivity. The olefin/paraffin (O/P) ratio also decreased with increasing $H_2$ concentration, indicating intensified hydrogenation. Interestingly, FeCoKAl consistently showed lower O/P ratios than FeKAl, supporting the hypothesis that Co promotes hydrogenation reactions.

Long-term stability tests (Fig. 4) under $H_2$:CO = 3:1 and 5:1 at 340 °C for 96 h confirmed the superior durability of FeCoKAl. FeKAl-3 exhibited severe deactivation, with STY of light olefins dropping from 22.1 to 3.1 mmol $g^{-1}$ $h^{-1}$. This decline corresponded with substantial carbon deposition and partial re-oxidation of $Fe_5C_2$, as confirmed by XRD and TEM. Conversely, FeCoKAl-3 retained 19.6 mmol $g^{-1}$ $h^{-1}$ with minimal change, correlating with reduced carbon formation and more stable $Fe_5C_2$ presence. Additionally, the Co-containing catalysts showed less wax accumulation and carbon fiber formation, allowing sustained accessibility of active sites. These findings underscore the critical role of Co in enhancing both reactivity and resistance to deactivation under syngas conversion conditions.

PPC & PETROMAT SYMPOSIUM 2025

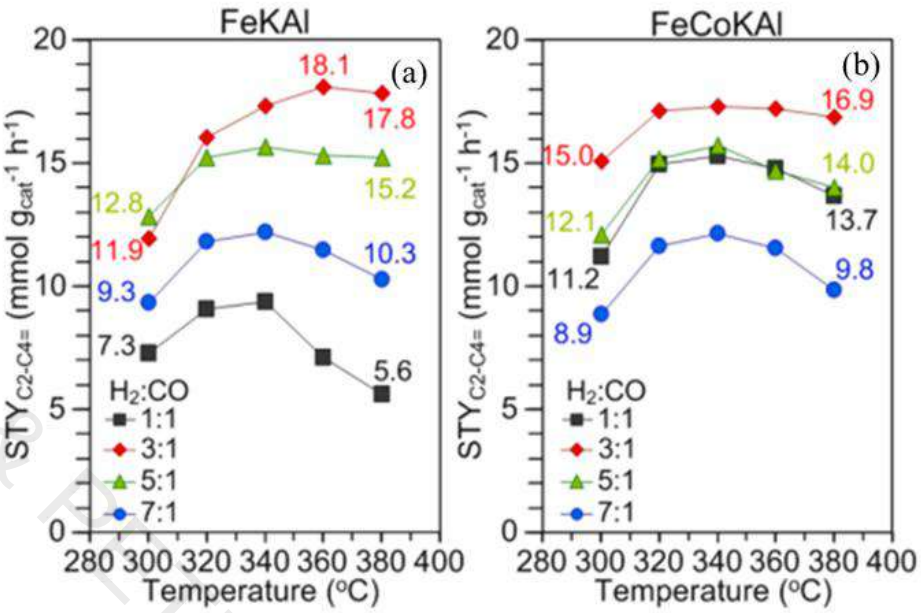


**Figure 3.** Comparison of Light Olefin Production over FeKAl and FeCoKAl Catalysts under Varying $H_2/CO$ Ratios and Reaction Temperatures.

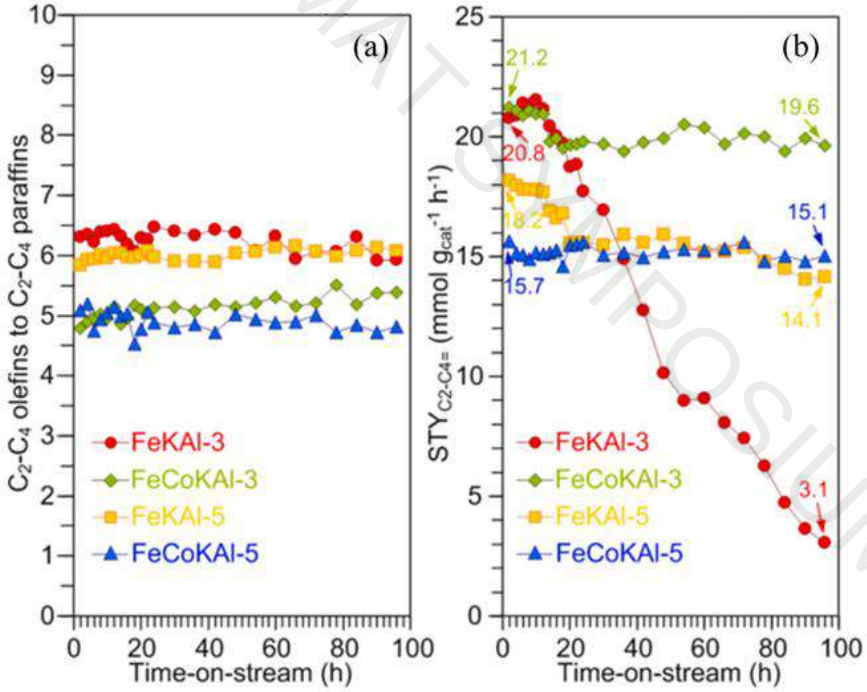


**Figure 4.** Long-Term Stability of FeKAl and FeCoKAl Catalysts at $H_2/CO$ Ratios of 3:1 and 5:1: Evolution of $C_2$-$C_4$ Light Olefin STY under Continuous Operation at 340 °C and 20 bar.

PPC & PETROMAT SYMPOSIUM 2025

The superior performance and stability of FeCoKAl arise from synergistic effects of Co with Fe, enhancing $H_2$ activation, minimizing carbon accumulation, and stabilizing carbide phases. Co also facilitates hydrogen spillover and moderates the $CO_2$ adsorption strength, contributing to selective and stable light olefin production.

## CONCLUSIONS

This study demonstrates that Co incorporates into K-promoted Fe-based catalysts (FeKAl) significantly enhances catalytic performance and stability in CO hydrogenation to light olefins. The addition of Co facilitates the reduction of iron species, improves hydrogen activation, and increases the formation of Fe–Co interfacial sites favorable for hydrocarbon production. Under optimized $H_2$/CO ratios (particularly 3:1), FeCoKAl exhibits higher CO conversion and light olefin space–time yield (STY) compared to FeKAl, especially at lower $H_2$/CO conditions. Importantly, Co-modified catalysts show superior resistance to deactivation during long-term operation, attributed to the suppression of wax and amorphous carbon formation and the stabilization of active iron carbide phases. The combined effects of potassium promotion, cobalt interaction, and appropriate $H_2$/CO feed ratio result in a more robust and efficient catalytic system.

## ACKNOWLEDGEMENTS

This work was financially supported by the Kasetsart University Research and Development Institute (KURDI) under grant number FF(KU)51.67, and by the Hub of Talent: Sustainable Materials for Circular Economy, National Research Council of Thailand (NRCT).

## REFERENCES

**Ding, X., Zhu, M., Han, Y.-F., Yang, Z.** (2023). Revisiting the syngas conversion to olefins over Fe-Mn bimetallic catalysts: Insights from the proximity effects. *J. Catal.*, *417*, 213–225.

**Ma, H., Yang, Y., Hu, H., Zhang, H., Qian, W., Sun, Q., et al.** (2024). Effect of alkaline-earth metals (Mg, Ca, Sr, and Ba) on promoting Fe-based catalysts for high-performance Fischer-Tropsch synthesis of light olefins. *Fuel*, *357*, 129605.

**Numpliai, T., Cheng, C. K., Limtrakul, J., Witoon, T.** (2021). Recent advances in light olefins production from catalytic hydrogenation of carbon dioxide. Process Saf. Environ. Prot., 151, 401–427.

**Tian, Z., Wang, C., Yue, J., Zhang, X., Ma, L.** (2019). Effect of a potassium promoter on the Fischer–Tropsch synthesis of light olefins over iron carbide catalysts encapsulated in graphene-like carbon. *Catal. Sci. Technol.*, *9*, 2728–41.

**Witoon, T., Lapkaseteree, V., Numpliai, T., Cheng, C. K., Limtrakul, J. C.** (2022). CO2 hydrogenation to light olefins over mixed Fe–Co–K–Al oxides catalysts prepared via precipitation and reduction methods. *Chem. Eng. J.*, *428*, 131389.

PROCEEDINGS FROM PPC & PETROMAT SYMPOSIUM 2025

# Workshop on Water

# Development of Biomass-Based Adsorbents for Metal Ion Removal from Agricultural Water Source

*Wasupon Wongvitvichot* [a,b], *Thanyalak Chaisuwan*[*a,b]

[a] The Petroleum and Petrochemical College, Chulalongkorn University
[b] Center of Excellence on Petrochemical and Materials Technology

Keywords: Water treatment, Bio-adsorbent, Activated carbon, Bio-chemicals, Electrostatic interactions

## Abstract

Metal ion contamination from agricultural runoffs is a critical issue affecting natural water bodies and posing risks to ecosystems and human health. This study investigates the effectiveness of activated carbon (AC)-based bio-adsorbents for removing metal ions from real agricultural water sources, collected to ensure practical relevance. All adsorbents were prepared using cost-effective and eco-friendly processes, and their metal adsorption capabilities were evaluated through batch experiments. Results demonstrate a significant reduction in calcium, potassium, and iron concentrations across all adsorbents. Carboxymethyl cellulose-Citric acid-AC (CMC-AC) exhibited the highest removal efficiency, reducing metal ion levels from approximately 178.67 mg/L to below 50 mg/L, attributed to the electrostatic interaction of abundant functional groups from biopolymers and enhanced surface area from AC. The FD-CMC-AC monolith achieved a removal of 84%. This comparative study confirms the potential of CMC-AC for use in decentralized water treatment applications in agricultural areas. Integrating natural biopolymers and accessible materials in adsorbent design offers a sustainable route to improve rural water quality and mitigate heavy metal pollution.

***thanyalak.c@chula.ac.th**

## INTRODUCTION

Worldwide, agricultural practices often lead to metal ion contamination in water resources (Saravanan et al., 2024). Metal ions, originating from various industrial and agricultural activities, are a group of chemicals that, while sometimes naturally occurring, can become severely problematic when present in excessive concentrations (Saravanan et al., 2024). The presence of heavy metals like lead, mercury, cadmium, and arsenic, even in trace amounts, can have detrimental effects on aquatic life and human populations (Qasem et al., 2021).

The pervasive nature of metal ion contamination makes its removal a critical challenge in water resource management and environmental conservation. Restoring water quality affected by metal ions requires practical and sustainable technologies and methods. However, current approaches often fall short of providing economically viable and long-term solutions (Wibowo, 2025).

PPC & PETROMAT SYMPOSIUM 2025

Various technologies exist for removing metal ions from water, including membrane filtration, precipitation, ion exchange, and adsorption (Laishram et al., 2025). Each of these methods has limitations, such as difficulties in scaling up for large-scale applications, high energy consumption, incomplete removal of metal ions, and the generation of secondary pollutants (Chen et al., 2025; Wibowo, 2025). Therefore, developing innovative, high-performance adsorbents to address this issue is essential. Ideal adsorbents should efficiently extract metal ions from water, be cost-effective, and environmentally friendly.

Research on metal-ion sorbents has primarily targeted high-porosity materials, with activated carbons made from agricultural wastes standing out for their low cost and tunable chemistry (Zhang et al., 2024; Wibowo, 2025). Surface modifications—such as metal impregnation, polymer grafting, or hetero-atom doping—can boost capacity (Huang et al., 2025), yet metal-loaded carbons often leach and lose efficiency, limiting long-term use (Wongvitvichot et al., 2023). Therefore, a key challenge is designing sorbents that combine high uptake with durability.

To address these limitations, this research focuses on developing a high-performance adsorbent prototype using biomass-derived materials such as activated carbon (AC) from agricultural waste, citric acid (CA), and carboxymethyl cellulose (CMC), enhanced with a freeze-drying technique to create a 3D structure (Wang et al., 2023) to remove metal ion contaminants resulting from agricultural processes. Furthermore, this research contributes to sustainable water pollution management strategies that can be applied in agriculture and environmental restoration from the local to the industrial level. This approach will reduce the impact on human and ecological health, as well as promote the development of cost-effective and environmentally friendly water treatment technologies in the future.

## EXPERIMENTAL

### *A. Materials*

Carboxymethyl cellulose (CMC) and citric acid (CA) were obtained from Siam Bakery Land Co., Ltd. (Bangkok, Thailand) and used as received. Granular activated carbon (G-AC, 12 × 40 mesh, 3.0 % ash) and powdered activated carbon (P-AC, 325 mesh) were supplied by Carbokarn Co., Ltd. (Thailand). A multi-layered filter foam, composed of alternating layers of nylon fiber, absorbent pads, carbon sheets, and a nano-biofilter layer, was purchased from Petslove (Thailand). Before use, the activated carbons and the foam were rinsed with de-ionized water until the effluent conductivity fell below 50 μS $cm^{-1}$.

### *B. Adsorbent Preparation*

For CMC-grafted AC (CMC-AC), CMC (2 % w/v) was dissolved in 10 mL of de-ionized water, after which CA (20 % w/v) was introduced, and the solution was stirred at ambient temperature until homogeneous. Five grams of either G-AC or P-AC were then added and mixed for 30 min. The suspension was cured at 120 °C (16 h) to complete esterification. Then it was

further washed with de-ionized water until the effluent conductivity fell below 50 μS $cm^{-1}$, and dried overnight at 100 °C, yielding CMC-AC (granular) and CMC-P-AC (powder).

For Freeze-dried 3D-CMC-AC (FD-CMC-AC), a second batch was prepared with the same CMC and CA concentrations. After dispersing AC, the mixture was frozen and freeze-dried to generate a three-dimensional porous network, then heat-treated at 120 °C for 16 h. Subsequent washing (< 50 μS $cm^{-1}$) and drying (100 °C, overnight) produced the 3-D adsorbents FD-CMC-AC (granular) and FD-CMC-P-AC (powder).

*C. Water Treatment*

Natural water samples were collected in Chiang Mai Province and subjected to two preliminary treatments: one batch was passed only through a coarse-sand bed, whereas a second batch underwent sequential filtration through coarse sand followed by a granular-carbon layer, called B1 and B2, respectively. To compare basic sorbent performance, three materials- foam, AC, and CMC-AC - were weighed out at 0.20 g, and each was contacted with 10 mL of both pretreated waters. The slurries were gently agitated for 24 h, then clarified by passage through a 0.22 μm nylon membrane.

A separate experiment evaluated whether three-dimensional structuring improved sorption efficiency. Four grafted carbons were tested: granular CMC-AC, powdered CMC-P-AC, freeze-dried three-dimensional CMC-AC (FD-CMC-AC), and its powdered FD-CMC-P-AC. Exactly 0.20 g of each adsorbent was mixed with 10 mL of the sand-plus-carbon-filtered water, left to equilibrate for 24 h, and filtered through the same 0.22 μm membrane.

For both studies, metal-ion concentrations ($Ca^{2+}$, $K^{+}$, and $Fe^{2+}$) before and after treatment were measured by atomic-absorption spectroscopy. Removal efficiency (%Removal) was calculated with the equation,

$$\%Removal = \frac{C_{initial} - C_{final}}{C_{initial}} \times 100$$

Where $C_{initial}$ and $C_{final}$ express the metal ion concentrations (mg/L) before and after adsorption, respectively.

*D. Characterization*

Morphological analysis of the adsorbents was carried out on a Phenom ProX field-emission scanning electron microscope (Thermo Fisher Scientific) after the samples had been mounted on carbon-taped metal stubs and sputter-coated with platinum at 20 mA using a Hitachi E-1010 ion coater. Surface chemistry and electrostatic properties were probed by X-ray photoelectron spectroscopy on a Kratos Axis Ultra DLD instrument operated with a monochromatic Al Kα source (15 kV, chamber pressure < 5 × $10^{-7}$ Torr); high-resolution spectra were collected at 40 eV pass energy and referenced to the C 1s hydrocarbon peak at 284.6 eV. Residual metal ions ($Ca^{2+}$, $K^{+}$, $Fe^{2+}$) were quantified by atomic-absorption spectroscopy using a GBC system controlled with Avant v2.02 software.

PPC & PETROMAT SYMPOSIUM 2025

## RESULTS AND DISCUSSION

Observing the structure of grafted adsorbents through the XPS data, illustrated in Figure 1, provides insight into the surface functional groups of the adsorbents. Activated carbon primarily displayed 59.22% graphitic carbon at 285.0 eV, 22.21% hydroxyl or ether (C-O) group at 286.4 eV, 15.66% carbonyl group at 287.4 eV, and 2.92% carboxyl (COO) group at 290.2 eV. The carbonyl group was evident in CMC-AC due to the grafting of long-chain anionic cellulose and citric acid onto AC.

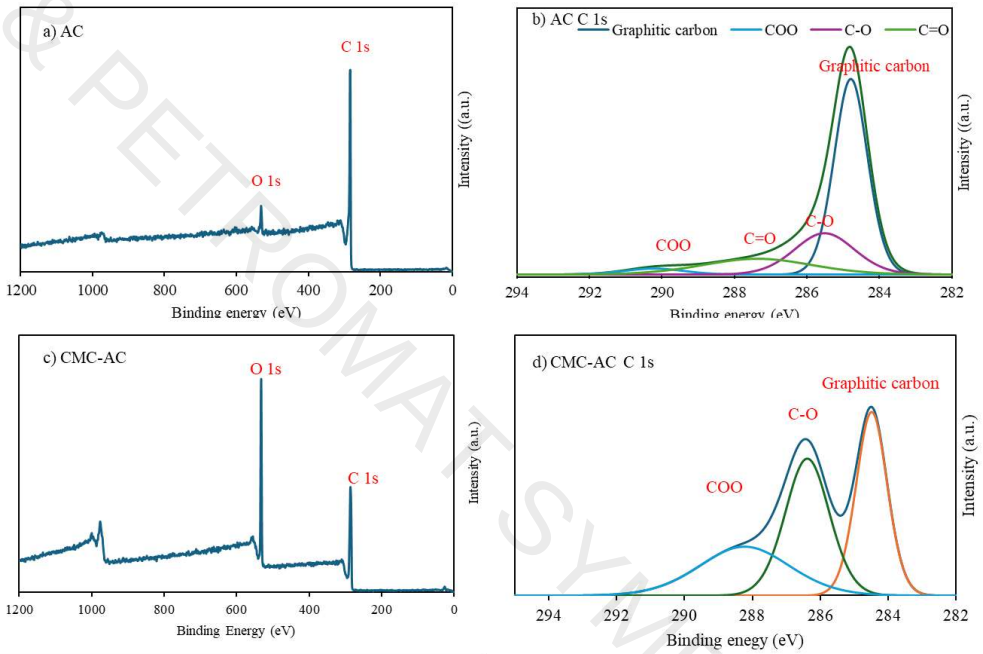


Fig. 1. XPS spectra results showing a) wide-scan of AC, b) narrow-scan of AC, c) wide-scan of CMC-AC, and narrow-scan of CMC-AC.

Raw water pre-filtered through coarse sand (B1) contained 178.7 mg $L^{-1}$ total dissolved metals ($Ca^{2+}$, $K^{+}$, and $Fe^{2+}$), whereas an additional AC (B2) reduced this to 119.1 mg $L^{-1}$. Both sources were subjected to different adsorbent treatments, as shown in Fig. 2a. The foam has the worst impurity adsorption capabilities. In the foam, the metal ion adsorptions of B1 and B2 were 5.78% and 13.52%, respectively. However, CMC-AC demonstrated that the maximum metal ion adsorption reached 73–74 %. The results clearly show that CMC-AC is more effective in adsorbing metal ions than AC, as the AC results in 29.39% of B2 water source and 36.95% of B1 water source. Through electrostatic adsorption, the carboxylic groups of CMC and CA can increase the effectiveness of metal ions. (Gupta et al., 2021).

Increasing the surface area provides more active sites, which enhances metal ion adsorption and improves efficiency. The freeze-drying process is another way to increase the active site by forming three-dimensional structures, and powdered activated carbon was utilized to compare with

granules to improve the surface area. Comparing the powdered and granular forms of activated carbon, the former only demonstrated 9.73% metal ion adsorption, while the latter demonstrated 71.71%. Grafted CMC (P-CMC-AC) in powder form displayed agglomeration of particles (Fig. 3e.), and the CMC and CA function as a binder, lowering surface area and obstructing pores. The 3D-structure metal ion removal result revealed 55.73% of FD-P-CMC-AC and 84.15% of FD-CMC-AC. By producing the three-dimensional structure seen in Figures 3c, 3d, and 3f, it is verified that the freeze-drying process increases the adsorption efficiency (Zeng et al., 2021).

These findings show that (i) high-affinity carboxyl sites are introduced by grafting AC with CMC/CA and (ii) performance is further enhanced by freeze-drying, which increases the accessible surface area and diffusion pathways.

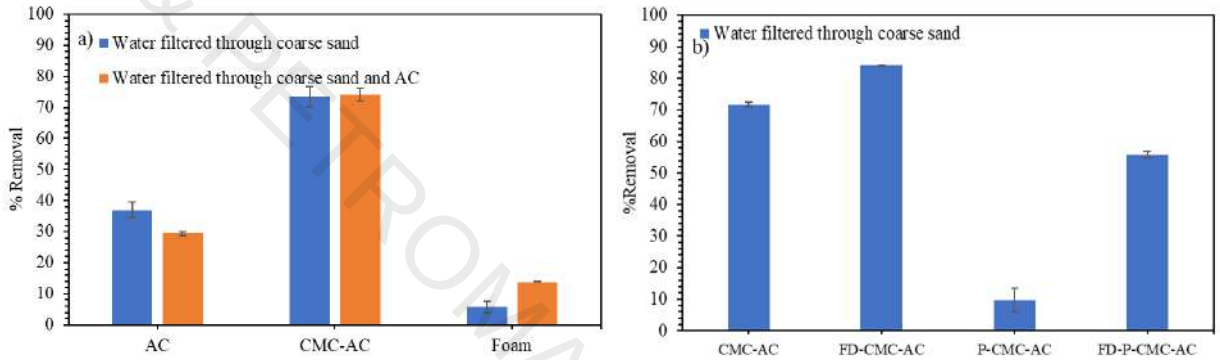


Fig. 2. Water treatment results varying a) types of adsorbent, and b) 3D-structural performance.

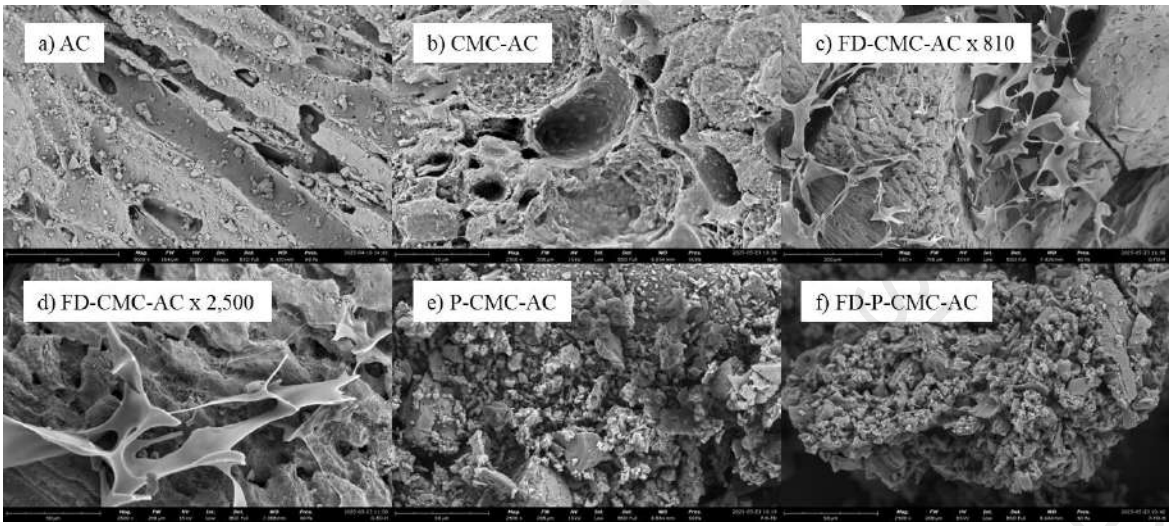


Fig. 3. SEM image of a) AC, b) CMC-AC, c) FD-CMC-AC at 810 magnitudes, d) FD-CMC-AC at 2,500 magnitudes, e) P-CMC-AC, and f) FD-P-CMC-AC.

## CONCLUSIONS

This study demonstrates that coupling biomass-derived activated carbon with carboxymethyl-cellulose and citric acid, followed by freeze-drying to create a three-dimensional

scaffold, yields a high-performance, low-cost adsorbent for metal-ion remediation. After grafting, XPS confirmed a substantial increase in surface carbonyl and carboxyl functionalities, providing strong coordination sites for dissolved metals. Batch tests using naturally contaminated waters from Chiang Mai showed that the grafted granular carbon (CMC-AC) removed ~74 % of total metals, roughly double the capacity of unmodified granular AC, and an order of magnitude higher than a commercial eight-layer foam. While powdered CMC-AC suffered from agglomeration and pore blockage, freeze-dried 3-D materials overcame these limitations: the FD-CMC-AC monolith achieved the highest removal (≈ 84 %), underscoring the dual benefits of chemical functionalization and hierarchical porosity.

## ACKNOWLEDGEMENTS

The authors sincerely thank the Petroleum and Petrochemical College, Chulalongkorn University, for providing the essential equipment and support. This research is financially supported by the Ratchadapisake Sompote Endowment Fund and the Center of Excellence for Petrochemical and Materials Technology, Chulalongkorn University, Thailand.

## REFRENCES

**Chen, J., Duan, Q., Liu, J., Zhang, S., Zhang, J., and Lin, S.** (2025). Adsorption of Fe-modified peanut shell biochar for Pb(II) in mixed Pb(II), Cu(II), Ni(II) solutions. Scientific Reports, 15(1), 13558.

**Gupta, A., Sharma, V., Sharma, K., Kumar, V., Choudhary, S., Mankotia, P., Kumar, B., Mishra, H., Moulick, A., Ekielski, A., and Mishra, P.K.** (2021). A Review of Adsorbents for Heavy Metal Decontamination: Growing Approach to Wastewater Treatment. Materials (Basel), 14(16).

**Laishram, D., Kim, S.-B., Lee, S.-Y., and Park, S.-J.** (2025). Advancements in Biochar as a Sustainable Adsorbent for Water Pollution Mitigation. Advanced Science, 12(19), 2410383.

**Qasem, N.A.A., Mohammed, R.H., and Lawal, D.U.** (2021). Removal of heavy metal ions from wastewater: a comprehensive and critical review. npj Clean Water, 4(1), 36.

**Saravanan, P., Saravanan, V., Rajeshkannan, R., Arnica, G., Rajasimman, M., Baskar, G., and Pugazhendhi, A.** (2024). Comprehensive review on toxic heavy metals in the aquatic system: sources, identification, treatment strategies, and health risk assessment. Environmental Research, 258, 119440.

**Wang, Y., Wang, Y., Qiu, S., Wang, C., Zhang, H., Guo, J., Wang, S., and Ma, H.** (2023). 3D-Printed Filters for Efficient Heavy Metal Removal from Water Using PLA@CS/HAP Composites. Polymers, 15(20), 4144.

**Wibowo, Y.G.** (2025). Carbon-Based adsorbents for heavy metal removal in Wastewater: Green technology or environmental Burden? Environmental Nanotechnology, Monitoring & Management, 23, 101051.

**Zeng, H., Xu, K., Wang, F., Sun, S., Li, D., and Zhang, J.** (2021). Preparation of adsorbent based on water treatment residuals and chitosan by homogeneous method with freeze-drying and

PPC & PETROMAT SYMPOSIUM 2025

its As(V) removal performance. International Journal of Biological Macromolecules, 184, 313-324.

PPC & PETROMAT SYMPOSIUM 2025

# The 9th SKY Symposium

# (SKY 2025)

# PRODUCTION OF ITACONIC ACID FROM SUGARCANE BAGASSE BY FERMENTATION *Aspergillus terreus*

*Syamsul Bakhri [a,f], Eka Triwahyuni [a,g], Olivia Bunga Pongtuluran [a,g], Afrinal Firmanda [a], Adella Nazwa Hanifa [a], Dyah Nurcahyani [a], Figo Alfino [a], Vanessa Natasha Johanes [a], Ibnu Maulana Hidayat [a], Farizal Farizal [c], Ambar Pertiwiningrum [d], Meilana Dharma Putra [e], Misri Gozan [a,b]**

[a] Department of Chemical Engineering, Faculty of Engineering, Universitas Indonesia, Kampus UI, Depok, 16424, Indonesia
[b] Research Centre of Biomass Valorization (RCBV-UI), Faculty of Engineering, Universitas Indonesia, Kampus UI, Depok, 16424, Indonesia
[c] Department of Industrial Engineering, Faculty of Engineering, Universitas Indonesia, Kampus UI, Depok, 16424, Indonesia
[d] Department of Animal Products Technology, Faculty of Animal Science, Universitas Gadjah Mada, Yogyakarta, 55281, Indonesia
[e] Department of Chemical Engineering, Faculty of Engineering, Universitas Lambung Mangkurat, Banjarbaru, 70714, Indonesia
[f] Department of Chemical Engineering, Faculty of Industrial Technology, Universitas Muslim Indonesia, Makassar, 90232, Indonesia
[g] Research Centre for Chemistry, National Research and Innovation Agency, Kawasan Puspiptek, Serpong, 15314, Indonesia

Keywords : Itaconic acid, Sugarcane bagasse, *Aspergillus terreus,* Fermentation, Techno-economic analysis

## ABSTRACT

Itaconic acid is a high-value bio-based chemical with diverse industrial applications, yet its commercial production is constrained by high costs. This study investigates the feasibility of producing itaconic acid from sugarcane bagasse, an abundant lignocellulosic by-product, using an integrated biorefinery approach. The process integrates physical and chemical pretreatment, enzymatic hydrolysis, and fermentation using Aspergillus terreus, simulated in SuperPro Designer® v13.0. From 10,000 kg of sugarcane bagasse per batch, the process yielded 3,091.6 kg of itaconic acid crystals with 89.85% purity. The plant is proposed to be located in South Lampung, Indonesia. Economic evaluation shows a net present value (NPV) of USD 10.7 million, an internal rate of return (IRR) of 34.49%, a return on investment (ROI) of 40.18%, and a payback period of 2.49 years. Sensitivity analysis highlights that profitability is most influenced by product pricing. These results demonstrate that sugarcane bagasse-based itaconic acid production is not only technically feasible but also economically attractive, paving the way for sustainable biorefinery development in tropical regions.

*mgozan@ui.ac.id

PPC & PETROMAT SYMPOSIUM 2025

## INTRODUCTION

Itaconic acid (IA) has garnered significant attention as a bio-based chemical due to its versatile applications in agriculture, plastics, textiles, paints, and pharmaceuticals. As a renewable alternative to petrochemical-derived acrylic and methacrylic acids, IA supports the transition toward sustainable industrial practices by enabling the production of superabsorbent polymers, synthetic resins, and pH-sensitive materials (Okabe et al., 2009). Despite its high potential, the major barrier to widespread IA commercialization lies in its elevated production cost, prompting the need for innovative, cost-efficient bioprocessing strategies.

One promising approach to lowering production costs is the utilization of low-cost, abundant lignocellulosic feedstocks such as sugarcane bagasse. As a by-product of the sugar industry, bagasse is readily available in large volumes across tropical regions and aligns with circular economy principles by transforming agricultural waste into high-value biochemicals. Efficient pretreatment and hydrolysis of this biomass are critical to unlocking its fermentable sugar content. (Harahap, 2019) demonstrated that microwave-assisted alkaline delignification significantly improves cellulose accessibility for enzymatic hydrolysis, enhancing sugar yields. Additionally, the techno-economic feasibility of utilizing bagasse-derived components has been supported by studies on encapsulated lignin production components (Ramadhan et al., 2022).

The fermentation of simple sugars into IA is commonly carried out using *Aspergillus terreus*, which possesses the enzyme aconitate decarboxylase, enabling the conversion of cis-aconitate to IA at relatively high yields (Karaffa & Kubicek, 2019). Optimization of fermentation parameters including oxygen levels, substrate concentrations, and nutrient ratios is critical for enhancing IA biosynthesis (Shahriarinour et al., 2011). Integrating these parameters into a coherent biorefinery scheme enables IA production and the co-generation of valuable co-products such as furfural and formic acid. (Muryanto et al., 2023) and (Panjaitan & Gozan, 2020) have demonstrated the feasibility of such valorization using catalytic and separation innovations applied to bagasse and corncob.

Given the complexity and capital intensive nature of biorefinery systems, comprehensive techno-economic assessments are necessary to ensure viability. Prior analyses by (Gozan et al., 2018) have underscored the importance of process integration and economic optimization in biorefinery operations in Indonesia. Building upon these findings, this study simulates IA production from sugarcane bagasse using SuperPro Designer v13.0, incorporating recent advances in pretreatment and fermentation technologies. By evaluating key performance indicators Net Present Value (NPV), Internal Rate of Return (IRR), Return on Investment (ROI), and Payback Period (PBP) this research aims to develop a scalable and sustainable production model that supports resource efficiency and industrial decarbonization in tropical settings.

## EXPERIMENTAL

*The SuperPro Designer V.13* (Academic Licensed to Universitas Indonesia) was employed to simulate itaconic acid production from sugarcane bagasse. The operational mode of the plant process was configured as a batch system, with each batch lasting 28.22 hours and a total of 279 batches conducted annually.

PROCEEDINGS PPC 2025

*A. Pretreatment*

The processes carried out in the pre-treatment stage are physical and chemical methods.Beginning with initial physical treatment, in which sugarcane bagasse obtained from sugar industry waste will be pretreated, which begins with washing sugarcane bagasse using a washing bulk conveyor. Followed by grinding to reduce the size of biomass particles. Lastly, the biomass is dried in a rotary dryer.

As for the chemical method, it begins with an acid hydrolysis process in which hemicellulose is converted into xylose, and cellulose is converted into cellobiose, acetic acid, and glucose. This is followed by neutralization, sedimentation, and enzymatic hydrolysis processes.

*B. Main Process*

Seed fermentation and fermentation process is done in a batch-stirred fermentor using *Aspergillus terreus*, glucose, xylose, and cellobiose are reacted to form itaconic acid. The fermentation process is done at a temperature of 37°C. For the first seed fermentation process, glucose and ammonia with a 9:1 wt ratio are pasteurized first at 121°C for 15 minutes. Then, the flow is split into two flows, with 90% of the flow going into the first seed fermentation process for the main fermentation process. *Aspergillus terreus* and water are fed into the fermentation tank with a 1:9 mass ratio. The seed fermentation is done at 37°C for 24 hours. Then, the product from the first seed fermentation is fed into the second seed fermentation tank. The 10 % glucose and ammonia mixture and about 10% simple sugar are also fed into the second seed fermentation tank. Here are the main reactions for the production of itaconic acid from the simple sugar and biomass formation reaction based on Nieder-Heitmann (2018) (Nieder-Heitmann et al., 2018):

$$1\ Glucose \rightarrow 1.39\ Itaconic\ Acid$$

$$1\ Cellobiose \rightarrow 2.63\ Itaconic\ Acid$$

$$1\quad Xylose \rightarrow 1.15\ Itaconic\ Acid$$

$$1\ A.\ terreus + 1\ Glucose + 1\ NH_3 \rightarrow 1.75\ A.terreus + CO_2 + H_2O$$

$$1\ A.\ terreus + 1\ Xylose + 1\ NH_3 \rightarrow 1.58\ A.terreus + CO_2 + H_2O$$

After these main processes, the separation processes for 4 hours and purification process for 1 hour. The flow chart of the Itaconic Acid production process are shown in Figure 1.

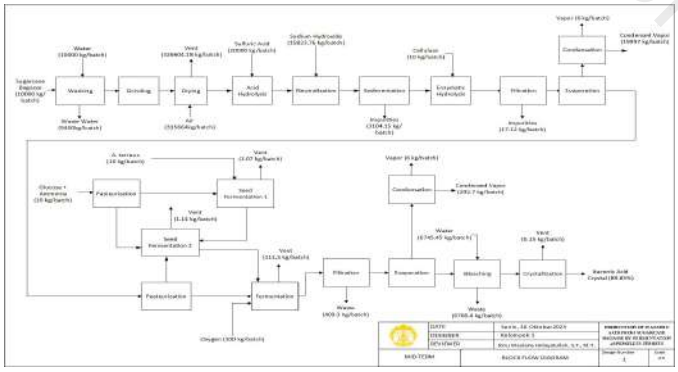

**Figure 1.** Block Flow Diagram of Itaconic Acid Production

PPC & PETROMAT SYMPOSIUM 2025

## RESULTS AND DISCUSSION

### *A. Itaconic Acid Production*

The production of itaconic acid involves a multistep fermentation process. The fermentation process is the longest stage in this simulation of itaconic acid production. One batch before optimisation with a closed flow and pH maintained within the range of 2.4–4.9 can take up to 97.72 hours, starting with a 12 hours pretreatment process, followed by the first and second pasteurisation processes of each lasting 0.25 hours, the first and second fermentation processes of each lasting 24 hours, the main fermentation process for 28. 22 hours, separation process (filtration and evaporation) for 4 hours, purification process lasting 1 hours, and a crystallisation process lasting 4 hours. Therefore, further testing and optimisation are required to maximise production efficiency. From the separation and purification process, we obtained Itaconic Acid as the final product, amounting to 3,091.61 kg/batch of IA crystals with a purity level of 89.85% after the main substrate passed through four operational units: filtration, evaporation, adsorption, and crystallisation. The purity level achieved is quite high, although lower than our reference simulation of 98.99%. Additionally, this itaconic acid production simulation can be analysed from an economic perspective and further optimised for large-scale or commercial applications.

### *B. Economic Analysis*

Several assumptions have been made to calculate the capital expenditure, including : (1) The plant will be constructed from the beginning of 2024 until the end of 2026, (2) The production runs 330 days a year, (3) The production capacity is 3091.6 kg/batch, (4) The Net Present Value (NPV) at 7% interest, and (5) Minimum Attractive Rate of Return (MARR) is assumed to be at 10%.
The economic analysis is as follows:

#### *1) Total Capital Investment*

For the total capital investment we can obtain it using the formula of :

*Capital Investment = Total Plant Cost + Contractor's fee & Contingency*.

Using an input that we already have for unit operation and its variable cost, the total capital investment for the plant is = US$ 4,076,000 at present value or time = 0 , here are the inputs for our capital investment calculation.

#### *2) Operating Cost*

For the operating cost of this project the basis of this calculation is annually so, we can calculate it using the formula of :

*AOC = Raw Material + Labor + Facility + Laboratory + Waste treatment + Utility*.

By using an input that we already obtain from literature, then we can calculate the AOC for this project. The AOC for this project are = US$ 6,013,000 / year.

#### *3) ProfitabilityAnalysis*

*a) Internal Rate of Return (IRR)*

The value of IRR must be compared with MARR to analyze the project's feasibility. If the IRR value is greater than MARR, then the project is feaesible. IRR of the itaconic acid production is obtained at 34.49%. Compared to MARR, which is 10%, the IRR value is

PPC & PETROMAT SYMPOSIUM 2025

much higher. Thus, this project will be interesting for investors compared to bank interest rates.

*b) Net Present Value (NPV)*

A project can be considered feasible if the NPV value is greater than zero as the project is profitable. If the NPV value equals zero, the project will gain neither profit or loss. If NPV is less than zero, the project is not eligible to run because it does not generate profit. From the economic analysis, it is found that the NPV value is $10,695,000, and the project is eligible to run.

*c) Payback Periode*

The payback period of a given investment or project is an important determinant of whether to undertake the position or project, with a shorter payback period meaning that the investment is better. If the payback period is less than a predetermined period, the project is acceptable. The payback period for this plant is 2.49 years, which is still in line with the predetermined period of 10 years. This means that the project of this plant is still stable.

*d) Sensitivity Analysis And Graph*

Examining the sensitivity of profitability is a critical aspect, focusing on key factors such as product price, raw material cost, and labor cost. These factors play a significant role in determining overall cost. The primary factor affecting cash inflow is the selling price. The costs of raw materials and labor are then chosen because they will most likely change over time. These settings might be adjusted or decreased based on the situation. These graphs in Figures 2, 3, and 4 illustrate the outcomes of the sensitivity analysis, portraying the fluctuations in key variables and their impact on the dependent parameters.

**Figure 2.** NPV Sensitivity Graph.

**Figure 3.** IRR Sensitivity Graph

**Figure 4.** PBP Sensitivity Graph

From all the graphs obtained, we use ± 20 percent deviation as a basis for our calculations. For product price deviation, the profitability is increasing and decreasing linearly, this indicates that this project is sensitive when it comes to its product price. The product is the main and only revenue stream for this project.. That's why it's very sensitive to it. For the raw material sensitivity. It's not as sensitive as the product price because there are other factors that influence the operating cost of this project. So it's not as sensitive as the product price. And lastly for the labor price deviation. It's the least sensitive because the labor cost has a small proportion of the annual operating cost. So a slight deviation will not affect the project as a whole and only change for a bit.

## CONCLUSIONS

In this work, different pretreatment technologies were integrated to convert sugarcane bagasse into fermentable sugars, enabling efficient itaconic acid (IA) production via *Aspergillus terreus* fermentation. Simulation using SuperPro Designer v13.0 demonstrated

PROCEEDINGS OF PPC & PETROMAT SYMPOSIUM 2025

that 10,000 kg of sugarcane bagasse per batch can yield 3,091.6 kg of IA crystals with 89.85% purity. Economic evaluation showed promising results, including an internal rate of return (IRR) of 34.49%, net present value (NPV) of USD 10.7 million, return on investment (ROI) of 40.18%, and a payback period of 2.49 years.

These findings suggest that the proposed biorefinery model is not only technically feasible but also economically attractive, especially for implementation in tropical regions such as Southeast Asia, where sugarcane bagasse is abundantly available. The process scalability and alignment with circular economy principles support broader efforts toward industrial sustainability in the region.

Moreover, itaconic acid—due to its reactive carboxylic and unsaturated groups—can be integrated into various bio-based value chains, including bioplastics, biodegradable resins, and pharmaceutical intermediates. This opens further opportunities for IA to serve as a key building block in high-value, green chemical manufacturing.

## ACKNOWLEDGEMENTS

We would like to express our gratitude to the organisers of the International Conference PPC & PETROMAT SYMPOSIUM 2025 in Thailand.

## REFERENCES

**Gozan, M., Ryan, B., & Krisnandi, Y.** (2018). Techno-economic assessment of Levulinic Acid Plant from Sorghum Bicolor in Indonesia. *IOP Conference Series: Materials Science and Engineering*, *345*(1), 012012. https://doi.org/10.1088/1757-899X/345/1/012012

**Harahap, I.** (2019). Ekonomi pembangunan: pendekatan transdisipliner.

**Karaffa, L., & Kubicek, C. P.** (2019). Citric acid and itaconic acid accumulation: variations of the same story? *Applied microbiology and biotechnology*, *103*(7), 2889-2902. https://doi.org/10.1007/s00253-018-09607-9

**Muryanto, M., Sudiyani, Y., Darmawan, M. A., Handayani, E. M., & Gozan, M.** (2023). Simultaneous Delignification and Furfural Production of Palm Oil Empty Fruit Bunch by Novel Ternary Deep Eutectic Solvent. *Arabian Journal for Science and Engineering*, *48*(12), 16359-16371. https://doi.org/10.1007/s13369-023-08211-y

**Nieder-Heitmann, M., Haigh, K. F., & Görgens, J. F.** (2018). Process design and economic analysis of a biorefinery co-producing itaconic acid and electricity from sugarcane bagasse and trash lignocelluloses. *Bioresource Technology*, *262*, 159-168.

**Okabe, M., Lies, D., Kanamasa, S., & Park, E. Y.** (2009). Biotechnological production of itaconic acid and its biosynthesis in Aspergillus terreus. *Applied microbiology and biotechnology*, *84*, 597-606.

**Panjaitan, J. R. H., & Gozan, M.** (2020). Sensitivity analysis of nitrocellulose production from palm oil empty fruit bunches. *IOP Conference Series: Earth and Environmental Science*, *537*(1), 012036. https://doi.org/10.1088/1755-1315/537/1/012036

**Ramadhan, M. Y. A., Salsabila, S., Darmawan, M. A., & Gozan, M.** (2022). Techno-Economic evaluation of oil palm empty fruit bunch-based encapsulated lignin production process. *AIP Conference Proceedings*, *2537*(1). https://doi.org/10.1063/5.0097937

**Shahriarinour, M., Wahab, M. N. A., Ariff, A. B., Mohamad, R., & Mustafa, S.** (2011). Kinetics of cellulase production by Aspergillus terreus at various levels of dissolved oxygen tension in a stirred tank bioreactor. *BioResources*, *6*(4), 4909-4921.

PPC & PETROMAT SYMPOSIUM 2025